Lecture Notes in Physics

H. J. Carmichael R. J. Glauber M. O. Scully (Eds.)

Directions in Quantum Optics

Selected Papers

Springer

Lecture Notes in Physics

Springer
Berlin
Heidelberg
New York
Barcelona
Hong Kong
London
Milan
Paris
Singapore
Tokyo

Physics and Astronomy ONLINE LIBRARY
http://www.springer.de/phys/

Editorial Policy

The series *Lecture Notes in Physics* (LNP), founded in 1969, reports new developments in physics research and teaching -- quickly, informally but with a high quality. Manuscripts to be considered for publication are topical volumes consisting of a limited number of contributions, carefully edited and closely related to each other. Each contribution should contain at least partly original and previously unpublished material, be written in a clear, pedagogical style and aimed at a broader readership, especially graduate students and nonspecialist researchers wishing to familiarize themselves with the topic concerned. For this reason, traditional proceedings cannot be considered for this series though volumes to appear in this series are often based on material presented at conferences, workshops and schools (in exceptional cases the original papers and/or those not included in the printed book may be added on an accompanying CD ROM, together with the abstracts of posters and other material suitable for publication, e.g. large tables, colour pictures, program codes, etc.).

Acceptance

A project can only be accepted tentatively for publication, by both the editorial board and the publisher, following thorough examination of the material submitted. The book proposal sent to the publisher should consist at least of a preliminary table of contents outlining the structure of the book together with abstracts of all contributions to be included.
Final acceptance is issued by the series editor in charge, in consultation with the publisher, only after receiving the complete manuscript. Final acceptance, possibly requiring minor corrections, usually follows the tentative acceptance unless the final manuscript differs significantly from expectations (project outline). In particular, the series editors are entitled to reject individual contributions if they do not meet the high quality standards of this series. The final manuscript must be camera-ready, and should include both an informative introduction and a sufficiently detailed subject index.

Contractual Aspects

Publication in LNP is free of charge. There is no formal contract, no royalties are paid, and no bulk orders are required, although special discounts are offered in this case. The volume editors receive jointly 30 free copies for their personal use and are entitled, as are the contributing authors, to purchase Springer books at a reduced rate. The publisher secures the copyright for each volume. As a rule, no reprints of individual contributions can be supplied.

Manuscript Submission

The manuscript in its final and approved version must be submitted in camera-ready form. The corresponding electronic source files are also required for the production process, in particular the online version. Technical assistance in compiling the final manuscript can be provided by the publisher's production editor(s), especially with regard to the publisher's own Latex macro package which has been specially designed for this series.

Online Version/ LNP Homepage

LNP homepage (list of available titles, aims and scope, editorial contacts etc.):
http://www.springer.de/phys/books/lnpp/

LNP online (abstracts, full-texts, subscriptions etc.):
http://link.springer.de/series/lnpp/

H. J. Carmichael R. J. Glauber M. O. Scully (Eds.)

Directions in Quantum Optics

A Collection of Papers
Dedicated to the Memory of Dan Walls
Including Papers Presented at the TAMU-ONR
Workshop Held at Jackson, Wyoming, USA,
26--30 July 1999

Springer

Editors

Howard J. Carmichael
Department of Physics
College of Arts and Sciences
1274 University of Oregon
Eugene, OR 97403-1274, USA

Roy J. Glauber
Lyman Laboratory of Physics
Harvard University
Cambridge, MA 02138, USA

Marlan O. Scully
Department of Physics
Texas A & M University
College Station, TX 77843-4242, USA

Library of Congress Cataloging-in-Publication Data applied for.

Die Deutsche Bibliothek - CIP-Einheitsaufnahme
Directions in quantum optics : a collection of papers dedicated to the memory of Dan Walls including papers presented at the TAMU ONR workshop held at Jackson, Wyoming, USA, 26 - 30 July 1999 / H. J. Carmichael ... (ed.). - Berlin ; Heidelberg ; New York ; Barcelona ; Hong Kong ; London ; Milan ; Paris ; Singapore ; Tokyo : Springer, 2001
(Lecture notes in physics ; Vol. 561)
(Physics and astronomy online library)
ISBN 3-540-41187-9

ISSN 0075-8450
ISBN 3-540-41187-9 Springer-Verlag Berlin Heidelberg New York

Typesetting: Camera-ready by the authors/editors;
Camera-data conversion by Steingraeber Satztechnik GmbH Heidelberg
Cover design: *design & production*, Heidelberg

Printed on acid-free paper
SPIN: 10785652 55/3141/du - 5 4 3 2 1 0

Preface

Dan Walls was a notable presence in quantum optics almost from the beginning of the modern era of intense research in the field, right up to the time of his untimely death. In the 30 years that have passed since his PhD at Harvard, he established a school of theoretical quantum optics in New Zealand, first at the University of Waikato and then at the University of Auckland, which gained an international reputation for its seminal contributions in the area of quantum fluctuations and noise, and as a leading center advancing and promoting the latest directions in quantum optics. Today his numerous students lead active research groups throughout New Zealand and Australia, and also in the United States. Dan is remembered by colleagues as an enthusiastic collaborator, and as a generous host during their visits to New Zealand as guest scientists or participants at the summer meetings arranged by Dan Walls and John Harvey.

To honor Dan's achievements, and in recognition of the influence of his enthusiasm, insight, and generosity, on them individually and on quantum optics research more widely, a group of Dan Walls' students and colleagues have assembled this collection of papers reviewing current research directions in quantum optics. At some stage in his career, Dan Walls contributed to each of the areas featured here. He was actively working on Bose–Einstein condensation right up until his last months, and we have included in this volume a completed, but unpublished, manuscript by Dan, Scott Parkins, and Atac Imamoğlu, the theme of which is developed around three topical research areas – cavity QED, nonlinear optics, and quantum information; this paper looks in anticipation towards the next advances of high importance and impact, as was so often the case in Dan's work. Recent developments in each of these areas are described in a number of the contributions. Other papers cover the areas of quantum interference, and the area of Dan's most significant accomplishments, quantum noise processes.

During the early part of Dan Walls' career, travel out of New Zealand was not at all a small undertaking. Dan was, nevertheless, from the beginning, renowned as an international traveller and regular attendee at meetings in Europe and the United States. It is fitting that over this last year he has been recognized, through special sessions or symposia, at a number of international meetings. He was so recognized at the TAMU-ONR Workshop on Quantum

Optics, held in Jackson, Wyoming in July of 1999. A number of the papers presented at that meeting are reproduced, in tribute, in this volume.

We wish to express our thanks to all those who have contributed to this book, either as authors or in the refereeing of the papers. With no explicit direction from us, the range of the contributed papers provides a review of the latest developments across virtually the entire field of quantum optics. The standard of the papers is high, as we hoped it would be, and the work of the referees has helped us in that. We also extend our appreciation and thanks to Colleen Vande Voorde at the Oregon Center for Optics, for her management of the editorial communications with authors and referees, and for her help in compiling the numerous electronic files, producing a book of pleasant appearance and a suitable tribute to the memory of our colleague Dan Walls.

Eugene, Cambridge, College Station
August 2000

Howard Carmichael
Roy Glauber
Marlan Scully

List of Contributors

P. Alsing
University of New Mexico
Albuquerque High Performance
Computing Center
Albuquerque, NM 87131, USA
alsing@arc.unm.edu

H.-A. Bachor
Department of Physics
Faculty of Science
The Australian National University
Canberra, ACT 0200, Australia
hans.bachor@anu.edu.au

R.J. Ballagh
Physics Department
University of Otago
Dunedin, New Zealand
ballagh@physics.otago.ac.nz

B. Berhane
School of Physics
Georgia Institute of Technology
Atlanta, GA 30332–0430, USA
bb49@anvil.gatech.edu

N. Bloembergen
Department of Physics
Harvard University
Cambridge, MA 02138, USA

P. Brick
Optical Sciences Center
University of Arizona
Tucson, AZ 85721, USA
brick@optics.arizona.edu

B.M. Caradoc-Davies
Physics Department
University of Otago
Dunedin, New Zealand
bmcd@physics.otago.ac.nz

H.J. Carmichael
Oregon Center for Optics
and Department of Physics
1274 University of Oregon
Eugene, OR 97403–1274, USA
hjcarm@oregon.uoregon.edu

C.M. Caves
Center for Advanced Studies
Department of Physics
and Astronomy
University of New Mexico
Albuquerque, NM 87131–1156, USA
caves@tangelo.phys.unm.edu

S. Chaturvedi
School of Physics
University of Hyderabad
Hyderabad, 500, 134, India
scsp@uohyd.ernet.in

G. Chen
Department of Mathematics
Texas A&M University
College Station, TX 77843–3368
USA
gchen@math.tamu.edu

Y.-T. Chough
Department of Physics
Korea Advanced Institute
of Science and Technology
Taejeon 305-701, South Korea
tak@cais.kaist.ac.kr

R. Côté
Department of Physics
University of Connecticut
2152 Hillside Road
Storrs, CT 06269–3046, USA
rcote@phys.uconn.edu

J.D. Cresser
Department of Physics
Macquarie University
New South Wales 2109, Australia
cresser@physics.mq.edu.au

D.G. Deppe
Department of Electrical and
Computer Engineering
Microelectronics Research Center
University of Texas
Austin, TX 78712-1084, USA
deppe@mail.utexas.edu

P. Deuar
Centre for Laser Science
Department of Physics
University of Queensland
Queensland 4072, Australia
deuar@physics.uq.edu.au

P.D. Drummond
Department of Physics
University of Queensland
Queensland 4072, Australia
drummond@physics.uq.oz.au

C. Ell
Optical Sciences Center
University of Arizona
Tucson, AZ 85721, USA
ell@optics.arizona.edu

M. Fleischhauer
Sektion Physik
Universität München
80333 München, Germany
mfleisch@mfl.sue.physik.
uni-muenchen.de

M. Fliesser
Fachbereich Physik
Universität–GH Essen
45117 Essen, Germany
fliesser@theo-phys.uni-essen.de

S.A. Fulling
Department of Mathematics
Texas A&M University
College Station, TX 77843–3368
USA
fulling@math.tamu.edu

H.M. Gibbs
Optical Sciences Center
University of Arizona
Tucson, AZ 85721, USA
gibbs@kilimanjaro.opt-sci.
arizona.edu

V. Giovannetti
Dipartimento di Matematica e Fisica
and Unitá INFM
Universitá di Camerino
via Madonna delle Carceri
62032 Camerino, Italy
vittorio@camcat.unicam.it

R. Graham
Fachbereich Physik
Universität–GH Essen
45117 Essen, Germany
graham@uni-essen.de

F. Haake
Fachbereich Physik
Universität–GH Essen
45117 Essen, Germany
fritz.haake@uni-essen.de

G.R. Hoy
Physics Department
Old Dominion University
Norfolk, VA 23529–0116, USA
hoy@physics.odu.edu

D.L. Huffaker
Department of Electrical and
Computer Engineering
Microelectronics Research Center
University of Texas
Austin, TX 78712-1084, USA
dhuf@mail.utexas.edu

A.F. Hughes
33 Woodlands Gate
Woodlands Way
Putney, London SW15 2SY, UK
ahughes@fenics.com

A. Imamoğlu
Department of Electrical and
Computer Engineering
and Department of Physics
University of California
Santa Barbara, CA 93106, USA
atac@xanadu.ece.ucsb.edu

T.A.B. Kennedy
School of Physics
Georgia Institute of Technology
Atlanta, GA 30332–0430, USA
brian.kennedy@physics.
gatech.edu

G. Khitrova
Optical Sciences Center
University of Arizona
Tucson, AZ 85721, USA
khitrova@kilimanjaro.opt-sci.
arizona.edu

M.I. Kolobov
Fachbereich Physik
Universität–GH Essen
45117 Essen, Germany
mkolobov@wanadoo.fr

E.S. Lee
Optical Sciences Center
University of Arizona
Tucson, AZ 85721, USA
esl@u.arizona.edu

H. Lee
California Institute of Technology
Jet Propulsion Laboratory
4800 Oak Grove Drive
MS 126-147
Pasadena, CA 91009-8099, USA
hwang.lee@jpl.nasa.gov

M. Lukin
ITAMP
Harvard–Smithsonian Center
for Astrophysics
Cambridge, MA 02138, USA
mlukin@phase.harvard.edu

U. Martini
Sektion Physik
Universität München
80333 München, Germany
ullrich.martini@physik.
uni-muenchen.de

K.-P. Marzlin
Fachbereich Physik
Universität Konstanz
Postfach 5560 M674
78457 Konstanz, Germany
peter@spock.physik.
uni-konstanz.de

K. McNeil
Department of East Asian Studies
University of Waikato
Hamilton, New Zealand
japn0149@Waikato.ac.nz

P. Meystre
Department of Physics
Optical Sciences Center
University of Arizona
Tucson, AZ 85721, USA
pierre.meystre@optics.arizona.edu

G.J. Milburn
Special Research Centre for
Quantum Computer Technology
and Department of Physics
University of Queensland
Queensland 4072, Australia
milburn@physics.uq.edu.au

M.G. Moore
Department of Physics
Optical Sciences Center
University of Arizona
Tucson, AZ 85721, USA

W.R. Munro
Centre for Laser Science
Department of Physics
University of Queensland
Queensland 4072, Australia
munro@physics.uq.edu.au

K. Nemoto
Centre for Laser Science
Department of Physics
University of Queensland
Queensland 4072, Australia
nemoto@physics.uq.edu.au

E. Ostrovskaya
Optical Sciences Centre
Australian National University
Canberra, ACT 0200, Australia
ost124@rsphy1.anu.edu.au

S. Park
Optical Sciences Center
University of Arizona
Tucson, AZ 85721, USA
sahnggi@samsung.co.kr

S. Parkins
Department of Physics
University of Auckland
Auckland, New Zealand
asp@phy.auckland.ac.nz

R. Pike
Physics Department
Kings College
University of London
Strand, London WC2R 2LS, UK
erp@maxwell.ph.kcl.ac.uk

L. Plimak
Department of Chemical Physics
The Weizmann Institute of Science
76100 Rehovot, Israel
lev.plimak@weizmann.ac.il

T.C. Ralph
Centre for Laser Science
Department of Physics
University of Queensland
Queensland 4072, Australia
ralph@physics.uq.edu.au

M.D. Reid
Department of Physics
University of Queensland
Queensland 4072, Australia
margaret@physics.uq.edu.au

N. Robins
Department of Physics
Australian National University
Canberra, ACT 0200, Australia
s9405885@student.anu.edu.au

Y.V. Rozhdestvensky
Institute for Laser Physics
S.I. Vavilov State Optical Institute
Birzhevaya Line 12
199034, St. Petersburg, Russia
RozdYu@soi.spb.su

P. Rungta
Center for Advanced Studies
Department of Physics
and Astronomy
University of New Mexico
Albuquerque, NM 87131–1156, USA
pranaw@unm.edu

J. Ruostekoski
Abteilung für Quantenphysik
Universität Ulm
89069 Ulm, Germany
ruostekoski@physik.uni-ulm.de

B.C. Sanders
Department of Physics
Macquarie University
Sydney, New South Wales 2109
Australia
barry@physics.mq.edu.au

C. Savage
Department of Physics
Australian National University
Canberra, ACT 0200, Australia
craig.savage@anu.edu.au

B. Segev
Department of Chemistry
Ben-Gurion University of the Negev
POB 653, Beer–Shiva 84105, Israel
bsegev@bgumail.bgu.ac.il

A. Schenzle
Sektion Physik
Universität München
80333 München, Germany
axel.schenzle@physik.
uni-muenchen.de

M.O. Scully
Department of Physics
and Institute for Quantum Studies
Texas A&M University
College Station, TX 77843-4242,
USA and
Max-Planck Institut für Quanten-
optik, Munich, Germany
scully@tamu.edu

C. Spiegelberg
Optical Sciences Center
University of Arizona
Tucson, AZ 85721, USA
christis@u.arizona.edu

M. Szymanska
Physics Department
Cavendish Laboratory
Theory of Condensed Matter Group
Madingley Road
Cambridge CB3 0HE, UK
mhs24@phy.cam.ac.uk

V.V. Temnov
Fachbereich Physik
Universität–GH Essen
45117 Essen, Germany and
Institute of Applied Physics
Russian Academy of Science
46 Ul'yanov str.
Nizhny Novgorod, 603600, Russia
temnov@next21.theo-phys.
uni-essen.de

E. Timmermans
Theoretical Division (T-4)
Los Alamos National Laboratory
MS B-268, Los Alamos, NM 87545,
USA
eddy@t4.lanl.gov

P. Tombesi
Dipartimento di Matematica e Fisica
and Unitá INFM
Universitá di Camerino
via Madonna delle Carceri
62032 Camerino, Italy
tombesi@campus.unicam.it

L. Tribe
Department of Physics
Macquarie University
Sydney, New South Wales 2109
Australia

D. Vitali
Dipartimento di Matematica e Fisica
and Unitá INFM
Universitá di Camerino
via Madonna delle Carceri
62032 Camerino, Italy
david@camcat.unicam.it

H.M. Wiseman
School of Science
Griffith University
Nathan, Queensland 4111, Australia
h.wiseman@mailbox.gu.edu.au

W. Zhang
Centre for Lasers and Applications
and Department of Physics
Macquarie University
Sydney, New South Wales 2109
Australia
weiping@physics.mq.edu.au

Contents

† Paper presented at the TAMU–ONR Workshop on Quantum Optics

Density Oscillations in Trapped Bose Condensates at Finite Temperature

Martin Fliesser and Robert Graham

Summary. Density fluctuations in Bose gases are investigated in the collisionless limit at finite temperature. First the density fluctuations of a homogenous Bose gas above the phase transition are analysed in linear response theory. Their complex velocity of sound is determined, finding a pure relaxation-mode for weak interactions. Then we consider the coupled dynamics of a condensate interacting with the density of non-condensed atoms, and determine numerically and in perturbation theory the temperature dependent damping rate of the Bogoliubov sound. Using a local-density-approximation we generalize this approach to inhomogeneous systems.

1 Introduction

The spectrum of collective excitations from a Bose condensate differs in a significant way from the spectrum of a cloud of thermal atoms, so the temperature dependence of these condensate modes poses an interesting problem. For trapped weakly interacting Bose condensates [1] these excitations have been investigated experimentally and theoretically under various aspects [2,3]. At vanishing temperatures almost all the atoms are condensed, and in a mean field description discrete real frequencies were determined. At finite temperature a fraction of all atoms is thermally excited and interacts with the condensate and physically it is obvious that this interaction will give rise to shifts of these frequencies and damping. In a static description, though, the interaction with these non-condensed atoms merely acts as an additional potential for the condensate, giving rise to frequency shifts, but not to any damping. To explain damping of these modes one has to consider the coupled *dynamics* of the condensed and the non-condensed atoms. Recently, progress with this problem has been made using a particular Greens-function approach called the dielectric formalism [4,5]. In the present paper we shall address this problem by an alternative approach using collisionless hydrodynamics for the Bose condensate and linear response theory for the thermal cloud of non-condensed atoms. We get results similar to those in [4,5]. The present approach is physically very direct and transparent, however, and therefore sheds new light on the physics behind the more powerful formalism used in [4,5].

In the next two sections we introduce the coupled dynamics of the condensate and the thermal cloud, the condensate being described by the Gross-

H.J. Carmichael, R.J. Glauber, M.O. Scully (Eds.): LNP 561, pp. 3–17, 2001.

Pitaevskii equation and the thermal cloud by linear response theory. We then investigate these coupled oscillations for homogenous Bose condensates and finally apply these results to trapped Bose gases.

2 The Dynamics of the Condensate

At finite temperature the condensate dynamics can be described by the Gross-Pitaevskii-equation extended by thermal contributions [6]. To derive it we consider the Heisenberg equation of motion for the field operator $\hat{\Psi}$ of a system of atoms interacting by a contact potential $V_0\delta(\mathbf{x}-\mathbf{y})$

$$i\hbar\frac{\partial}{\partial t}\hat{\Psi}(\mathbf{r},t) = \left[-\frac{\hbar^2}{2m}\nabla^2 + V_{\rm ext}(\mathbf{r})\right]\hat{\Psi}(\mathbf{r},t) + V_0\,\hat{\Psi}^\dagger(\mathbf{r},t)\hat{\Psi}(\mathbf{r},t)\hat{\Psi}(\mathbf{r},t)\,. \quad (1)$$

The interaction constant $V_0 = 4\pi\hbar^2 a/m$ is proportional to the s-wave scattering length a and describes effectively the scattering of atoms at low energies. The Bose condensate is described by the macroscopic wave function introduced as $\langle\hat{\Psi}(\mathbf{r},t)\rangle = \Phi(\mathbf{r},t)$ [8,9]. $\langle\cdot\rangle$ denotes here a restricted thermal average. The decomposition of the field operator in a classical field and an operator describing fluctuations follows as

$$\hat{\Psi}(\mathbf{r},t) = \Phi(\mathbf{r},t) + \hat{\varphi}(\mathbf{r},t)\,, \quad (2)$$

which gives for the cubic product in (1)

$$\hat{\Psi}^\dagger\hat{\Psi}\hat{\Psi} = |\Phi|^2\Phi + 2|\Phi|^2\hat{\varphi} + \Phi^2\hat{\varphi}^\dagger + 2\Phi\hat{\varphi}^\dagger\hat{\varphi} + \Phi^*\hat{\varphi}\hat{\varphi} + \hat{\varphi}^\dagger\hat{\varphi}\hat{\varphi}\,. \quad (3)$$

Upon averaging the second and third term vanish. In a dilute system we can neglect the last term cubic in the fluctuation operator $\hat{\varphi}$. The three remaining terms give finite contributions: The normal average

$$n_{\rm th}(\mathbf{r},t) = \langle\hat{\varphi}^\dagger(\mathbf{r},t)\hat{\varphi}(\mathbf{r},t)\rangle \quad (4)$$

is the density of atoms excited from the condensate. In the Bose condensed region also the anomalous average

$$m(\mathbf{r},t) = \langle\hat{\varphi}(\mathbf{r},t)\hat{\varphi}(\mathbf{r},t)\rangle \quad (5)$$

takes a finite value. Both $n_{\rm th}$ and m are determined by the thermal occupation of excited states. For the classical field follows the Gross-Pitaevskii-equation

$$i\hbar\frac{\partial}{\partial t}\Phi(\mathbf{r},t) = \Big[-\frac{\hbar^2}{2m}\nabla^2 + V_{\rm ext}(\mathbf{r}) + V_0\,|\Phi(\mathbf{r},t)|^2 + 2V_0\,n_{\rm th}(\mathbf{r},t) + V_0\,m(\mathbf{r},t)\Big]\Phi(\mathbf{r},t)\,. \quad (6)$$

The equilibrium is given by the time-independent solution Φ_0 of (6), depending again on the static solutions for $n_{\rm th}$ and m. Thus all mean fields in equilibrium have to be determined self consistently.

Small fluctuations of this equilibrium are described by a wave function with two component u and v, fulfilling the Bogoliubov equations [8,10], which can be obtained by linearizing (6) with the classical ansatz

$$\Phi(\mathbf{r},t) = \left(\Phi_0(\mathbf{r}) + u(\mathbf{r})\, e^{-i\omega t} + v^*(\mathbf{r})\, e^{i\omega t}\right) e^{-i\mu t/\hbar}\,. \tag{7}$$

In the simplest approximation $n_{\rm th} = n_{\rm th}^0$ und $m = m^0$ are considered as static mean fields, describing the interaction of the condensate with the non-condensed atoms at rest. However for the homogenous systems this spectrum exhibits an energy gap $E(k=0) = 2V_0\sqrt{-m_0|\Phi_0|^2}$ and violates the Goldstone theorem, which requires in the case of a spontaneously broken continuous symmetry excitations of arbitrarily small energy. This static approximation does not fulfill the Hugenholtz-Pines-theorem [11].

For this reason we restrict ourselves here to the so called Popov approximation [12] and neglect the anomalous average [13]:

$$m(\mathbf{r},t) \equiv 0 \tag{8}$$

In this approximation the energy gap vanishes. Here we are interested in the coupled dynamics of the condensed and the thermally excited atoms [6,7]. The thermal density also oscillates with a small amplitude about its mean value $n_{\rm th}^0$

$$n_{\rm th}(\mathbf{r},t) = n_{\rm th}^0(\mathbf{r}) + \tilde{n}_{\rm th}(\mathbf{r})e^{-i\omega t} + \tilde{n}_{\rm th}^*(\mathbf{r})e^{i\omega t}\,. \tag{9}$$

The fluctuations of the condensate and of the thermal density interact with each other and coupled oscillations of these two components occur. Linearizing the Gross-Pitaevskii equation according to (7) and (9) with $\tilde{n}_{\rm th} = \tilde{n}_{\rm th}^*$ gives the two Bogoliubov type equations

$$\begin{aligned} \hbar\omega\, u(\mathbf{r}) &= H_{\rm HF}\, u(\mathbf{r}) + V_0\Phi_0^2\, v(\mathbf{r}) + 2V_0\Phi_0\, \tilde{n}_{\rm th} \\ -\hbar\omega\, v(\mathbf{r}) &= H_{\rm HF}\, v(\mathbf{r}) + V_0\Phi_0^{*2}\, u(\mathbf{r}) + 2V_0\Phi_0^*\, \tilde{n}_{\rm th} \end{aligned} \tag{10}$$

with the Hartree-Fock operator

$$\hat{H}_{\rm HF} = -\frac{\hbar^2}{2m}\nabla^2 + V_{\rm ext}(\mathbf{r}) + 2V_0\left(|\Phi_0(\mathbf{r})|^2 + n_{\rm th}^0(\mathbf{r})\right) - \mu\,. \tag{11}$$

The linear combinations $u \pm v$ are proportional to the density- and phase fluctuations of the condensate, respectively [14–16]. The first order equation of motion for the density fluctuation $\tilde{n}_c = \Phi_0(u+v)$ is the continuity equation, and depends only on the condensate velocity $(u-v)/\Phi_0$. This means, that no particle exchange between the condensate and the thermal density occurs, both components fulfill separate continuity equations. Such a particle exchange can only be described by mean values of operators not conserving particle number as the anomalous average, which we neglected in the approximation (8).

In the following we are interested in the dynamics at long wave lengths and for low energies $E \ll \mu$. In this limit we can derive a wave equation

for the condensate fluctuations by a gradient expansion of the equations (10) [15,16]:

$$\left(\frac{\partial}{\partial t}\right)^2 \tilde{n}_c = \frac{V_0}{m}\nabla\cdot\left(|\Phi_0|^2\nabla(\tilde{n}_c + 2\tilde{n}_{\rm th})\right). \tag{12}$$

In the static approximation $n_{\rm th} = n_{\rm th}^0$ the speed of sound for excitations with wave vectors $k^2 \ll 8\pi a|\Phi_0|^2$ is simply given by $c^2 = V_0\,|\Phi_0(T)|^2/m$ and no damping occurs. In the limit of vanishing temperature this reduces to the Bogoliubov result.

3 Linear Response of the Homogenous Bose–gas Above T_c

In this section we consider the homogenous Bose gas for $T > T_c$. Density fluctuations in the thermal cloud of non-condensed atoms can be described by linear response theory [9,18,19]. To illustrate this we consider a system of atoms with density n interacting via the contact potential introduced above. We describe their interaction in Hartree-Fock approximation, giving identical terms $V_0\,n$ for the direct and the exchange term. The atoms interact locally with the mean density of all atoms n. Starting from the equilibrium with density n^0 we apply a small perturbation potential U_p coupling to the density and ask which density response $\tilde{n}$ is caused. However since the mean field is a dynamic quantity, we have to linearize also the Hartree-Fock operator in the density fluctuation giving

$$\hat{H} = -\frac{\hbar^2}{2m}\nabla^2 + 2V_0\,(n^0+\tilde{n}) + U_p = \hat{H}_{\rm HF} + 2V_0\,\tilde{n} + U_p\,.$$

In addition to the external perturbation U_p the density of the system also responds to the fluctuation of its own mean field and the effective perturbation potential is $2V_0\,\tilde{n} + U_p$ [17]. For a homogenous system the density response to a perturbation with given wave vector $\mathbf{k}$ and frequency ω (with positive infinitesimal imaginary part due to the adiabatic switch-on of the perturbation from $t = -\infty$) is given by the algebraic equation

$$\begin{aligned}\tilde{n}(\mathbf{k},\omega) &= \chi^0(\mathbf{k},\omega)\left(2V_0\,\tilde{n}(\mathbf{k},\omega) + U_p(\mathbf{k},\omega)\right)\\ &= \frac{\chi^0(\mathbf{k},\omega)}{1-2V_0\,\chi^0(\mathbf{k},\omega)}\;U_p(\mathbf{k},\omega)\,.\end{aligned} \tag{13}$$

Here we introduced the response function of a homogenous system [9,18]

$$\chi^0(\mathbf{k},\omega) = \int\frac{d^3q}{(2\pi)^3}\,\frac{f_0(E(\mathbf{q})) - f_0(E(\mathbf{q}+\mathbf{k}))}{\omega - (E(\mathbf{q}+\mathbf{k}) - E(\mathbf{q}))/\hbar}\,. \tag{14}$$

with the single-particle spectrum of the Hartree-Fock operator in equilibrium $E(\mathbf{k}) = (\hbar\mathbf{k})^2/2m + 2V_0\,n^0$ and the equilibrium Bose distribution

$$f_0(E(k)) = \frac{1}{\exp\left[\beta(E(k)-\mu)\right]-1}\,. \tag{15}$$

The effective response function to an external perturbation in (13) has a pole for

$$1 - 2V_0\,\chi^0(\mathbf{k},\omega) = 0 \tag{16}$$

which gives the condition for eigenmodes of density fluctuations of the thermal system. This pole describes collective behavior of an interacting system of atoms and follows only from the *dynamical* treatment of the mean field. For the poles to describe physical decaying modes $\sim e^{-i\omega t}$ they have to lie in the lower complex half-plane of ω .

Condition (16) can be read as an implicit equation for ω at a given $\mathbf{k}$, giving one (or several) branches of solutions $\omega(k)$ for the collective motion. These solutions are in general not on the real axis but rather in the complex plane and describe so the frequency and the damping of an oscillation with given wave vector.

As for the condensate dynamics we are in the following again interested in the behavior at long wave lengths, i.e. for wave vectors with $k\Lambda \ll 1$ where $\Lambda = \sqrt{2\pi\hbar^2/mk_BT}$ denotes the thermal wave length. For small k we can approximate in the denominator of (14)

$$E(\mathbf{p}+\hbar\mathbf{k}) - E(\mathbf{p}) \approx \frac{\hbar}{m}\,\mathbf{k}\cdot\mathbf{p}\,.$$

The difference of the Bose factors in the numerator can be approximated by a derivative and the response function, describing density fluctuations of long wave length in a cloud of bosons, can be written as

$$\chi^0(\mathbf{k},\omega) = \int \frac{d^3p}{h^3}\;\frac{\mathbf{k}\cdot\nabla_p f_0(\mathbf{p})}{\omega - \mathbf{p}\cdot\mathbf{k}/m}\,. \tag{17}$$

With this response function the collective behavior is determined by (16). In the context of a different formalism this response function was already investigated in [20]. To evaluate (17) further we choose $\mathbf{k}$ in x-direction and integrate first in $p_y\,, p_z$ with the result

$$\chi^0(k_x,\omega) = \frac{1}{\Lambda^2}\frac{1}{2mk_BT}\int \frac{dp_x}{h}\;\frac{2\,p_x}{\omega/k - p_x/m}\,f_0(E(p_x))\,.$$

This response only depends on the ratio ω/k , which introduces the (in general complex) speed of sound $c = \omega/k$ in the long wave length limit. Scaling p_x by $\sqrt{2mk_BT}$ and measuring the speed of sound c in units of the thermal velocity $c_T = \sqrt{2k_BT/m}$, the response function reads

$$\chi^0(c) = \frac{\Lambda^{-3}}{k_BT}\;\tilde{\chi}^0(c/c_T)\,. \tag{18}$$

The scaled velocity of sound $s = c/c_T$ only occurs as an argument of the dimensionless response function

$$\tilde{\chi}^0(s) = \frac{1}{\sqrt{\pi}}\int_{-\infty}^{\infty} dt\;\frac{t}{s-t}\,\frac{z}{e^{t^2}-z}\,. \tag{19}$$

Besides the appearance of T in the prefactor in (18) the temperature dependence of $\chi^0(c)$ is given by that of the fugacity $z = e^{\beta\mu}$.

The integral can be evaluated by the method of residua [20]. The physical boundary condition is, that in the derivation ω is the frequency of an external perturbation which has to vanish for large negative times $t \to -\infty$, i.e. $\mathrm{Im}[s] > 0$ and the integral has to be evaluated with s in the upper complex half-plane. To obtain a sufficiently fast decaying integrand we write first

$$\frac{t}{s-t} = -1 + \frac{s^2}{s^2-t^2} + \frac{st}{s^2-t^2}\,.$$

The integral over the last term, which is odd in t, vanishes identically. The integral over the first term gives

$$\int_{-\infty}^{\infty} dt\ \frac{-z}{e^{t^2}-z} = -\sqrt{\pi}\, g_{1/2}(z)\,.$$

For the remaining integration we close the integration contour with a semicircle in the upper plane. In this region the Bose factor has poles at

$$\left.\begin{matrix} a_n \\ b_n \end{matrix}\right\} = i\sqrt[4]{4\pi^2\, n^2 + \gamma^2}\ e^{\pm i\phi_n/2}$$

with $\gamma = -\mu/k_BT = |\mu|/k_BT$, and $\phi_n = \arctan(2\pi n/\gamma)$ for $n \geq 0$. The summation of the different residua finally gives the dimensionless response function

$$\begin{aligned}\tilde{\chi}^0(s) = -g_{1/2}(z) - \sqrt{\pi} i\, \frac{sz}{e^{s^2}-z} + \sqrt{\frac{\pi}{\gamma}}\ \frac{s^2}{s^2+\gamma} \\ + \sqrt{\pi} i \sum\nolimits_{n=1}^{\infty}\ \frac{s^2}{s^2-a_n^2}\,\frac{1}{a_n} + \frac{s^2}{s^2-b_n^2}\,\frac{1}{b_n}\,. \end{aligned} \tag{20}$$

For small γ one can expand $g_{1/2}(e^{-\gamma}) = \sqrt{\pi/\gamma} + \zeta(1/2) + O(\gamma)$. The divergence for $\gamma \to 0$ is cancelled by the third term in (20), the response function is finite in this limit.

When we ask for solutions of (16), we are looking for eigenmodes of the system, which have to decay exponentially for physical reasons and the poles we look for have to be located in the lower complex half-plane. In condition (16) the analytical continuation of the integral from the upper to the lower complex half-plane has to be used.

The numerically determined solutions of (16) are shown in Fig.1 for different interactions. We can see the following behavior: at high temperatures the Bose distribution can be replaced by the Boltzmann distribution $f_{\mathrm{B}}(E(\mathbf{k})) = z\, e^{-\beta \mathbf{p}^2/2m}$ and only the ratio $V_0 z \Lambda^{-3}/k_BT = V_0 n^0/k_BT$ enters in (16) as a parameter. The solutions $s = c/c_T$ for different interactions can be obtained from each other by simply scaling the temperature.

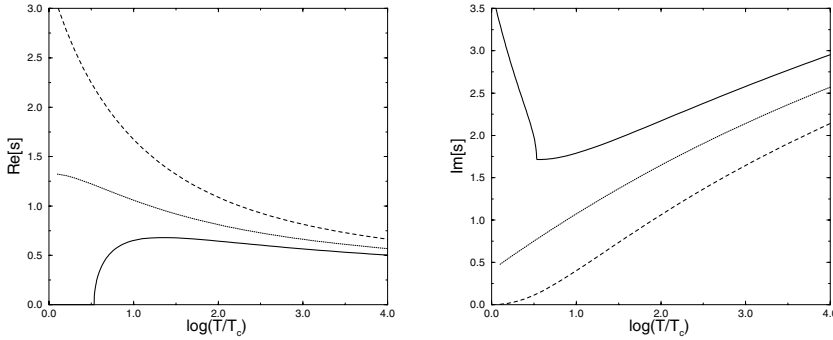

Fig. 1. Real part (left) and imaginary part (right) of the velocity of sound $c = \omega/k$ from (16) in units $\sqrt{2kT/m}$ for different interactions $V_0 n^0/kT_c = 0.1, 1, 10$ (solid, dotted, dashed) in dependence of the logarithmic temperature $\log_{10}(T/T_c)$

At low temperatures the observed behavior depends qualitatively on the interaction. From an expansion of the integrand in (19) in t/s we get as the dominant behavior for large s

$$\tilde{\chi}^0(s;z) \approx \frac{g_{3/2}(z)}{2s^2} - 2\sqrt{\pi} i \, \frac{s\,z}{e^{s^2} - z}\,, \tag{21}$$

where the second term has to be added for the analytical continuation. For strong interactions $V_0\, n^0 \gg k_B T$ the first term dominates and the second term vanishes exponentially, and $c = s\, c_T$ converges to the real solution $c_n^2 = 2\, V_0\, n^0/m$ independent of the temperature. This agrees with thermodynamical velocity of sound of a thermal gas with a pressure determined by the mean field interaction only neglecting the kinetic pressure. For small interaction $V_0\, n^0 \ll k_B T$ the full response function can be approximated by the second term in (21). Below a certain temperature T_0 depending on the interaction the condition (16) can be fulfilled by a purely imaginary solution, which takes for $s \gg 1$ the form

$$c_{\rm im} = -\frac{i}{4\sqrt{\pi}} \, \frac{k_B T}{V_0 \Lambda^{-3}} \, c_T$$

and which is again independent of the temperature. Above T_0 the approximate response function gives rise to the characteristic growth of the real part, see Fig.1. This case of weak interaction is realized in alkali gases. In a homogenous gas of alkali atoms above the phase transition $T > T_c$ density waves decay as a mere relaxation with a rate inversely proportional to the interaction strength.

4 Homogenous Bose Gases Below T_c

Let us now investigate sound waves in the homogenous Bose gas below the phase transition. The equilibrium is given by $|\Phi_0|^2 = n_c^0$ and n_{th}^0, the chemical potential by the Gross-Pitaevskii equation as $\mu = V_0\,(n_c^0 + 2n_{\rm th}^0)$. The excited atoms are described in Hartree-Fock approximation interacting with the mean field of the total density $U = 2V_0\,(n_{\rm th} + n_c)$. So the dispersion of the plane waves is $E(\mathbf{k}) = (\hbar\mathbf{k})^2/2m + 2V_0\,(n_c^0 + n_{\rm th}^0)$ in equilibrium. By integrating the Bose factor over the momenta the thermal equilibrium density is obtained as $n_{\rm th}^0 = g_{3/2}(z)/\Lambda^3$. Here we introduced the effective chemical potential $\bar{\mu} = \mu - 2V_0\,(n_{\rm th}^0 + n_c^0) = -V_0 n_c^0$ and the fugacity as $z = e^{\beta\bar{\mu}}$. For a given total density $n_{\rm tot}^0$ and temperature the equilibrium is determined by the implicit equation

$$n_{\rm tot}^0 = n_c^0 + \frac{1}{\Lambda^3}\, g_{3/2}(e^{-\beta V_0 n_c^0})\,. \tag{22}$$

However it turns out that, as an artefact of the Popov approximation, the phase transition is no longer continuous, but the condensate exhibits a finite jump at the critical temperature

$$\Delta n_c(T_c) = \frac{4\pi\bar{V}_0}{(1-\zeta(1/2)\bar{V}_0)^2} + O(\bar{V}_0^{5/2})\,.$$

For $T = T_c$ both states with $n_c = 0$ and with $n_c = \Delta n_c$ are thermodynamically allowed.

Below T_c the thermal density responds to the internal fluctuation in the mean field $\tilde{U} = 2V_0\,(\tilde{n}_{\rm th} + \tilde{n}_c)$. So the equation of motion reads now

$$\tilde{n}_{\rm th} = 2V_0\,\chi^0(c)\,(\tilde{n}_{\rm th} + \tilde{n}_c)\,, \tag{23}$$

with the response function (17). This description is also arrived at within the dielectric formalism [5] and therefore from here on the further evaluation in this section parallels that of [5]. Together with the condensate dynamics (12) we get as the determinant condition for the solvability of these two equations

$$(c^2 - c_B^2) = (c^2 + c_B^2)\,2V_0\,\chi^0(c)\,, \tag{24}$$

where we introduced the Bogoliubov speed of sound $c_B = \sqrt{V_0\,n_c^0/m}$. This is the condition for collective motion in the homogenous system below the phase transition. The ratio of the two amplitudes $\tilde{n}_c, \tilde{n}_{th}$ is

$$\frac{\tilde{n}_c}{\tilde{n}_{th}} = \frac{1 - 2V_0\chi^0}{2V_0\chi^0} = \frac{2c_B^2}{c^2 - c_B^2}\,. \tag{25}$$

From this one can see whether mainly one or both components contribute to a density oscillation and whether they oscillate in or out of phase.

Here we consider the case of weakly interacting systems given by the condition $V_0 n_c^0 \ll k_B T$. It follows $V_0\chi^0(c_B) \ll 1$. To see this we consider the

behavior of the response function for small arguments $|s| = |c/c_T| \ll 1$ and for small interactions $\gamma = \beta V_0 n_c^0 \ll 1$ [20]. The terms in leading order in (20) in s, γ can be put in the form

$$\tilde{\chi}^0(s) = -\sqrt{\pi}\,\frac{is+\sqrt{\gamma}}{s^2+\gamma} = \frac{-i\sqrt{\pi}}{s+i\sqrt{\gamma}}\,. \tag{26}$$

This shows that $V_0\chi^0(c_B; z)$ is indeed of the order $O(\gamma^{1/2}) \ll 1$. So one solution of (24) is near the Bogoliubov speed of sound c_B. The numerically determined solutions for weak interaction of different strengths are presented in Fig.2, together with the unperturbed result $c = c_B$. In the scaling chosen c converges for $T \to 0$ to the dimensionless interaction $V_0 n_{\rm tot}^0/k_B T_c$. Since the velocity of sound c is a slight perturbation of the Bogoliubov result c_B, the amplitude ratio (25) shows, that mainly the condensate is oscillating in this mode.

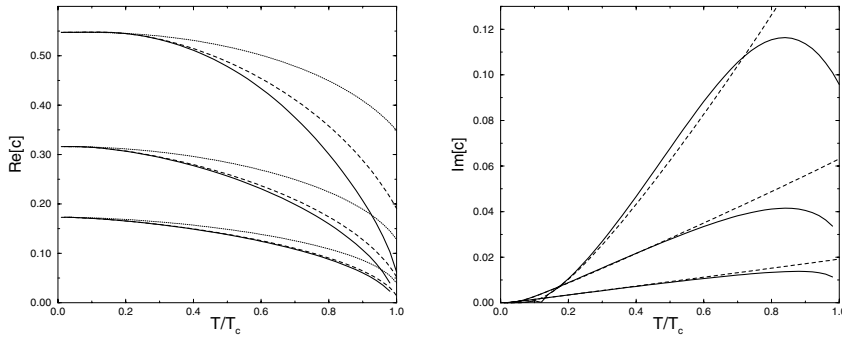

Fig. 2. Real part (**a**) and imaginary part (**b**) of the velocity of sound $c = \omega/k$ from (24) in units $\sqrt{k_B T_c/m}$ for different interactions $V_0 n_{\rm tot}^0/k_B T_c = 0.3, 0.1, 0.03$ (solid curves, from top down) depending on the temperature T/T_c. Result of the perturbation theory (27) (dashed curve). Popov-result $c_B = \sqrt{V_0 n_c^0/m}$ in (a) (weak, dotted curve)

Let us compare this self consistent solution with perturbation theory, which is much simpler and is therefore usually applied in this or a related context (cf.[30–32]). Taking the right hand side in (24) as a perturbation to the Bogoliubov speed of sound $c = c_B$, we get to first order in V_0 the complex correction

$$c = c_B + 2c_B\,\chi^0(c_B)\,. \tag{27}$$

These results are also displayed in Fig.2. Already for not too small interactions both results agree very well for low and intermediate temperatures. Near the phase transition for $T \gtrsim 0.8T_c$ perturbation theory does not agree any more with the exact solutions.

5 Inhomogeneous Bose Condensates

In the experiments with alkali condensates trapped atoms are investigated. In these inhomogeneous systems the equation of motion for the thermal density (23) takes the form of an integral equation

$$\tilde{n}_{\rm th}(\mathbf{r}) = 2V_0 \int d^3r'\, \chi^0(\mathbf{r},\mathbf{r}',\omega)\left(\tilde{n}_c(\mathbf{r}') + \tilde{n}_{\rm th}(\mathbf{r}')\right). \tag{28}$$

The exact response function has to be calculated from all discrete excited states of the inhomogeneous systems [19]. To determine the complex frequencies from this integral equation together with the condensate dynamics (12) numerically one has to represent these equations in matrix form in some basis and solve the determinant condition as an implicit equation for the complex frequency, which presents a rather demanding problem.

Instead of this self-consistent solution we determine complex frequency shifts to the discrete modes of the condensate dynamics in perturbation theory as we determined corrections to the Bogoliubov speed of sound in the preceding section. Thus we consider the thermal density in (12) again as a small perturbation to the condensate dynamics. Furthermore we consider the thermal density in (28), as a response to the condensate fluctuation only, neglecting its self interaction:

$$\tilde{n}_{\rm th}(\mathbf{r}) = 2V_0 \int d^3r'\, \chi^0(\mathbf{r},\mathbf{r}',\omega)\, \tilde{n}_c(\mathbf{r}')\,.$$

The equation of motion for the condensate fluctuation then becomes

$$\omega^2\, \tilde{n}_c = \frac{V_0}{m}\nabla\cdot\left(n_c^0\nabla\big(\tilde{n}_c + 4V_0 \int d^3r'\, \chi^0(\mathbf{r},\mathbf{r}',\omega)\, \tilde{n}_c(\mathbf{r}')\big)\right). \tag{29}$$

The term in leading order in V_0 is the wave equation in the static approximation with the normalized solutions

$$\omega_\mu^2\, \psi_\mu^{(0)} = \frac{V_0}{m}\nabla\cdot\left(n_c^0\nabla\psi_\mu^{(0)}\right). \tag{30}$$

At vanishing temperature these low lying modes can be determined analytically in the Thomas-Fermi limit $N_0\, a/d \to \infty$ [15,16,21], where N_0 is the number of atoms in the condensate and d the zero-point amplitude in the trap, and they turn out to be independent of N_0. At finite temperature $T \lesssim 0.6T_c$ with a thermally depleted condensate the modes can be described as oscillations of a condensate at $T = 0$ with a thermally reduced number of atoms $N_0(T)$ [22]. The frequency shifts for finite particle numbers due these effects have also been investigated in the static approximation in [23,24]. Here we restrict ourselves to the Thomas-Fermi limit at finite temperature with $V_0|\Phi_0(\mathbf{R})|^2 = \max(\mu(T) - V_{\rm ext}(\mathbf{R}) - 2V_0 n_{\rm th}^0(\mathbf{R}), 0)$, and the real discrete frequencies ω_μ only depend on the shape, but not on the size of the condensate.

We consider the second term of order V_0^2 in (29) as a small perturbation. Writing the frequency as $\omega = \omega_\mu + \Delta\omega_\mu$, one obtains from (29) in leading order the correction

$$\Delta\omega_\mu = 2V_0\,\omega_\mu \int d^3r\,\psi_\mu^{(0)}(\mathbf{r}) \int d^3r'\,\chi^0(\mathbf{r},\mathbf{r}',\omega_\mu;z)\,\psi_\mu^{(0)}(\mathbf{r}')\,. \tag{31}$$

The imaginary part of this frequency shift gives the damping of the mode. In the following we wish to evaluate this correction analytically. Numerical solutions have already been determined in [25,4].

As mentioned above the determination of the exact response function for the inhomogeneous system is quite complicated. Instead we use here as a suitable simplification the local density approximation [26]. We consider the inhomogeneous system as locally homogenous and take the inhomogeneity into account only via the use of a space dependent dispersion relation $E(k,\mathbf{R})$. In the Hartree-Fock approximation this local spectrum of excitations is $E(k,\mathbf{R}) = (\hbar\mathbf{k})^2/2m + V_{\rm ext}(\mathbf{R}) + 2V_0(n_c^0(\mathbf{R}) + n_{\rm th}^0(\mathbf{R}))$. Sums over states can then be performed analytically. For slowly changing values, like the mean atom density in the center of the trap, this approximation is justified. For the density of excited atoms inside the condensate we obtain in the Thomas-Fermi approximation

$$n_{\rm th}^0(\mathbf{R}) = \frac{1}{\Lambda^3}\,g_{3/2}(e^{-\beta V_0 n_c^0(\mathbf{R})})\,, \tag{32}$$

where we introduced the space dependent fugacity $z(\mathbf{R}) = \exp(-\beta V_0 n_c^0(\mathbf{R}))$. In [27] thermodynamical properties of condensed Bose gases in traps were investigated in this approximation.

To apply this local density approximation to the response function we transform first to center of mass and relative coordinates $\mathbf{R} = (\mathbf{r}+\mathbf{r}')/2$ and $\mathbf{r}-\mathbf{r}'$ and Fourier transform with respect to the relative coordinate

$$\chi^0(\mathbf{r},\mathbf{r}',\omega) = \int \frac{d^3k}{(2\pi)^3} e^{i\mathbf{k}(\mathbf{r}-\mathbf{r}')}\chi^0(\mathbf{R},\mathbf{k},\omega)\,. \tag{33}$$

In the homogenous system χ^0 only depends on the relative coordinate, we have $\chi^0(\mathbf{R},\mathbf{k},\omega) = \chi^0(\mathbf{k},\omega)$. The local density approximation for the response function of the inhomogeneous system $\chi^0(\mathbf{R},\mathbf{k},\omega)$ now consists in replacing the fugacity in the homogenous response function by its space dependent value:

$$\chi^0\left(\mathbf{R},\mathbf{k},\omega;z\right) \approx \chi^0\left(\mathbf{k},\omega;z(\mathbf{R})\right)\,. \tag{34}$$

We consider the limiting case of a weakly interacting system with $V_0 n_c^0(R) \ll k_B T$, which is approximately fulfilled in the experiments with alkali condensates at the measured temperatures. For the experiments with ^{87}Rb [28] one can estimate for the condensate density in the center of the trap $V_0 n_c^0(0)/k_B T_{\rm c} \approx 0.3$, for the experiments with ^{23}Na [29] one can estimate $V_0 n_c^0(0)/k_B T_{\rm c} \approx 0.2$. So we want to use approximation (26) for χ^0 for

the inhomogeneous system. Putting there $c = \omega_\mu/k$, the response function reads

$$\chi^0(\omega_\mu, k; z(R)) = -\frac{\Lambda^{-3}}{k_B T}\sqrt{\frac{\pi k_B T}{V_0 n_c^0(R)}}\;\frac{k}{k - i\sqrt{\frac{m\omega_\mu^2}{2V_0 n_c^0(R)}}}\,. \tag{35}$$

So using (31) we determine the complex frequency shifts $\Delta\omega_\mu$ explicitly as:

$$\Delta\omega_\mu = -2\,\omega_\mu\,\frac{V_0\Lambda^{-3}}{k_B T}\sqrt{\frac{\pi k_B T}{\mu}}\,A_0 = -4\,\omega_\mu\,\frac{a}{\Lambda}\sqrt{\frac{\pi k_B T}{\mu}}\,A_0\,. \tag{36}$$

The frequency shift is linear in the temperature T. The complex numerical coefficient A_0 is given by the integral

$$A_0 = -\int\frac{d^3k}{(2\pi)^3}\int d^3R\int d^3r\,\sqrt{\frac{\mu}{V_0 n_c^0(\mathbf{R})}}$$
$$\times\,\psi_\mu^{(0)}(\mathbf{R}-\mathbf{r}/2)^*\psi_\mu^{(0)}(\mathbf{R}+\mathbf{r}/2)\,k\,e^{i\mathbf{k}\cdot\mathbf{r}}\left(k - i\sqrt{\frac{m\omega_\mu^2}{2V_0 n_c^0(R)}}\right)^{-1}\,.$$

Similar expressions for the damping rate have been derived in [6,30–32]. However in these papers either the explicit form of the mode function was not considered and the damping was only calculated up to a numerical factor, or only the damping of higher lying modes with frequencies $\hbar\omega_\mu$ of the order of μ was determined.

In the following we are interested only in the damping rates from (36). So we neglect the frequency shifts in (30) due to finite temperature and take as our zeroth order solutions the frequencies and mode functions at $T = 0$ from [15,16,21]. A_0 converges to a constant value in the Thomas-Fermi limit $N_0 a/d \gg 1$ and the damping rates depend only via the chemical potential on the particle number in the condensate N_0, giving $\Delta\omega_\mu \propto N_0^{-1/5}$. The 9-fold integral in the explicit determination of A_0 can hardly be evaluated analytically. Even in isotropic traps the integrand depends on the different components of the relative coordinate for non isotropic modes, and the integration limits for the relative coordinate depend on $\mathbf{R}$ and on the direction of $\mathbf{r}$. In anisotropic traps even a numerical evaluation turns out to be difficult. For this reason we determine the coefficient A_0 in the following approximation:

i. Since we consider fluctuations of long wave lengths, we can neglect gradients in the expansion of the mode functions $\psi_\mu^{(0)}$ at point $\mathbf{R}$ in $\mathbf{r}$ and approximate $\psi_\mu^{(0)}(\mathbf{R}-\mathbf{r}/2)^*\;\psi_\mu^{(0)}(\mathbf{R}+\mathbf{r}/2) \approx |\psi_\mu^{(0)}(\mathbf{R})|^2$.

ii. For axially symmetric potentials the center of mass coordinate is integrated over the volume $X^2+Y^2+(\omega_z/\omega_x Z)^2 \equiv \tilde{R}^2 \le R_{\mathrm{TF}}^2$ in the Thomas-Fermi approximation, with R_{TF} the Thomas-Fermi-Radius in x-direction. To perform the integral over the relative coordinate, we approximate the exact range of

integration by a sphere with radius r_a given by the condition of equal integration volume in both cases. From this it follows $r_a = (h^2(3R_{\rm TF} - h)/2)^{1/3}$ with $h^2 = R_{\rm TF}^2 - \tilde{R}^2$. The integral of the exponential over this sphere gives $4\pi\, r_a^2\, j_1(kr_a)/k$, with the spherical Bessel function j_1. We obtain as an approximate expression for the coefficient A_0

$$A_0 = -\frac{2}{\pi}\int_0^\infty dk \int_{V_{\rm TF}} d^3R \sqrt{\frac{\mu}{V_0 n_c^0(\mathbf{R})}} \times |\psi_\mu^{(0)}(\mathbf{R})|^2\ (kr_a)^2\, j_1(kr_a) \left(k - i\sqrt{\frac{m\omega_\mu^2}{2V_0 n_c^0(R)}} \right)^{-1} .$$

Let us compare our description with the experiments [28] and determine the damping rates for the two measured modes. The quadrupole mode has the frequency $\omega_{(0,2)} = \omega_x\sqrt{2}$, the mode function is $\psi^{(0)}(\rho,\phi,z) = \rho^2\, e^{i2\phi}/N$ with $N^2 = 32\pi/105 R_{\rm TF}^3\, \omega_x/\omega_z$. The numerical evaluation of the integral gives for this mode the imaginary part $\mathrm{Im}[A_0] = 0.87$. The monopole mode is given by $\omega_{(2,0)} = \omega_x\sqrt{14 - 2\sqrt{29}} \approx \omega_x 1.797$ at the anisotropy $\omega_z^2/\omega_x^2 = 8$, the mode function is $\psi^{(0)}(\rho,\phi,z) = (\rho^2 + bz^2 + c)/N$ with $b = \omega_{(2,0)}^2/\omega_x^2 - 4$ and $c = 2\omega_x^2/\omega_{(2,0)}^2 - 1$, the normalization is $N^2 = 0.109$. For this mode we obtain $\mathrm{Im}[A_0] = 0.94$. The damping rates linear in the temperature are compared in Fig.3a and b for both modes with the measurements [28].

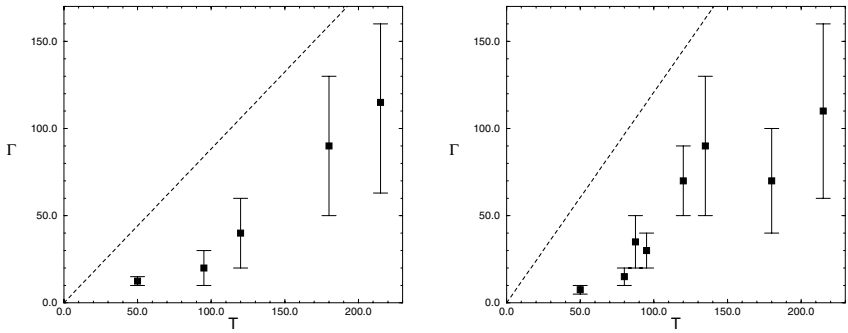

Fig. 3. Damping Γ in s of the quadrupole mode $\omega_\mu = \sqrt{2}\omega_x$ (left) and of the monopole mode $\omega_\mu = 1.797\omega_x$ (right) according to (36) (dashed line) depending on the temperature T in nK for the parameter from [3]. Squares are the experimental values

6 Conclusions

In both cases the calculated damping rates (36) are above the measured values. This is in accordance with our results for the homogenous system, where

the damping rates from perturbation theory were bigger than the exact results, see Fig.2. The dimensionless interaction for [28] was estimated to be $V_0 n_c^0 / k_B T_c \approx 0.3$, what can explain the large deviations in Fig.3 for small temperatures $T \leq T_c/2$. In the range $T \gtrsim T_c/2$ the linear growth of the experimental damping rates agrees rather well with our results, except for the two last measured values for the monopole mode. However, for these measured values also a growth of the frequency was observed, which is not fully understood yet. In general we can say, that the complex frequency shifts described in this paper can explain the measured damping rates in a qualitative or even semi-quantitative way, however, for a fully quantitative explanation the applied approximations are not yet sufficient. More detailed numerical evaluations like in [4] are then necessary.

Acknowledgments

We wish to dedicate this work to the memory of Dan Walls with whom we enjoyed fruitful collaboration also on BEC-related problems. We wish to thank Jürgen Reidl and Péter Szépfalusy for useful discussions and remarks. This work was supported by the Deutsche Forschungsgemeinschaft through the Sonderforschungsbereich Unordnung und große Fluktuationen.

References

1. A.S. Parkins, D.F. Walls: Physics Reports **303**, 1 (1998)
2. F. Dalfovo, S. Giorgini, L. Pitaevskii, S. Stringari: Rev. Mod. Phys. **71**, 463 (1999)
3. W. Ketterle, D.S. Durfee, D.M. Kurn: Lecture given at the Varenna summer school, 1998
4. J. Reidl, A. Csordás, R. Graham, P. Szépfalusy, Phys. Rev. A**61**, 043606 (2000)
5. M. Fliesser, J. Reidl, P. Szépfalusy, R. Graham: cond-mat/0006475 (2000)
6. S. Giorgini: Phys. Rev. A **57**, 2949 (1998)
7. S. Giorgini: Phys. Rev. A **61**, 063615 (2000)
8. N. Bogoliubov: J. Phys. USSR **1**, 23 (1947)
9. A.L. Fetter, J.D. Walecka: *Quantum Theory of Many-Particle Systems* (McGraw Hill, New York 1971)
10. A.L. Fetter: Ann. Phys. (N.Y.) **70**, 67 (1972)
11. N. Hugenholtz, D. Pines: Phys. Rev. **116**, 489 (1959)
12. A. Griffin: Phys. Rev. B. **53**, 9341 (1996)
13. V. N. Popov: *Functional Integrals and Collective Modes* (Cambridge University Press, New York 1987), Chap. 6
14. A.L. Fetter: Phys. Rev. A **53**, 4245 (1996)
15. S. Stringari: Phys. Rev. Lett. **77**, 2360 (1996)
16. W.-C. Wu, A. Griffin: Phys. Rev. A. **54**, 4204 (1996)
17. H.T.C. Stoof: In: *Dynamics: Models and Kinetic Methods for Non-Equilibrium Many-Body Systems*, ed. John Karkheck (Kluwer, Dordrecht, in press) e-print: cond-mat/9812424

18. L.P. Kadanoff, G. Baym: *Quantum Statistical Mechanics* (W. A. Benjamin, California 1962)
19. A. Minguzzi, M.J. Tosi: J. Phys. : Condens. Matter **9**, 10211 (1998)
20. P. Szépfalusy, I. Kondor: Ann. Phys. (N.Y.) **82**, 1 (1974)
21. M. Fliesser, A. Csordás, P. Szépfalusy, R. Graham: Phys. Rev. A **56**, R2533 (1997)
22. R.J. Dodd, M. Edwards, C.W. Clark, K. Burnett: Phys. Rev. A **57**, R32 (1998)
23. D.A.W. Hutchinson, E. Zaremba, A. Griffin: Phys. Rev. Lett. **78**, 1842 (1997)
24. J. Reidl, A. Csordás, R. Graham, P. Szépfalusy: Phys. Rev. A **59**, 3816 (1999)
25. G. Bene, P. Szépfalusy: Phys. Rev. A **58**, R3391 (1998)
26. P. Szépfalusy: Acta Phys. Hung. Tom XVII, Fasc.1-2, 229 (1964)
27. S. Giorgini, L.P. Pitaevskii, S. Stringari: J. Low Temp. Phys. **109**, 309 (1997)
28. D.S. Jin, M.R. Matthews, J.R. Ensher, C.E. Wieman, E.A. Cornell: Phys. Rev. Lett. **78**, 764 (1997)
29. M.-O. Mewes, M.R. Andrews, N.J. van Druten, D.M. Kurn, D.S. Durfee, W. Ketterle: Phys. Rev. Lett. **77**, 416 (1996)
30. M.V. Liu: Phys. Rev. Lett. **79**, 4056 (1997)
31. P.O. Fedichev, G.V. Shlyapnikov, J.T.M. Walraven: Phys. Rev. Lett. **80**, 2269 (1998)
32. L.P. Pitaevskii, S. Stringari: Phys. Rev. Lett. **74**, 3352 (1998)

Coherent Vortex Dynamics in Two- and Three-Dimensional Bose–Einstein Condensates

R.J. Ballagh and B.M. Caradoc-Davies

1 Introduction

Vortices have been a major interest in Bose-condensed systems since the early studies of superfluid He II. These topological objects in the quantum field have a 2π phase circulation about a point of zero amplitude, and thus allow circulating flow in the (otherwise) irrotational quantum fluid. A classic experiment in superfluidity demonstrated that vortices form as the preferred stable state in a rotating cylinder of He II [1], a result explained theoretically in terms of the equilibrium energy properties of vortices [2]. The recently realised gaseous Bose-Einstein condensates (BEC) provide important new opportunities for the study of vortices in quantum fluids, and in particular of vortex dynamics. *A priori* theoretical calculations can be more readily made for these weakly interacting gases than for strongly interacting quantum liquids such as He II, and the experiments can make direct and detailed dynamical observations. Initial theoretical studies of vortices in BEC concentrated on static properties including stability and excitation spectra [3–6]. Recently, however, a number of dynamical studies of vortices have been made using the Gross-Pitaevskii equation (GPE) for the mean field wavefunction $\psi(\mathbf{r}, t)$, which is known to be accurate near $T = 0$. Jackson *et al.* [7] showed that vortices may be generated by movement of a localised potential through a condensate, while Marzlin and Zhang [8] investigated vortex production using four laser beams in a ring configuration. A potentially important scheme for vortex detection using phase sensitive detection was formulated by Bolda and Walls [9]. Experimental realisation of vortices has now been achieved by the JILA group in a two-component condensate [10], in confirmation of a theoretical prediction by Williams and Holland [11], and also by Madison *et al.* [12] who reported the first observation of vortices in a single-component condensate.

In this paper we present a study of the dynamics of vortex production in a trapped dilute single-component condensate stirred rotationally with a repulsive Gaussian potential (representing for example a focussed far blue detuned laser beam). This scheme is similar in spirit to the rotating cylinder of He II, with the laser mimicking surface roughness of the cylinder. However, in contrast to the case of He II, there is a tractable theoretical model for the stirred condensate, and this enables us to interpret the dynamics (in

H.J. Carmichael, R.J. Glauber, M.O. Scully (Eds.): LNP 561, pp. 18–27, 2001.

a certain regime) in terms of a relatively simple coherent mechanism. In previous work we investigated the stirring model in the case of two spatial dimensions [13]. Such a case can have real physical application: experimental observation of a two-dimensional condensate has recently been reported [14]. However, most contemporary BEC experiments are three dimensional. In this paper we extend our earlier analysis, and in particular simulate the model numerically in both two and three spatial dimensions. We present an analytic model that explains the main features of the vortex dynamics, and gives a quantitative prediction for the critical speed of rotation for vortex formation. We also investigate the question of vortex stability in the mean field limit.

Our treatment is based on the Gross-Pitaevskii equation for the condensate wavefunction $\psi(\mathbf{r},t)$

$$i\frac{\partial\psi(\mathbf{r},t)}{\partial t} = -\nabla^2\psi(\mathbf{r},t) + V(\mathbf{r},t)\psi(\mathbf{r},t) + C|\psi(\mathbf{r},t)|^2\psi(\mathbf{r},t)\ , \tag{1}$$

in which time has units of ω^{-1} (where ω is the harmonic trap frequency in the x and y directions), length and energy are in units of $\sqrt{\hbar/2m\omega}$ and $\hbar\omega$ respectively, and C is proportional to the number of atoms in the condensate and the s-wave scattering length. The total external potential $V(\mathbf{r},t)$ is given by $V_{trap}+W(\mathbf{r},t)$, where V_{trap} is a cylindrically symmetric trapping potential and $W(\mathbf{r},t)$ represents the stirrer (a narrow moving potential). In two dimensions we consider coordinates x and y, so that V_{trap} is $(x^2+y^2)/4$, while in 3D the z axis is the symmetry axis of the trap, so that V_{trap} is $(x^2+y^2+\lambda^2z^2)/4$ with λ the trap anisotropy parameter. The stirring potential is given by

$$W(\mathbf{r},t) = W_0(t)\exp\left[-4\left(\frac{|\boldsymbol{\rho}-\boldsymbol{\rho}_s(t)|}{w_s}\right)^2\right]\ , \tag{2}$$

where $\boldsymbol{\rho}$ is the projection of $\mathbf{r}$ into the x-y plane, and $\boldsymbol{\rho}_s$ is the centre of the Gaussian stirrer in that plane. In the three-dimensional case, $W(\mathbf{r},t)$ is cylindrically symmetric about a line parallel to the z axis.

2 Simulations

In this paper, we begin all our simulations with the condensate in an eigenstate of the time independent GPE [i.e. (1) with $W_0 = 0$ and the LHS set to $\mu\psi$], usually the ground state. The condensate is stirred by moving the stirrer in a circle of constant radius ρ_s at a constant angular velocity ω_f and we minimise transient effects by linearly increasing the stirrer height W_0 from zero to its final value between $t = 0$ to $t = \pi$.

We have carried out a wide range of simulations, varying the angular stirring speed, the width, depth and radial position of the stirrer, and the number of atoms in the condensate. Due to the constraints imposed by computer resources, most of the simulations are carried out in two spatial dimensions,

but in this paper we have also performed fully three dimensional simulations to confirm that the types of behaviour found in two dimensions also occur in three dimensions. Our numerical simulations were carried out using an efficient fourth order spectral method, which will be described elsewhere [15]. Vortices are found in the resultant wavefunction by an algorithmic procedure which searches for a 2π phase circulation. It is worth emphasising that in a gaseous condensate, the density varies, and vortices form easily in the very low density regions right out to the edge of the computational grid. Unlike the case of He II, where density is constant and all vortices carry the same angular momenta, in the gas, vortices in very low density regions have negligible significance. Hence we ignore all vortices where the density curvature (calculated by finite difference) is less than a predefined value (typically 10^{-3}).

2.1 Overview of Behaviour

Specific cases will be presented in subsequent sections, but it is useful to survey the main overall trends that we have found. At low stirring speeds, no vortices form in the 'visible' region of the condensate. For fast stirring speeds, numerous vortices are generated, typically at the visible edge of the condensate, or in other low density regions that form during stirring. In the fast stirring case the behaviour can be very complex, with vortices moving in complicated trajectories, and pairs of opposite circulation annihilating during close encounters [16]. However, a regime of simply characterised behaviour emerges at intermediate stirring speeds, in which a single vortex forms at the edge of the condensate and is drawn towards the centre, before cycling back to the edge. Perhaps counterintuitively, neither the linear speed of the stirrer, nor the value of the local speed of sound of condensate near the stirrer appears to be of particular significance. The nonlinearity, parameterised via C, plays a role but not a crucial one: in the linear case ($C = 0$) vortices can form or remain absent. The key parameter is the angular stirring speed ω_f. For a given value of C we find that there is a *critical angular speed* ω_c below which the system operates in a 'single vortex' regime. When $\omega_f = \omega_c$ the single vortex is drawn right to the centre of the condensate, and for $\omega_f > \omega_c$ multiple vortices form. It turns out that the critical angular frequency (in our dimensionless units) is predicted with very good accuracy as the difference between the energy of the first excited vortex state of condensate E_v and the energy of the ground state E_g. In the next section we present a simple model which explains these features, and shows that the trap, with its well separated energy levels, plays a central role in the system dynamics and gives rise to behaviour that is qualitatively distinct from that of the homogeneous case studied in the context of He II.

3 The Single Vortex Regime

The main features of the single vortex regime are illustrated in the two dimensional simulation shown in Fig. 1 where evolution of the condensate during stirring is shown as a sequence of subfigures. We see a single vortex appear first at the edge of the visible region of the condensate, then cycle between the edge and the centre. The accompanying phase plots in Fig. 1 confirm that the feature is indeed a vortex. The amplitude of the cycling is reduced as the stirring frequency is reduced below the critical speed, and even at the critical speed, the cycling amplitude may be small if the stirring potential is too small or located too far from the centre of the condensate. A quantitative measure of the cycling amplitude can be obtained by plotting $\langle L_z \rangle$, the (dimensionless) angular momentum expectation value, as a function of time. We show in Fig. 2 the case corresponding to Fig. 1, plotted as a solid line. When the vortex reaches the centre of the condensate $\langle L_z \rangle$ takes the value 1. Stirring above the critical angular speed causes additional vortices to appear and $\langle L_z \rangle$ periodically exceeds 1 as shown with the narrow line in Fig. 2. In the corresponding simulation (not shown) two vortices are eventually formed in the condensate, and at $t > 40$ these vortices develop a regular oscillation which is echoed in $\langle L_z \rangle$.

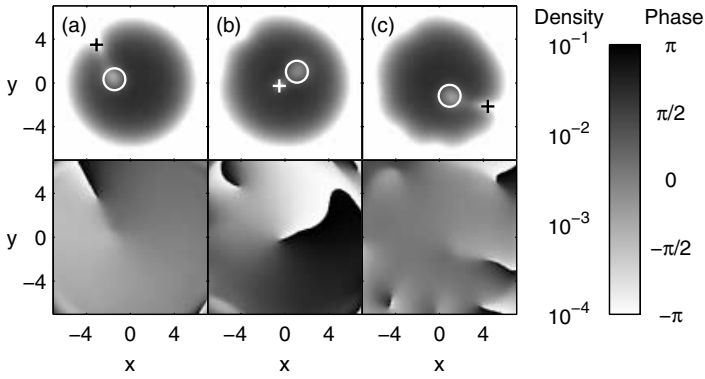

Fig. 1. Probability density (top row) and phase of ψ (bottom row) for a sequence of states for a two-dimensional condensate stirred from rest as described in the text. In (**a**) $t = 7.29$, (**b**) $t = 17.59$, and (**c**) $t = 29.15$. The vortex, which has positive circulation, is marked with a + sign. The circle denotes the stirrer. Parameters are $C = 200$, $\omega_f = 0.4$, $\rho_s = 1.5$, $W_0 = 10$, and $w_s = 2$

Our simulations show that the critical angular speed reduces as C increases, and we plot in Fig. 3 the values of ω_c found for different values of C. On the same graph we show the difference in energy between the first excited vortex and the ground states, $E_v - E_g$ for a various values of C.

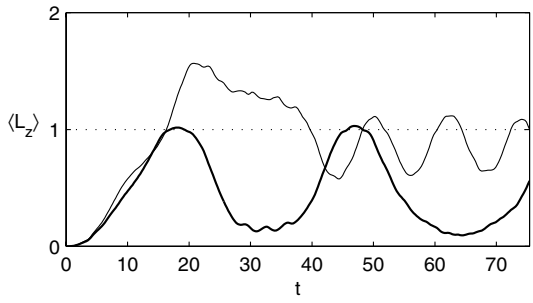

Fig. 2. Angular momentum expectation value versus time for $\omega_f = 0.4$ (thick line), $\omega_f = 0.45$ (thin line). Other parameters as in Fig. 1

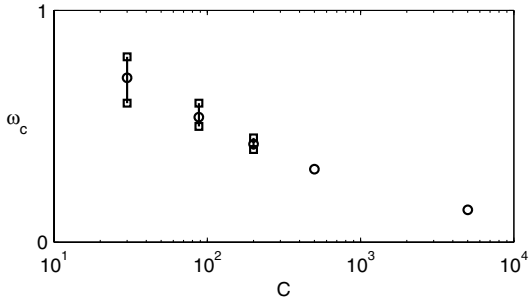

Fig. 3. Critical angular frequencies as a function of C. The squares give bounds for ω_c found from simulations. The circles give the values $E_v - E_g$

3.1 Formalism for a Nonlinear Two-State Model

The single-vortex behaviour can be understood quantitatively in terms of a nonlinear 'two-state' model, which has a formal similarity to the Rabi cycling model familiar from quantum optics, or the Josephson model familiar in condensed matter physics. The essential idea is that the stirring potential causes the condensate to cycle between the ground and first vortex state, analogous to the Rabi cycling of an atom between the ground and excited level in the presence of a light field. However, the model has additional complexity compared to the case familiar from linear quantum mechanics. The 'basis' states are modified by their nonlinear self and mutual interaction [the term containing C in (1)], and thus the appropriate basis states vary according to the vortex fraction. We make the ansatz that the condensate wavefunction can be decomposed onto a basis of an axially symmetric part ϕ_s (ground-state-like) and a vortex part ϕ_v (axially symmetric with an anticlockwise phase circulation), according to

$$\psi(\mathbf{r}, t) = a_s(t)\phi_s(\rho, n_v) + a_v(t)\phi_v(\rho, n_v)e^{i\theta} \; . \tag{3}$$

Here $n_v = |a_v|^2$ is the fraction of the condensate in the vortex component, and ρ and θ are the cylindrical polar components of $\mathbf{r}$. We have chosen (3) to represent the two-dimensional case, and we present the formal development of the model in this geometry. However, we illustrate in Sect. 4 with three-dimensional simulations that the two-state concept does provide the

framework for a quantitative understanding of single-vortex dynamics, even in the three dimensional case. The functions $\phi_s(\rho, n_v)$ and $\phi_v(\rho, n_v)$ are real valued, nonnegative, and normalised as $\int \phi_\sigma^2 d\mathbf{r} = 1$, (here σ represents either s or v) and their form depends on their relative weighting via n_v. The eigenfunctions ϕ_s and $\phi_v e^{i\theta}$ are automatically orthogonal and are found as the lowest energy coupled eigenstates for the coupled time-independent radial GP equations

$$\mu_s \phi_s = \left[-\frac{1}{\rho}\frac{d}{d\rho}\left(\rho \frac{d}{d\rho}\right) + \frac{\rho^2}{4} + C\left(n_s\phi_s^2 + 2F n_v \phi_v^2\right)\right]\phi_s \ , \tag{4a}$$

$$\mu_v \phi_v = \left[-\frac{1}{\rho}\frac{d}{d\rho}\left(\rho \frac{d}{d\rho}\right) + \frac{1}{\rho^2} + \frac{\rho^2}{4} + C\left(n_v\phi_v^2 + 2F n_s \phi_s^2\right)\right]\phi_v \ , \tag{4b}$$

where $n_s = 1 - n_v$. The eigenvalues $\mu_s(n_v)$ and $\mu_v(n_v)$ are obtained along with their eigenfunctions by solving (1.4) for a particular value of n_v. The parameter F is a constant which in principle is equal to one, but we have introduced it as an adjustable parameter to improve quantitative agreement, as we discuss further below. The superposition (3) produces a condensate with angular momentum expectation value $\langle L_z \rangle = n_v$, and a vortex whose distance from the centre of the trap decreases as $n_v \to 1$. Figure 4 illustrates how the functions ϕ_s and ϕ_v vary as the vortex fraction increases. The mutual repulsion between the vortex and the symmetric state is enhanced by a factor of 2 compared to the self repulsion, so that the vortex and symmetric states tend to separate.

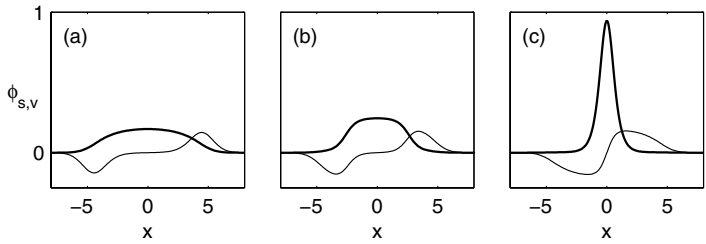

Fig. 4. The eigenstates ϕ_s (thick line) and $\phi_v e^{i\theta}$ (thin line) for vortex fractions (**a**) $n_v = 0$, (**b**) $n_v = 0.5$, (**c**) $n_v = 1$. The eigenstates are for the two-dimensional case with $C = 200$, and we have plotted a slice along the x axis

The ansatz of (3) allows us to recast the full GPE (1) into a suggestive form. Using the method outlined in [13] and writing $\tilde{a}_s = a_s e^{i\alpha_s}$ and $\tilde{a}_v = a_v e^{i(\alpha_s + \omega_f t)}$, where $\alpha_s(t) = \int_0^t \mu_s(t')dt'$, and transforming to a frame which rotates with the stirring potential we obtain the equations

$$\frac{d\tilde{a}_s}{dt} = -i\delta_s(n_v)\tilde{a}_s - \frac{i}{2}\Omega(n_v)\tilde{a}_v \ , \tag{5a}$$

$$\frac{d\tilde{a}_v}{dt} = -i[\Delta(n_v) + \delta_v(n_v)]\tilde{a}_v - \frac{i}{2}\Omega^*(n_v)\tilde{a}_s \ . \tag{5b}$$

Here $\Delta(n_v) = \mu_v(n_v) - \mu_s(n_v) - \omega_f$ and,

$$\delta_\sigma(n_v) = \int \phi_\sigma(n_v)W'(\mathbf{r})\phi_\sigma(n_v)d\mathbf{r} \ , \tag{6a}$$

$$\Omega(n_v) = 2\int \phi_s(n_v)W'(\mathbf{r})\phi_v(n_v)e^{i\theta}d\mathbf{r} \ . \tag{6b}$$

3.2 Interpretation of Coherent Cycling

Equations (1.5) are nonlinear, but as we have shown previously [13], with some care they can accurately reproduce the results of single vortex cycling. The value of (1.5) is not so much that it provides another (numerical) means of solving the GPE, but that they have a formal resemblance to the well known linear Rabi equations [17] with Ω corresponding to the bare Rabi frequency, Δ the detuning, and δ_σ to the frequency shifts. We therefore recognise that the stirring potential couples and causes coherent cycling between the ground state and the first excited vortex state of the condensate in the harmonic trap, in a manner analogous to linear Rabi cycling. Although the nonlinearity of (1.5) means caution is required in applying certain results from the linear Rabi model to vortex cycling, energy conservation remains a valid and central part of the model. In the frame rotating with the stirrer the potential is static so the condensate energy in the rotating frame $E' = E - \omega_f\langle L_z\rangle$ is constant (E is the lab frame energy). The wavefunction evolution is thus constrained by the requirement to conserve E'. The implications of this on the system behaviour can be understood from Fig. 5, where the expectation value E' is plotted for the range of superposition states of (3), for two cases. In both Fig. 5(a) and (b) the frame rotation frequency is chosen to be the difference $E_v - E_g$ so that the energy E' is the same for the pure ground and pure vortex states. Figure 5(a) shows an energy barrier between the ground and vortex states which arises from the repulsive interaction of the condensate and prevents transitions from the ground to vortex states. Fig. 5(b) shows that the presence of the stirrer can distort the energy surface to permit constant E' paths along which a superposition of varying fractions of vortex and symmetric states can evolve. It is clear that for critical cycling (i.e. where the condensate transfers entirely to the first excited vortex state), the rotating frame energies of the ground and first vortex state must be equal, and including the level shifts we obtain the equation for the critical frequency

$$\omega_c = E_v - E_g + \delta_v(1) - \delta_s(0) \ . \tag{7}$$

Of course complete cycling will not occur unless the stirrer potential overlaps sufficiently with the ground and vortex states that the energy surface distorts enough to allow a constant E' path from the ground to the vortex state. The

energy surface plots also help explain why the adjustable parameter F in (1.4) is needed to obtain quantitative agreement with the full time dependent GPE simulation. The basis set in (3) is not complete and thus leads to energy values which exceed the true energy, and in particular the energy barrier is exaggerated. Indeed we see in Fig. 5(b) that even with the stirrer present, the energy barrier is still too high to allow significant cycling out of the ground state. We have found that by setting $F \approx 0.8$, the solution to the cycling equations (1.5) very closely matches the full time dependent GPE.

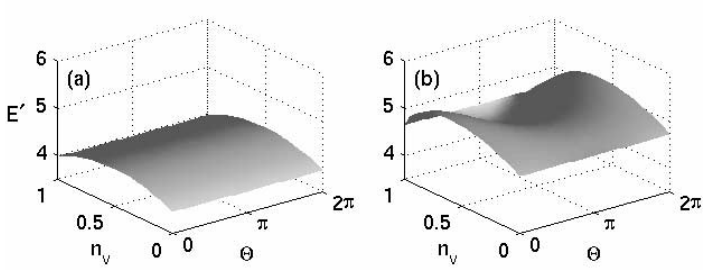

Fig. 5. Energy E' in the rotating frame as a function of the superposition state ψ. The horizontal axes are n_v the vortex fraction, and $\Theta = \mathrm{Arg}\{\tilde{a}_v/\tilde{a}_s\}$. In (**a**) there is no stirrer, while in (**b**) the stirrer is present. Parameters are $C = 200$, $\omega_f = 0.4$, $\rho_s = 1.5$, $W_0 = 10$, $w_s = 2$, and $F = 1$

4 Three-Dimensional Simulations

The underlying assumption in our two-state model is that the ground state is coupled primarily to the lowest energy vortex state, and all other couplings are much smaller. The two state model works well in 2D geometry, because the state closest in energy to the ground state is the first vortex state, and couplings to most of the other states nearby in energy are forbidden by symmetry considerations. The model begins to fail when ω_f exceeds ω_c (see Fig. 2) because more states are accessible at the corresponding energy E'.

In three dimensional cylindrically symmetric traps, many more condensate trap eigenstates exist, in either the oblate (pancake shaped; $\lambda > 1$) or prolate (cigar shaped; $\lambda < 1$) trap geometry. Nevertheless, energy and symmetry considerations may combine to restrict the coupling primarily to just the ground and first vortex states. We will consider here only the case of the oblate traps, which are realised in practice by TOP traps ($\lambda = \sqrt{8}$). We have carried out a number of simulations in this geometry and found that once again a regime of single vortex behaviour occurs. Figure 6 illustrates a vortex partway through its initial cycle to the centre, for a case corresponding to a condensate of about 10^4 atoms of ^{87}Rb with a laser stirrer of about 10

μm beam diameter. The hole that appears in the condensate is an almost vertical vortex line. The angular momentum cycles regularly between 0 and 1 as before, and the observed critical angular speed ω_c is very close to the prediction (7).

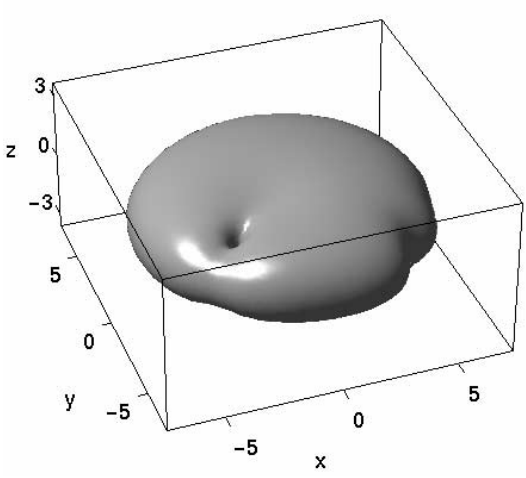

Fig. 6. Probability density isosurface at $|\psi|^2 = 10^{-4}$ for a three-dimensional condensate at $t = 13.82$, stirred as described in text. Parameters are $W_0 = 4$, $w_s = 4$, $\rho_s = 2$, $\omega_f = 0.3 < \omega_c = 0.323$, $C = 1000$, and $\lambda = \sqrt{8}$

We have also used our three dimensional simulations to investigate the question of vortex dynamical stability (which differs from thermodynamical stability [18]). Taking as the initial state the lowest energy $l = 1$ vortex, we insert then withdraw the stirring potential at a fixed position in the laboratory frame. We find that this rather vigorous perturbation causes significant oscillation of the condensate but the vortex line simply wobbles about a small region in the centre of the condensate. Our two state model provides an explanation for this dynamical stability. In the rotating frame (which now corresponds to the lab frame) the ground and vortex states are well separated in energy, and there can be little mixing.

5 Conclusion

We have found from two and three dimensional numerical simulations of the GPE that a regime of simple one-vortex behaviour occurs for a rotationally stirred condensate. The key parameter controlling the vortex dynamics is the *angular* stirring frequency, and we have shown that the underlying coherent dynamics can be understood in terms of a two state model.

Acknowledgments

We thank K. Burnett and P. B. Blakie for valuable contributions. This work was supported by The Marsden Fund of New Zealand under contract PVT603 and PVT902.

References

1. R.E. Packard, T.M. Sanders, Jr.: Phys. Rev. A **6**, 799 (1972)
2. D.R. Tilley, J. Tilley: *Superfluidity and Superconductivity*, 3rd edn. (Institute of Physics Publishing, Bristol 1990)
3. F. Dalfovo, S. Stringari: Phys. Rev. A **53**, 2477 (1996)
4. R.J. Dodd, K. Burnett, M. Edwards, C.W. Clark: Phys. Rev. A **56**, 587 (1997)
5. A.L. Fetter: J. Low Temp. Phys. **113**, 189 (1998)
6. D.A. Butts, D.S. Rokhsar: Nature **397**, 327 (1998)
7. B. Jackson, J.F. McCann, C.S. Adams: Phys. Rev. Lett. **80**, 3903 (1998)
8. K.-P. Marzlin, W. Zhang: Phys. Rev. A **57**, 4761 (1998)
9. E.L. Bolda, D.F. Walls: Phys. Rev. Lett. **81**, 5477 (1998)
10. M.R. Matthews *et al.*: Phys. Rev. Lett. **83**, 2498 (1999)
11. J.E. Williams, M.J. Holland: Nature **401**, 568 (1999)
12. K.W. Madison, F. Chevy, W. Wohlleben, J. Dalibard: Phys. Rev. Lett. **84**, 806 (2000)
13. B.M. Caradoc–Davies, R.J. Ballagh, K. Burnett: Phys. Rev. Lett. **83**, 895 (1999)
14. A.I. Safonov *et al.*: Phys. Rev. Lett. **81**, 4545 (1998)
15. C. Fox, R.J. Ballagh, A. Wall: in preparation
16. MPEG movies showing these results are available from: `<http://www.physics.otago.ac.nz/research/bec>`
17. L. Allen, J.H. Eberly: *Optical Resonance and Two-Level Atoms* (John Wiley and Sons, New York 1975)
18. D.S. Rokhsar: Phys. Rev. Lett. **79**, 2164 (1997)

Quasicondensate Droplet Formation in Hydrogen

Robin Côté

1 Introduction

Over the last few years, the experimental realization of Bose-Einstein condensation (BEC) in dilute alkali-metal atoms [1] and atomic hydrogen [2] has stimulated studies of the formation and evolution of condensates [3]. The kinetics of the condensate formation from a nonequilibrium initial state to a final coherent state has been explored in many systems [4], and particularly in dilute atomic gases [5,6]. Recently, effects of quasicondensates on the three-body recombination rate in a two-dimensional gas of atomic hydrogen have been observed [7]. The 1S-2S two-photon absorption lineshapes measured at MIT [2,8] show distortions that may originate from the formation of metastable quasicondensate droplets [9].

The formation of metastable condensates as a first step in atomic BEC has been discussed in several theoretical models [3,5,6]. Here, we develop a model based on a first-order phase transition treatment [9], and evaluate the effect of their existence on the 1S-2S lineshape under conditions similar to the experimental ones [2].

2 Review of the Experiment

The four hyperfine levels of the hydrogen 1S ground state exhibit the usual Zeeman splitting in the presence of a magnetic field (see Fig. 1). In the MIT experiment [2,8], a Ioffe-Pritchard magnetic trap is used to capture the purely spin-polarized d state [10], a low field seeker state (see Fig. 1). The cooling process starts by precooling the atoms to a temperature T of 0.5 K (the trap depth) or less via cryogenic techniques (no adequate light source exists for driving the 1S-2P transition at 121.6 nm, preventing laser cooling [10]). With such methods, the trapped atoms reach temperatures around 40 mK and density near 2×10^{13} cm^{-3}. The sample of cold atoms is located in the central low field trap created by strong magnetic fields at both ends of the apparatus (see Fig. 1). To cool further, evaporation over a magnetic saddlepoint at one end of the trap is used : temperatures close to 120 μK with densities near 6×10^{13} cm^{-3} are reached by this technique. To obtain lower temperatures still, rf evaporation is used [2]: the hotter atoms are ejected by

H.J. Carmichael, R.J. Glauber, M.O. Scully (Eds.): LNP 561, pp. 28–40, 2001.

induced spin flip, and the remaining atoms thermalize to a lower T through elastic collisions. Although the total number of atoms is reduced, the density is increased (the total volume of the trap decreases more rapidly [2]): however, inelastic collisions limit the maximal densities reachable (e.g. dipolar decay or three body recombination). In 25 s of rf evaporation, the sample can cool from about 120 μK to about 30 μK, and be in the degenerate regime, with densities around 2×10^{14} cm^{-3}. The entire cooling process takes about 5 minutes. The final trap has an elongated cigar shape with a very tight radial confinement (corresponding to a frequency $\omega_\rho = 2\pi \times 3.90$ kHz) and a weaker axial confinement (with $\omega_z = 2\pi \times 10.2$ Hz).

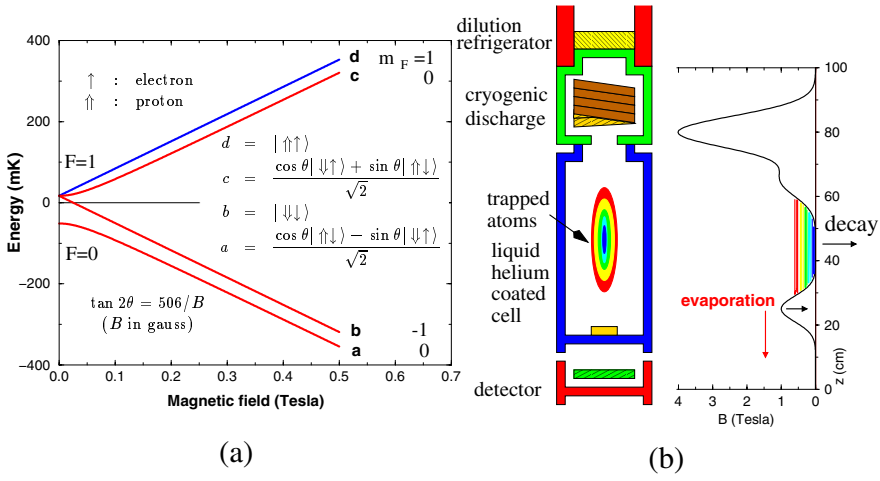

Fig. 1. Trapping low-field seekers: (**a**) the purely stretched spin-polarized state d of the 1S level (with $F = 1$ and $m_F = 1$) is a low field seeker state: it minimizes its energy by moving towards regions of lower magnetic field. Atoms in this state are trapped in the middle of the apparatus (**b**): by thermalizing with the helium-coated walls, they reach temperatures near 40 mK. To cool further, saddle and rf evaporation techniques are used (see text). Figures inspired from [10]

To detect the condensate, the MIT group uses high resolution spectroscopy, contrary to the alkali BEC's which rely on imaging techniques [1]. The temperature and the density distribution are measured via the two-photon spectroscopy of the 1S-2S transition [2]. Two 243 nm photons excite the 1S d state to the 2S state (metastable with lifetime of 122 ms). Once the laser pulse (lasting typically $\sim$ 400 μs) has been applied, the 2S state is Stark mixed to the 2P state by an electric field pulse (duration $\sim$ 12 μs) after a short time delay ($\sim$ 150 μs): the 2P state decays rapidly (lifetime of 1.6 ns) by spontaneous emission (see Fig. 2). The Lyman-alpha photons emitted are detected at the base of the apparatus. Due to the small solid angle of the detector ($\sim 2 \times 10^{-2}$ sr.), the number of photons detected represents a small

fraction of the total amount of photons emitted (about 10^{-5} [2,10]). This sequence, from firing the laser to detecting the photons, is repeated 10-100 times for a given frequency of the two photons: the delay between two successive sequences is typically 800 μs, giving a measurement time of 40 ms for 50 repetitions.

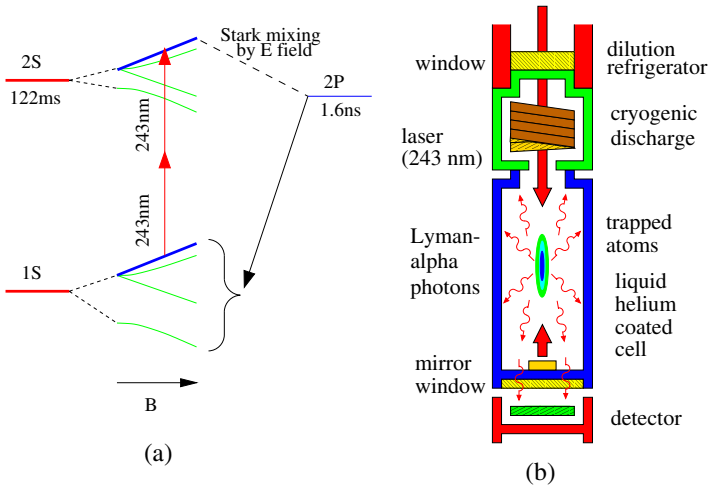

Fig. 2. Detection scheme: (**a**) trapped $F = 1$, $m_F = 1$ 1S atoms are excited to the metastable $F = 1$, $m_F = 1$ 2S state by absorption of two 243 nm photons. An applied electric field Stark mixes some 2P character and causes prompt radiative decay into all the m_F sublevels of 1S through emission of a single Lyman-alpha photon (121.6 nm). 1S and 2S $F = 1, m_F = 1$ atoms see the same magnetic trapping potential. A small mirror reflects the 243 nm laser to allow Doppler free absorption (**b**). The Lyman-alpha photons are detected by a microchannel plate at the bottom of the apparatus. Figures inspired from [10]

The 1S-2S two-photon absorption frequency is sensitive to the local density. A frequency shift, due essentially to elastic collisions, has been evaluated by Jamieson et al. [11]. In the ultralow temperature limit, it takes the form

$$\Delta\nu_{1S-2S} = (a_{1S-2S} - a_{1S-1S})\,\frac{hn}{\pi m} = \alpha n\,, \tag{1}$$

where m is the mass of the atoms, a_{1S-1S} and a_{1S-2S} are the scattering lengths between atoms in the 1S state with atoms in the 1S and 2S state, respectively, and n is the density of the 1S atoms (see Fig. 3). The measured value of α [8] is in good agreement with the predicted value [11]: $-3.8 \pm 0.8 \times 10^{-10}$ Hz cm^3 and -3.0×10^{-10} Hz cm^3, respectively. Atoms located in regions of higher densities will make the 1S-2S transition at a frequency more red detuned than atoms in regions of lower densities: the density profile in

the trap can be obtained by varying the frequency $\nu_{243\,\mathrm{nm}}$ of the two-photon beam.

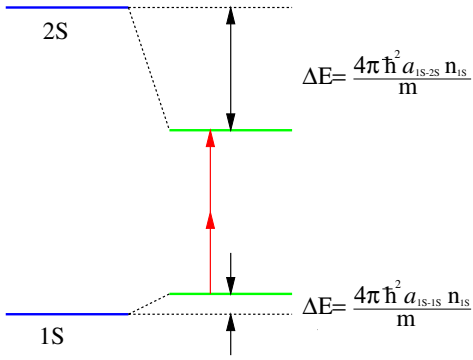

Fig. 3. $\Delta\nu_{1S-2S}$ can be calculated from the mean field energy ΔE. Few 2S atoms are created: 2S-2S interactions can be neglected. The shift of the 1S level is proportional to $a_{1S-1S} = 1.2a_0$ and the density of the surrounding atoms (basically n_{1S}). For the 2S level, ΔE is given to first order by $a_{1S-2S} = -43a_0$ [11] and n_{1S}. $\Delta\nu_{1S-2S}$ is negative: the positive 1S shift is much smaller than the negative 2S shift

The two-photon absorption can take place with two co-propagating or two counter-propagating photons: in the first case, the absorption will depend on the velocity of the atom (Doppler sensitive), and in the second case, it will not (Doppler free). In Fig. 4, a composite plot of the two types of signals is presented. As the temperature decreases and the density increases, the system comes closer to the BEC conditions (Fig. 4(a)). Away from the transition line, only the Doppler free and Doppler sensitive signals of the normal gas (noncondensed) appear: the Doppler free is centered near zero detuning and is very sharp, and the Doppler sensitive is broadly distributed around the two-photon recoil value of 6.7 MHz (Fig. 4(b)). The Doppler broadening can be used to measure the absolute temperature of the sample [2]. When the sample is brought at the transition conditions, additional features appear in the spectrum, indicating the onset of BEC. The Doppler free normal and BEC signals are well separated: the density of the condensate is much larger than the normal gas, hence a larger frequency shift.

The Doppler free signal of the normal component for three different conditions is illustrated in Fig. 5. The three curves correspond to the three points shown in the phase space plot of Fig. 4(a), with temperatures of 120 μK, 53 μK, and 44 μK, respectively. In the first two cases, no BEC signals were observed, and both curves are symmetric, centered near the frequency corresponding to the shift at half the maximum density $n_g^{\max}$ of the normal gas in the trap. The third curve (at $T \sim 44$ μK) exhibits a strong asymmetry, with a long red detuned tail corresponding to normal gas densities larger than the peak density $n_g^{\max}$ in the trap: about 20-30% [2,12] of the atoms are contained in the tail. The tail extends to about -100 kHz and is well separated from the observed BEC signal centered near -750 kHz (see Fig. 4(b)). Notice that each data point requires ~ 40 ms (average of ~ 50 firing sequences), so that a full spectrum of 45 points is obtained in about 1.8 s.

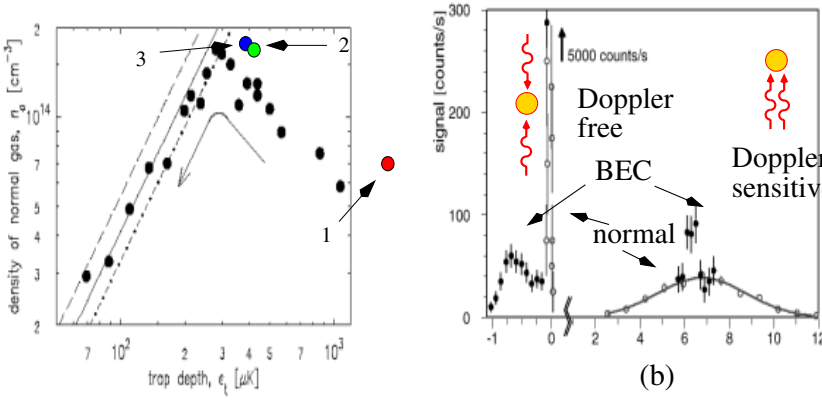

Fig. 4. Phase space plot of the normal (noncondensed) gas (**a**): each of these points correspond to different conditions at which spectra were obtained. The lines (dashed, solid, dot-dashed) indicate the BEC phase transition line, assuming a sample temperature of ($\frac{1}{5}$th, $\frac{1}{6}$th, $\frac{1}{7}$th) the trap depth. The points labelled 1, 2 and 3 represent systems far, near, and at the transition conditions. In (**b**), a composite spectrum shows the Doppler free and Doppler sensitive signals for the normal component ∘, and the corresponding BEC signals •. The BEC signal appears for $n_g^{\max} \simeq 1.8 \times 10^{14}$ cm^{-3} and $T \sim 50$ μK. Figures adapted from [2]

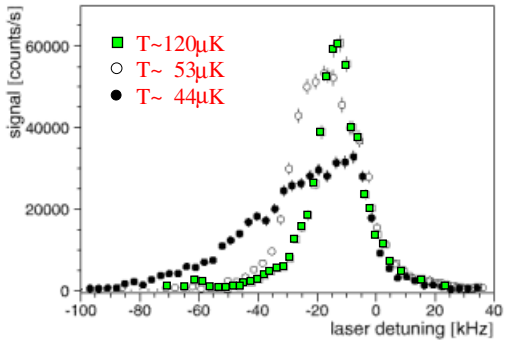

Fig. 5. Doppler free spectra for the normal component corresponding to conditions 1,2 and 3 of Fig.4(a). When transition conditions are reached, a long red detuned tail appears ($T \sim 44$ μK) that includes 20-30% of the total area of the spectrum. Figure adapted from [2]

3 Conditions in the Trap

A useful dimensionless parameter to describe the conditions in the trap is

$$\xi_g \equiv n_g \lambda^3 \qquad \text{with} \qquad \lambda = \sqrt{2\pi\hbar^2/mk_BT}\,, \tag{2}$$

where n_g is the gas density and λ is the thermal de Broglie wavelength for atoms of mass m at temperature T. ξ_g represents the number of atoms in the volume λ^3: if $\xi_g > 1$ more than one atom occupy the same volume, a sign of Bose-Einstein condensation. At the first stage of evaporative cooling, the temperature of the gas is high enough and the density low enough so that

the gas is in the dilute limit, i.e. $\xi_g \ll 1$. Under these conditions, the gas is well described by a Maxwellian distribution and thermalization is rather fast: it was shown by Snoke and Wolfe, and Luiten et al. [13], that only four collisions or so are necessary to reach a new equilibrium. In the experiment [2,10], rf evaporative cooling starts at $T \sim 100$ μK and $n_g \sim 3.6 \times 10^{13}$ cm^{-3}: the average speed is $v = \sqrt{8k_BT/\pi m} \sim 145$ cm/s, and the collision time $\tau_{\text{coll.}} = 1/8\pi a^2 n_g v \sim 0.2$ s. The system is dilute, with $\xi_g \sim 0.2$, and one can consider the system in equilibrium.

As T decreases and n_g increases, the trapped atoms "migrate" closer to the degenerate regime, and the system is not at equilibrium anymore. For $\xi_g \gtrsim 1$ simulations show that it takes between 50 to over 100 collisions to thermalize (see also Snoke and Wolfe, and Holland et al. [13]). At the onset of BEC, $T \sim 50$ μK and the average density $n_g \sim 1.1 \times 10^{14}$ cm^{-3} so that $v \sim 103$ cm/s. The collision time $\tau_{\text{coll.}} \sim 0.1$ s, which means that the system takes between 5.0 to 10.0 s to reach equilibrium. With the above conditions, $\xi_g \sim 1.6$, and although the collisional time is not very different than for the dilute case, the degenerate nature of the system changes its behavior.

During most of the measurements [14], the system is out of equilibrium, and the metastable gas can be described by a Boltzmann-like distribution [9,13]. Such a supercooled gas has a positive chemical potential whose fluctuations provide the nucleation conditions for the quasicondensate droplets [15]. Positive chemical potential has been used for the theoretical description of BEC by Gardiner, Zoller and co-workers [6]. A positive chemical potential describes the depopulation of low energy states: the lower states of the Bose-Einstein distribution are difficult to fill, and the distribution shows a Boltzmann-like character before equilibrium is reached [9,13].

4 The Model

Although interactions play an important role in thermalization, we explore here the case of an ideal gas, i.e. with the scattering length $a = 0$ (this is a good approximation for hydrogen, with $a = 1.2a_0$; see [9] for a treatment to first order in a). We consider a spherical quasicondensate droplet locally formed by density fluctuations within the metastable gas. The droplet radius R_d is determined by the local mechanical equilibrium conditions: the pressure induced by the quasicondensate droplet equals the external pressure of the surrounding normal gas [16]. We estimate the quantal pressure P_d in the droplets using a solvable model for the dependence of the droplet energy E_d on the droplet radius R_d. If we assume that the coherent wavefunction of the quasicondensate is localized inside a spherical region [17] and that the quasicondensate containing $\tilde{N}$ atoms of mass m is in its ground-state with entropy $S_d = 0$, we get

$$E_d = \tilde{N}\frac{\hbar^2\pi^2}{2mR_d^2} \quad \Longrightarrow \quad P_d = \frac{\hbar^2\pi}{4m}\frac{\tilde{N}}{R_d^5}\,, \tag{3}$$

where we used $P = -(\partial E/\partial V)_{\tilde{N},S}$ to get the droplet quantal pressure.

For the metastable bath gas with effective temperature T, the pressure is simply $P_g = n_g k_B T$, where $n_g = n_g(\boldsymbol{r})$ is the local normal gas density. Equating P_g and P_d, we obtain R_d as a function of $T, \tilde{N}$, and n_g:

$$R_d = \left(\frac{\hbar^2 \pi \tilde{N}}{4 m n_g k_B T}\right)^{1/5} = \lambda \left(\frac{\tilde{N}}{8\xi_g}\right)^{1/5} . \tag{4}$$

The density of the coherent phase inside a droplet is then simply

$$n_d \equiv \frac{3\tilde{N}}{4\pi R_d^3} = \frac{3 n_g}{\pi}\left(\frac{\tilde{N}}{\sqrt{2}\xi_g}\right)^{2/5} . \tag{5}$$

For large $\tilde{N}$, the droplet density is much larger than the surrounding normal gas density.

To determine the most probable number of atoms in a droplet, $\tilde{N}_d$, we follow a first-order phase transition treatment based on an activation energy similar to the phase nucleation of small droplets or bubbles in a metastable vapor-liquid system [18]. Small droplets ($\tilde{N} < \tilde{N}_d$) have large quantal energy and are dissolved back into the normal gas phase. We define an activation energy A as the difference between the free energies of the final and initial systems. For the initial system of total volume V made of N atoms in the normal gas phase, the free energy is simply $F_{\text{initial}} = F_g(N)$. In the final system, the appearance of one droplet containing $\tilde{N}$ atoms gives a free energy $F_{\text{final}} = F_g(N-\tilde{N}) + F_d(\tilde{N})$, where $F_d(\tilde{N})$ is the droplet free energy. Assuming that the number of atoms $\tilde{N}$ converted from the gas state to the coherent state is small, $\tilde{N} \ll N$, we expand $F_g(N-\tilde{N})$ and use the definition of the chemical potential for the normal gas $\mu_g \equiv (\partial F_g/\partial N)_{V,T}$ to obtain

$$A = F_d(\tilde{N}) - \tilde{N}\mu_g + \mathcal{O}(\tilde{N}/N) . \tag{6}$$

For an ideal gas, the chemical potential of the initial metastable gas phase is [19] $\mu_g = k_B T \ln \xi_g$, and the quasicondensate droplet free energy $F_d = E_d - TS_d$ is simply given by E_d (since $S_d = 0$). Thus the activation energy A becomes

$$A = \tilde{N}\frac{\hbar^2 \pi^2}{2 m R_d^2} - \tilde{N} k_B T \ln \xi_g , \tag{7}$$

where R_d is a function of $\tilde{N}$. In Fig. 6, A is shown as a function of $\tilde{N}$ for various conditions. The results from the treatment with $a = 1.2a_0$ [9] are also shown to illustrate the effect of a: interactions reduce the probability of formation of large size nascent droplets. The position $\tilde{N}_d$ of the maximum value of A is also illustrated in Fig 6. For $\tilde{N} < \tilde{N}_d$, the droplet will minimize its free energy by lowering $\tilde{N}$ until it disappears: such droplets are unstable and will vaporize back into the normal gas phase. Droplets with $\tilde{N} > \tilde{N}_d$ will

decrease their free energy by growing: they are stable [18]. The maximum of A gives a threshold value $A_{\rm th}$ which determines if a droplet is stable or not. This model is well behaved for $\xi_g > 1$: near the critical conditions for BEC for an ideal infinite homogeneous bosonic gas, $\xi_g = 2.612$.

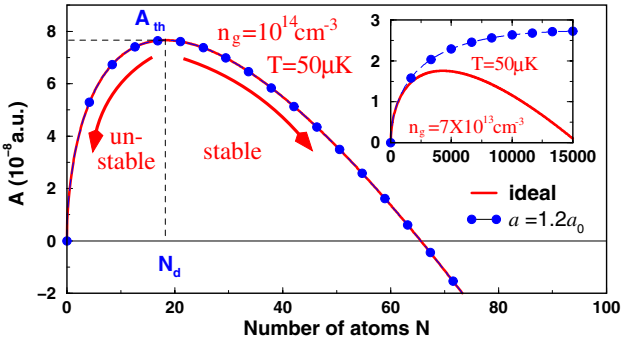

Fig. 6. Plot of A as a function of $\tilde{N}$ with and without interactions. The quantities $A_{\rm th}$ and $\tilde{N}_d$ regulate the stability of the droplets (see text). As shown in the inset, the activation energy is increased and the probability of droplet formation is reduced when the effect of repulsive interactions is considered. Adapted from [9]

Setting $dA/d\tilde{N} = 0$, we obtain $\tilde{N}_d$ and the corresponding $A_{\rm th}$

$$\tilde{N}_d = \left(\frac{3\pi}{5}\right)^{5/2} \frac{\xi_g}{4} \left[\ln \xi_g\right]^{-5/2} \quad \text{and} \quad \frac{A_{\rm th}}{k_B T} = \left(\frac{3\pi}{5}\right)^{5/2} \frac{\xi_g}{6} \left[\ln \xi_g\right]^{-3/2} . \quad (8)$$

The formation time τ_f of a droplet containing $\tilde{N}$ atoms can be estimated from the local density fluctuations via $\tau_f \sim \tau_g \tilde{N}^{1/2}$ [5,9], where $\tau_g^{-1} = 4\pi\hbar a n_g/m$: with $a = 0$, we get an infinite formation time. Of course, although small, $a = 1.2a_0 \neq 0$ and with $n_g \sim 10^{14}$ cm^{-3} [2], we estimate $\tau_g = 200$ μs. Although density fluctuations in the normal gas may create droplets of any size, the smallest stable droplets containing $\tilde{N}_d$ atoms are formed faster than the larger ones. The probability of having a nascent droplet with $\tilde{N}_d$ is given by $P(\tilde{N}_d) \propto \exp(-A_{\rm th}/k_B T)$, and its density n_d by $n_d = 9n_g/10 \ln \xi_g$. For atomic hydrogen gas at $T = 50$ μK, there is no droplet phase for $n_g < 6.7 \times 10^{13}$ cm^{-3}, corresponding to $\xi_g < 1$.

5 Lineshape

To compare with experimental data, we find the effect of the droplet formation on the 1S-2S two-photon absorption lineshape. We are focussing our attention on the Doppler free lineshape only. The line profile is assumed to be due essentially to the local density shift $\Delta\nu_{1S-2S} = \alpha n(\boldsymbol{r})$, where

$\alpha = -3.8 \pm 0.8 \times 10^{-10}$ Hz cm^3 [8]. The line intensity at a given value of the 243 nm laser detuning $\nu \equiv \Delta\nu_{243\,\mathrm{nm}}$ is proportional to the number of atoms absorbing the two photons with a frequency shift $\Delta\nu_{1S-2S} = 2\nu = \alpha n_d$. The total number of atoms contained within droplets of density n_d is $\tilde{N}_d$ times the total number of droplets, assumed to be proportional to the probability $\exp(-A_{\mathrm{th}}/k_BT)$ of being formed. The droplet contribution to the line profile is therefore

$$I_d(n_g) = I_d^0 \tilde{N}_d(n_g) \exp\left(-\frac{A_{\mathrm{th}}(n_g)}{k_BT}\right) , \tag{9}$$

where I_d^0 is a normalization constant. Since the gas density n_g varies within the trap, the Doppler free line profile as a function of $\nu = \Delta\nu_{1S-2S}/2$ is

$$I_d(\nu) = \int_{n_{\min}}^{n_0} dn_g p(n_g) I_d(n_g) \delta[2\nu - \alpha n_d(n_g)] , \tag{10}$$

where $n_{\min} = \lambda^{-3}$ corresponds to $\xi_g = 1$. Here, $p(n_g)$ is the probability of having a local density of n_g in the line of sight of the laser beams, and it is given by

$$p(n_g) \equiv \frac{1}{N_g} \int d^3r\; n(\boldsymbol{r}) P_L(\boldsymbol{r}) \delta[n_g - n(\boldsymbol{r})] , \tag{11}$$

where N_g is the total number of atoms in the normal gas phase, and $P_L(\boldsymbol{r})$ is the laser intensity profile which depends on the geometry (see Fig. 7). For two-photon absorption of counter-propagating laser beams, $P_L(\boldsymbol{r}) = I_L^2(\boldsymbol{r})/I_0^2$, with axial symmetry [2,8] such that $I_L(\boldsymbol{r}) = I_L(\rho) = I_0 \exp(-\rho^2/2\sigma_L^2)$, where σ_L is the laser intensity half-width and I_0 its intensity. The spatial density distribution of a gas described by a Maxwell-Boltzmann distribution in a harmonic trap corresponds to a Gaussian distribution. For the normal gas density, we consider $n(\boldsymbol{r})$ to be Gaussian with axial symmetry [20]

$$n(\boldsymbol{r}) = n(\rho, z) = n_0 \exp\left[-\frac{m}{2k_BT}\left(\omega_\rho^2\rho^2 + \omega_z^2 z^2\right)\right] , \tag{12}$$

with the maximum density n_0 given by $n_0 = N_g(m/2\pi k_BT)^{3/2}\omega_\rho^2\omega_z = 1.8 \times 10^{14}$ cm^{-3} [2]. The probability $p(n_g)$ becomes

$$p(n_g) = \frac{2}{\sqrt{\pi}} \frac{1}{n_0} \left(\frac{n_g}{n_0}\right)^\beta \sqrt{\ln\left(\frac{n_0}{n_g}\right)} , \tag{13}$$

where $n_g < n_0$, and $\beta = 1/3$ for the MIT experiment [21]. In Fig. 8, we illustrate $I_d(n_g)/I_d^0$ as well as $p(n_g)$ and $p(n_g)I_d(n_g)/I_d^0$ for an ideal gas.

Similarly, the normal gas line profile is given by [9]

$$\begin{aligned} I_g(\nu) &= I_g^0 \int_0^{n_0} dn_g p(n_g) \delta(2\nu - \alpha n_g) , \\ &= \frac{I_g^0}{|\alpha|} \left(\frac{2\nu}{\alpha}\right)^\beta \frac{2}{\sqrt{\pi}} \frac{1}{n_0} \sqrt{\ln\left(\frac{\alpha n_0}{2\nu}\right)} . \end{aligned} \tag{14}$$

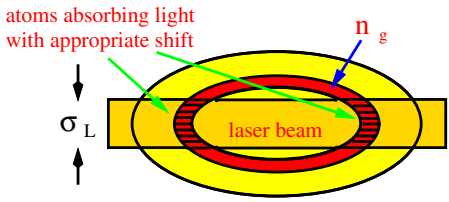

Fig. 7. Geometry of the laser and the trap: the atoms absorbing the two photons frequency shifted by ν are located in a shell of the Gaussian density profile corresponding to n_g, and in the line of sight of the laser beam of width $\sigma_L \sim 50\ \mu$m

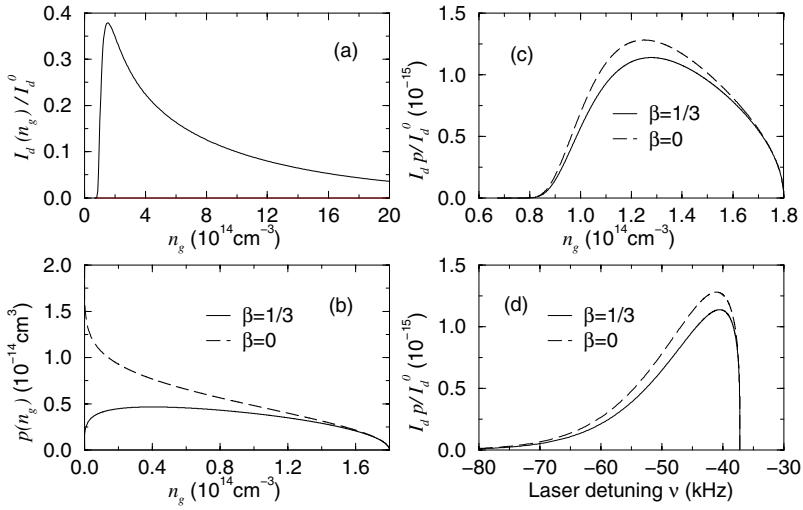

Fig. 8. Plot of (**a**) $I_d(n_g)/I_d^0$, (**b**) $p(n_g)$, and (**c**) $p(n_g)I_d(n_g)/I_d^0$ as a function of n_g for $n_0 = 1.8 \times 10^{14}$ cm^{-3} and $T = 50\ \mu$K: $p(n_g)$ cuts the long tail of $I_d(n_g)/I_d^0$. (**d**) shows the same as (c) but as a function of the laser detuning ν. In (b)-(d) we give the curves for two values of β corresponding to the actual experiment geometry ($\beta = 1/3$) and the case of a uniform laser intensity ($\beta = 0$). Adapted from [9]

The laser detuning ν is limited to values between 0 and $\alpha n_0/2$. In Fig. 9, we show the contribution of the normal gas and quasicondensate droplet phases to the line profile of an ideal gas corresponding to the experimental conditions [2]. The normal line alone cannot reproduce the experimental curve: the droplet line contribution gives rise to a long tail at large detunings as well as a shoulder. The large asymmetry measured in the Doppler-free normal gas lineshape is well reproduced by the model, and the experiment [2] provides a strong evidence of quasicondensate formation.

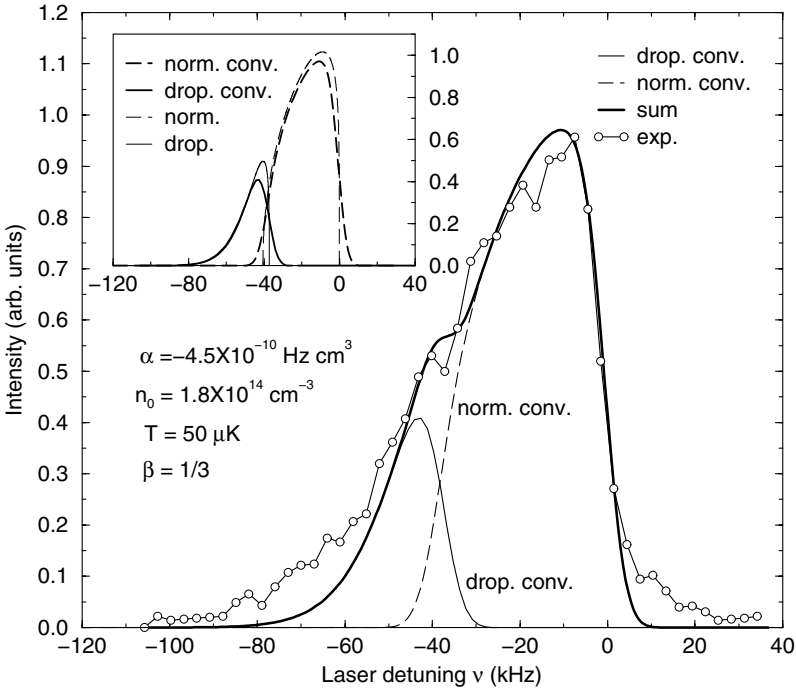

Fig. 9. Plot of $I_d(\nu)$ and $I_g(\nu)$ as a function of ν for an ideal gas with $\beta = 1/3$. The normal and droplet lines have been convoluted with a Gaussian of 3kHz width (corresponding to the experimental frequency step). The sum of those two lines is compared to the experimental signal [2]. The inset shows the same lines with and without convolution. Adapted from [9]

6 Conclusion

The model described here is based on simple ideas. Thermalization is slow near transition conditions (small a) and the gas is out of equilibrium. Such a metastable gas can be described by a Boltzmann-like distribution, and fluctuations of the resulting positive chemical potential provide the nucleation condition for metastable quasicondensate droplets. Local mechanical equilibrium sets the properties of the droplets.

However, for small droplets with $R_d \sim \lambda$, the spherical box approximation should be relaxed to allow the coherent wavefunction to penetrate the walls: pressure and droplet density would decrease. Such corrections could bring the lineshape in even better agreement with the experimental one. Other mechanisms may prove important to explain the wings (both red and blue) of the experimental spectra, like decays in the population of 2S atoms (e.g. ionization due to 2S-2S collisions). Rates for such processes are not known in the ultracold regime.

Because the data were taken over a period of a second [12], growth and decay of the metastable droplets may play an important role in explaining the large spread of the measured line. However, since the time-evolution of the droplet line is slow (it can be observed for many seconds [12]), the static model presented here should be broadly applicable. A more thorough study, including the role of interactions, and the time-evolution of the droplets, should help in the design of experiments to determine the detailed properties of the droplets.

Finally, the quasicondensate droplets discussed here are metastable. They exist because the system is out of equilibrium. When equilibrium will be reached, the gas will follow the Bose-Einstein distribution: the chemical potential will no longer be positive, and the droplets will have vaporized back into the normal gas or coalesce with the main central condensate.

Acknowlegments

The author gratefully acknowledges helpful discussions with V. Kharchenko, A. Dalgarno, D. Kleppner, T.J. Greytak, T.C. Killian, D.G. Fried, L. Willmann, D. Landhuis, and S.C. Moss. The work was supported by the National Science Foundation through the Grant PHY-9970757.

References

1. K.B. Davis *et al.*: Phys. Rev. Lett. **75**, 3969 (1995); M.H. Anderson *et al.*: Science **269**, 198 (1995); C.C. Bradley *et al.*: Phys. Rev. Lett **75**, 1687 (1995)
2. D.G. Fried *et al.*: Phys. Rev. Lett. **81**, 3811 (1998)
3. E. Levich, V. Yakhot: J. Low Temp. Phys. **27**, 107 (1977); Phys. Rev. B **15**, 243 (1977); J. Phys. A **11**, 2237 (1978); H.T.C. Stoof: Phys. Rev. Lett. **66**, 3148 (1991); Phys. Rev. A **49**, 3824 (1994); Phys. Rev. Lett. **78**, 768 (1997); D.W. Snoke, J.P. Wolfe: Phys. Rev. B **39**, 4030 (1989); D.V. Semikov, I.I. Tkachev: Phys. Rev. Lett. **74**, 3093 (1995); K. Damle, S.N. Majumdar, S. Sachdev: Phys. Rev. A **54**, 5037 (1996)
4. C. Josserand, S. Rica: Phys. Rev. Lett. **78**, 1215 (1997); L.M. Smith, V. Yakhot: Phys. Rev. Lett. **71**, 352 (1993); W. Zhao, P. Stenuis, A. Imamoğlu: Phys. Rev. B **56**, 5306 (1997)
5. Yu.M. Kagan, B.V. Svistunov, G.V. Shlyapnikov: Sov. Phys. JETP **74**, 279 (1992); Sov. Phys. JETP **75**, 387 (1992); Yu. Kagan., B.V. Svistunov: Sov. Phys. JETP **78**, 187 (1994); Phys. Rev. Lett. **79**, 3331 (1997); Yu. Kagan: *Bose-Einstein Condensation*, p. 202, ed. by A. Griffin, D.W. Snoke, S. Stringari (Cambridge University Press, Cambridge 1995)
6. C.W. Gardiner *et al.*: Phys. Rev. Lett. **79**, 1793 (1997); C.W. Gardiner *et al.*: Phys. Rev. Lett. **81**, 5266 (1998)
7. A.I. Safonov *et al.*: Phys. Rev. Lett. **81**, 4545 (1998)
8. T.C. Killian *et al.*: Phys. Rev. Lett. **81**, 3807 (1998)
9. R. Côté, V. Kharchenko: Phys. Rev. Lett. **83**, 2100 (1999)

10. T.C. Killian: 1S-2S Spectroscopy of Trapped Hydrogen: The Cold Collision Frequency Shift and Studies of BEC, Ph.D. thesis, MIT, Cambridge (1999); D.G. Fried: Bose-Einstein Condensation in Atomic Hydrogen, Ph.D. thesis, MIT, Cambridge (1999)
11. M.J. Jamieson, A. Dalgarno, J.M. Doyle: Mol. Phys. **87**, 817 (1996)
12. D. Kleppner, T. Greytak et al. (private communication)
13. D.W. Snoke, J.P. Wolfe: Phys. Rev. B **39**, 4030 (1989); O.J. Luiten, M.W. Reynolds, J.T.M. Walraven: Phys. Rev. A **53**, 381 (1996); M. Holland, J. Williams, J. Cooper: Phys. Rev. A **55**, 3670 (1997)
14. It takes over 1 s to obtain the Doppler-free normal line spectrum, and the central condensate can be detected for about 5 s [12].
15. Spatial density fluctuations of the metastable gas create fluctuations of the value of the positive chemical potential, which can be seen as an internal random potential for the single particle atomic wavefunction in the non-linear equation.
16. The nascent coherent phase, while attempting to spread throughout the trap, will interact with the surrounding thermal atoms, and its wave function final size will be attained as local equilibrium is reached.
17. The surrounding normal gas restricts the coherent wavefunction spatial extension. If the infinite wall constraint is relaxed, the quasicondensate wavefunction penetrates the walls, and pressure and droplet density decrease.
18. E.M. Lifshitz, L.P. Pitaevskii: *Physical Kinetics, Course of Theroretical Physics*, Vol.10, by L.D. Landau, E.M. Lifshitz (Pergamon Press, New York 1981)
19. The expression for μ_g is valid even for nonequilibrium systems: see L.D. Landau, E.M. Lifshitz: *Statistical Physics* (Pergamon Press, New York 1980)
20. We adopt the Gaussian density profile describing the system before it reaches BEC conditions: because thermalization is slow, we assume that the density profile remains constant during the measurement of the spectrum.
21. This functional dependence is valid for σ_L larger than the equivalent width of the normal gas distribution. For $T = 50$ μK, $n_0 = 1.8 \times 10^{14}$ cm^{-3} and $\sigma_L = 50$ μm, $\beta = 1/3$: this value varies with T, n_0 and σ_L. If the laser intensity is spatially constant (or $\sigma_L \to \infty$), $\beta = 0$.

Polarization Decay in a BCS Paired Fermi Gas

Bereket Berhane and T.A.B. Kennedy

Summary. A trapped gas of atomic fermions is polarized by an incident laser pulse. The induced polarization decays through emission of radiation. The radiative coupling of the atoms, and the angular distribution of radiation is shown to be sensitive to the interactions between the fermions, including anomalous pair correlations which characterize the superfluid state.

1 Introduction

Trapped atomic gases provide exciting opportunities for the observation of quantum many body effects with weakly interacting neutral particles. Following successful experiments with bosonic atoms [1], there is now a drive to observe related quantum statistical signatures with atomic fermions [2]. These include the possibility for observation of Cooper pairing of a mixture of two hyperfine states of a Fermi gas [3]. In contrast to Bose Einstein condensation, the change in density and momentum distribution of Cooper paired atomic fermions is predicted to be very small [4]. Recently, a number of proposals for the detection of Cooper pairing in these vapors via optical interactions have been put forward. These include the effect of pairing on the lineshapes in a superfluid Fermi gas [5], off-resonant light scattering [6,7], and resonant light induced tunneling [8].

In this paper we investigate the decay of a polarized Fermi gas induced by a short light pulse. In contrast to the earlier theoretical work on optical signatures of BCS pairing, we include spontaneous emission and reabsorption of radiation within the trapped vapor in our model. We calculate the radiation emitted as the collective polarization of the trapped vapor decays, and discuss its sensitivity to the presence of BCS pairing of atomic fermions in different hyperfine ground states.

The paper is organised as follows. In section 1 we give a general description of the theoretical model. In section 2 we show how the scattered field depends on the matter polarization and compute the polarization induced by a short laser pulse using linear response theory. The decay in time of this polarization is computed via master equation methods, and shown to depend on various many body correlations, including the anomalous pair correlation which characterizes the superfluid state. In section 3 we illustrate the

H.J. Carmichael, R.J. Glauber, M.O. Scully (Eds.): LNP 561, pp. 41–49, 2001.

angular radiation intensity distribution, and its dependence on pairing. Our conclusions are given in section 4.

2 General Description of the Model

We consider the resonant interaction of a short laser light pulse with a degenerate trapped atomic Fermi gas. The atoms are modeled as two level systems with ground and excited state angular momenta J_g and J_e, respectively, and atomic transition energy $\hbar\omega_A$. The interaction between the atoms and the electromagnetic field, in the dipole approximation, is given by

$$H_I = -\frac{1}{\varepsilon_0}\int d^3r \hat{\mathbf{D}}(\mathbf{r})\cdot\hat{\mathbf{P}}(\mathbf{r}) \tag{1}$$

where $\hat{\mathbf{D}}(\mathbf{r})$ is the electric displacement operator, and $\hat{\mathbf{P}}(\mathbf{r}) = \hat{\mathbf{P}}^{+}(\mathbf{r}) + H.c.$ is the polarization density operator. The positive frequency component of the latter can be written

$$\mathbf{P}^{+}(\mathbf{r}) = \wp\sum_{Mn}\mathcal{C}_{M\ n}\mathbf{e}_{n-M}\Psi^{\dagger}_{gM}(\mathbf{r})\Psi_{en}(\mathbf{r}) \tag{2}$$

where, $\wp$ is the reduced dipole matrix element between the excited and ground atomic states, $\Psi^{\dagger}_{gM}(\mathbf{r})$ creates an atom in the electronic ground state $|g, M\rangle$ at position $\mathbf{r}$ and $\Psi_{en}(\mathbf{r})$ annihilates an atom in the electronic excited state $|e, n\rangle$ at position $\mathbf{r}$. These annihilation and creation operators satisfy the usual anticommutation relation for fermions. We have also used the shorthand $\mathcal{C}_{Mn} \equiv \langle J_g 1 J_e M n - M | J_g 1 J_e n\rangle$ for the Clebsh-Gordon coefficients, and as usual $\mathbf{e}_q$, $(q = -1, 0, 1)$, denotes a spherical unit vector. We note that the interaction Hamiltonian H_I includes the resonant dipole-dipole interaction between atoms.

To be specific, we will consider a harmonically trapped gas of ultracold atoms in a mixture of two hyperfine ground states, $|J_g = 1/2, M = \pm 1/2\rangle$ (the electronic excited state is chosen to have $J_e = 3/2$). Atoms in different hyperfine states interact via s-wave scattering, and such a system may exhibit Cooper pairing of the ground states, when the scattering length is negative [3]. The incident pulse is assumed to be linearly polarized in the z direction, and induces a polarization in the degenerate vapor. The polarization subsequently decays with the emission of light, to which we now turn our attention.

2.1 The Scattered Field

Using the Heisenberg equations for the electromagnetic field, the scattered field can be readily expressed in terms of the polarization density operator as follows [9],

$$\hat{\mathbf{E}}^{+}_{s}(\mathbf{r}, t) = \int d^3r' \mathbf{G}(\mathbf{r} - \mathbf{r}', k_A)\cdot\hat{\mathbf{P}}^{+}(\mathbf{r}', t). \tag{3}$$

Here $\mathbf{G}$ is the dyadic Green function for dipole radiation and $k_A = \omega_A/c$. In the far field ($k_A|\mathbf{r}-\mathbf{r}'| \gg 1$) it is given, including retardation, by

$$\mathbf{G}(\mathbf{r}-\mathbf{r}') \simeq \frac{k_A^3 e^{ik_A r}}{4\pi\epsilon_0 r}\left[1-\hat{\mathbf{k}}_s\hat{\mathbf{k}}_s\right] e^{-ik_A\hat{\mathbf{r}}\cdot\mathbf{r}'} \tag{4}$$

and, hence, the scattered electric field,

$$\hat{\mathbf{E}}_s^+(\mathbf{r},t) = \frac{k_A^3 e^{ik_A r}}{4\pi\epsilon_0 r}[\mathbf{1}-\hat{\mathbf{k}}_\mathbf{s}\hat{\mathbf{k}}_\mathbf{s}]\cdot\hat{\mathbf{P}}^+(\mathbf{k}_s,t), \tag{5}$$

where $\mathbf{k}_s = k_A\hat{\mathbf{r}}$, and

$$\hat{\mathbf{P}}^+(\mathbf{k}_s,t) = \wp\sum_q \mathbf{e}_q\hat{p}_q^+(\mathbf{k}_s,t) = \int d^3r' e^{-i\mathbf{k}_s\cdot\mathbf{r}'}\hat{\mathbf{P}}^+(\mathbf{r}',t) \tag{6}$$

is the spatial Fourier transform of the polarization density operator.

We note that a mean polarization of the atomic sample produces a mean scattered field. In this paper we will compute the contribution of this mean field to the angular distribution of intensity, ignoring the contributions due to light field fluctuations. The mean field contribution to the photon flux scattered in the direction $\hat{\mathbf{k}}_s$, and detected at position $\mathbf{r}$, is proportional to $|\langle\hat{\mathbf{E}}_s^+(\mathbf{r},t)\rangle|^2 = \sum_{\alpha=1,2} I_s(\mathbf{k}_s,\boldsymbol{\epsilon}_\alpha,t)$, where $\mathbf{k}_s$, $\boldsymbol{\epsilon}_1$ and $\boldsymbol{\epsilon}_2$ form a mutually orthogonal set. The contribution of the scattered field component polarized in the direction $\boldsymbol{\epsilon}_\alpha$, is given by

$$I_s(\mathbf{k}_s,\boldsymbol{\epsilon}_\alpha,t) = \left(\frac{3\Gamma_A}{4r}\right)^2\sum_q |(\boldsymbol{\epsilon}_\alpha\cdot\mathbf{e}_q)|^2\left|\left\langle\hat{p}_q^+(\mathbf{k}_s,t)\right\rangle\right|^2, \tag{7}$$

where we have introduced the single atom linewidth $\Gamma_A = \wp^2 k_A^3/3\hbar\epsilon_o\pi$.

2.2 Initial Polarization of the Trapped Vapor

The atomic sample is polarized by a short laser pulse, and subsequently decays with the emission of photons. In this section we use linear response theory to compute the initial quantum state of the polarized medium. We consider a classical laser pulse perturbation incident on the sample. The Hamiltonian can be divided into two parts, $\hat{H} = \hat{H}_0 + \hat{V}_{ext}(t)$, where $\hat{H}_0$ governs the dynamics in the absence of the perturbation potential which we denote by $\hat{V}_{ext}(t)$. For a system initially in the state $\rho(0)$, linear response theory gives that

$$\rho(t) = U_0(t,0)\rho(0)U_0^\dagger(t,0) + \frac{1}{i\hbar}U_0(t,0)\int_0^t dt'\left[\tilde{V}_{ext}(t'),\rho(0)\right]U_0^\dagger(t,0) \tag{8}$$

where $\tilde{V}_{ext}(t) = U_0^\dagger(t,0)\hat{V}_{ext}(t)U_0(t,0)$, and $U_0(t,0) = \exp\left\{-it\hat{H}_0/\hbar\right\}$ is the time evolution operator in the absence of the external laser field.

We assume the linearly polarized laser pulse (polarization vector $\hat{\varepsilon}_L$) has a duration $\tau \ll 1/\Gamma_A$ and $1/|\omega_L - \omega_A|$, wave vector $\mathbf{k}_L$, frequency ω_L and peak Rabi frequency Ω_L. Thus,

$$\tilde{V}_{ext}(t) = -i\hbar\Omega_L h(t)\left(e^{-i\omega_L t}\int d^3r \hat{\varepsilon}_L \cdot \tilde{\mathbf{P}}^-(\mathbf{r},t)e^{i\mathbf{k}_L\cdot\mathbf{r}} - H.c.\right) \tag{9}$$

where $h(t) = 1$ for $0 \leq t \leq \tau$ while it vanishes everywhere else. It is reasonable then to assume that the polarization operator evolves freely during this short time, so that

$$U_0^\dagger(t,0)\hat{\mathbf{P}}^-(\mathbf{r})U_0(t,0) \approx e^{i\omega_A t}\hat{\mathbf{P}}^-(\mathbf{r}),\ 0 < t < \tau. \tag{10}$$

With the above approximation, Eqn. (8) takes the form

$$\rho(t) = U_0(t,0)\rho(0)U_0^\dagger(t,0) + U_0(t,0)\rho_i U_0^\dagger(t,0), \tag{11}$$

where

$$\rho_i = \frac{\tau\Omega_L}{\wp}\hat{\varepsilon}_L \cdot \hat{\mathbf{P}}^-(\mathbf{k}_L)\rho(0) + H.c. \tag{12}$$

The latter equation also holds if we replace the density operators on both sides by the corresponding reduced atomic density operators, $\rho_A = Tr_{rad}\rho$, as is easily seen by tracing over the radiation field degrees of freedom. The first term on the RHS of (11) describes the time evolution of the system without the perturbation, while the second term gives the linear response due to the induced polarization. This contributes to the mean polarization of the sample, and, as we shall see, produces a non-trivial angular distribution of radiation at order $(\Omega_L\tau)^2$. We suppose that $\rho_A(0) = Tr_{rad}\rho(0)$ is an unpolarized state, with all atoms in the ground state. We note that this contributes a background noise to the emitted spectrum at order $(\Omega_L\tau)^2$, which for an isotropic trap, is also isotropic [10]. For this reason we will not consider its contribution further here.

Having established the quantum state of the matter induced by the laser pulse, we will now proceed to compute its subsequent time dependence, and determine the scattered field.

2.3 Time Dependence of Matter Polarization

The master equation for the reduced atomic density matrix, $\rho_A(t)$, can be obtained by standard methods [11], and in interaction picture is given by

$$\dot{\rho}_A(t) = (\mathcal{S} + \mathcal{J})\rho_A(t) \tag{13}$$

where,

$$\mathcal{S}\rho_A(t) = i(H_{eff}\rho_A(t) - \rho_A(t)H_{eff}^\dagger) \tag{14}$$

$$\mathcal{J}\rho_A(t) = \Gamma_A \int d^3r \int d^3r' \sum_{nM}\sum_{n'M'} \mathbf{e}^*_{n-M} \cdot \Re\ \left[\mathbf{g}(\mathbf{r}-\mathbf{r}')\right] \cdot\ \mathbf{e}_{n'-M'}$$
$$\times \Psi^\dagger_{gM'}(\mathbf{r}')\Psi_{en'}(\mathbf{r}')\rho_A(t)\Psi^\dagger_{en}(\mathbf{r})\Psi_{gM}(\mathbf{r}) \tag{15}$$

and the effective Hamiltonian

$$H_{eff} = -i\frac{\Gamma_A}{2} \int d^3r \int d^3r' \sum_{nM}\sum_{n'M'} \mathbf{e}^*_{n-M} \cdot\ \mathbf{g}(\mathbf{r}-\mathbf{r}') \cdot\ \mathbf{e}_{n'-M'}$$
$$\times \Psi^\dagger_{en}(\mathbf{r})\Psi_{gM}(\mathbf{r})\Psi^\dagger_{gM'}(\mathbf{r}')\Psi_{en'}(\mathbf{r}') \tag{16}$$

The resonant dipole-dipole interaction among the atoms is mediated by the dipole dyadic

$$\mathbf{g}(\mathbf{r}-\mathbf{r}', k_A) = \frac{3i}{2k_A}\left[\nabla\nabla - \nabla^2\right] \frac{\exp\{ik_A|\mathbf{r}-\mathbf{r}'|\}}{4\pi k_A^2|\mathbf{r}-\mathbf{r}'|}, \tag{17}$$

which relates the field observed at $\mathbf{r}$ to a source dipole oscillator at $\mathbf{r}'$.

We recall that we consider a mixture of two hyperfine ground states, $|J_g = 1/2, M = \pm 1/2\rangle$ confined by an isotropic harmonic potential $V(r) = m\Omega^2 r^2/2$. The s-wave interactions between the atoms may lead to Cooper pairing if the interaction is attractive. In order to describe the paired states of the matter we use Bogoliubov theory [12], to expand the matter field operators in terms of quasiparticle operators and corresponding eigenmodes $u_{i,M}(\mathbf{r})$ and $v_{i,M}(\mathbf{r})$, namely

$$\Psi_{gM}(\mathbf{r}) = \sum_i \left(u_{i,M}(\mathbf{r})b_{i,M} + v_{i,M}(\mathbf{r})b^\dagger_{i,-M}\right) \tag{18}$$

where $M = \pm 1/2$, and the quasiparticle operators, $b_{i,M}, b^\dagger_{i,M}$, satisfy fermionic anticommutation relations. The quasiparticle eigenmodes are computed from the Bogoliubov-de Gennes equations [13,14],

$$\left[H_{cm} - \mu + W_M(\mathbf{r})\right] u_{i,M}(\mathbf{r}) + \Delta_M(\mathbf{r})v_{i,M}(\mathbf{r}) = E_{i,M}u_{i,M}(\mathbf{r})$$
$$-\left[H_{cm} - \mu + W_M(\mathbf{r})\right] v_{i,M}(\mathbf{r}) + \Delta_M(\mathbf{r})u_{i,M}(\mathbf{r}) = E_{i,M}v_{i,M}(\mathbf{r}). \tag{19}$$

Here, $H_{cm} = -\hbar^2\nabla^2/2m + V(r)$ is the center of mass motion Hamiltonian, μ is the chemical potential which we assume to be the same for both hyperfine states, $W_M(\mathbf{r}) = (4\pi a\hbar^2/m)\langle\Psi^\dagger_{gM}(\mathbf{r})\Psi_{gM}(\mathbf{r})\rangle$ is the Hartree potential and $\Delta_M(\mathbf{r}) = -(4\pi a\hbar^2/m)\langle\Psi_{gM}(\mathbf{r})\Psi_{g-M}(\mathbf{r})\rangle$ is the *pair potential* or *gap function*, and describes the influence of Cooper pairing. For a given μ, Eqn. (19) together with the definitions of $W_M(\mathbf{r})$ and $\Delta_M(\mathbf{r})$ can be solved self consistently with the use of (18). It is also useful to expand the excited state matter field operator in terms of the eigenstates $\phi_j(\mathbf{r})$ of H_{cm}, as

$$\Psi_{en}(\mathbf{r}) = \sum_j \phi_j(\mathbf{r})e_{jn}. \tag{20}$$

The effective Hamiltonian can now be written as

$$H_{eff} = -i\frac{\Gamma_A}{2}\left(n_e - h_{ex} - h_I\right), \tag{21}$$

where all single atom contributions are contained in

$$n_e = \int d^3r \sum_n \Psi^\dagger_{en}(\mathbf{r})\Psi_{en}(\mathbf{r}) = \sum_{jn} e^\dagger_{jn} e_{jn}. \tag{22}$$

In a dilute gas the single atom contributions are dominant. The term h_{ex} accounts for quasiparticle exchange mediated by the electromagnetic field, and is given by

$$h_{ex} = \int d^3r \int d^3r' \sum_{nM} \mathbf{e}^*_{n-M} \cdot \ \mathbf{g}(\mathbf{r}-\mathbf{r}') \cdot \ \mathbf{e}_{n-M}\phi_j(\mathbf{r})\phi_j(\mathbf{r}') \tag{23}$$

$$\left[u_{i,M}(\mathbf{r})u_{i,M}(\mathbf{r}')b^\dagger_{i,M}b_{i,M} + v_{i,M}(\mathbf{r})v_{i,M}(\mathbf{r}')b_{i,-M}b^\dagger_{i,-M}\right] e^\dagger_{jn}e_{jn} \tag{24}$$

The remaining term represents resonant dipole-dipole interactions between atoms, and is given by

$$h_I = \int d^3r \int d^3r' \sum_{nM}\sum_{n'M'} \mathbf{e}^*_{n-M} \cdot \ \mathbf{g}(\mathbf{r}-\mathbf{r}') \cdot \ \mathbf{e}_{n'-M'} \tag{25}$$

$$\times \Psi^\dagger_{en}(\mathbf{r})\Psi^\dagger_{gM'}(\mathbf{r}')\Psi_{gM}(\mathbf{r})\Psi_{en'}(\mathbf{r}') - h_{ex}. \tag{26}$$

We now assume that initially (before the arrival of the laser pulse) the atoms are in a BCS ground state, $\rho_A(0) = |BCS\rangle\langle BCS|$ and, therefore from (12),

$$\rho_{Ai} = \frac{\tau\Omega_L}{\wp}\hat{\varepsilon}_L \cdot \hat{\mathbf{P}}^-(\mathbf{k}_L)|BCS\rangle\langle BCS| + H.c. \tag{27}$$

With the above initial condition, Eqn. (13) has the exact solution

$$\rho_A(t) = e^{\mathcal{S}t}\rho_{Ai}. \tag{28}$$

We will use perturbation theory to take into account the resonant dipole-dipole interactions. These involve the physics of *reabsorption*, i.e., photon emission, absorption and reemission cycles within the medium. In the dilute medium limit of interest to us, single reabsorption processes dominate, and by using perturbation theory we ignore multiple reabsorption cycles. Thus we separate $\mathcal{S}$ into two parts, $\mathcal{S} = \mathcal{S}_0 + \mathcal{S}_I$, with

$$\mathcal{S}_0\rho = -\frac{\Gamma_A}{2}\left[\left(n_e - h_{ex}\right)\rho + \rho\left(n_e - h_{ex}\right)^\dagger\right], \tag{29}$$

$$\mathcal{S}_I\rho = \frac{\Gamma_A}{2}\left[h_I\rho + \rho h_I^\dagger\right], \tag{30}$$

and approximate

$$e^{\mathcal{S}t} \approx e^{\mathcal{S}_0 t} + \int_0^t dt' e^{\mathcal{S}_0(t-t')} \mathcal{S}_I e^{\mathcal{S}_0 t'}. \tag{31}$$

In this approximation the effects of $\mathcal{S}_0$ are treated exactly. Besides single atom effects, this part contains exchange interactions which lead to a narrowing of the collective radiative linewidth due to the Fermi blocking factor [10,15]

$$f = \sum_{Mn} \int d^3r \int d^3r' \mathbf{e}^*_{n-M} \cdot \Re \left[\mathbf{G}(\mathbf{r} - \mathbf{r}', k_A) \right] \cdot \mathbf{e}_{n-M} \times \left\langle \Psi^\dagger_{gM}(\mathbf{r}) \Psi_{gM}(\mathbf{r}') \right\rangle \left\langle \Psi^\dagger_{en}(\mathbf{r}') \Psi_{en}(\mathbf{r}) \right\rangle . \tag{32}$$

Fermi blocking is of course present even in an ideal Fermi gas. The atomic interactions and pairing can modify f, but pairing has only a small influence on the linewidth in the regime of interest here.

3 Angular Spectrum of Radiation

Using (31) and (28), we compute the time resolved angular spectrum of radiation. The incident light pulse is assumed to be polarized in the z-direction, and propagates in the y-direction. We will compute the angular distribution of scattered radiation in the x-y plane ($\theta_s = \pi/2$), with $\hat{z}$-polarization, as a function of the azimuthal angle ϕ_s. The result is, to a very good approximation

$$I_s(\mathbf{k}_s, \hat{z}, t) = \frac{2}{3}(\Omega_L \tau)^2 e^{-\Gamma_A t(1-f)} \left| S_0(\mathbf{k}_s - \mathbf{k}_L) - \frac{\Gamma_A t}{2} S_1(\mathbf{k}_s) \right|^2 \tag{33}$$

where as noted $\mathbf{k}_s$ lies in the xy plane, and the form factor

$$S_0(\mathbf{q}) = \int d^3r e^{i\mathbf{q}\cdot\mathbf{r}} \sum_M \rho_M(\mathbf{r}), \tag{34}$$

is the Fourier transform of the average density of the gas evaluated at the wave vector $\mathbf{q} = \mathbf{k}_s - \mathbf{k}_L$, and

$$\rho_M(\mathbf{r}) = \left\langle \Psi^\dagger_{gM}(\mathbf{r}) \Psi_{gM}(\mathbf{r}) \right\rangle \tag{35}$$

is the average density of atoms in the electronic state $|J_g, M\rangle$. If reabsorption of radiation within the sample is ignored, this term gives the complete angular spectrum of scattered radiation.

The leading correction to the scattered intensity due to reabsorption is given by

$$S_1(\mathbf{k}_s) = \sum_{MM'} \mathcal{C}^2_{M'M} \int d^3r d^3r' \left[\mathbf{e}^*_{M-M'} \cdot \mathbf{g}(\mathbf{r}-\mathbf{r}') \cdot \mathbf{e}_{\mathbf{M}-\mathbf{M}'}\right] e^{i\mathbf{k}_s\cdot\mathbf{r} - i\mathbf{k}_L\cdot\mathbf{r}'} \\ [\rho_M(\mathbf{r})\rho_{M'}(\mathbf{r}') - \rho_M(\mathbf{r},\mathbf{r}')\rho^*_{M'}(\mathbf{r},\mathbf{r}') + \xi_M(\mathbf{r},\mathbf{r}')\xi^*_{M'}(\mathbf{r},\mathbf{r}')] \\ + c.c., \tag{36}$$

where we have defined the ground state density matrix

$$\rho_M(\mathbf{r},\mathbf{r}') = \left\langle \Psi^\dagger_{gM}(\mathbf{r})\Psi_{gM}(\mathbf{r}')\right\rangle \tag{37}$$

and the anomalous pair amplitude, which vanishes in the absence of pairing, is given by

$$\xi_M(\mathbf{r},\mathbf{r}') = \langle \Psi_{gM}(\mathbf{r})\Psi_{g-M}(\mathbf{r}')\rangle\,. \tag{38}$$

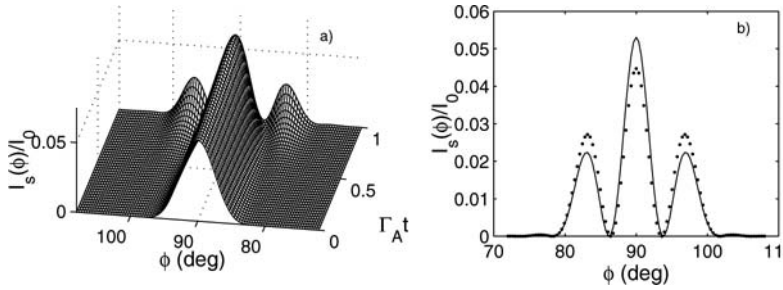

Fig. 1. (**a**) The angular distribution of the normalized scattered intensity for a BCS paired gas for an isotropic trap of frequency Ω and for $\mu/E_R = 2/3$ and $\mu = 20\hbar\Omega$. (**b**) The angular spectrum for a paired($\Delta \neq 0$) Fermi vapor (*dotted line*) and a normal Fermi vapor (*solid line*) for $\Gamma_A t \approx 1$ and the same parameters as (a)

In Fig. (1a) we show the distribution of the scattered intensity in the xy-plane as a function of time for $\mu/E_R = 2/3$ and $\mu = 20\hbar\Omega$ where $E_R = \hbar^2 k_A^2/2m$ is the recoil energy. This corresponds to approximately 10^4 trapped atoms. For such particle numbers, the forward scattering is less pronounced than for larger samples. At each time step the intensity has been normalized by the total intensity $I_0(t) = \int d\phi_s I_s(\phi_s, t)$. Initially the scattering is predominantly in the forward direction with a characteristic angular width of about $\Delta\phi_s = 8/k_A R_F$ where the Fermi radius $R_F \approx 2\sqrt{\mu E_R}/\hbar\Omega$. For $\Gamma_A t \to 1$, reabsorption effects cause side lobes corresponding to first order diffraction, to grow, and the spectrum is sensitive to both particle interactions and pairing. In Fig. (1b) we show the profile of the normalized intensity for $\Gamma_A t \approx 1.0$ for a Fermi vapor with pairing ($\Delta \neq 0$) and a normal vapor ($\Delta = 0$). The

pair function is calculated using the local density approximation applied to (19) [4,6,13]. The effect of pairing is to enhance the side lobes relative to the forward scattering peak.

4 Conclusion

We considered a trapped gas of atomic fermions in which a matter polarization is induced by a short laser pulse. The subsequent decay of the polarization, through radiative emission, produces an intensity distribution which was shown to be sensitive to BCS pairing correlations. The technique may therefore prove useful in the detection of such correlations.

Acknowledgments

In honor of our late friend and colleague Dan Walls. We acknowledge support from the NSF grant PHY-9803180.

References

1. M.H. Anderson *et al.*: Science **269**, 198 (1995); K.B. Davis *et al.*: Phys. Rev. Lett. **75**, 3969 (1995); C.C. Bradley: *et al.*: Phys. Rev. Lett. **75**, 1687 (1995)
2. B. DeMarco, J.L. Bohn, J.P Burke Jr., M. Holland, D.S. Jin: Phys. Rev. Lett. **82**, 4208 (1999)
3. J. Bardeen, L. Cooper, J.R. Schrieffer: Phys. Rev. **108**, 1189 (1957); H.T.C. Stoof, M. Houbiers, C.A. Sackett, R.G. Hulet: Phys. Rev. Lett **76**, 10 (1996)
4. M. Houbiers, R. Ferweda, H.T.C. Stoof, W.I. McAlexander, C.A. Sackett, R.G. Hulet: Phys. Rev. A **56**, 4864 (1997)
5. J. Ruostekoski: Phys. Rev. A **60**, 1775 (1999)
6. F. Weig, W. Zwerger: Europhys. Lett. **49**, 1 (2000)
7. W. Zhang, C.A. Sackett, R.G. Hulet: Phys. Rev. A **60**, 504 (1999)
8. P. Torma, P. Zoller: cond-mat/0001341
9. J. Javanainen, J. Ruostekoski: Phys. Rev. A **52**, 3033 (1995);
10. B. Berhane, T.A.B. Kennedy: Phys. Rev. A (2000) (to be published);
11. G.J. Milburn, D.F. Walls: *Quantum Optics* (Springer-Verlag, Berlin 1994)
12. N.N. Bogoliubov: J. Exptl. Theor. Phys. (USSR) **34**, 58 (1958)
13. G. Bruun, Y. Castin, R. Dum, K. Burnett: cond-mat/9810013
14. P.G. de Gennes: *Superconductivity of Metals and Alloys* (Addison-Wesley, New York 1966)
15. Th. Busch, J.R. Anglin, J.I. Cirac, P. Zoller: Europhys. Lett. **44**, 1 (1998)

A Model of a Pumped Continuous Atom Laser

Nicholas Robins, Craig Savage, and Elena Ostrovskaya

1 Introduction

At the end of the millennium a continuous wave (cw) pumped atom laser remains to be experimentally demonstrated. The prototype atom lasers that have been operated have used rapidly pulsed or continuous output coupling, but lacked pumping of the trapped atom laser mode [1,2], as is needed for a cw laser system. Indeed, apart from simple rate equation descriptions, existing theoretical models do not incorporate both pumping of the laser mode and propagation of the out-coupled beam.

We have used the macroscopic wave-function approximation, or mean field approximation, which leads to the Gross-Pitaevskii (GP) equation, as the basis for a complete cw atom laser model. The macroscopic wave-function is the order parameter for a Bose-Einstein condensate of atoms. Our model system is schematically illustrated in Fig. 1. It includes a pumped reservoir of un-condensed atoms irreversibly coupled to the atom laser mode [3]. The condensed atoms in this mode, and in the output beam, undergo two-body interactions and three body recombination. The atoms are reversibly coupled from the atom laser mode to the output beam by a Raman process [1,3]. We solve the resulting system of coupled differential equations numerically in one spatial dimension. The macroscopic wave-function of the output atoms is analysed to determine quantities such as linewidth. Previous work based on systems of coupled equations of the complex Ginzburg-Landau type (GP equations with gain and loss) has either neglected important physics, such as the pumping [4,5] or has concentrated solely on the condensate, ignoring the spatio-temporal structure of the output atom beam [6].

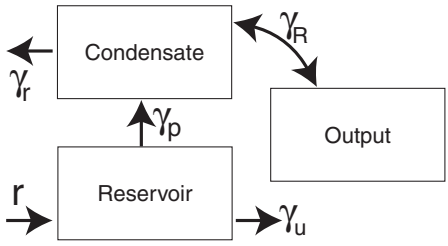

Fig. 1. Schematic representation of the model system. The symbols stand for the coupling, pumping and loss rates and are defined in the text

H.J. Carmichael, R.J. Glauber, M.O. Scully (Eds.): LNP 561, pp. 50–59, 2001.

2 The Model

We consider the trapped atom laser mode, which we refer to as the "laser mode", to be a one-dimensional condensate in a highly anisotropic, cigar-shaped harmonic trapping potential. The atoms in the laser mode and in the output beam are described by the macroscopic wave-functions $\Psi_a(x,t)$ and $\Psi_b(x,t)$ respectively. They experience two-body repulsive atom-atom interactions and three-body recombination. A novel feature of our model is the saturated loss due to the three-body recombination process [7,8].

To describe pumping we use the phenomenological model of Kneer et.al. [6] which mimics the pumping mechanism of a conventional optical laser. The number of atoms in the uncondensed pump reservoir is $N_u(t)$, and their spatial distribution is not modeled. The reservoir is fed at a rate r, loses atoms at the rate $\gamma_u N_u$, and pumps the laser mode at the rate $\gamma_p N_u N_a$, where $N_a(t) = \int_{-\infty}^{\infty} |\Psi_a|^2 dx$ is the total number of atoms in the laser mode.

The laser mode is coupled, by a reversible two-photon Raman transition, to an untrapped electronic state which is the output atom laser beam $\Psi_b(x,t)$ [1,3]. The Raman transition may also give a momentum kick to the out-coupled atoms. In an experiment the magnitude of this kick depends on the relative geometry of the two Raman laser beams. The output atom beam accelerates due to gravity. Inside the trap it overlaps, and hence interacts with, the laser mode atoms. This interaction has both a linear contribution, due to the Raman coupling, and a nonlinear contribution due to the inter-species atom-atom interactions.

Mathematically, our model is described by the following dimensionless equations:

$$\begin{aligned}
i\frac{\partial \Psi_a}{\partial t} &= -\frac{1}{2}\frac{\partial^2 \Psi_a}{\partial x^2} + \frac{1}{2}x^2\Psi_a + U_a\Psi_a|\Psi_a|^2 + U_{ab}\Psi_a|\Psi_b|^2 \\
&\quad -i\gamma_r\Psi_a(|\Psi_a|^4 + |\Psi_b|^4) + \gamma_R e^{ikx}\Psi_b + \frac{i}{2}\gamma_p N_u \Psi_a, \\
i\frac{\partial \Psi_b}{\partial t} &= -\frac{1}{2}\frac{\partial^2 \Psi_b}{\partial x^2} + Gx\Psi_b + U_b\Psi_b|\Psi_b|^2 + U_{ab}\Psi_b|\Psi_a|^2 \\
&\quad -i\gamma_r\Psi_b(|\Psi_a|^4 + |\Psi_b|^4) + \gamma_R e^{-ikx}\Psi_a, \\
\frac{dN_u}{dt} &= r - \gamma_u N_u - \gamma_p N_u N_a,
\end{aligned} \tag{1}$$

where U_a and U_b are the intra- and U_{ab} the inter- species two-body interaction coefficients, γ_r is the three-body recombination coefficient, and γ_R is the Raman coupling coefficient.

The model is made dimensionless using the characteristic unit of length $l = (\hbar/\omega m)^{1/2}$ and time, $\tau = \omega^{-1}$, where ω is the trap frequency in the direction of the weak confinement. We use $\omega \approx 125$ Hz and $m \approx 10^{-26}$ kg. The dimensionally correct [5] two-body interaction coefficients, which we assume

to be equal, can be written as $U_{a,b,ab} = 4\pi a_s/l$ where a_s is the s-wave scattering length for the relevant process. There is some arbitrariness in how the $U_{a,b,ab}$ relate to their three dimensional counterparts. The scaling we have chosen gives a realistic condensate size [5]. Similar reasoning applies to the choice of the three-body recombination rate, γ_r. We have set it to give feasible lifetimes for the laser mode condensate: it is typically between 10^{-7} and 10^{-9} in our simulations. In accordance with experimentally reasonable values, we allow the dimensionless Raman coefficient, $\gamma_R = \Omega_1\Omega_2/(\omega\Delta)$, to range up to 10^4, where $\Omega_{1,2}$ are the Rabi frequencies of the Raman lasers and Δ is the laser detuning [3], and we take the dimensionless Raman momentum kick to lie in the range $0 \leq k \leq 100$. The dimensionless gravitational coefficient $G = g(m\omega^{-3}\hbar^{-1})^{1/2}$ varies in the range $0 \leq G \leq 68$, with $G = 68$ corresponding to $g = 9.8$ ms^{-2}. Physically, we may think of the output atomic beam propagating in a tilted atom waveguide [9], with the tilt angle determining the value of G.

3 Rate Equations

Given the complexity of the model equations (1), a numerical method is the only feasible method of solution. However, some understanding of the dynamics of the system can be gained by deriving approximate rate equations for the populations of the reservoir, condensate and output fractions [10]. We proceed by projecting the condensate and output mean fields onto the stationary state modes $\Phi_a(x)$ and $\Phi_b(x)$ defined by:

$$\Psi_a(x,t) = a(t)\Phi_a(x) \qquad \Psi_b(x,t) = b(t)\Phi_b(x)e^{-ikx}, \tag{2}$$

where $\Phi_{a,b}$ satisfy the time independent, lossless, and decoupled form of the equations (1):

$$\begin{aligned} \frac{1}{2}\frac{\partial^2\Phi_a}{\partial x^2} &= -\mu_a\Phi_a + \frac{1}{2}x^2\Phi_a + U_a\Phi_a|\Phi_a|^2, \\ \frac{1}{2}\frac{\partial^2\Phi_b}{\partial x^2} &= -\mu_b\Phi_b + Gx\Phi_b + U_b\Phi_b|\Phi_b|^2. \end{aligned} \tag{3}$$

We are free to choose the magnitude of the chemical potentials μ_a and μ_b. In order to simplify the analysis we set the momentum kick, k, equal to zero. By doing so, we neglect the main effect the momentum kick has on the dynamics of the system, that is, the change in the spatial overlap between the condensate and the out-coupled field.

The first equation in (3) describes the eigenfunction of a trap with chemical potential μ_a. The equation for the output mode describes a falling wave and can be solved numerically or perturbatively, using a superposition of Airy functions in the linear limit [11]. We now substitute the ansatz (2) into the original system (1), and use the equations (3) to simplify the result. We then integrate out the spatial dependence in the equations and separate the time

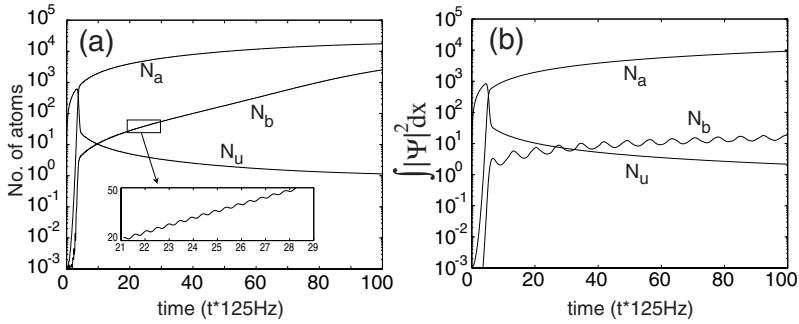

Fig. 2. Typical population dynamics without three-body recombination. (**a**) From the rate equations (4) showing the growth of the laser mode. We have tested that this growth continues in the long time limit ($\tau > 600$). Parameters are $r = 200$, $\gamma_p = \gamma_u = 0.01$, $\gamma_R = 0.5$, $U_a = U_b = 0.02$, $U_{ab} = 0.01$, $\delta\mu = 0.02$, $N_a(t = 0) = 0.001$, $N_b(t = 0) = 10$ and $\gamma_r = 0$. Values of the spatial integrals are as given in the text. The inset shows the Rabi-type oscillations, present in all three fields. (**b**) From the full GP equations (1). Parameters are the same as for part (a) and G=68, $k = 5$. The GP simulations predict a much smaller number of atoms in the output beam, N_b, than the rate equations, because there is an effective loss of atoms due to the boundary absorber at the edge of the numerical grid

dependence of the modal amplitudes as $a = n_a(t)e^{i\theta_a(t)}$ and $b = n_b(t)e^{i\theta_b(t)}$. By noting that the relationship between the modal amplitudes and the population numbers is given by $N_a = I_6\delta n_a^2$ and $N_b = I_5\delta n_b^2$, we arrive at the following system of equations for the real population numbers $N_{a,b}$, N_u, and phase difference $\theta = \theta_b - \theta_a$:

$$\begin{aligned}
\frac{dN_a}{dt} &= -(\alpha N_a^3 + \beta N_a N_b^2) + \gamma_p N_u N_a + 2\gamma_R\sqrt{I_5 I_6 N_a N_b}\sin(\theta),\\
\frac{dN_b}{dt} &= -(\beta N_b^3 + \alpha N_b N_a^2) - 2\gamma_R\sqrt{I_5 I_6 N_a N_b}\sin(\theta),\\
\frac{d\theta}{dt} &= \delta\mu + \delta_{NL} + \frac{\gamma_R\sqrt{I_5 I_6}}{\sqrt{N_a N_b}}\cos(\theta)(N_b - N_a)\\
\frac{dN_u}{dt} &= r - \gamma_u N_u - \gamma_p N_u N_a,
\end{aligned} \tag{4}$$

where $\delta\mu = (\mu_a - \mu_b)$, $\alpha = (2\gamma_r I_3)/(\delta I_6)^2$, $\beta = (2\gamma_r I_4)/(\delta I_5)^2$, and $\delta_{NL} = U_b(1 - N_b/(\delta I_5))I_2 + U_a(N_a/(\delta I_6) - 1)I_1 + U_{ab}((N_a I_1)/(\delta I_6) - (N_b I_2)/(\delta I_5))$.

The constant coefficients I_s, where $s = 1, 2, 3, 4, 5, 6$, and δ are determined by spatial overlap integrals as follows:

$$I_1 = \delta^{-1} \int \Phi_a \Phi_b |\Phi_a|^2 dx, \qquad I_2 = \delta^{-1} \int \Phi_a \Phi_b |\Phi_b|^2 dx,$$
$$I_3 = \delta^{-1} \int \Phi_a \Phi_b |\Phi_a|^4 dx, \qquad I_4 = \delta^{-1} \int \Phi_a \Phi_b |\Phi_b|^4 dx, \tag{5}$$
$$I_5 = \delta^{-1} \int |\Phi_b|^2 dx, \qquad I_6 = \delta^{-1} \int |\Phi_a|^2 dx, \qquad \delta = \int \Phi_a \Phi_b dx.$$

For realistic parameters, and using the stationary solutions of (3) we numerically calculated these integrals to have the approximate values $\delta = 233$, $I_1 = 875$, $I_2 = 1.45$, $I_3 = 8.39 \times 10^5$, $I_4 = 2.79$, $I_5 = 0.13$ and $I_6 = 41.3$.

From the rate equations it is seen that the populations of the condensate and the output mode undergo nonlinear Rabi-type oscillations [12] with the effective frequency determined, in part, by the strength of the interactions through $\delta_{NL}(U_a, U_b, U_{ab})$, and the Raman coupling γ_R. In the presence of pumping and without the three-body loss terms, the condensate fraction acquires a fast growing component which prevents the system from reaching a steady state defined by $dN_{a,b}/dt = 0$. A typical solution to the system (4) is shown in Fig. 2(a). An important feature of this regime is the unbounded growth of the laser mode in the absence of three-body recombination, which would not be the case for a realistic atom laser. This emphasises the need to include three-body recombination in atom laser models, as we do in subsequent sections. The qualitative predictions of the rate equation model are confirmed by direct integration of (1), with the results shown in Fig. 2(b). It is important to note that the values of the spatial integrals, I_s and δ, play a large part in the time evolution of the rate equations.

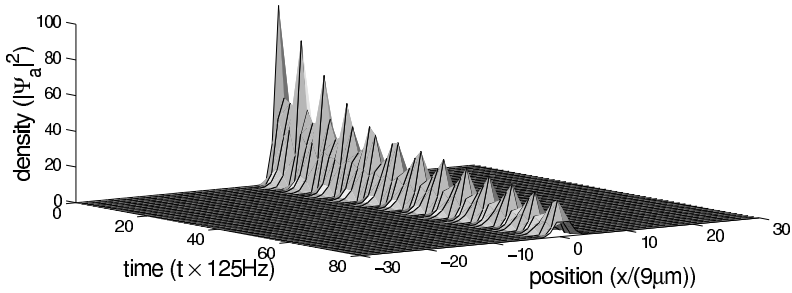

Fig. 3. The time evolution of an unpumped condensate. Parameters are $\gamma_R = 0.5$, $\gamma_r = 10^{-7}$, $U_a = U_b = 0.02$, $U_{ab} = 0.01$, $G = 12$, $k = 5$, and $N_a(t = 0) = 140$

4 Numerical Results

With this initial understanding of the behavior of the atom laser to guide us, we proceed to investigate the numerical solution of our full model equations (1). We use a split-step method [13] to analyse the spatio-temporal behavior of the laser mode and the output beam. An absorbing boundary is used at the edges of the spatial grid. We have ensured that our results are insensitive to the size of the spatial grid and time-step.

Our model is at its simplest with the pump mechanism turned off, so that the out-coupling depletes the atom laser mode. The laser mode population changes rapidly at the beginning of the first Rabi oscillation, as can be seen in Fig.3, so the approximation of a stationary mode may be false even on short time scales [14]. One of the results of this paper is that it might be more realistic to make this approximation on the assumption of a steady state achieved through a balance of pumping and loss due to three body recombination.

We next consider the pumped system. Without the effects of gravity and interactions we find the bound state predicted by Hope et al. [15]. This is produced by the Raman coupling. A fraction of the output field remains localised around the laser mode, see Fig.4, and hence the population in the laser mode increases indefinitely due to the pumping. Hope et al. found that including gravity or two-body interactions could destroy this bound state by introducing a repulsive effective potential acting on the output mode. A large fraction of the atoms then quickly leave the interaction region. However we find that when both gravity *and* interactions act together they tend to recreate the exponentially growing output state. The population dynamics of the laser mode and the output is approximately described by (4) in this case. The output beam's spatio-temporal structure, in the absence of three-body recombination, is shown in Fig.5.

Adding three body recombination destroys the bound state as can be seen in Fig. 6 and Fig. 7(a). This occurs because the loss rate increases as the square of the atomic density. In addition, the three-body recombination effect suppresses the atomic density noise in the output field, as well as suppressing the collective excitations of the condensate, see Fig. 7(b). Remarkably, the three body recombination process assists in creating a steady state, both in the output and laser modes, as can be seen in Fig. 7(a).

5 Linewidth Narrowing

One of the characteristic properties of a continuous wave optical laser is the dramatic reduction in linewidth that occurs above threshold. The ultimate quantum mechanical limit to the linewidth is given by the Schawlow-Townes formula [16,17]. Graham has proposed a related limit for the atom laser due to interaction with the thermal reservoir of uncondensed atoms [18]. Our model

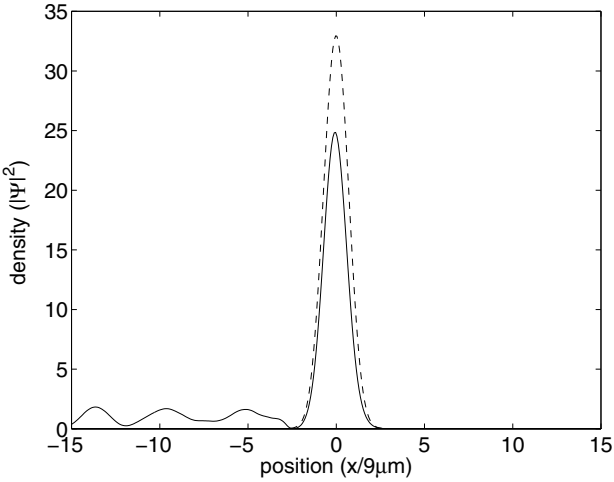

Fig. 4. The bound state of the laser mode (*dashed line*) and the output beam (*solid line*) at $t = 200$. The laser mode is multiplied by 0.003. The output beam, for $x < -2.5$ only, is multiplied by a factor of 10. Parameters are $r = 200$, $\gamma_R = 0.5$, $\gamma_r = 0$, $U_a = U_b = U_{ab} = 0$, $G = 0$, $k = 5$, $N_a(t = 0) = 0.001$, $N_b(t = 0) = 10$

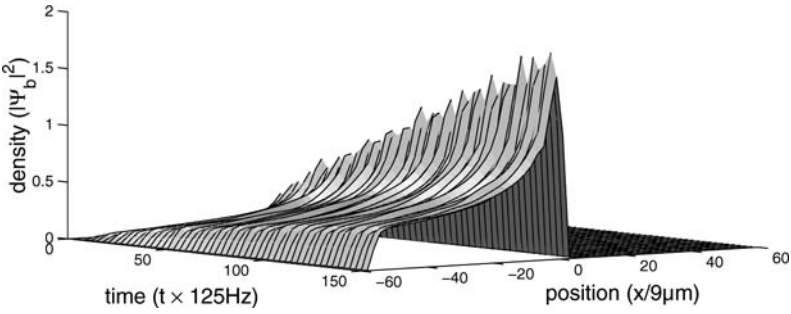

Fig. 5. Atom laser beam density as a function of position and time, with no three-body recombination, showing the steady growth of the output. The beam propagates in the negative x direction from the condensate centered at $x = 0$. Parameters are $r = 200$, $\gamma_R = 0.5$, $\gamma_u = 0.1$, $\gamma_p = 0.1$, $\gamma_r = 0$, $U_a = U_b = 0.02$, $U_{ab} = 0.01$, $G = 68$, $k = 5$, $N_a(t = 0) = 0.001$, $N_b(t = 0) = 10$

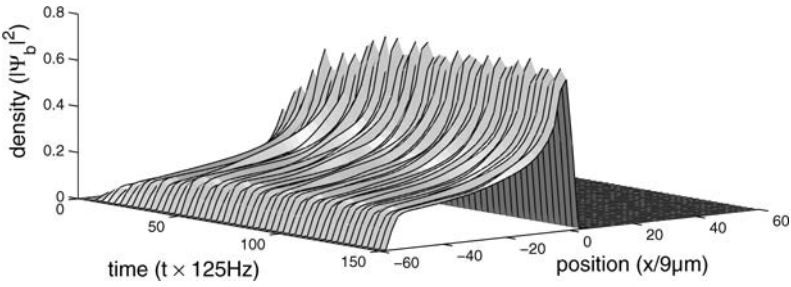

Fig. 6. Atom laser beam density as a function of position and time, with three-body recombination included $\gamma_r = 10^{-7}$, showing a quasi-steady state. Parameters are otherwise the same as for Fig. 5

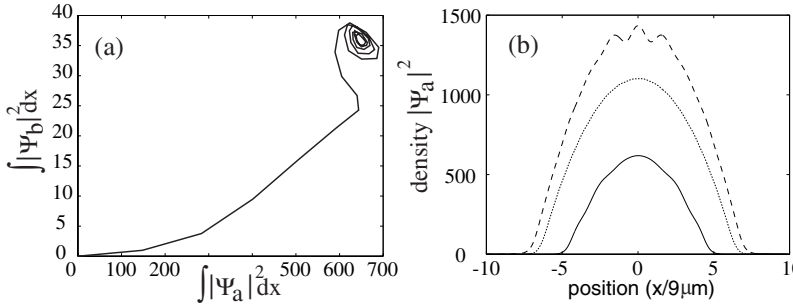

Fig. 7. Steady state operation of the system with three-body recombination. (**a**) Atom number in the output versus atom number in the laser mode. Parameters are $r = 100$, $\gamma_R = 0.5$, $\gamma_u = 0.1$, $\gamma_p = 0.1$, $\gamma_r = 10^{-5}$, $U_a = U_b = 0.02$, $U_{ab} = 0.01$, $G = 12$, $k = 5$, $N_a(t = 0) = 0.001$, $N_b(t = 0) = 100$. (**b**) The quasi-steady state density profile of the laser mode at $t = 150$ for pumping of $r = 200$ (*solid*) and $r = 1600$ (*dotted*) Other parameters are $\gamma_R = 0.5$, $\gamma_u = 0.1$, $\gamma_p = 0.1$, $\gamma_r = 10^{-7}$, $U_a = U_b = 0.02$, $U_{ab} = 0.01$, $G = 68$, $k = 5$, $N_a(t = 0) = 0.001$, $N_b(t = 0) = 10$. By contrast the laser mode at $t = 150$ for pumping of $r = 200$ (*dashed*), with *no* three body recombination, is continuing to grow and change shape

does not incorporate the many-body quantum physics that determines the ultimate atom laser linewidth. However, in practice we might expect that the linewidth is not determined by fundamental factors, but rather by the dynamics of the particular system; for example, in the optical case by relaxation oscillations [19]. Our model is suitable for determining the linewidth due to this type of dynamical effect.

To determine the linewidth of the output we have calculated the instantaneous spatial Fourier transforms of particular regions of the output field. The results are shown in the inset to Fig.8. The atoms are accelerated by gravity according to $v = \sqrt{v_0^2 + 2gx}$ and hence, the velocity linewidth narrows as the

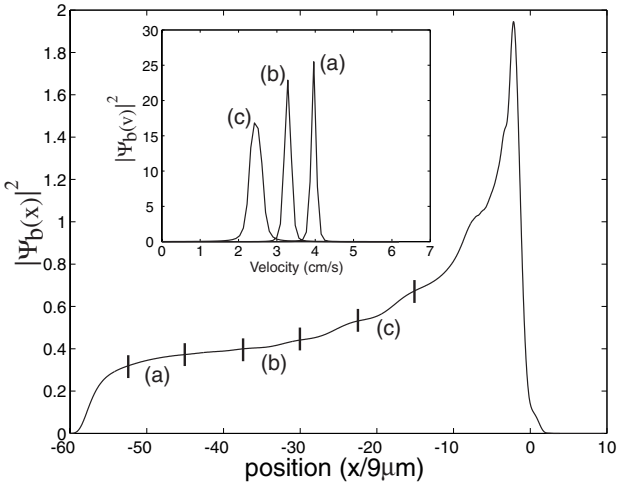

Fig. 8. The density of the output beam as a function of position. The inset shows the velocity linewidth over three regions of the atom laser output. These regions are labeled (a), (b), and (c) and are indicated by the bars on the main curve. Their width is about 7.5 dimensionless units, or 68 μm. The number of atoms in each region is approximately the dimensionless density times the length; e.g. $7.5 \times 0.4 = 3$ for region (b). Parameters are as in Fig.7(a)

atoms fall away from the trap [20]. We are currently investigating the effect of the pump rate, r, on the output linewidth of our model, in both the spatial and temporal domains.

6 Conclusion

We have presented a model of an atom laser in which we have endeavored to include the important physics of an experimental atom laser system. The resulting model exhibits a rich and complex dynamics. A novel aspect of our model is the inclusion of three-body recombination, which we believe plays an important part in achieving steady state laser operation. We demonstrated that the complex interplay of effects in our model can lead to a steady output with low atomic density fluctuations. The output of our atom laser is locally monochromatic, its linewidth dominated by gravitational acceleration. We are in the process of generalising this one dimensional model to three dimensions.

Acknowledgments

We acknowledge continuing discussions with J. Hope, and thank G. Moy for his input.

References

1. E.W. Hagley, L. Deng, M. Kozuma, J. Wen, K. Helmerson, S.L. Rolston, W.D. Phillips: Science **283**, 1706 (1999)
2. I. Bloch, T.W. Hansch, T. Esslinger: Phys. Rev. Lett. **82**, 3008 (1999)
3. G.M. Moy, J.J. Hope, C.M. Savage: Phys. Rev. A **55**, 3631 (1997)
4. J. Schneider, A. Schenzle: App. Phys. B **69**, 353 (1999)
5. M. Edwards, D.A. Griggs, P.L. Holman, C.W. Clark, S.L. Rolston, W.D. Phillips: J. Phys. B: At. Mol. Opt. Phys. **32**, 2935 (1999)
6. B. Kneer, T. Wong, K. Vogel, W.P. Schleich, D.F. Walls: Phys. Rev. A **58**, 4841 (1998)
7. Yu. Kagan, A.E. Muryshev, G.V. Shlyapnikov: Phys. Rev. Lett. **81**, 933 (1998)
8. E.A. Burt, R.W. Ghrist, C.J. Myatt, M.J. Holland, E.A. Cornell, C.E. Wieman: Phys. Rev. Lett. **79**, 337 (1997)
9. S. Marksteiner, C.M. Savage, P. Zoller, S.L. Rolston: Phys. Rev. A **50**, 2680 (1994)
10. N. Robins: Honours Thesis, Australian National University (2000)
11. J. Schneider, A. Schenzle: App. Phys. B **69**, 353 (1999)
12. R.J. Ballagh, K. Burnett, T.F. Scott: Phys. Rev. Lett. **78**, 1607 (1997)
13. T.R. Taha, M.J. Ablowitz: J. Comp. Phys. **55**, 203 (1984)
14. M. Naraschewski, A. Schenzle, H. Wallis: Phys. Rev. A **56**, 603 (1997)
15. J.J. Hope, G.M. Moy, M.J. Collett, C.M. Savage: cond-mat/9907023, Phys. Rev. A **61**, 023603 (2000)
16. A.L. Schawlow, C.H. Townes: Phys. Rev. **112**, 1940 (1958)
17. H.M. Wiseman: Phys. Rev. A **60**, 4083 (1999)
18. R. Graham: Phys. Rev. Lett. **81**, 5262 (1998)
19. A.E. Siegman: *Lasers* (University Science Books, Mill Valley 1986)
20. H.M. Wiseman: Phys. Rev. A **56**, 2068 (1997)

The BEC Near a Feshbach Resonance: A Superfluid of Mutually Coherent Condensates

Eddy Timmermans

1 Introduction

To gain a true appreciation of how extraordinary many of the properties of the atomic-trap Bose-Einstein condensates (BEC's) [1] are, we only have to remind ourselves of their dilute gas nature. As such, the fact that their dynamics is extremely sensitive to the inter-particle interactions is remarkable, for instance. Since these BEC's are amenable to atomic and optical techniques that can modify the inter-atomic interactions [2], it is also a relevant remark. In this paper, we discuss one of the proposed schemes: the magnetically controlled low energy Feshbach resonance. Near resonance, a magnetic field variation alters the detuning and, hence, the binary atom interactions. The response of the condensate to sudden changes of the inter-particle interaction is macroscopic [3] and the experimentalist who can control it is insured of performing interesting dynamical BEC-experiments. This prospect motivated a great deal of research, both in theory [4]– [5] and experiment [6].

Our investigations of the near-resonant condensate [7] reveal that the Feshbach resonance is responsible for a different – and more interesting – many-body structure of the BEC. The interaction that creates the intermediate quasi-bound molecule in the binary atom resonance creates a second condensate component of molecules in the atomic BEC. The resulting system consists of *two* coexisting condensates: an atomic and a molecular BEC, which are, moreover, *mutually coherent*. From the point of view of BEC-physics, the molecular Bose-Einstein condensate is interesting. Traditional schemes to achieve molecular condensation with internal state cooling appear problematic, partly due to collisional 'quenching' of the internal ro-vibrational states. From the point of view of superfluidity, the relative phase introduces an interesting generalization of the usual boson superfluidity, such as manifested by the ^{3}He-fluids. Its corresponding broken symmetry state is characterized by a single long-range phase, the spatial variation of which gives rise to superfluid flow. In contrast, the Feshbach resonant condensate is characterized by two long-range quantum phases, the complex phases of the atomic and molecular BEC's. Moreover, the mutual coherence implies that the relative phase is a dynamical variable. Its canonical conjugate is the population imbalance and any disturbance of this imbalance leads to Josephson-like oscillations of the atomic and molecular populations.

H.J. Carmichael, R.J. Glauber, M.O. Scully (Eds.): LNP 561, pp. 60–69, 2001.

In addition, we show that the dependence of the ground state energy on density suggests the surprising liquid-like property of a self-determined density.

2 Single Condensate Dynamics

The BEC 'condensation' occurs in Fock space: a significant fraction of the bosonic particles occupies the same single particle state χ_0. In fact, to a good approximation, all particles of the zero temperature dilute condensate reside in that same single particle state:

$$\psi(\mathbf{r}_1, \mathbf{r}_2, ..., \mathbf{r_N}; \mathbf{t}) \approx \chi_\mathbf{0}(\mathbf{r_1}; \mathbf{t})\chi_\mathbf{0}(\mathbf{r_2}; \mathbf{t})....\chi_\mathbf{0}(\mathbf{r_N}, \mathbf{t}) \tag{1}$$

Such wave function assumes a total lack of inter-particle correlations. In reality, we know that the atomic motion is strongly correlated, but only for short inter-particle distances (of the order of the range of the interatomic interaction). This length scale is much shorter than any distance of relevance to the many-body behavior of the system. Under those circumstances, one can indeed use an uncorrelated wave function of the type (1), provided one evolves the state according to an effective Hamiltonian $\hat{H}$,

$$\hat{H} = \sum_j^N \frac{-\hbar^2\nabla^2}{2m} + V(\mathbf{r}_j) + \lambda \sum_{i \neq j} \delta(\mathbf{r}_i - \mathbf{r}_j) \ , \tag{2}$$

with an effective inter-particle contact interaction. We determine the value of the parameter λ, which we will call the interaction strength by requiring the contact interaction to give the correct binary atom scattering length, a, in the Born approximation:

$$\lambda = \left(\frac{4\pi\hbar^2}{m}\right) a \ . \tag{3}$$

The Born approximation assumes precisely the total lack of correlation exhibited by the product wavefunction.

The evolution of this ansatz wave function according to the many-body Hamiltonian (2) is described by the Hartree-Fock equation,

$$i\hbar\dot{\chi}_0 = \left(\frac{-\hbar^2\nabla^2}{2m} + V(\mathbf{r}) + \lambda[N-1]|\chi_0(\mathbf{r};t)|^2\right)\chi_0(\mathbf{r};t) \ . \tag{4}$$

In all condensates reported so far, the number of particles, N, is large enough that the $[N-1]$ factor can safely be replaced by N, which gives the Gross-Pitaevskii equation [8] – [9]. Moreover, since N is indeed large, the contribution of the non-linear interaction dominates the time evolution. Since it is also proportional to the value of the interaction strength and, hence, the scattering length, it is clear that the dynamics is very sensitive to the inter-particle interactions.

Before proceeding with a description of the proposed Feshbach resonant scheme to modify the scattering length, we will show how the Gross-Pitaevskii equation may be derived in a second quantization formalism. Although we don't learn any new single condensate physics, second quantization provides a very useful framework for describing the more subtle Feshbach resonant condensates. In this description, the Hamiltonian (2) takes on the form

$$\hat{H} = \int d^3r \; \hat{\psi}^\dagger \left(\frac{-\hbar^2\nabla^2}{2m} + V + \frac{\lambda}{2}\hat{\psi}^\dagger\hat{\psi} \right) \hat{\psi} \;\; , \tag{5}$$

where $\hat{\psi}$ and $\hat{\psi}^\dagger$ represent the annihilation and creation field operators, and where the dependence on the position $\mathbf{r}$ is understood. In the Heisenberg picture, the field operator obeys the Heisenberg commutator equation:

$$\begin{aligned} i\hbar\frac{d}{dt}\hat{\psi} &= \left[\hat{H}, \hat{\psi}\right]_- \\ &= \left(\frac{-\hbar^2\nabla^2}{2m} + V + \lambda\hat{\psi}^\dagger\hat{\psi} \right) \hat{\psi} \;\; . \end{aligned} \tag{6}$$

In the broken symmetry formulation, the Bose condensation is characterized by the emergence of a complex valued order parameter: $\langle\hat{\psi}\rangle = \phi \neq 0$, which we will call the condensate field. The expectation value over the Heisenberg equation (6) then yields a meaningful equation of motion for the condensate field. Finally, for the weakly interacting zero temperature condensates, we may assume 'complete coherence', implying that the expectation value of products of field operators may be replaced by the product of the expectation values, i.e., $\langle\hat{\psi}^\dagger\hat{\psi}\rangle \approx \phi^*\phi$, $\langle\hat{\psi}\hat{\psi}\rangle \approx \phi\phi$ etc... The resulting equation,

$$i\hbar\dot{\phi} = \left[\frac{-\hbar^2\nabla^2}{2m} + V + \lambda|\phi|^2 \right] \phi \;\; , \tag{7}$$

is equivalent to the Gross-Pitaevskii equation (5) with $\phi = \sqrt{N}\chi_0$.

3 Binary Atom Feshbach Resonance

To bring the inter-particle interactions near-resonance, the trapped alkali atoms are placed in an external magnetic field. A high magnetic field [10] aligns the valence electron spins of the alkali atoms and two atoms interact in a triplet state. However, the hyperfine interactions can rearrange the spins of the interacting atoms, bringing the binary atom system to a molecular quasi-bound singlet state. A second hyperfine interaction can flip the electron spins again, breaking up the molecule after which the atoms separate.

What is the role of the magnetic field in this process? Since the intermediate state is created by means of a spin flip process that takes place in an external magnetic field, the intermediate state continuum is shifted. The energy shift Δ depends on the value of the magnetic field strength B, $\Delta(B)$. On

resonance, $B = B_m$, the energy of the m-th bound state of the intermediate channel lines up with the continuum of the incident channel. Near-resonance, the energy difference of the intermediate m-state and the initial state, i.e. the 'detuning' ϵ, is approximately proportional to the magnetic field variation: $\epsilon \approx \partial\Delta/\partial B \times [B - B_m]$. Thus, the magnetic field controls the detuning and, hence, the binary atom interaction.

To be more quantitative, we calculate the effective scattering of the binary atom interactions as the negative of the scattering amplitude $f(k)$ in the limit of vanishing relative momentum k,

$$\begin{aligned} a_{eff} &= -\lim_{k\to 0} f(k) \\ &= a_0 - \lim_{k\to 0} f_{res}(k) \ , \end{aligned} \tag{8}$$

where the scattering amplitude consists of a non-resonant contribution, $-a_0$, and a resonant scattering amplitude, f_{res}. The resonant scattering amplitude can be written in terms of the 'width' Γ_m and the difference in energies of the initial and intermediate state energies, $\epsilon - \hbar^2 k^2/m$ (in the center-of-mass frame):

$$f_{res} = \frac{1}{k} \frac{\Gamma_m/2}{(\epsilon - \hbar^2 k^2/m)^2 + (\Gamma_m/2)^2} \ . \tag{9}$$

We determine the width from Fermi's 'golden rule':

$$\Gamma_m = \frac{2\pi}{\hbar} \sum_k |_{2atom}\langle \mathbf{k}, -\mathbf{k}|V_{spinflip}|\mathbf{K} = 0\rangle_{molecule}|^2 \delta(\epsilon - \hbar^2 k^2/m) \ . \tag{10}$$

The interaction matrix element in the above equation is a '2 atom– 1 molecule' matrix element. Its evaluation involves an integral over the positions of both atomic nuclei. Alternatively, we integrate over the relative and center-of-mass position. Using box normalization, the center-of-mass integral yields $\sqrt{\Omega}^{-1}$, where Ω denotes the macroscopic volume of the box. The matrix element of the spin flip interaction reduces to an amplitude α that is energy-independent in the relevant low energy regime. The result contains a phase space factor $\Omega^{-1} \sum_{\mathbf{k}} \delta(\epsilon - \hbar^2 k^2/m)$ that measures phase space volume the molecule can decay into. Evidently, in the limit $\lim_{k\to 0}$ this volume vanishes, as the molecule can only decay back into the initial state. More precisely, the phase space volume vanishes linearly with k,

$$\Gamma_m = 2\alpha^2 \left(\frac{m}{4\pi\hbar^2}\right) k = \ 2\,\gamma\,k \ , \tag{11}$$

where the constant γ is known as the reduced width.

In the expression of the effective scattering length (8) the k-factor of (11) cancels the k in the denominator of (9), resulting in a simple dispersive dependence on the detuning ϵ:

$$\lambda_{eff} = \frac{4\pi\hbar^2}{m} a_{eff} = \lambda - \frac{\alpha^2}{\epsilon} \ . \tag{12}$$

Note that the effective interaction strength diverges as $\epsilon \to 0$.

This divergence represents one symptom of the illness suffered by the many-body description that treats the system as a single condensate with interactions described by the effective scattering length. Indeed, physically relevant quantities such as the pressure and chemical potential are proportional to the interaction strength and similarly diverge on-resonance. Although one could take this as an indication that the system becomes strongly interacting, the vanishing width indicates that the molecules become long-lived entities near the resonance. In a sense, the molecules lose their virtual character and become 'real'. Under these circumstances, it becomes necessary to describe the system by a many-body theory that includes the molecules explicitly.

4 The Condensate Near a Feshbach Resonance

We revisit the many-body treatment while including the molecules into the description. For that purpose, we introduce two field operators: $\hat{\psi}_a$ for the atoms and $\hat{\psi}_m$ for the quasi-bound molecules. The Feshbach resonant interaction contributes the following term to the Hamiltonian:

$$\int d^3r \left\{ \frac{\alpha}{\sqrt{2}} \hat{\psi}_m^\dagger \hat{\psi}_a \hat{\psi}_a + h.c. \right\} \quad , \tag{13}$$

which gives the correct resonant behavior in the binary atom system.

In describing the many-body physics, we account for the atom-atom (λ_a), molecule-molecule (λ_m) and molecule-atom (λ) interactions and the external potentials experienced by the atoms (V_a) and the molecules (V_m). Measuring the energies relative to the continuum of the incident channel, the detuning ϵ appears as the single molecule energy. The Hamiltonian is

$$\begin{aligned} \hat{H} = \int d^3r \, \Bigg\{ & \hat{\psi}_a^\dagger \left(\frac{-\hbar^2 \nabla^2}{2m} + V_a + \frac{\lambda_a}{2} \hat{\psi}_a^\dagger \hat{\psi}_a \right) \hat{\psi}_a \\ & + \hat{\psi}_m^\dagger \left(\frac{-\hbar^2 \nabla^2}{4m} + \epsilon + V_m + \frac{\lambda_m}{2} \hat{\psi}_m^\dagger \hat{\psi}_a \right) \hat{\psi}_m \\ & + \lambda \hat{\psi}_m^\dagger \hat{\psi}_m^\dagger \hat{\psi}_a \hat{\psi}_a + \left(\frac{\alpha}{\sqrt{2}} \hat{\psi}_m^\dagger \hat{\psi}_a \hat{\psi}_a + h.c. \right) \Bigg\} \quad . \end{aligned} \tag{14}$$

The corresponding Heisenberg equations, $i\hbar \dot{\hat{\psi}}_a = \left[\hat{\psi}_a, \hat{H} \right]_-$ and $i\hbar \dot{\hat{\psi}}_m = \left[\hat{\psi}_m, \hat{H} \right]_-$, read

$$\begin{aligned} i\hbar \dot{\hat{\psi}}_a &= \left(\frac{-\hbar^2 \nabla^2}{2m} + V_a + \lambda_a \hat{\psi}_a^\dagger \hat{\psi}_a + \lambda \hat{\psi}_m^\dagger \hat{\psi}_m \right) \hat{\psi}_a + \sqrt{2} \alpha \hat{\psi}_m \hat{\psi}_a^\dagger \quad , \\ i\hbar \dot{\hat{\psi}}_m &= \left(\frac{-\hbar^2 \nabla^2}{4m} + \epsilon + V_m + \lambda_m \hat{\psi}_m^\dagger \hat{\psi}_m + \lambda \hat{\psi}_a^\dagger \hat{\psi}_a \right) \hat{\psi}_a + \frac{\alpha}{\sqrt{2}} \hat{\psi}_a \hat{\psi}_a \quad . \end{aligned} \tag{15}$$

We take the expectation value of the above operator equations, assuming that the atoms are Bose condensed, $\langle\hat{\psi}_a\rangle = \phi_a \neq 0$. Furthermore, we also allow the molecules to Bose-condense, $\langle\hat{\psi}_a\rangle = \phi_m$. In the assumption of total coherence, we obtain two coupled Gross-Pitaevskii-like equations:

$$
\begin{aligned}
i\hbar\dot{\phi}_a &= \left(\frac{-\hbar^2\nabla^2}{2m} + V_a + \lambda_a|\phi_a|^2 + \lambda|\phi_m|^2\right)\phi_a + \sqrt{2}\alpha\phi_m\phi_a^* \ , \\
i\hbar\dot{\phi}_m &= \left(\frac{-\hbar^2\nabla^2}{4m} + \epsilon + V_m + \lambda_m|\phi_m|^2 + \lambda|\phi_a|^2\right)\phi_m + \frac{\alpha}{\sqrt{2}}\phi_a^2 \ . \qquad (16)
\end{aligned}
$$

Note that the ϕ_m-field experiences a source term $\sim \alpha\phi_a^2$, so that it cannot remain zero. It follows that the coherent atom-molecule interaction forms a molecular condensate in the presence of an atomic Bose condensate. The α-terms in the equations of motion (16) describe the coherent inter-condensate exchange of atom pairs so that the condensates are mutually coherent. Here, the coherent atom-molecule coupling is associated with the Feshbach resonance, but coherent photoassociation may provide an alternative scheme [11] – [12].

5 Josephson-Like Population Oscillations

The aspect of inter-condensate boson exchange is reminiscent of the Josephson junction. In the original paper that earned its author a Nobel price [13], Josephson predicted that a voltage difference over a junction separating superconductors results in a measurable oscillating current. This current reflects oscillations of the relative superfluid populations on either side of the junction, caused by a difference in their chemical potentials. These superfluids are also mutually coherent in the sense that they coherently exchange bosons (fermion pairs, in the case of superconductors).

Likewise, the near-resonant condensate consists of two mutually coherent superfluids. Furthermore, the Feshbach resonance provides a means of creating a chemical potential difference. A sudden change of the near-resonant magnetic field modifies the detuning ϵ and, through ϵ, the molecular chemical potential. In Fig. 1, we show the atomic and molecular densities of a homogeneous condensate of initial density $10^{14}cm^{-3}$ after the detuning was suddenly changed from fifty times to twice the initial atomic chemical potential. The atomic and molecular populations show pronounced oscillations on a time scale that is amenable to experimental detection. Note also that the number of particles decreases with time. Typically, the experiments resonate on rather loosely bound states of high vibrational quantum number. Such molecules are likely to lower their vibrational quantum number in an interaction with another particle. The energy released in this process leads to the loss of the particles, not only to the condensate, but also to the trap system. In addition, the vibrational relaxation damps the population oscillations. We

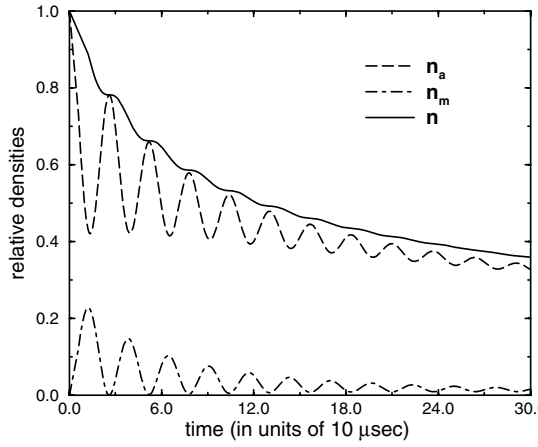

Fig. 1. Plot of the particle densities: the total condensate density, $n = n_a + 2n_m$, is shown in full line, the atomic density n_a in dashed line and the molecular density n_m in dash-dotted line. The condensate is homogeneous with an initial density of $n = 10^{14}\,\mathrm{cm}^{-3}$. At this point, the detuning experienced a sudden shift from $\epsilon = 50\lambda n$ to $\epsilon = 2\lambda n$. The interaction parameters, $\lambda n = \lambda_m n = \lambda_a n = \alpha\sqrt{n} = 10^5\,\mathrm{Hz}$, and collision rates, $c_{ma} = c_{mm} = 5 \times 10^{-10}\,\mathrm{cm}^3\mathrm{sec}^{-1}$ are realistic

estimated the rate constant for vibrational relaxation used in computing Fig. (1) from calculations on Hydrogen and Helium [14].

Although the oscillations superficially resemble Rabi-oscillations, there is a crucial difference. While Rabi oscillations appear in classically moving atoms, the Feshbach atom/molecule population oscillations imply long-range order. While a binary atom Feshbach resonance can cause oscillations in the atom-molecule population of individual atom pairs, these oscillations start when the atoms 'meet'. For classically moving atoms, the collisions occur randomly and the oscillations 'wash out'. Thus, the prediction of macroscopically coherent the population oscillations is remarkable. In a sense, they represent macroscopically coherent chemistry.

6 Statistics

For reasons that we detail below, the dependence of the energy per particle, E/N, on density can have a local minimum. Therefore, the ground state system, unrestrained by physical boundaries, would take on the value that gives minimal energy – a self-determined density. To see that, we start by calculating the many-body energy E as the expectation value of the Hamiltonian:

$$E = \int d^3r \, \left\{ \phi_a^* \left(\frac{-\hbar^2\nabla^2}{2m} + V_a + \frac{\lambda_a}{2}|\phi_a|^2 \right) \phi_a \right.$$

$$+\phi_m^* \left(\frac{-\hbar^2 \nabla^2}{4m} + \epsilon + V_m + \frac{\lambda_m}{2} |\phi_m|^2 \right) \phi_m$$
$$+\lambda |\phi_a|^2 |\phi_m|^2 + \alpha \sqrt{2} |\phi_m| |\phi_a|^2 \cos(\theta_m - 2\theta_a) \Big\} \quad . \tag{17}$$

The atom-molecule coupling is the only phase-dependent contribution and its minimization leads to a definite phase relation, $\theta_m - 2\theta_a = \pi$. With this phase condition, the expression for the ground state energy reduces to integrals over the field amplitudes. For a homogeneous system, $|\phi_a| = \sqrt{N_a/\Omega}$, where N_a denotes the expectation value of the number of atoms and Ω the macroscopic volume of the system. The coherent atom-molecule energy reduces to

$$-\sqrt{2}\alpha \int d^3r \; n_m^{1/2} n_a = -\sqrt{2}\alpha N \sqrt{\frac{N}{\Omega}} \sqrt{\frac{N_m}{N}} \frac{N_a}{N} \quad , \tag{18}$$

where N denotes the total number of atomic particles, $N = N_a + 2N_m$.

The energy-per-particle consists of three types of contributions:

$$\frac{E}{N} = \frac{N}{\Omega} \left(\frac{\lambda_a}{2} f_a^2 + \frac{\lambda_m}{2} f_m^2 + \lambda f_m f_a \right) - \alpha \sqrt{\frac{2N}{\Omega}} f_a \sqrt{f_m} + \epsilon f_m \quad , \tag{19}$$

where we have denoted the fraction of atoms and molecules by f, $f_a = N_a/N, f_m = N_m/N$. The interaction contribution is, as usual, inversely proportional to the volume Ω. The single molecule energy is volume-independent, and the atom-molecule contribution is negative and inversely proportional to $\sqrt{\Omega}$. Since $f_a + 2f_m = 1$, the expression (19) can easily be minimized with respect to the fraction of molecules. However, even without minimization, simple considerations lead to interesting conclusions. We specialize to the on-resonant system, $\epsilon = 0$, in the dilute limit, $\Omega \to \infty$. As $\Omega \to \infty$, the interaction energy vanishes more quickly, and the atom-molecule energy dominates. The latter energy is negative and, moreover, its derivative with respect to the volume yields a negative pressure. While the negative pressure is not surprising – the effective scattering length goes negative in the same limit – the fact that the resulting mechanical instability does not necessarily imply collapse, is. As the system responds to the negative pressure by decreasing its volume, the interaction contributions ($\sim \Omega^{-1}$) grow faster than the atom-molecule energy ($\sim \Omega^{-1/2}$) and may stabilize the system. In the high density limit, the interaction term dominates, giving the energy of an ordinary mixture of atomic and molecular gases. If the mixture is stable, this energy is linear with density of positive slope. In between both density limits, the slope changes sign and E/N goes through a minimum.

The magnitude of the self-determined density follows from equating the interaction energy with the coherent atom-molecule interaction. For realistic values of the α parameter this condition yields densities of the order of $10^{14} cm^{-3}$. That this value is so low – eight to nine orders of magnitude below the densities of usual (classical) liquids – is both significant and important. It

is important, because at these densities the system may survive the bothersome, but unavoidable, destructive recombination processes. It is significant, because it suggests the possibility of creating the first laboratory example of a truly rarefied liquid.

7 Summary

In conclusion, we have discussed the BEC-structure near a magnetically controlled low energy Feshbach resonance. The many-body system consists of mutually coherent atomic and molecular condensates. A practical signature for detecting this new bosonic superfluid state of matter is the observation of Josephson-like population oscillations in response to a sudden change of the magnetic field. Furthermore, the density dependence of the ground state energy suggests the unusual property of a liquid-like self-determined density.

Acknowledgements

This paper is dedicated to the memory of Dan Walls who, I think, would have been particularly interested in the mutual matter-wave coherence of this system.

Acknowledgment

It is a pleasure to acknowledge many fruitful interactions with the people that have collaborated with me on this and related topics: Paolo Tommasini, Peter Milonni, Arthur Kerman, Robin Côté and Mahir Hussein.

References

1. M.H. Anderson *et al.*: Science **269**, 198-201 (1995); K.B. Davis *et al.*: Phys. Rev. Lett. **75**, 3969-3973 (1995); C.C. Bradley *et al.*: Phys. Rev. Lett. **75**, 1687-1690 (1995); and **78**, 985 (1997)
2. In addition to the Feshbach resonance, other schemes have been proposed e.g. by means of external electric fields, see P.W. Milonni, A. Smith: Phys. Rev. A **53**, 3484 (1996), and P.O. Fedichev *et al.*: Phys. Rev. Lett. **77**, 2913 (1996)
3. Y. Kagan, E.L. Surkov, G.V. Shlyapnikov: Phys. Rev. Lett. **79** 2604 (1997)
4. The first discussion of the Feshbach resonance in the context of atom traps appeared very early on: W. Stwalley: Phys. Rev. Lett. **37**, 1628 (1976)
5. The binary atom physics was explored in detail by B. Verhaar and his group and, more recently by the AMO-group at JILA: E. Tiesinga *et al.*: Phys. Rev. A. **46**, R1167-R1170 (1992); E. Tiesinga *et al.*: Phys. Rev. A **47**, 4114-4122 (1993); A.J. Moerdijk *et al.*: Phys. Rev. A **51**, 4852-4861 (1995); J.M. Vogels *et al.*: Phys. Rev. A R1067-1070 (1997); H.M.J.M. Boesten *et al.*: Phys. Rev. A **54**, R3726-R3729 (1996); J.P. Burke, C.H. Greene, J.L. Bohn: Phys. Rev. Lett. **81**, 3355 (1998)

6. S. Inouye *et al.*: Nature **392**, 151-154 (1998); Ph. Courteille *et al.*: Phys. Rev. Lett. **81**, 69 (1998); J.L. Roberts *et al.*: Phys. Rev. Lett. **81**, 5109 (1998) V. Vuletic *et al.* (1998)
7. P. Tommasini *et al.*: preprint, cond-mat/9804015 (1998); E. Timmermans *et al.*: preprint, cond-mat/9805323 (1998); R. Côté *et al.*: proceedings of E.U. meeting on 'New Directions in Atomic Physics,' eds. C.T. Whelan *et al.* (Plenum Press, New York, in press); E. Timmermans: Proceedings of international meeting on "Collective Excitations in Bose and Fermi systems," held September 1998, Serra Negra, Sao Paulo, Brazil (World Scientific, Singapore 1999); E. Timmermans *et al.*: Phys. Rep. **315**, 199 (1999); Phys. Rev. Lett. **83**, 2691(1999)
8. E.P. Gross: Nuovo Cimento **20**, 454 (1961)
9. L.P. Pitaevskii: Sov. Phys. -JETP **13**, 451 (1961)
10. Although this is not the limit that the current experiments operate in, the high-magnetic field limit offers the advantage of simplifying the multichannel analysis.
11. P.D. Drummond *et al.*: Phys. Rev. Lett. **81**, 3055 (1998)
12. J. Javanainen, M. Mackie: Phys. Rev. A. **59**, R3186(1999)
13. B.D. Josephson: Phys. Lett. **1**, 251 (1962); Adv. Phys. **14**, 419 (1965)
14. N. Balakrishnan *et al.*: Phys. Rev. Lett. **80**, 3224 (1998)

Collisional and Collapse Dynamics of a Twin Bose–Einstein Condensate with Negative Scattering Length

Weiping Zhang, Karl-Peter Marzlin, Leon Tribe, and Barry C. Sanders

Summary. We study the collisional and collapse dynamics of a twin Bose–Einstein condensate with an attractive interatomic interaction. We show that the collision between two Bose–Einstein components with densities higher than the critical density for instability can first lead to a collapse due to the attractive interatomic interaction followed by a cessation of collapse due to the mutual nonlinear interaction.

1 Introduction

Atomic gases, which have undergone Bose–Einstein condensation, exhibit macroscopic quantum coherence. Mean-field theory may be applied which leads to a description of these condensates by the Gross-Pitaevskii equation (GPE). The GPE describes the condensate in terms of an effective single–atom wave function. In the GPE, the nonlinear interaction of the Bose–Einstein condensate (BEC) arises from, and depends directly on, the interatomic interaction. For BECs which have thus far been realised in atomic gases, the ^{87}Rb BEC[1], the ^{23}Na BEC[2] and the ^{1}H BEC[3] have a repulsive interaction, and the ^{7}Li BEC[4,5] has an attractive interaction. Both the magnitude and sign of the interactions are responsible for quite different behaviours of these BECs. For ^{7}Li, the attractive interaction may lead to a critical density above which the single BEC system is unstable and consequently undergoes collapse.

Collapse is a feature of BECs with an attractive interaction, but the collision between two BECs can mitigate this collapse as we show here. We solve the GPE numerically for the collisional dynamics of a twin BEC with two different spin components. The stability of a single BEC with attractive interaction has been studied in detail both theoretically and experimentally[6–18]. A motivation for this study is to determine the effect of two components on the stability of a single BEC. For simplicity, we treat the case of a BEC in an effective two–dimensional geometry. A weak harmonic potential confines the BEC in the y–dimension, and a strong harmonic potential confines the BEC in the z–dimension. The x–dimension is open to allow for free collisional dynamics. Free collisional dynamics has been of interest, for example, in the study of propagating BEC pulses[19–21].

H.J. Carmichael, R.J. Glauber, M.O. Scully (Eds.): LNP 561, pp. 70–76, 2001.

2 Theory

We begin with two coupled nonlinear equations which describe the coherent collisional dynamics of a twin BEC in two different spin states. The twin BEC is represented by two macroscopic quantum wave functions ψ_1 and ψ_2 in the mean–field approximation. The interatomic interaction between the two components is characterised by the scattering strengths a_{11}, a_{22} and a_{21}. The resultant mean–field equations for the two components has the following form

$$\begin{aligned} i\hbar\frac{\partial\psi_1}{\partial t} &= \left(-\frac{\hbar^2}{2m}\nabla^2 + U(\boldsymbol{r})\right)\psi_1 + \frac{4\pi\hbar^2}{m}\left(a_{11}|\psi_1|^2 + a_{12}|\psi_2|^2\right)\psi_1, \\ i\hbar\frac{\partial\psi_2}{\partial t} &= \left(-\frac{\hbar^2}{2m}\nabla^2 + U(\boldsymbol{r})\right)\psi_2 + \frac{4\pi\hbar^2}{m}\left(a_{22}|\psi_2|^2 + a_{21}|\psi_1|^2\right)\psi_2 \end{aligned} \tag{1}$$

with the two macroscopic wave functions normalised by the relation

$$\int d^3\boldsymbol{r}\,|\psi_i|^2 = \mathcal{N}_i,\ i \in \{1,2\}, \tag{2}$$

with $\mathcal{N}_i$ the (conserved) number of atoms in each component i, $\mathcal{N} = \mathcal{N}_1 + \mathcal{N}_2$ the total number of atoms, and $\boldsymbol{r} \equiv (x,y,z)^T$.

Our interest here is in collisional dynamics with a trap–confining potential $U(\boldsymbol{r})$, which is specified in two dimensions (y,z) by a two–dimensional (2D) harmonic trap. The x–dimension is unconfined, thereby allowing free collisions. Furthermore, we have assumed that the dynamics along the z–dimension can be ignored by applying an appropriate trapping potential.

For $\boldsymbol{r}_\perp \equiv (x,y)^T$, we make the ansatz

$$\psi_1(\boldsymbol{r},t) = \phi_1(\boldsymbol{r}_\perp,t)f(z), \psi_2(\boldsymbol{r},t) = \phi_2(\boldsymbol{r}_\perp,t)f(z) \tag{3}$$

where $f(z)$ is the shape function of the initial BEC along the z axis. We assume that the shape function is normalised according to

$$\int_{-\infty}^{\infty}|f|^2dz = 1, \tag{4}$$

which yields the normalisation relation

$$\int d^2\boldsymbol{r}_\perp\,|\phi_i|^2 = \mathcal{N}_i,\ i \in \{1,2\}. \tag{5}$$

To simplify the equations, we introduce the dimensionless variables and normalised macroscopic wave functions

$$\bar{x} \equiv x/w_x, \bar{y} \equiv y/w_y, \bar{z} \equiv z/w_z, \tau \equiv \nu t, \phi_j = \sqrt{\mathcal{N}}\bar{\phi}_j/w, \tag{6}$$

with $w_{x,y,z}$ the widths of the initial BEC in the x,y,z directions, respectively. We assume that $w \equiv w_x = w_y$, and the effective frequency parameter is set as

$\nu = \hbar/2mw^2$. For $\bar{\nabla}_\perp$ the transverse gradient with respect to the normalised coordinates $\bar{\boldsymbol{r}}_\perp = (\bar{x}, \bar{y})^T$, the normalised equations are

$$i\frac{\partial\bar{\phi}_1}{\partial\tau} = \left(-\bar{\nabla}_T^2 + \beta\bar{y}^2\right)\bar{\phi}_1 + \left(V_{11}|\bar{\phi}_1|^2 + V_{12}|\bar{\phi}_2|^2\right)\bar{\phi}_1,$$
$$i\frac{\partial\bar{\phi}_2}{\partial\tau} = \left(-\bar{\nabla}_T^2 + \beta\bar{y}^2\right)\bar{\phi}_2 + \left(V_{22}|\bar{\phi}_2|^2 + V_{21}|\bar{\phi}_1|^2\right)\bar{\phi}_2 \tag{7}$$

with

$$\beta = \frac{m\omega^2 w^2}{2\hbar\nu}, V_{ij} = \frac{\rho_0}{\nu}\frac{4\pi\hbar\bar{a}_{ij}}{m}. \tag{8}$$

The effective peak density is defined by $\rho_0 = \mathcal{N}/\mathcal{V}$, with $\mathcal{N}$ the effective particle number (5) and $\mathcal{V} \equiv w_x w_y w_z$the effective volume. The effective scattering length corresponds to $\bar{a}_{ij} \equiv a_{ij}\Gamma$, with

$$\Gamma = \int_{-\infty}^{\infty} |f(\bar{z})|^4 d\bar{z} \tag{9}$$

the shape factor.

Our central interest is in the collisional dynamics of twin BECs with negative scattering lengths. Hence the natural choice is to study the ^{7}Li BEC[4,5] with corresponding parameters

$$\bar{a}_{11} = \bar{a}_{22} \approx -27.3a_0 = -1.44\text{nm} \tag{10}$$

and $\omega = 160 \times 2\pi\text{Hz}$. We introduce the effective trap size $d_c \sim 0.67\sqrt{\hbar/m\omega}$. With this definition we also obtain

$$w = d_c = 0.67\sqrt{\hbar/m\omega} \approx 2 \times 10^{-4}\,\text{cm},\ \nu \approx 1123\,\text{Hz},\ \beta \approx 0.2. \tag{11}$$

In this paper, we have assumed the simple case $\chi \equiv V_{12} = V_{21} = V_{11} = V_{22}$.

3 Simulation and Results

For the normalised equations presented in the previous section, we have developed computer codes to simulate a one–dimensional collision dynamics in a two–dimensional geometry. We apply the standard split-operator technique to solve the coupled nonlinear equations. The initial condensate wave functions are Gaussians and identical for the two components.

For Bose–Einstein condensates with attractive interactions, there is a critical density above which collapse is inevitable. However, collisional dynamics can yield stability even above the critical density as we show here. Let us assume a density for each condensate higher than the critical density which in the simulation results in correspondingly large nonlinear coefficients $V_{11} = V_{12} = V_{22} = -12.2$.

The simulated results are presented in Fig. 1. Although the two components overlap at certain times during the collision, the figure presents the two

components separately. This distinctive representation is essential to convey clearly the dynamic nonlinear effect which is evident in Fig. 1. The dynamics are presented for three values of the time parameter: the initial time (0 ms), the early stage of the collision where dynamic nonlinear interactions can be observed (2 ms) and a latter stage of the collision (3 ms).

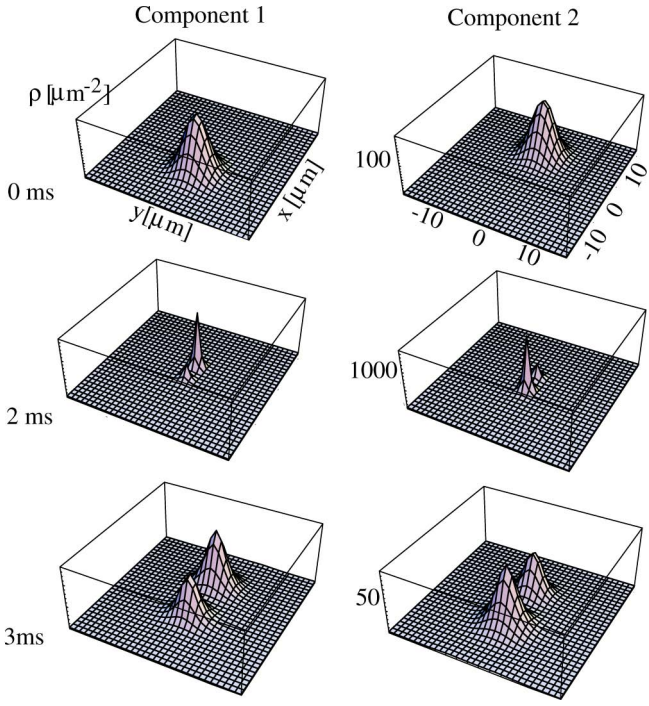

Fig. 1. The two–component Bose–Einstein condensate (BEC), initially separated and moving towards each other with velocities ±4 mm/s in the x–direction. The initial states are Gaussians with equal widths in both the x– and y–directions of 2 μm, and the total atomic number is 6750. The density of the BEC is $\rho_0 = 8.4 \times 10^{13}$ cm^{-3}. The nonlinear coupling coefficients are $V_{11} = V_{12} = V_{22} = -12.2$. The two components are depicted separately but overlap during the collision. The state of the two–component BEC is shown at three times: at 0 ms, 2 ms and 3 ms

During the collision, the two condensates overlap and experience a nonlinear interaction. This nonlinear interaction induces a redistribution of the density for each of the two BEC components. The density redistribution is effectively a nonlinear interaction between the positions of the two BEC com-

ponents, which can be understood via a hydrodynamic analysis. We employ the transformation

$$\psi_j = \sqrt{\rho_j} e^{i\theta_j} \tag{12}$$

for $j = 1, 2$. Eq (1) can be written in the hydrodynamic form

$$\begin{aligned} 0 &= \frac{\partial \rho_j}{\partial t} + \nabla \cdot (\rho_j \boldsymbol{v}_j), \\ m\frac{d\boldsymbol{v_j}}{dt} &= \nabla\left(\frac{1}{4m}\frac{\nabla\rho_j}{\rho_j}\right) - \nabla U - \chi\nabla(\rho_1 + \rho_2), \end{aligned} \tag{13}$$

with $\boldsymbol{v_j} \equiv \hbar\nabla\theta_j/m\,(j = 1, 2)$, and we have assumed equal scattering lengths for the two components with $\chi = 4\pi\hbar^2 a/m$.

For the initial conditions of the simulation presented in Fig. 1, which is given by two counterpropagating Gaussian wavepackets, one can prove that, because $U(-\bar{\mathbf{r}}) = U(\bar{\mathbf{r}})$ and $V_{ij} = \chi$, the following symmetry between the two components is preserved,

$$\phi(\bar{\mathbf{r}}, t) \equiv \phi_1(\bar{\mathbf{r}}, t) = \phi_2(-\bar{\mathbf{r}}, t). \tag{14}$$

The hydrodynamic expression (13) then can be simplified by exploiting the wavefunction symmetry. For $\phi(\bar{\mathbf{r}}, t) = \sqrt{\rho(\bar{\mathbf{r}}, t)}\exp\{i\theta(\bar{\mathbf{r}}, t)\}$, we obtain the hydrodynamic expressions

$$\begin{aligned} 0 &= \frac{\partial \rho(\bar{\mathbf{r}}, t)}{\partial t} + \nabla\left(\rho(\bar{\mathbf{r}}, t)\mathbf{v}(\bar{\mathbf{r}}, t)\right), \\ m\frac{\partial \mathbf{v}(\bar{\mathbf{r}}, t)}{\partial t} &\approx \nabla\left[\frac{1}{4m}\frac{\nabla\rho(\bar{\mathbf{r}}, t)}{\rho(\bar{\mathbf{r}}, t)} - \chi\left(\rho(\bar{\mathbf{r}}, t) + \rho(-\bar{\mathbf{r}}, t)\right)\right]. \end{aligned} \tag{15}$$

The contribution by the potential U has been neglected in this expression.

In order to understand (15), it is helpful to first consider the case of a single BEC component for which $\rho(-\bar{\mathbf{r}}, t)$ is absent. For the condition of stability, the curvature term in (15) cancels the contribution from the nonlinear interaction term. However, a strong nonlinearity leads to a collapse. In our simulations the collapse time of a single BEC component was about 2 ms.

The collapse dynamics for the twin BEC is entirely different. For example we can consider a BEC component with a Gaussian profile. Provided that the two BEC components are well–separated, the contribution of $\rho(-\bar{\mathbf{r}}, t)$ to the overall dynamics is negligible, and the collapse can take place. If, however, the two BEC components are moving towards each other, the contribution of $\rho(-\bar{\mathbf{r}}, t)$ can offset the collapse dynamics to some extent by an overlap between the two BEC components. The effect is most pronounced when the two components completely overlap and $\rho(\bar{\mathbf{r}}, t) = \rho(-\bar{\mathbf{r}}, t)$. For this case of total overlap the collapse is, in fact, accelerated, and the curvature of the BEC is enhanced: the Gaussian is therefore becoming narrower.

The density $\rho(\bar{\mathbf{r}}, t)$ is, of course, time–dependent, and the two components eventually become well–separated. That is, after sufficient time, $\rho(\bar{\mathbf{r}}, t)$ and

$\rho(-\bar{\mathbf{r}}, t)$ approach the situation of having negligible overlap. As the two components separate, the nonlinear interaction energy reduces to near its original value, but the BEC component has been left in a narrow state, that is, one with strong curvature. This strong curvature induces an expansion of the BEC, and the collapse time is thereby increased. In this way, the collapse dynamics are mitigated by temporary overlap of the two components of the BEC.

The relative velocity of the two BEC components is an important parameter in reducing the collapse of the BEC. For a relative velocity with a small magnitude, the separation of the two components of the BEC is not rapid enough to allow the nonlinear interaction energy to quickly return to near its original value, and collapse occurs even faster (after about 1 ms). For a large relative velocity, the duration of the overlap is too short to permit sufficient narrowing of the BEC peak (and therefore growth in the curvature) to halt or slow the collapse: the collision does not, in the case of large relative velocities, prevent collapse.

For a relatively long time evolution (about 3 ms), our simulation shows that the collapse, which usually should occur after about 2 ms, has been prevented by the collision between the two components of the BEC. Therefore, the co–existence of two colliding BEC components can stabilise each other under conditions for which each component would otherwise undergo collapse.

Acknowledgments

This work was supported by an Australian Research Council Small Grant. LT has been supported by an Australian Postgraduate Research Award. K-PM has been supported by the Optik-Zentrum Konstanz. We thank R. G. Hulet and C. A. Sackett for helpful discussions.

References

1. M.H. Anderson, J.R. Ensher, M.R. Matthews, C.E. Wieman, E.A. Cornell: Science **269**, 198 (1995)
2. K.B. Davis, M.-O. Mewes, M.R. Andrews, N.J. van Druten, D.S. Durfee, D.M. Kurn, W. Ketterle: Phys. Rev. Lett. **75**, 3969 (1995)
3. D.G. Fried, T.C. Killian, L. Willmann, D. Landhuis, S.C. Moss, D. Kleppner, T.J. Greytak: Phys. Rev. Lett. **81**, 3811 (1998)
4. C.C. Bradley, C.C. Bradley, C.A. Sackett, J.J. Tollett, R.G. Hulet: Phys. Rev. Lett. **75**, 1687 (1995)
5. C.C. Bradley, C.A. Sackett, R.G. Hulet: Phys. Rev. Lett. **78**, 985 (1997)
6. M. Houbiers, H.T.C. Stoof: Phys. Rev. A **54**, 5055 (1996)
7. C.A. Sackett, H.T.C. Stoof, R.G. Hulet: Phys. Rev. Lett. **80**, 2031 (1998)
8. C.A. Sackett, J.M. Gerton, M. Welling, R.G. Hulet: Phys. Rev. Lett. **82**, 876 (1999)

9. W. Zhang, B.C. Sanders, A. Mann: J. Phys. I (France) **6**, 1411 (1996)
10. Yu. Kagan, A.E. Muryshev, G.V. Shlyapnikov: Phys. Rev. Lett. **81**, 933 (1998)
11. D. Gordon, C.M. Savage: Phys. Rev. A **58**, 1440 (1998)
12. J.A. Freire, D.P. Arovas: Phys. Rev. A **59**, 1461 (1999)
13. A. Parola, L. Salasnich, L. Reatto: Phys. Rev. A **57**, R3180 (1998)
14. M.J. Davis, D.A.W. Hutchinson, E. Zaremba: cond-mat/9906334
15. L. Berge, T.J. Alexander, Y.S. Kivshar: cond-mat/9907408
16. E.J. Mueller, G. Baym: cond-mat/9908133
17. A.Eleftheriou, K. Huang: cond-mat/9908229
18. V.M. Perez–Garcia, V.V. Konotop, J.J. Garcia–Ripoll: cond-mat/9912301
19. G. Lenz, P. Meystre, E.M. Wright: Phys. Rev. Lett. **71**, 3271 (1993)
20. W. Zhang, D.F. Walls, B.C. Sanders: Phys. Rev. Lett. **72**, 60 (1994); S. Dyrting, W. Zhang, B.C. Sanders: Phys. Rev. A **56**, 2051 (1997)
21. W. Zhang, D.F. Walls: Phys. Rev. A **49**, 3799 (1994)
22. W. Zhang, B.C. Sanders, W. Tan: Phys. Rev. A **56**, 1433 (1997)

Schrödinger Cat State of a Bose–Einstein Condensate in a Double-Well Potential

J. Ruostekoski

Summary. We consider a weakly interacting coherently coupled Bose-Einstein condensate in a double-well potential. We show by means of stochastic simulations that the system could possibly be driven to an entangled macroscopic superposition state or a Schrödinger cat state by means of a continuous quantum measurement process.

1 Introduction

Since the first observations of Bose-Einstein condensation in dilute alkali-metal atomic gases [1–3] the ultra-cold atomic gases have stimulated significant theoretical and experimental interest [4]. The scientific progress has been rapid and examples of recent experiments include the development of accurate detection methods [5], the state preparation of topological structures [6], and the applications in nonlinear atom optics [7]. Due to the macroscopic quantum coherence Bose-Einstein condensates (BECs) could possibly be also used in the future as a test for the foundations of quantum mechanics. One particularly puzzling and controversial issue has been the existence of macroscopic quantum superposition states in many-particle quantum systems. In this paper we propose a method of creating the Schrödinger cat states of different atom occupation numbers in a weakly interacting BEC confined in a double-well potential.

The existence of the superpositions of macroscopically distinguishable states in BECs has been addressed by several authors [8–12]. The superposition state may arise as the ground state of a coherently coupled BEC in a double-well potential [9,10]. Under certain conditions it could be reached as a result of a unitary time evolution [11]. Previously, we proposed a method of creating Schrödinger cat states in BECs by means of scattering light from two BECs moving with opposite velocities [8]. The nonunitary evolution due to the detections of scattered photons drives the condensates to macroscopic quantum superposition states. In this paper we show that a continuous quantum measurement process could also drive a trapped coherently coupled BEC in a double-well potential to a Schrödinger cat state. The advantage of the proposed scheme is that the BEC is almost stationary and trapped. Moreover, as a result of the back-action of quantum measurement process the superpo-

H.J. Carmichael, R.J. Glauber, M.O. Scully (Eds.): LNP 561, pp. 77–87, 2001.

sition state could be reached rapidly unlike in a slow unitary evolution, which may be very sensitive to decoherence.

The paper is organized as follows: We begin in Sect. 2.1 by introducing the unitary system Hamiltonian. The scattering of light and the measurement geometry is described in Sect. 2.2. In Sect. 2.3 we study the dynamics of the open quantum system in terms of stochastic trajectories of state vectors. The results of the numerical simulations are presented in Sect. 3. Finally, a few concluding remarks are made in Sect. 4.

2 System Dynamics

2.1 Unitary Evolution

We consider the evolution of a BEC in a double-well potential in a two-mode approximation. Macroscopic quantum coherence of BECs results in coherent quantum tunneling of atoms between the two modes representing 'two BECs'. This is analogous to the coherent tunneling of Cooper pairs in a Josephson junction [13–18]. To obtain the system Hamiltonian in the two-mode approximation for the unitary evolution of the BEC we approximate the total field operator by the two lowest quantum modes $\psi(\boldsymbol{r}) \simeq \psi_b(\boldsymbol{r})b+\psi_c(\boldsymbol{r})c$, where ψ_b and ψ_c stand for the local mode solutions of the individual wells with small spatial overlap. The corresponding annihilation operators are denoted by b and c. The Hamiltonian in the two-mode approximation reads [14]:

$$\frac{H_S}{\hbar} = \xi b^\dagger b + \Omega(b^\dagger c + c^\dagger b) + \kappa[(b^\dagger)^2 b^2 + (c^\dagger)^2 c^2] \,. \tag{1}$$

Here ξ is the energy difference between the modes. The tunneling between the two wells is described by Ω, which is proportional to the overlap of the spatial mode function of the opposite wells. The short-ranged two-body interaction strength is obtained from $\kappa = 2\pi a\hbar/m \int |\psi_b(\boldsymbol{r})|^4$, where a and m denote the scattering length and the atomic mass, respectively. For simplicity, here we have assumed that $\int |\psi_b(\boldsymbol{r})|^4 = \int |\psi_c(\boldsymbol{r})|^4$. A necessary condition for the validity of the single-mode approximation in a harmonic trap is that the oscillation energy of the atoms do not dominate over the mode energy spacing of the trap.

According to the Josephson effect, the atom numbers of the BECs determined by the Hamiltonian (1) may oscillate even if the number of atoms in each well is initially equal. Due to the nonlinear self-interaction the number oscillations also exhibit collapses and revivals. These have been studied numerically in [14]. We may also obtain a simple analytical description by solving the dynamics in the rotating wave approximation in the limit $\Omega \gg N\kappa$ as described in [19]. Here N denotes the total number of atoms. In particular, we may solve the number of atoms $N_b \equiv \langle b^\dagger b\rangle$ in well b. We consider a coherent state in the both wells as an initial state. Then we obtain

$$N_b = \frac{N}{2}\left[1 + \mathrm{e}^{N[\cos(\kappa t)-1]}(\sqrt{1-\beta^2}\cos\eta - \beta\sin\varphi\sin\eta)\right] , \tag{2}$$

with $\eta \equiv N\beta \sin(\kappa t)\cos\varphi - 2\Omega t$. Here all the operators on the right-hand side have been evaluated at $t = 0$. It is useful to define the real expectation values β and φ in the following way:

$$\beta e^{i\varphi} \equiv \frac{2}{N}\langle b^\dagger c\rangle \ . \tag{3}$$

For a coherent state with equal atom numbers in the two wells we obtain the visibility $\beta = 1$. The relative phase between the wells is φ. For a number state there is no phase information and $\beta = 0$. For unequal atom numbers the maximum visibility is $\beta_{\max} = 2(N_b N_c)^{1/2}/N$. We see that the number of atoms in (2) may oscillate in the case of initially equal atom numbers $\beta = 1$. The amplitude of sinusoidal oscillations, representing the macroscopic coherence, collapses. For instance, for $\varphi = \pi/2$ and $\beta = 1$ we may obtain the short time decay by considering the time scales $N\kappa t \ll 1 \ll \Omega t$. Then the decay of the oscillations has the form $\exp(-N\kappa^2 t^2/2)$. This is the rate of the phase diffusion and it may be interpreted as the width of the relative phase $\langle \Delta\varphi^2(t)\rangle \simeq N\kappa^2 t^2 \sim \kappa^2 t^2/\langle \Delta\varphi^2(0)\rangle$. Perhaps surprisingly the functional dependence of the width in this case is the same as in the case of two uncoupled BECs [4].

If the phase is unknown we may obtain the ensemble average by integrating over the relative phase φ in (2):

$$N_b = \frac{N}{2}\left\{1 + e^{N[\cos(\kappa t)-1]}\sqrt{1-\beta^2}\cos(2\Omega t)\, J_0[N\beta\sin(\kappa t)]\right\} \ , \tag{4}$$

where J_0 is the 0th order Bessel function. If the both wells have initially equal number of atoms, $\beta = 1$, the atom numbers do not oscillate. For unequal atom numbers the oscillations collapse at the first zero of the Bessel function $t \simeq 2.4/(N\beta\kappa)$ for $(N_b N_c)^{1/2} \gg 1$.

2.2 Quantum Measurement Process

The time evolution of the system is nonunitary, when we include the effect of quantum measurement process. We consider the nondestructive measurement of the number of atoms in the both wells by means of shining coherent light beams through the atom clouds. The scattered light beams are combined by a 50-50 beam splitter. We display the measurement setup in Fig. 1.

We assume that the incoming light fields are detuned far from the atomic resonance. For instance, if the shape of the gas is flat and the light is shone through a thin dimension, the multiple scattering is negligible and the sample can be considered optically thin. A BEC atom scatters back to the BEC via coherent spontaneous scattering, stimulated by a large number of atoms in the BEC. Coherently scattered photons are emitted into a narrow cone in the forward direction. By spontaneous scattering we mean that the emission is not stimulated by light, although it is stimulated by atoms. The decay into noncondensate center-of-mass states is also stimulated by the Bose-Einstein

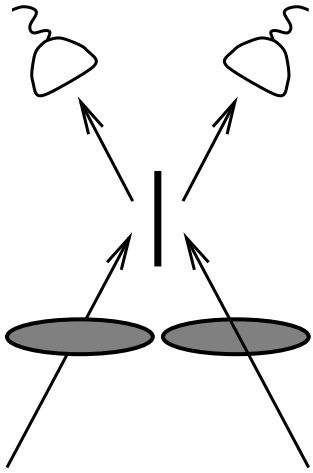

Fig. 1. The measurement setup. Two incoming light fields are scattered from two coherently coupled BECs. The two scattered photon beams are combined by a 50-50 beam splitter. The photons are detected from the two output channels of the beam splitter. One of the output channels introduces only a constant phase shift and it may be ignored

statistics. However, at very low temperatures this stimulation is much weaker because most of the particles are in the BEC. As a first approximation we ignore the scattering from and to the noncondensate modes. Then the measurement is nondestructive in the sense that BEC atoms in the modes b and c scatter back to the same modes b and c. Because the overlap of the mode functions of the different wells is assumed to be small, the scattering between the two wells is ignored.

The detection rate of photons on the detectors is the intensity of the scattered light $I(\boldsymbol{r})$ integrated over the scattering directions divided by the energy of a photon $\hbar ck$. Here k and c stand for the wave number and the velocity of light. We obtain the detection rate at the channel j:

$$\gamma_j = \frac{1}{\hbar ck} \int d\Omega_{\hat{\boldsymbol{n}}}\, r^2 I_j(\boldsymbol{r}) = 2\Gamma \langle C_j^\dagger C_j \rangle \; . \tag{5}$$

The photon annihilation operator at the output channel j of the beam splitter is denoted by C_j. For a symmetric measurement geometry we obtain

$$C_1 = \frac{1}{\sqrt{2}}(b^\dagger b - c^\dagger c) \; , \quad C_2 = \frac{1}{\sqrt{2}}(b^\dagger b + c^\dagger c) \; . \tag{6}$$

Because the total number of atoms is assumed to be conserved, the operator $\hat{N} \equiv b^\dagger b + c^\dagger c$ contributes to the measurements only through a constant phase shift. Therefore, we may ignore the effect of the scattering channel 2 on the dynamics.

The scattered intensity may be written in terms of the positive frequency component of the scattered electric field $\boldsymbol{E}^+(\boldsymbol{r})$

$$I(\boldsymbol{r}) = 2c\varepsilon_0 \langle \boldsymbol{E}^-(\boldsymbol{r}) \cdot \boldsymbol{E}^+(\boldsymbol{r}) \rangle \; , \tag{7}$$

Here ε_0 denotes the permittivity of the vacuum.

We assume that the driving electric fields may be approximated by plane waves $\boldsymbol{E}_d^+(\boldsymbol{r}) = \mathcal{E}\hat{\boldsymbol{e}}\, e^{i(\boldsymbol{k}\cdot\boldsymbol{r}-\Omega t)}/2$. In the limit of large atom-light detuning Δ we use the first Born approximation and write the electric fields in the far radiation zone ($kr \gg 1$). Then the scattered field from the well b has the following form [20]:

$$\boldsymbol{E}^+(\hat{\boldsymbol{n}}r) = \frac{k^2\mathcal{R}\mathrm{e}^{\mathrm{i}kr}}{4\pi\varepsilon_0\Delta r}\,\hat{\boldsymbol{n}}\times(\hat{\boldsymbol{n}}\times\boldsymbol{d})\int d^3r'\mathrm{e}^{\mathrm{i}(\boldsymbol{k}-k\hat{\boldsymbol{n}})\cdot\boldsymbol{r}'}|\psi_b(\boldsymbol{r}')|^2 b^\dagger b\,. \tag{8}$$

Here we have defined the Rabi frequency $\mathcal{R}$ of the atomic dipole matrix element $\boldsymbol{d}$ by $\mathcal{R} \equiv d\mathcal{E}/(2\hbar)$. We also assumed that $\boldsymbol{d}\cdot\hat{\boldsymbol{e}} = d$. In the limit that the characteristic length scale ℓ of the BECs is much larger than the inverse of the wave number of the incoming light $\ell \gg 1/k$, the momentum of the scattered photon is approximately conserved, and we obtain in (8):

$$\int d^3r'\mathrm{e}^{\mathrm{i}(\boldsymbol{k}-k\hat{\boldsymbol{n}})\cdot\boldsymbol{r}'}|\psi_b(\boldsymbol{r}')|^2 \simeq \delta(k\hat{\boldsymbol{n}}-\boldsymbol{k})\,. \tag{9}$$

In this simple case the scattering rate Γ may be easily evaluated:

$$\Gamma = \frac{3\gamma\mathcal{R}^2}{8\pi\Delta^2}\,, \tag{10}$$

Here $\gamma = d^2k^3/(6\pi\hbar\varepsilon_0)$ denotes the optical linewidth of the atom.

2.3 Stochastic Schrödinger Equation

The dissipation of energy from the quantum system of macroscopic light fields and the BEC in a double-well potential is described by the coupling to a zero temperature reservoir of vacuum modes, resulting in a spontaneous emission linewidth for the atoms. The dynamics of the continuous quantum measurement process may be unraveled into stochastic trajectories of state vectors [21–23]. The procedure consists of the evolution of the system with a non-Hermitian Hamiltonian H_{eff}, and randomly decided quantum 'jumps'. In our case the quantum jumps correspond to the detections of spontaneously emitted photons. The system evolution is thus conditioned on the outcome of a measurement. The non-Hermitian Hamiltonian has the following form:

$$H_{\mathrm{eff}} = H_S - \mathrm{i}\hbar\Gamma C_1^\dagger C_1\,, \tag{11}$$

where the unitary system Hamiltonian H_S is determined by (1).

Equation (11) corresponds to the modification of the state of the system associated with a zero detection result for scattered photons. Because the output is being continuously monitored, we gain information about the system even if no photons have been detected.

The Hamiltonian H_{eff} determines the evolution of the state vector $\psi_{\mathrm{sys}}(t)$. If the wave function $\psi_{\mathrm{sys}}(t)$ is normalized, the probability that a photon from

the output channel 1 of the beamsplitter is detected during the time interval $[t, t+\delta t]$ is

$$P(t) = 2\Gamma \langle \psi_{\rm sys}(t) \,|\, C_1^\dagger C_1 \,|\, \psi_{\rm sys}(t)\rangle \, \delta t \; . \tag{12}$$

We implement the simulation algorithm as follows: At the time t_0 we generate a quasi-random number ϵ which is uniformly distributed between 0 and 1. We assume that the state vector $\psi_{\rm sys}(t_0)$ at the time t_0 is normalized. Then we evolve the state vector by the non-Hermitian Hamiltonian $H_{\rm eff}$ iteratively for finite time steps Δt. At each time step n we compare ϵ to the reduced norm of the wave function, until

$$\langle \psi_{\rm sys}(t_0 + n\Delta t) \,|\, \psi_{\rm sys}(t_0 + n\Delta t)\rangle < \epsilon \; , \tag{13}$$

when the detection of a photon occurs. If the photon has been observed during the time step $t \to t + \Delta t$ we take the new wave function at $t + \Delta t$ to be

$$|\, \psi_{\rm sys}(t + \Delta t)\rangle = \sqrt{2\Gamma}\, C_1 \,|\, \psi_{\rm sys}(t)\rangle \; , \tag{14}$$

which is then normalized.

3 Numerical Results

We simulate the effect of the system Hamiltonian H_S and the quantum measurement process of scattered photons by means of the stochastic Schrödinger equation. For simplicity, we set the total number of atoms to be reasonably small $N = 200$. We start from a slightly asymmetric initial state with the two modes in number states $N_b = 102$ and $N_c = 98$. We choose $\Gamma/\Omega = 5 \times 10^{-6}$.

After just a few detected photons we observe the emergence of two well-separated amplitude maxima in the occupation number of atoms in one of the two wells. These correspond to a macroscopic number state superposition or a Schrödinger cat state. Because the total number of atoms is assumed to be conserved, the atom numbers in the two wells are entangled and we have a Bell-type of superposition state. In Fig. 2 we display the absolute value of the wave function $|\psi_b|$ in mode b in number state basis in a single run at two different times. In this case the nonlinearity vanishes $\kappa = 0$ and $\xi/\Omega = 0.1$. We clearly recognize the two distinct peaks in the number distribution. For instance, the peaks in Fig. 2 (b) are centered at $N_b \simeq 10$ and $N_b \simeq 190$ corresponding to maxima at $N_c \simeq 190$ and $N_c \simeq 10$, respectively. In Fig. 3 we show the absolute value of the wave function for a different run with $N\kappa/\Omega = 0.2$ and $\xi/\Omega = 0.001$.

We also describe the state of the BEC in terms of the quasiprobability Q distribution. For the number state distribution of atoms $|\psi_b\rangle = \sum_n c_n |n\rangle$ in mode b we obtain [24]:

$$Q(\alpha) = \frac{|\langle \alpha | \psi_b \rangle|^2}{\pi} = \frac{{\rm e}^{-|\alpha|^2}}{\pi} \left| \sum_{n=0}^{N} \frac{\alpha^n c_n^*}{\sqrt{n!}} \right|^2 \; . \tag{15}$$

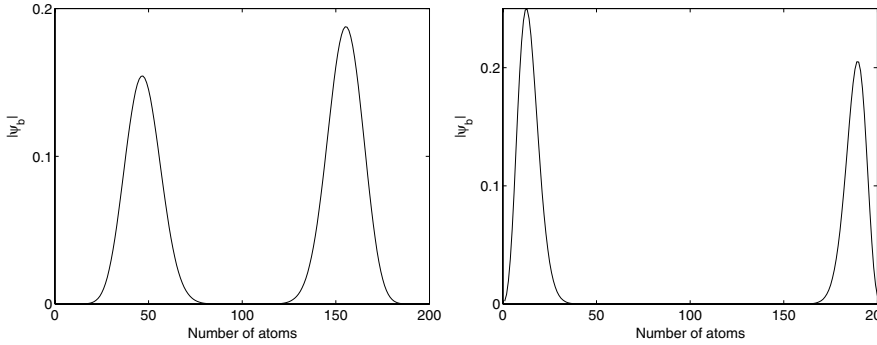

Fig. 2. The entangled Schrödinger cat states of atoms with different atom numbers. We show the absolute value of the wave function $|\psi_b|$ in the number state basis for the atoms in well b during one realization of stochastic measurement process of spontaneously scattered photons after (**a**) 750 and after (**b**) 1700 detections. The two maxima correspond to the superposition states. The nonlinearity $\kappa = 0$ and the total number of atoms $N = 200$

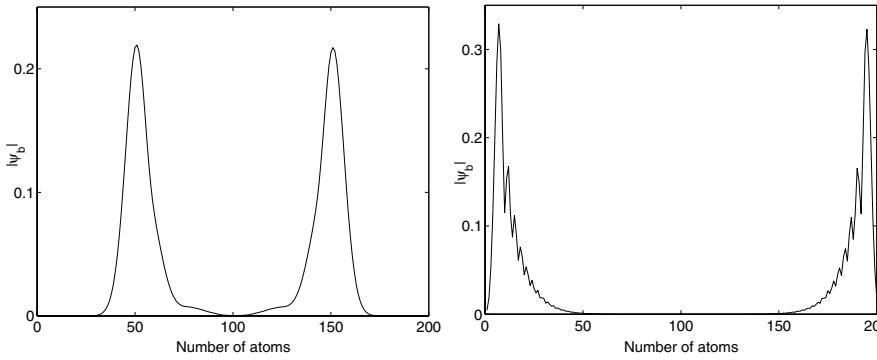

Fig. 3. The entangled Schrödinger cat states of atoms with different atom numbers. We show the absolute value of the wave function $|\psi_b|$ during one realization of stochastic trajectory after (**a**) 100 and after (**b**) 1250 detections. The nonlinearity $N\kappa = 0.2$

The Q function represents the phase-space distribution. The amplitude and phase quadratures are denoted by X and Y. In polar coordinates the radius in the xy plane is equal to $N_b^{1/2}$ and the polar angle is the relative phase between the atoms in the two wells. In Fig. 4 we show the Q function distribution of the number state superposition displayed in Fig. 2(a).

It is interesting to emphasize that the measurement of the number of atoms in only one of the wells affects the system dynamics quite differently. In that case the number state distribution remains well localized and approximately approaches a coherent state [17]. Even though we start from a number state with no phase information, the detections of spontaneously scattered

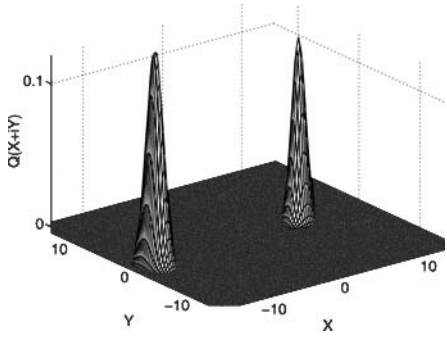

Fig. 4. The Q function of the Schrödinger cat state. We show the Q function of the quantum state displayed in Fig. 2 (a). The two peaks are located at different value of the radius $N_b^{1/2}$ representing the different maxima of the occupation numbers

photons establish a macroscopic coherence or the off-diagonal long-range order (ODLRO) between the atoms in the two separate wells. This is similar to establishing the coherence between two BECs as a result of the counting of atoms [25,26]. However, in the present case the continuous measurement process drives the system to a Schrödinger cat state and the ODLRO remains small. We may describe the visibility of the macroscopic coherence between the two wells by the real parameter β defined in (2). We show the relative visibility $\beta_r \equiv \beta/\beta_{\max}$ and the number of atoms in well b as a function of the number of measurements for $\kappa = 0$ in Fig. 5 and for $N\kappa/\Omega = 0.2$ in Fig. 6. Due to the emergence of the superposition state the visibility remains below one. The measurement process of the scattered photons significantly complicates the dynamics of the number of atoms predicted by the unitary time evolution of (1).

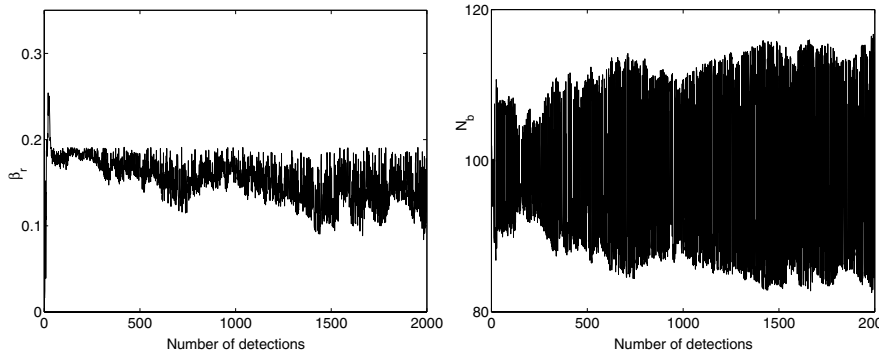

Fig. 5. The (**a**) relative visibility of the interference β_r and the (**b**) number of atoms N_b in one of the wells as a function of the number of detected photons. Due to the Schrödinger cat state the visibility never reaches one. Here the nonlinearity $\kappa = 0$

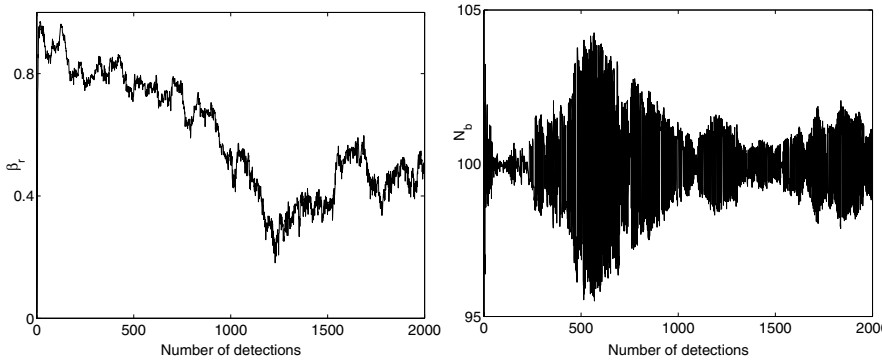

Fig. 6. The (**a**) relative visibility of the interference β_r and the (**b**) number of atoms N_b in one of the wells as a function of the number of detected photons. The nonlinearity $N\kappa/\Omega = 0.2$

4 Final Remarks

We studied the generation of the macroscopic superposition states or the Schrödinger cat states of a BEC in a double-well potential. The Schrödinger cat state was shown to emerge as a result of the continuous quantum measurement process of scattered photons. The particular detection geometry increases the fluctuations of the relative atom number between the two wells. Therefore the superposition states are more stable in the detection process. The proposed setup is an open quantum system and the creation of the Schrödinger cat state in this case is not based on reaching the ground state of a BEC in a double-well potential [9,10]. The advantage over previously proposed open systems schemes [8] is that the BEC is stably trapped and the superposition state for a small BEC could be created by scattering only a few photons.

In the present discussion we ignored the effect of decoherence [27]. The interaction of the BEC with its environment results in the decoherence of the superposition states. We can identify several sources of decoherence. Decoherence by amplitude damping or by phase damping has been estimated in [28]. The inelastic two-body and three-body collisions between the condensate atoms and the noncondensate atoms change the number of condensate atoms and introduce amplitude damping. The phase damping corresponds, e.g., to elastic collisions between the condensate and noncondensate atoms in which case the number of BEC atoms is conserved. If the number of atoms in a BEC is not large, the scattering between the condensate and noncondensate atom fractions may not be negligible. This also introduces amplitude decoherence. Additional sources of decoherence may be, e.g., the imperfect detection of the scattered photons and the fluctuations of the magnetic trap. In [12] it was proposed that the decoherence rate of a BEC could be dramatically reduced by symmetrization of the environment and by changing the geometry of the

trapping potential to reduce the size of the thermal cloud. Moreover, the continuous measurement process increases the information about the system and therefore it could also reduce the decoherence rate.

Acknowledgments

We are indebted to the late Prof. Walls for his support, inspiration, and encouragement during his last years. This work was financially supported by the EC through the TMR Network ERBFMRXCT96-0066.

References

1. M.H. Anderson, J.R. Ensher, M.R. Matthews, C.E. Wieman, E.A. Cornell: Science **269**, 198 (1995)
2. C.C. Bradley, C.A. Sackett, J.J. Tollett, R.G. Hulet: Phys. Rev. Lett. **75**, 1687 (1995)
3. K.B. Davis, M.-O. Mewes, M.R. Andrews, N.J. van Druten, D.S. Durfee, D.M. Kurn, W. Ketterle: Phys. Rev. Lett. **75**, 3969 (1995)
4. See the review of theoretical studies of BECs of alkali-metal atomic gases: A.S. Parkins, D.F. Walls: Phys. Rep. **303**, 1 (1998), and references therein
5. D.M. Stamper–Kurn, A.P. Chikkatur, A. Görlitz, S. Innouye, S. Gupta, D.E. Pritchard, W. Ketterle: Phys. Rev. Lett. **83**, 2876 (1999)
6. M.R. Matthews, B.P. Anderson, P.C. Haljan, D.S. Hall, C.E. Wieman, E.A. Cornell: Phys. Rev. Lett. **83**, 2498 (1999)
7. L. Deng, E. Hagley, J. Wen, M. Trippenbach, Y. Band, P. Julienne, J. Simsarian, K. Helmerson, S. Rolston, W. Phillips: Nature **398**, 218 (1999)
8. J. Ruostekoski, M.J. Collett, R. Graham, D.F. Walls: Phys. Rev. A **57**, 511 (1998)
9. J.I. Cirac, M. Lewenstein, K. Mølmer, P. Zoller: Phys. Rev. A **57**, 1208 (1998)
10. M.J. Steel, M.J. Collett: Phys. Rev. A **57**, 2920 (1998)
11. D. Gordon, C.M. Savage: Phys. Rev. A **59**, 4623 (1999)
12. D.A.R. Dalvit, J. Dziarmaga, W.H. Zurek: e-print cond-mat/0001301
13. J. Javanainen: Phys. Rev. Lett. **57**, 3164 (1986)
14. G.J. Milburn, J. Corney, E.M. Wright, D.F. Walls: Phys. Rev. A **55**, 4318 (1997)
15. A. Smerzi, S. Fantoni, S. Giovanazzi, S.R. Shenoy: Phys. Rev. Lett. **79**, 4950 (1997)
16. I. Zapata, F. Sols, A.J. Leggett Phys. Rev. A **57** R28 (1998)
17. J. Ruostekoski, D.F. Walls: Phys. Rev. A **58**, R50 (1998)
18. J. Williams, R. Walser, J. Cooper, E. Cornell, M. Holland: Phys. Rev. A **59**, R31 (1999)
19. N. Korolkova, J. Perina, Opt. Comm. **136**, 135 (1997)
20. J. Javanainen, J. Ruostekoski: Phys. Rev. A **52**, 3033 (1995)
21. J. Dalibard, Y. Castin, K. Mølmer: Phys. Rev. Lett. **68**, 580 (1992)
22. C.W. Gardiner, A.S. Parkins, P. Zoller: Phys. Rev. A **46**, 4363 (1992)
23. H.J. Carmichael: *An Open Systems Approach to Quantum Optics*, Lecture Notes in Physics, Vol. m18 (Springer, Berlin 1993)

24. D.F. Walls, G.J. Milburn: *Quantum Optics* (Springer, Berlin 1994)
25. J. Javanainen, S.M. Yoo: Phys. Rev. Lett. **76**, 161 (1996); S.M. Yoo, J. Ruostekoski, J. Javanainen: J. Mod. Opt. **44**, 1763 (1997)
26. M.W. Jack, M.J. Collett, D.F. Walls: Phys. Rev. A **54**, R4625 (1996)
27. W.H. Zurek: Phys. Today **44** (10), 36 (1991) and references therein
28. D.F. Walls, G.J. Milburn: Phys. Rev. A **31**, 2403 (1985)

A Historical Perspective on Lasing Without Inversion

Nicolaas Bloembergen and Galina Khitrova

Summary. The objective of this article is to put the concepts of lasing without inversion, electromagnetically induced transparency, and quantum interferences into a broad historical perspective.

1 Introduction

Quantum optics remains a very active field of scientific investigation. In a recent textbook with this title, Scully and Zubairy devoted one chapter to "lasing without inversion and other effects of atomic coherence and interference" [1]. An extensive and still growing literature is concerned with the effects of lasing without inversion, denoted by the acronym LWI, and electromagnetically induced transparency, denoted by the acronym EIT. These two novel concepts have been the subject of several review papers, which in turn contain many references to the original literature [2–4]. This note is an attempt to put the concepts of LWI and EIT and atomic coherent states in a broader historical context. A brief review of the precursors of these phenomena in radiofrequency and microwave spectroscopy is presented, as well as some early examples of optical amplification and oscillation without population inversion based on parametric and damping effects. The highlights of the intense activity during the past two decades are summarized to complete this historical perspective.

2 Precursors in Magnetic Resonance

The ubiquitous use of the "Rabi frequency" in quantum optics has its origin in Rabi's description [5] of the evolution of a two-level nuclear spin system, $I = 1/2$, in a magnetic field H_0; the spin precesses about H_0 with an angular frequency $\omega_0 = \gamma H_0$, where γ is the gyromagnetic ratio. When a circularly polarized radiofrequency magnetic field with amplitude H_1 is applied at frequency ω_1 perpendicular to H_0, the motion of the spin can be described exactly in the co-rotating frame as sketched in Fig. 1. Exactly at resonance, $\omega = \omega_0$, the spin precesses around H_1 with the Rabi frequency $\Omega_\mathrm{R} = \gamma H_1$. If the radiofrequency field has a square pulse duration t_p, the spin rotates through an angle $\Omega_\mathrm{R} t_\mathrm{p}$. A 180° pulse ($\Omega_\mathrm{R} t_\mathrm{p} = \pi$), flips the spin. For

H.J. Carmichael, R.J. Glauber, M.O. Scully (Eds.): LNP 561, pp. 91–106, 2001.

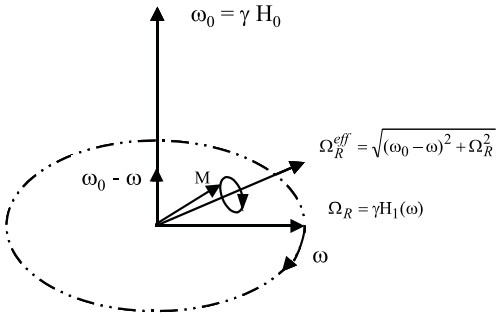

Fig. 1. Response of a magnetic spin $I = 1/2$ system in a rotating magnetic field. The magnetization precesses with angular frequency $\Omega_{\mathrm{R}}^{\mathrm{eff}}$ in a rotating frame that precesses around the dc magnetic field H_0 with an angular frequency ω. The same response is valid for any two-level system without damping in the rotating wave approximation (compare Refs. [6,8])

$\Omega_{\mathrm{R}} t_{\mathrm{p}} = \pi/2$ a state of maximum coherence is obtained, in which the spin is stationary and perpendicular to H_0 in the rotating frame. The exact quantum mechanical solution is discussed in detail in a review paper by Rabi, Ramsey, and Schwinger [6]. The motion of a macroscopic magnetization, described by a two-by-two density matrix, follows the same equation of motion. In the Bloch equations, damping terms are added phenomenologically [7]. The longitudinal relaxation time T_1 describes the return of the thermal equilibrium components of magnetization parallel to H_0. The transverse relaxation time T_2 describes the decay of the coherence, or the perpendicular precessing component of magnetization.

While the magnetic resonance situation corresponds literally to the physical description outlined above, the same formalism may be applied to any two-level system. This point was emphasized by Feynman et al. [8] and is described as the vector model of the density matrix in a textbook by Sargent et al. [9]. If this system consists of two atomic levels coupled by an electric dipole matrix element to an optical field with amplitude E at resonance, the Rabi frequency $\Omega_{\mathrm{R}} = er_{ba}E\hbar^{-1}$ describes the strength of interaction. Since there is usually no permanent electric dipole moment, the longitudinal component of the magnetization is replaced by the difference in population, or the difference in the diagonal elements $\varrho_{bb} - \varrho_{aa}$ of the density matrix. For linear polarization of the applied fields, the counter-rotating components are usually ignored.

Inversion of population in a nuclear spin system, $I = 1/2$, can be obtained by three methods. Bloch and coworkers [10] introduced adiabatic rapid passage in 1946. They observed a change in sign of the nuclear induction signal in traversing back and forth through resonance.

Purcell and Pound [11] inverted the spin system non-adiabatically by a sudden reversal of the magnetic field H_0. It was switched from a value of

+10 gauss to −10 gauss in about a microsecond. This time interval is shorter than T_2 and the spins have no time to change their orientation. Purcell and Pound observed the negative absorption or gain, which lasted for a time T_1.

The third method to achieve population inversion is the π-pulse discussed earlier. It was demonstrated experimentally by Carr and Purcell [12].

While the small gain in a nuclear spin system at radiofrequencies is of no practical interest, the gain obtainable on electronic paramagnetism at microwave frequencies led to the solid state maser. Combrisson, Honig, and Townes [13] used spin resonance of a donor level in silicon to obtain a transient gain.

A cw gain can be obtained in systems with more than two energy levels, for example magnetic ions with total spin $S > 1/2$. Bloembergen proposed to utilize a double irradiation scheme [14]. A strong pump field saturates the resonance between two non-adjacent energy levels and equalizes their populations. Gain occurs at a microwave transition involving an intermediate level with a different population. In the three-level solid state maser scheme it is not necessary to take into account coherences in the three-level system. Even if pumping is performed by a coherent microwave source such as a klystron, the condition $T_2 \ll T_1$ prevails in the paramagnetic crystal (ruby) at liquid helium temperature. Saturation of the resonance is achieved for $\gamma^2 H_1^2 T_1 T_2 \gg 1$, while $\gamma H_1 T_2 \ll 1$. Clogston [15] took account of the coherences, which might be induced by the coherent pump field in a density matrix calculation of the three-level paramagnetic system and confirmed that the coherence effects were negligible. Coherences in magnetic resonance did play a role in parametric devices, which have been reviewed by Louisell [16].

The pumping scheme between non-adjacent energy levels is also utilized in most lasers. The first operating laser, the (ruby) laser of Maiman [17] used the same material, which was a favorite substance in low-noise microwave maser receivers. In the laser the incoherent pumping was provided by the black-body radiation from a xenon-flash discharge.

The influence of a strong radiofrequency field on the response of a probe near the same resonance was also investigated in magnetic resonance before the advent of optical lasers. The probe response may be described as a resonance in the rotating frame, in which the pump field is time-independent. Bloch [18] analyzed the response in this situation, and Anderson [19] carried out an early experiment. These are forerunners of optical experiments discussed in Sect. 3.

The influence of a strong pump field on other transitions in a system with three or more energy levels is described in Sect. 4. Here a precursor in molecular microwave spectroscopy was described by Autler and Townes [20]. They observed dynamic Stark shifts in the microwave transition between two rotational levels of the OCS molecule, induced by a strong radiofrequency field tuned in the vicinity of the lambda doubling of the rotational levels.

Transitions involving the absorption of two microwave quanta and radiofrequency Raman-type processes were also demonstrated before the advent of lasers and nonlinear optics [21]. It is clear that laser spectroscopy owes a significant debt to earlier developments in microwave and radiofrequency spectroscopy. In turn, these spectroscopies owe a lot to optics of the 19th and early 20th century, when the concepts of transitions between energy levels induced by electromagnetic fields were developed.

3 Early Examples of Parametric Amplification Without Population Inversion

In this section we present several examples of coherent light beam amplification dating back to the sixties, without population inversion in the material energy levels. The term "parametric" is often used to describe these processes. The origin of the term derives from the modulation of circuit parameters, such as capacitance and inductance, in radiofrequency and microwave circuits [16]. In optical parametric processes the real index of refraction of a probe beam is modulated by the presence of other electromagnetic modes. As resonances are approached the imaginary part of the index may also be modulated. It is not clear when the designation "parametric" loses its original meaning, as imaginary parts of the dielectric response function come into play. Low-order perturbation theories have been used to describe these phenomena of parametric amplification [22].

The nomenclature LWI, introduced in the late eighties, specifically excludes these parametric situations and is sometimes used only in situations where an incoherent pump supplies energy to a material system that is subsequently converted to coherent energy of an electromagnetic mode. It excludes parametric processes, in which energy is transferred coherently between different EM modes, while no material energy is either supplied or exchanged. The subject of nonlinear optics in nonabsorbing dielectrics provides numerous examples of parametric harmonic generation, and parametric up- and down-conversion. Optical parametric oscillators were developed in the sixties and are now widely used to obtain tunable sources of radiation [23]. The operation of these devices can be described by assuming that the material system remains in the ground state. There is no population inversion, and light amplification without inversion occurs in a literal sense.

Stimulated Raman scattering involves gain without population inversion at the Stokes-shifted frequency. The material system remains in the electronic ground state, while it makes a transition to a vibrationally excited state. The Stokes gain is not phase-sensitive since the phase of the vibrational excitation adjusts itself. The process may be regarded as a parametric one, in which a laser photon is down-converted to a Stokes photon and a Raman-active phonon. This phonon excitation is usually heavily damped in comparison

with the optical waves. The vibrational, coherently driven mode adjusts itself to conserve both energy and momentum.

Stimulated Brillouin scattering may also be considered as a parametric process, involving the down-conversion of a laser pump photon to a Brillouin-shifted scattered photon and an acoustical phonon. Stimulated Rayleigh wing scattering, first reported in CS_2 by Mash et al. [24], may be considered as a Raman-type process between rotational states of the molecule. These rotational states in liquid CS_2 are unresolved and overdamped. Bloembergen and Lallemand [25] explicitly calculated a dispersive-type gain feature. There is loss for frequencies higher than the pump frequency and gain on the low frequency side. Extrema occur for a frequency shift equal to the width of the Rayleigh wing scattering. A rotational orientation grating is produced by the two coherent light waves. The pump wave is diffracted by this grating to add energy to the probe beam at lower frequencies by the two coherent light waves. This process may again be considered as parametric in a certain sense.

The role of damping in stimulated Rayleigh wing scattering is an early example of how damping mechanisms may have a profound influence on coherent interactions [26]. Extra resonances in four wave light mixing induced by collisional interaction were demonstrated in 1981 by Prior et al. [27]. A collision may destroy the destructive interference between different coherent pathways to the same final state. In Rayleigh wing scattering, collisions permit a net energy transfer from the coherent electromagnetic modes to the material system. Grynberg and Berman have analyzed in depth the influence of collisions in nonlinear optical processes in a series of papers [28,29].

4 Optical Response of a Two-Level System in a Strong Coherent Field

Consider a two-level system with energy separation $\hbar\omega_0$ irradiated by a strong pump field at frequency ω and a weaker probe field at ω'.

A general procedure, which would take account of all powers in Ω_{R}, or the pump field amplitude, involves a transformation to the rotating frame in which the near-resonant pump field is time-independent [30]. Several early papers [31,32] were concerned with the off-diagonal elements of the density matrix, or the atomic coherence, induced by the coherent field in atomic gas lasers, but the first detailed calculation of the response of a weak probe beam as a function of ω, ω' and Ω_{R} was presented by Mollow [33]. He observed that "a striking feature of the expression of the (probe's) absorption line shape function is that in some cases it takes on negative values, even though population inversion never occurs." His theoretical predictions were strikingly confirmed five years later in experiments with a beam of Na atoms, traversed by laser pump and probe beams at right angles to minimize Doppler effects. Wu, et al. [34] showed that the probe absorption is negative in the domain

$\omega_0 - \Omega_R < \omega' < \omega_0 + \Omega_R$ for a strong resonant pump field, $\omega = \omega_0$. Theoretical predictions and experimental results are reproduced in Fig. 2

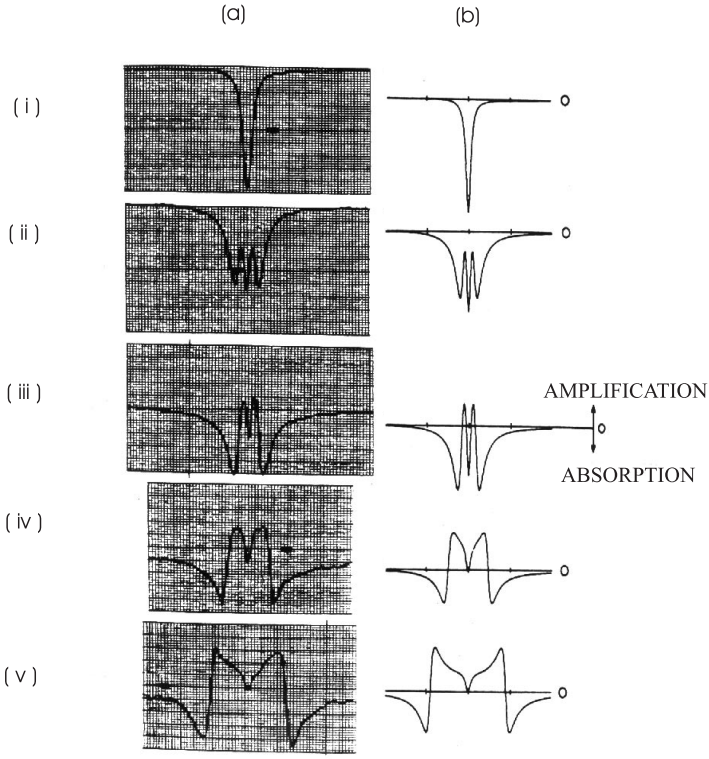

Fig. 2. Experimental (**a**) and theoretical (**b**) line shapes of a probe beam, when a closed two-level system is pumped exactly at resonance for values of the pump Rabi frequency varying from zero (top) to $\Omega_R = 8\Gamma$ (bottom) where Γ is the natural line width caused by spontaneous emission. (with permission from Ref. [34])

The situation off-resonance, with $|\omega - \omega_0| > \Omega_R > \Gamma$, where Γ is the natural linewidth of the transition, allows for a more detailed discussion of various physical processes involved. It is sketched in Fig. 3. Haroche and Hartmann showed already in 1972 that one can expect a strong absorption peak at ω_0' equal to ω_0 plus or minus a Stark shift proportional to Ω_R [35]. There is gain for $\omega' = 2\omega - \omega_0'$. This has been interpreted by Cohen–Tannoudji and Reynaud [36] as an inversion of population between two energy levels of the atom dressed by the pump field. This gain was also observed by Wu et al. in their atomic beam experiment. It can be described as a hyper-Raman process, in which two pump photons are absorbed, one probe photon is emitted, while the upper level is reached, from which spontaneous emission to the lower level takes place. In a sodium vapor cell this gain is Doppler broad-

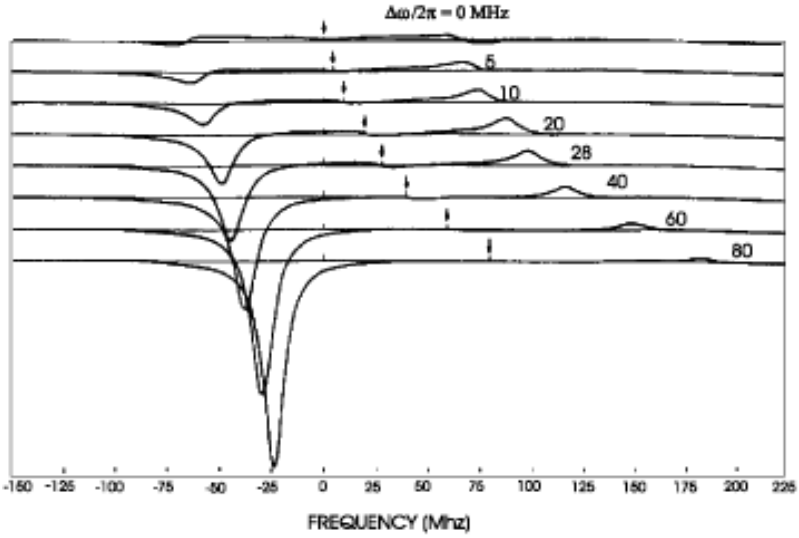

Fig. 3. Calculated response of a probe beam in a closed two-level system with natural line width $\Gamma/2\pi = 10\,\mathrm{MHz}$, in the presence of a pump beam with Rabi frequency $\Omega/2\pi = 66\,\mathrm{MHz}$. The pump detuning $(\omega - \omega_0)/2\pi$ is varied from 0 (top) to 80 MHz (bottom). Arrows indicate the frequency of the driving field. (with permission from Ref. [34])

ened [37]. Khitrova showed that integration over the velocity distribution should still lead to an observable gain. Pump-probe measurements of the Doppler-broadened gain profile were reported in [38]. Laser action based on this gain was observed in 1988 by off-axis pumping of the sodium cell in an optical ring cavity with a cw beam of a few hundred milliwatts of power [39]. This lasing was unidirectional with the lasing beam making an angle of 0.9° with the pump beam. The lasing occurred about 3 GHz away from the frequency of the pump, corresponding to twice the pump detuning from resonance. The broad gain supported lasing of several longitudinal modes. The group of Mossberg used an atomic beam to avoid the complications associated with Doppler broadening and studied not only the stimulated, but, also the spontaneous regimes [40].

The dispersive-like gain/absorption feature around $\omega' \approx \omega$ requires a more subtle explanation. It is a Doppler-free resonance, so its shape is the same for sodium atoms in a cell or in an atomic beam. It was first observed in the same experiment by Wu et al. in 1977. The gain can be either above or below the pump frequency depending upon whether the latter is below or above the atomic resonance. Lasing based on this gain for Na atoms in an evacuated cell was first observed in 1988 by Khitrova et al. [39]. This is an observation of lasing in a system without inversion in both the dressed and bare bases. As discussed at the end of this section, it was preceded by LWI with the aid of a

buffer gas. It is not a simple parametric process. In a closed two-level system, when spontaneous emission from the upper to the lower level constitutes the only stochastic process, this dispersive gain/absorption feature can only be explained as an interference between various processes involving the spontaneous emission into two modes of the vacuum field. Using an amplitude approach for a single atom, one can calculate the probability that the probe field is amplified or absorbed. This approach has the advantage that it allows one to separate the individual contributions to absorption and emission. This separation is not possible in density matrix calculations. The use of the amplitude (Schrödinger) picture requires extensive tedious algebraic manipulations. The first amplitude calculation for this problem was performed by Grynberg and Cohen–Tannoudji [41] in the dressed-atom basis. They showed that the dispersive-like resonance arises from an interference term that appears in absorption and not in emission. The dressed-atom approach uses quasi-stationary states of the atom dressed by the pump field, allowing one to apply Fermi's Golden Rule to the calculation of transition probabilities. Its main limitation is that it does not give results directly in powers of the pump field intensity; nor is it useful for arbitrary pump field detuning. The bare-atom amplitude calculations by Berman and Khitrova [42] describe interesting atom-fields dynamics, which becomes more complex with increasing pump field strength. The origin of the dispersive-like gain is still related to interference effects in the bare state calculations. In Ω_{R}^4 order, three pump photons are absorbed and transformed into a probe photon and two photons spontaneously emitted into vacuum modes k_1 and k_2. The main diagrams in the bare-atom picture leading to this dispersive gain/absorption feature, proportional to Ω_{R}^4, are shown in Fig. 4. The gain is nonvanishing over a range of detunings determined by the excited state decay rate for a closed two-level system. The origin of this gain, occurring without population inversion in either the bare or dressed atom picture, is also not parametric in nature. It represents a unique case of LWI.

Lasing with a two-photon downward transition in barium vapor has been reported by Mossberg and coworkers [43–45] who explain this phenomenon on the basis of a population inversion in the dressed atom picture, in a manner similar to the one-photon lasing at $2\omega - \omega_0'$ [36].

The situation in an open two-level system is qualitatively different. In this case the dispersive gain/absorption feature around $\omega' \approx \omega$ is proportional to Ω_{R}^2 rather than Ω_{R}^4 [46]. In the open system spontaneous emission may occur from both the upper and lower level to additional levels of the atomic system, or elastic collisions with a buffer gas may cause a decay of the off-diagonal elements of the density matrix without changing the populations in the bare system.

Grandclément et al. [47] first observed gain without population inversion and laser oscillation in a Na-vapor cell with a high pressure noble buffer gas. They describe the effect in terms of a population grating similar to the

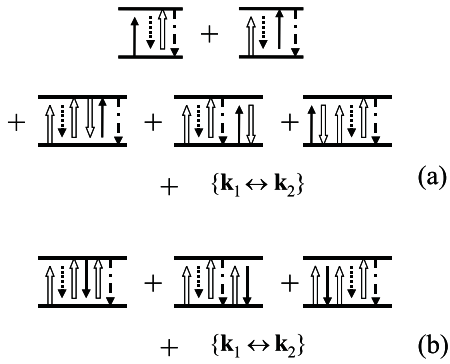

Fig. 4. The dominant diagrams that lead to the dispersive gain/absorption feature in a closed two-level system, proportional to Ω_{R}^4. The symbol $k_1 \leftrightarrow k_2$ indicates that diagrams in which the order of two spontaneously emitted photons is interchanged must be added. The dotted arrows indicate spontaneous emission, the open arrows indicate pump photons and the solid arrows indicate probe photons. Diagrams (**a**) correspond to probe absorption and diagrams (**b**) correspond to probe emission. Their interference causes the observed effect

description of stimulated Rayleigh wing scattering described in Sect. 2. It should be noted, however, that both the laser and the probe were detuned from the atomic resonance at ω_0 by an amount large compared to the collisionally induced line width, although the detuning was small compared to an inverse collision time, i.e. the impact approximation is valid. A density matrix calculation shows that a population difference grating results with phase shifts appropriate to explain the observed dispersive gain/absorption feature, but the analysis of Berman and Khitrova [42] in terms of the evolution of Schrödinger amplitudes in the open two-level system may be more appropriate. In this picture an interference occurs between processes involving the spontaneous emission of one photon. Both descriptions lead to a dispersive feature proportional to Ω_{R}^2, in agreement with experiment. In our opinion this feature in the open two-level system is not a parametric process, but is another case of lasing without inversion in both the bare and dressed bases. It is different from the processes in multi-level systems, to which the LWI designation is usually applied.

5 LWI and EIT in Three-Level Systems

Consider three levels with energy eigenvalues $\omega_a < \omega_b < \omega_c$ and eigenstates $|a\rangle, |b\rangle$, and $|c\rangle$. In earlier sections, two extreme cases were mentioned. Incoherent pumping at ω_{ca} between nonadjacent levels $|c\rangle$ and $|a\rangle$ starting with the system in the ground state, $\varrho_{aa}(0) = 1$, will lead to population inversion, $\varrho_{cc} > \varrho_{bb}$ if the relaxation times for depopulation of level $|b\rangle$ are sufficiently

short. This inversion may be calculated without paying attention to coherences.

In parametric down conversion the frequencies of the three electromagnetic waves are all far off resonance. In this situation, the coherences $\varrho_{ca}, \varrho_{ba}$ and ϱ_{cb} may be calculated to second order without paying attention to population changes, i.e. $\varrho_{aa}(0) = 1$. The nonvanishing coherences of course imply $\varrho_{bb} \neq 0$ and $\varrho_{cc} \neq 0$, but these terms only play a role in higher order nonlinear optics effects.

The concept of LWI and EIT gained much attention, when situations were considered where electromagnetic waves interact with the system close to the three resonant frequencies ω_{ca}, ω_{ba} and ω_{cb} with Rabi frequencies satisfying the inequality $\Omega_{\mathrm{R}} > \Gamma$, so that large atomic coherences are induced. Javan [31] discussed the combined role of coherences and population differences in a three-level system in an early paper. He called attention to the combined role of single photon and two-photon transitions between the three levels. This interference between single photon and Raman-type processes in a three-level system was also discussed by Bloembergen and Shen [30].

During the last quarter century an extensive literature has grown, which reports the detailed calculation of the state amplitudes and the evolution of all density matrix elements of the three-level system for a variety of initial conditions, damping mechanisms, and amplitudes and frequencies of electromagnetic fields.

An introduction to this vast literature may be found in review papers by Kocharovskaya [2], Arimondo [3], Harris [4], Khurgin and Rosencher [48], and Alam [49], and in a textbook by Scully and Zubairy [1]. Some of the first references on LWI suggest the use of Fano-type interference [50,51] in the absorption profile of an atomic transition to an ionization continuum via a doublet of excited states embedded in the continuum. The emission, following the excitation of one discrete level in the continuum, shows no such interference. Kovarovskaya and Khanin [52] and Scully et al. [53], proposed schemes based on three discrete atomic levels, in which light amplification may be traced to an inversion of population occurring between dressed atomic levels, while the bare atomic levels in the laboratory frame have no population inversion. Consider the Λ-type configuration shown in Fig. 5a, where levels $|a\rangle$ and $|b\rangle$ are nearly degenerate Zeeman-levels of the atomic ground state, with electric dipole matrix elements er_{ca} and er_{cb} connecting to the excited state. A short quasi-monochromatic pulse may induce both transitions. Suitable sidebands separated by ω_{ba} may also occur in coherent pulse sequences, or a bichromatic laser field may simultaneously be resonant near ω_{ca} and ω_{cb}. Under the influence of such illumination the system will be excited from both levels $|a\rangle$ and $|b\rangle$. Subsequent spontaneous decays will be followed by renewed excitation by pumping fields. Eventually the system will be driven to a coherent dark state, $\lambda_a|a\rangle + \lambda_b|b\rangle$, such that the matrix element $\lambda_a E(\omega_{ca}) er_{ba} + \lambda_b E(\omega_{cb}) er_{cb} = 0$. The system in this coherent state is de-

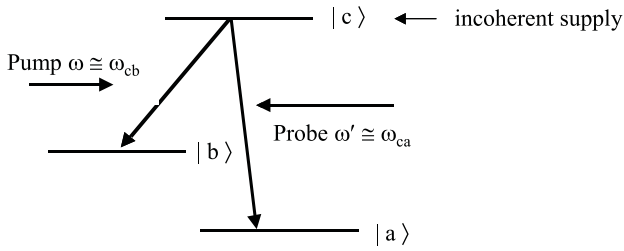

Fig. 5. LWI in a three-level Λ-configuration. The simultaneous presence of the coherent pump and probe beams creates a coherent dark-state superposition of states $|a\rangle$ and $|b\rangle$. An incoherent supply of atoms in state $|c\rangle$ causes gain in transitions to the orthogonal coupled state

coupled from the electromagnetic fields [3]. The system becomes transparent. No further absorption occurs. The decoupled dark states were discovered by Alzetta et al. [54] in 1976, and are the basis of EIT in three-level systems [4].

Now inject by incoherent pumping a small population into the excited state $|c\rangle$ so that $\varrho_{cc} \neq 0$. Stimulated emission will take place to the unpopulated coupled state, $\lambda_a^*|b\rangle - \lambda_b^*|a\rangle$, which is orthogonal to the dark state. No matter how large the population in the dark state is, gain will occur for the transition to the coupled state. This situation can also be described in terms of the existence of population inversion for the dressed state, while $\varrho_{aa} + \varrho_{bb} >> \varrho_{cc}$ for the bare atomic levels. Lasing in this situation was reported by Padmabandu et al. [55].

The close relationship between LWI and EIT can be illustrated by the example in which a strong coherent pump field is applied at the exact resonant frequency ω_{cb} but the energy splitting ω_{ba} is sufficiently large so that transitions to level $|a\rangle$ are not affected. The initial populations in levels $|b\rangle$ and $|c\rangle$ are not important. The dynamic Stark shift will cause a Rabi splitting $2\Omega_{\mathrm{R}}$ of the dressed atomic level $|c\rangle$. A weak probe field at the exact undressed resonant frequency ω_{ca} will experience increased transparency, as the strong absorption features are shifted to $\omega_{ca} \pm \Omega_{\mathrm{R}}$.

When the probe field $E(\omega_{ca})$ is gradually applied in the presence of the large pump field $E(\omega_{cb})$, the two-state vector spanning the two-level system ab will evolve adiabatically from the pure state $|a\rangle$ to the coherent dark state. It was noted by Harris [4] that this transparent coherent state can be established in a time shorter than the radiative lifetime from level $|c\rangle$.

The main interest in the Λ-type configuration lies now in its relevance to the experimental situation of Raman-type transitions between hyperfine and Zeeman levels in the electronic ground state of alkali-atoms. These transitions are intrinsically narrow and have little Doppler broadening. They can also be enhanced by collisional processes [56,57]. Relatively low powers obtainable from cw diode lasers are sufficient to cause Rabi splittings at the resonance lines of Na and Rb atoms. The linear index of refraction varies extremely

rapidly between the dynamic Stark doublet resonant lines where EIT occurs as shown in Fig. 6. A probe pulse in this transparent domain should travel

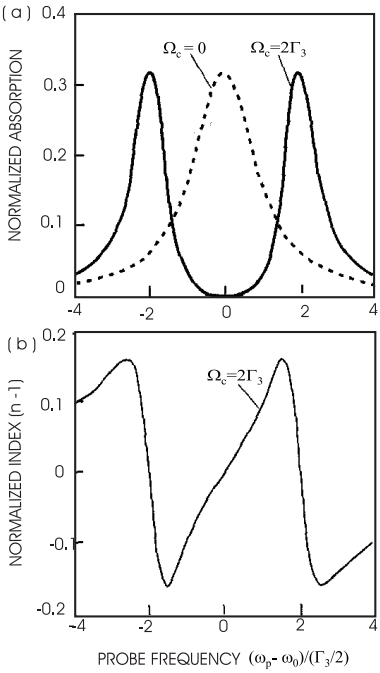

Fig. 6. A coherent pump causes a Rabi-type splitting in a two-level system. (**a**) The solid curve shows the response of a probe, when $\Omega_{\mathrm{R}} = 2\Gamma$. (**b**) The dispersion of the probe index of refraction is large at the point of EIT, where $\omega' = \omega = \omega_{ba}$. (with permission from Ref. [4])

with a very slow group velocity due to the large value of $\mathrm{d}n/\mathrm{d}\omega$. As the probe pulse propagates through the alkali vapor in the presence of the cw pump field, the required coherent state is established adiabatically. At the leading edge of the probe pulse photons are transferred to the pump field, which returns them to the probe at the trailing edge. This pictorial description makes it plausible that the probe propagates without significant attenuation at low velocities. Recent experiments have confirmed this behavior. Hau et al. [58] demonstrated a pulse propagation in a Bose–Einstein condensate of Na atoms with a group velocity of 17 meters/second. Other groups have reported group velocities of 90 and 8 meters/second in Rb vapor at room temperature [59,60]. These group velocities of 10^{-7}c are much slower than the c/3000 seen in coherent pulse propagation (self-induced transparency) [61].

When these near resonant effects are expressed in terms of nonlinear susceptibilities, extremely large values are obtained [62,63]. Scully and Zubairy [1] have also called attention to the fact that it is possible to obtain a real value of the index of refraction of ten or higher, at a wavelength where the imaginary part vanishes. This opens possibilities for studying optical lattices. It

is clear, however, that these conditions could only exist in extremely narrow frequency intervals.

When levels $|b\rangle$ and $|c\rangle$ are close together in an excited electron configuration, while level $|a\rangle$ belongs to the ground state manifold, one speaks of a V-configuration if optical fields are applied near ω_{ba} and ω_{ca}. Kocharovskaya et al. [64] have shown that in this situation optical gain can only be achieved when the total population in the excited configuration exceeds that in the ground state, $\varrho_{bb} + \varrho_{cc} > \varrho_{aa}$, but, ϱ_{bb} may be smaller than ϱ_{aa}. There may be gain at ω_{ba} in either the bare or the dressed pictures. An experimental confirmation of this situation of LWI in Rb vapor has been reported by Zibrov et al. [65]. The arduous and illuminating amplitude picture is used by Cohen and Berman to analyze this case [66].

Another situation arises when the transition ω_{cb} is coherently pumped by a strong microwave field. If no optical transitions are allowed at ω_{ba} one speaks of a p-configuration, shown in Fig. 7. Light at ω_{ca} is in an EIT region

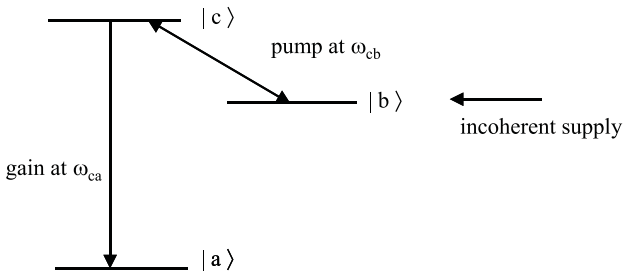

Fig. 7. LWI in the three-level p-configuration. A low-frequency field creates a coherent superposition of the two upper levels. An incoherent supply into level $|b\rangle$ may lead to gain at the high frequency ω_{ca}

because of dynamic Stark splitting of level $|c\rangle$ by the microwave pump. If an incoherent mechanism injects some population in level $|b\rangle$, it may be possible to obtain gain at ω_{ca} by anti-Stokes scattering of the microwave photon from $|b\rangle$ to $|a\rangle$. This scheme would be really useful if a nuclear isomer could be identified with a pair of energy levels, which could be pumped by optical radiation, with subsequent γ-ray emission to a lower level. In this connection the following quotation by Narducci et al. [67] is relevant: "An inversionless laser may indeed become a useful device, if it can produce light amplification at a frequency that differs enough from the driving source. Ideally one would want to operate this system in regions of the e.m. spectrum where lasing action is impractical with conventional schemes."Similar observations have been made by Kocharovskaya [2].

In a combination of the V- and p-configuration, i.e. when two coherent optical fields and a microwave field are simultaneously present, the microwave field provides an additional parametric coupling between the two

optical fields. Kocharovskaya et al. [64] have presented detailed calculations which lead to complex conditions between the populations and the relaxation and incoherent pumping mechanisms in the three-level system. The conclusion is that in certain situations gain of a parametric nature [68] may occur without population inversion in either the dressed or bare level systems. This should perhaps not be so surprising since optical parametric amplifiers with three electromagnetic waves far from any resonance in multi-level solid state systems, in which only the ground state is populated, have been known for a long time.

Imamoglu et al. [69] have described a three-level LWI situation without inversion either in the bare or dressed state pictures. There is, however, some type of inversion in the reservoir, which must provide suitable relaxation mechanisms for the populations between the three levels. There are also special conditions on the spontaneous decay rates in this closed atomic system. No experimental realization of this situation has been reported.

Most atomic systems will of course have more than three energy levels playing a role in these optical pumping experiments. For example, in a four or five level scheme a double Λ-type configuration may occur. It falls outside the scope of this historical overview to discuss detailed situations in multi-level systems. The basic physical phenomena of LWI and EIT are all exhibited by the three-level scheme.

6 Conclusion

EIT and LWI are interesting manifestations, which occur when large atomic coherences are induced by one or more coherent electromagnetic fields with Rabi frequencies larger than the line width. Precursors of such situations occurred in magnetic resonance before the advent of lasers. Precursors of optical parametric processes, where the detuning is larger than the Rabi frequency, have also been identified.

Detailed calculations of the evolution of the density matrix in two- and three-level material systems exhibit a complex interplay between the action of coherent fields with incoherent mechanisms, including spontaneous emission, collisional processes and incoherent pumping. Atomic coherences result in constructive or destructive interferences for one-, two-, and multi-photon processes. It is often helpful to visualize the situation in a rotating frame of reference, in which the strongest pump field is time independent, or alternatively in terms of a level scheme for dressed atoms.

Experiments have confirmed the theoretical descriptions of LWI configurations, without inversion in both the bare and dressed schemes. LWI has not (yet) yielded new coherent sources at frequencies much higher than the needed coherent pump field.

Conditions of EIT have recently been achieved in alkali vapors, where the probe pulse group velocity has been slowed down to meters per second

without much attenuation. A regime of extremely high optical nonlinearities has been created, albeit in a very narrow frequency range, where useful applications of EIT may arise.

Acknowledgments

N. B. acknowledges support from the Air Force Office of Scientific Research, and G. K. from NSF AMOP.

References

1. M.O. Scully, M.S. Zubairy: *Quantum Optics* (Cambridge University Press, New York 1997) Chap. 7
2. O. Kocharovskaya: Physics Reports **219**, 175 (1992)
3. E. Arimondo: 'Coherent Population Trapping in Laser Spectroscopy'. In: *Progress in Optics 35*, ed. by E. Wolf (Elsevier, Amsterdam 1996), p. 258
4. S.E. Harris: Physics Today, July, 36 (1997)
5. I.I. Rabi: Phys. Rev. **51**, 652 (1937)
6. I.I. Rabi, N.F. Ramsey, J. Schwinger: Rev. Mod. Phys. **26**, 167 (1954)
7. F. Bloch: Phys. Rev. **70**, 460 (1946)
8. R.P. Feynman, F.L. Vernon, R.W. Hellwarth: J. App. Phys. **28**, 49 (1957)
9. M. Sargent III, M.O. Scully, W.E. Lamb Jr.: *Laser Physics* (Addison-Wesley, Reading 1974) pp. 91-95
10. F. Bloch, W.W. Hansen, M. Packard: Phys. Rev. **70**, 474 (1946)
11. E.M. Purcell, R.V. Pound: Phys. Rev. **81**, 279 (1950)
12. H.Y. Carr, E.M. Purcell: Phys. Rev. **94**, 630 (1954)
13. J. Combrisson, A. Honig, C.H. Townes: Comptes Rend **242**, 2451 (1956)
14. N. Bloembergen: Phys. Rev. **104**, 324 (1956)
15. A.M. Clogston: J. Chem. Phys. Solids **4**, 271 (1958)
16. W.H. Louisell: *Coupled Modes and Parametric Electronics* (Wiley, New York 1960) Chap. 7
17. T.H. Maiman: Nature **187**, 493 (1960)
18. F. Bloch: Phys. Rev. **102**, 104 (1956)
19. W.A. Anderson: Phys. Rev. **102**, 151 (1956)
20. S.H. Autler, C.H. Townes: Phys. Rev. **100**, 703 (1955)
21. J.M. Winter: J. Phys. Radium **19**, 802 (1958)
22. See for example, N. Bloembergen: *Nonlinear Optics* (W.A. Benjamin, New York 1965, World Science Publ., Singapore 1996, fourth edition)
23. See for example, R.L. Byer: J. Nonlinear Opt. Phys. and Mat. **6**, 549 (1997)
24. D.I. Mash, V.V. Morozov, V.S. Starunov, I.I. Fabelinskii: JETP Letter **2**, 25 (1965)
25. N. Bloembergen, P. Lallemand: Phys. Rev. Lett. **16**, 81 (1966)
26. N. Bloembergen, H. Lotem, R.T. Lynch Jr.: Indian J. Pure and App. Phys. **36**, 865 (1978)
27. Y. Prior, A.R. Bogdan, M. Dagenais, N. Bloembergen: Phys. Rev. Lett. **46**, 111 (1981)

28. P.R. Berman, G. Grynberg: Phys. Rev. A **39**, 570 (1989) and **40**, 6921 (1989)
29. G. Grynberg, P.R. Berman: Phys. Rev. A **39**, 4016 (1989) and **41**, 2677 (1990)
30. N. Bloembergen, Y.R. Shen: Phys. Rev. **133**, A37 (1964)
31. A. Javan: Phys. Rev. **107**, 1579 (1957)
32. S.G. Rautian, I.I. Sobelman: JETP **14**, 328 (1962)
33. B.R. Mollow: Phys. Rev. A **5**, 2217 (1972)
34. F.Y. Wu, S. Ezechiel, M. Ducloy, B.R. Mollow: Phys. Rev. Lett. **38**, 1077 (1977)
35. S. Haroche, F. Hartmann: Phys. Rev. A **6**, 1280 (1972)
36. C. Cohen–Tannoudji, S. Reynaud: J. Phys. Bio. **10**, 345 (1977)
37. G. Khitrova: Theory of Pump-Probe and 4-Wave Mixing Spectroscopy. Ph.D. Thesis, New York University, New York (1986)
38. M.T. Gruneisen, K.R. MacDonald, R.W. Boyd: J. Opt. Soc. Am. B **5**, 123 (1988)
39. G. Khitrova, J.F. Valley, H.M. Gibbs: Phys. Rev. Lett. **60**, 1126 (1988)
40. A. Lezama, Y. Zhu, M. Kanskar, T.W. Mossberg: Phys. Rev. A **41**, 1576 (1990)
41. G. Grynberg, C. Cohen–Tannoudji: Opt. Commun. **96**, 150 (1993)
42. P.R. Berman, G. Khitrova: Opt. Commun. to be published
43. M. Lewenstein, Y. Zhu, T.W. Mossberg: Phys. Rev. Lett. **64**, 3131(1990)
44. Y. Zhu, Q. Wu, S. Morin, T.W. Mossberg: Phys. Rev. Lett. **65**, 1200 (1990)
45. D.J. Gauthier, Q. Wu, S.E. Morin, T.W. Mossberg: Phys. Rev. Lett. **68**, 464 (1992)
46. P.R. Berman, G. Khitrova, J.F. Lam: In: *Spectral Line Shapes*, ed. by F. Rostas (W. de Gruyter, Berlin 1985), Vol. 3, p. 258
47. D. Grandclément, G. Grynberg, M. Pinard: Phys. Rev. Lett. **59**, 40 (1987)
48. J.B. Khurgin, E. Rosencher: IEEE J. Qu. El. **32**, 1882 (1996)
49. S. Alam: *Lasers without Inversion and Electomagnetically Induced Transparency* (SPIE Optical Engineering Press, Bellingham 1999)
50. V.G. Arkhipkin, Yu.I. Heller: Phys. Lett. A **98**, 12 (1983)
51. S.E. Harris: Phys. Rev. Lett. **62**, 1033 (1989)
52. O. Kocharovskaya, Ya.I. Khanin: JEPT Lett. **48**, 630 (1988)
53. M.O. Scully, S.-Y. Zhu, A. Gavridiles: Phys. Rev. Lett. **62**, 2813 (1989)
54. G. Alzetta, A. Gozzini, L. Moi, G. Orriols: Nuovo Cimento **B36**, 5 (1976)
55. G.G. Padmabandu, G.R. Welch, I.N. Shubin, E.S. Frey, D.E. Nikonov, M.D. Lukin, M.O. Scully: Phys. Rev. Lett. **76**, 2053 (1996)
56. N. Bloembergen, Y.H. Zou: Phys. Rev. A **33**, 1730 (1986)
57. N. Bloembergen: Ann. de Physique (Paris) **10**, 681 (1985)
58. L.V. Hau, S.E. Harris, Z. Dutton, C.H. Behroozi: Nature **397**, 594 (1999)
59. M.M. Kash, V.A. Sautenkov, A.S. Zibrov, L. Hollberg, G.R. Welch, M.D. Lukin, Y. Rostovtsev, E.S. Fry, M.O. Scully: Phys. Rev. Lett. **82**, 5220 (1999)
60. R. Fitzgerald: Phys. Today, July, 17 (1999)
61. R.E. Slusher, H.M. Gibbs: Phys. Rev. A **5**, 1634 (1972)
62. H. Schmidt, A. Imamoglu: Opt. Lett. **21**, 1936 (1996)
63. S.E. Harris, L.V. Hau: Phys. Rev. Lett. **82**, 4611 (1999)
64. O. Kocharovskaya, P. Mandel, Y.V. Radeonychev: Phys. Rev. A **45**, 1997 (1992)
65. A.S. Zibrov, M.D. Lukin, D.E. Nikonov, L. Hollberg, M.O. Scullt, V.L. Velichansky, H.G. Robinson: Phys. Rev. Lett. **75**, 1499 (1995)
66. J.L. Cohen, P.R. Berman: Phys. Rev. A **55**, 3900 (1997)
67. L.M. Narducci, M.O. Scully, C.H. Kittle, S.Y. Zhu, H.M. Doss: Opt. Comm. **86**, 324 (1991)
68. G.S. Agarwal: Phys. Rev. A **44**, R28 (1991)
69. A. Imamoglu, J.E. Field, S.E. Harris: Phys. Rev. Lett. **66**, 1154 (1991)

The Coherent-Path Approach to Forward Scattering of Recoil-Free Resonant Gamma Radiation

Gilbert R. Hoy

Summary. A coherent-path approach is developed to describe nuclear-resonant gamma-ray transmission through nuclear-resonant matter. The solution is based on mathematical techniques, developed by Heitler and Harris, using time-dependent perturbation theory in the frequency domain. The nuclear-resonant absorber is modeled as a one-dimensional chain of N "effective" nuclei. A closed-form solution is obtained for the forward scattering of recoil-free radiation. The solution is given as a finite sum over $N + 1$ indistinguishable coherent paths the radiation takes going from the radioactive source through the absorber to the detector. The solution agrees numerically with the well-established theories although it has a completely different form. The major features of the time-differential Mössbauer spectroscopic result, namely the "speed-up" and "dynamical beat" effects, are easily explained in terms of the interference between the different contributing amplitudes. The model is so physically transparent that extension to other situations, e.g. synchrotron radiation, the "gamma-echo" effect, and incoherent processes, is not difficult.

1 Introduction

In this paper I will focus on a new approach to describe the processes by which gamma radiation passes through nuclear-resonant matter. In particular imagine there is a radioactive source that emits recoil-free gamma radiation when the radioactive nuclei decay from the first-excited state to the ground state. Next place a detector to record the resonant radiation, but interpose between the source and the detector a nuclear-resonant absorber. We can think of this absorber as a kind of gamma-ray filter. I will use the words "absorber" and "filter" interchangeably. If we now consider recoil-free processes in the filter, we are essentially treating the famous Mössbauer effect [1,2]. Furthermore, if there is a "signal" event, which allows us to determine the time at which the first-excited nuclear level in the source is formed, it is possible to record the radiation coming through the nuclear-resonant filter as a function of time after the signal event. This technique has been called "time differential Mössbauer spectroscopy" (TDMS).

When the first TDMS experimental results were obtained, they showed that the time-dependent intensity has an unusual shape. In a celebrated paper [3] Hamermesh explained the unusual shape, described below, of the time-dependent data using a semi-classical optical model. Subsequently Harris [4],

H.J. Carmichael, R.J. Glauber, M.O. Scully (Eds.): LNP 561, pp. 107–115, 2001.

following a development due to Heitler [5], treated the problem quantum mechanically and obtained the same result. In this paper I will use the methods of Harris and Heitler. However, I will represent the nuclear-resonant filter as a linear "chain" of "effective" nuclei. I say effective nuclei because the representation of a real three-dimensional solid as a linear chain is certainly a drastic assumption. In fact one might argue that such a representation would produce a theory that has little to do with actual experimental results. As will be seen below this is not the case and, in fact, the results of the model have a direct correspondence to the observed experimental results. Furthermore the model gives a clear physical picture of the multiple scattering processes occurring in the filter.

The solution has the form of a sum over coherent indistinguishable amplitudes. This form is completely different from that obtained using the classical optical model or the other quantum mechanical solutions. In spite of this, the predicted shape of the time-dependent data agrees with the other theories, as well as the experimental data.

Before starting into the mathematical methods for obtaining the solution, let me first describe two "unusual" features of the observed time-dependent spectrum mentioned above. In the first place, the initial slope of the spectrum does not correspond to the normal lifetime value, of the first excited state of the source, that one would obtain if the filter were absent. This has been called the "speed-up" effect, since it appears that the source is decaying more rapidly than normal. It is also possible for the spectrum to show a local maximum, at a time greater than $t = 0$, if the filter is sufficiently thick. This effect has been called a "dynamical beat." Both these effects have been seen more recently using synchrotron radiation [6] as the source.

2 The Quantum Mechanical Approach

Following Harris and Heitler, the general approach is to use time-dependent perturbation as described in any text on quantum mechanics. The state of the system at time t is described by

$$|\Psi(t)\rangle = \sum_l a_l(t) e^{-i(E_l/\hbar)t} |\psi_l(0)\rangle. \tag{1}$$

Solving the Schrödinger equation, using the appropriate boundary conditions [5] at $t = 0$, leads to a set of coupled differential equations relating the expansion coefficients $a_l(t)$

$$i\hbar \frac{a_l}{dt} = \sum_q a_q(t) e^{i(\omega_l - \omega_q)t} \langle \psi_l(0)|V|\psi_q(0)\rangle + i\hbar\delta_{l,n}\delta(t) \tag{2}$$

where $\omega_l - \omega_q = (E_l - E_q)/\hbar$. In order to obtain a set of coupled *linear* equations the Fourier transform is introduced

$$a_l(t) = -\frac{1}{2\pi i} \int_{-\infty}^{\infty} d\omega A_l(\omega) e^{i(\omega_l - \omega)t}. \tag{3}$$

The resulting set of coupled linear equations is

$$(\omega - \omega_l + i\epsilon)A_l(\omega) = \sum_q A_q(\omega)\frac{V_{lq}}{\hbar} + \delta_{ln} \tag{4}$$

where V_{lq} is the matrix element inducing a transition from the q^{th} unperturbed state to the l^{th} unperturbed state, and a pole is introduced into the lower half of the complex plane ($\epsilon > 0$) to insure that all amplitudes $a_l(t)$ are zero for $t < 0$. This procedure is described in Heitler [5].

3 Defining the Frequency-Dependent Amplitudes

Next we need to consider what frequency-dependent amplitudes are needed to solve the problem at hand. These amplitudes are $A(\omega)$: corresponding to the amplitude for finding the source nucleus excited at time $t = 0$ when all absorber nuclei are in the ground state and there are no photons or conversion electrons present; $B_k(\omega)$ corresponding to the amplitude for finding all nuclei in the ground state and only a photon of wave number k and energy $\hbar\omega_k$ is present; $C_m(\omega)$ corresponding to the amplitude when only the absorber nucleus located at $x = x_m$ is excited and no photons or conversion electrons are present; $D_p(\omega)$ corresponding to the amplitude for finding a conversion electron from the source nucleus present, all nuclei in their ground states and no photons are present; and $E_{mp}(\omega)$ corresponding to the amplitude for finding a conversion electron from the absorber nucleus located at $x = x_m$ present, all nuclei in their ground states and no photons are present.

Using these amplitudes, the resulting set of coupled linear equations is

$$(\omega - \omega_0 + i\epsilon)A(\omega) = 1 + \sum_k \frac{B_k(\omega)H_k}{\hbar} + \sum_p \frac{D_p(\omega)H_p}{\hbar} \tag{5}$$

$$(\omega - \omega_k + i\epsilon)B_k(\omega) = \frac{A(\omega)H_k^*}{\hbar} + \sum_m \frac{C_m(\omega)H_k^*}{\hbar}e^{-ikx_m} \tag{6}$$

$$(\omega - \omega_0' + i\epsilon)C_m(\omega) = \sum_k \frac{B_k(\omega)H_k}{\hbar}e^{ikx_m} + \sum_p \frac{E_{mp}(\omega)H_p}{\hbar}e^{i(p/\hbar)x_m} \tag{7}$$

$$(\omega - \omega_p + i\epsilon)D_p(\omega) = \frac{A(\omega)H_p^*}{\hbar} \tag{8}$$

$$(\omega - \omega_p + i\epsilon)E_{mp}(\omega) = \frac{C_m(\omega)H_p^*}{\hbar}e^{-i(p/\hbar)x_m} \tag{9}$$

where H_k and H_k^* are the matrix elements corresponding to absorption and emission of a photon, respectively. Also H_p and H_p^* are the matrix elements corresponding to absorption and emission of a conversion electron, respectively.

The details, showing the solution for $B_k(\omega)$ and the resulting expression for the time-dependent intensity of the recoil-free radiation reaching the

detector due to forward scattering, are given in [7]. The result for the time-dependent intensity is

$$I_{\mathrm{recoil-free}}(t) = \frac{\gamma_r f_s}{2\hbar} e^{-(\Gamma/\hbar)t} \left[1 + \sum_{n=1}^{N} \binom{N}{n} \left(\frac{-f_a \gamma_r t}{2\hbar} \right)^n \frac{1}{n!} \right]^2 \tag{10}$$

where γ_r is the radiative width of the first excited-state nuclear level, f_s is the recoil-free fraction for the source, f_a is the recoil-free fraction for the absorber, Γ is the total width of the first excited-state nuclear level, N is the effective number of nuclei in the one-dimensional chain representation of the nuclear-resonant absorber (filter) and $\binom{N}{n}$ is the binomial coefficient. In this treatment I have assumed that the gamma rays have only a single frequency, i.e. the nuclear first-excited and ground states are assumed to be unsplit.

Going back one step in the derivation the total amplitude, as a function of time, for recoil-free radiation to reach the detector after passing through the resonant absorber is

$$amp_{\mathrm{recoil-free}}(t) = \sqrt{\frac{\gamma_r f_s}{2\hbar}} e^{-(\Gamma/2\hbar)t} \left[1 + \sum_{n=1}^{N} \binom{N}{n} \left(\frac{-f_a \gamma_r t}{2\hbar} \right)^n \frac{1}{n!} \right]. \tag{11}$$

Of course to obtain intensity from amplitude one simple needs to take the absolute value squared of the amplitude.

4 Discussion

4.1 Simple Cases

In order to understand the meaning of the results presented above; consider the expression for the total amplitude (11). Suppose the absorber (filter) is not present. In that case the second term in the brackets of (11), the summation, is absent. The intensity reaching the detector is then given by

$$I_{\mathrm{source-alone}}(t) = \frac{\gamma_r f_s}{2\hbar} e^{-(\Gamma/\hbar)t}. \tag{12}$$

As expected the source radiates with a lifetime $\tau = \hbar/\Gamma$. Half the radiation goes forward and the gamma-ray emission rate is reduced by the recoil-free fraction if one considers recoil-free emission alone.

Thus the effect due to the nuclear-resonant absorber (filter) is contained in the summation term in (11). According to this model the thinnest absorber is one having one "effective" nucleus, i.e. $N = 1$. In this case the total amplitude for recoil-free radiation reaching the detector is

$$amp_{N=1}(t) = \sqrt{\frac{\gamma_r f_s}{2\hbar}} e^{-(\Gamma/2\hbar)t} \left[1 + \left(\frac{-f_a \gamma_r t}{2\hbar} \right) \right]. \tag{13}$$

The first term is the amplitude for the source to radiate directly to the detector. The second term corresponds to the amplitude when the source radiation interacts with the absorber, in this case the thinnest possible absorber ($N = 1$). To simply the language I will say, that when radiation is absorbed and re-emitted in a recoil-free manner, the radiation "hops" on that effective nucleus. It is important to notice that the "one-hop" amplitude is negative, compared to the direct source radiation, due to the negative sign in (13). Because I am only considering recoil-free processes, it is impossible to detect which "path" the radiation took in reaching the detector. Thus these two amplitudes must be added, as in (13), before calculating the intensity. In this case the amplitudes destructively interfere. It is perhaps already clear that the resulting time-dependent intensity decreases more rapidly in time than would be the case if the resonant absorber were absent.

4.2 General Case

Now consider an absorber (filter) that is not necessarily thin, i.e. N can take on any integer value. Referring back to (11) the first term is, as we know, the amplitude for the source radiation to reach the detector without interacting with the absorber. The second term, the summation term, describes the interaction with the absorber. The source radiation can "hop" on any or all of the effective nuclei. The term in the summation with $n = 1$ corresponds to the "one-hop" amplitude: this amplitude can happen N ways i.e. $\binom{N}{1} = N$. Notice again that the "one-hop" amplitude has a negative sign. The $n = 2$ term corresponds to the "two-hop" amplitude containing the appropriate binomial coefficient, answering the question, how many ways can two hops occur on N objects. Notice that the "two-hop" amplitude has a positive sign. Thus, the "two-hop" amplitude interferes constructively with the direct source radiation. In a similar fashion the terms with $n > 2$ correspond to higher order multiple scattering processes: paths containing more hops.

4.3 General Comments

Notice that the positions of the effective nuclei do not appear in the solution, (10) and (11). This is because, for forward scattering, all optical paths from the source nucleus to the detector are equal. The solution simply says that all we must do is keep track of the phase of each contribution as we make a coherent summation over all indistinguishable "paths", i.e. multiple scattering (hopping) paths, that the radiation takes in getting to the detector. The odd-number hopping paths interfere destructively with the direct source radiation, while the even-number hopping paths interfere constructively. This is due to the minus sign, as noted above, appearing in the solution.

The parameter N, in the model, is a measure of the thickness of the absorber. The number and type of hopping paths that must be summed over depend on the number N, since the summation in the solution goes from $n = 1$ to $n = N$. The total amplitude is obtained by summing over all the $N + 1$ indistinguishable paths.

4.4 Example Calculations

In order to give a pictorial representation of the results, some simulation calculations are presented below using the parameters corresponding to the well-known Mössbauer transition in ^{57}Fe. In Fig. 1 the first three, of the $N + 1$, amplitudes are shown according to (11) for the ^{57}Fe case assuming a nuclear-resonant absorber of thickness corresponding to $N = 50$. We see the destructive interference between the direct source amplitude and the one-hop amplitude. This is the main cause of the "speed-up" effect. Furthermore, since the two-hop amplitude is positive, the dynamical beat will be present at some time t when the magnitude of the sum of the direct source and two-hop amplitudes is greater than the magnitude of the one-hop amplitude. These remarks are a little oversimplified because one must do the total calculation to obtain the correct result.

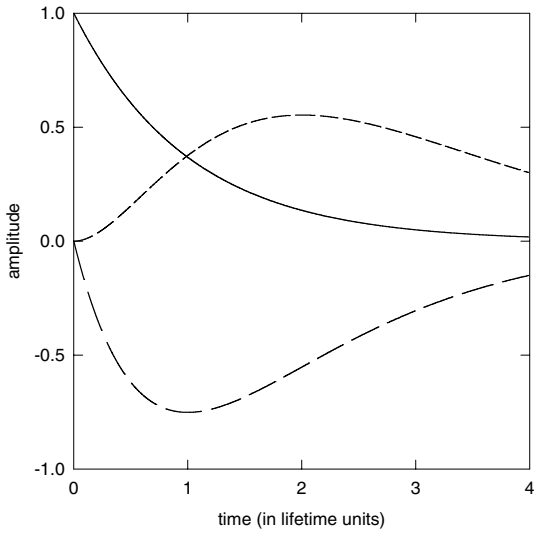

Fig. 1. Of the total $N + 1$ amplitudes, three amplitudes are shown. The direct source radiation amplitude, i.e. the "no hop" amplitude, is the solid line. The longer dashed line gives the "one-hop" amplitude, and the "two-hop" amplitude is shown as the shorter dash line. The case shown corresponds to $N = 50$ and the parameters for the well-known Mössbauer transition in ^{57}Fe are used. The final result requires summation over all $N + 1$ amplitudes

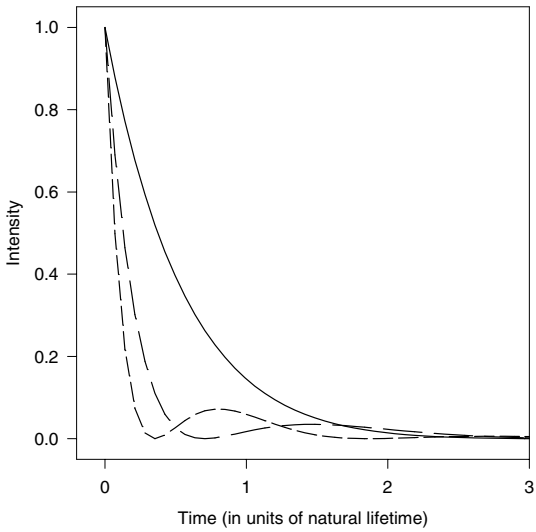

Fig. 2. The time-dependent intensity of recoil-free forward-scattered gamma radiation is shown. The solid-line curve corresponds to an absorber having thickness equivalent to $N = 10$. The longer dashed curve corresponds to an absorber having thickness equivalent to $N = 50$, and the shorter dashed curve corresponds to an absorber having thickness equivalent to $N = 100$. Again the parameters for the well-known Mössbauer transition in ^{57}Fe have been used

Figure 2 shows the time-dependent intensity of gamma radiation reaching the detector after forward scattering from an absorber. Results are shown for three absorbers differing only in thickness. Notice that as the thickness increases the speed-up effect increases, and the presence of the dynamical beat becomes more prominent. All such effects are due to the interference of the coherent amplitudes.

The relationship, between the "thickness" in the one-dimensional model of the absorber represented by N and the thickness of the three-dimensional real absorber, is not immediately apparent. In fact one can simply view N as a parameter that can be adjusted to fit the data. However, it is possible to obtain a relationship by noting that, even though the formula for the result using the classical optical model is completely different from the one-dimensional model, the calculated numerical results agree. To establish this relationship, consider the thin-absorber limit. In the classical optical model [3], when the source and absorber are in resonance, this amounts to expanding the J_0 Bessel function. In the one-dimensional model the thin "absorber" limit is set by putting $N = 1$. Comparing the two results in this limit gives

$$N = \frac{\beta\Gamma}{2f_a\gamma_r} \tag{14}$$

where the usual thickness parameter β is equal to $N_0 f_a \sigma_0 d$. N_0 is the number of real resonant nuclei/cm^3 in the absorber, f_a is the recoil-free fraction of the absorber, σ_0 is the maximum cross section evaluated on resonance, and d is the thickness of the absorber. Equation (14) is a curious result. The left-hand side of the equation takes on only integer values. On the other hand, the right-hand side of the equation will, in general, not be equal to an integer. To apply the one-dimensional model to an experimental result one would pick the value of N that is nearest to the value of the right-hand side of (14). It is not clear at this time whether or not there is some physical significance to (14). For example, with respect to gamma ray forward scattering, can an actual solid be represented in some fundamental way as a series of layers as suggested by (14).

5 Summary and Conclusions

First consider some previous results, mentioned above, in the field of nuclear-resonant forward scattering of gamma radiation. Hamermesh [3] developed the semi-classical optical model that has been frequently used to explain many features of nuclear-resonant forward scattering of gamma radiation, in particular TDMS. It spite of its success the model is not physically transparent and has difficulty including gamma-ray scattering events that occur with recoil in the scatterer itself. The resulting equations are in the form of an infinite series and, in the TDMS case, the scattering events with recoil are assumed to occur only in the source. Harris [4] calculated the Mössbauer transmission result starting from the quantum mechanical approach developed by Heitler [5]. Harris was able to show that the result was in the same form as the semi-classical model. Harris did not obtain a separate distinguishable quantum mechanical result. In Ref. [7] a detailed calculation, using the approach of Heitler and Harris, was applied assuming the scatterer could be represented as a one-dimensional chain of effective nuclei. The present paper is a distillation of the work in [7] with an emphasis on the meaning and interpretation of the results.

The one-dimensional quantum mechanical model gives a clear physical explanation of the important features of nuclear-resonant forward scattering. These prominent features are the speed-up and dynamical beat effects. All features are explained as interference effects arising from the summation over all coherent indistinguishable paths the gamma radiation takes in going from the source through the absorber to the detector. It appears that some paths lead to absorption and others do not. When the "path" of the gamma radiation involves interaction in a recoil-free fashion with a single "effective" nucleus, absorption occurs. In fact, if the path involves interaction with an odd number of effective nuclei, absorption occurs. If absorption occurs, then energy is lost to the forward-scattered beam due to re-radiation in non-forward directions, as well as through the inelastic channel of internal

conversion. By contrast, a path that involves an even number of effective nuclei does not appear to give rise to absorption. Such paths seem to correspond to suppression of the inelastic channel, or one may say, to a type of self-stimulated emission such that the radiation passes through the absorber with no energy loss.

It is not difficult to include inelastic processes, such as emission with recoil, in the theory. For example, one can consider processes in which an "effective" absorber nucleus, after excitation, emits radiation but in the process recoils. This re-emitted radiation is not in resonance with the other absorber "nuclei" and thus passes through the rest of the absorber without resonant absorption. Furthermore such a process is incoherent with the recoil-free processes, as well as other recoil processes. Details for calculating such processes are given in [7].

The model is so physical transparent that one is easily able to extend the theory to several other interesting cases, e.g. when synchrotron radiation is the source. Furthermore the effect known as the "gamma-echo" effect [8], when using a radioactive source, can be easily explained as a phase shift induce transparency [9].

References

1. R.L. Mössbauer: Z. Phys. **151**, 124 (1958)
2. See for example G.R. Hoy: *Encyclopedia of Physical Science and Technology*, Vol. 10 (Academic Press, New York 1992) pp. 469-483
3. F.J. Lynch, R.E. Holland, M. Hamermesh: Phys. Rev. **120**, 513 (1960)
4. S.M. Harris: Phys. Rev. **124**, 1178 (1961)
5. W. Heitler: *The Quantum Theory of Radiation*, 3rd edn. (Oxford University Press, Oxford 1957)
6. G.V. Smirnov: Hyperfine Interactions **97/98**, 81 (1996)
7. G.R. Hoy: J. Phys.: Condens. Matter **9**, 8749 (1997)
8. I. Tittonen, M. Lippmaa, P. Helistö, T. Katila: Phys. Rev. B **47**, 7840 (1993)
9. G.R. Hoy, J. Odeurs: unpublished

Parametric Amplification of Coupled Atomic and Optical Fields

Michael G. Moore and Pierre Meystre

1 Introduction

One of the earliest and still most important spin-offs of the invention of the laser is without a doubt nonlinear optics. Following the pioneering experiments carried out by P. A. Franken and his students [1], N. Bloembergen, Y. R. Shen and their collaborators made a series of crucial advances that led to the rapid development of the field [2]. In the early days, it was generally understood that what made nonlinear optics possible was the high optical powers provided by lasers. For such fields, a classical description of the light fields was clearly sufficient. Yet, a few visionaries insisted on a fully quantum mechanical description of radiation in the analysis of nonlinear optical phenomena such as parametric amplification. A central character in these developments was R. J. Glauber, who, together with his students, developed many of the tools, and much of the early quantum theory of nonlinear optics [3,4]. One of his students was Dan Walls, who upon his return to New Zealand after spending a short time in Germany developed one of the leading schools of quantum optics in the world.

It is impossible in a brief introduction to recount all of the important contributions of Dan Walls. Suffice it to say that he made a number of trailblazing advances, one of the most important being the prediction of photon antibunching in resonance fluorescence [5]. The demonstration of this effect is one of the few low energy proofs of the quantized nature of light [6]. Together with his students, he went on to develop novel theoretical tools to analyze nonlinear problems in the quantum description of light-matter interactions [7]. These methods were applied with considerable success in the analysis of the generation of squeezed states of the electromagnetic field [8,9]. He also devoted much of his enormous energy to the study of the "paradoxes" of quantum mechanics associated with quantum entanglement [10].

In the 1980's, when Bose-Einstein condensation [11,12] was still a distant experimental goal, he was amongst the first to realize the raising importance of atom optics. At nearly the same time as we did, and independently of us, he and his collaborator W. Zhang recognized that collisions play in atom optics a role similar to that of a nonlinear medium in optics, thereby leading to nonlinear atom optics [13,14]. This opened up a completely new direction of research, which is now starting to witness its first experimental successes [15].

H.J. Carmichael, R.J. Glauber, M.O. Scully (Eds.): LNP 561, pp. 116–125, 2001.

Nonlinear atom optics is in many ways at the same state as early nonlinear optics, with the intense source being now a Bose-Einstein condensate or an "atom laser" rather than a laser. Yet, the same trend will develop in this field, and soon experimentalists will start investigating "weak" signals where the effects of quantum statistics become important. Already, phase-coherent matter-wave amplifiers have been demonstrated, based on the four-wave mixing between two optical and two matter waves [16,17]. It is not difficult to imagine that this work will soon lead to the study of subtle effects such as the quantum entanglement between optical and matter waves [18], the generation of "nonclassical matter waves"— as opposed to present-day condensates and atom laser, which are in many ways the de Broglie wave equivalent of classical light fields, etc. In many ways, this is a legacy of Dan's work and vision. We think that it is a fitting tribute to Dan Walls to discuss these kind of problems in this book.

The paper is organized as follows: Section 2 introduces an effective Hamiltonian that describes the far off-resonant interaction between optical and matter-wave fields. Using a standard mode expansion, it is cast in the form of a four-wave mixing interaction, with two of the fields being atomic and the other two optical. This model is applied in section 3 to a discussion of the creation of atom-photon pairs in an atom-optical extension of the optical parametric oscillator. We briefly review the gain of the system, as well as the generation of nonclassical correlations between the atoms and the light. A more detailed analysis of this system can be found in [19,18,20]. A central element in this discussion is the use of an optical resonator to limit the number of electromagnetic modes available. Section 4, which is a conclusion and outlook, discusses in general terms a situation where this is no longer necessary, with mode selection resulting from the geometry of the atomic sample. This is an application of the "end-fire mode" ideas of Dicke to atom optics, and has recently lead to the experimental demonstration of four-wave mixing between light and matter waves [21,22].

2 Four-Wave Mixing with Atoms and Light

In this section we derive the form of the effective interaction between the ground state atomic field and a far off-resonant optical field. We begin with the Hamiltonian describing a field of two-level atoms coupled via the dipole interaction to a set of quantized optical field modes. Because we are trying to gain insight into the atom-field interaction, we neglect atomic collisions and trapping potentials for the sake of simplicity. In the rotating wave approximation the atom-field Hamiltonian is then given by

$$\hat{H} = \sum_{j=g,e} \int d^3\, q \hat{c}_j^\dagger(\mathbf{q}) \left[\frac{\hbar^2 q^2}{2m} + \hbar\omega_a \delta_{je} \right] \hat{c}_j(\mathbf{q}) + \sum_{\mathbf{k}\lambda} \hbar c |\mathbf{k}| \hat{b}_{\mathbf{k}\lambda}^\dagger \hat{b}_{\mathbf{k}\lambda}$$

$$- i\hbar \sum_{\mathbf{k}\lambda} \int d^3q \left[g_{\mathbf{k}\lambda} \hat{c}_e^\dagger(\mathbf{q}+\mathbf{k}) \hat{c}_g(\mathbf{q}) \hat{b}_{\mathbf{k}\lambda} - g_{\mathbf{k}\lambda}^* \hat{b}_{\mathbf{k}\lambda}^\dagger \hat{c}_g^\dagger(\mathbf{q}) \hat{c}_e(\mathbf{q}+\mathbf{k}) \right], \quad (1)$$

where the operator $\hat{c}_j(\mathbf{q})$ annihilates an atom with mass m, momentum $\hbar\mathbf{q}$, and internal state j, $\hat{b}_{\mathbf{k}\lambda}$ annihilates a photon with momentum $\hbar\mathbf{k}$ and polarization λ, ω_a is the energy difference between the ground and excited atomic states and $g_{\mathbf{k}\lambda}$ is the atom field coupling constant. The field operators are assumed to obey the usual bosonic commutation relations.

We are interested in wave-mixing phenomena between atomic and far-off resonant light fields. Hence, we assume that the frequencies of the optical fields are centered around a central frequency ω_0 satisfying the condition $|\Delta| \gg \gamma$, where $\Delta = \omega_0 - \omega_a$ and γ is the lifetime of the excited atomic state. After removing the fast oscillations via the transformations $\hat{c}_e(\mathbf{q}) \to \hat{c}_e(\mathbf{q}) \exp(-i\omega_0 t)$ and $\hat{b}_{\mathbf{k}\lambda} \to \hat{b}_{\mathbf{k}\lambda} \exp(-i\omega_0 t)$, the equation of motion for the excited state field operator is found to be

$$\frac{\mathrm{d}}{\mathrm{d}t} \hat{c}_e(\mathbf{q}) = -i \left[\frac{\hbar q^2}{2m} - \Delta \right] \hat{c}_e(\mathbf{q}) - \sum_{\mathbf{k}\lambda} g_{\mathbf{k}\lambda} \hat{c}_g(\mathbf{q}-\mathbf{k}) \hat{b}_{\mathbf{k}\lambda}. \quad (2)$$

With the assumption that the optical and atomic ground-state fields are slowly varying compared to the frequency Δ, (2) has the approximate solution

$$\hat{c}_e(\mathbf{q}) = \hat{c}_e(\mathbf{q},0) \mathrm{e}^{i(\Delta - \hbar q^2/2m)t} - \frac{i}{\Delta} \sum_{\mathbf{k}\lambda} \hat{c}_g(\mathbf{q}-\mathbf{k}) \hat{b}_{\mathbf{k}\lambda}). \quad (3)$$

The first term can be neglected for most considerations if we assume that there are no excited atoms at $t = 0$, in which case the operator $\hat{c}_e(\mathbf{k}, 0)$ acting on the initial state gives zero. Dropping the first term and substituting (3) into the equations of motion for $\hat{c}_g(\mathbf{q})$ and $\hat{b}_{\mathbf{k}\lambda}$ then gives

$$\frac{\mathrm{d}}{\mathrm{d}t} \hat{c}_g(\mathbf{q}) = -i \frac{\hbar q^2}{2m} \hat{c}_g(\mathbf{q}) - i \sum_{\mathbf{k}\lambda\mathbf{k}'\lambda'} \frac{g_{\mathbf{k}\lambda}^* g_{\mathbf{k}'\lambda'}}{\Delta} \hat{b}_{\mathbf{k}\lambda}^\dagger \hat{b}_{\mathbf{k}'\lambda'} \hat{c}_g(\mathbf{q}+\mathbf{k}-\mathbf{k}') \quad (4)$$

and

$$\frac{\mathrm{d}}{\mathrm{d}t} \hat{b}_{\mathbf{k}\lambda} = -i\delta_{\mathbf{k}} \hat{b}_{\mathbf{k}\lambda} - i \sum_{\mathbf{k}'\lambda'} \int d^3q \, \frac{g_{\mathbf{k}\lambda}^* g_{\mathbf{k}'\lambda'}}{\Delta} \hat{c}_g^\dagger(\mathbf{q}) \hat{b}_{\mathbf{k}'\lambda'} \hat{c}_g(\mathbf{q}+\mathbf{k}-\mathbf{k}'), \quad (5)$$

where $\delta_{\mathbf{k}} = c|\mathbf{k}| - \Delta$. Equations (4) and (5) can be derived from the effective Hamiltonian

$$\hat{H} = \int d^3q \, \frac{\hbar^2 q^2}{2m} \hat{c}^\dagger(\mathbf{q}) \hat{c}(\mathbf{q}) + \sum_{\mathbf{k}\lambda} \hbar\delta_{\mathbf{k}} \hat{b}_{\mathbf{k}\lambda}^\dagger \hat{b}_{\mathbf{k}\lambda}$$
$$+ \sum_{\mathbf{k}\lambda\mathbf{k}'\lambda'} \int d^3q \, \hbar \frac{g_{\mathbf{k}\lambda}^* g_{\mathbf{k}'\lambda'}}{\Delta} \hat{b}_{\mathbf{k}\lambda}^\dagger \hat{b}_{\mathbf{k}'\lambda'} \hat{c}^\dagger(\mathbf{q}) \hat{c}(\mathbf{q}+\mathbf{k}-\mathbf{k}'), \quad (6)$$

where we have dropped the subscript g from the atomic field operators as it is no longer needed. From (4-6) we see that the interaction between the

ground-state atomic field and a far off-resonant optical field takes the form of a third order nonlinearity.

The nonlinearity in (6) allows for cross-phase modulation and four wave mixing phenomena between the atomic and optical fields, but does not allow them to undergo self-phase modulation, as that would require terms which involve four atomic or four optical field operators. By formally eliminating the atomic field from our system we must recover standard nonlinear optics. This means that phenomena related to optical self-phase modulation, such as self-focusing and soliton formation, must be contained within (6). From the symmetric way in which the atomic and optical fields appear, it is clear that atomic self-focusing and atomic soliton formation occur as well. In fact this was the subject of much of the early work on nonlinear atom optics [13,14]. The phase shift which the optical field acquires due to cross-phase modulation with the atomic field is

$$\Delta\phi_{opt} = \frac{|g_{\mathbf{k}\lambda}|^2 \hat{N}}{\Delta} t, \tag{7}$$

where $\hat{N}$ is the operator for the total number of atoms, which may or may not be a constant of motion. Particularly in closed systems where the number of atoms is fixed, this nonlinear phase shift is nothing more than the dispersive shift to the index of refraction found in linear optics. Non-trivial effects may occur in open systems, e.g., if the number of atoms fluctuates in response to changes in the optical field, but otherwise this phase shift leads only to a negligible shift in the optical dispersion relation. Similarly the phase shift acquired by the atomic field due to cross-phase modulation

$$\Delta\phi_{at} = \sum_{\mathbf{k}\lambda} \frac{|g_{\mathbf{k}\lambda}|^2 \hat{b}^\dagger_{\mathbf{k}\lambda} \hat{b}_{\mathbf{k}\lambda}}{\Delta} t, \tag{8}$$

is simply the spatially independent part of the Stark shift, which has no dynamical effect on the atomic density.

In the examples we consider in the following sections the Stark shift and the dispersion of the optical field play no real roles and may be safely neglected. We shall instead focus on the effects of four-wave mixing between atomic and optical fields, which we shall see leads to parametric amplification and the generation of entanglement between atomic and optical fields. Of course to observe four-wave mixing atomic and optical sources must be developed which can achieve a high enough phase-space density so that Bose-stimulated effects dominate spontaneous noise. In optics this usually requires a laser and we are fortunate that the atomic analog to the laser now exists in the form of atomic Bose-Einstein condensates (BECs).

3 Coupling to Single Optical Cavity Mode

There are two limiting cases in which the system (6) can be significantly simplified. They are (I) when light from an intense pump laser is scattered

into a single mode of an optical cavity, and (II) when the atomic system is of sufficiently low density and sufficiently localized that pump photons are at most only singly scattered before escaping the interaction region. This paper considers specifically the first case, which leads to a very simple theoretical model describing the parametric amplification of light and matter waves.

We remark at the onset that the optical gain achievable in practical systems is most likely insufficient to overcome losses in even the best high-Q optical cavities. Thus, while effective single mode systems can be achieved, they will in general be dominated by losses. It is however important to realize that even in those cases where losses prevent the optical field from building up, the atomic field may still experience gain and exponential growth. As a matter of fact, this is the key to the matter-wave superradiance recently observed by the MIT group. This being said, in order to extract the basic physics underlying the four-wave mixing of optical and matter waves, we ignore cavity losses in the following. Our model system therefore consists of an atomic field coupled to both a strong pump laser and a single optical ring-cavity mode (the probe). The dynamics of the pump may be safely neglected, in which case the effective Hamiltonian for the system is

$$\hat{H} = \hbar\omega_r \left[\delta \hat{b}^\dagger \hat{b} + \int d^3q \, \frac{q^2}{K^2} \hat{c}^\dagger(\mathbf{q}) \hat{c}(\mathbf{q}) + \chi \left[\hat{c}^\dagger(\mathbf{q}) \hat{c}(\mathbf{q} - \mathbf{K}) \hat{b} + H.c. \right] \right], \quad (9)$$

where $\mathbf{K}$ is the difference between the pump and probe wavevectors, $\omega_r = \hbar K^2/2m$ is the atomic two-photon recoil frequency, $\hat{b}$ is the photon annihilation operator for the probe mode, whose frequency is detuned from that of the pump by $\hbar\omega_r\delta$. The effective atom-probe coupling constant is given by $\chi = g\Omega_0/2|\Delta|\omega_r$, where g is $g_{\mathbf{k}\lambda}$ for the probe mode and Ω_0 is the pump Rabi frequency.

3.1 Instability and Gain

We consider specifically the case where the atomic field initially consists of a BEC well below the critical temperature. Assuming that the initial momentum width of the BEC is small compared to the recoil momentum $\hbar\mathbf{K}$ it is reasonable to approximate it as a plane wave at $\mathbf{q} = 0$. The effect of the optical fields is then to couple the BEC to matter-wave side modes separated from the BEC in momentum space by integer multiples of $\hbar\mathbf{K}$. Making use of the familiar symmetry-breaking ansatz, we replace the condensate field operator $\hat{c}(0)$ by a c-number plus a perturbation

$$\hat{c}(0) = \sqrt{N} + \hat{c}_0, \quad (10)$$

where N is number of atoms initially in the BEC. In the case where the number of photons initially in the probe mode is much less than N, both the momentum side mode and probe field operators, as well as $\hat{c}_0$, can be considered as infinitesimal relative to $\sqrt{N}$. Thus for times short enough that

the fraction of atoms transferred into the side modes remains negligible, the Hamiltonian (9) can be linearized, leading to

$$\hat{H}_{lin} = \hbar\omega_r \left[\hat{c}_-^\dagger \hat{c}_- + \hat{c}_+^\dagger \hat{c}_+ + \delta \hat{b}^\dagger \hat{b} + \chi\sqrt{N}\left(\hat{b}^\dagger \hat{c}_-^\dagger + \hat{b}^\dagger \hat{c}_+ + H.c.\right)\right], \quad (11)$$

where $\hat{c}_\pm = \hat{c}(\pm\mathbf{K})$. This Hamiltonian yields a 3×3 set of linear equations for the three coupled field modes

$$\frac{\mathrm{d}}{\mathrm{d}\tau}\begin{pmatrix} \hat{b} \\ \hat{c}_-^\dagger \\ \hat{c}_+ \end{pmatrix} = i\begin{pmatrix} -\delta & -\chi\sqrt{N} & -\chi\sqrt{N} \\ \chi\sqrt{N} & 1 & 0 \\ -\chi\sqrt{N} & 0 & -1 \end{pmatrix}\begin{pmatrix} \hat{b} \\ \hat{c}_-^\dagger \\ \hat{c}_+ \end{pmatrix}, \quad (12)$$

where $\tau = \omega_r t$. The time dependence of the three field modes is therefore determined by the eigenvalues of the 3×3 matrix on the r.h.s. of (12). These are found by solving the characteristic equation

$$\omega^3 + \delta\omega^2 - \omega - \delta + 2\chi^2 N = 0, \quad (13)$$

which has complex solutions provided that

$$\chi^2 N > \left[(3 + \delta^2)^{3/2} - \delta^3 + 9\delta\right]/27. \quad (14)$$

When the condition (14) is satisfied, the system is unstable and the three fields initially exhibit exponential growth. This growth will of course be arrested by saturation effects in the nonlinear regime. In the case where $\chi^2 N \gg |\delta|^3$ the rate of exponential growth is well approximated by

$$\Gamma = \sqrt{3}(\chi^2 N/4)^{1/3}, \quad (15)$$

which shows that the growth scales as the cube root of the atomic density. The presence of the $\hat{b}^\dagger \hat{c}_-^\dagger$ term in (11) describes the creation of correlated atom-photon pairs, and is analogous to the term found in the optical parametric amplifier [7] which describes the generation of correlated photon pairs. The instability is strongest in the vicinity of $\delta = -1$, where the generation of atom-photon pairs conserves energy, allowing the efficient transfer of atoms from the condensate into the $-\mathbf{K}$ side mode. The transfer of atoms into the $+\mathbf{K}$ side mode does not conserve energy, and hence the population of this mode remains negligible compared to the populations of the other two modes. If we do not include this mode in our model, however, we would fail to predict the $N^{1/3}$ dependence of the gain.

It is straightforward to compute the intensities of the three modes in the case where they each begin in the vacuum state. We find

$$N_1 \equiv \langle \hat{b}^\dagger \hat{b} \rangle = |a_{12}(\tau)|^2, \quad (16)$$

$$N_2 \equiv \langle \hat{c}_-^\dagger \hat{c}_- \rangle = |a_{22}(\tau)|^2 - 1, \quad (17)$$

and

$$N_3 \equiv \langle \hat{c}_+^\dagger \hat{c}_+ \rangle = |a_{32}(\tau)|^2, \quad (18)$$

where

$$a_{ij}(\tau) = \sum_{k=1}^{3} U_{ik} U_{kj}^{-1} \mathrm{e}^{i} \omega_k \tau. \tag{19}$$

Here ω_k is the kth eigenvalue of the 3×3 system, and the elements U_{ik} comprise the matrix U whose columns are the corresponding eigenvectors. Equations (16-18) show that even vacuum fluctuations in the atomic density and in the electric field are sufficient to trigger the instability, resulting in spontaneous parametric amplification of the atomic and optical fields.

3.2 Entanglement Between Atomic and Optical Fields

One of the most interesting applications of the optical parametric amplifier is the generation of entangled quantum optical states. A similar entanglement occurs in the present system, only now it is between atomic and optical field modes. A useful measure of quantum entanglement is the second-order equal-time intensity correlation function, defined as

$$g_{ij}^{(2)} = \frac{\langle \hat{N}_i \hat{N}_j \rangle - \delta_{ij} \langle \hat{N}_i \rangle}{\langle \hat{N}_i \rangle \langle \hat{N}_j \rangle}. \tag{20}$$

These two-mode correlation functions ($i \neq j$) arise, e.g., if we consider a measurement of the intensity difference between two modes, described by the operator

$$\hat{N}_{ij} = \hat{N}_i - \hat{N}_j, \tag{21}$$

whose variance is given by

$$(\Delta N_{ij})^2 = (\Delta N_i)^2 - 2 N_i N_j \left(g_{ij}^{(2)} - 1 \right) + (\Delta N_j)^2 . \tag{22}$$

For uncorrelated fields, $g_{ij}^{(2)} = 1$, and we have the usual rule for the addition of uncorrelated noise sources

$$(\Delta N_{ij})^2 = (\Delta N_i)^2 + (\Delta N_j)^2 . \tag{23}$$

If, however, there are correlations between the fluctuations in the intensities of the two modes, then we have $g_{ij}^{(2)} > 1$, and the variance ΔN_{ij} will be less than that given by (23).

For classical fields (positive P-function), the two-mode ($i \neq j$) correlations are constrained by the Cauchy-Schwartz inequality

$$g_{ij}^{(2)} \leq \left[g_{ii}^{(2)} \right]^{1/2} \left[g_{jj}^{(2)} \right]^{1/2} . \tag{24}$$

Quantum mechanical fields, however, can violate this inequality and are instead constrained by

$$g_{ij}^{(2)} \leq \left[g_{ii}^{(2)} + \frac{1}{\langle \hat{N}_i \rangle} \right]^{1/2} \left[g_{jj}^{(2)} + \frac{1}{\langle \hat{N}_j \rangle} \right]^{1/2}, \tag{25}$$

which reduces to the classical result in the limit of large intensities. When triggered from the vacuum, it is readily found that the single-mode correlation functions are those of thermal fields $g^{(2)}(\tau) = 2$. In this case the cross-correlation functions are found to be

$$g_{12}^{(2)} = g_{23}^{(2)} = \left[2 + \frac{1}{N_1 + N_3} \right]^{1/2} \left[2 + \frac{1}{N_2} \right]^{1/2}, \tag{26}$$

and

$$g_{13}^{(2)} = 2, \tag{27}$$

where 1 corresponds to the probe mode, 2 to the $-\mathbf{K}$ side mode and 3 to the $+\mathbf{K}$ mode. As $N_1 \gg N_3$ we see that the intensity correlations between the probe and $-\mathbf{K}$ side mode are very close to the maximum allowed by quantum mechanics, whereas the other two-mode correlations are considerably more classical.

4 Outlook

The simplified model of the preceding section used an optical cavity to select the probe optical field mode. Recent experiments by W. Ketterle and coworkers, however, have demonstrated that under appropriate conditions mode selectivity can be achieved without the use of cavities.[21] They observed highly directional scattering of pump photons along the long axis of a cigar shaped condensate when the pump polarization and wavevector were both perpendicular to the condensate axis. The optical mode is therefore selected by the condensate geometry, and this results in the build-up of population in a condensate side-mode with a single well-defined momentum.

To see how this works, we note that typical condensates are sufficiently localized in space that scattered photons immediately exit the condensate, with a negligible cross-section for multiple scattering. Due to photon recoil, however, each such scattering event transfers an atom from the condensate state into a state which is shifted in momentum space by the two-photon recoil momentum, as discussed in the preceding section. The positive feedback which leads to instability and parametric gain is then provided solely by the recoiling atoms, which due to their slow velocity remain in the condensate volume long enough to influence the direction of subsequent photon scattering. This influence occurs due to bosonic stimulation as the probability that subsequent atoms will recoil in a given direction is proportional to

$n + 1$, where n is the number of atoms which have already recoiled in that direction.

The finite size of the BEC implies that it has a finite extent in momentum space as well. This means that two final states shifted by different photon recoil momenta may in fact have significant overlap if the directions of the scattered photons are within a small enough solid angle. Hence, despite there being a continuum of final states that the photon can scatter into, the atoms can only recoil into a finite number of distinct quantum states. If the number of distinct quantum states into which the atoms are likely to recoil can be made small compared to total number of scattered atoms, then certain modes will undergo a 'winner-takes-all' effect, in which those few modes receive all of the atoms due to Bose-stimulation.

This effect was recently demonstrated by the group of Ketterle at MIT [21], where highly directional scattering of light was observed when an off-resonant laser was shined on a highly asymmetrical BEC. The asymmetry of the condensate results in certain final atomic states having a slightly larger gain than others. These states, corresponding to the 'end-fire' photon scattering of Dicke [23], gain enough of an advantage that all other directions are squelched by mode competition.

In the absence of a "seed" signal, the parametric amplification of the side mode builds up from quantum density fluctuations, the atom-optical version of "vacuum fluctuations". Recent experiments at MIT and in Tokyo [16,17] have gone one step further and demonstrated phase-coherent matter-wave amplification. To demonstrate the phase-preserving nature of the amplification, it was necessary to amplify an injected signal with known properties. In the experiments just reported, this seed was generated by exposing the condensate to a pulsed optical standing wave that transferred atoms into the appropriate side mode. The phase of the amplified signal was then determined with an atom interferometer, using a second matter wave derived from the condensate as the reference beam.

Since coherent amplification is an essential element of many proposed applications of atom optics, just as it is central to electronics and optics, this work is likely to have a major impact in the future development of the field. Potential applications include sensors, precision measurements and lithography. The combination of atom lasers and coherent matter-wave amplifiers will provide exciting new possibilities for atom optics, both pure and applied. In addition, these new techniques will allow atom opticians to perform many experiments on the fundamentals of quantum theory that currently are only possible with photons.

Acknowledgements

This work is supported in part by the U.S. Office of Naval Research under Contract No. 14-91-J1205, by the National Science Foundation under Grant

No. PHY98-01099, by the U.S. Army Research Office, and by the Joint Services Optics Program.

References

1. P. Franken, A.E. Hill, C.W. Peters, G. Weinreich: Phys. Rev. Lett. **7**, 118 (1961)
2. Y.R. Shen: *The Principles of Nonlinear Optics* (Wiley, New York 1984)
3. R.J. Glauber: Phys. Rev. **131**, 2766 (1963)
4. B.R. Mollow, R.J. Glauber: Phys. Rev. **160**, 1076-1108 (1967)
5. H.J. Carmichael, D.F. Walls: J. Phys. B. **9**, 1199 (1976)
6. D.F. Walls: Nature **280**, 451 (1979)
7. D.F. Walls, G.J. Milburn: *Quantum Optics*, 1st edn. (Springer-Verlag, Berlin 1994)
8. G. Milburn, D.F. Walls: Opt. Commun. **39**, 401 (1981)
9. D.F. Walls: Nature **306**, 141 (1983)
10. M.D. Reid, D.F. Walls: Phys. Rev. A **34**, 1260 (1986)
11. M.H. Anderson *et al.*: Science **269**, 198 (1995)
12. K.B. Davis: Phys. Rev. Lett. **75**, 3969 (1995)
13. G. Lenz, P. Meystre, E. M. Wright: Phys. Rev. Lett. **71**, 3271 (1993)
14. W. Zhang, D.F. Walls, B.C. Sanders: Phys. Rev. Lett. **72**, 60 (1994)
15. L. Deng *et al.*: Nature **398**, 218 (1999)
16. S. Inouye *et al.*: Nature **402**, 6762 (1999)
17. M. Kozuma *et al.*: Science **286**, 5448 (1999)
18. M.G. Moore, P. Meystre: Phys. Rev. A **59**, R1754 (1999)
19. M.G. Moore, P. Meystre: Phys. Rev. A **58**, 3248 (1998)
20. M.G. Moore, O. Zobay, P. Meystre: Phys. Rev. A **60**, 1491 (1999)
21. S. Inouye *et al.*: Science **285**, 571 (1999)
22. M.G. Moore, P. Meystre: Phys. Rev. Lett. **83**, 5202 (1999)
23. R.H. Dicke: Phys. Rev. **93**, 99 (1954)

Quantum and QED Effects on Reflection from an Atomic Mirror

Bilha Segev

Summary. I review recent work on the evanescent wave atomic mirror [B. Segev, R. Côté, and M.G. Raizen, PRA **56**, R3350 (1997); R. Côté, B. Segev, and M.G. Raizen, PRA **58**, 3999 (1998)] in which we demonstrated that reflection of cold sodium atoms from such a mirror is expected to exhibit both quantum and quantum–electrodynamic (QED) effects. I then present a new phase–space wave–packet analysis of the time dependent reflection process. The time dependent distribution of cold atoms reflected from an atomic mirror can be used to probe the effective potential of the 'mirror'.

1 Introduction

Recent work in atom–optics has emphasized, on the one hand, the need to develop elements, like mirrors and lenses, for the coherent manipulation of atomic matter waves [1]. On the other hand, the experimental progress brought about the ability to cool and launch atoms with extremely low and well defined velocities [2–4].

The evanescent–wave atomic mirror is a useful tool for reflecting coherent matter–waves. By measuring the flux and distribution of the reflected atoms, quantum and quantum–electrodynamic (QED) effects would be probed [5,6]. Among Dan Walls' contributions to the field of atom–optics, his seminal work on the position measurement of moving atoms should be mentioned in this context [7–10]. Definition and previous work on the evanescent–wave atomic mirror are presented in Sect.2. Predictions of QED regarding the atom–surface long–range interaction that could be studied with this system, are discussed in Sect.3. Atoms incident on the evanescent–wave atomic mirror see an effective potential barrier which is a combination of a light induced repulsive potential and the attractive atom–wall interaction. The fundamental quantum processes of tunneling and above–barrier reflection from this barrier could be studied. In Sects.4 and 5 time–independent and time–dependent aspects of the quantum reflection are discussed, respectively. Conclusions are presented in Sect.6.

H.J. Carmichael, R.J. Glauber, M.O. Scully (Eds.): LNP 561, pp. 126–135, 2001.

2 The Evanescent-Wave Atomic Mirror

An evanescent–wave atomic mirror is obtained when blue–detuned laser light undergoes total internal reflection inside a dielectric prism. The exponentially declining evanescent light field outside the surface of the prism creates an effective repulsive optical potential for incident cold atoms. The reflecting force is the induced atom–laser dipole interaction. For large detuning the dipole force dominates the atom–laser interaction and the optical potential reduces to a simple form:

$$V_{\text{dipole}} \overset{\text{large } \delta}{\longrightarrow} \frac{\hbar \Omega^2}{4\delta} , \tag{1}$$

with $\Omega^2 \propto I d^2$ where I is the laser intensity and d is the atomic dipole. The dipole potential is proportional to the intensity of the laser and inversely proportional to detuning. The dipole force can be attractive or repulsive, according to the sign of the detuning. For red detuning, $\delta < 0$, and the atom is attracted by high intensity, in accordance with the classical intuition for a dipole in a field. However, for blue detuning, $\delta > 0$, and the atom is repelled by high intensity. This repulsion is the reflecting force used in the evanescent–wave atomic mirror.

Such an electromagnetic mirror for neutral atoms was first suggested by Cook and Hill in 1982 [11], and realized experimentally by Balykin et al. [12]. Normal incidence reflection in the form of an atomic "trampoline" has also been demonstrated [13,14]. Experimental applications of the evanescent–wave mirror already include a variety of studies. It was recently incorporated into an atomic interferometer [15]. The phase–shift of the reflected laser beam can be used to detect the passage of a cloud of atoms without destroying the coherence of the reflection [16]. Experiments with a time–dependent mirror, in which the potential changes rapidly and continuously by controlled modulation of the intensity of the laser light, were performed [17]. The penetration depth and wave vector of the evanescent electromagnetic waves were studied using on resonance laser atomic spectroscopy [18]. Atom guiding using evanescent waves in small hollow optical fibers was demonstrated [19–21], and an interferometric approach to the van der Waals interactions in atomic mirrors was suggested [22]. Transmission grating diffraction of molecular beams was recently used to measure atom–surface van der Waals potentials [23]. Other recent related works can be found in [24–29].

3 Retardation Effects on the Potential Curves

The interaction between an atom and a dielectric or conducting wall has been investigated theoretically and experimentally [30–42]. Theoretical studies have been performed at different levels, from a simple model of a dipole–dipole interaction of the atom and its mirror image, to the full QED relativistic quantum treatment.

The simplest model for the interaction of a ground state atom and a wall of dielectric constant n^2 considers the interaction between a dipole $\boldsymbol{d}$ and its mirror image and gives the Lennard–Jones potential

$$V_{\mathrm{LJ}} = -\left(\frac{n^2-1}{n^2+1}\right)\left(\frac{\langle d_{||}^2\rangle + 2\langle d_{\perp}^2\rangle}{64\pi\varepsilon_0}\right) z^{-3} = -\frac{C_3^{(n)}}{z^3}\ , \tag{2}$$

where z is the distance between the atom and the surface, $\langle d_{||}^2\rangle$ and $\langle d_{\perp}^2\rangle$ are the expectation values of the squared dipole parallel and perpendicular to the surface, and n is the index of refraction of the dielectric [30]. This expression for the potential is approximately valid for constant n and small z.

Taking into account retardation effects, the Casimir–Polder potential is obtained where the finite propagation time between the dipole and its image results in a different asymptotic behavior: $\lim_{z\to\infty} V_{CP}(z) \propto z^{-4}$ [31].

The complete QED treatment gives

$$V_{\mathrm{QED}}(z) = -\frac{\alpha^3}{2\pi}\int_0^\infty \mathrm{d}\xi\xi^3 \boldsymbol{d}(\mathrm{i}\xi)\int_1^\infty \mathrm{d}p\ \mathrm{e}^{-2\xi z p\alpha}\zeta(p,n^2)\ , \tag{3}$$

where

$$\zeta(p,n^2) \equiv \frac{\sqrt{n^2-1+p^2}-p}{\sqrt{n^2-1+p^2}+p} + (1-2p^2)\frac{\sqrt{n^2-1+p^2}-n^2p}{\sqrt{n^2-1+p^2}+n^2p}\ , \tag{4}$$

and $\boldsymbol{d}(\mathrm{i}\xi)$ is the dynamic dipole polarizability function [32].

Reflection from an atomic mirror in the classical regime was used to measure the van der Waals force between a dielectric surface and an atom in its ground state [39]. We have shown that retardation effects on the atom surface potential could be observed by measuring the reflection flux while gradually changing the intensity of the laser, provided the atoms are cold enough and the mirror is homogeneous enough [5,6].

The exponentially decaying optical potential and the attractive atom–wall interaction add up to generate an effective potential barrier. It is given by one of the following two formulas, which, respectively, neglect retardation effects or take them into account,

$$V_{\mathrm{noret}}(z) = C_0\exp(-2\kappa z) - \frac{C_3^{(n)}}{z^3}, \tag{5}$$

$$V_{\mathrm{exact}}(z) = C_0\exp(-2\kappa z) + V_{\mathrm{QED}}(z)\ , \tag{6}$$

where C_0 and κ depend on the parameters of the mirror.

By calculating and comparing reflection probabilities from the two barriers, we have shown that the long range (Casimir) interactions due to retardation have in this case an observable effect on the quantum reflection probabilities and that the classically–forbidden above–barrier reflection is particularly sensitive to details of the atom–surface potential. If measured, this would constitute a low energy experimental signature of QED effects, and would supplement recent different measurements of the Casimir forces.

4 Above Barrier Reflection

Côté, Raizen, and I have shown that cold atoms incident on an evanescent–wave atomic mirror with sufficiently small velocities, (e.g. 10 cm/s for sodium atoms), will exhibit quantum dynamics: tunneling and over–barrier reflection [5,6]. We predicted an S-shaped probability curve, which is typical of quantum behavior, for the fraction of reflected atoms as a function of the logarithm of the laser intensity, and suggested a way to measure it by minimizing the variation of the intensity across the atomic mirror.

Unlike reflection in the classical domain, quantum reflection depends on the details of the potential, both at short and large distances. This sensitivity and the ability to control the optical potential is what enables to probe the atom–wall interaction, including the retardation effects, as discussed in the previous section.

Traditionally, one compares the de Broglie wave length of the particle, $\lambda_{dB} = 2\pi\hbar/mv$, with some scale in the potential, say the width of the potential barrier, to determine if substantial quantum behavior should be expected. One can define "badlands" at the regions of space where the Wentzel–Kramers–Brillouin (WKB) approximation breaks down [43]. WKB applies where the de Broglie wave length varies sufficiently slowly, i.e.

$$\delta\lambda \equiv \frac{1}{2\pi}\left|\frac{d\lambda}{dx}\right| = \hbar\left|\frac{m}{p^3}\frac{dV}{dx}\right| \ll 1 \quad . \tag{7}$$

The badlands, are therefore defined as regions of space where this condition breaks. According to our analysis, while the under–barrier transmission is mostly sensitive to the width and height of the barrier, the over–barrier reflection is determined by regions of the potential where the semiclassical treatment fails. We have shown that for under barrier energies the badlands are centered around the turning points, their height extending to infinity. For above barrier energies there are no turning points, but two badlands can still be recognized. In this respect the concept of the badlands includes the concept of turning points but is more general. Note that close enough to the dielectric–vacuum interface there is no badland and WKB applies. It is generally true that the quantum reflection effect is enhanced by rapid changes in the potential. Thus, by measuring quantum reflection one is probing the most rapidly changing region of the potential. In the case of atomic mirrors the significant region is in the inner side of the barrier.

Quantum effects may be used for very sensitive measurements. In the classical regime, for example, reflection yields can only be used to identify thresholds. In the semiclassical regime, the yields are also sensitive to the curvature near the top of the barrier. Quantum reflection probabilities are determined by the complete potential curve.

5 Reflected Wave Packets

In the experimental setting of reflection of cold atoms from an evanescent wave mirror, it may become possible to measure the time dependence of the reflection process in line with the ideas and methods developed by Dan Walls and his collaborators [7–10].

In a previous research on the problem of time dependence in barrier penetration [44–46], scattering was considered in phase space, using the Wigner representation of quantum mechanics, [47,48]. The insufficiency of semiclassical methods (such as WKB) for time–dependent evaluation of classically forbidden processes was demonstrated. Analytic results were obtained for the probability distribution of the transmitted particles, and a solution to the long lasting controversy regarding the definition, calculation, and measurement of the tunneling time, emphasizing the effect of causality on the particle propagation, was obtained. The mathematical methods, and the physical insight into quantum dynamics that was gained, are applicable more generally, and will be applied here to the reflected wave packet.

The asymptotic solution to the stationary Schrödinger equation for a particle with mass m and momentum k, e.g. a sodium atom, incident on a one dimensional potential barrier, is given in terms of the transmission and reflection amplitudes, $A(k)$ and $B(k)$ respectively,

$$\begin{aligned} \psi_k(q) &= A(k)\ \mathrm{e}^{\mathrm{i}kq} \qquad\qquad \text{for } q \to +\infty \\ &= B(k)\ \mathrm{e}^{-\mathrm{i}kq} + \ \mathrm{e}^{\mathrm{i}kq} \quad \text{for } q \to -\infty\ . \end{aligned} \tag{8}$$

We assume reflection from a symmetric barrier. The generalization to non-symmetric barriers is straightforward.

The Wigner representation of quantum mechanics can then be used in order to obtain the time dependent evolution of the atoms. The Wigner phase–space representation of quantum mechanics. has several advantages. Both coordinate and momentum are considered at once without violating Heisenberg uncertainty relations. Both pure and mixed initial states can be considered, and analogies to classical distributions can be used to emphasize purely quantum effects. The particle initial state at $t = 0$ is given in phase space by its Wigner quasi-distribution $\varrho_0(q,p)$ with the initial coordinate and momentum expectation values, (Q_0, P_0), and the initial dispersions, $(\Delta q_0, \Delta p_0)$.

When there is no potential the particle state at a latter time t is given by the free propagation of its initial state:

$$\varrho_t^f(q,p) = \varrho_0(q - tp/m, p)\ . \tag{9}$$

The time–dependent coordinate probability distribution of the free particle is given by:

$$\mathcal{P}_t^f(q) = \int_{-\infty}^{\infty} \mathrm{d}p\ \varrho_t^f(q,p)\ , \tag{10}$$

and the first momentum moment of the free particle quasi-distribution projected into coordinate space is given by:

$$\mathcal{M}_t^f(q) \equiv \frac{1}{\hbar}\int_{-\infty}^{\infty} \mathrm{d}p(p-P_0)\varrho_t^f(q,p)\ . \tag{11}$$

The probability of finding a reflected particle at the time t at the coordinate q can be expressed in terms of the following transform over the initial phase–space quasi-distribution $\varrho_0(q,p)$ and the complex reflection coefficient $B(k)$:

$$\begin{aligned}\mathcal{P}_t^R(q) = \frac{1}{2\pi\hbar}\int_{-\infty}^{\infty}\mathrm{d}p\int_{-\infty}^{\infty}dr\int_{-\infty}^{\infty}\mathrm{d}\sigma\exp[\mathrm{i}\sigma r/\hbar] \\ \times B(p-\sigma/2)B(-p-\sigma/2)\varrho_0(-q+tp/m+r,-p)\ ,\end{aligned} \tag{12}$$

where the time t was assumed large enough for the reflected and transmitted wave packets not to overlap [45], and use was made of the identity $\overline{B(p)} = B(-p)$ [44]. A similar expression was used to obtain the transmitted wave packets coordinate distribution [46].

The time dependent transmitted and reflected coordinate distributions are sensitive to the phase shifts of the respective amplitudes. Yet, the definition of the phase of the reflection amplitude is ambiguous. It is different for different choices of the point $q = 0$. Under the translation $V(q) \longrightarrow V(q-d)$, the reflection amplitude changes its phase $B_0(p) \longrightarrow B_d(p) \equiv B_0(p)\exp(-2ipd)$. Physical observables, while sometimes sensitive to the phase, must be invariant to this translation. One can verify that the coordinate probability distribution is indeed invariant to translations by re-defining the integration variable r,

$$\begin{aligned}\mathcal{P}_t^R(q) &= \frac{1}{2\pi\hbar}\int_{-\infty}^{\infty}\mathrm{d}p\int_{-\infty}^{\infty}\mathrm{d}r\int_{-\infty}^{\infty}\mathrm{d}\sigma\exp[\mathrm{i}\sigma r/\hbar] \\ &\quad\times B_0(p-\sigma/2)B_0(-p-\sigma/2)\varrho_0(-q+tp/m+r,-p) \qquad (13)\\ &= \frac{1}{2\pi\hbar}\int_{-\infty}^{\infty}\mathrm{d}p\int_{-\infty}^{\infty}\mathrm{d}r\int_{-\infty}^{\infty}\mathrm{d}\sigma\exp[\mathrm{i}\sigma r/\hbar] \\ &\quad\times B_d(p-\sigma/2)B_d(-p-\sigma/2)\varrho_0(2d-q+tp/m+r,-p)\ . \qquad (14)\end{aligned}$$

The coordinate probability distribution does not depend on the choice of the point $q = 0$. For different choices the amplitude would have different phases but the coordinate reflection in the argument of the quasi-distribution would be with respect to different reflection points. $B_d(k)$ is the reflection amplitude with the correct phase shift for the reflection point at d. $\mathcal{P}_t^R(q)$ is invariant to the choice of d because one can not distinguish reflection from a given point with a given phase shift from reflection from another point with a different phase shift.

Expanding $\varrho_0(2d - q + tp/m + r, -p)$ in powers of r around $r = 0$ and using the definition of the Dirac δ function and its derivatives,

$$\delta^{(n)}(\sigma) = \frac{1}{2\pi\hbar}\int_{-\infty}^{\infty} \mathrm{d}r \exp[\mathrm{i}\sigma r/\hbar](\mathrm{i}r/\hbar)^n \ , \tag{15}$$

one gets

$$\begin{aligned}\mathcal{P}_t^R(q) = \sum_n \frac{(\mathrm{i}\hbar)^n}{n!}\int_{-\infty}^{\infty}\mathrm{d}p \ \Bigg[\left(\frac{\partial}{\partial q}\right)^n \varrho_0(2d - q + tp/m, -p) \qquad (16)\\ \times \int_{-\infty}^{\infty}\mathrm{d}\sigma\delta^{(n)}(\sigma)B_d(p - \sigma/2)B_d(-p - \sigma/2)\Bigg]\\ = \int_{-\infty}^{\infty}\mathrm{d}p \ |B_d(-p)|^2 \ \varrho_0(2d - q + tp/m, -p) \qquad (17)\\ +\hbar\int_{-\infty}^{\infty}\mathrm{d}p \ |B_d(-p)|^2 \ \frac{\partial \arg B_d(p)}{\partial p}\frac{\partial}{\partial q}\varrho_0(2d - q + tp/m, -p)\\ + \ \ ...\end{aligned}$$

Higher order terms involve higher coordinate–derivatives of the initial quasi-distribution and higher momentum–derivatives of the amplitude. Assuming that the initial state had a well defined momentum, with a small dispersion, one gets to first order in $\Delta p_0/P_0$,

$$\begin{aligned}\mathcal{P}_t^R(q) = |B_d(-P_0)|^2 \ \int_{-\infty}^{\infty}\mathrm{d}p \ \varrho_0(2d - q + tp/m, -p) \qquad (18)\\ + \ \frac{\partial|B(P_0)|^2}{\partial P_0} \ \int_{-\infty}^{\infty}\mathrm{d}p \ (p - P_0) \ \varrho_0(2d - q + tp/m, -p)\\ + \ \hbar \ |B_d(-P_0)|^2 \ \frac{\partial \arg B_d(P_0)}{\partial P_0} \ \frac{\partial}{\partial q}\int_{-\infty}^{\infty}\mathrm{d}p \ \varrho_0(2d - q + tp/m, -p) \ .\end{aligned}$$

The third term vanishes for the choice $d = D$ where D is defined by:

$$\frac{\partial \arg B_D(P_0)}{\partial P_0} = 0 \ . \tag{19}$$

Thus, the coordinate distribution of reflected atoms is given, for a narrow initial momentum distribution and to first order in $\Delta p_0/P_0$, by

$$\mathcal{P}_t^R(q) = |B(P_0)|^2 \left[\mathcal{P}_t^f(2D - q) + \ 2\delta \ M_t^f(2D - q)\right] \ , \tag{20}$$

where

$$\delta = \hbar\frac{\partial \ln|B(P_0)|}{\partial P_0} \ . \tag{21}$$

δ is negative if the reflection probability decreases with increasing energies. The dispersion term $2\delta M_t^f(2D - q)$ is the leading–order correction to mirror–like reflection. The phase shift is taken into account by choosing the effective

reflection point D,

$$2D = \hbar \, \frac{\partial \arg B_0(P_0)}{\partial P_0} \, . \tag{22}$$

Note that the expansion of ϱ_0 around $r = 0$ is only appropriate when the reflection is a direct process and there are no resonances or recurrences. This is consistent with the assumption of perfect sticking for atoms that have crossed the barrier.

In the specific case of a Gaussian initial quasi-distribution,

$$\varrho_0(q,p) = (2\pi \Delta p_0 \Delta q_0)^{-1} \exp\left[-\frac{(p-P_0)^2}{2(\Delta p_0)^2} - \frac{(q-Q_0)^2}{2(\Delta q_0)^2} \right] \, , \tag{23}$$

$\Delta p_0 \Delta q_0 \geq \hbar/2$, and the peak of the reflected wave packet is at the time t at:

$$Q_{\max} = 2D - Q_0 - tP_0/m + \frac{2s\Delta q}{\Delta q + \sqrt{(2s)^2 + (\Delta q)^2}} \, , \tag{24}$$

where Δq is the width of the freely propagating coordinate distribution and s is proportional to the time,

$$\Delta q \equiv \sqrt{(\Delta q_0)^2 + (t\Delta p_0/m)^2} \, , \tag{25}$$

$$s \equiv -2 \, \delta \, \left(\frac{t(\Delta p_0)^2}{\hbar m} \right) \, . \tag{26}$$

For short propagation times, $s < \Delta q$

$$Q_{\max} \approx 2D - Q_0 + tP_R/m \, , \tag{27}$$

and the velocity of the peak is shifted:

$$P_R = -P_0 \; - \; (\Delta p_0)^2 \, \frac{\partial \ln |B(P_0)|^2}{\partial P_0} \, . \tag{28}$$

For $s > \Delta q$,

$$Q_{\max} \approx 2D - Q_0 - tP_0/m + \Delta q \, . \tag{29}$$

The shift in the peak is bounded by the width of the freely propagating wave packet. The propagation of any other initial wave packet can be studied in a similar way.

6 Conclusions

Some theoretical fundamental aspects of the atom–mirror and future molecule–mirror interaction remain to be studied.

The theoretical analysis usually employed is divided into two steps. First, the effective potential is found, and second, the time evolution of the particle in this potential is analyzed. Note the apparent contradiction between the

two steps. The internal structure of the atom is essential for the evaluation of the potential curves in the first step. In general, an effective potential for an atom or a molecule is the result of changes to its internal structure. In the second step, however, after a potential curve has been determined, one solves for the dynamics i.e. for the time evolution of the particle in the given potential, treating the atom as a pointlike structureless particle. The disregard of the internal structure of the atom, at the second step of the calculation is justified by the assumption that actual changes to this internal structure can be neglected, while the space dependence of the effective potentials is the result of virtual, not actual, transitions. For optical potentials, for example, this amounts to neglecting spontaneous emission. This approximation is meaningful only in the large detuning regime. Recent experiments demonstrate and emphasize the entanglement between internal and external degrees of freedom in atom optics. Observed effects that go beyond the two level model include state–selective properties of the reflection [12,49], cooling during the reflection through a spontaneous Raman transition between two hyperfine levels [21], and in general, an interplay between internal state transitions and the center of mass motion [50].

It is not trivial to find observables that explicitly exhibit QED effects. We have shown that the long range (Casimir) interactions due to retardation may have an observable effect on the quantum reflection probabilities from evanescent waves atomic mirrors, as the above–barrier, classically forbidden reflection is particularly sensitive to details of the atom–surface potential [5,6]. Identifying and using parameters in the quantum regime, i.e. looking for experiments that cannot be described by semiclassical approximations, is a promising new way to study long–range and short–range atom–surface interactions. Casimir and retardation potential for a cold atom or a cold molecule and dielectric surfaces of different geometries, multilayered dielectrics, metallic surfaces, and temperature effects on the potentials, remains to be studied.

Finally, a phase–space approach for analyzing the time–dependence of reflected wave packets was considered. Some specific properties of this phase–space wave packet approach, such as the proper inclusion of dispersion and the insensitivity to the choice of an initial state, could make it particularly useful for analyzing present and future atom–optics experiments.

References

1. C.S. Adams, M. Sigel, J. Mlynek: Phys. Rep. **240**, 143 (1994)
2. M. Ben Dahan *et al.*: Phys. Rev. Lett. **76**, 4508 (1996)
3. S.R. Wilkinson *et al.*: Phys. Rev. Lett. **76**, 4512 (1996)
4. M.G. Raizen, C. Salomon, Q. Niu: Physics Today **50**, 30 (July 1997)
5. B. Segev, R. Côté, M.G. Raizen: Phys. Rev. A **56**, R3350 (1997)
6. R. Côté, B. Segev, M.G. Raizen: Phys. Rev. A **58**, 3999 (1998)
7. P. Storey, M. Collett, D. Walls: Phys. Rev. Lett. **68**, 472 (1992)
8. P. Storey, M. Collett, D. Walls: Phys. Rev. A **47**, 405 (1993)

9. P. Storey, M. Collett, T. Sleator, D. Walls: Phys. Rev. A **49**, 2322 (1994)
10. P. Storey, S. Tan, M. Collett, D. Walls: Nature **367**, 626 (1994)
11. R.J. Cook, R.K. Hill: Opt. Commun. **43**, 258 (1982)
12. V.I. Balykin *et al.*: Pis'ma Zh. Eksp. Theor. Fiz. **45**, 282 (1987) [Sov. Phys. JETP Lett. **45**, 353 (1987)]; Phys. Rev. Lett. **60**, 2137 (1988)
13. M.A. Kasevich, D.S. Weiss, S. Chu: Opt. Lett. **15**, 667 (1990)
14. C.G. Aminoff *et al.*: Phys. Rev. Lett. **71**, 3083 (1993)
15. P. Szriftgiser *et al.*: Phys. Rev. Lett. **77**, 4 (1996)
16. A. Aspect *et al.*: Phys. Rev. A **52**, 4704 (1995)
17. M. Arndt *et al.*: Phys. Rev. A **53**, 3369 (1996)
18. T. Matsudo *et al.*: Phys. Rev. A **55**, 2406 (1997)
19. M.J. Renn *et al.*: Phys. Rev. A **53**, R648 (1996)
20. B. Pape *et al.*: Quantum Semiclass. Opt. **9**, 419 (1997)
21. H. Nha, W. Jhe: Phys. Rev. A **56**, 2213 (1997)
22. M. Gorlicki *et al.*: Phys. Rev. A **61**, 013603 (2000)
23. R.E. Grisenti *et al.*: Phys. Rev. Lett. **83**, 1755 (1999)
24. C. Henkel *et al.*: Laser Phys. **4**, 1042 (1994)
25. J.-Y. Courtois et al.: Phys. Rev. A **53**, 1862 (1996)
26. H. Ito *et al.*: Phys. Rev. A **56**, 712 (1997)
27. Y.B. Ovchinnikov *et al.*: Phys. Rev. Lett. **79**, 2225 (1997)
28. L. Cognet *et al.*: Phys. Rev. Lett. **81**, 5044 (1998)
29. C. Henkel, J.-Y. Courtois: Eur. Phys. J. D **3**, 129 (1998)
30. L.E. Lennard–Jones: Trans. Faraday Soc. **28**, 333 (1932)
31. H.B.G. Casimir, D. Polder: Phys. Rev. **73**, 360 (1948)
32. I.E. Dzyaloshinskii *et al.*: Adv. Phys. **10**, 165 (1961)
33. P.W. Milonni, P.B. Lerner: Phys. Rev. A **46**, 1185 (1992)
34. V. Sandoghdar *et al.*: Phys. Rev. Lett. **68**, 3432 (1992)
35. C.I. Sukenik *et al.*: Phys. Rev. Lett. **70**, 560 (1993)
36. L. Spruch, Y. Tikochinsky: Phys. Rev. A **48**, 4213 (1993); Y. Tikochinsky, L. Spruch: *ibid.*, **48**, 4223 (1993); *ibid.*, **48**, 4236 (1993)
37. M. Fichet *et al.*: Phys. Rev. A **51**, 1553 (1985)
38. F. Zhou, L. Spruch: Phys. Rev. A **52**, 297 (1995)
39. A. Landragin *et al.*: Phys. Rev. Lett. **77**, 1464 (1996)
40. M. Marinescu, A. Dalgarno, J.F. Babb: Phys. Rev. A **55**, 1530 (1997)
41. P. Kharchenko, J.F. Babb, A. Dalgarno: Phys. Rev. A **55**, 3566 (1997)
42. E.A. Hinds *et al.*: Phys. Rev. Lett. **80**, 645 (1998)
43. R. Côté, H. Friedrich, J. Trost: Phys. Rev. A **56**, 1781 (1997)
44. M.S. Marinov, B. Segev: J. Phys. A: Math. and General **29**, 2839 (1996)
45. M.S. Marinov, B. Segev: Phys. Rev. A **54**, 4752 (1996)
46. M.S. Marinov, B. Segev: Phys. Rev. A **55**, 3580 (1997)
47. E.P. Wigner: Phys. Rev. **40**, 749 (1932)
48. M. Hillery, R.F. O'Connell, M.O. Scully, E.P. Wigner: Phys. Rep. **106**, 121 (1984)
49. W. Zhang, D.F. Walls: Phys. Rev. Lett. **68**, 3287 (1992)
50. C. Henkel *et al.*: Phys. Rev. A **55**, 1160 (1997); Phys. Rev. A **56**, R9 (1997)

Atom Wave Lithography via Adiabatic Passage in Multilevel Systems

Yuri Rozhdestvensky and Lev Plimak

1 Introduction

Atom optics [1] seeks to study phenomena associated with the wave nature of matter. In recent years, several versions of atom interferometers have been demonstrated [2–4], and a variety of precision measurements utilising atom-interferometry techniques have been performed [5,6]. In a search for an efficient robust wide-angle atomic beam-splitter, a number of schemes based on the well-known effect of coherent population transfer (aka adiabatic passage, aka STIRAP) have been implemented [7,8], following the proposal by Marte and Zoller [3]. (For a general discussion of STIRAP see [9].) Chu and co-authors [4] demonstrated that employing experimental techniques based on STIRAP, the initial momentum splitting can be scaled up orders of magnitude.

Atom interferometry may have an important technological application as atom lithography [5], which consists of depositing an atomic interference pattern on a substrate to create a periodical structure. To this end, one should prepare a wave packet consisting of two coherent momentum components of the same internal atomic state. As to our knowledge, this problem has so far not had a satisfactory solution. Methods like scattering cold atoms on a periodic microfabricated structure [5] convert only a small fraction of atoms in the superposition state sought, and hence require additional atomic-state selection. Atomic beam splitters (e.g. that demonstrated by Bergmann in Ref. [8]) typically produce atoms in a coherent superposition of different internal atomic states which does not yield a spatial interference pattern.

To utilize experimental advances of atom interferometry in atom-wave lithography, a coherent superposition of momentum components of different states should be converted into that within a single atomic state. The idea we are exploring in this paper is to use an adiabatic-passage sequence which is in a certain sense inverted compared to that leading to the superposition of different states. This naive idea does not work exactly as expected: First, atoms end in a superposition of different internal states, with two momentum components in each; interference patterns due to different states cancel each other. Second, the process we observe (via numerical simulations) is not STIRAP proper; in particular, substantial population of the excited state is created. The good news, however, is that by fine-tuning the amplitudes

H.J. Carmichael, R.J. Glauber, M.O. Scully (Eds.): LNP 561, pp. 136–145, 2001.

of laser pulses, the fraction of atoms ending in the excited states can be reduced to less than one and a half percent. Furthermore, interference patterns coming from different internal states move relative to each other. Then, by simply allowing the atomic wave packet to propagate freely, a revival of interference is achieved. As a result, a quality spatial interference pattern may be obtained without atomic-state selection, by just properly locating the substrate. This simplicity might outweigh drawbacks connected with the intermediate population in excited states.

To be specific, we imply a Gedanken experiment which follows, as close as possible, experimental conditions in the work by Bergmann and co-authors [8]. In that paper, adiabatic passage was shown to coherently split population between a number of lower atomic states coupled to a common excited state (a "tripod" configuration). The reason we have chosen this situation is robustness of the tripod scheme, and the fact that the initial splitting may be scaled up by applying Chu's technique to either of the Λ's comprising the tripod (see Fig. 1). At the same time the idea we are exploring is quite general and is not confined to the experimental conditions of Ref. [8].

2 Adiabatic Passage in an M Configuration

In the experiment [8], a beam of metastable Ne atoms in the $(2p^5 3s)\ ^3P_0$ state propagating along x axis was incident on a combination of three laser beams: A pair of σ^+ and σ^--polarized beams counter-propagating along z axis, and a π-polarized beam propagating along y axis. The π-polarised beam was tuned to the $(2p^5 3s)\ ^3P_0$–$(2p^5 3p)\ ^3P_1$ transition, while the σ-polarised beams were tuned to the $(2p^5 3s)\ ^3P_2$–$(2p^5 3p)\ ^3P_1$ transition, see Fig. 1. As illustrated in this Figure, selection rules confine the set of interacting magnetic sublevels to a tripod configuration. Further, the interaction of an atom with the π-polarized beam was delayed by shifting the latter along the x axis. An atom thus saw a synchronous pair of σ-polarised pulses overlapping with a delayed π-polarised pulse. This pulse sequence put an atom into a coherent combination of the $^3P_2, M = +1$, and $^3P_2, M = -1$, Zeeman states, with a momentum splitting of $2\hbar\boldsymbol{k}_\sigma$. ($\boldsymbol{k}_\sigma$ and $\boldsymbol{k}_\pi$ denote the wave vectors of, respectively, the σ and π-polarised optical fields.) In this paper, we consider an M configuration with 3 lower states (1,2 and 3) and two excited states (4 and 5), shown schematically in Fig. 2. Figure 1 illustrates how the schematic level diagram, Fig. 2, may be implemented as the actual M configuration of magnetic sublevels. Namely, the σ-polarised beams should be tuned to the $^3P_0$–$^3P_1$ transition, and the π-polarised beam—to the $^3P_2$–$^3P_1$ transition. Note that this leaves freedom in the direction of propagation of the laser beams, and hence freedom in momenta passed to atoms.

In the M configuration, the same splitting effect may be achieved as in the tripod configuration, if the σ-polarised pulses acting on the 'inner' transitions 1–4 and 1–5 are delayed relative to the π-polarised pulse (or pulses) acting

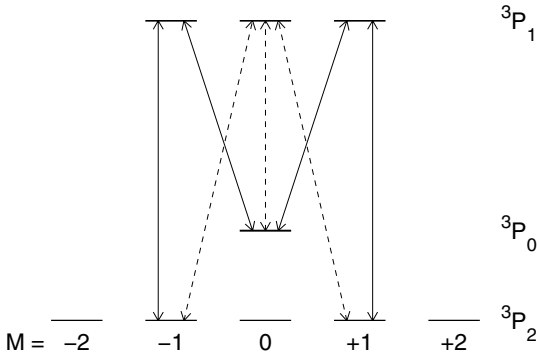

Fig. 1. The M scheme realised on magnetic sublevels of Ne. The corresponding transitions are drawn in solid lines. Dashed lines show transitions comprising Bergmann's tripod scheme [8].

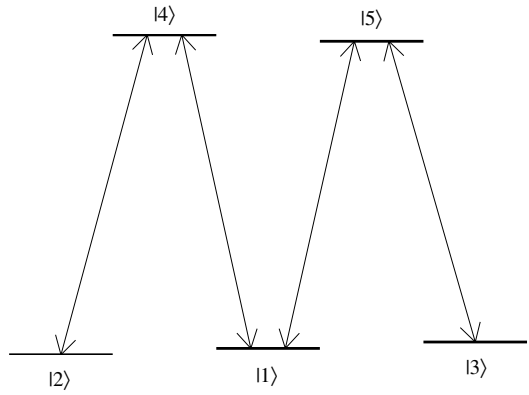

Fig. 2. Schematic diagram of the M configuration

on the 'outer' transitions 2–4 and 3–5. So we consider, for simplicity, the M configuration on both splitting and combining stages. Assume, to start with, that the incident atomic beam has a zero transverse momentum component ($\boldsymbol{p}_\perp = 0$). After interaction with the optical pulses, the coherent components in states 2 and 3 will have transverse momenta, $\boldsymbol{p}_\perp = \hbar\,(-\boldsymbol{k}_\pi \pm \boldsymbol{k}_\sigma)$. Swapping the time order of the pulses acting on the 'inner' and 'outer' transitions, this combination can be transferred back into state 1 with transverse momentum zero. This is the general property of reversibility of adiabatic passage. However, consider what happens if on the top of swapping the time order, one also swaps polarizations of the σ-polarized beams. The aforementioned components in the states 2 and 3 are then 'routed' into two coherent momentum components of the state 1, with $\boldsymbol{p}_\perp = \pm 2\hbar\boldsymbol{k}_\sigma$ (we stress similarity between this point and Chu's techniques [4]). That is, the final atomic state should contain a coherent combination of two momentum components of the same internal state 1.

Following these initial considerations, the system in Fig. 2 was simulated numerically in the Raman-Nath approximation. Interaction of atoms with the

optical fields was treated in a dipole approximation. Spontaneous processes were neglected. The laser beams were regarded as running plain waves, on resonance for atoms with $\boldsymbol{p}_\perp = 0$. Time dependence of the Rabi frequencies of the optical fields was as follows, (cf also Fig. 5)

$$\Omega_\pi^{(1)}(t) = \Omega_0 \mathrm{e}^{-\left[t-t^{(1)}\right]^2/\Delta t^2}, \tag{1}$$

$$\Omega_\sigma^{(1)}(t) = \Omega_0 \mathrm{e}^{-\left[t-t^{(1)}-\tau_\mathrm{d}\right]^2/\Delta t^2}, \tag{2}$$

$$\Omega_\pi^{(2)}(t) = \Omega_0 \mathrm{e}^{-\left[t-t^{(2)}-\tau_\mathrm{d}\right]^2/\Delta t^2}, \tag{3}$$

$$\Omega_\sigma^{(2)}(t) = \Omega_0 \mathrm{e}^{-\left[t-t^{(2)}\right]^2/\Delta t^2}. \tag{4}$$

Here, $\Omega_{\sigma,\pi}^{(1)}(t)$ and $\Omega_{\sigma,\pi}^{(2)}(t)$ are, respectively, pulses of the first sequence (splitting $1 \to 2+3$) and of the second sequence (combining $2+3 \to 1$). The times $t^{(1)}$ and $t^{(2)}$ determine overall positioning of the first and second pulse sequences in time, τ_d is the time delay within a sequence, and Ω_0 and Δt are the Rabi frequency and duration of an individual pulse. In our simulations we assumed that $\Omega_0 = 200$, and the time parameters were as follows: $\Delta t = 0.075$, $\tau_\mathrm{d} = .1$, and $t^{(2)} - t^{(1)} = .45$, cf Fig. 5. Note that in the Raman-Nath approximation the presence of the y component (brought in by the π-polarised pulses) is irrelevant. Our simulations could therefore be confined to 1D. The initial wave function of state 1 was assumed to be, $\psi_1(p) \propto \mathrm{e}^{-p^2/\Delta p^2}$, where $\Delta p = 0.2\hbar k$ and $p = p_z$ is the z component of the atomic momentum (brought in by the σ-polarised pulses).

Results of the simulation with this set of parameters are shown in Figs. 3–5. We see that approximately 50% of the total population is indeed transferred into a coherent superposition of momentum components of state 1 centred at $p_z = \pm 2\hbar k$. At the same time, the 'combining' stage is very far from the adiabatic passage proper. What is observed is pronounced Rabi oscillations between the levels, with substantial intermediate population of excited atomic states. Even worse, a large fraction (another 50%) of atoms end in the excited states.

As to the final excited-state population, below it is shown that a simple cure exists for this problem. Then, intermediate excited-state population may be taken care of by confining optical pulse durations to a nanosecond region, which does not appear a fundamental problem. Importantly, the loss of spectral resolution associated with short pulses is of no concern, because the magnetic sublevels comprising the M configuration (cf Fig. 1) are resolved based solely on selection rules.

It is worthy of stressing that no population in excited states exists on the splitting stage and between the splitting and combining stages. That is, the splitting stage may in principle follow the experimental design of Ref. [8], and only the combining stage should be based on optical-pulse techniques. However, we do not try to design a real experiment utilising pulsed optical fields, leaving this point open to discussion.

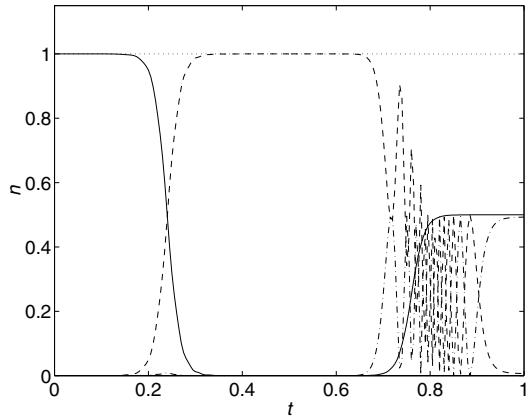

Fig. 3. Results of the numerical simulation assuming all pulse amplitudes are equal: time dependence of the level populations n_k, $k = 1, \cdots, 5$. Solid line: n_1; dashed line: $n_2 + n_3$; dash-dotted line: $n_4 + n_5$; dotted line: $n_1 + n_2 + n_3 + n_4 + n_5$

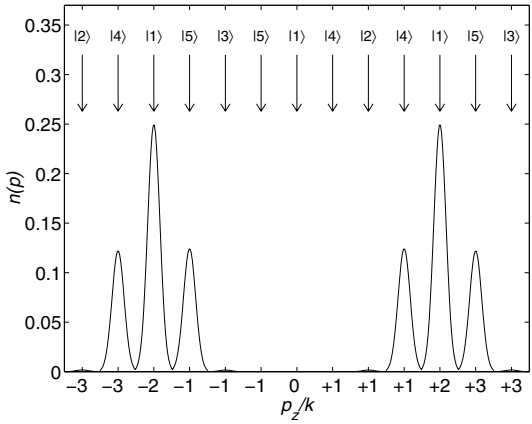

Fig. 4. Results of the numerical simulation assuming all pulse amplitudes are equal: the final distribution over the z component of the atomic momentum, normalised to a unity maximum of the initial distribution. Note that a momentum component at $p_z = -3\hbar k$ exists in two states, 2 and 4. To show them separately, we repeat the abscissa region [-3.5 -2.5] twice, each time marking its centre as -3. Other momentum components are shown in a similar way. The states to which they correspond are shown on the top of the graph

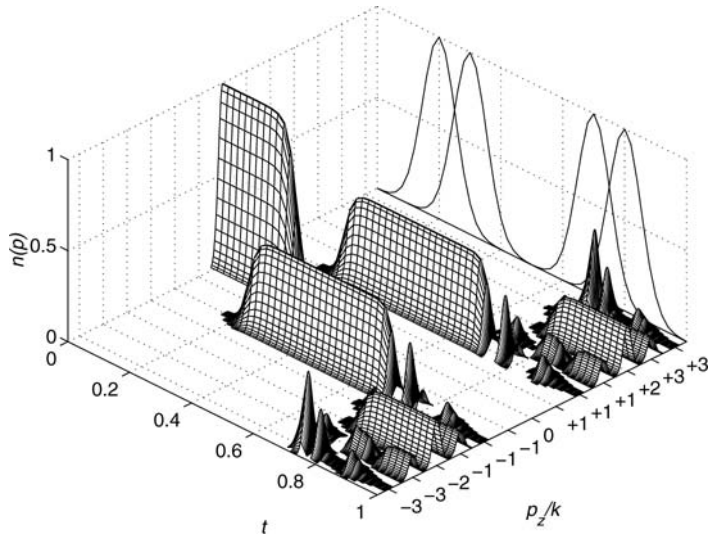

Fig. 5. Time dependence of the atomic momentum distribution, assuming all pulse amplitudes are equal. Refer to Fig. 4 to attribute different momentum components to the levels. Synchronisation of the laser pulses is shown on the axes box wall as a guide to the eye. The initial distribution was arbitrarily normalized to a unity maximum, and only values of $n(p) \geq 10^{-3}$ were retained

3 Optimisation of Pulse Amplitudes

As was already noted, on the combining stage the system undergoes Rabi oscillations (cf Figs. 3 and 5). The final distribution of atoms over levels should strongly depend on the frequency of these oscillations and hence on pulse amplitudes. This led us into the idea to 'tune' the amplitudes so as to minimise the fraction of atoms transferred into the excited states. The amplitude of the second π-polarised pulse in the sequence (1–4) was made a variable parameter,

$$\Omega_{\pi}^{(2)}(t) = \kappa\Omega_0 \mathrm{e}^{-\left[t-t^{(2)}-\tau_\mathrm{d}\right]^2/\Delta t^2}. \tag{5}$$

Simulations were then run repeatedly looking for a minimum in the final population of excited states. For $\kappa < 1$, this minimum was achieved at $\kappa \approx 0.238$. It corresponds to approximately 1.4% of the total population transferred into the excited states. Results of the simulation with the optimised set of parameters may be seen in Figs. 6 and 7. We see that the fraction of atoms ending in the state sought remains close to 50%. An approximately equal fraction of atoms end in states 2 and 3.

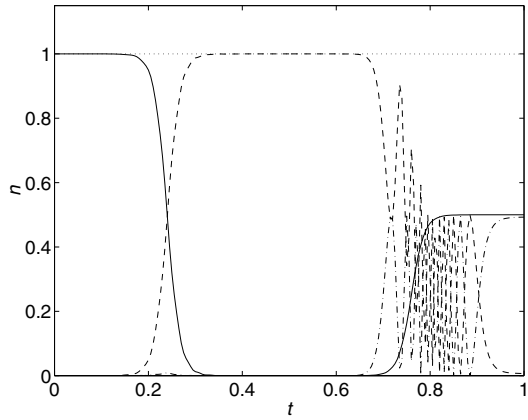

Fig. 6. Results of the numerical simulation with optimised pulse amplitudes: time dependence of the level populations n_k, $k = 1, \cdots, 5$. Solid line: n_1; dashed line: $n_2 + n_3$; dash-dotted line: $n_4 + n_5$; dotted line: $n_1 + n_2 + n_3 + n_4 + n_5$.

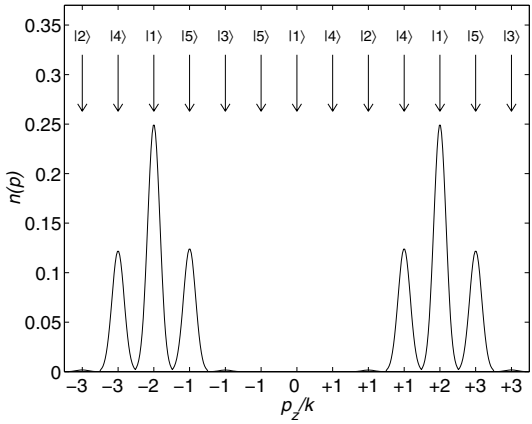

Fig. 7. Results of the numerical simulation with optimised pulse amplitudes: the final distribution over the z component of the atomic momentum, normalised to a unity maximum of the initial distribution. Note that a momentum component at $p_z = -3\hbar k$ exists in two states, 2 and 4. To show them separately, we repeat the abscissa region [-3.5 -2.5] twice, each time marking its centre as -3. Other momentum components are shown in a similar way. The states to which they correspond are shown on the top of the graph.

4 Revival of Interference

Consider in more detail the momentum structure of the atomic wave packet obtained via the 'optimised' pulse sequence. Neglecting the minor fraction of atoms ending in excited states, each of the states 1, 2 and 3 has two momentum components. They are centered, respectively, at $\boldsymbol{p}_\perp = \pm 2\hbar \boldsymbol{k}_\sigma$, $\boldsymbol{p}_\perp = \pm 2\hbar \boldsymbol{k}_\sigma - \hbar\,(\boldsymbol{k}_\pi + \boldsymbol{k}_\sigma)$, and $\boldsymbol{p}_\perp = \pm 2\hbar \boldsymbol{k}_\sigma - \hbar\,(\boldsymbol{k}_\pi - \boldsymbol{k}_\sigma)$. Each state thus produces an interference pattern with a period (along z) of $\lambda/4$, where $\lambda = 2\pi/k$ is the optical wavelength. However the components of state 1 are in phase, whereas those of states 2 and 3—in counterphase. As a result, interference patterns coming from state 1 and from states 2 and 3 are π out of phase and cancel each other (Fig. 8).

Nevertheless, consider what happens if the atom wave packet were simply allowed to propagate freely. Atoms in state 1 have an average transverse velocity equal to zero. The interference pattern due to state 1 thus stays in place (relative to the atomic beam axis). Atoms in states 2 and 3 have average transverse velocities in the z direction equal to $\pm v_\mathrm{R}$, where $v_\mathrm{R} = \hbar k/m$ is the recoil velocity and m is the atomic mass. The interference patterns due to states 2 and 3 thus slide along the z axis with velocities $\pm v_\mathrm{R}$. After $t_\mathrm{rev} = \lambda/(8v_\mathrm{R})$, all three interference patterns turn out to be in phase, and a revival of interference is observed. How complete this revival is, depends on the initial collimation of the atomic beam. For a perfect revival, the spatial separation of the momentum components of each state, $4v_\mathrm{R}t_\mathrm{rev}$, should stay small compared to the transverse coherence length of the wave packet, $\hbar/\Delta p$, where Δp is the transverse momentum spread. This yields,

$$\Delta p \ll \frac{\hbar k}{\pi}. \tag{6}$$

In [8], $\Delta p \sim 0.4\hbar k$, which is fairly close to the collimation needed.

Figure 8 shows the revival of the interference pattern calculated with $\Delta p = 0.2\hbar k$, assuming values as for the ${}^3P_2$–${}^3P_1$ transition in Ne employed in [8]: $R = \hbar k^2/2m\gamma \approx 3{\cdot}10^{-3}$ and $t_\mathrm{rev} = \pi/(8R\gamma) \approx 2.5$ μsec, where $\gamma \approx 5{\times}10^7$ sec is the lifetime of the exited atomic state. It is evident from the Figure that the collimation of $0.2\hbar k$ suffices for purposes of initial demonstration.

5 Conclusion

Although the 'first-split-then-combine' optical pulse sequence in the M scheme does not exactly lead to a coherent superposition of momentum components of a single internal state, the resulting atomic state has all the necessary properties for atom-wave lithography. A high-visibility spatial interference pattern, utilising nearly 100% of the initial atomic-beam intensity, may be created by purely optical means, without the need to separate atoms in different internal states. Among drawbacks of the scheme, the major one is a

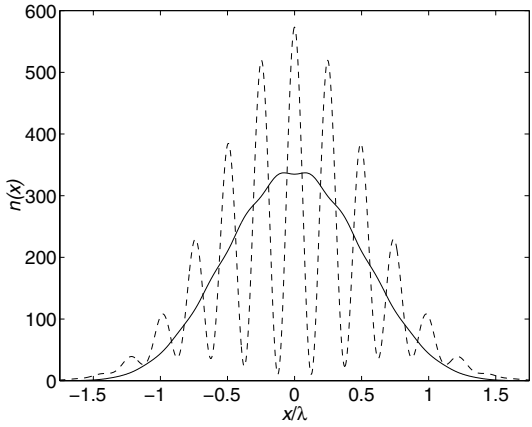

Fig. 8. Spatial distribution along z axis of the atomic density (arbitrary units) at $t = 0$, showing no interference (solid line), and revival of interference after free propagation time $t = t_{\mathrm{rev}}$ (dashed line), for $\Delta p = 0.2\hbar k$ and other conditions as in Ref. [8]

substantial intermediate population of the optically excited states, forcing one to opt for nanosecond pulse durations. Further improvement of the scheme may be sought by fine tuning pulse shapes as well as amplitudes, employing the optimal control theory [10]. One could, e.g., try to reduce population of the excited states on the combining stage. This will be subject to further investigation.

Acknowledgments

One of us (Yu.R.) is grateful to Prof. K. Bergmann for a stimulating discussion. This work was supported in part by the US office of Naval Research, the Israel Science Foundation, and the Minerva Foundation, Munich, Germany.

References

1. *Optics and Interferometry with Atoms*, Appl. Phys. B **54**, 319–485 (1992)
2. S. Glasgow, P. Meystre, M. Wilkens, E.M. Wright: Phys. Rev. A **43**, 2455 (1991); T. Pfau, C. Kurtsiefer, C.S. Adams, M. Sigel, J. Mlynek: Phys. Rev. Lett. **71**, 3427 (1993); S.Z. Tan, D.F. Walls: Opt. Commun. **118**, 412 (1995); T. Wong, M.K. Olsen, S.Z. Tan, D.F. Walls: Phys. Rev. A **52**, 2161 (1995); A.P. Chu, K.S. Johnson, M. Prentiss: J. Opt. Soc. Am. B **13**, 1352 (1996)
3. P. Marte, P. Zoller, J.L. Hall: Phys. Rev. A **44**, 4118 (1991)
4. M. Weitz, B.C. Young, S. Chu: Phys. Rev. Lett. **73**, 2563 (1994)
5. P.R. Berman: *Atom Interferometry* (Academic Press, Boston 1997)

6. K. Sengstock *et al.*: Appl. Phys. B **59**, 99 (1994); K. Zeiske, G. Zinner, F. Riehle, L. Helmcke: Appl. Phys. B **60**, 205 (1995); A. Morinaga, T. Tako, N. Ito: Phys. Rev. A **48**, 1364 (1993); V. Rieger, K. Sengstock, U. Sterr, J.H. Muller, W. Ertmer: Opt. Commun. **99**, 172 (1993)
7. L.S. Goldner *et al.*: Phys. Rev. Lett. **72**, 997 (1994); J. Lawall, M. Prentiss: Phys. Rev. Lett. **72**, 993 (1994)
8. H. Theuer, R.G. Unayan, B.W. Shore, K. Bergmann: Optics Express **4**, 77 (1999)
9. K. Bergmann, H. Theuer, B.W. Shore: Rev. Mod. Phys. **70**, 1003 (1998)
10. V. Malinovsky, D.J. Tannor: Phys. Rev. A **56**, 4929 (1997); Phys. Rev. A **60**, 3081 (1999)

Qudit Entanglement

P. Rungta, W.J. Munro, K. Nemoto, P. Deuar, G.J. Milburn, and C.M. Caves

Summary. We consider the separability of various joint states of D-dimensional quantum systems, which we call "qudits." We derive two main results: (i) the separability condition for a two-qudit state that is a mixture of the maximally mixed state and a maximally entangled state; (ii) lower and upper bounds on the size of the neighborhood of separable states surrounding the maximally mixed state for N qudits.

1 Introduction

One of the distinguishing features of quantum mechanics, not found in classical physics, is the possibility of entanglement between subsystems. It lies at the core of many applications in the emerging field of quantum information science [1], such as quantum teleportation [2] and quantum error correction [3,4]. Entanglement is a distinctly quantum-mechanical correlation between subsystems, which cannot be created by actions on each subsystem separately; moreover, correlations between subsystem measurements on an entangled composite system cannot be explained in terms of correlations between local classical properties inherent in the subsystems. Thus one often says that an entangled composite system is nonseparable. Formally, the state of a composite system, pure or mixed, is *separable* if the state has an ensemble decomposition in terms of product states. A separable state has no quantum entanglement, and a nonseparable state is entangled. Though the nonclassical nature of quantum entanglement has been recognized for many years [5,6], only recently has considerable attention been focused on trying to understand and characterize its properties precisely.

This paper focuses on the question of whether various joint quantum states of D-dimensional quantum systems are entangled. For convenience, we call a D-dimensional quantum system a "qudit," by analogy with the name "qubit" for $D = 2$ and "qutrit" for $D = 3$. We now have a general method for quantifying the degree of entanglement of a pair of qubits [7], and we have a criterion, the partial transposition condition of Peres [8], which determines whether a general state of two qubits is entangled and whether a general state of a qubit and a qutrit is entangled [9]. The partial-transposition condition fails, however, to provide a criterion for entanglement in other cases, where the constituents have higher Hilbert-space dimensions [10,11] or where there

H.J. Carmichael, R.J. Glauber, M.O. Scully (Eds.): LNP 561, pp. 149–164, 2001.

are more than two constituents. Indeed, at present there is no general criterion for determining whether the joint state of N qudits is entangled, nor is there any general way to quantify the degree of entanglement if such a state is known to be entangled.

In Sect. 2 we review an operator representation of qudit states, which is applied in Sect. 3, where we consider states of two qudits that are a mixture of the maximally mixed state and a maximally entangled state. We show that such states are separable if and only if the probability for the maximally entangled state in the mixture does not exceed $1/(1+D)$. A more general result, of which ours is a special case, was first obtained by Vidal and Tarrach [12]. In Sect. 4 we consider the separability of mixed states of N qudits near the maximally mixed state. We find both lower and upper bounds on the size of the neighborhood of separable states around the maximally mixed state. Our results generalize and extend the results obtained by Braunstein et al. for qubits [13] and by Caves and Milburn for qutrits [14]. Before tackling the upper and lower bounds, we present, in Sect. 4.1, various mathematical results which are used to obtain the lower bound, but which might prove useful in other contexts as well.

2 Operator Representation of Qudit States

In this section we review an operator representation of qudit states, analogous to the Pauli, or Bloch-sphere, representation for qubits. We begin with the set of Hermitian generators of SU(D); the generators, denoted by λ_j, are labeled by a Roman index taken from the middle of the alphabet, which takes on values $j = 1, \ldots, D^2-1$. We represent the generators in an orthonormal basis $|a\rangle$, labeled by a Roman letter taken from the beginning of the alphabet, which takes on values $a = 1, \ldots, D$. With these conventions the generators are given by

$$
\begin{aligned}
&j = 1, \ldots, D-1 : \\
&\quad \lambda_j = \Gamma_a \equiv \frac{1}{\sqrt{a(a-1)}} \left(\sum_{b=1}^{a-1} |b\rangle\langle b| - (a-1)|a\rangle\langle a| \right) \ , \ 2 \le a \le D \ , \qquad (1) \\
&j = D, \ldots, (D+2)(D-1)/2 : \\
&\quad \lambda_j = \Gamma_{ab}^{(+)} \equiv \frac{1}{\sqrt{2}} \left(|a\rangle\langle b| + |b\rangle\langle a| \right) \ , \ 1 \le a < b \le D \ , \qquad (2) \\
&j = D(D+2)/2, \ldots, D^2-1 : \\
&\quad \lambda_j = \Gamma_{ab}^{(-)} \equiv \frac{-\mathrm{i}}{\sqrt{2}} \left(|a\rangle\langle b| - |b\rangle\langle a| \right) \ , \ 1 \le a < b \le D \ . \qquad (3)
\end{aligned}
$$

In (2) and (3), the Roman index j stands for the pair of Roman indices, ab, whereas in (1), it stands for a single Roman index a. The generators are traceless and satisfy

$$\lambda_j\lambda_k = \frac{1}{D}\delta_{jk} + d_{jkl}\lambda_l + \mathrm{i}f_{jkl}\lambda_l \ . \tag{4}$$

Here and wherever it is convenient throughout this paper, we use the summation convention to indicate a sum on repeated indices. The coefficients f_{jkl}, the structure constants of the Lie group SU(D), are given by the commutators of the generators and are completely antisymmetric in the three indices. The coefficients d_{jkl} are given by the anti-commutators of the generators and are completely symmetric.

By supplementing the $D^2 - 1$ generators with the operator

$$\lambda_0 \equiv \frac{1}{\sqrt{D}} I \ , \tag{5}$$

where I is the unit operator, we obtain a Hermitian operator basis for the space of linear operators in the qudit Hilbert space. This is an orthonormal basis, satisfying

$$\mathrm{tr}(\lambda_\alpha\lambda_\beta) = \delta_{\alpha\beta} \ . \tag{6}$$

Here the Greek indices take on the values $0, \ldots, D^2 - 1$; throughout this paper, Greek indices take on D^2 or more values. Using this orthonormality relation, we can invert (1)–(3) to give

$$|a\rangle\langle a| = \frac{I}{D} + \frac{1}{\sqrt{a(a-1)}}\left(-(a-1)\Gamma_a + \sum_{b=a+1}^{D}\Gamma_b\right) \ , \tag{7}$$

$$|a\rangle\langle b| = \frac{1}{\sqrt{2}}(\Gamma_{ab}^{(+)} + \mathrm{i}\Gamma_{ab}^{(-)}) \ , \quad 1 \le a < b \le D \ , \tag{8}$$

$$|b\rangle\langle a| = \frac{1}{\sqrt{2}}(\Gamma_{ab}^{(+)} - \mathrm{i}\Gamma_{ab}^{(-)}) \ , \quad 1 \le a < b \le D \ . \tag{9}$$

Any qudit density operator can be expanded uniquely as

$$\varrho = \frac{1}{D} c_\alpha \lambda_\alpha \ , \tag{10}$$

where the (real) expansion coefficients are given by

$$c_\alpha = D\mathrm{tr}(\varrho\lambda_\alpha) \ . \tag{11}$$

Normalization implies that $c_0 = \sqrt{D}$, so the density operator takes the form

$$\varrho = \frac{1}{D}\left(I + c_j\lambda_j\right) = \frac{1}{D}(I + \boldsymbol{c}\cdot\boldsymbol{\lambda}) \ . \tag{12}$$

Here $\boldsymbol{c} = c_j\boldsymbol{e}_j$ can be regarded as a vector in a $(D^2 - 1)$-dimensional real vector space, spanned by the orthonormal basis $\boldsymbol{e}_j$, and $\boldsymbol{\lambda} = \lambda_j\boldsymbol{e}_j$ is an

operator-valued vector. If $\varrho = |\psi\rangle\langle\psi|$ is a pure qudit state, then $\mathrm{tr}(\varrho^2) = 1$, from which it follows that

$$|\boldsymbol{c}\,|^2 = \boldsymbol{c}\cdot\boldsymbol{c} = D(D-1)\;. \tag{13}$$

We could represent a pure state by a unit vector $\boldsymbol{n} = \boldsymbol{c}/\sqrt{D(D-1)}$ on the unit sphere in D^2-1 dimensions, but in contrast to the situation with the Bloch sphere ($D = 2$), most vectors on this unit sphere do not represent a pure state or, indeed, any state at all.

3 Mixtures of Maximally Mixed and Maximally Entangled States

In this section we deal with two qudits, labeled A and B. We consider a class of two-qudit states, specifically mixtures of the maximally mixed state, $M_{D^2} = I\otimes I/D^2$, with a maximally entangled state, which we can choose to be

$$|\Psi\rangle = \frac{1}{\sqrt{D}}\sum_{a=1}^{D}|a\rangle\otimes|a\rangle\;. \tag{14}$$

Such mixtures have the form

$$\varrho_\varepsilon = (1-\varepsilon)M_{D^2} + \varepsilon|\Psi\rangle\langle\Psi|\;, \tag{15}$$

where $0 \le \varepsilon \le 1$.

In analogy to (10), any state ϱ of two qudits can be expanded uniquely as

$$\varrho = \frac{1}{D^2}c_{\alpha\beta}\lambda_\alpha\otimes\lambda_\beta\;, \tag{16}$$

where the expansion coefficients are given by

$$c_{\alpha\beta} = D^2\mathrm{tr}(\varrho\lambda_\alpha\otimes\lambda_\beta)\;, \tag{17}$$

with $c_{00} = D$ determined by normalization. Using (17) or (7)–(9), we can find the operator expansion for the maximally entangled state (14):

$$|\Psi\rangle\langle\Psi| = \frac{1}{D^2}\Bigg(I\otimes I + D\sum_a \Gamma_a\otimes\Gamma_a + D\sum_{a<b}\left(\Gamma_{ab}^{(+)}\otimes\Gamma_{ab}^{(+)} - \Gamma_{ab}^{(-)}\otimes\Gamma_{ab}^{(-)}\right)\Bigg)\;, \tag{18}$$

from which we can read off the expansion coefficients for the state ϱ_ε of (15):

$$c_{0j} = c_{j0} = 0\;, \tag{19}$$

$$c_{jk} = \begin{cases} 0\;, & j\neq k,\\ D\varepsilon\;, & j = k = 1,\ldots,(D+2)(D-1)/2.\\ -D\varepsilon\;, & j = k = D(D+2)/2,\ldots,D^2-1.\end{cases} \tag{20}$$

A state of the two qudits is *separable* if it can be written as an ensemble of product states. In this section we show that the mixed state (15) is separable if and only if

$$\varepsilon \leq \frac{1}{1+D} \ . \tag{21}$$

Our method is to prove the necessity of the condition (21) by considering the restrictions that separability places on the correlation coefficients (20) and then to construct an explicit product ensemble when $\varepsilon \leq 1/(1+D)$. Vidal and Tarrach [12] found the separability boundary for a mixture of M_{D^2} with *any* pure state by using the partial transpose condition [8] to show that any state with ε outside the boundary is nonseparable and by constructing an explicit product ensemble for states with ε within the separability boundary. The reason for presenting our more limited proof in this section is, first, that our proof of necessity has a nice physical interpretation in terms of the correlation coefficients (20) and, second, that the product ensemble we use is different from the one used by Vidal and Tarrach.

The product pure states for two qudits, $|\psi_A\rangle\langle\psi_A|\otimes|\psi_B\rangle\langle\psi_B|$, constitute an overcomplete operator basis. Thus we can expand any two-qudit density operator in terms of them,

$$\varrho = \int d\mathcal{V}_A \, d\mathcal{V}_B \, w(\psi_A, \psi_B) \, |\psi_A\rangle\langle\psi_A|\otimes|\psi_B\rangle\langle\psi_B| \ . \tag{22}$$

Here the integral for each system runs over all of projective Hilbert space, i.e., the space of Hilbert-space rays, and the volume elements $d\mathcal{V}_A$ and $d\mathcal{V}_B$ are the unitarily invariant integration measures on projective Hilbert space. Because of overcompleteness of the pure-state projectors, the expansion function $w(\psi_A, \psi_B)$ is not unique. Notice that the expansion coefficients $c_{\alpha\beta}$ of (17) can be written as integrals over the expansion function,

$$c_{\alpha\beta} = \int d\mathcal{V}_A \, d\mathcal{V}_B \, w(\psi_A, \psi_B) \, (c_A)_\alpha (c_B)_\beta \ , \tag{23}$$

where $(c_A)_\alpha = D\langle\psi_A|\lambda_\alpha|\psi_A\rangle$ and $(c_B)_\alpha = D\langle\psi_B|\lambda_\alpha|\psi_B\rangle$ are the expansion coefficients for the pure states $|\psi\rangle_A$ and $|\psi\rangle_B$, satisfying $\boldsymbol{c}_A \cdot \boldsymbol{c}_A = D(D-1) = \boldsymbol{c}_B \cdot \boldsymbol{c}_B$.

A two-qudit state is separable if and only if there exists an expansion function $w(\psi_A, \psi_B)$ that is everywhere nonnegative. In this case $w(\psi_A, \psi_B)$ can be thought of as a normalized classical probability distribution for the pure states ψ_A and ψ_B, and the integral for $c_{\alpha\beta}$ in (23) can be interpreted as a classical expectation value of the product of the random variables $(c_A)_\alpha$ and $(c_B)_\beta$, i.e.,

$$c_{\alpha\beta} = E\left[(c_A)_\alpha (c_B)_\beta\right] \ . \tag{24}$$

If the state ϱ_ε is separable, we have from (20) that for each value of j,

$$D\varepsilon = |c_{jj}| = \Big| E\left[(c_A)_j (c_B)_j\right] \Big| \leq \frac{1}{2}\big(E[(c_A)_j^2] + E[(c_B)_j^2]\big) \ . \tag{25}$$

Adding over the D^2-1 value of j gives

$$D(D^2-1)\varepsilon \le \frac{1}{2}\Big(E[\boldsymbol{c}_A\cdot\boldsymbol{c}_A]+E[\boldsymbol{c}_B\cdot\boldsymbol{c}_B]\Big)=D(D-1)\;. \tag{26}$$

We conclude that if ϱ_ε is separable, then $\varepsilon \le 1/(1+D)$.

To prove the converse, we construct an explicit product ensemble for the state ϱ_ε with $\varepsilon = 1/(1+D)$. We define a vector $\boldsymbol{z} = (z_1,\ldots,z_D)$ whose components z_a take on the values ±1 and $\pm i$, so that

$$\sum_{z_j} z_j = \sum_{z_j} z_j^2 = 0\;,\;\sum_{z_j}|z_j|^2 = 4\;. \tag{27}$$

Associated with each vector $\boldsymbol{z}$ is a pure state

$$|\Phi_{\boldsymbol{z}}\rangle = \frac{1}{\sqrt{D}}\sum_{a=1}^{D} z_a|a\rangle\;. \tag{28}$$

There are 4^D vectors and thus that many states $\Phi_{\boldsymbol{z}}$, although only 4^{D-1} of these states are distinct in that they differ by more than a global phase. Now we define a product state for the two-qudit system:

$$\varrho_{\boldsymbol{z}} = |\Phi_{\boldsymbol{z}}\rangle\langle\Phi_{\boldsymbol{z}}|\otimes|\Phi_{\boldsymbol{z}^*}\rangle\langle\Phi_{\boldsymbol{z}^*}|\;. \tag{29}$$

The ensemble consisting of all 4^D of these states, each contributing with the same probability, produces the density operator

$$\frac{1}{4^D}\sum_{\boldsymbol{z}}\varrho_{\boldsymbol{z}} = \frac{1}{4^D D^2}\sum_{a,b,c,d}\left(\sum_{\boldsymbol{z}} z_a z_b^* z_c^* z_d\right)|a\rangle\langle b|\otimes|c\rangle\langle d|\;. \tag{30}$$

Since

$$\sum_{\boldsymbol{z}} z_a z_b^* z_c^* z_d = 4^D(\delta_{ab}\delta_{cd}+\delta_{ac}\delta_{bd}-\delta_{ab}\delta_{cd}\delta_{ac})\;, \tag{31}$$

it follows that

$$\frac{1}{4^D}\sum_{\boldsymbol{z}}\varrho_{\boldsymbol{z}} = \frac{I\otimes I}{D^2}+\frac{1}{D}|\Psi\rangle\langle\Psi| - \frac{1}{D^2}\sum_{a=1}^{D}|a\rangle\langle a|\otimes|a\rangle\langle a|\;. \tag{32}$$

Multiplying by $D/(D+1)$ and rearranging yields

$$\begin{aligned}\frac{D}{1+D}\frac{I\otimes I}{D^2}+\frac{1}{1+D}|\Psi\rangle\langle\Psi| \\ = \frac{D}{1+D}\frac{1}{4^D}\sum_{\boldsymbol{z}}\varrho_{\boldsymbol{z}}+\frac{1}{1+D}\frac{1}{D}\sum_{a=1}^{D}|a\rangle\langle a|\otimes|a\rangle\langle a|\;.\end{aligned} \tag{33}$$

The left-hand side of (33) is the state (15) with $\varepsilon = 1/(1+D)$, and the right-hand side is an explicit product ensemble for the state. This concludes the proof that ϱ_ε is separable if and only if $\varepsilon \le 1/(1+D)$.

4 Separability of States Near the Maximally Mixed State

This section deals with N-qudit states of the form

$$\varrho_\varepsilon = (1-\varepsilon)M_{D^N} + \varepsilon\varrho_1 \ , \tag{34}$$

where $M_{D^N} = I\otimes\cdots\otimes I/D^N$ is the maximally mixed state for N qudits and ϱ_1 is any N-qudit density operator. We establish lower and upper bounds on the size of the neighborhood of separable states surrounding the maximally mixed state. In particular, we show, first, that for

$$\varepsilon \le \frac{1}{1+D^{2N-1}} \ , \tag{35}$$

all states of the form (34) are separable and, second, that for

$$\varepsilon > \frac{1}{1+D^{N-1}} \ , \tag{36}$$

there are states of the form (34) that are not separable (i.e., they are entangled). These results generalize and extend the work of Braunstein et al. for qubits [13] and of Caves and Milburn for qutrits [14].

4.1 Mathematical Preliminaries

Before turning to the lower and upper bounds, it is useful to develop some mathematical apparatus that will be used in deriving the bounds.

Superoperator Formalism

We begin by reviewing a formalism for handling superoperators, introduced by Caves [15] and used by Schack and Caves [16] to generate product ensembles for separable N-qubit states.

The space of linear operators acting on a D-dimensional complex vector space is a D^2-dimensional complex vector space. In this space we introduce operator "kets" $|A) = A$ and "bras" $(A| = A^\dagger$, distinguished from vector kets and bras by the use of smooth brackets. The natural operator inner product can be written as $(A|B) = \mathrm{tr}(A^\dagger B)$. An orthonormal basis $|a\rangle$ induces an orthonormal operator basis,

$$|c\rangle\langle a| = \tau_{ca} = \tau_\alpha \ , \tag{37}$$

where the Greek index α is an abbreviation for the pair of Roman indices, ca. Not all orthonormal operator bases are of this outer-product form.

The space of superoperators, i.e., linear maps on operators, is a D^4-dimensional complex vector space. Any superoperator $\mathcal{S}$ is specified by its "matrix elements"

$$\mathcal{S}_{ca,db} = \langle c|\,\mathcal{S}(|a\rangle\langle b|)|d\rangle \ , \tag{38}$$

for the superoperator can be written in terms of its matrix elements as

$$\begin{aligned}\mathcal{S} &= \sum_{c,a,d,b} \mathcal{S}_{ca,db}|c\rangle\langle a| \odot |b\rangle\langle d| \\ &= \sum_{c,a,d,b} \mathcal{S}_{ca,db}\, \tau_{ca} \odot \tau_{db}^{\dagger} \\ &= \sum_{\alpha,\beta} \mathcal{S}_{\alpha\beta}|\tau_\alpha)(\tau_\beta| \ . \end{aligned} \tag{39}$$

The tensor product here is an ordinary operator tensor product, but we use the symbol $\odot$ to distinguish it from a tensor product between objects associated with different systems, which is denoted by $\otimes$. In the final form of (39), the tensor product is written as an operator outer product, with $\alpha = ca$ and $\beta = db$.

The ordinary action of $\mathcal{S}$ on an operator A, used to generate the matrix elements, is obtained by dropping an operator A into the center of the representation of $\mathcal{S}$, in place of the tensor-product sign,

$$\mathcal{S}(A) = \sum_{\alpha,\beta} \mathcal{S}_{\alpha\beta}\, \tau_\alpha A \tau_\beta^{\dagger} \ . \tag{40}$$

There is clearly another way that $\mathcal{S}$ can act on A, the left-right action,

$$\mathcal{S}|A) = \sum_{\alpha,\beta} \mathcal{S}_{\alpha\beta}|\tau_\alpha)(\tau_\beta|A) \ , \tag{41}$$

in terms of which the matrix elements are

$$\mathcal{S}_{\alpha\beta} = (\tau_\alpha|\,\mathcal{S}|\tau_\beta) = (\tau_{ca}|\,\mathcal{S}|\tau_{db}) = \langle c|\,\mathcal{S}(|a\rangle\langle b|)|d\rangle \ . \tag{42}$$

This expression provides the fundamental connection between the two actions of a superoperator. We can define an operation, called *sharp*, that exchanges the ordinary and left-right actions:

$$\mathcal{S}^{\#}(A) = \mathcal{S}|A) \ . \tag{43}$$

Equation (42) implies that

$$\mathcal{S}^{\#}_{ca,db} = \langle c|\,\mathcal{S}^{\#}(|a\rangle\langle b|)|d\rangle = (\tau_{cd}|\mathcal{S}|\tau_{ab}) = \mathcal{S}_{cd,ab} \tag{44}$$

or, equivalently, that

$$\mathcal{S}^{\#} = \sum_{c,a,d,b} \mathcal{S}_{ca,db}|c\rangle\langle d| \odot |b\rangle\langle a| \ . \tag{45}$$

With respect to the left-right action, a superoperator works just like an operator. Multiplication of superoperators $\mathcal{R}$ and $\mathcal{S}$ is given by

$$\mathcal{R}\mathcal{S} = \sum_{\alpha,\beta,\gamma} \mathcal{R}_{\alpha\gamma}\mathcal{S}_{\gamma\beta}|\tau_\alpha)(\tau_\beta| \ , \tag{46}$$

and the adjoint is defined by

$$(A|\mathcal{S}^\dagger|B) = (B|\mathcal{S}|A)^* \quad \Longleftrightarrow \quad \mathcal{S}^\dagger = \sum_{\alpha,\beta} \mathcal{S}^*_{\beta\alpha} |\tau_\alpha)(\tau_\beta| \; . \tag{47}$$

With respect to the ordinary action, superoperator multiplication, denoted as a composition $\mathcal{R} \circ \mathcal{S}$, is given by

$$\mathcal{R} \circ \mathcal{S} = \sum_{\alpha,\beta,\gamma,\delta} \mathcal{R}_{\gamma\delta} \mathcal{S}_{\alpha\beta} \, \tau_\gamma \tau_\alpha \odot \tau_\beta^\dagger \tau_\delta^\dagger \; . \tag{48}$$

The adjoint with respect to the ordinary action, denoted by $\mathcal{S}^\times$, is defined by

$$\mathrm{tr}\big([\mathcal{S}^\times(B)]^\dagger A\big) = \mathrm{tr}\big(B^\dagger \mathcal{S}(A)\big) \quad \Longleftrightarrow \quad \mathcal{S}^\times = \sum_{\alpha,\beta} \mathcal{S}^*_{\alpha\beta} \, \tau_\alpha^\dagger \odot \tau_\beta \; . \tag{49}$$

The identity superoperator with respect to the left-right action can be written as

$$\mathbf{I} = \sum_\alpha |\tau_\alpha)(\tau_\alpha| = \sum_{c,a} |c\rangle\langle a| \odot |a\rangle\langle c| \; . \tag{50}$$

When sharped, $\mathbf{I}$ becomes the identity superoperator with respect to the ordinary action, denoted by $\mathcal{I}$:

$$\mathbf{I}^\# = \sum_{c,a} |c\rangle\langle c| \odot |a\rangle\langle a| = I \odot I \equiv \mathcal{I} \; . \tag{51}$$

The final ingredient we need is the superoperator trace relative to the left-right action, defined by

$$\mathrm{Tr}(\mathcal{S}) = \sum_\alpha (\tau_\alpha|\mathcal{S}|\tau_\alpha) = \sum_{c,a} \langle c| \, \mathcal{S}(|a\rangle\langle a|)|c\rangle = \mathrm{tr}(\mathcal{S}(I)) \; . \tag{52}$$

Notice that $\mathbf{I}(I) = DI$ and $\mathcal{I}(I) = I$, which give $\mathrm{Tr}(\mathbf{I}) = D^2$ and $\mathrm{Tr}(\mathcal{I}) = D$.

Now suppose the operators $|N_\alpha)$ constitute a complete or overcomplete operator basis; i.e., let the operator kets $|N_\alpha)$ span the vector space of operators. It follows that the superoperator $\mathcal{G}$ defined by

$$\mathcal{G} = \sum_\alpha |N_\alpha)(N_\alpha| = \mathcal{G}^\dagger \tag{53}$$

is invertible with respect to the left-right action. The operators

$$|Q_\alpha) = \mathcal{G}^{-1} |N_\alpha) \tag{54}$$

form a dual basis, which gives rise to the following expressions for the identity superoperator:

$$\mathbf{I} = \sum_\alpha |Q_\alpha)(N_\alpha| = \sum_\alpha |N_\alpha)(Q_\alpha| \; . \tag{55}$$

An arbitrary operator A can be expanded in terms of the original basis or the dual basis:

$$A = \sum_\alpha |N_\alpha)(Q_\alpha|A) = \sum_\alpha N_\alpha \mathrm{tr}(Q_\alpha^\dagger A) \ , \tag{56}$$

$$A = \sum_\alpha |Q_\alpha)(N_\alpha|A) = \sum_\alpha Q_\alpha \mathrm{tr}(N_\alpha^\dagger A) \ . \tag{57}$$

These expansions are unique if and only if the operators $|N_\alpha)$ are linearly independent. Later in this section we apply expansions of this sort to density operators.

Pure States and Their Dual Basis

The set of all pure-state projectors in a D-dimensional Hilbert space,

$$P_\psi = |\psi\rangle\langle\psi| \ , \tag{58}$$

forms an overcomplete operator basis. To develop operator expansions in terms of the pure-state projectors, we follow the discussion in the preceding subsection and consider the superoperator

$$\mathcal{G} = \int d\mathcal{V} \, |P_\psi)(P_\psi| = \int d\mathcal{V} \, |\psi\rangle\langle\psi| \odot |\psi\rangle\langle\psi| \ , \tag{59}$$

where $d\mathcal{V}$ is the unitarily invariant integration measure on projective Hilbert space.

The only Hilbert-space integrals we need to calculate explicitly are those for which the integrand is a function only of an angle θ defined by $\cos\theta = |\langle e|\psi\rangle|$, where $|e\rangle$ is some particular unit vector (pure state). The angle θ, which runs over the range $0 \le \theta \le \pi/2$, can be thought of as a "polar angle" relative to the "polar axis" defined by $|e\rangle$. For integrals of this sort, a convenient form of the integration measure is [17]

$$d\mathcal{V} = (\sin\theta)^{2D-3} \cos\theta \, d\theta \, d\mathcal{S}_{2D-3} \ , \tag{60}$$

where $d\mathcal{S}_{2D-3}$ is the standard integration measure on a $(2D-3)$-dimensional unit sphere. Thus the total volume of D-dimensional projective Hilbert space is [17]

$$\mathcal{V} = \mathcal{S}_{2D-3} \int_0^{\pi/2} d\theta \, (\sin\theta)^{2D-3} \cos\theta \, d\theta = \frac{\mathcal{S}_{2D-3}}{2(D-1)} = \frac{\pi^{D-1}}{(D-1)!} \ , \tag{61}$$

where $\mathcal{S}_{2D-3} = 2\pi^{D-1}/(D-2)!$ is the volume of a $(2D-3)$-dimensional unit sphere.

To use the expansions (56) and (57), we need the dual basis $|Q_\psi)$, and for that purpose, we need to invert $\mathcal{G}$. Since $\mathcal{G}$ is Hermitian relative to the left-right action, we can invert it by diagonalizing it with respect to the left-right action. Given an orthonormal basis $|a\rangle$, we can write $\mathcal{G}$ as in (39),

$$\mathcal{G} = \sum_{c,a,d,b} \mathcal{G}_{ca,db} |c\rangle\langle a| \odot |b\rangle\langle d| = \sum_{c,a,d,b} \mathcal{G}_{ca,db} |\tau_{ca})(\tau_{db}| \ , \tag{62}$$

where the matrix elements are given by (38):

$$\mathcal{G}_{ca,db} = \langle c|\,\mathcal{G}(|a\rangle\langle b|)|d\rangle = \int d\mathcal{V}\,\langle c|\psi\rangle\langle\psi|a\rangle\langle b|\psi\rangle\langle\psi|d\rangle\ . \tag{63}$$

The unitary invariance of the integration measure places stringent constraints on the matrix elements (63). Since the integral in (63) remains unchanged under a change in the sign of the amplitude $\langle a|\psi\rangle$ corresponding to a particular basis vector $|a\rangle$, the matrix elements vanish except when (i) $a = b \neq c = d$ or $a = c \neq b = d$ or (ii) $a = b = c = d$. Furthermore, unitary invariance implies that for each of these cases, all the matrix elements have the same value. Gathering these conclusions together, we have

$$\mathcal{G}_{ca,db} = \begin{cases} \alpha\ , & a = b \neq c = d \text{ or } a = c \neq b = d, \\ \gamma\ , & a = b = c = d, \\ 0\ , & \text{otherwise.} \end{cases} \tag{64}$$

We get a relation between α and γ by noting that

$$D(D-1)\alpha + D\gamma = \sum_{c,a=1}^{D} \mathcal{G}_{ca,ca} = \mathcal{V}\ , \tag{65}$$

where the second equality follows from doing the sum within the integral in (63). We need one more relation, which we get by evaluating explicitly the integral for γ:

$$\begin{aligned} \gamma &= \int d\mathcal{V}|\langle a|\psi\rangle|^4 \\ &= \mathcal{S}_{2D-3}\int_0^{\pi/2} d\theta\,(\sin\theta)^{2D-3}(\cos\theta)^5 = \frac{2\mathcal{V}}{D(D+1)} \equiv 2K\ . \end{aligned} \tag{66}$$

It follows that $\alpha = K$. As a result, we have

$$\begin{aligned} \mathcal{G} &= K\left(2\sum_a |\tau_{aa})(\tau_{aa}| + \sum_{\substack{a,b \\ a\neq b}} \Big(|\tau_{ab})(\tau_{ab}| + |\tau_{aa})(\tau_{bb}|\Big)\right) \\ &= K(\mathbf{I} + \mathcal{I})\ . \end{aligned} \tag{67}$$

This result gives us immediately that [17]

$$\int d\mathcal{V}\,|\psi\rangle\langle\psi| = \mathcal{G}(I) = \frac{\mathcal{V}}{D} I\ . \tag{68}$$

The operators λ_α introduced in Sect. 2 constitute a complete, orthonormal operator basis, so we can write $\mathbf{I}$ as

$$\mathbf{I} = \sum_\alpha |\lambda_\alpha)(\lambda_\alpha| = \frac{|I)(I|}{D} + \mathcal{T}\ , \tag{69}$$

where

$$\mathcal{T} = \sum_j |\lambda_j)(\lambda_j| \tag{70}$$

is the superoperator that projects onto the subspace of traceless operators. Plugging (69) into (67) gives the diagonal form of $\mathcal{G}$:

$$\mathcal{G} = K\left((D+1)\frac{|I)(I|}{D} + \mathcal{T}\right) . \tag{71}$$

Orthonormal eigenoperators of $\mathcal{G}$ are $\lambda_0 = I/\sqrt{D}$, with eigenvalue $K(D+1) = \mathcal{V}/D$ and the traceless operators λ_j, which are degenerate with eigenvalue $K = \mathcal{V}/D(D+1)$.

We are now prepared to write the inverse of $\mathcal{G}$ with respect to the left-right action as

$$\mathcal{G}^{-1} = \frac{1}{K}\left(\frac{1}{D+1}\frac{|I)(I|}{D} + \mathcal{T}\right) = \frac{1}{K}\left(\mathbf{I} - \frac{\mathcal{I}}{D+1}\right) . \tag{72}$$

Thus the dual operators of (54) are given by

$$|Q_\psi) = \mathcal{G}^{-1}|P_\psi) = \frac{1}{K}\left(|P_\psi) - \frac{|I)}{D+1}\right) = \frac{D}{\mathcal{V}}\Big((D+1)P_\psi - I\Big) . \tag{73}$$

Alternative Diagonalization of $\mathcal{G}$

In this subsection we rederive (71) using the special properties of the superoperator $\mathcal{G}$. These properties are evident from the integral form of $\mathcal{G}$ in (59).

- The superoperator $\mathcal{G}$ is Hermitian relative to the left-right action, which implies that it has a complete, orthonormal set of eigenoperators η_α, $\alpha = 1, \ldots, D^2$, with real eigenvalues q_α:

$$\mathcal{G} = \mathcal{G}^\dagger \quad \Longrightarrow \quad \mathcal{G} = \sum_\alpha q_\alpha |\eta_\alpha)(\eta_\alpha| = \sum_\alpha q_\alpha \eta_\alpha \odot \eta_\alpha^\dagger . \tag{74}$$

- The superoperator $\mathcal{G}$ is Hermitian relative to the ordinary action,

$$\mathcal{G} = \mathcal{G}^\times = \sum_\alpha q_\alpha \eta_\alpha^\dagger \odot \eta_\alpha = \sum_\alpha q_\alpha |\eta_\alpha^\dagger)(\eta_\alpha^\dagger| , \tag{75}$$

  which implies that if η_α is an eigenoperator of $\mathcal{G}$, then $\eta_\alpha^\dagger$ is also an eigenoperator with the same eigenvalue. This means that we can choose all the eigenoperators to be Hermitian.
- The superoperator $\mathcal{G}$ is unitarily invariant, i.e.,

$$\mathcal{G} = U \odot U^\dagger \circ \mathcal{G} \circ U^\dagger \odot U = \sum_\alpha q_\alpha U\eta_\alpha U^\dagger \odot U\eta_\alpha^\dagger U^\dagger , \tag{76}$$

  for any unitary operator U, which implies that if η_α is an eigenoperator of $\mathcal{G}$, then $U\eta_\alpha U^\dagger$ is also an eigenoperator with the same eigenvalue.

The upshot of these three properties is that the eigensubspaces of $\mathcal{G}$ are invariant under Hermitian conjugation and under all unitary transformations. It is not hard to show that the only such operator subspaces are the subspace of traceless operators and its orthocomplement, the one-dimensional subspace spanned by the unit operator. The result is that $\mathcal{G}$ must have the form

$$\mathcal{G} = K\left(\mu \frac{I \odot I}{D} + \mathcal{T}\right) = K\left(\mathbf{I} + \frac{\mu - 1}{D}\mathcal{I}\right) , \tag{77}$$

where K is the eigenvalue of any traceless operator and $K\mu$ is the eigenvalue of $\lambda_0 = I/\sqrt{D}$. Now we use the final property to evaluate μ.

- The superoperator $\mathcal{G}$ is invariant under exchange of the two kinds of action:

$$\mathcal{G} = \mathcal{G}^{\#} = K\left(\mathcal{I} + \frac{\mu - 1}{D}\mathbf{I}\right) . \tag{78}$$

  This implies that $\mu = D+1$, thus bringing $\mathcal{G}$ into the form (67), but with K not yet determined.

We find the value of K by evaluating the superoperator trace, first using (59),

$$\mathrm{Tr}(\mathcal{G}) = \mathrm{tr}(\mathcal{G}(I)) = \mathcal{V} , \tag{79}$$

and then using (67),

$$\mathrm{Tr}(\mathcal{G}) = K\Big(\mathrm{Tr}(\mathbf{I}) + \mathrm{Tr}(\mathcal{I})\Big) = KD(D+1) . \tag{80}$$

This gives $K = \mathcal{V}/D(D+1)$, in agreement with (66).

4.2 Separability Bounds

We turn now to demonstrating the lower and upper bounds (35) and (36) on the size of the neighborhood of separable states surrounding the maximally state.

To establish the lower bound, we use the results of Sect. 4.1 to formulate operator expansions in terms of product pure states. For a single qudit, any density operator can be expanded as

$$\varrho = \int d\mathcal{V}\, |P_\psi)(Q_\psi|\varrho) = \int d\mathcal{V}\, w_\varrho(\psi) P_\psi , \tag{81}$$

where

$$w_\varrho(\psi) = \mathrm{tr}(\varrho Q_\psi) = \frac{D}{\mathcal{V}}\Big((D+1)\langle\psi|\varrho|\psi\rangle - 1\Big) \tag{82}$$

is a quasi-probability distribution, normalized to unity, but possibly having negative values. The analogous product representation for an N-qudit density operator is

$$\varrho = \int d\mathcal{V}_1 \cdots d\mathcal{V}_N \, w_\varrho(\psi_1, \ldots, \psi_N) \, P_{\psi_1} \otimes \cdots \otimes P_{\psi_N} \, , \tag{83}$$

where

$$w_\varrho(\psi_1, \ldots, \psi_N) = \mathrm{tr}(\varrho Q_{\psi_1} \otimes \cdots \otimes Q_{\psi_N}) \, . \tag{84}$$

The N-qudit quasi-distribution obeys the bound

$$w_\varrho(\psi_1, \ldots, \psi_N) \geq \begin{pmatrix} \text{smallest eigenvalue of} \\ Q_{\psi_1} \otimes \cdots \otimes Q_{\psi_N} \end{pmatrix} = -\frac{D^{2N-1}}{\mathcal{V}^N} \tag{85}$$

This follows from the fact that Q_ψ has a nondegenerate eigenvalue, $D^2/\mathcal{V}$, and a $(D-1)$-fold degenerate eigenvalue, $-D/\mathcal{V}$. Thus the most negative eigenvalue of the product operator $Q_{\psi_1} \otimes \cdots \otimes Q_{\psi_N}$ is $(-D/\mathcal{V})(D^2/\mathcal{V})^{N-1} = -D^{2N-1}/\mathcal{V}^N$.

We can use the lower bound (85) to place a similar lower bound on the quasi-distribution for the mixed state ϱ_ε of (34). Since the quasi-distribution for the maximally mixed state, M_{D^N}, is the uniform distribution $1/\mathcal{V}^N$, we have

$$w_{\varrho_\varepsilon}(\psi_1, \ldots, \psi_N) = \frac{1-\varepsilon}{\mathcal{V}^N} + \varepsilon w_{\varrho_1} \geq \frac{1 - \varepsilon(1 + D^{2N-1})}{\mathcal{V}^N} \, . \tag{86}$$

We conclude that if $\varepsilon \leq 1/(1 + D^{2N-1})$, then w_{ϱ_ε} is nonnegative and the qudit state ϱ_ε is separable. This establishes the lower bound (35) on the size of the neighborhood of separable states surrounding the maximally mixed state.

The upper bound (36) on the size of the separable neighborhood can be established with the help of an exact separability condition for a particular N-qubit state, obtained by Dür, Cirac, and Tarrach [18] and also by Pittenger and Rubin [19]. We consider the N-qudit state,

$$\varrho_\varepsilon = (1-\varepsilon) M_{D^N} + \varepsilon |\Psi_{\mathrm{cat}}\rangle\langle\Psi_{\mathrm{cat}}| \, , \tag{87}$$

where

$$|\Psi_{\mathrm{cat}}\rangle = \frac{1}{\sqrt{D}} \sum_{a=1}^{D} |a\rangle \otimes \cdots \otimes |a\rangle \, , \tag{88}$$

is an N-qudit "cat state." We call the mixed state (87) an ε-cat state.

Now project each qudit onto the two-dimensional (qubit) subspace spanned by $|1\rangle$ and $|2\rangle$. The local projection operator on each qudit is $\Pi = |1\rangle\langle 1| + |2\rangle\langle 2|$, and the normalized N-qubit state after projection is

$$\varrho'_\varepsilon = \frac{\Pi^{\otimes N} \varrho_\varepsilon \Pi^{\otimes N}}{\mathrm{tr}(\Pi^{\otimes N} \varrho_\varepsilon)} = (1-\varepsilon') M_{2^N} + \varepsilon' |\Phi_{\mathrm{cat}}\rangle\langle\Phi_{\mathrm{cat}}| \, , \tag{89}$$

where

$$|\Phi_{\rm cat}\rangle \equiv \frac{1}{\sqrt{2}}\Big(|1\rangle\otimes\ldots\otimes|1\rangle + |2\rangle\otimes\ldots\otimes|2\rangle\Big) \tag{90}$$

is the cat state for N qubits and

$$\varepsilon' = \frac{2\varepsilon/D}{(2/D)^N(1-\varepsilon)+2\varepsilon/D}\ . \tag{91}$$

Dür, Cirac, and Tarrach [18] and also Pittenger and Rubin [19] have shown that the N-qubit ε-cat state (89) is nonseparable (entangled) if and only if $\varepsilon' > 1/(1+2^{N-1})$, a condition equivalent to $\varepsilon > 1/(1+D^{N-1})$. Since local projections on each qudit cannot create entanglement, we can conclude that the N-qudit ε-cat state (87) is nonseparable under the same condition. This establishes the upper bound (36) on the size of the separable neighborhood around the maximally mixed state.

Pittenger and Rubin [20] have recently extended the result of Dür, Cirac, and Tarrach [18] for the N-qubit ε-cat state. They have shown directly that the N-qudit ε-cat state (87) is nonseparable if $\varepsilon > 1/(1+D^{N-1})$, and they have also shown that the same condition is a necessary and sufficient condition for entanglement when D is prime. Their argument is akin to the correlation-coefficient argument we give in Sect. 3.

Acknowledgments

Work at UNM was supported in part by the U.S. Office of Naval Research (Grant No. N00014-93-1-0116). WJM acknowledges the support of the Australian Research Council, and KN thanks the Australian International Education Foundation (AIEF) for financial support.

References

1. *Introduction to Quantum Computation and Information*, ed. by H.-K. Lo, S. Popescu, T. Spiller (World Scientific, Singapore 1998)
2. C.H. Bennett, G. Brassard, C. Crépeau, R. Jozsa, A. Peres, W.K. Wootters: Phys. Rev. Lett. **70**, 1895 (1993)
3. P.W. Shor: Phys. Rev. A **52**, R2493 (1995)
4. A.M. Steane: Phys. Rev. Lett. **77**, 793 (1996)
5. A. Einstein, B. Podolsky, N. Rosen: Phys. Rev. **47**, 777 (1935)
6. J.S. Bell: Physics (N.Y.) **1**, 195 (1964)
7. W.K. Wootters: Phys. Rev. Lett. **80**, 2245 (1998)
8. A. Peres: Phys. Rev. Lett. **77**, 1413 (1996)
9. M. Horodecki, P. Horodecki, R. Horodecki: Phys. Lett. A **223**, 1 (1996)
10. P. Horodecki: Phys. Lett. A **232**, 333 (1997)
11. M. Lewenstein, J.I. Cirac, S. Karnas: unpublished, `quant-ph/9903012`
12. G. Vidal R. Tarrach: Phys. Rev. A **59**, 141 (1999)

13. S.L. Braunstein, C.M. Caves, R. Jozsa, N. Linden, S. Popescu, R. Schack: Phys. Rev. Lett. **83**, 1054 (1999)
14. C.M. Caves, G.J. Milburn: Opt. Commun. to be published, quant-ph/9910001
15. C.M. Caves: J. Superconductivity **12**, 707 (1999)
16. R. Schack, C.M. Caves: J. Mod. Opt. to be published, quant-ph/9904109
17. R. Schack, G.M. D Ariano, C.M. Caves: Phys. Rev. E **50**, 972 (1994)
18. W. Dür, J.I. Cirac, R. Tarrach: Phys. Rev. Lett. **83**, 3562 (1999); see also W. Dür, J.I. Cirac: unpublished, quant-ph/9911044
19. A.O. Pittenger, M.H. Rubin: unpublished, quant-ph/9912116
20. A.O. Pittenger, M.H. Rubin: unpublished, quant-ph/0001014

Grover's Algorithm for Multiobject Search in Quantum Computing

Goong Chen, Stephen A. Fulling, Hwang Lee, and Marlan O. Scully

Summary. L.K. Grover's search algorithm in quantum computing gives an optimal, square-root speedup in the search for a single object in a large unsorted database. In this paper, we expound Grover's algorithm in a Hilbert-space framework that isolates its geometrical essence, and we generalize it to the case where more than one object satisfies the search criterion.

1 Introduction

A quantum computer (QC) is envisaged as a collection of 2-state "quantum bits", or *qubits* (e.g., spin 1/2 particles). Quantum computation does calculations on data densely coded in the entangled states that are the hallmark of quantum mechanics, potentially yielding unprecedented parallelism in computation, as P. Shor's work on factorization [10, 11] proved in 1994. Two years later, L. K. Grover [6] showed that for an unsorted database with N items in storage, it takes an average number of $\mathcal{O}(\sqrt{N})$ searches to locate a single desired object by his quantum search algorithm. If N is a very large number, this is a significant square-root speedup over the exhaustive search algorithm in a classical computer, which requires an average number of $\frac{N+1}{2}$ searches. Even though Grover's algorithm is not logarithmically fast (as Shor's is), it has been argued that the wide range of its applicability compensates for this [4]. Furthermore, the quantum speedup of the search algorithm is *indisputable*, whereas for factoring the nonexistence of competitively fast classical algorithms has not yet been proved [1, 2].

Grover's original papers [6, 7] deal with search for a single object. In practical applications, typically more than one item will satisfy the criterion used for searching. In the simplest generalization of Grover's algorithm, the number of "good" items is known in advance (and greater than 1). Here we expound this generalization, along the lines of a treatment of the single-object case by Farhi and Gutmann [5, Appendix] that makes the Hilbert-space geometry of the situation very clear.

The success of Grover's algorithm and its multiobject generalization is attributable to two main sources:

H.J. Carmichael, R.J. Glauber, M.O. Scully (Eds.): LNP 561, pp. 165–175, 2001.

(i) the notion of amplitude amplication; and
(ii) the dramatic reduction to invariant subspaces of low dimension for the unitary operators involved.

Indeed, the second of these can be said to be responsible for the first: A proper geometrical formulation of the process shows that all the "action" takes place within a *two-dimensional, real* subspace of the Hilbert space of quantum states. Since the state vectors are normalized, the state is confined to a one-dimensional unit circle and (if moved at all) initially has nowhere to go except toward the place where the amplitude for the sought-for state is maximized. This accounts for the robustness of Grover's algorithm — that is, the fact that Grover's original choice of initial state and of the Walsh–Hadamard transformation can be replaced by (almost) any initial state and (almost) any unitary transformation [8, 9, 4].

The notion of amplitude amplification was emphasized in the original works [6, 7, 8] of Grover himself and in those of Boyer, Brassard, Høyer and Tapp [3] and Brassard, Høyer and Tapp [4]. (See also [1, 2].) Dimensional reduction is prominent in the papers by Farhi and Gutmann [5] and Jozsa [9]. We applied dimensional reduction to multiobject search independently of references [3] and [4] and later learned that the same conclusions about multiobject search (and more) had been obtained there in a different framework. (We modestly suggest that our framework is clearer.)

The rest of the paper is divided into two parts. In §2, we reformulate the original Grover algorithm, and in §3, a multiobject search algorithm is studied.

2 Introduction to Grover's Algorithm

In this section, we review Grover's algorithm for searching a single element in an unsorted database containing $N \gg 1$ items, following [5]. This proof is presented in a way that makes possible the generalization of the algorithm to perform multiobject search in an unstructured database.

Grover treated the following abstract problem: We are given a Boolean function $f(a)$, $a = 1, 2, \ldots, N$, which is known to be zero for all a except at a single point, say at $a = w$, where $f(w) = 1$. The problem is to find the value w. (The function is an "oracle" or "black box": all we know about it is its output for any input we care to insert.) On a classical computer we have to evaluate the function $\frac{N+1}{2}$ times on average to find the answer to this problem. In contrast, Grover's quantum algorithm finds w in $\mathcal{O}(\sqrt{N})$ steps.

The quantum-mechanical statement of the problem is that given an orthonormal basis $\{\,|\,a\rangle\,:\,a = 1, 2, \ldots, N\}$ we want to single out the basis element $|\,w\rangle$ for which $f(w) = 1$. (More concretely, each $|\,a\rangle$ is to be an eigenstate of the qubits making up the QC. If $N = 2^n$, then n qubits will be needed.)

At $t = 0$, we prepare the state of the system $|\psi\rangle$ in a superposition of the states $\{|a\rangle\}$, each with the same probability:

$$|\psi\rangle = \frac{1}{\sqrt{N}} \sum_{1}^{N} |a\rangle \equiv |s\rangle \ . \tag{1}$$

By the Gram–Schmidt construction we extend $|w\rangle$ to an orthonormal basis for the subspace spanned by $|w\rangle$ and $|s\rangle$. That is, we introduce a normalized vector $|r\rangle$ orthogonal to $|w\rangle$,

$$|r\rangle = \frac{1}{\sqrt{N-1}} \sum_{a \neq w} |a\rangle \ , \tag{2}$$

and find that the initial state has the representation

$$|s\rangle = \sqrt{\frac{N-1}{N}} |r\rangle + \frac{1}{\sqrt{N}} |w\rangle \ . \tag{3}$$

Following Grover, we now define the unitary operator of *inversion about average*,

$$I_s = \boldsymbol{I} - 2|s\rangle\langle s| \ . \tag{4}$$

Notice that the only action of this operator is to flip the sign of the state $|s\rangle$; that is, $I_s |s\rangle = -|s\rangle$ but $I_s |v\rangle = |v\rangle$ if $\langle s|v\rangle = 0$. Using (3) we write I_s as

$$I_s = -\left(1 - \frac{2}{N}\right)(|r\rangle\langle r| - |w\rangle\langle w|) - 2\frac{\sqrt{N-1}}{N}(|r\rangle\langle w| + |w\rangle\langle r|) \ . \tag{5}$$

In other words, with respect to the orthonormal basis the operator I_s is represented by the orthogonal (real unitary) matrix

$$\begin{bmatrix} 1 - \frac{2}{N} & -2 \cdot \frac{\sqrt{N-1}}{N} \\ -2 \cdot \frac{\sqrt{N-1}}{N} & -\left(1 - \frac{2}{N}\right) \end{bmatrix} .$$

Similarly, the operator I_w is defined by

$$I_w = \boldsymbol{I} - 2|w\rangle\langle w| \tag{6}$$

and satisfies $I_w |w\rangle = -|w\rangle$. The crucial fact is that in terms of the oracle function f,

$$I_w |a\rangle = (-1)^{f(a)} |a\rangle \tag{7}$$

for each $|a\rangle$ in the original basis for the full state space of the QC. Therefore, to execute the operation I_w one does not need to know w; one only needs to know f. (And conversely, being able to execute I_w does not mean that one can immediately determine w; $\sqrt{N}$ steps will be needed.)

A "Grover iteration" is the unitary operator $U \equiv -I_s I_w$. This product can be calculated easily in either the bra-ket or the matrix formalism. In particular, for the transition element $\langle w \,|\, U \,|\, s \rangle$ we obtain

$$\begin{aligned}
\langle w \,|\, U \,|\, s \rangle &= \langle w \,|\, \left[\left(1 - \frac{2}{N} \right) \boldsymbol{I} + \frac{2\sqrt{N-1}}{N} (\,|\, w \rangle\langle r \,|\, - \,|\, r \rangle\langle w \,|\,) \right] \,|\, s \rangle \\
&= \left(1 - \frac{2}{N} \right) \frac{1}{\sqrt{N}} + 2 \left(1 - \frac{1}{N} \right) \frac{1}{\sqrt{N}} \qquad (8) \\
&= \frac{1}{\sqrt{N}} + \frac{2}{\sqrt{N}} + \mathcal{O}(N^{-3/2}) \, .
\end{aligned}$$

The fact that the matrix element $\langle w \,|\, U \,|\, s \rangle$ is nonzero can be used to reinforce the probability amplitude of the unknown state $|\, w \rangle$. If we use U as our unitary search operation, then after $m \gg 1$ trials the value $\langle w \,|\, U^m \,|\, s \rangle$ can be evaluated as follows:

$$\begin{aligned}
\langle w|U^m|s\rangle &= [1 \quad 0] \begin{bmatrix} 1 - \dfrac{2}{N} & 2 \cdot \dfrac{\sqrt{N-1}}{N} \\ -2 \cdot \dfrac{\sqrt{N-1}}{N} & 1 - \dfrac{2}{N} \end{bmatrix}^m \begin{bmatrix} \dfrac{1}{\sqrt{N}} \\ \sqrt{\dfrac{N-1}{N}} \end{bmatrix} \\
&= [1 \quad 0] \begin{bmatrix} \cos\theta & \sin\theta \\ -\sin\theta & \cos\theta \end{bmatrix}^m \begin{bmatrix} \dfrac{1}{\sqrt{N}} \\ \sqrt{\dfrac{N-1}{N}} \end{bmatrix} \left(\theta \equiv \sin^{-1} \frac{2\sqrt{N-1}}{N} \right) \\
&= [1 \quad 0] \begin{bmatrix} \cos m\theta & \sin m\theta \\ -\sin m\theta & \cos m\theta \end{bmatrix} \begin{bmatrix} \dfrac{1}{\sqrt{N}} \\ \sqrt{\dfrac{N-1}{N}} \end{bmatrix} \\
&= \frac{1}{\sqrt{N}} \cos m\theta + \sqrt{\frac{N-1}{N}} \sin m\theta \, ,
\end{aligned}$$

or

$$\langle w|U^m|s\rangle = \cos(m\theta - \alpha), \qquad \alpha \equiv \cos^{-1} \frac{1}{\sqrt{N}} \, . \qquad (9)$$

Setting $\cos^2(m\theta - \alpha) = 1$, we can maximize the amplitude of $U^m|s\rangle$ in $|w\rangle$; thus

$$\begin{aligned}
m\theta - \alpha &= 0 \, , \\
m &= \tfrac{\alpha}{\theta} \, . \qquad (10)
\end{aligned}$$

(If no integer satisfies this equation exactly, take the closest one.) When N is large, $\theta \approx \frac{2}{\sqrt{N}}$, $\alpha \approx \frac{\pi}{2}$, from (10) we obtain

$$m \approx \frac{\pi}{2} \Big/ \left(\frac{2}{\sqrt{N}} \right) = \frac{\pi}{4} \sqrt{N} \, . \qquad (11)$$

Therefore, after $m = \mathcal{O}(\sqrt{N})$ trials the state $|w\rangle$ will be projected out, which is precisely Grover's result. By observing the qubits, we will learn w. *By constructive interference, we have constructed* $|w\rangle$! (Since m only approximately satisfies (10), there is a small chance of getting a "bad" w. But because evaluating $f(w)$ is easy, in that case one will recognize the mistake and start over.)

3 Generalization of Grover's Algorithm to Multiobject Search

Here we generalize Grover's search algorithm in its original form [6, 7] to the situation where the number of objects satisfying the search criterion is greater than 1.

Let a database $\{w_i \mid i = 1, 2, \ldots, N\}$, with corresponding orthonormal eigenstates $\{|w_i\rangle : i = 1, 2, \ldots, N\}$ in the QC, be given. Let f be an oracle function such that

$$f(w_j) = \begin{cases} 1, \; j = 1, 2, \ldots, \ell \; , \\ 0 \;\; j = \ell + 1, \ell + 2, \ldots, N \; . \end{cases}$$

Here the ℓ elements $\{w_j \mid 1 \le j \le \ell\}$ are the desired objects of search. (To avoid introducing another layer of subscripts, we pretend in this theoretical discussion that these good objects are the first ℓ items in the list. In a real search application they would appear in the list in random order; in other words, all N items w_i are subjected to some unknown permutation, which we do not indicate explicitly.) Let $\mathcal{H}$ be the Hilbert space generated by the orthonormal basis $\mathcal{B} = \{|w_j\rangle \mid j = 1, \ldots, N\}$. Let $L = \text{span}\{|w_j\rangle \mid 1 \le j \le \ell\}$ be the subspace of $\mathcal{H}$ spanned by the vectors of the good objects.

Define a linear operation in terms of the oracle function f as follows:

$$I_L|w_j\rangle = (-1)^{f(w_j)}|w_j\rangle \; , \qquad j = 1, 2, \ldots, N \; . \tag{12}$$

Then since I_L is linear, the extension of I_L to the entire space $\mathcal{H}$ is unique, with an "explicit" representation

$$I_L = \boldsymbol{I} - 2\sum_{j=1}^{\ell} |w_j\rangle\langle w_j| \; , \tag{13}$$

where $\boldsymbol{I}$ is the identity operator on $\mathcal{H}$. I_L is the operator of *rotation (by π) of the phase* of the subspace L. Note again that the explicitness of (13) is misleading because explicit knowledge of $\{|w_j\rangle \mid 1 \le j \le \ell\}$ in (13) is not available. Nevertheless, (13) is a well-defined (and unitary) operator on $\mathcal{H}$ because of (12). (Unitarity is a requirement for all operations in a QC.)

We now again define $|s\rangle$ as

$$|s\rangle = \frac{1}{\sqrt{N}} \sum_{i=1}^{N} |w_i\rangle = \frac{1}{\sqrt{N}} \sum_{i=1}^{\ell} |w_i\rangle + \sqrt{\frac{N-\ell}{N}}|r\rangle \; , \tag{14}$$

where now

$$|r\rangle = \frac{1}{\sqrt{1-(\ell/N)}}\left(|s\rangle - \frac{1}{\sqrt{N}}\sum_{i=1}^{\ell}|w_i\rangle\right) .$$

As before, we use

$$I_s = \boldsymbol{I} - 2|s\rangle\langle s| . \tag{15}$$

Note that I_s in (15) is unitary and hence quantum-mechanically admissible. I_s is explicitly known, constructible with the so-called Walsh–Hadamard transformation.

Lemma 1 *Let $\widetilde{L} = \mathrm{span}(L \cup \{|r\rangle\})$. Then $\{|w_i\rangle, |r\rangle \mid i = 1, 2, \ldots, \ell\}$ forms an orthonormal basis of $\widetilde{L}$. The orthogonal direct sum $\mathcal{H} = \widetilde{L} \oplus \widetilde{L}^{\perp}$ is an orthogonal invariant decomposition for both operators $I_{\widetilde{L}}$ and I_s. Furthermore,*

(i) The restriction of I_s to $\widetilde{L}$ admits this real unitary matrix representation with respect to the orthonormal basis $\{|w_1\rangle, |w_2\rangle, \ldots, |w_\ell\rangle, |r\rangle\}$:

$$A = [a_{ij}]_{(\ell+1)\times(\ell+1)} ,$$

$$a_{ij} = \begin{cases} \delta_{ij} - \dfrac{2}{N} , & 1 \le i, j \le \ell , \\ -\dfrac{2\sqrt{N-\ell}}{N}(\delta_{i,\ell+1} + \delta_{j,\ell+1}) , & i = \ell+1 \text{ or } j = \ell+1 , i \ne j , \\ \dfrac{2\ell}{N} - 1 , & i = j = \ell+1 . \end{cases} \tag{16}$$

(ii) The restriction of I_s of $\widetilde{L}^{\perp}$ is $\mathbb{P}_{\widetilde{L}^{\perp}}$, the orthogonal projection operator onto $\widetilde{L}^{\perp}$. Consequently, $I_s|_{\widetilde{L}^{\perp}} = \boldsymbol{I}_{\widetilde{L}^{\perp}}$, where $\boldsymbol{I}_{\widetilde{L}^{\perp}}$ is the identity operator on $\widetilde{L}^{\perp}$.

Proof. We have, from (14) and (15),

$$\begin{aligned} I_s &= \boldsymbol{I} - 2\left[\frac{1}{\sqrt{N}}\sum_{i=1}^{\ell}|w_i\rangle + \sqrt{\frac{N-\ell}{N}}|r\rangle\right]\left[\frac{1}{\sqrt{N}}\sum_{j=1}^{\ell}\langle w_j| + \sqrt{\frac{N-\ell}{N}}\langle r|\right] \\ &= \left[\sum_{i=1}^{\ell}|w_i\rangle\langle w_i| + |r\rangle\langle r| + \mathbb{P}_{\widetilde{L}^{\perp}}\right] - \left\{\frac{2}{N}\sum_{i=1}^{\ell}\sum_{j=1}^{\ell}|w_i\rangle\langle w_j| \right. \\ &\quad \left. + \frac{2\sqrt{N-\ell}}{N}\left[\sum_{i=1}^{\ell}(|w_i\rangle\langle r| + |r\rangle\langle w_i|)\right] + 2\left(\frac{N-\ell}{N}\right)|r\rangle\langle r|\right\} \\ &= \sum_{i=1}^{\ell}\sum_{j=1}^{\ell}\left(\delta_{ij} - \frac{2}{N}\right)|w_i\rangle\langle w_j| - \frac{2\sqrt{N-\ell}}{N}\left[\sum_{i=1}^{\ell}(|w_i\rangle\langle r| + |r\rangle\langle w_i|)\right] \\ &\quad + \left(\frac{2\ell}{N} - 1\right)|r\rangle\langle r| + \mathbb{P}_{\widetilde{L}^{\perp}} . \end{aligned} \tag{17}$$

The conclusion follows.

The generalized "Grover search engine" for multiobject search is now constructed as

$$U = -I_s I_L \ . \tag{18}$$

Lemma 2 *The orthogonal direct sum $\mathcal{H} = \widetilde{L} \oplus \widetilde{L}^{\perp}$ is an invariant decomposition for the unitary operator U, such that the following holds:*

(1) With respect to the orthonormal basis $\{|w_1\rangle, \ldots, |w_\ell\rangle, |r\rangle\}$ of $\widetilde{L}$, U admits the real unitary matrix representation

$$U|_{\widetilde{L}} = [u_{ij}]_{(\ell+1)\times(\ell+1)} \ ,$$

$$u_{ij} = \begin{cases} \delta_{ij} - \dfrac{2}{N} \ , & 1 \le i,j \le \ell \ , \\ \dfrac{2\sqrt{N-\ell}}{N}(\delta_{j,\ell+1} - \delta_{i,\ell+1}) \ , & i = \ell+1 \text{ or } j = \ell+1 \ , i \ne j \ , \\ 1 - \dfrac{2\ell}{N} \ , & i = j = \ell+1 \ . \end{cases} \tag{19}$$

(2) The restriction of U to $\widetilde{L}^{\perp}$ is $-\mathbf{P}_{\widetilde{L}^{\perp}} = -\boldsymbol{I}_{\widetilde{L}^{\perp}}$.

Proof. Substituting (13) and (17) into (18) and simplifying, we obtain

$$\begin{aligned} U = -I_s I_L &= \cdots (\text{simplification}) \\ &= \sum_{i=1}^{\ell}\sum_{j=1}^{\ell}\left(\delta_{ij} - \frac{2}{N}\right)|w_i\rangle\langle w_j| + \frac{2\sqrt{N-\ell}}{N}\sum_{i=1}^{\ell}(|w_i\rangle\langle r| - |r\rangle\langle w_i|) \\ &\quad + \left(1 - \frac{2\ell}{N}\right)|r\rangle\langle r| - \mathbf{P}_{\widetilde{L}^{\perp}} \ . \end{aligned}$$

The lemma follows.

Lemmas 1 and 2 above effect a reduction of the problem to an invariant subspace $\widetilde{L}$. However, $\widetilde{L}$ is an $(\ell+1)$-dimensional subspace where ℓ may also be fairly large. Another reduction of dimensionality is needed to further simplify the operator U.

Proposition 3 *Define $\mathcal{V}$ by*

$$\mathcal{V} = \left\{ |v\rangle \in \widetilde{L} \ : \ |v\rangle = a\sum_{i=1}^{\ell}|w_i\rangle + b|r\rangle \ ; \ a,b \in \mathbb{C} \right\} \ .$$

Then $\mathcal{V}$ is an invariant two-dimensional subspace of U such that

(1) $r, s \in \mathcal{V}$;
(2) $U(\mathcal{V}) = \mathcal{V}$.

Proof. Straightforward verification.

Let $|\widetilde{w}\rangle = \frac{1}{\sqrt{\ell}} \sum_{i=1}^{\ell} |w_i\rangle$. Then $\{|\widetilde{w}\rangle, |r\rangle\}$ forms an orthonormal basis of $\mathcal{V}$. We have the second reduction, to dimensionality 2.

Theorem 4 *With respect to the orthonormal basis $\{|\widetilde{w}\rangle, |r\rangle\}$ in the invariant subspace $\mathcal{V}$, U admits the real unitary matrix representation*

$$U = \begin{bmatrix} \frac{N-2\ell}{N} & \frac{2\sqrt{\ell(N-\ell)}}{N} \\ \frac{-2\sqrt{\ell(N-\ell)}}{N} & \frac{N-2\ell}{N} \end{bmatrix} = \begin{bmatrix} \cos\theta & \sin\theta \\ -\sin\theta & \cos\theta \end{bmatrix},$$

$$\theta \equiv \sin^{-1}\left(\frac{2\sqrt{\ell(N-\ell)}}{N}\right). \tag{20}$$

Proof. Use the matrix representation (19) and the definition of $|\widetilde{w}\rangle$.

Since $|s\rangle \in \mathcal{V}$, we can calculate $U^m|s\rangle$ efficiently using (20):

$$\begin{aligned} U^m|s\rangle &= U^m\left(\frac{1}{\sqrt{N}}\sum_{i=1}^{\ell}|w_i\rangle + \sqrt{\frac{N-\ell}{N}}|r\rangle\right) \qquad \text{(by (14))} \\ &= U^m\left(\sqrt{\frac{\ell}{N}}|\widetilde{w}\rangle + \sqrt{\frac{N-\ell}{N}}|r\rangle\right) \\ &= \begin{bmatrix} \cos\theta & \sin\theta \\ -\sin\theta & \cos\theta \end{bmatrix}^m \begin{bmatrix} \sqrt{\frac{\ell}{N}} \\ \sqrt{\frac{N-\ell}{N}} \end{bmatrix} \\ &= \begin{bmatrix} \cos(m\theta-\alpha) \\ -\sin(m\theta-\alpha)] \end{bmatrix} \quad \left(\alpha \equiv \cos^{-1}\sqrt{\frac{\ell}{N}}\right), \qquad (21) \\ &= \cos(m\theta-\alpha)\cdot|\widetilde{w}\rangle - \sin(m\theta-\alpha)\cdot|r\rangle . \end{aligned}$$

Thus, the probability of reaching the state $|\widetilde{w}\rangle$ after m iterations is

$$P_m = \cos^2(m\theta-\alpha) . \tag{22}$$

If $\ell \ll N$, then α is close to $\pi/2$ and, therefore, (22) is an increasing function of m initially. This again manifests the notion of amplitude amplification. This probability P_m is maximized if $m\theta - \alpha = 0$, implying

$$m = \left[\frac{\alpha}{\theta}\right] = \text{the integral part of } \frac{\alpha}{\theta} .$$

When ℓ/N is small, we have

$$\theta = \sin^{-1}\left(\frac{2\sqrt{\ell(N-\ell)}}{N}\right)$$

$$= \sin^{-1}\left(2\sqrt{\frac{\ell}{N}}\left[1 - \frac{1}{2}\frac{\ell}{N} - \frac{1}{8}\left(\frac{\ell}{N}\right)^2 \pm \cdots\right]\right)$$

$$= 2\sqrt{\frac{\ell}{N}} + \mathcal{O}((\ell/N)^{3/2}),$$

$$\alpha = \cos^{-1}\sqrt{\frac{\ell}{N}} = \frac{\pi}{2} - \left[\sqrt{\frac{\ell}{N}} + \mathcal{O}((\ell/N)^{3/2})\right] .$$

Therefore

$$m \approx \frac{\frac{\pi}{2} - \left[\sqrt{\frac{\ell}{N}} + \mathcal{O}((\ell/N)^{3/2})\right]}{2\sqrt{\frac{\ell}{N}} + \mathcal{O}((\ell/N)^{3/2})}$$

$$= \frac{\pi}{4}\sqrt{\frac{N}{\ell}}\left[1 + \mathcal{O}\left(\frac{\ell}{N}\right)\right] . \tag{23}$$

Corollary 5 *The generalized Grover algorithm for multiobject search with operator U given by (18) has success probability $P_m = \cos^2(m\theta - \alpha)$ of reaching the state $|\widetilde{w}\rangle \in L$ after m iterations. For ℓ/N small, after $m = \frac{\pi}{4}\sqrt{N/\ell}$ iterations, the probability of reaching $|\widetilde{w}\rangle$ is close to 1.* □

The result (23) is consistent with Grover's original algorithm for single object search with $\ell = 1$, which has $m \approx \frac{\pi}{4}\sqrt{N}$; cf. (11).

Theorem 6 (Boyer, Brassard, Høyer and Tapp [3]). *Assume that ℓ/N is small. Then any search algorithm for ℓ objects, in the form of*

$$U_p U_{p-1} \ldots U_1 |w_I\rangle ,$$

where each U_j, $j = 1, 2, \ldots, p$, is a unitary operator and $|w_I\rangle$ is an arbitrary superposition state, takes in average $p = \mathcal{O}(\sqrt{N/\ell})$ iterations in order to reach the subspace L with a positive probability $P > \frac{1}{2}$ independent of N and ℓ. Therefore, the generalized Grover algorithm in Corollary 5 is of optimal order.

Proof. This is the major theorem in [3]; see Section 7 and particularly Theorem 8 therein. Note also the work of Zalka [12].

Unfortunately, if the number ℓ of good items is not known in advance, Corollary 5 does not tell us when to stop the iteration. This problem was addressed in [3], and in another way in [4]. In a related context an equation arose that was not fully solved in [3]. We consider it in the final segment of this paper. As in [3, §3], consider stopping the Grover process after j iterations, and, if a good object is not obtained, starting it over again from the beginning. From Corollary 5, the probability of success after j iterations is

$\cos^2(j\theta-\alpha)$. By a well-known theorem of probability theory, if the probability of success in one "trial" is p, then the expected number of trials before success is achieved will be $1/p$. (The probability that success is achieved on the kth trial is $p(1-p)^{k-1}$. Therefore, the expected number of trials is

$$\sum_{k=1}^{\infty} kp(1-p)^{k-1} = -p\sum_{k=1}^{\infty}\frac{d}{dp}(1-p)^k = -p\,\frac{d}{dp}\frac{1-p}{p}\,, \tag{24}$$

which is $1/p$.) In our case, each trial consists of j Grover iterations, so the expected number of iterations before success is

$$E(j) = j\cdot\sec^2(j\theta-\alpha)\,.$$

The optimal number of iterations j is obtained by setting the derivative $E'(j)$ equal to zero:

$$\begin{aligned} 0 = E'(j) &= \sec^2(j\theta-\alpha) + 2j\theta\sec^2(j\theta-\alpha)\tan(j\theta-\alpha),\\ 2j\theta &= -\cot((j\theta-\alpha))\,. \end{aligned} \tag{25}$$

(In [3, §3], this equation is derived in the form $4\vartheta j = \tan((2j+1)\vartheta)$, which is seen to be equivalent to (25) by noting that $\vartheta = \frac{\theta}{2} = \frac{\pi}{2}-\alpha$. Those authors then note that they have not solved the equation $4\vartheta j = \tan((2j+1)\vartheta)$ but proceed to use an ad hoc equation $z = \tan(z/2)$ with $z = 4\vartheta j$ instead.) Let us now approximate the solution j of (25) iteratively as follows. From (25),

$$\begin{aligned} &2j\theta\sin(j\theta-\alpha) + \cos(j\theta-\alpha) = 0\,,\\ &e^{2i(\theta j-\alpha)} = (i2\theta j+1)/(i2\theta j-1)\,, \end{aligned} \tag{26}$$

and by taking the logarithm of both sides, we obtain

$$2i(\theta j-\alpha) = 2i\pi n + i\arg\left(\frac{i2\theta j+1}{i2\theta j-1}\right) + \ln\left|\frac{i2\theta j+1}{i2\theta j-1}\right|\,, \tag{27}$$

for any integer n. Assume that ℓ/N is small so that j is large, but we are looking for the smallest such positive j. Note that the logarithmic term in (27) vanishes, and

$$\begin{aligned} \arg\left(\frac{i2\theta j+1}{i2\theta j-1}\right) &= -2\tan^{-1}\frac{1}{2\theta j}\\ &= 2\left[\sum_{q=0}^{\infty}\frac{(-1)^{q+1}}{2q+1}\left(\frac{1}{2\theta j}\right)^{2q+1}\right]\\ &= -\frac{1}{\theta j} + \mathcal{O}((\theta j)^{-3})\,; \end{aligned}$$

by taking $n=0$ in (27), we obtain

$$\begin{aligned} j &= \frac{1}{2i\theta}\left[2i\alpha - i\cdot\frac{1}{\theta j} + \mathcal{O}((\theta j)^{-3})\right]\\ &= \frac{1}{\theta}\left[\alpha - \frac{1}{2\theta j} + \mathcal{O}((\theta j)^{-3})\right]\,. \end{aligned} \tag{28}$$

The first order approximation j_1 for j is obtained by solving

$$j_1 = \frac{1}{\theta}\left(\alpha - \frac{1}{2\theta j_1}\right) ,$$
$$j_1^2 - \frac{1}{\theta}\,\alpha j_1 + \frac{1}{2\theta^2} = 0 ,$$
$$j_1 = \frac{1}{2\theta}(\alpha + \sqrt{\alpha^2 - 2}) . \tag{29}$$

Higher order approximations j_{n+1} for $n = 1, 2, \ldots$, may be obtained by successive iterations

$$j_{n+1} = \frac{1}{\theta}\left(\alpha - \tan^{-1}\frac{1}{2\theta j_n}\right)$$

based on (25). This process will yield a convergent solution j to (25).

Acknowledgments

We thank B.-G. Englert and M. Hillery for acquainting us with some of the literature of quantum computation, M. M. Kash for a technical discussion, and J. D. Malley and D. A. Lidar for comments on the manuscript.

References

1. E. Biham, O. Biham, D. Biron, M. Grassl, D.A. Lidar: Phys. Rev. A **60**, 2742 (1999)
2. D. Biron, O. Biham, E. Biham, M. Grassl, D.A. Lidar: 'Generalized Grover Search Algorithm for Arbitrary Initial Amplitude Distribution'. In: *Quantum Computing and Quantum Communications*, Lec. Notes. Comp. Sci. **1509** (Springer, New York 1998) pp. 140–147
3. M. Boyer, G. Brassard, P. Høyer, A. Tapp: Fortsch. Phys. **46**, 493 (1998)
4. G. Brassard, P. Høyer, A. Tapp: `quant-ph/9805082`, May 1998
5. E. Farhi, S. Gutmann: Phys. Rev. A **57**, 2403 (1998)
6. L.K. Grover: 'A Fast Quantum Mechanical Algorithm for Database Search'. In: *Proc. 28th Annual Symposium on the Theory of Computing* (ACM Press, New York 1996) pp. 212–218
7. L.K. Grover: Phys. Rev. Lett. **79**, 325 (1997)
8. L.K. Grover: Phys. Rev. Lett. **80**, 4329 (1998)
9. R. Jozsa: `quant-ph/9901021`, Jan. 1999
10. P. Shor: 'Algorithms for Quantum Computation: Discrete Logarithms and Factoring'. In: *Proc. 35th IEEE Symposium on the Foundations of Computer Sci.* (1994) pp. 124–134
11. P. Shor: SIAM J. Comp. **26**, 1484 (1997)
12. C. Zalka: `quant-ph/9711070`, Nov. 1997

New Tests of Macroscopic Local Realism

M.D. Reid

Summary. We show that quantum mechanics predicts an Einstein-Podolsky-Rosen paradox (EPR), and also a contradiction with local hidden variable theories, for photon number measurements which have limited resolving power, to the point of imposing an uncertainty in the photon number result which is macroscopic in absolute terms. We show how this can be interpreted as a failure of a new, very strong premise, called macroscopic local realism. We link this premise to the Schrodinger-cat paradox. Our proposed experiments ensure all fields incident on each measurement apparatus are macroscopic. We show that an alternative measurement scheme corresponds to balanced homodyne detection of quadrature phase amplitudes. The implication is that where either EPR correlations or failure of local realism is predicted for quadrature phase amplitude measurements, one can potentially perform a modified experiment which would lead to conclusions about the much stronger premise of macroscopic local realism.

1 Introduction

In 1935 Einstein, Podolsky and Rosen [1] (EPR) formulated an argument, now experimentally realised [2], in an attempt to show that quantum mechanics is an incomplete theory. The EPR argument is based on the premise of local realism. Bell [3] in 1966 showed that the premise of local realism (local hidden variable theories) was incompatible quantum mechanics. "Local realism" has now been essentially disproved by experiments [4] based on Bell's theorem or those of Greenberger, Horne and Zeilinger (GHZ) [3].

To date the EPR and Bell theorems and experimental efforts focus on measurements intrinsically microscopic, in that one requires to clearly distinguish between results (eigenvalues of the appropriate quantum operator) which are microscopically distinct. Previous results [5] have indicated failure of local realism for macroscopic systems, but the violations are still apparently only indicated where measurements must resolve microscopically different results, such as adjacent photon number or spin values. It is not clear whether one is testing a premise different to that tested in the microscopic experiments.

We propose a strategy for testing local realism at a macroscopic level, in the sense emphasised by Schrodinger [6,7] in his famous "cat" paradox and also by Leggett and Garg [8], where one considers macroscopically distinct outcomes. We define in section 2 the premise of "macroscopic local

H.J. Carmichael, R.J. Glauber, M.O. Scully (Eds.): LNP 561, pp. 176–186, 2001.

realism" [9], in such a way that it relates to the Schrodinger-cat example of macroscopically distinct states.

In section 3 we present an EPR argument based on the validity of "macroscopic local realism", which has not yet been questioned. We suggest that modifications to an experiment already performed by Ou et al [2] would realise this macroscopic EPR argument and would leave no logical alternative except to deny the validity of macroscopic local realism or else to accept the incompleteness of quantum mechanics, in the sense proposed by EPR.

In section 4 we present a quantum state which allows a violation of a Bell-inequality even where all uncertainties in measurements are macroscopic, and show how this implies a predicted failure of macroscopic local realism.

2 Definition of Macroscopic Local Realism

In 1935 Einstein, Podolsky and Rosen [1] defined "local realism". "Realism" implies that if one can predict with certainty the result of a measurement of a physical quantity at A, without disturbing the system A, then the results of the measurement were predetermined. One has an "element of reality" corresponding to this physical quantity. The element of reality is a variable which assumes one of a set of values which are the predicted results of the measurement. This value gives the result of the measurement, should it be performed. Locality states that events at A cannot, instantaneously, disturb a second system at B spatially separated from A. Taken together "local realism" implies that, if one can predict the result of a measurement of a physical quantity at A, by making a simultaneous measurement at B, then the result of the measurement at A is described by an element of reality.

EPR assumed quantum mechanics to be correct in predicting the existence of two spatially separated particles with correlated positions, and also correlated momenta. The key quantity in establishing the EPR argument is the precision (call the associated error Δ) to which the result of the potential position measurement at A can be inferred by the measurement at B. This specifies an associated indeterminacy (error Δ) in the "element of reality" x. In the original EPR gedanken example, Δ is zero. "Local realism" establishes two "elements of reality", x and p which simultaneously exist to give precisely the result of a potential position or momentum measurement, respectively. No description of this nature exists within quantum mechanics, since any quantum wavefunction gives an indeterminacy Δx and Δp in position and momentum respectively, in accordance with the uncertainty relation $\Delta x \Delta p \geq \hbar/2$. In this way, the EPR argument, based on the validity of "local realism", allows one to conclude that quantum mechanics is incomplete.

Macroscopic local realism [9] is defined as a premise stating the following. If one can predict the result of a measurement at A by performing a simultaneous measurement on a spatially separated system B, then the result of the measurement at A is predetermined but described by an element of reality

which has an indeterminacy in each of its possible values, so that only values macroscopically different to those predicted are excluded.

Macroscopic local realism is based on a "macroscopic locality", which states that measurements at a location B cannot instantaneously induce macroscopic changes (for example the dead to alive state of a cat, or a change between macroscopically different photon numbers) in a second system A spatially separated from B. Macroscopic local realism also incorporates a "macroscopic realism", since it implies elements of reality with (up to) a macroscopic indeterminacy. Suppose our "Schrodinger's cat [6]" is correlated with a second spatially separated system, for example a gun used to kill the cat. The strength of macroscopic local realism is understood when one realises that its rejection in this example means we cannot think of the cat as being either dead or alive, even though we can predict the dead or alive result of "measuring" the cat, without disturbing the cat, by measurement on the correlated spatially-separated second system.

3 An EPR Argument Based on Macroscopic Local Realism

We consider a new EPR situation, depicted in Figure 1, where uncertainties in "elements of reality" become macroscopic. The $\hat{a}_\pm$ and $\hat{b}_\pm$ are boson operators for four fields, described by the quantum state $|\psi\rangle$. Fields $\hat{a}_\pm$ and $\hat{b}_\pm$ propagate towards the spatially separated locations A and B respectively. We measure simultaneously at A and B the Schwinger spin operators

$$\begin{aligned}\hat{S}^A_\theta &= \hat{S}^A_x \cos\theta + \hat{S}^A_y \sin\theta \\ &= (\hat{a}^\dagger_+ \hat{a}_- \exp(-i\theta) + \hat{a}_+ \hat{a}^\dagger_- \exp(i\theta))/2 \end{aligned} \tag{1}$$

and

$$\begin{aligned}\hat{S}^B_\phi &= \hat{S}^B_x \cos\phi + \hat{S}^B_y \sin\phi \\ &= (\hat{b}^\dagger_+ \hat{b}_- \exp(-i\phi) + \hat{b}_+ \hat{b}^\dagger_- \exp(i\phi))/2 \end{aligned} \tag{2}$$

respectively, where $\hat{S}^A_x = (\hat{a}^\dagger_+ \hat{a}_- + \hat{a}^\dagger_- \hat{a}_+)/2, \hat{S}^A_y = (\hat{a}^\dagger_+ \hat{a}_- - \hat{a}^\dagger_- \hat{a}_+)/2i$ and $\hat{S}^A_z = (\hat{a}^\dagger_+ \hat{a}_+ - \hat{a}^\dagger_- \hat{a}_-)/2$, and similarly for the modes at B.

We propose to measure, at A, $\hat{S}^A_x$ or $\hat{S}^A_y$, by selecting $\theta = 0$ or $\theta = \pi/2$. At B the measurement is either S^B_x or S^B_y. In Figure 1 the measurement at A is performed by first mixing $\hat{a}_\pm$ using phase shifts and beam splitters to give two new fields $\hat{a}'_- = (\hat{a}_- - \hat{a}_+)/\sqrt{2}$ and $\hat{a}'_+ = i(\hat{a}_- + \hat{a}_+)/\sqrt{2}$. Similarly $\hat{b}_\pm$ are mixed to give outputs $\hat{b}'_\pm$. The fields a_+, b_+ are coherent states of large amplitude. The mixing is incorporated so that both fields, $\hat{a}'_\pm$ say at A, incident on the measuring apparatus are macroscopic. The final measurements are made with the transformations (using polarisers or beam splitters with variable transmission) $c_+ = \hat{a}'_+ \cos\theta/2 + \hat{a}'_- \sin\theta/2$ and $c_- = \hat{a}'_+ \sin\theta/2 - \hat{a}'_- \cos\theta/2$,

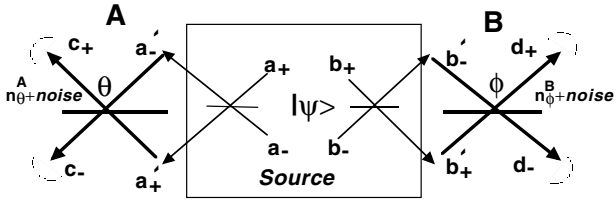

Fig. 1. Schematic diagram of the experimental arrangement used to give the two different tests, described in sections 3 and 4, of macroscopic local realism. The a_+ and b_+ represent strong coherent states. For the macroscopic EPR experiment of section 3, the quantum state is chosen to ensure that the output fields a_-, b_- are EPR correlated with respect to quadrature phase amplitudes

at A, and $d_+ = \hat{b}'_+ \cos\phi/2 + \hat{b}'_- \sin\phi/2$ and $d_- = \hat{b}'_+ \sin\phi/2 - \hat{b}'_- \cos\phi/2$, at B, followed by photodetection to give $\hat{S}^A_\theta = (\hat{c}^\dagger_+ \hat{c}_+ - \hat{c}^\dagger_- \hat{c}_-)/2$ and $\hat{S}^B_\phi = (\hat{d}^\dagger_+ \hat{d}_+ - \hat{d}^\dagger_- \hat{d}_-)/2$. The measurement is one of photon number, and we define $\hat{n}^A_\theta = 2\hat{S}^A_\theta = \hat{c}^\dagger_+ \hat{c}_+ - \hat{c}^\dagger_- \hat{c}_-$ and $\hat{n}_\phi = 2\hat{S}^B_\phi = \hat{d}^\dagger_+ \hat{d}_+ - \hat{d}^\dagger_- \hat{d}_-$.

In Figure 2 we demonstrate how the measurement $\hat{S}^A_\theta$ can be performed using an alternative arrangement, by introducing a relative phase shift θ and mixing with a 50/50 beam splitter to produce $\hat{c}'_\pm = (\hat{a}_+ \pm \hat{a}_- \exp(-i\theta))/\sqrt{2}$, followed by photodetection to give $\hat{S}^A_\theta = (\hat{c}'^\dagger_+ \hat{c}'_+ - \hat{c}'^\dagger_- \hat{c}'_-)/2$. It is to be clarified below that this measurement scheme corresponds to homodyne measurement [10] (used [2,11] to detect subshot noise, or "squeezed", radiation) of the quadrature phase amplitudes of a_- and b_-.

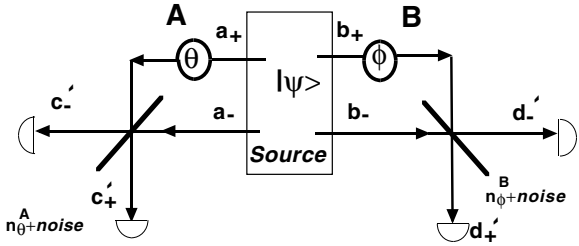

Fig. 2. An alternative arrangement used to measure n^A_θ and n^B_ϕ. Fields a_+, b_+ are in coherent states of large amplitude $\alpha = \beta = E$. This measurement scheme corresponds to balanced homodyne detection of the quadrature phase amplitudes $\hat{X}^A_\theta$ and $\hat{X}^B_\phi$ (defined in section 4), the a_+, b_+ being "local oscillator" fields

For certain systems the results for $\hat{S}^A_x$ and $\hat{S}^B_x$, and also $\hat{S}^A_y$ and $\hat{S}^B_y$, are predicted by quantum mechanics to be correlated, so that elements of

reality may be deduced for the physical quantities S_x^A and S_y^A respectively. We consider the relevant uncertainty relation for $\hat{S}_x^A$ and $\hat{S}_y^A$ [12].

$$\Delta\hat{S}_x^A \Delta\hat{S}_y^A \geq \left|\left\langle \hat{S}_z^A \right\rangle\right| /2 = (\hat{a}_+^\dagger \hat{a}_+ - \hat{a}_-^\dagger \hat{a}_-)/4 \tag{3}$$

Fields $\hat{a}_+$ and $\hat{b}_+$ are coherent states $|\alpha>$ and $|\beta>$ respectively with $\alpha = \beta = E$ real and large, so that $\hat{a}_+$ is replaced by c-number E giving

$$\begin{aligned} \hat{S}_x^A &= E\left(\hat{a}_- + \hat{a}_-^\dagger\right)/2 = E\hat{X}_0^A/2 \\ \hat{S}_y^A &= E\left(\hat{a}_- - \hat{a}_-^\dagger\right)/2i = E\hat{X}_{\pi/2}^A/2 \end{aligned} \tag{4}$$

where $\hat{X}_0^A = \hat{a}_- + \hat{a}_-^\dagger$ and $\hat{X}_{\pi/2}^A = \left(\hat{a}_- - \hat{a}_-^\dagger\right)/i$ are quadrature phase amplitudes. We denote the indeterminacy in the "element of reality" s_x^A by Δ_x, and in the "element of reality" s_y^A by Δ_y. In order to exclude the possibility that the "elements of reality" cannot be described by a quantum wavefunction, it is sufficient to establish (here $\left\langle \hat{a}_+^\dagger \hat{a}_+ \right\rangle >> \left\langle \hat{a}_-^\dagger \hat{a}_- \right\rangle$)

$$\Delta_x \Delta_y < \left|\left\langle \hat{S}_z^A \right\rangle\right| /2 = E^2/4 \tag{5}$$

The new feature of this EPR situation is the macroscopic nature of the minimum uncertainty product: $2\left|\left\langle \hat{S}_z^A \right\rangle\right| = E^2$ is a macroscopic (photon) number. The implication is that one need only use the premise of "macroscopic local realism", rather than local realism in its entirety, to arrive at the conclusion that quantum mechanics is incomplete. With "macroscopic local realism", one can only exclude the possibility of macroscopic changes to the system at A, as a result of measurements made at B. One can predict with some error (Δ_1 and Δ_2 say for the x and y spin components respectively) the result of the spin measurement at A. By macroscopic local realism, the spin is predetermined, but only to a precision which excludes values macroscopically different to those in the range predicted. The "element of reality" for the x component of spin has a range of possible values, given by $\pm\Delta_x$ where $\Delta_x = \Delta_1 + \delta$ and δ is microscopic or mesoscopic. The "element of reality" for the y component has an indeterminacy $\pm\Delta_y$ where $\Delta_y = \Delta_2 + \delta$. This can still be sufficient to imply the EPR criterion (5) since the uncertainty limit E^2 is a macroscopic number. We only require for example the differences $E/2 - \Delta_1$ and $E/2 - \Delta_2$ to be macroscopic numbers and we satisfy (5).

To meet the situation of a macroscopic EPR experiment, where macroscopic local realism is used in the EPR conclusions, one needs $\Delta_1\Delta_2 < \left|\left\langle \hat{S}_z^A \right\rangle\right| /2 = E^2/4$ satisfied, but where $2\left|\left\langle \hat{S}_z^A \right\rangle\right| = E^2$, and $2(E/2 - \Delta_1)$ and $2(E/2 - \Delta_2)$ are macroscopic photon numbers. From the point of view of performing an experiment which is convincingly macroscopic, the preference would be to satisfy these criteria where measurement errors, and therefore also Δ_1 and Δ_2, are also large (photon) numbers.

So far we have assumed the existence of the required correlations for the spin operators. Such correlated fields are predicted when a_-, b_- are fields with "EPR correlations" for quadrature phase amplitudes, and a_+, b_+ are strong coherent fields. EPR correlations for quadrature phase amplitudes were defined in [12], and have received much interest as fields enabling quantum teleportation for continuous variables [13]. EPR fields may be generated by the parametric interaction $H = i\hbar\kappa\left(\hat{a}_-^\dagger \hat{b}_-^\dagger - \hat{a}_- \hat{b}_-\right)$, where here κ represents the strength of nonlinear interaction. This represents the logical choice for the quantum state $|\phi\rangle$ in Figure 1. It is also possible to generate the required EPR correlations from a single-mode squeezed state passed through a 50/50 beam splitter [12,13].

Using the parametric example, we consider the quadrature phase amplitudes $\hat{X}_0^A, \hat{X}_{\pi/2}^A$, and $\hat{X}_0^B, \hat{X}_{\pi/2}^B$ where $\hat{X}_0^B = b_- + b_-^\dagger$ and $\hat{X}_{\pi/2}^B = \left(\hat{b}_- - \hat{b}_-^\dagger\right)/i$. With vacuum inputs, the output solutions after a time t, for $\kappa t \to \infty$, satisfy $\hat{X}_0^A(t) = \hat{X}_0^B(t)$ and $\hat{X}_{\pi/2}^A(t) = -\hat{X}_{\pi/2}^B(t)$, indicating a maximum correlation[13] between the results of measurements $\hat{X}_0^A(t)$ and $\hat{X}_0^B(t)$, and also $\hat{X}_{\pi/2}^A(t)$ and $\hat{X}_{\pi/2}^B(t)$. The $\hat{a}_+, \hat{b}_+$ fields are coherent states $|\alpha\rangle$ and $|\beta\rangle$ of large intensity so that $\hat{S}_x^A = \alpha\hat{X}_0^A(t)/2$, $\hat{S}_x^B = \beta\hat{X}_0^B(t)/2$, $\hat{S}_y^A = \alpha\hat{X}_{\pi/2}^A(t)/2$ and $\hat{S}_y^B = \beta\hat{X}_{\pi/2}^B?(t)/2$, and we have the required correlations. The reader is referred to articles [2,12,9] for information on the evaluation of Δ_1 and Δ_2.

The macroscopic EPR experiment performed with results in accordance with quantum mechanics would logically lead to the conclusion that: either macroscopic local realism is invalid; or that quantum mechanics is incomplete. EPR experiments have not widely been considered important in their own right, since previously they have been based on local realism, a premise dismissed by Bell inequality experiments. In our macroscopic example this is not correct. The validity of macroscopic local realism has not been tested.

The macroscopic EPR experiment has been performed in a partly satisfactory way by Ou et al [2], with the arrangement of Figure 2. For a conclusive result the arrangement of Figure 1 is preferred. The experimental scheme of Ou et al suffers the disadvantage that fields a_-, b_- are microscopic. This is irrelevant in that the quantity measured, and to which the elements of reality relate, is not $\hat{X}_\theta^A$ but $\hat{S}_\theta^A$. Nevertheless, the microscopic nature of $\hat{a}_-, \hat{b}_-$ incident on the measurement apparatus gives the impression of a microscopic experiment. The scheme of Figure 1 where both fields incident on the measurement apparatus are macroscopic is more transparent, making it clear that the "local oscillator" fields a_+, b_+ form part of the system. It is also essential to ensure measurement events (the selection of θ or ϕ) at A and B causally separated, as in delayed-choice Bell inequality experiments [4]. Since a wide variety of squeezing experiments have been performed, including squeezing in pulsed fields, an experimental realisation of the macroscopic EPR experiment would seem very feasible.

4 A Direct Test of Macroscopic Local Realism: Bell Inequalities Based on Macroscopic Local Realism

We prove that for coarse measurements with macroscopic uncertainties, Bell inequalities can be derived using only the premise of macroscopic local realism [14]. Our proposed experiment is again depicted in Figure 1, except that the quantum state $|\phi>$ will be chosen differently. The parametric interaction used as a source for EPR correlations in the Ou et al experiment is not directly suitable for this experiment, as in this case a positive Wigner function exists. This positive Wigner function can act as a local hidden variable theory to describe the quantum predictions [3], and thus prevent a violation of a Bell inequality as we derive here. With an appropriate choice of quantum state then, we measure simultaneously at A and B the Schwinger operators $\hat{S}_\theta^A$ and $\hat{S}_\phi^B$. The result for the photon number differences $\hat{n}_\theta^A$ and $\hat{n}_\phi^B$ is of the form $n+noise$, where n is the result in the absence of the noise. We introduce a random noise function (Gaussian distribution of standard deviation σ) at each of A and B, and define probabilities such as $P^A(noise \geq x)$, that the $noise$ at A is greater than or equal to the value x.

The results of measurements are classified as $+1$ if the photon number difference is positive or zero, and -1 otherwise. We determine the following probability distributions: $P_+^A(\theta)$ for obtaining $+$ at A; $P_+^B(\phi)$ for obtaining $+$ at B; and $P_{++}^{AB}(\theta,\phi)$ the joint probability of $+$ at both A and B.

We define the probability $P_{ij}^{0,AB}(\theta,\phi)$ for obtaining results i and j respectively upon joint measurement of $\hat{n}_\theta^A$ at A, and $\hat{n}_\phi^B$ at B, in the absence of the applied noise σ. With noise present, measured probabilities become

$$P_{++}^{AB}(\theta,\phi) = \sum_{i,j=-\infty}^{\infty} P_{ij}^{0,AB}(\theta,\phi) P^A(noise \geq -i) P^B(noise \geq -j) \qquad (6)$$

Local realism as defined by Einstein-Podolsky-Rosen, Bell and Clauser-Horne [1] implies the well known expression.

$$P_{ij}^{0,AB}(\theta,\phi) = \int \rho(\lambda) \quad p_i^A(\theta,\lambda) p_j^B(\phi,\lambda) \quad d\lambda \qquad (7)$$

Local realism implies a set of elements of reality, or hidden variables λ (with probability distribution $\rho(\lambda)$), not specified by quantum theory. For our experiment, a precise prediction of $\hat{n}_\theta^A$ is not possible given a measurement at B, for any choice ϕ at B. The elements of reality then do not take on definite values and local realism is only sufficient to imply a probability $p_i^A(\theta,\lambda)$ for the result i of the measurement $\hat{n}_\theta^A$, for a given λ. The independence of $p_i^A(\theta,\lambda)$ on ϕ is based on the locality assumption.

With macroscopic local realism the locality condition is relaxed, but only up to the level of M photons, where M is not macroscopic, by maintaining

that the measurement at B cannot instantaneously change the result at A by an amount exceeding M photons. Where our predicted result at A is $i^{'}$ using local realism, macroscopic local realism allows the result to be $i = i^{'} + m_A$ where m_A can be any number not macroscopic. Importantly, while $i^{'}$ is not dependent on the choice ϕ at B, the value m_A which is not macroscopic can be. The macroscopic local realism assumption is that the conditional probability $p_i^A(\theta, \lambda)$ in equation (7) is expressible as the convolution:

$$p_i^A(\theta, \phi, \lambda) = \sum_{m_A=-M}^{+M} p_{m_A}^A(i^{'}, \theta, \phi, \lambda) p_{i'=i-m_A}^A(\theta, \lambda). \tag{8}$$

The original local probability $p_{i'}^A(\theta, \lambda)$ can be convolved with a microscopic nonlocal probability function $p_{m_A}^A(i^{'}, \theta, \phi, \lambda)$, the only restriction being that the nonlocal distribution does not provide macroscopic perturbations, so that the probability of getting a nonlocal change outside the range $m_A = -M, ..., +M$ is zero. Equivalently we must have

$$\sum_{m_A=-M}^{M} p_{m_A}^A(i^{'}, \theta, \phi, \lambda) = 1. \tag{9}$$

We substitute the macroscopic locality assumption (8) into (7) to obtain the prediction for the measured probabilities (6). Recalling $i = i' + m_A$, $j = j' + m_B$ we change the i, j summation to one over i', j' to get

$$\begin{aligned} P_{++}^{AB}(\theta, \phi) = & \sum_{i',j'=-\infty}^{\infty} \int \rho(\lambda) p_{i'}^A(\theta, \lambda) \\ & \times \left[\sum_{m_A=-M}^{M} p_{m_A}^A(i^{'}, \theta, \phi, \lambda) p_{j'}^B(\phi, \lambda) P^A(noise \geq -(i' + m_A)) \right] \\ & \times \left[\sum_{m_B=-M}^{M} p_{m_B}^B(j^{'}, \phi, \theta, \lambda) P^B(noise \geq -(j' + m_B)) \right] d\lambda \end{aligned} \tag{10}$$

We assume that the noise function *noise* is slowly varying over the microscopic (or mesoscopic) range $-m_A, .. + m_A$ for which nonlocal perturbations are possible according to macroscopic local realism:

$$\begin{aligned} & \sum_{m_A=-M}^{M} p_{m_A}^A(i^{'}, \theta, \phi, \lambda) P^A(noise \geq -(i' + m_A)) \\ & \quad \approx P^A(noise \geq -i') \sum_{m_A=-M}^{M} p_{m_A}^A(i^{'}, \theta, \phi, \lambda). \end{aligned} \tag{11}$$

This is only valid if σ is macroscopic. Using (11), one simplifies to get the final form $P_{++}^{AB}(\theta, \phi) = \sum_{i',j'} \int \rho(\lambda) p_{i'}^A(\theta, \lambda) p_{j'}^B(\phi, \lambda) d\lambda \times P^A(noise \geq$

$-i')P^B(noise \geq -j')$. This prediction of the hidden variable theory is now given in a (local) form like that of (7), from which Bell- Clauser-Horne inequalities [3] follow, for example:

$$S = \frac{P^{AB}_{++}(\theta,\phi) - P^{AB}_{++}(\theta,\phi') + P^{AB}_{++}(\theta',\phi) + P^{AB}_{++}(\theta',\phi')}{P^A_+(\theta') + P^B_+(\phi)} \leq 1. \qquad (12)$$

Violation of Bell inequalities (12) with macroscopic noise terms (σ macroscopic) is evidence of a failure of macroscopic local realism. We propose a quantum state with this property (I_0 is a modified Bessel function, $r_0 = 1.1$).

$$|\psi\rangle = [I_0(2r_0^2)]^{-1/2}|\alpha>_{a_+}|\beta>_{b_+}\left(\sum_{n=0}^{\infty}\frac{(r_0^2)^n}{n!}|n>_{a_-}|n>_{b_-}\right). \qquad (13)$$

$|\alpha>_{a_+}$ and $|\beta>_{b_+}$ are coherent states with α, β real and large. $|n>_k$ is a Fock state for field k. The fields $\hat{a}_-$ and $\hat{b}_-$ are microscopic and are generated in a pair-coherent state [15]. The quantum prediction for (13) is shown in Figure 3. Violations of the Bell inequality (12) in the absence of *noise* are shown in curve (a). Violations are still possible (curve (b)) in the presence of increasingly larger absolute noise σ, simply by increasing $\alpha = \beta = E$. This violation of the Bell inequality (12) with macroscopic noise σ implies the failure of macroscopic local realism.

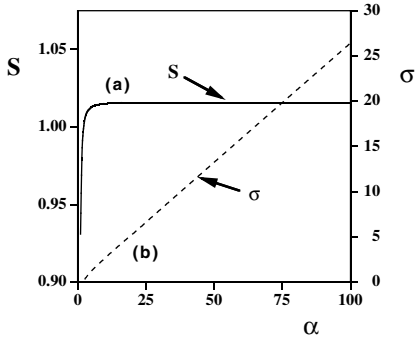

Fig. 3. (**a**) S versus $\alpha = \beta$, for $\theta = 0, \phi = -\pi/4, \theta' = \pi/2, \phi' = -3\pi/4$ for the quantum state (13) with no noise present. (**b**) Maximum noise σ still giving a violation of the Bell inequality (12), versus α

The large α,β limit is crucial in determining whether the violation of macroscopic local realism will occur. We see from (1) and (2) that (letting $\alpha = \beta = E$) $\hat{S}^A_\theta = E\hat{X}^A_\theta/2$ and $\hat{S}^B_\phi = E\hat{X}^B_\phi/2$, where $\hat{X}^A_\theta = \hat{a}_- exp(-i\theta) + \hat{a}^\dagger_- exp(i\theta)$ and $\hat{X}^B_\phi = \hat{b}_- exp(-i\phi) + \hat{b}^\dagger_- exp(i\phi)$ are the quadrature phase amplitudes of fields $\hat{a}_-$ and $\hat{b}_-$. Violations of Bell inequalities for measurements $\hat{X}^A_\theta$, $\hat{X}^B_\phi$ on state (13) have recently been predicted [16], confirming Figure 3(a). It is always the case that such violations of a Bell inequality will vanish when Gaussian noise of sufficiently large standard deviation σ_0 is added to the measurements $\hat{X}^A_\theta, \hat{X}^B_\phi$. With $\alpha = E$ sufficiently large, this corresponds

to a macroscopic noise value of $E\sigma_0$ in the photon number measurement $\hat{n}_\theta^A$. Therefore any state $|\psi\rangle$ which shows a failure of local realism for measurements $\hat{X}_\theta^A$ and $\hat{X}_\phi^B$ will also indicate a violation of macroscopic local realism, provided α, β are large. This is relevant since other such states have been recently predicted [17], such as an odd or even coherent state passed through a beam splitter and parametric interaction [16].

This Bell inequality test is logically more straightforward than the EPR test, and is stronger, potentially leading to the rejection of macroscopic local realism outright. Appropriate states however are likely to be difficult to prepare. Unlike the EPR test it becomes strictly necessary to ensure the measurement uncertainty in photon number is macroscopic in absolute terms, because of assumption (11).

References

1. A. Einstein, B. Podolsky, N. Rosen: Phys. Rev. **47**, 777 (1935)
2. Z.Y. Ou, S.F. Pereira, H.J. Kimble, K.C. Peng: Phys. Rev. Lett. **68**, 3663 (1992)
3. J.S. Bell: Physics **1**, 195 (1965); J.F. Clauser, A. Shimony: Rep. Prog. Phys. **41**, 1881 (1978); D.M. Greenberger, M. Horne, A. Zeilinger: In: *Bell's Theorem, Quantum Theory and Conceptions of the Universe*, ed. by M. Kafatos (Kluwer, Dordrecht, The Netherlands 1989), p. 69
4. A. Aspect, P. Grangier, G. Roger: Phys. Rev. Lett. **49**, 91 (1982); A. Aspect, J. Dalibard, G. Roger: *ibid.* **49**, 1804 (1982); W. Gregor, T. Jennewein, A. Zeilinger: Phys. Rev. Lett. **81**, 5039 (1998)
5. N.D. Mermin: Phys. Rev. D **22**, 356 (1980); P.D. Drummond: Phys. Rev. Lett. **50**, 1407 (1983); A. Garg, N.D. Mermin: Phys. Rev. Lett. **49**, 901 (1982) S.M. Roy, V. Singh: Phys. Rev. Lett. **67**, 2761 (1991); A. Peres: Phys. Rev. A **46**, 4413 (1992); M.D. Reid, W.J. Munro: Phys. Rev. Lett. **69**, 997 (1992); G.S. Agarwal: Phys. Rev. A **47**, 4608 (1993); D. Home, A.S. Majumdar: Phys. Rev. A **52**, 4959 (1995); W.J. Munro, M.D. Reid: Phys. Rev. A **47**, 4412 (1993); C. Gerry: Phys. Rev. A **54**, 2529, (1996); N.D. Mermin: Phys. Rev. Lett. **65**, 1838 (1990); B.J. Sanders: Phys. Rev. A **45**, 6811, (1992)
6. E. Schrödinger: Naturwissenschaften **23**, 812 (1935)
7. C. Monroe, D.M. Meekhof, B.E. King, D.J. Wineland: Science **272**, 1131 (1996); M. Brune, E. Hagley, J. Dreyer, X. Maitre, A. Maali, C. Wunderlich, J.M. Raimond, S. Haroche: Phys. Rev. Lett. **77**, 4887 (1996); M.W. Noel, C.R. Stroud: Phys. Rev. Lett. **77**, 1913 (1996)
8. A.J. Leggett, A. Garg: Phys. Rev. Lett. **54**, 857 (1985)
9. M.D. Reid: Europhys. Lett. **36**, 1 (1996); M.D. Reid: Quantum Semiclass. Opt. **9**, 489 (1997); M.D. Reid, P. Deuar: Ann. Phys. **265**, 52 (1998)
10. H.P. Yuen, V.W.S. Chan: Opt. Lett. **8**, 177 (1983)
11. M.D. Levenson, R.M. Shelby, M.D. Reid, D.F. Walls: Phys. Rev. Lett. **57**, 2473 (1986)
12. M.D. Reid: Phys. Rev. A **40**, 913 (1989)
13. A. Furasawa, J. Sorensen, S. Braunstein, C. Fuchs, H. Kimble, E. Polzik: Science **282**, 706 (1998)
14. M.D. Reid: Phys. Rev. Lett. in press

15. G.S. Agarwal: Phys. Rev. Lett. **57**, 827, (1986); M.D. Reid, L. Krippner: Phys. Rev. A **47**, 552 (1993)
16. A. Gilchrist, P. Deuar, M.D. Reid: Phys. Rev. Lett. **80**, 3169 (1998); Phys. Rev. A **60**, 4259 (1999)
17. B. Yurke, M. Hillery, D. Stoler: quant-ph/9909042; W.J. Munro, G.J. Milburn: Phys. Rev. Lett. **81**, 4285 (1998); W.J. Munro: Phys. Rev. A **59**, 4197 (1999)

Teleportation Criteria: Form and Significance

T.C. Ralph

Summary. Our criteria for continuous variable quantum teleportation [T.C. Ralph and P.K. Lam, Phys. Rev. Lett. **81**, 5668 (1998)] take the form of sums, rather than products, of conjugate quadrature measurements of the signal transfer coefficients and the covariances between the input and output states. We discuss why they have this form. We also discuss the physical significance of the covariance inequality.

Recently we have proposed criteria for the characterization of continuous variable quantum teleportation [1]. It was shown that for any classical teleportation scheme (i.e. where no entanglement is shared) the following inequalities cannot be violated for minimum uncertainty Gaussian input states:

$$T_t = T_s^+ + T_s^- \leq 1 \tag{1}$$

$$V_t = \frac{1}{2}(V_{cv}^+ + V_{cv}^-) \geq 1 \tag{2}$$

Here T_s^+ (T_s^-) are the amplitude (phase) quadrature signal transfer functions from the input to output fields of the teleporter defined by

$$T_s^\pm = \frac{\mathrm{SNR}_{\mathrm{out}}^\pm}{\mathrm{SNR}_{\mathrm{in}}^\pm} \tag{3}$$

where the SNR are the signal to noise ratios of small classical test signals. The RF frequency test signals are placed on each quadrature of the input beam. The conditional variances between the input and output for each of the quadrature amplitudes are defined by

$$V_{cv}^\pm(\omega) = V_{\mathrm{out}}^\pm(\omega)(1 - C^\pm(\omega)) \tag{4}$$

where $V_{\mathrm{out}}^\pm(\omega) = \langle |\delta X_{\mathrm{out}}^\pm(\omega)|^2 \rangle$ are the standard spectral variances for the amplitude (δX^+) and phase (δX^-) quadrature fluctuations of the output state assessed at some RF frequency ω. The correlation function, C, is defined by

$$C^\pm = \frac{|\langle \delta X_{\mathrm{in}}^\pm \delta X_{\mathrm{out}}^\pm \rangle|^2}{V_{\mathrm{in}}^\pm V_{\mathrm{out}}^\pm} \tag{5}$$

and is directly related to the SNR's via $C^\pm = T_s^\pm$ [2] when cross-coupling between the quadratures can be ignored [3]. The criteria in (1) and (2) are

H.J. Carmichael, R.J. Glauber, M.O. Scully (Eds.): LNP 561, pp. 187–192, 2001.

semi-independent. Violation of either inequality indicates entanglement is present. A strong test of teleportation would require both inequalities be violated simultaneously.

Although there is no question of the validity of the inequalities in (1) and (2) there has been some discussion about their significance [4]. In particular, it has been queried as to why sums are formed of the conjugate quadrature measurements instead of the "usual" procedure of forming products (cf: Heisenberg uncertainty principle). In the following we justify the form of T_t and V_t by deriving them from more fundamental expressions.

Suppose the quantum fluctuations of our input field are described in the usual way by the zero-mean annihilation operator $\delta a_{\rm in}$ whilst our output field is described by $\delta a_{\rm out}$. The amplitude and phase quadrature fluctuations of the input field are defined respectively by $\delta X^+_{\rm in} = \delta a_{in} + \delta a^\dagger_{in}$ and $\delta X^-_{\rm in} = i(\delta a^\dagger_{in} - \delta a_{in})$. The quadrature fluctuations of the output field can be described by

$$\delta X^\pm_{\rm out} = Y^\pm \delta X^\pm_{\rm in} + Z^\pm \delta X^\pm_N \tag{6}$$

where $Y^\pm$ and $Z^\pm$ are c-numbers and $\delta X^\pm_N$ includes all added noise sources. Here again we will assume there is no cross coupling between the amplitude and phase quadratures of the input and output [2],[3]. Then

$$V^\pm_{\rm out} = |Y^\pm|^2 V^\pm_{\rm in} + |Z^\pm|^2 V^\pm_N \tag{7}$$

and

$$T^\pm_s = \frac{V^\pm_{\rm in}|Y^\pm|^2}{|Y^\pm|^2 V^\pm_{\rm in} + |Z^\pm|^2 V^\pm_N} \tag{8}$$

Because the information used to produce the output field traveled through a classical channel the added noise terms must be sufficient to ensure the generalized uncertainty principle is maintained for the photo-currents in the classical channels [2],[5], this implies

$$\frac{|Z^+|^2}{|Y^+|^2} V^+_N \frac{|Z^-|^2}{|Y^-|^2} V^-_N \geq 1 \tag{9}$$

For a minimum uncertainty input state ($V^+_{\rm in} V^-_{\rm in} = 1$) and using (8) the inequality in (9) reduces to that of (1). Thus we see that the origin of the signal transfer inequality is, in fact, the standard product uncertainty. In quantum teleportation the shared entanglement acts as a "quantum key" that enables the inaccessible (because of the added noise) quantum information on the classical channel to be retrieved [1,6]. The noise on the output field can then be less than the minimum required for the classical channel thus allowing the inequality to be violated.

We now consider how one might generalize the conditional variance used in QND [2,7] to teleportation. In QND one is only interested in how well the properties of one quadrature are preserved. In teleportation we wish to quantify how well the entire state is preserved. As we are working in the

Heisenberg picture, in which it is the operators which evolve in time, this is equivalent to quantifying how well the field operator, a, is preserved. Caves [8] defined the variance of the field operator as

$$V_f = \frac{1}{2}\langle \delta a^\dagger \delta a + \delta a \delta a^\dagger \rangle \tag{10}$$

Following the standard procedure for constructing a conditional variance we are thus motivated to consider the field correlation

$$C_f = \frac{|\frac{1}{2}\langle \delta a^\dagger_{\rm out}\delta a_{\rm in} + \delta a_{\rm in}\delta a^\dagger_{\rm out} + \delta a_{\rm out}\delta a^\dagger_{\rm in} + \delta a^\dagger_{\rm in}\delta a_{\rm out}\rangle|^2}{\langle \delta a^\dagger_{\rm out}\delta a_{\rm out} + \delta a_{\rm out}\delta a^\dagger_{\rm out}\rangle\langle \delta a^\dagger_{\rm in}\delta a_{\rm in} + \delta a_{\rm in}\delta a^\dagger_{\rm in}\rangle} \tag{11}$$

If the fields are identical, i.e. $\delta a_{\rm in} = \delta a_{\rm out}$, then $C_f = 1$. If the fields are completely independent, i.e. $[a_{\rm out}, a^\dagger_{\rm in}] = [a_{\rm in}, a^\dagger_{\rm out}] = 0$, then $C_f = 0$. We then construct the field conditional variance as

$$V_{cvf} = \langle \delta a^\dagger_{\rm out}\delta a_{\rm out} + \delta a_{\rm out}\delta a^\dagger_{\rm out}\rangle(1 - C_f) \tag{12}$$

Using $\delta a = \frac{1}{2}(\delta X^+ + i\delta X^-)$, we can rewrite (12) as

$$\begin{aligned} V_{cvf} &= \frac{1}{2}(V^+_{\rm out} + V^-_{\rm out} - \frac{|\langle \delta X^+_{\rm out}\delta X^+_{\rm in} + \delta X^-_{\rm out}\delta X^-_{\rm in}\rangle|^2}{V^+_{\rm in} + V^-_{\rm in}}) \\ &= \frac{1}{2}(V^+_{\rm out} + V^-_{\rm out} - \frac{(\sqrt{T_s^+ V^+_{\rm out} V^+_{\rm in}} + \sqrt{T_s^- V^-_{\rm out} V^-_{\rm in}})^2}{V^+_{\rm in} + V^-_{\rm in}}) \end{aligned} \tag{13}$$

For independent fields $V_{cvf} \geq 1$. If we assume that $Y^+ = Y^-$, i.e. the teleporter acts symmetrically on the two quadratures of the input field, then it is straightforward to show that in fact

$$V_{cvf} = V_t \tag{14}$$

Thus the inability of classical teleportation schemes to violate the inequality of (2) can be seen as showing that in a certain sense the input and output remain independent fields. The sum form of the inequality is seen to have its origin in the structure of the field operator as a sum of the two quadrature components. For asymmetric manipulations of the input quadratures ($Y^+ \neq Y^-$) we find $V_{cvf} \neq V_t$. Our analysis suggests that V_{cvf} may be the more appropriate measure when quantifying such asymmetric schemes.

We now discuss the physical significance of violating the field covariance inequality (2). It has been argued by some that our criteria are too stringent because the presence of entanglement in the teleporter can be demonstrated without exceeding our inequalities. For example the field covariance of a lossless, symmetric teleportation scheme which has an entanglement resource V_{ent} ($V_{ent} = 1$ represents no entanglement whilst $V_{ent} \to 0$ represents maximal entanglement) and a gain of λ (assumed real) is given by [1,9]

$$V_{cvf} = \frac{1}{2}(1+\lambda)^2 V_{ent} + \frac{1}{2}(1-\lambda)^2 \frac{1}{V_{ent}} \tag{15}$$

Consider the case of unity gain ($\lambda = 1$). Without entanglement ($V_{ent} = 1$) we find $V_{cvf} = 2$. Only by introducing entanglement ($V_{ent} < 1$) can we obtain $V_{cvf} < 2$. However it is not till we have introduced more than 50% entanglement ($V_{ent} < .5$) that we can obtain $V_{cvf} < 1$ as per (2). Indeed it is in this intermediate region, where $2 > V_{cvf} > 1$, that the only experimental demonstration of continuous variable teleportation presently lies [10]. One may ask if there is any *qualitative* difference between the types of correlation that can be observed when $2 > V_{cvf} > 1$ and those that can be observed when $1 > V_{cvf} > 0$. If qualitative differences exists then the more stringent definition of teleportation may be justified. We now give brief examples which illustrate that such differences do exist.

Entanglement Requirements. Firstly, it should be pointed out that true EPR entanglement is not required to reach the intermediate region. A single-mode squeezed beam, split on a 50:50 beamsplitter, is a sufficient resource [11]. Although entangled [12], the beams so produced will exhibit non-classical correlations on only one quadrature with classical correlations on the conjugate quadrature. The signature of true EPR entanglement is non-classical correlations on both quadratures. The field covariance for a beam teleported with such a resource is given by [13]

$$V_{cvf} = \frac{1}{4}(1+\lambda)^2(1+V_s) + \frac{1}{4}(1-\lambda)^2(1+\frac{1}{V_s}) \tag{16}$$

where V_s is the level of single-mode squeezing in the resource. The value of Eq.(16) can never fall below 1 for any level of the squeezing or gain. Only when non-classical correlations can be observed on both quadratures can the field covariance fall below 1. Thus only with true EPR entanglement can we observe $V_{cvf} < 1$.

Preservation of Non-classical Statistics. It is clearly of interest to ask under what conditions can teleportation of states with a non-classical character result in output states which retain that non-classical character. Suppose our input state is squeezed along the amplitude quadrature. We may ask under what conditions will the output still be squeezed. For symmetric, lossless teleportation the spectral variance of the output amplitude quadrature is given by [1]

$$\begin{aligned} V^+_{out} &= \frac{1}{2}(1+\lambda)^2 V_{ent} + \frac{1}{2}(1-\lambda)^2 \frac{1}{V_{ent}} + \lambda^2 V^+_{in} \\ &= V_{cvf} + \lambda^2 V^+_{in} \end{aligned} \tag{17}$$

It is immediately clear from Eq.(17) that it is impossible for squeezing to appear on the output unless $V_{cvf} < 1$ is satisfied. In the limit of very strong squeezing ($V^+_{sq} \to 0$) squeezing on the output is guaranteed when the field covariance is less than 1, however in general a field covariance less than 1 is a necessary but not sufficient condition for squeezing to be preserved.

Preservation of Entanglement. Of even greater importance for quantum information applications is to ask under what conditions entanglement be-

tween two systems, of which one has been teleported, is preserved. We have recently quantified this question by looking at the violation of a Bell-type inequality [14]. In particular we looked at the value of the Clauser-Horne variable [15,16], S, between entangled photon beams when one of the beams is teleported using a continuous variable method. Local realistic hidden variable theories place the following restriction on the value of S; $S \leq 1$. Quantum mechanical states allow S to violate this inequality. The maximum violation occurs for non-maximally entangled states [17] and has the value; $S = 1.5$ [18]. Our result (in the limit of no loss) can be written

$$S = \frac{\frac{1}{2}(V_{cvf} - 1) + \lambda^2(S_i + \frac{1}{2})}{(V_{cvf} - 1) + 2\lambda^2} \tag{18}$$

where S_i is the value of S which would be obtained between the beams before teleportation. Eq.(18) shows that if $V_{cvf} < 1$ and $S_i = 1.5$ then $S > 1$. That is, provided that the entangled beams show a maximum violation of S before teleportation, then some violation of local realism is guaranteed after teleportation if the field covariance falls below 1. As for squeezing this condition is necessary, but not sufficient if S_i does not have its maximum value.

We have derived the criteria for continuous variable teleportation from more fundamental arguments. We have shown by example that the properties that can be exhibited by the teleported system when the strong inequality $V_{cvf} < 1$ is satisfied are qualitatively more "quantum mechanical" than in the region $2 < V_{cvf} < 1$. We have also noted that the strong inequality can only be satisfied by using true EPR entanglement in the teleporter.

Acknowledgment

This work was supported by the Australian Research Council.

References

1. T.C. Ralph, P.K. Lam: Phys. Rev. Lett. **81**, 5668 (1998)
2. J.-Ph. Poizat, J.-F. Roch, P. Grangier: Ann. Phys. Fr. **19**, 265 (1993)
3. Cross coupling between the quadratures can always be eliminated by a suitable quadrature phase rotation.
4. P. van Loock, S.L. Braunstein: LANL quant-ph/9902030 (1999); S.L. Braunstein, C.A. Fuchs, H.J. Kimble: LANL quant-ph/9910030 (1999)
5. E. Arthurs, M.S. Goodman: Phys. Rev. Lett. **24**, 2447 (1988)
6. D. Deutsch, P. Hayden: LANL quant-ph/9906007 (1999)
7. M.J. Holland, M.J. Collett, D.F. Walls: M.D. Levenson, Phys. Rev. A **42**, 2995 (1990)
8. C.M. Caves: Phys. Rev. D **26**, 1817 (1982)
9. T.C. Ralph, P.K. Lam, R.E.S. Polkinghorne: J. Opt. B **1**, 483 (1999)

10. A. Furusawa, J.L. Sorensen, S.L. Braunstein, C.A. Fuchs, H.J. Kimble, E.S. Polzik: Science **282**, 706 (1998)
11. P. van Loock, S.L. Braunstein: Phys. Rev. Lett. A **61**, 010302(R) (2000)
12. Y. Aharonov *et al.*: Ann. Phys. (N.Y.) **39**, 498 (1966)
13. T.C. Ralph: Phys. Rev. A **61**, 044301 (2000)
14. R.E.S. Polkinghorne, T.C. Ralph: Phys. Rev. Lett. **83**, 2095 (1999)
15. D.F. Walls, G. J. Milburn: *Quantum Optics* (Springer-Verlag, Berlin 1994)
16. J.F. Clauser, M.A. Horne: Phys. Rev. D **10**, 526 (1974)
17. P.H. Eberhard: Phys. Rev. A **47** R747 (1993)
18. R.E.S. Polkinghorne: Department of Physics, University of Queensland, private communication (1999)

Quantum Information Processing Based on Cavity QED with Mesoscopic Systems*

Mikhail Lukin, Michael Fleischhauer, and Atac Imamoğlu

1 Introduction

Recent developments in quantum communication and computing [1–3] stimulated an intensive search for physical systems that can be used for coherent processing of quantum information. It is generally believed that quantum entanglement of distinguishable quantum bits (qubits) is at the heart of quantum information processing. Significant efforts have been directed towards the design of elementary logic gates, which perform certain unitary processes on pairs of qubits. These gates must be capable of generating specific, in general entangled, superpositions of the two qubits and thus require a strong qubit-qubit interaction. Using a sequence of single and two-bit operations, an arbitrary quantum computation can be performed [2].

Over the past few years many systems have been identified for potential implementations of logic gates and several interesting experiments have been performed. Proposals for strong qubit-qubit interaction involve e.g. the vibrational coupling of cooled trapped ions [4], near dipole-dipole or spin-spin interactions such as in nuclear magnetic resonance [5], collisional interactions of confined cooled atoms [6] or radiative interactions between atoms in cavity QED [7]. The possibility of simple preparation and measurement of qubit states as well as their relative insensitivity to a thermal environment makes the latter schemes particularly interesting for quantum information processing.

Most theoretical proposals on cavity-QED systems focus on fundamental systems involving a small number of atoms and few photons. These systems are sufficiently simple to allow for a first-principle description. Their experimental implementation is however quite challenging. For example, extremely high-Q micro-cavities are needed to preserve coherence during all atom-photon interactions. Furthermore, single atoms have to be confined inside the cavities for a sufficiently long time. This requires developments of novel cooling and trapping techniques, which is in itself a fascinating direction of current research. Despite these technical obstacles, a remarkable progress has been made in this area: quantum processors consisting of several coupled qubits now appear to be feasible.

* This work is dedicated to the memory of Professor Dan Walls

H.J. Carmichael, R.J. Glauber, M.O. Scully (Eds.): LNP 561, pp. 193–203, 2001.

On the other hand, some of the above difficulties are related to the microscopic nature of the system and may be avoided if mesoscopic systems are used. Proposals based on mesoscopic systems are also very attractive for possible large-scale implementation in the (presumably distant) future. Here collective (i.e. many-particle) excitations can be used as qubits, but it is in general difficult to control the coupling between them.

Motivated by this we here consider an approach that combines elements of cavity QED with mesoscopic systems. Specifically, we consider an N-atom system coupled to a few-photon cavity field. We investigate the conditions under which quantum entanglement can be created and manipulated in this mesoscopic system. Although entanglement manipulation involves collective rather than single-particle excitations, the system is still sufficiently simple to allow for a first principle description.

The central feature of our approach is the ability to manipulate collective excitations of light and matter by coherent control of the atom-field interaction using atomic dark resonances [8]. The present work demonstrates that the essential elements of QED-based quantum information processing can be implemented and that some of them can be considerably improved in a mesoscopic system. We show in particular that (*i*) quantum information contained in polarization states of single photons can be stored in collective atomic excitations; (*ii*) simple two-bit operations can be performed; (*iii*) entanglement can easily be transfered and distributed among collective excitations of distant atomic ensembles.

2 Collective Excitations as Qubits

A convenient way of encoding quantum information in optics is via the analogy between spin-1/2 systems and polarization states of light waves. We therefore begin by associating qubits with polarization states of single photons, and show that the states of these qubits can be mapped onto collective excitations of ensembles of atoms. We are here interested in single-photon excitations of cavity modes described by a superposition of right ($|1_+\rangle$) and left ($|1_-\rangle$) circularly polarized components

$$|\Psi_i\rangle = \alpha_i|1_{i,+}\rangle + \beta_i|1_{i,-}\rangle, \tag{1}$$

with $|\alpha_i|^2+|\beta_i|^2 = 1$. In the following we focus on the case that involves a pair of such single-photons states, i.e. $i = 1, 2$. For simplicity let us assume that the two photons occupy different frequency bands and hence are associated with different cavity modes.

In order to manipulate quantum information stored in such qubits we consider optical cavities filled with N identical multilevel atoms. The frequency of a particular pair of transitions is assumed to be close to resonance frequencies of the cavity. The corresponding coupling strengths of the atoms

to the two cavity modes $\hat{a}_{1+}$ and $\hat{a}_{1-}$ are assumed to be equal and are denoted by g (see Fig.1a). In addition some time-dependent classical fields with Rabi-frequencies $\Omega_{1\pm}(t)$ couple the lower (meta-stable) states $|c_{\pm 1}\rangle$ of these atoms to the excited states $|a_{\pm 1}\rangle$ as shown. The excited states decay with (equal) decay rate γ and all atoms are initially prepared in a certain hyperfine sub-level, i.e. in a pure state.

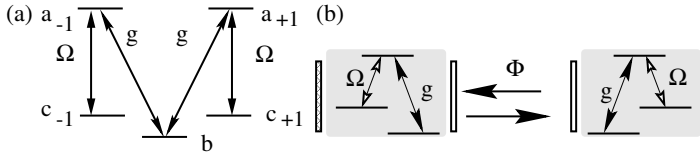

Fig. 1. (**a**) Schematic of the system for storing photon qubits in collective atomic excitations. (**b**) Quantum communication system based on photon trapping and release

The basic Hamiltonian of the cavity + atom system can be written in terms of collective operators $\hat{\Sigma}_{a_j,b} = \sum_{i=1}^{N} \hat{\sigma}^i_{a_j,b}$ and $\hat{\Sigma}_{a_j,c_j} = \sum_{i=1}^{N} \hat{\sigma}^i_{a_j,c_j}$ as

$$\hat{V} = \sum_j \hbar g \hat{a}_j \hat{\Sigma}_{a_j,b} + \hbar \Omega_j(t) \hat{\Sigma}_{a_j,c_j} + \text{h.c.}, \tag{2}$$

where $j = 1\pm$, and $\hat{\sigma}^i_{\mu\nu} = |\mu\rangle_{ii}\langle\nu|$ is the flip operator of the ith atom between states $|\mu\rangle$ and $|\nu\rangle$. Here and below we work in a frame rotating with the optical frequencies.

Of special interest are certain superposition states of light and collective states of matter that do not interact with the optical fields. These so-called dark-states [8] correspond to elementary excitations of bosonic quasi-particles, so-called dark-state polaritons [9]. They are defined by the following canonical transformation

$$\hat{d}_j = \cos\theta_j \, \hat{a}_j - \sin\theta_j \, \frac{1}{\sqrt{N}} \hat{\sigma}_{bc_j}, \qquad \tan\theta_j(t) = g\sqrt{N}/\Omega_j(t) \tag{3}$$

In the limit of small excitation the operators $\hat{d}_j$ and $\hat{d}_j^\dagger$ fulfill Bose commutation relations. The $\hat{d}_j^\dagger$'s create a family of dark states which do not have an excited-state component and are decoupled from both optical fields:

$$|D_{ji..}, n_j, k_i ...\rangle = \frac{1}{\sqrt{n!k!...}} \left(\hat{d}_j^\dagger\right)^n \left(\hat{d}_i^\dagger\right)^k ... |0\rangle |b\rangle_1 ... |b\rangle_N, \tag{4}$$

$\hat{V}|D_{ji..}, n_j, k_i ...\rangle = 0$. These states are composed of cavity field states and symmetric Dicke-like atomic states $|\mathbf{c}_j^n \, \mathbf{c}_i^k ..\rangle$ containing n atoms in level $|c_j\rangle$,

k atoms in level $|c_i\rangle$ etc, and all others in the ground state $|b\rangle$:

$$|\mathbf{b}\rangle \equiv |b\rangle_1 ... |b\rangle_N, \qquad |\mathbf{c}_j\rangle \equiv \sum_{l=1}^{N} \frac{-1}{\sqrt{N}} |b\rangle_1 ... |c_j\rangle_l ... |b\rangle_N, \tag{5}$$

$$|\mathbf{c}_j^2\rangle \equiv \sum_{l\neq m=1}^{N} \frac{1}{\sqrt{2N(N-1)}} |b\rangle_1 ... |c_j\rangle_l ... |c_j\rangle_m .... |b\rangle_N, \quad \text{etc.} \tag{6}$$

We here assumed that the number of atoms is much larger than the number of photons in the light field.

The essence of the present approach is that a quantum bit stored in photo states can be transfered to collective atomic excitations (and vice versa) by adiabatic passage in dark-polariton states. Specifically single-mode dark states (4) have the following asymptotic behavior in the two limiting cases:

$$|D_j, n_j\rangle \rightarrow |n_j\rangle\, |\mathbf{b}\rangle, \quad \text{when} \quad \Omega \gg g\sqrt{N}, \tag{7}$$

$$|D_j, n_j\rangle \rightarrow |0\rangle\, |\mathbf{c}_j^n\rangle, \quad \text{when} \quad \Omega \ll g\sqrt{N}. \tag{8}$$

It is most important that by varying the strength of the driving field $\Omega(t)$, the state of the combined atom+cavity system can be changed from cavity-like (in which excitation is mostly of photon nature) to atom-like (in which excitations are shared among the atoms). In the latter case the lifetime of excitations will not be sensitive to cavity decay; it will be limited solely by the decay of the meta-stable atomic states. In this process qubit states encoded in the photon field are mapped onto symmetric collective excitations of atomic ensembles. Since all dark states are orthogonal to each other, copying of all states can proceed in parallel.

It is known that adiabatic following takes place in the stimulated Raman process considered here, if the characteristic time scale T exceeds the ratio of the optical decay rate γ to the square of the characteristic Rabi-frequency. For the present system this condition translates into $g^2 N/\gamma T \gg 1$. One recognizes that using a mesoscopic system with $N \gg 1$ considerably improves the adiabaticity condition as compared to the single-atom case. This is a result of the well-known enhancement of the single-atom coupling by a factor $\sqrt{N}$ due to the collective nature of the interaction [10,11]. It should be noted that as long as the atom density is much lower than $1/\lambda^3$ there is no corresponding (superradiant) enhancement of the radiative decay rate γ.

3 Quantum Entanglement of Collective Excitations

A pair of qubits stored in collective excitations can be entangled using a number of different processes. Here we consider the resonantly enhanced Kerr effect [12] in combination with a cavity-QED setup to construct an elementary logic gate. The resonantly enhanced Kerr interaction in a 4-level configuration

is the basis for the so-called "photon blockade" in a cavity configuration [13] and results in extremely strong photon-photon interactions of pulses [14].

To implement a two-bit gate we consider a pair of photons resonant with different transitions of the same multi-state atom. We use a level configuration and optical fields as indicated in Fig.2.

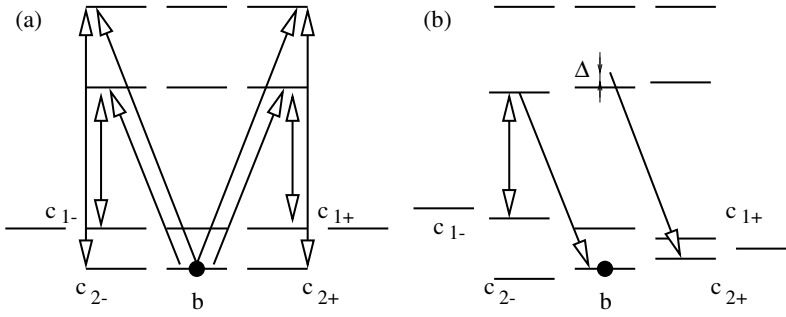

Fig. 2. Schematic of the system for an entanglement operation in atomic Rb. Only the coupling to the relevant transitions is shown

In order to entangle qubit states the following sequence of operations can be used. In the first step [15], the photon state $|1_1\rangle = \alpha_1|1_{1+}\rangle + \beta_1|1_{1-}\rangle$ is transfered to collective atomic states composed of $|\mathbf{c}_{1\pm}\rangle$ with the adiabatic technique described above. This operation corresponds to:

$$\Big(\alpha_1|1_{1+}\rangle + \beta_1|1_{1-}\rangle\Big)|\mathbf{b}\rangle \rightarrow |0_1\rangle\Big(\alpha_1|\mathbf{c}_{1+}\rangle + \beta_1|\mathbf{c}_{1-}\rangle\Big). \tag{9}$$

In the next step, the state of the second photon $|1_2\rangle$ is mapped onto the different atomic sub-levels $|\mathbf{c}_{2\pm}\rangle$:

$$\Big(\alpha_2|1_{2+}\rangle + \beta_2|1_{2-}\rangle\Big)\Big(\alpha_1|\mathbf{c}_{1+}\rangle + \beta_1|\mathbf{c}_{1-}\rangle\Big) \longrightarrow |0_2\rangle \times \tag{10}$$
$$\Big(\alpha_1\alpha_2|\mathbf{c}_{1+}\mathbf{c}_{2+}\rangle + \alpha_1\beta_2|\mathbf{c}_{1+}\mathbf{c}_{2-}\rangle + \beta_1\alpha_2|\mathbf{c}_{1-}\mathbf{c}_{2+}\rangle + \beta_1\beta_2|\mathbf{c}_{1-}\mathbf{c}_{2-}\rangle\Big).$$

We now want to generate a conditional phase shift on only *one* of the collective states, say $|\mathbf{c}_{1-}\mathbf{c}_{2_+}\rangle$. For this we first apply a weak magnetic field in such a way that the transition $|\mathbf{c}_{1-}\rangle \rightarrow |\mathbf{b}\rangle$ becomes close to the frequency of some cavity mode (different from the one used for trapping of the photon $|1_1\rangle$). Note that this mode also couples off-resonantly (with detuning Δ) the transition $|\mathbf{c}_{2+}\rangle \rightarrow |e_2, M_F = 0\rangle$, where $|e\rangle$ denotes the excited state. The shift of the atomic energy levels will also result in undesired different phase shifts for the components of the collective atomic states. These phase shifts can be compensated however (e.g. by reversing the direction of the field for an appropriate time) and shall not be considered here.

By applying a classical field of appropriate frequency we can transfer one component of the collective state $|\mathbf{c}_{1-}\rangle$ back into the photonic mode:

$$|0\rangle\,|\mathbf{c}_{1-}\mathbf{c}_{2+}\rangle \;\rightarrow\; |1_{1-}\rangle\,|\mathbf{c}_{2+}\rangle, \qquad |0\rangle\,|\mathbf{c}_{1-}\mathbf{c}_{2-}\rangle \;\rightarrow\; |1_{1-}\rangle\,|\mathbf{c}_{2-}\rangle. \tag{11}$$

At this point the energies of the states $|1_{1-}\rangle\,|\mathbf{c}_{2+}\rangle$ and $|1_{1-}\rangle\,|\mathbf{c}_{2-}\rangle$ differ in a nontrivial way. Namely the state $|1_{1-}\rangle\,|\mathbf{c}_{2+}\rangle$ exhibits an AC-Stark shift $\delta = g^2/\Delta$, since it is coupled by the off-resonant cavity mode containing one photon. In order to avoid decoherence associated with two-photon absorption, Δ should exceed the optical decay rate γ. By simply letting the system evolve for a time τ a conditional phase $\Phi = \delta\,\tau$ is accumulated. By transferring the photonic components $|1_{1-}\rangle$ back to the atoms and reversing the magnetic field for a time appropriate to eliminate the single-bit phase shifts, the following state is obtained:

$$\alpha_1\alpha_2|\mathbf{c}_{1+}\mathbf{c}_{2+}\rangle + \alpha_1\beta_2|\mathbf{c}_{1+}\mathbf{c}_{2-}\rangle + \mathrm{e}^{i\Phi}\beta_1\alpha_2|\mathbf{c}_{1-}\mathbf{c}_{2+}\rangle + \beta_1\beta_2|\mathbf{c}_{1-}\mathbf{c}_{2-}\rangle. \tag{12}$$

In the language of quantum information, this operation corresponds to a universal logic gate (a so-called phase gate) [1]. It is clear that by selecting a proper value of the conditional phase Φ and by performing independent single bit rotations, arbitrary entangled states of two qubits can be generated. This can be achieved however only if the system preserves coherence during the characteristic time required to accumulate a large phase shift. Hence, in the present approach $g^2\tau/\Delta \sim 1$ is required to achieve arbitrary entanglement of collective states. Thus while transfer operations as discussed in the previous section do not require a strong-coupling regime, two-bit operations still do.

4 Effects of Decoherence

In this section we discuss the effect of decoherence on the manipulation of collective atomic excitations. In general, decoherence mechanisms depend on the particular implementation. In order to be specific we consider an ensemble of laser-cooled Rb atoms in a magneto-optic trap (MOT). The main sources of decoherence and dissipation are then (*i*) spontaneous emission from the excited states (with the rate γ), (*ii*) the finite lifetimes of hyperfine and Zeeman coherences within the ground state (corresponding decay rate is γ_g) and, (*iii*) the photon decay of the optical cavity with rate γ_c.

For the present problem dephasing of the collective states is of interest. One finds that the states corresponding to single collective excitations are dephased at the same rate as the average coherences corresponding to individual atoms. For instance

$$\frac{\mathrm{d}}{\mathrm{d}t}\langle\mathbf{b}|\rho|\mathbf{a}_i\rangle = \frac{\mathrm{d}}{\mathrm{d}t}\frac{1}{\sqrt{N}}\sum_{\mu=1}^{N}\langle\mathbf{b}|\rho|\mathbf{a}_i^{\mu}\rangle = -\gamma\langle\mathbf{b}|\rho|\mathbf{a}_i\rangle. \tag{13}$$

By the same argument, coherences between hyperfine and Zeeman sub-levels decay at a rate γ_g. The states containing a single photon in a cavity mode

will decay with an additional rate γ_c. In the following we assume that γ_g is small on the time scales of interest and can be neglected.

Both processes considered in the previous sections are affected by decoherence, but in a different way. In the case of quantum state transfer, decoherence due to spontaneous emission can be avoided if the transfer time T is sufficiently long such that the adiabatic following condition is fulfilled. However, in order to avoid decoherence due to cavity decay the transfer time T should be short compared to γ_c. Hence, ideal quantum state transfer between cavity mode and collective excitations is only possible if

$$g^2 N \gg \gamma_c \gamma. \tag{14}$$

In the case of two-bit operations, spontaneous emission causes two-photon absorption at a rate $\sim g^2/\Delta^2\gamma$. Here, two-photon absorption can be avoided when the detuning Δ (see Fig.2) is sufficiently large $\Delta \gg \gamma$. At the same time, the entanglement generation should be fast compared to the cavity decay $\tau\gamma_c \ll 1$. Hence, in order to accumulate a large conditional phase without dissipation it is necessary that

$$g^2 \gg \gamma_c \Delta \gg \gamma_c \gamma. \tag{15}$$

The main conclusion of this section is that in principle increasing the number of atoms does not make it harder to create quantum entanglement. Other operations such as the reliable quantum state transfer between light and matter become much easier. The reason for this behavior is that the basic decoherence mechanisms are not enhanced as the number of atoms is increased. At the same time the coupling of the cavity mode to the *ground* state is enhanced by a factor $\sqrt{N}$.

We note that in practice decoherence mechanisms exist that do scale with the number of atoms. For instance, off-resonant scattering of the external coherent fields on the transition from the ground $|b\rangle$ to the excited states $|e^i\rangle$ will result in dephasing of the collective states which is clearly enhanced: $\tilde{\gamma} = N\gamma\Omega^2/\tilde{\Delta}^2$. Here $\tilde{\Delta}$ is the (large) detuning of the coupling field from the $|b\rangle \rightarrow |e^i\rangle$ transition frequency. Therefore, in experiments extra care should be taken to avoid these decoherence mechanisms.

5 Entanglement Distribution

One of the most intriguing aspects of quantum information is the use of entanglement as information resource for purposes such as super-dense information transfer [16], quantum teleportation [17] and secure communication [18]. In this section we show that the quantum state of *collective* atomic excitations including possible entanglements can be transferred form a given cavity system to other systems under much improved conditions as compared to single-atom QED systems. The technique is based on the possibility

to map quantum correlations from traveling-wave light fields to collective atomic states and vice versa with nearly 100% efficiency [19,20].

The basic mechanism is again the adiabatic procedure discussed in section 2 with the additional ingredient of a coupling to a continuum of free-space modes. We will outline the basic features for a single traveling-wave quantum field. In a suitable system, this operation can proceed in parallel for several field components and the corresponding generalization is straightforward.

We consider a cavity with N identical multi-level atoms as before. In addition we include the coupling of the cavity mode to a 1-D continuum of free-space modes with creation operators $b_k^\dagger$ described by the effective Hamiltonian $\hat{V} = \hbar \sum_k \kappa \hat{a}^\dagger \hat{b}_k + \text{h.c.}$; κ being the coupling constant. We assume that initially all atoms are in the ground state $|b\rangle$ and that there is no photon in the cavity. Thus the combined cavity-atom system is initially in the dark-state $|D,0\rangle$ (see (4)). The initial state of the free field is taken to be $|\Psi_{\text{in}}\rangle = \sum_k \xi_k^1 |1_k\rangle + \sum_{k,m} \xi_{k,m}^2 |1_k 1_m\rangle + \ldots$. It is convenient to work with correlation amplitudes, i.e. Fourier transforms of $\xi_{k\ldots l}^j$:

$$\Phi_j(t_1 \ldots t_j) = \langle 0 | \hat{E}(t_1) \ldots \hat{E}(t_j) | \Psi \rangle, \tag{16}$$

where $\hat{E}(t) = L/(2\pi c) \int d\omega_k \exp(i\omega_k t) \hat{b}_k$, and L is the quantization length. E.g. Φ_1 describes the envelope of a single-photon wave packet, Φ_2 is the coincidence amplitude etc. We now consider a broad class of pulsed fields that are characterized by a single common envelope function $h(t)$ such that

$$\Phi_j(t_1, t_2, \ldots t_j) = \alpha_j \sqrt{j!}\, h(t_1) h(t_2) \ldots h(t_j). \tag{17}$$

Any pure state or mixture of such pulses can be described by a single-mode density matrix $\rho_{nm} = \alpha_n^* \alpha_m$. The corresponding mode function is a superposition of plane waves proportional to $h(z/c) = \int \mathrm{d}\omega_k\, \xi_k\, \mathrm{e}^{i\omega_k z/c}$.

Due to the interaction of the cavity mode with the environment, the dark states of the cavity + atoms system are coupled to the continuum states. When only single-photon pulses are involved the evolution equations of the corresponding state amplitudes are [19]:

$$\dot{D}_1(t) = i\kappa \cos\theta(t) \sum_k \xi_k(t), \tag{18}$$

$$\dot{\xi}_k(t) = -i\Delta_k\, \xi_k(t) + i\kappa \cos\theta(t)\, D(t). \tag{19}$$

$D_1(t)$ denotes here the amplitude of the dark-state $|D,1\rangle$ and $\theta(t) \equiv \theta_1(t)$ is defined in (3). We proceed by formally integrating (19), substituting the result into (18) and invoking a Markov approximation. Assuming that no photons arrive to the cavity before t_0 we find for the dark state amplitude $D_1(t) = -i\alpha_1 D(t)$ with

$$D(t) = \sqrt{\gamma_c \frac{c}{L}} \int_{t_0}^{t} \mathrm{d}\tau\, \cos\theta(\tau)\, h(\tau) \times \exp\left\{ -\frac{\gamma_c}{2} \int_{\tau}^{t} \mathrm{d}\tau'\, \cos^2\theta(\tau') \right\}. \tag{20}$$

Here we have introduced the empty-cavity decay rate $\gamma_c = \kappa^2 L/c$. Substituting this result back into (19) one finds that the outgoing field is described by the common envelope function $h_{\rm out}(t) = h(t) - \sqrt{\gamma_c L/c}\, D(t)$.

In order to trap photons we require that the envelope of the outgoing field and its first derivative vanish identically. I.e. $h_{\rm out}(t) = \dot{h}_{\rm out}(t) = 0$. Differentiating the above relation for $h_{\rm out}(t)$ yields

$$-\frac{\mathrm{d}}{\mathrm{d}t} \ln \cos\theta(t) + \frac{\mathrm{d}}{\mathrm{d}t} \ln h(t) = \frac{\gamma_c}{2} \cos^2\theta(t). \tag{21}$$

If $\Omega(t)$ is chosen such that $\theta(t)$ obeys this equation with the asymptotic condition $\cos\theta \to 0$ the output field remains zero and the incoming light pulse is completely transferred to the atomic system.

The above condition corresponds to a quantum or dynamical impedance matching [19]. The term on the r.h.s. of (21) is the effective cavity decay rate reduced due to intracavity electromagnetically induced transparency (EIT) [21]. The first term on the l.h.s. describes internal "losses" due to coherent Raman adiabatic passage and the second term is due to the time-dependence of the input field. As in the case of classical impedance matching [22], (21) reflects the condition for complete destructive interference resulting in a vanishing outgoing wave. Solving (21) yields

$$\cos^2\theta(t) = \frac{h^2(t)}{\gamma_c \int_{-\infty}^{t} \mathrm{d}\tau h^2(\tau)}, \tag{22}$$

which corresponds to $D(t \to +\infty) \to 1$. Hence, by suitable variation of the classical driving field any single-photon pulse can be trapped ideally, if its pulse length is longer than the bare-cavity decay time.

Generalizations of the above considerations to multi-photon states can proceed along the same lines, but involve more tedious algebra. In particular, for the two-photon states one finds $D_2(t) = -\alpha_2 D(t)^2$, and in general

$$D_k(t) = (-i)^k \alpha_k\, d(t)^k \tag{23}$$

can be proved. Under conditions of quantum impedance matching $D_k(t \to \infty) \to (-i)^k \alpha_k$ for arbitrary k. Hence pulsed fields in a generalized single mode with arbitrary quantum state can be mapped onto the atomic ensemble.

Releasing the stored quantum state into a pulse of desired shape can be accomplished in a straightforward way. A simple reversal of the time dependence of the control field at a later time t_d leads to a perfect mirror-image of the initial pulse. This can be verified directly from (20).

Before concluding we note that the quantum transfer protocol described here is based solely on the adiabatic rotation of the dark state described in Section 2. Hence, this operation can be nearly ideal whenever inequality (14) is fulfilled [19]. Therefore, perfect quantum communication can be achieved in the present system without invoking the strong coupling regime of cavity QED.

6 Conclusions

In conclusion, we have shown that quantum information stored in collective excitations of an N-atom system can be coherently processed using cavity QED techniques. The use of a many-atom system will simplify practical implementations of cavity-QED systems as it eliminates the problem of trapping exactly one atom inside the resonator. We showed that certain network operations such as the transfer of excitation between atomic and photonic degrees of freedom and entanglement distribution can be performed without invoking the strong coupling condition of cavity QED. This will allow much faster network operations as in single-atom based schemes. However other operations, such as two-bit rotations resulting in quantum entanglement still require a strong coupling. Studies of possible ways to alleviate these requirements, and to avoid the strong coupling regime altogether are currently under way. This includes, for instance, resonant nonlinearities in a traveling wave geometry, so-called photon-exchange interactions or cold collisions.

Acknowledgments

This work was supported by the National Science Foundation via the grant to the Institute for Theoretical Atomic and Molecular Physics. We thank Susanne Yelin for stimulating discussions and collaboration on a related project. One of us (ML) especially thanks her and little Theodor for their patience that allowed to complete this contribution.

References

1. R.P. Feynman: Int. J. Theor. Phys. **21**, 467 (1982); D. Deutsch: Proc. R. Soc. London A **425**, 73 (1989)
2. See e.g.: D.P. DiVincenzo, Science **270**, 255 (1995); C.H. Bennett: Phys. Today **48**, No. 10, 24 (1995); A. Ekert, R. Josza: Rev. Mod. Phys. **68**, 733 (1996); A. Steane: Rep. Prog. Phys. **61**, 117 (1998)
3. D. Deutsch: Proc. R. Soc. London A **400**, 97 (1985)
4. J.I. Cirac, P. Zoller: Phys. Rev. Lett. **74**, 4091 (1995)
5. N.A. Gershenfeld, I.L. Chuang: Science **275**, 350 (1997)
6. D. Jaksch *et al.*: Phys. Rev. Lett. **82**, 1975 (1999)
7. T. Pellizzari *et al.*: Phys. Rev. Lett. **75**, 3788 (1995); for a review of cavity QED experiments see e.g. *Cavity Quantum Electrodynamics*, ed. by P. Berman (Academic Press, San Diego 1994)
8. See e.g.: E. Arimondo: Progr. in Optics **35**, 259 (1996)
9. M. Fleischhauer, M.D. Lukin: Phys. Rev. Lett. in press, quant-ph/0001094
10. R.H. Dicke: Phys. Rev. **93**, 99 (1954); M. Sargent III, M.O. Scully, W.E. Lamb Jr.: *Laser Physics*, (Addison-Wesley, Reading 1974); for collective enhancement effects in the interaction of single photons with atomic ensembles see e.g. G.S. Agarwal: Phys. Rev. Lett. **53**, 1732 (1984); see also: H.J. Carmichael: Phys. Rev. A **33**, 3262 (1986); S.L. Mielke *et al.*: Opt. Lett. **22**, 325 (1992)

11. The use of collective couplings in the context of quantum information processing has also been proposed in: J. Franson *et al.*: Phys. Rev. A **60**, 917 (1999)
12. H. Schmidt, A. Imamoğlu: Opt. Lett. **21**, 1936 (1996)
13. A. Imamoğlu *et al.*: Phys. Rev. Lett. **79**, 1467 (1997); P. Grangier, D.F. Walls, K. Gheri: Phys. Rev. Lett. **81**, 2833 (1998)
14. M.D. Lukin, A. Imamoğlu: Phys. Rev. Lett. **84**, 1419 (2000)
15. Note that the order in which the qubits are trapped is in principle important. The corresponding correction can be disregarded however when $N \gg 1$.
16. C.H. Bennet, S.J. Wiesner: Phys. Rev. Lett. **69**, 2881 (1992); K. Mattle *et al.*: Phys. Rev. Lett. **76**, 4656 (1996)
17. C.H. Bennett *et al.*: Phys. Rev. Lett. **70**, 1895 (1990); B. Bouwmeester *et al.*: Nature **390**, 575 (1997); D. Boschi *et al.*: Phys. Rev. Lett. **80**, 1121 (1998); A. Furusawa *et al.*: Science **282**, 706 (1998)
18. C.H. Bennett, G. Brassard: Proc. of IEEE Int. Conf. on Comp. Systems and Signal Processing, Banglore India (IEEE, New York 1984); A.K. Ekert: Phys. Rev. Lett. **67**, 661 (1991)
19. M. Fleischhauer, S.F. Yelin, M.D. Lukin: Opt. Comm. in press
20. M.D. Lukin, S.F. Yelin, M. Fleischhauer: Phys. Rev. Lett. **84**, 4232 (2000)
21. M.D. Lukin *et al.*: Opt. Lett. **23**, 295 (1998)
22. A. Siegmann: *Lasers* (University Science Books, Mill Valley 1986).

Quantum State Protection Using All-Optical Feedback

Paolo Tombesi, Vittorio Giovannetti, and David Vitali

Summary. An all-optical feedback scheme in which the output of a cavity mode is used to influence the dynamics of another cavity mode is considered. We show that under ideal conditions, perfect preservation against decoherence of a generic quantum state of the source mode can be achieved.

1 Introduction

Electromagnetic fields in cavities have already been used for quantum information processing. For example, one of the first experimental demonstration of a quantum gate has been implemented using two cavity modes characterized by a nonlinear dispersive interaction mediated by a beam of Cs atoms [1]. In particular, quantum information can be stored in high-Q electromagnetic cavities, and with this respect it is important to develop schemes able to increase the quantum information storage time as much as possible, and provide therefore a good *quantum state protection* against the effects of the decoherence due to cavity leakage.

We have developed schemes for the preservation of generic quantum states in cavities based on feedback loops originating from homodyne measurements [2,3], or associated with direct photodetection supplemented with the injection of an appropriately prepared atom [4,5]. These schemes provide a significative increase of the decoherence time of an initially prepared quantum state, but are both characterized by some limitations. In the case of homodyne-mediated feedback, the scheme is "anisotropic" in phase-space [2], that is, it does not protect all the quantum states in the same way. This is due to the fact that the dynamics in the presence of feedback has a privileged direction, coinciding with that of the measured quadrature. In the case of photodetection-mediated feedback, the scheme is isotropic but it is affected by phase diffusion, which, although very slowly, leads to destruction of quantum phases [5].

The schemes considered in [2–5] employ the usual implementation of optical feedback, i.e., electro-optical feedback, in which the light exiting the cavity enters a detector and the photocurrent produced is used to control the cavity dynamics by some electro-optical device. Here we show that a promising way to obtain perfect quantum state protection, that is, the preservation of an initially prepared quantum state for an arbitrarily large time, can be

H.J. Carmichael, R.J. Glauber, M.O. Scully (Eds.): LNP 561, pp. 204–213, 2001.

obtained by using an *all-optical feedback* scheme. In these schemes, the output light is not detected, but it is reflected around a feedback loop and sent into another cavity (the driven cavity) which is coupled to the first in some way. This scheme is an actual feedback scheme if the loop is one-way, i.e., it goes from the source to the driven cavity and it cannot go backward. This can be achieved by inserting in the loop a system analogous to a Faraday isolator. With this respect, all-optical feedback schemes are an example of cascaded quantum systems, introduced and described by Gardiner [6] and Carmichael [7]. In these systems, the output from a source mode is used as an input for a second mode. The new feature introduced by feedback is the presence of an interaction term between the two modes, so that the source mode dynamics is affected by the driven mode.

All-optical feedback schemes have been already studied by Wiseman and Milburn in [8]. However they focus their attention to the adiabatic regime, where the linewidth of the driven cavity is much larger than that of the source mode, so that the driven mode can be adiabatically eliminated. In this case, an all-optical feedback scheme reduces to an analogous electro-optical feedback scheme whenever the interaction between driven and source mode has a quantum non demolition (QND)-like form, that is, it is a product of source and driven mode operators. In this case, in fact, the role of the driven mode is completely equivalent to that of a detection apparatus [8]. On the contrary, all-optical feedback cannot be reduced to an electro-optical analogous in the case of a non-factorized form of interaction Hamiltonian. This is the most interesting case and in this work we shall only consider this case, which can be experimentally realized, for example, using a simple set up involving a single cavity. In this case, one polarization mode plays the role of the source mode and an orthogonal polarization mode plays the role of the driven system. The unidirectional coupling is provided by an optically active element supplemented with two polarized beam splitter and a polarizer. We shall see that the scheme is able to provide an "isotropic", i.e. phase-independent, quantum state protection for the source mode. More interestingly, we show that in the ideal limit of unit efficiency of the feedback loop, feedback parameters can be chosen so to achieve perfect state protection, i.e., perfect freezing of the source mode dynamics.

2 The All-Optical Feedback Scheme

Let us briefly recall the theory of cascaded quantum systems developed by Gardiner and Carmichael in [6,7] and reconsidered by Wiseman and Milburn in [8]. This theory describes two systems, the source system and the driven system, which are unidirectionally coupled. This broken symmetry can be naturally obtained in optical systems when the coupling is realized by a reservoir of electromagnetic waves traveling in one direction. Experimentally this one-way isolation can be obtained using a Faraday rotator. This means

that the source emits photons influencing the dynamics of the driven system, while the radiation emitted by the driven system does not affect the source. The source and the driven system can be generic quantum system, but here we shall consider the case of two optical cavities. If we denote with a_1 and γ_1' the annihilation operator and the decay rate of the source cavity mode, and with a_2 and γ_2' the corresponding quantities for the driven cavity mode, the dynamics of a generic operator $c(t)$ can be obtained using the input-output theory [9], yielding the following quantum Langevin equation [6]:

$$\begin{aligned}
\dot{c}(t) = &-\frac{i}{\hbar}\left[c(t), H\right] - \left[c(t), a_1^\dagger(t)\right]\left\{\frac{\gamma_1'}{2}a_1(t) + \sqrt{\gamma_1'}a_{in}(t)\right\} \\
&+ \left\{\frac{\gamma_1'}{2}a_1^\dagger(t) + \sqrt{\gamma_1'}a_{in}^\dagger(t)\right\}\left[c(t), a_1(t)\right] \\
&- \left[c(t), a_2^\dagger(t)\right]\left\{\frac{\gamma_1'}{2}a_2(t) + \sqrt{\gamma_1'\gamma_2'}a_1(t-\tau) + \sqrt{\gamma_2'}a_{in}(t-\tau)\right\} \\
&+ \left\{\frac{\gamma_2'}{2}a_2^\dagger(t) + \sqrt{\gamma_1'\gamma_2'}a_1^\dagger(t-\tau) + \sqrt{\gamma_2'}a_{in}^\dagger(t-\tau)\right\}\left[c(t), a_2(t)\right] \ .
\end{aligned} \tag{1}$$

We have considered the presence of a total system Hamiltonian H; then $a_{in}(t)$ is the input noise at the source cavity, with $[a_{in}(t), a_{in}(t')] = \delta(t-t')$, and τ is such that $c\tau$ is the distance between the two cavities. When $H = H_1 + H_2$ is the sum of a source Hamiltonian H_1 and a driven mode Hamiltonian H_2, we have a cascaded system and the meaning of (1) is evident. The equation of an operator of the source cavity does not involve the last two lines of (1), and one has the usual quantum Langevin for the source cavity, since the driven cavity has no effect on it. On the contrary, in the case of a driven cavity operator, the second and third term of the right hand side of (1) is zero and one has the usual quantum Langevin equation but with an input field equal to the output field from the source cavity, delayed by τ. In the case of cascaded systems, the delay τ is an arbitrary constant, which is essentially irrelevant for the physics of the problem. In fact, the results for a given value of the delay τ can be obtained from those with another value for τ with simple, appropriate, adjustments. It is evident that the easiest case is the limiting case of a vanishingly small delay $\tau \to 0$, which involves the input noise at time t, $a_{in}(t)$, only, and this explains why the zero delay case is usually considered.

The delay τ becomes an important physical parameter in the presence of some feedback process, i.e., when the driven mode can affect in some way the source mode dynamics. This could be done, for example, simply by removing the Faraday isolation, i.e., restoring the inversion symmetry, but this simply means going back to the trivial case of two interacting systems. A more interesting situation is obtained when the unidirectional coupling is left unchanged, and feedback from the driven to the source system is obtained through a coupling Hamiltonian term. This means that the Langevin equation (1) is still valid, but with a non-decomposable total system Hamiltonian $H = H_1 + H_2 + H_{int}$, so that the two cavity modes are no more real cas-

caded systems. The presence of the interaction term H_{int} implies that the two cavities have to overlap spatially, at least partially. In this case one essentially realizes an *all-optical feedback scheme*, because in this way one tries to implement a control of the source mode dynamics through an optical loop involving the driven cavity and its interaction with the source mode. In this case, the delay τ acquires the meaning of a feedback loop transit time and the $\tau \neq 0$ case now corresponds to a truly non-Markovian dynamics [3]. The Markovian limiting case $\tau \to 0$ becomes now a well specified physical assumption, which is justified only in the case when the feedback delay τ is much smaller than the typical timescale of the dynamics of the system of interest, i.e., of the source mode. Since we are concerned with the preservation of a generic quantum state generated in the source cavity, the relevant timescale here is the decoherence time, which is given by $t_{dec} \simeq (\gamma_1' \bar{n})^{-1}$, where $\bar{n}$ is the mean number of photons [10]. The feedback loop delay time is instead of the order of a single cavity transit time $\tau \simeq 2L/c$ (L is the cavity length) and since $1/\gamma_1' = 2L/cT$, where T is the cavity mirror transmittivity, it is evident that for good cavities, the Markovian limit $\tau \to 0$ can be safely assumed even for quantum states of the source mode with a quite large number of photons.

In the Markovian limit $\tau \to 0$, the quantum Langevin equation (1) becomes equivalent to a master equation for the joint density matrix $D(t)$ of the source and driven modes. We consider the most common case of a vacuum reservoir, that is, $\langle a_{in}(t) a_{in}^{\dagger}(t) \rangle = \delta(t - t')$ (the case of more general input white noises is considered in [8]). Moreover we generalize to the realistic situation in which the losses in each cavity are not due only to coupling with the vacuum electromagnetic modes responsible for the unidirectional coupling between the source and the driven mode (with rates γ_i'), but also to the coupling with some other unwanted modes (absorption and diffraction losses), with rates η_i. The general master equation for all-optical feedback in the $\tau \to 0$ limit is therefore

$$\begin{aligned} \dot{D} = & -\frac{i}{\hbar}[H, D] + \frac{\gamma_1' + \eta_1}{2}\left(2a_1 D a_1^{\dagger} - a_1^{\dagger} a_1 D - D a_1^{\dagger} a_1\right) \\ & + \frac{\gamma_2' + \eta_2}{2}\left(2a_2 D a_2^{\dagger} - a_2^{\dagger} a_2 D - D a_2^{\dagger} a_2\right) \\ & + \sqrt{\gamma_1' \gamma_2'}\left\{\left[a_1 D, a_2^{\dagger}\right] + \left[a_2, D a_1^{\dagger}\right]\right\} . \end{aligned} \tag{2}$$

In this work we apply this master equation to a set up which could be realized experimentally in a quite straightforward way and which is schematically shown in Fig. 1. The source and the driven cavity coincide and the two annihilation operators a_1 and a_2 describe two frequency degenerate, orthogonally polarized modes of the cavity. As discussed in detail in [8], in order to have a feedback scheme with no electro-optical analog, one has to choose an interaction Hamiltonian H_{int} which cannot be factorized into a source and a driven term. We choose the simplest case, a mode conversion term, which can be realized even without a nonlinear medium, but with a simple half-wave

plate, i.e., a polarization rotator. In the frame rotating at the frequency of the modes, one has

$$H = i\hbar \frac{g\sqrt{\gamma_1'\gamma_2'}}{2} \left(a_1^\dagger a_2 - a_2^\dagger a_1 \right) , \tag{3}$$

where we have defined the coupling in terms of the dimensionless constant g. In this case the unidirectional coupling can be simply realized using two polarized beam splitters, a Faraday rotator and an half-wave plate (see Fig. 1).

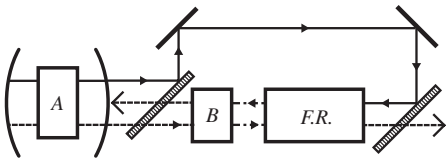

Fig. 1. Scheme of the proposed all-optical feedback loop. The source mode (full line) and the driven mode (dashed line) are, respectively, horizontally and vertically polarized and are coupled within the cavity by the half-wave plate A. The source mode passes through an optically active element $F.R.$ and the half-wave plate B, both rotating its polarization by $\pi/4$ radians, so that it finally drives the driven mode in the cavity. The output from the driven mode cannot come back into the cavity because of the action of the optically active element and of the polarized beam splitter

3 The Dynamics of the System

Before studying the dynamics of the two coupled cavity modes, it is convenient to consider the adiabatic regime where the driven mode bandwidth $\gamma_2 = \gamma_2' + \eta_2$ is much larger than that of the source mode. This limit will show in which way the optical feedback loop is able to inhibit the decohering effects of photon leakage. When γ_2 is much larger than the other parameters, the driven mode can be adiabatically eliminated so to get a master equation for the reduced density matrix of the source mode alone ϱ. The driven mode will always be very close to the vacuum state, so that we can expand the total density matrix D as

$$\begin{aligned} D = {} & w_0 \otimes |0\rangle\langle 0| + w_1 \otimes |1\rangle\langle 0| + w_1^\dagger \otimes |0\rangle\langle 1| \\ & + w_2' \otimes |1\rangle\langle 1| + w_2 \otimes |2\rangle\langle 0| + w_2^\dagger \otimes |0\rangle\langle 2| \, , \end{aligned} \tag{4}$$

where $|n\rangle$, $n = 0, 1, 2$, are the lowest driven mode Fock states. Inserting this expression in the master equation (2), one gets a set of coupled equations for

w_i, which, at lowest order in γ_2^{-1}, yields the following master equation for the source mode reduced density matrix $\varrho = w_0 + w_2'$

$$\dot{\varrho}(t) = \frac{\gamma_1}{2}\left[1 + g(2+g)\frac{\gamma_1'\gamma_2'}{\gamma_1\gamma_2}\right]\left(2a_1\varrho a_1^\dagger - a_1^\dagger a_1\varrho - \varrho a_1^\dagger a_1\right) , \tag{5}$$

where $\gamma_1 = \gamma_1' + \eta_1$ is the total decay rate of the source mode. Equation (5) shows that, in the adiabatic limit, the dynamics of the source mode in the presence of the optical feedback loop is still described by the standard vacuum optical master equation, but with a *renormalized decay rate* $\gamma_1^{eff} = \gamma_1\left[1 + g(2+g)\eta^2\right]$, where we have defined the feedback efficiency $\eta = \sqrt{\gamma_1'\gamma_2'/\gamma_1\gamma_2}$ (a decay rate renormalization in the adiabatic limit is already predicted in [8]). It is easy to see that the feedback is optimal, i.e., the effective decay rate γ_1^{eff} is minimized, when the dimensionless mode conversion coupling $g = -1$, and in this case $\gamma_1^{eff} = \gamma_1\left[1 - \eta^2\right]$. Therefore in the ideal limit of perfect feedback $\eta = 1$ (i.e., no light is lost in the loop due to diffraction or absorption), when $g = -1$ and $\gamma_2 \gg \gamma_1$, all-optical feedback completely freezes the source mode dynamics, that is, it realizes perfect preservation of an initial quantum state. In this ideal case, the whole source mode output is collected and converted by the all-optical loop into driven mode light, which is then efficiently converted again within the cavity into source mode light. No source mode photon is lost in the loop, and more importantly, when $g = -1$, optical feedback acts *in phase*, yielding a complete suppression of photon leakage. This phase-sensitive aspect of all-optical feedback cannot be achieved with electro-optical feedback. For example in [5], we have studied a direct-photodetection based electro-optical feedback loop, feeding back a photon in the cavity through atomic injection, whenever a photon is lost and detected. In this case, perfect state preservation is not achieved even in the ideal limit of unit feedback efficiency, because the fed back photon has no phase relationship with those in the cavity, and one is left with an unavoidable, even though slow, phase diffusion. This study of the adiabatic limit $\gamma_1/\gamma_2 \ll 1$ shows that, with all-optical feedback, perfect state preservation is in principle possible using the scheme of Fig. 1. We now study the exact dynamics of the two coupled modes by solving the master equation (2) in order to see the performance of the scheme as a function of the feedback efficiency η and of the adiabaticity parameter γ_1/γ_2. We shall consider a factorized initial condition $D(0) = \varrho_1(0) \otimes \varrho_2(0)$. It is convenient to expand the initial conditions $\varrho_j(0)$ using the R representation [9]

$$\varrho_j(0) = \frac{1}{\pi^2}\int \mathrm{d}^2\alpha_j \mathrm{d}^2\beta_j \; R_j(\beta_j^*, \alpha_j)\; |\beta_j\rangle\langle\alpha_j|\; e^{-(|\alpha_j|^2 + |\beta_j|^2)/2} , \tag{6}$$

where $|\alpha_j\rangle$ and $|\beta_j\rangle$ are coherent states and

$$R_j(\beta_j^*, \alpha_j) = \langle\beta_j|\varrho_j(0)|\alpha_j\rangle\; e^{(|\alpha_j|^2 + |\beta_j|^2)/2} \tag{7}$$

is the R function, analytic in the two complex variables α_j and β_j^*. We are interested in the dynamics of the source mode only and, even though we do

not adiabatically eliminate the driven mode, we shall always consider it more damped than the source mode. It is therefore reasonable to assume an initial vacuum state for the driven mode $\varrho_2(0) = |0\rangle\langle 0|$, which means $R_2(\beta_2^*, \alpha_2) = 1$. Moreover we shall trace over the driven mode and focus on the reduced Wigner function of the source mode $W_1(\alpha, \alpha^*, t) = \int \mathrm{d}^2\beta\, W(\alpha, \alpha^*, \beta, \beta^*, t)$. The time evolution of this reduced Wigner function can be determined exactly in terms of the R representation of the source mode initial condition, and after some Gaussian integrations one gets

$$W_1(\alpha, \alpha^*, t) = \frac{2}{\pi^3} \int \mathrm{d}^2\alpha_1 \mathrm{d}^2\beta_1 \; R_1(\beta_1^*, \alpha_1)\; e^{-|\alpha_1|^2 - |\beta_1|^2 + \beta_1 \alpha_1^*} \times \\ \times \; \exp\left[2\big(\alpha - \mathcal{F}(t)\beta_1\big)\big(\mathcal{F}(t)\alpha_1^* - \alpha^*\big)\right], \tag{8}$$

where

$$\mathcal{F}(t) = \frac{m + \gamma_1 - \gamma_2}{2m} \mathrm{e}^{-(\gamma_1+\gamma_2+m)t/4} + \frac{m - \gamma_1 + \gamma_2}{2m} \mathrm{e}^{-(\gamma_1+\gamma_2-m)t/4} \tag{9}$$

and $m = \sqrt{(\gamma_1 - \gamma_2)^2 - 4\gamma_1\gamma_2\eta^2(2+g)g}$. It is interesting to notice that the exact dynamics of the source mode is completely characterized by the function $\mathcal{F}(t)$ of (9) only. It can be shown that $\mathcal{F}(t)$ is always a nonincreasing function of time. In particular, in the absence of feedback ($g = 0$) one has $\mathcal{F}(t) = \exp(-\gamma_1 t/2)$, since the source mode is not affected by the driven mode. In the adiabatic limit, one can see from (9) that, at first order in γ_1/γ_2, one has $\mathcal{F}(t) = \exp\left(-\gamma_1\left(1 + \eta^2(2+g)g\right)t/2\right)$, implying (see also section 2), that in the ideal case $\eta = 1$ and $g = -1$, it is $\mathcal{F}(t) = 1$ and therefore the source mode dynamics is completely frozen.

It is instructive to apply the general expression of the time evolved Wigner function of (8) to some specific initial states of the source mode. The paradigm case for decoherence studies is the Schrödinger cat case, $\varrho_1(0) = |\psi(0)\rangle\langle\psi(0)|$, with

$$|\psi(0)\rangle = \frac{1}{\sqrt{2(1 + e^{-2|\alpha_0|^2}\cos\varphi)}}\big(|\alpha_0\rangle + e^{i\varphi}|-\alpha_0\rangle\big)\,; \tag{10}$$

applying (8) one gets that the corresponding time evolution of the Wigner function is

$$W_1(\boldsymbol{x}, t) = \frac{1}{\pi(1 + e^{-2|\boldsymbol{\alpha_0}|^2}\cos\varphi)}\Big(e^{-2|\boldsymbol{x} - \boldsymbol{\alpha_0}\mathcal{F}(t)|^2} + e^{-2|\boldsymbol{x} + \boldsymbol{\alpha_0}\mathcal{F}(t)|^2} \\ + 2e^{-2\left(|\boldsymbol{x}|^2 - |\boldsymbol{\alpha_0}\mathcal{F}(t)|^2 + |\boldsymbol{\alpha_0}|^2\right)} \cos\Big(4(\boldsymbol{x} \wedge \boldsymbol{\alpha_0}) \cdot \hat{z} - \varphi\Big)\Big)\,, \tag{11}$$

where $\boldsymbol{x} = (\mathrm{Re}\{\alpha\}, \mathrm{Im}\{\alpha\}, 0)$, $\boldsymbol{\alpha_0} = (\mathrm{Re}\{\alpha_0\}, \mathrm{Im}\{\alpha_0\}, 0)$ and $\hat{z} = (0, 0, 1)$. From (11) one can see the isotropic properties of the all-optical feedback scheme studied here, since the state of the source mode depends upon the angle between $\boldsymbol{x}$ and $\boldsymbol{\alpha_0}$ only. The time evolution of a Schrodinger cat state with $\alpha_0 = 2\mathrm{i}$ and $\varphi = 0$ is displayed in Fig. 2: in (a) the initial condition is

shown, while in (b) and in (c) the state evolved in the presence of feedback after two decoherence times $t_{dec} = 1/(2\gamma_1|\alpha_0|^2)$ and $20t_{dec}$ are respectively shown. In (d) the state evolved after $2t_{dec}$ in the *absence* of feedback is instead shown. What is relevant is that, with achievable feedback parameters $g = -1$, $\eta = 0.95$, and $\gamma_1/\gamma_2 = 10^{-3}$, one gets a very good preservation of the initial mesoscopic Schrödinger cat state ($\bar{n} = 4$) after two decoherence times. With all-optical feedback, one has a decohered cat state similar to that obtained in the absence of feedback after $2t_{dec}$, only after 20 decoherence times.

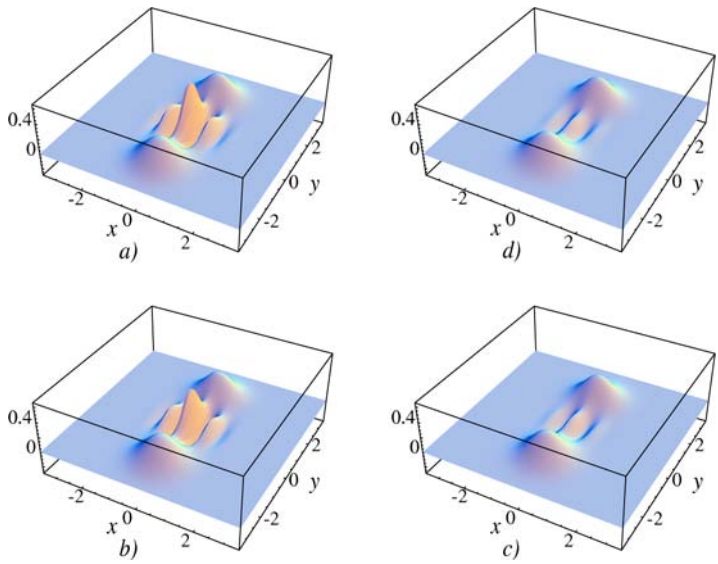

Fig. 2. Time evolution of the source mode Wigner function of the cat state of equation (10) with $\alpha_0 = 2\mathrm{i}$, $\varphi = 0$. (**a**) Initial Wigner function; (**b**) state after two decoherence times t_{dec} in the presence of feedback; (**c**) state after $t = 20t_{dec}$ in the presence of feedback. Parameter values are $g = -1$, $\eta = 0.95$, and $\gamma_1/\gamma_2 = 10^{-3}$. (**d**) shows the state after $t = 2t_{dec}$ in the absence of feedback ($g = 0$)

Similar qualitative results are obtained with a different initial pure quantum state of the source mode, i.e., the linear superposition of Fock states $\psi(0)\rangle = \left(|2\rangle + \sqrt{2}|4\rangle\right)/\sqrt{3}$. The time evolution of the Wigner function is shown in Fig. 3, where, again, (a) shows the initial state, (b) and (c) show the state evolved in the presence of feedback after $2t_{dec}$ and after $20t_{dec}$ respectively, and (d) shows the state evolved after $2t_{dec}$ in the absence of feedback. The feedback parameters are the same as in Fig. 2. One has again a very good preservation of quantum coherence after two decoherence times.

A more quantitative characterization of the preservation properties of the all-optical feedback scheme is obtained from the study of the fidelity of the initial state, $F(t) = \mathrm{Tr}\{\varrho_1(t)\varrho_1(0)\}$. Using (8) it is possible to write the

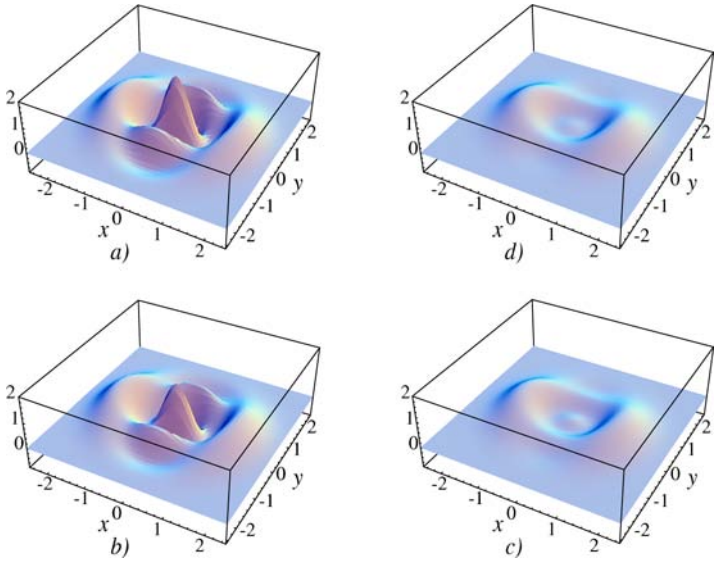

Fig. 3. Time evolution of the source mode Wigner function of the linear superposition of Fock states $|\psi(0)\rangle = \left(|2\rangle + \sqrt{2}|4\rangle\right)/\sqrt{3}$. (**a**) Initial Wigner function; (**b**) state after two decoherence times t_{dec} in the presence of feedback; (**c**) state after $t = 20t_{dec}$ in the presence of feedback; (**d**) state after $t = 2t_{dec}$ in the absence of feedback. Parameter values are the same as in Fig. 2

fidelity of a generic initial state in terms of its R representation (7) and the function $\mathcal{F}(t)$ as

$$F(t) = \frac{1}{\pi^2}\int \mathrm{d}^2\alpha_1 \mathrm{d}^2\beta_1 e^{-|\alpha_1|^2-|\beta_1|^2} \times R_1(\beta_1^*, (1-\mathcal{F}^2(t)\beta_1 + \mathcal{F}(t)\alpha_1) R_1(\alpha_1^*, \mathcal{F}(t)\beta_1) \; . \tag{12}$$

The time evolution of the fidelity in the case of the initial Schrödinger cat state of (10) is shown in Fig. 4. In (a) $F(t)$ is plotted for different values of the feedback efficiency η and with fixed values for the coupling constant g (the optimal choice $g = -1$ is considered) and for the ratio γ_1/γ_2. As expected, the preservation of the quantum state worsens for decreasing efficiencies. In (b) the effect of the timescale separation between source and driven mode is studied and $F(t)$ is plotted for different values of γ_1/γ_2 at fixed values for the coupling and the feedback efficiency (the optimal values $g = -1$ and $\eta = 1$ are considered). We notice in particular that the decay rates ratio γ_1/γ_2 plays an important role and that only in the adiabatic limit $\gamma_1/\gamma_2 \ll 1$ one gets a fidelity very close to one. Even in the adiabatic regime and in the ideal case (see for example the curve corresponding to $\gamma_1/\gamma_2 = 10^{-3}$), a finite value for γ_2 determines an appreciable initial slip from the condition $F(t) = 1$ at small times, before the fidelity saturates to its asymptotic value.

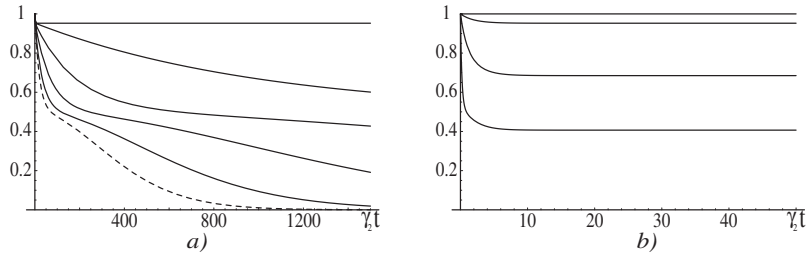

Fig. 4. Time evolution of the fidelity $F(t)$ in the case of an initial Schrödinger cat state (see (10) with $\alpha_0 = 5$ and $\varphi = 0$). (**a**) shows $F(t)$ for different values of the feedback efficiency η, with $g = -1$ and $\gamma_1/\gamma_2 = 10^{-3}$. From the top to the bottom: $\eta = 1$, $\eta = 0.99$, $\eta = 0.97$, $\eta = 0.95$, $\eta = 0.90$; the dashed line refers to $g = 0$ (absence of feedback). (**b**) shows $F(t)$ for different values of the decay rates ratio γ_1/γ_2 with $g = -1$ and $\eta = 1$ kept fixed. From top to bottom: $\gamma_1/\gamma_2 = 0$, $\gamma_1/\gamma_2 = 10^{-3}$, $\gamma_1/\gamma_2 = 10^{-2}$, $\gamma_1/\gamma_2 = 10^{-1}$

We have studied the behavior of the fidelity for a large class of initial states, as for example the linear superposition of Fock states of Fig. 3, and we have always found a behavior completely analogous to that shown in Fig. 4.

In conclusion, we have proposed an all-optical feedback scheme involving two orthogonally polarized modes in a cavity. The output light from the source mode is sent back using a Faraday isolator into the other, driven, mode and feedback is achieved by coupling the two modes within the cavity via a half-wave plate. In the adiabatic limit in which the driven mode is much more damped than the source mode, it is possible to choose the coupling constant so that in the ideal case of unit feedback efficiency one has freezing of the source mode dynamics, and therefore perfect preservation of quantum coherence. We have also shown that the protection capabilities of the scheme remain good even in the case of realistic values of the feedback efficiency.

References

1. Q.A. Turchette, C.J. Hood, W. Lange, H. Mabuchi, H.J. Kimble: Phys. Rev. Lett. **75**, 4710 (1995)
2. P. Goetsch, P. Tombesi, D. Vitali: Phys. Rev. A **54**, 4519 (1996)
3. V. Giovannetti, P. Tombesi, D. Vitali: Phys. Rev. A **60**, 1549 (1999)
4. D. Vitali, P. Tombesi, G.J. Milburn: Phys. Rev. Lett **79**, 2442 (1997)
5. D. Vitali, P. Tombesi, G.J. Milburn: Phys. Rev. A **58**, 4930 (1998)
6. C.W. Gardiner: Phys. Rev. Lett. **70**, 2269 (1993)
7. H.J. Carmichael: Phys. Rev. Lett. **70**, 2273 (1993)
8. H.M. Wiseman, G.J. Milburn: Phys. Rev. A **49**, 4110 (1994)
9. D.F. Walls, G.J. Milburn: *Quantum Optics* (Springer, Berlin 1994)
10. D.F. Walls, G.J. Milburn: Phys. Rev. A **31**, 2403 (1985)

Single-Photon Nonlinear Optics and Quantum Control*

Scott Parkins, Dan Walls and Atac Imamoğlu

Summary. Experiments using single atoms coupled strongly to high-finesse optical resonators are pushing nonlinear optics into a new realm where strong interactions between single-photon fields can be realized. In combination with subtle quantum interferences between different atomic transitions, which produce the phenomenon of electromagnetically-induced transparency, modifications of these experiments should enable such strong interactions to be implemented in an environment with minimal dissipation. Such an optical system is ideally suited to quantum information processing in a distributed network.

1 Introduction

Nonlinear optics is concerned with the interaction of light fields with media in which the induced polarization exhibits a nonlinear dependence on the electric field. Typically, the nonlinear terms in the polarization, which can give rise to effects such as harmonic generation, four-wave mixing and parametric down-conversion, are much smaller than the linear terms, and it requires very high intensities of the light fields for nonlinear effects to become significant. For example, in conventional nonlinear optical systems, the so-called Kerr nonlinearity, which gives rise to intensity-dependent phase shifts (associated with terms in the polarization of order 3 in the electric field), only yields effective field-field interactions at the level of roughly 10^{10} photons. That is, it generally requires powerful laser light sources producing essentially classical electromagnetic fields.

However, a fundamental challenge for nonlinear optics now being confronted by theorists and experimentalists alike is the realization of nonlinear systems able to mediate strong interactions between light fields at the *few-photon level*, or more generally where the *quantum* nature of the fields is manifest, in an environment with minimal dissipation. The possibility to address fundamental issues in physics such as quantum coherence and quantum measurement might seem motivation enough for this challenge, but perhaps

* This article was initiated by Dan Walls shortly before his death. Dan felt strongly that this particular area of research holds many exciting prospects for quantum optics. We have completed this article in tribute to Dan's remarkable insight and contributions to the advancement of the field.

H.J. Carmichael, R.J. Glauber, M.O. Scully (Eds.): LNP 561, pp. 217–229, 2001.

the major force now driving this research is the explosion of interest in quantum logic and computing and its possible implementation using quantum optical systems.

Remarkably, nonlinear systems operating in this quantum regime have in fact been demonstrated in the laboratory [1,2]. These pioneering demonstrations were based on effects in cavity quantum electrodynamics (cavity QED), using single atoms coupled strongly to high finesse microwave or optical cavity modes to generate Kerr-type nonlinearities capable of inducing large conditional phase shifts (on a probe atom or weak probe light field) *per photon* inside the cavity. Further exciting progress in the pursuit of giant optical nonlinearities has also been supplied recently, in quite dramatic form, by experiments using a dense ultracold atomic gas and a fascinating phenomenon known as electromagnetically induced transparency (EIT) [3]. EIT amounts to a cancellation of absorption associated with optical resonances and is a result of destructive quantum interference [4,5]. Surprisingly, and very fortuitously, this cancellation can occur in conjunction with the generation of large, resonantly-enhanced optical nonlinearities [6]. The ultracold-gas experiment demonstrated this possibility emphatically by realizing a perturbative Kerr nonlinearity enhanced by many orders of magnitude over conventional values. Indeed, the nonlinearity was of a magnitude where single photon effects should be significant [7], highlighting the potential of the EIT system, as suggested in [6], as a quantum logic device.

Encouraged by the theoretical and experimental results, a number of related proposals have appeared for the realization of, for example, single-photon "switches" or "blockades" using an EIT-based Kerr medium [8–14], possibly *inside* a high finesse optical cavity; that is, trying to utilize the combined potential of the cavity-QED- and EIT-based approaches to single-photon nonlinear optics. Since the energy level diagram of the EIT based schemes is generic to all alkali atoms, recent cavity QED experiments with single alkali atoms offer great encouragement for such schemes [15–17].

As further motivation for the present review, we begin with an overview of quantum computation and conditional quantum dynamics, outlining in somewhat more detail why quantum optical systems are being considered so actively in this context. We then describe briefly the first experimental demonstrations of single-photon nonlinear dynamics in cavity QED systems, after which we describe the EIT effect and discuss the proposed cavity-EIT schemes.

2 Quantum Computation and Cavity QED

The superposition principle of quantum mechanics and the phenomenon of quantum entanglement offer the possibility of fundamentally new forms of computation. While this possibility has been known for some time now, finding ways to exploit it in a specific and useful fashion has proved very chal-

lenging. However, quantum algorithms for the prime factorization of large integers and for performing fast searches on databases, recently developed by Peter Shor [18] and Lou Grover [19], respectively, have helped to transform quantum computation (QC) into a dynamic and rapidly expanding field of research, on both theoretical and experimental sides [20–22]. A further boost to the field has come with the invention of quantum error correction (QEC) and fault-tolerant QC, which demonstrates that (inevitable) decoherence need not be an obstacle to QC. However, the decoherence rate (normalized to the rate at which controlled gate operations can be carried out) has to be below an *accuracy threshold* in order to carry out reliable QC [22].

The fundamental variable in a classical computer is the bit, which can exist in *either* of two states, $|0\rangle$ or $|1\rangle$ say. The quantum equivalent, for a two-state variable, is known as a *qubit*, which, in accordance with quantum mechanics, can exist in any coherent *superposition* of $|0\rangle$ or $|1\rangle$; that is, both states can contribute to a single qubit, and hence to the behaviour and properties of that variable, *at the same time*. Naturally, a quantum computer that consists of n-qubits can, at any given time, be in a superposition of 2^n distinct states. Due to the linearity of quantum mechanics, the sequence of controlled quantum operations (that constitute QC) will be carried out for all 2^n states in parallel: this is sometimes referred to as *quantum parallelism* and is at the heart of the potential power of quantum computing [22].

Quantum logic gates must be able to operate on quantum variables and, preserving coherence, themselves generate quantum superpositions and entanglement in the output variables. The caveat to QC is the immense difficulty of engineering a sizeable network of quantum logic gates while minimizing dissipation, or decoherence, in the system so as to satisfy the accuracy threshold. The fragility of quantum superposition and entangled states is already well understood and appreciated. The larger and more macroscopic the system the more likely it is that quantum information will be distributed to uncontrollable degrees of freedom, spoiling the computational process. The challenge, therefore, is to engineer microscopic systems in which qubits can interact with each other, in sufficient isolation from the surrounding environment that repeated operations can be performed.

In order to achieve QC, we need to be able to modify the state of a quantum system (qubit), conditioned on another quantum variable: the simplest example for such *conditional quantum dynamics* is the controlled-not gate. It is perhaps not surprising that the cavity-QED experiments that we detail in the next section provided the first experimental realization of conditional dynamics at the quantum level. Over the last 20 years, quantum optics in general, and cavity-QED in particular, have proved to be an invaluable tool in investigating and understanding quantum phenomena. This is primarily due to the fact that the fundamental systems in quantum optics are relatively well isolated from their environment, and at the same time, they can be manipulated with a very high degree of precision using lasers. However, the residual

coupling to the electromagnetic environment through both atomic spontaneous emission and cavity losses severely limit the scalability of a quantum information processing scheme that is based on cavity-QED.

Scalability is a major problem arising in practically all of the vastly different physical implementations of QC: this is true even in schemes, such as the ion-trap quantum computer, where decoherence is much less of a problem in comparison to conventional cavity-QED schemes. As a result, it has been argued that an actual QC architecture is more likely to look like a quantum network, consisting of quantum information processing units that have a relatively small number of qubits, and that communicate with each other via quantum channels. All of the *quantum communication* schemes that have been proposed to that end are based on cavity-QED systems which establish the link between distant quantum systems via single-photon pulses [23–25]. Even though these schemes rely on linear pulse propagation, one can envision future schemes where conditional manipulation of single-photon pulses will also be important.

3 First Experimental Steps: Cavity QED

In quantum optics, cavity QED is concerned with the interaction of one or many atoms with a mode of the electromagnetic field supported by a resonator, or cavity [26]. In general, this cavity is formed by a pair of high-finesse mirrors whose spacing is carefully tuned to resonate with a particular transition between two internal states of the atomic species involved. If the dipole moment of the atomic transition is sufficiently large and the cavity mode volume sufficiently small (maximizing the "electric field per photon"), then the *single-photon* dipole coupling strength between an atom and the field mode can in fact exceed dissipative rates in the system due to mirror losses (i.e., finite mirror reflectivities) and atomic spontaneous emission; this corresponds to the strong-coupling regime of cavity QED.

Tremendous progress in experimental cavity QED over the past 10-15 years has pushed research squarely into this regime and opened the door to a variety of unique possibilities for investigating coherent quantum dynamics in a relatively simple and isolated system *at the few-photon level* [26]. In the present context, more particularly, it has enabled the demonstration of conditional quantum dynamics at the single-quantum level.

The first such demonstration, by Brune et al. [1], involved single Rydberg atoms interacting with a microwave field inside a superconducting cavity. Operating in the so-called *dispersive* regime, where the cavity mode and atomic transition frequencies are somewhat detuned from each other (such that energy exchange between the atom and the field is negligible), they effected a Kerr-type nonlinearity able to induce phase shifts of the atomic wave function at the level of 0.62 radians per photon in the field mode. How such a system

might be employed to implement an elementary two-bit quantum logic gate has been considered in Refs. [27,28].

Complementing this work, but dealing with *optical* fields and nonlinear photon-photon interactions, was the cavity QED experiment of Turchette et al. [2]. Their experiment involved a cesium atomic beam crossing a microscopic cavity mode (mirror separation 56 microns) such that there was, on average, one atom in the cavity at any time. Two laser beams, detuned from the joint atom-cavity resonance at slightly different frequencies, traversed the cavity together through its mirrors. The "pump" beam was either + or − circularly polarized and its intensity was such that the average photon population of the cavity mode ranged from less than 0.1 to more than 1. The second "probe" beam was linearly polarized and much weaker than the pump beam, with an intensity corresponding to approximately 10^{-4} photons on average in the cavity mode. Prepared in the appropriate internal ground state, the cesium atoms could interact appreciably only with + circularly polarized light, allowing a polarization-dependent Kerr-type nonlinearity (or circular birefringence) to be set up in the strongly coupled atom-cavity system. In this way, a relative phase shift between + and − circular polarization states of the probe beam could be induced, conditioned upon the intensity and polarization of the pump beam. This shift manifested itself as a polarization rotation of the (linearly-polarized) probe beam; from the measured rotation, a nonlinear phase shift of 0.28 radians per photon pair (if both pump and probe photons are + circularly polarized) could be inferred from the experiment. This is enormous compared to conventional nonlinear optics, dramatically illustrating the potential of cavity QED for conditional quantum dynamics.

Intensity-dependent phase shifts together with minimal absorption of the pump and probe beams are features also sought after for quantum nondemolition (QND) measurement, another very active subfield of quantum optics research aimed at developing strategies for evading the limitations on repeated measurements of quantum states imposed by Heisenberg's uncertainty principle [29]. Indeed, certain schemes developed recently for QND measurements employ effects and configurations similar to the EIT-based schemes that we consider below [30,31]. That is, they also make use of quantum interferences between atomic transitions to minimize loss while allowing resonantly-enhanced optical nonlinearities.

4 Electromagnetically Induced Transparency

Electromagnetically induced transparency (EIT) is a technique that uses a quantum interference effect to eliminate the optical response (polarization) of a medium [4,5]. The principal requirement for EIT is the existence of a forbidden optical transition with a long dephasing time. Even though such transitions are found in a wide range of atomic systems, here we will consider the hyperfine transitions of an alkali atom (Fig. 1). To attain transparency

for a given optical probe field (of frequency ω_a) that couples the ground atomic state $|1\rangle$ to an optically allowed excited state $|3\rangle$, one needs to apply a second nonperturbative electromagnetic field whose frequency differs from the first field by the frequency of the forbidden transition. Provided that the two-photon Raman resonance condition is satisfied, the atomic population is *coherently trapped* in a superposition state of the two hyperfine states ($|1\rangle$ and $|2\rangle$); that is, there is no amplitude in the excited state $|3\rangle$, and the atomic polarizability vanishes.

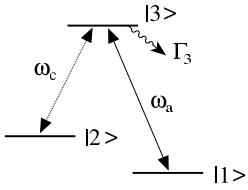

Fig. 1. Three-state EIT system. The upper state linewidth is Γ_3

The principal motivation for the large body of work on EIT as a technique to eliminate resonant absorption have come from the realization that in multi-level systems that are subject to quantum interference effects, the line shape of emission or nonlinear susceptibilities need not be the same as that of absorption [5]. This *nonreciprocity* opens up the possibility of resonant enhancement of nonlinear optical response while keeping linear absorption (and phase-shifts) negligible. Even though linear susceptibility vanishes for an ideal EIT system (where the dephasing rate of the hyperfine transition is zero), the medium still exhibits large dispersion that can exceed that of resonant atomic transitions: such a loss-free dispersive medium makes it possible to attain orders-of-magnitude reduction in the group velocity of the optical pulses [5]. When an EIT medium with large dispersion is introduced inside a cavity, the cavity response is significantly modified and exhibits ultranarrow resonances [32,33].

During the last decade, numerous experiments have demonstrated the existence and usefulness of EIT, in systems ranging from neutral atom-traps to semiconductors. Perhaps the most fascinating of these in the context of nonlinear quantum optics is the recent experiment by Hau et al. [3], in which a sodium Bose-Einstein condensate (BEC) was utilized to demonstrate Kerr nonlinearities almost 7 orders of magnitude larger than those reported previously with conventional cold atomic gases.

5 EIT and Giant Nonlinearities

Even though the possibility for resonant enhancement of sum-frequency generation and four-wave-mixing using EIT has been known for some time [5],

the possibility of using quantum interference effects to enhance the Kerr nonlinearity was first pointed out by Schmidt and Imamoğlu [6]. In their semiclassical perturbative analysis, appropriate for weak continuous-wave (cw) optical fields in a travelling-wave geometry, it was shown that in addition to the elimination of linear loss and phase shifts, the EIT system will, in certain limits, have a Kerr nonlinearity that is orders-of-magnitude larger than that of conventional resonant three-level systems.

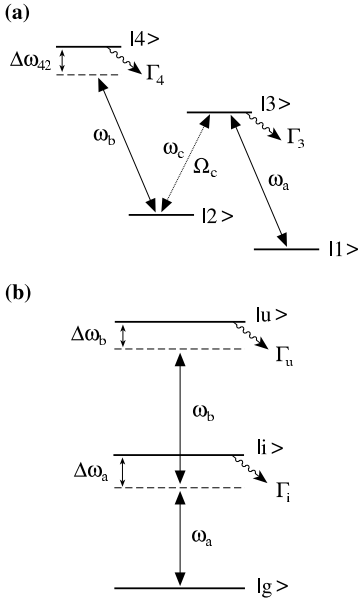

Fig. 2. Atomic energy level diagrams for the implementation of Kerr-type optical nonlinearities. The frequencies of the fields involved in the nonlinear process are $\omega_{\rm a}$ and $\omega_{\rm b}$. $\{\Gamma_k\}$ are the linewidths of the excited atomic states. (**a**) Four-level EIT-Kerr scheme of Schmidt and Imamoğlu. $\Omega_{\rm c}$ is the Rabi frequency of the coupling laser. (**b**) Conventional cross-phase modulation scheme using a three-level atomic medium

Fig. 2(a) shows the energy level diagram of the EIT-Kerr scheme that is at the heart of the proposals that follow: the only modification as compared to the basic EIT scheme is the introduction of a third electromagnetic field, of frequency $\omega_{\rm b}$, that couples state $|2\rangle$ to a higher energy (opposite parity) state $|4\rangle$. Solving the coupled amplitude equations in the perturbative regime yields the following expression for the real part of the Kerr nonlinearity $\chi^{(3)}$:

$$\mathrm{Re}[\chi^{(3)}]_{\rm EIT} = \frac{N|\mu_{13}|^2|\mu_{24}|^2}{2\epsilon_0\hbar^3\Omega_{\rm c}^2(\Delta\omega_{42})}\,. \tag{1}$$

Here, N is the atomic density, μ_{ij} denotes the dipole matrix element of the $|i\rangle \leftrightarrow |j\rangle$ transition, $\Omega_{\rm c}$ is the Rabi frequency of the coupling field, and $(\Delta\omega_{42}) = \omega_{42} - \omega_{\rm b}$. This expression is to be compared with the result for a conventional Kerr nonlinearity established using the atomic scheme shown in Fig. 2(b),

$$\mathrm{Re}[\chi^{(3)}]_{3-\rm Level} = \frac{N|\mu_{gi}|^2|\mu_{iu}|^2}{8\epsilon_0\hbar^3(\Delta\omega_{\rm gi})^2(\Delta\omega_{\rm iu})}\,. \tag{2}$$

The vital difference between the two expressions is that the detuning from the intermediate level in the conventional scheme, ($\Delta\omega_{\rm gi}$), is replaced by the Rabi frequency of the coupling laser, $\Omega_{\rm c}$, in the EIT scheme. The detuning ($\Delta\omega_{\rm gi}$) must be large in order to suppress spontaneous emission from the intermediate level $|i\rangle$; in particular, one requires ($\Delta\omega_{\rm gi}$) $\gg \Gamma_i$. In contrast, the lower limit for the Rabi frequency is given by the condition for EIT, $\Omega_{\rm c}^2 > \Gamma_2\Gamma_3$, but now $\Omega_{\rm c}$ can be much less than Γ_3 provided that $\Gamma_2 \simeq 0$, as is the case for a metastable level. Hence, as shown by Schmidt and Imamoğlu, in a four-level system exhibiting EIT one can achieve values for the Kerr nonlinearity that are orders of magnitude larger than in conventional systems.

A further important aspect of the EIT scheme is that it is generic to all alkali atoms and alkali-like ions, which in turn implies that it can be implemented in practically any cavity-QED set-up with the single addition of a non-perturbative coupling field. In addition, when hyperfine-split states are utilized, all three optical fields involved can be generated from a single source using acousto-optic modulators.

6 EIT and Cavity QED Combined: Photon "Blockade"

Suppose that one has a device which, when excited by a single photon, is unable to absorb a second incident photon, causing it to be reflected. In analogy with the phenomenon of Coulomb blockade of quantum well electrons, one might label such an effect as *photon blockade* [8]. As a possible realization of a photon blockade device, Imamoğlu et al. [8] have suggested using a nonlinear optical cavity (Fig. 3): provided that one can adiabatically eliminate the atomic degrees of freedom from the system dynamics, a simple effective Hamiltonian for the cavity field mode alone (annihilation operator $\hat{a}$) can be derived as

$$\hat{\mathcal{H}}_{\rm eff} = \hbar\omega_{\rm cav}\hat{a}^\dagger\hat{a} + \hbar\chi(\hat{a}^\dagger)^2\hat{a}^2 \tag{3}$$

where χ is the photon-photon interaction coefficient. Due to the finite reflectivities of the mirrors, the cavity mode has an inevitable loss rate, or linewidth, $\Gamma_{\rm cav}$. If the nonlinearity is large enough that $\chi \gg \Gamma_{\rm cav}$ is satisfied, photon blockade becomes possible via the following mechanism.
When the cavity mode is in the vacuum state, $|n = 0\rangle$, a photon from an external driving field tuned to the cavity frequency $\omega_{\rm cav}$ will excite the mode to the state $|n = 1\rangle$ with a probability determined by the driving field strength. However, excitation of the mode by a second photon at that frequency will be blocked because, due to the nonlinearity of (3), excitation of the system from $|n = 1\rangle$ to $|n = 2\rangle$ requires an additional energy $2\hbar\chi$, which cannot be supplied by the driving field (provided its amplitude and bandwidth are smaller than χ). Such a situation is depicted in Fig. 4. Hence, only after the first photon exits the cavity can a second photon enter.

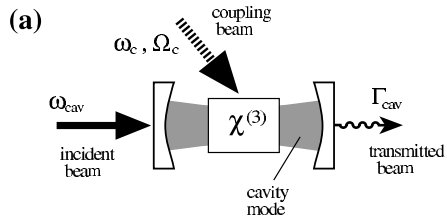

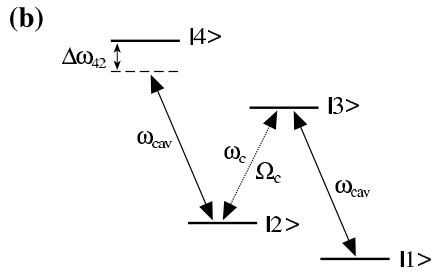

Fig. 3. (**a**) Nonlinear optical cavity. For simplicity, it is assumed that the mirror on the right has a smaller reflectivity and provides the dominant cavity output channel. (**b**) Energy level scheme of the intracavity atomic medium

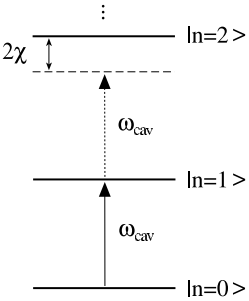

Fig. 4. Lowest three energy levels of the nonlinear optical cavity. Absorption of two photons from the incident laser is strongly suppressed due to the uneven spacing of the energy levels caused by the nonlinearity χ

This behaviour amounts to an effective *two-state* system, which is of course a well-studied problem in quantum optics in the context of resonance fluorescence from a two-level atom [34]. In analogy with that system, we expect the light transmitted through the cavity, as shown in Fig. 3, to exhibit *antibunching*. That is, an ideal detector counting photons emitted from the cavity should show a very low probability of registering two photons in a time interval shorter than the cavity mode lifetime. This effect is quantified by the normalized second-order coherence function,

$$g^{(2)}(\tau) = \frac{\langle \hat{a}^\dagger(t)\hat{a}^\dagger(t+\tau)\hat{a}(t+\tau)\hat{a}(t)\rangle}{|\langle \hat{a}^\dagger(t)\hat{a}(t)\rangle|^2}\,, \tag{4}$$

with antibunching characterized explicitly by having $g^{(2)}(0) < 1$. Ideal operation for a photon blockade or switch device requires $g^{(2)}(0) \simeq 0$ and a response time, or rise time, of $g^{(2)}(\tau)$ (to a value of the order of one) on the order of the cavity lifetime, $\Gamma_{\rm cav}^{-1}$ (perhaps 10–100 ns at optical frequencies). Strictly speaking, photon blockade and photon antibunching are closely related but distinct properties of a nonlinear atom-cavity system. Nevertheless,

when the coupled system behaves like a single two-level system, $g^2(0) \ll 1$ implies photon blockade [12].

Reference [8] suggested that an intracavity EIT-based Kerr medium could satisfy the requirements for photon blockade: with the (single) cavity mode coupled to both of the transitions $|1\rangle \leftrightarrow |3\rangle$ and $|2\rangle \leftrightarrow |4\rangle$, one can obtain, for the reasons discussed before, a large resonant enhancement in nonlinearity without creating any single-photon (or any significant two-photon) loss. However, more careful examination of the theoretical analysis, and in particular the adiabatic elimination procedure used to reach the simple model of (3), has shown that the ideal operating regime of the system is more restricted than originally thought [9,12]. Due to the dispersion properties of the atomic medium, elimination of the atomic variables actually requires $(g_{13}/\Omega_c)^2 n_{\rm atom} < 1$, which in turn implies that χ (in the perturbative limit) has an upper bound given by

$$\chi < \frac{|g_{24}|^2}{\Delta\omega_{42}} \,. \tag{5}$$

Here, $n_{\rm atom}$ is the total number of atoms and $g_{ij} = (\omega_{ij}/2\epsilon_0\hbar V_{\rm cav})^{1/2}\mu_{ij}$ ($V_{\rm cav}$ is the cavity mode volume). This upper limit simply indicates that the photon-photon interaction cannot exceed the ac-Stark shift of atomic level $|2\rangle$.

The breakdown of the adiabatic elimination procedure along with the fundamentally nonlinear nature of the problem implies that a fully quantum-mechanical analysis is needed in order to test the observability of photon blockade in the intracavity EIT system. To this end, Rebić et al. [13] have carried out a numerical calculation of the second-order coherence function for a *single* EIT atom inside a cavity, without making any approximations. Their results clearly demonstrate that such a system should indeed exhibit photon blockade, for parameters close to those of existing optical cavities [15]. For example, values of $g^{(2)}(0)$ of the order of 10^{-3} are possible with these parameters (see also [14]).

An analytical calculation based on the exact eigenstates of the atom-cavity system [12] reveals that the upper limit for the anharmonicity of the cavity-EIT scheme in the nonperturbative limit is g_{24}. Werner and Imamoğlu [12] have also shown that this upper limit can be attained for a single atom in a cavity, in agreement with the results of Rebić et al.. However, their investigations also demonstrate that the anharmonicity and the photon blockade effect closely associated with it, could have a very strong dependence on the number of atoms participating in the process; more precisely, when the cavity mode is exactly on resonance with the $|1\rangle \leftrightarrow |3\rangle$ transition and the atom number exceeds unity there is a sharp reduction in χ due to the appearance of a new eigenstate of the many-atom-cavity system that is decoupled from the state $|4\rangle$ and therefore does not experience an energy shift proportional to g_{24}. This eigenstate at energy $2\hbar\omega_{\rm cav}$ forces the atom-cavity system to

respond harmonically and consequently the photon blockade effect is essentially lost. For example, addition of a second atom to the numerical model mentioned above causes a jump in the simulated value of $g^{(2)}(0)$ to approximately 0.8 [14]. It is interesting to note that this result implies that for this particular detuning $\Delta\omega_{31} = \omega_{31} - \omega_{cav} = 0$, the adiabatic elimination of atomic variables is not justified even in the limit $(|g_{13}|/\Omega_c)^2 n_{\rm atom} < 1$.

In contrast, if we choose $\Delta\omega_{31} \sim \pm g_{13}$ while maintaining exact two-photon resonance (i.e., the EIT condition), then the nonlinearity as measured by the degree of photon antibunching in the limit of a large number of atoms is comparable to that of a single atom [12]. This possibility of observing strong photon antibunching and photon blockade in a cavity containing many atoms, where the atom number fluctuations become unimportant, opens up new possibilities for experimental cavity-QED research.

Finally, we note that a nonlinear optical cavity mode exhibiting effectively two-state behaviour can also arise with a single *two-level* atom coupled strongly and resonantly to the cavity mode [35]. The excitation frequencies of the lowest resonances of the coupled system (i.e., the *vacuum Rabi resonances*) are, as in the EIT scheme, different from all other frequencies in the spectrum of the atom-cavity system, allowing a two-state subsystem to be isolated. However, these lowest excited states have contributions from the atomic excited state and are therefore susceptible to atomic spontaneous emission. This, and the nature of the spectrum of the excited states for this system, result in a less favourable performance than the equivalent single-atom EIT scheme [14].

7 Summary and Outlook

The spectacular advances in experimental cavity QED and EIT over the past decade look set to usher in a remarkable new era in nonlinear optics and quantum control. Kerr nonlinearities such as those discussed above will enable the coherent interaction and manipulation of single-photon fields *with single-photon fields*. This represents the ultimate limit in nonlinear optics and achieving this goal has taken on particular significance in recent years with the tremendous upsurge of interest in the fields of quantum communication and quantum computation.

Beyond initial proof-of-principle demonstrations, the real test of the kinds of systems discussed here will lie in their ability to be incorporated into a (quantum) network of some kind, as appropriate, for example, to distributed quantum computation as discussed in Section II. Interestingly, Lloyd and Braunstein [36] have recently elucidated the necessary and sufficient conditions for constructing a universal quantum computer over continuous variables; required elements, for an optical realization (where the relevant variables are the quadrature phase amplitudes of the electromagnetic field), are simple linear devices such as beam splitters and phase shifters, squeezers

such as optical parametric oscillators, and, appropriately, devices supplying a strong Kerr effect with minimal losses. Another related, but perhaps more immediate application, might be to Bell-state analysis and measurement, in particular with regards to the quantum teleportation of the polarization state of a photon [37–39]. High-efficiency Bell-state analysis in such a case also requires a strong nonlinear interaction between single photons (see, e.g., [40] and references therein). These potential applications are, of course, fascinating in themselves; they serve here to emphasize once again some of the unique and special possibilities that single-photon nonlinear devices are likely to offer researchers in the near future.

Acknowledgments

We thank Stojan Rebić, Sze Tan and Mike Werner for helpful discussions. We also acknowledge support from the Marsden Fund of the Royal Society of New Zealand and a David and Lucile Packard Foundation Fellowship.

References

1. M. Brune *et al.*: Phys. Rev. Lett. **72**, 3339 (1994)
2. Q.A. Turchette *et al.*: Phys. Rev. Lett. **75**, 4710 (1995)
3. L.V. Hau, S.E. Harris, Z. Dutton, C.H. Behroozi: Nature **397**, 594 (1999)
4. A. Imamoğlu, S.E. Harris: Opt. Lett. **14**, 1344 (1989)
5. S.E. Harris: Phys. Today **50**(**7**), 36 (1997)
6. H. Schmidt, A. Imamoğlu: Opt. Lett. **21**, 1936 (1996)
7. S.E. Harris, L.V. Hau: Phys. Rev. Lett. **82**, 4611 (1999)
8. A. Imamoğlu, H. Schmidt, G. Woods, M. Deutsch: Phys. Rev. Lett. **79**, 1467 (1996); *ibid.* **81**, 2836 (1998)
9. P. Grangier, D.F. Walls, K.M. Gheri: Phys. Rev. Lett. **81**, 2833 (1998)
10. M.J. Dunstan *et al.*: 'Single photon quantum control via high-$\chi^{(3)}$ media'. In: *Quantum Communication, Computing, and Measurement 2*, ed. by P. Kumar, G.M. D Ariano, O. Hirota (Plenum Press, New York 1998)
11. S.E. Harris, Y. Yamamoto: Phys. Rev. Lett. **81**, 3611 (1998)
12. M. Werner, A. Imamoğlu: Phys. Rev. A **61**, 011801(R) (1999)
13. S. Rebić, S.M. Tan, A.S. Parkins, D.F. Walls: J. Opt. B: Quantum Semiclass. Opt. **1**, 490 (1999)
14. S. Rebić, D.F. Walls, M. Werner, A. Imamoğlu: 'Photon-photon interactions in cavity QED', unpublished
15. C.J. Hood, M.S. Chapman, T.W. Lynn, H.J. Kimble: Phys. Rev. Lett. **80**, 4157 (1998)
16. J. Ye, D.W. Vernooy, H.J. Kimble: Phys. Rev. Lett. **83**, 4987 (1999)
17. P. Münstermann, T. Fischer, P.W.H. Pinkse, G. Rempe: Opt. Commum. **159**, 63 (1999)
18. P.W. Shor: 'Polynomial-time algorithms for prime factorization and discrete logarithms on a quantum computer'. In *Proc. 35th Annual Symp. on Foundations of Computer Science* (IEEE Computer Society Press, Santa Fe, quant-ph/9508027, revised version)

19. L.K. Grover: Phys. Rev. Lett. **79**, 325 (1997)
20. C.H. Bennett: Phys. Today **48**(**10**), 24 (1995)
21. A. Ekert, R. Jozsa: Rev. Mod. Phys. **68**, 733 (1996)
22. A. Steane: Rep. Prog. Phys. **61**, 117 (1998)
23. J.I. Cirac, P. Zoller, H.J. Kimble, H. Mabuchi: Phys. Rev. Lett. **78**, 3221 (1997)
24. S.J. van Enk, J.I. Cirac, P. Zoller: Phys. Rev. Lett. **78**, 4293 (1997)
25. T. Pellizzarri: Phys. Rev. Lett. **79**, 5242 (1997)
26. P.R. Berman (ed.): *Cavity Quantum Electrodynamics* (Academic, San Diego 1994)
27. T. Sleator, H. Weinfurter: Phys. Rev. Lett. **74**, 4087 (1995)
28. P. Domokos, J.M. Raimond, M. Brune, S. Haroche: Phys. Rev. A **52**, 3554 (1995)
29. P. Grangier, J.A. Levenson, J.-P. Poizat: Nature **396**, 537 (1998)
30. K.M. Gheri, P. Grangier, J.-P. Poizat, D.F. Walls: Phys. Rev. A **46**, 4276 (1992)
31. J.-F. Roch *et al.*: Phys. Rev. Lett. **78**, 634 (1997)
32. G. Müller *et al.*: Phys. Rev. A **56**, 2385 (1997)
33. M.D. Lukin, M. Fleischauer, M.O. Scully: Opt. Lett. **23**, 295 (1998)
34. D.F. Walls, G.J. Milburn: *Quantum Optics* (Springer, Berlin 1994)
35. L. Tian, H.J. Carmichael: Phys. Rev. A **46**, R6801 (1992)
36. S. Lloyd, S.L. Braunstein: Phys. Rev. Lett. **82**, 1784 (1999)
37. C.H. Bennett *et al.*: Phys. Rev. Lett. **70**, 1895 (1993)
38. D. Boschi *et al.*: Phys. Rev. Lett. **80**, 1121 (1998)
39. D. Bouwmeester *et al.*: Nature **390**, 575 (1997)
40. L. Vaidmann, N. Yoran: Phys. Rev. A **59**, 116 (1999)

Normal-Mode Coupling of Excitons and Photons in Laterally Confined Nanocavities – Toward the Quantum Statistical Limit

Eun S. Lee, Sahnggi Park, Peter Brick, Claudia Ell, Christine Spiegelberg, Hyatt M. Gibbs, Galina Khitrova, Dennis G. Deppe, and Diana L. Huffaker

Summary. The observation of normal–mode coupling in a linear transmission measurement is demonstrated in an oxide–apertured microcavity which is capable of confining the light field three–dimensionally. A splitting–to-linewidth ratio of 4.9 was obtained for an aperture size of 2 μm. We also investigated the bare cavity modes for different aperture sizes, showing that lateral confinement is well achieved in cavities with high Q values.

1 Introduction

Semiconductor Fabry-Pérot microcavities have been used not only for some applications of enhancing the device performance, but also for fundamental studies of light-matter interactions. Since its first observation by Weisbuch et al. [1], normal–mode coupling in quantum–well–embedded semiconductor microcavities has been studied in the nonperturbative regime by many groups [1–4]. All present-day semiconductor microcavities still operate far from the strong coupling limit or the quantum statistical limit, i.e. many potential excitons are collectively involved in the light-matter coupling. However, only one single dipole oscillator with a large transition strength inside a microcavity of small volume and a high cavity quality factor (Q) can give vacuum Rabi splitting in the strong coupling regime. Eventually one hopes that this will be achieved with a single quantum dot in a laterally confined nanocavity [5]. Since the vacuum-field Rabi splitting is given by the product of the dipole moment and the vacuum field and since the dipole moment of a quantum dot is only about one order of magnitude larger than that of an atom, it is essential to maximize the vacuum field. The latter scales with one over the square root of the mode volume. Since the confinement length in the normal direction in a semiconductor microcavity is already close to its minimum value, lateral confinement of the electromagnetic field to about one micron diameter is required. Just focusing of the laser beam will not work, because the large angles involved in a tight focus lead to walk–off effects and broadening of the microcavity resonance. External lateral confinement is therefore necessary. Here we fabricate and test such nanocavities with cavity mode diameters ranging from 7 to1 μm. In nonlinear experiments performed

H.J. Carmichael, R.J. Glauber, M.O. Scully (Eds.): LNP 561, pp. 230–237, 2001.

on a planar semiconductor microcavity, we found that it takes about 10^5 photons to be absorbed from a 150 fs long laser pulse in a 50 μm spot to reduce the normal–mode–coupling transmission by a factor of two. By extrapolation, the same absorption should be induced by a single photon if the cavity diameter is ever reduced to 158 nm. Clearly, this would be a candidate for the quantum limit. For the case of the 3 μm diameter achieved here, the extrapolation gives 360 photons.

2 Sample Preparation

The recent progress in microfabrication techniques involving reactive ion etching has allowed a three-dimensional engineering of nanostructures starting from planar microcavities grown by molecular beam epitaxy[6–10]. Most structures are pillar shaped; large parts of the top mirror layers and the spacer are etched away all the way down to the bottom DBR mirror. The 3D confinement in this type of nanocavity is due to a large change of the refractive index in the lateral direction, thus the cavity quality factor Q is very sensitive to the roughness of the side walls [8]. In such structures, nonperturbative coupling of photons and excitons has been observed in photoluminescence measurements [7]. Other interesting studies involving a reduced number of electromagnetic modes have been carried out, for instance, controlling the spontaneous lifetime of excitons in quantum wells or dots [6].

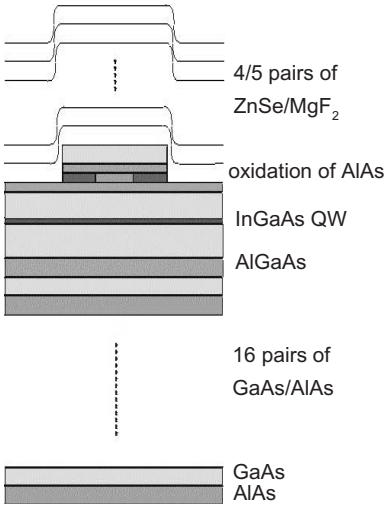

Fig. 1. Schematic of oxide–aperture microcavity

A different approach to achieve lateral confinement was demonstrated earlier by Deppe et al. [9]. They placed a thin dielectric (native oxide) aperture layer on top of the spacer to confine the current, and found lateral confinement as well. The physics of this effect was not clear at first sight. In the

meantime, the lateral confinement in this type of nanostructure has been associated with cut–off frequencies of a planar waveguide induced by the big difference in the refractive indices of the AlAs and the oxide [10]. In this article, we present experiments performed in the nonperturbative regime using such an oxide–aperture nanocavity. The sample under investigation is shown in Fig. 1, and it was prepared as follows. The DBR bottom mirror consists of 16 periods of GaAs/AlAs and a $\lambda/4$n layer of $Al_{0.8}Ga_{0.2}As$, a 1–λ spacer, and one GaAs/$Al_{0.8}Ga_{0.2}As$ period of the top mirror grown by molecular beam epitaxy. The spacer of GaAs and a 25–nm–wide $Al_{0.24}Ga_{0.76}As$ top layer contains one 8.5–nm–wide $In_{0.04}Ga_{0.96}As$ quantum well located in the antinode of the electromagnetic field. A 50–nm–wide AlAs layer was grown in the $Al_{0.8}Ga_{0.2}As$ layer of the top mirror for later oxidization. Photolithography and etching down to just above the spacer produced several arrays of posts with various diameters. The thin AlAs layer of these posts is then gradually oxidized in hot steam conditions resulting in various sizes of unoxidized AlAs apertures ranging from 1 to 7 μm. As a final step, the entire sample was coated with 4 or 5 periods of $ZnSe/MgF_2$ acting as the top mirror. Since the lateral spacing between the adjacent apertures is 100 μm, coupling between apertures can be excluded.

3 Experimental Results

Transmission experiments were performed using a spectrally broad 100 fs pulse from a Ti:saphire laser pumped by a 6 W Ar–ion laser. The sample was mounted in an optical cryostat equipped with an x–y–z stage. To make the probe spot size small enough to be comparable with an aperture size, a microscope objective with a numerical aperture of 0.3 was used as a focusing lens. The transmitted light was dispersed and detected by a monochromator and an optical multichannel analyzer.

First, we investigated the behavior of bare cavity modes for various aperture sizes. The layer thickness changes of our sample across the wafer allow us to measure at an energy of about 1.415 eV, far off–resonance from the exciton transition at 1.485 eV; this avoids the coupling of the optical mode to the quantum well exciton. Fig. 2 shows the transmission spectra of the modes for various aperture diameters. The data were taken at a solid angle of 30°. As expected, one clearly sees a number of transverse modes due to the lateral confinement of the cavity mode.

The first quantized mode shifts to higher energies with respect to the two–dimensional (2D) reference. As 2D reference we use a large aperture size of 25 μm, where we do not expect any significant lateral confinement effects. The smaller the aperture size, the stronger is the confinement of the cavity mode, the larger is the blue shift of the ground state photon energy, and the larger is the splitting of the higher transverse modes. To verify the three–dimensional confinement further, angular transmission measurements have

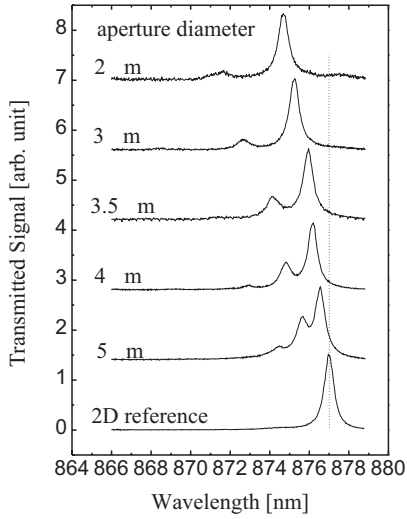

Fig. 2. Transmission spectra of oxide–aperture microcavities with varying aperture size at 10 K

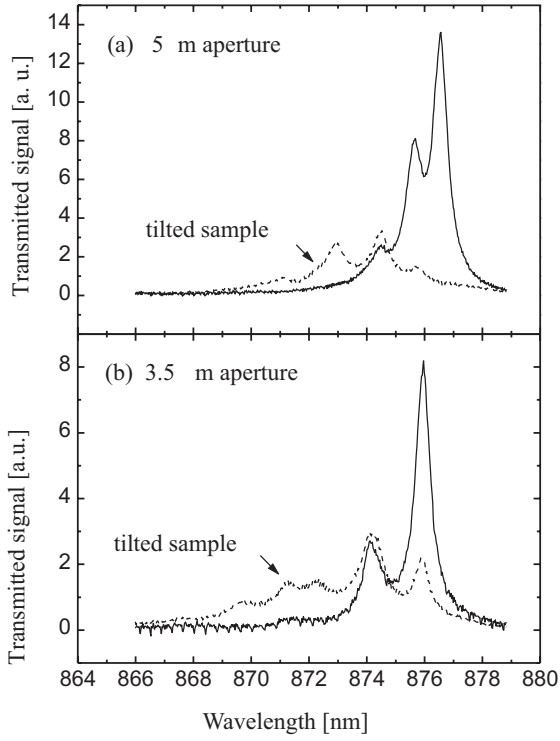

Fig. 3. Transmission spectra at 10° from normal for (**a**) 5 μm, (**b**) 3.5 μm aperture size

been performed by tilting the sample about 10^o from normal incidence; see Fig. 3. For the 2D reference, a blue shift of the cavity peak of about 0.6 nm was observed. In contrast, the spectral position of each transverse mode in the confining aperture did not change, verifying the lack of lateral dispersion of the quantized modes. However, with increased angle of observation, the intensities of the individual modes redistribute toward the higher energy states.

Linewidth measurements of the first quantized cavity mode were performed with high resolution, and the cavity quality factor $Q = \Delta\lambda/\lambda$, was estimated for each aperture size as shown in Fig. 4.

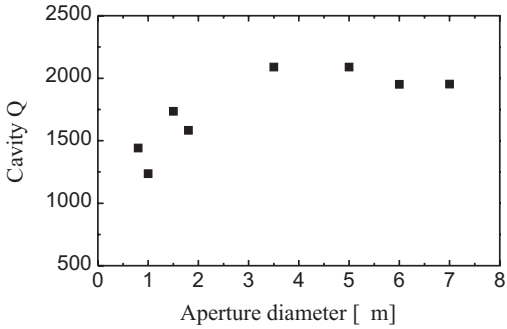

Fig. 4. Cavity Q versus aperture diameter

We found a decrease of the Q value for smaller aperture diameters. The Q reduction is much less pronounced compared to the pillar shaped nanocavities reported previously [8]. We believe this is due to an already lower quality factor in our unconfined samples. We have deliberately made the reflection of the bottom mirror low to make sure that lateral losses would not dominate the cavity behavior at all diameters. We expect to get an even higher Q value after improving the fabrication and processing of the sample. In a recently processed sample we already obtained a little higher Q of $\approx$ 2000 for 2 μm by just adding one more period to the top mirror. Together with our high–quality quantum well exciton of $\approx$ 0.6 meV FWHM absorption linewidth these Q values are high enough to show normal mode coupling with small apertures.

To find the resonance condition of the exciton and the photon mode for normal mode coupling, we used both possibilities: Taking advantage of the varying sample thickness in growth direction and scanning the probe spot keeping the same aperture size, and varying the temperature using the stronger dependence of the exciton transition energy to tune through the cavity resonances. We see a well–resolved normal–mode coupling and an anticrossing behavior by both approaches, although the discrete spacing of adjacent apertures and some aperture–size fluctuations made the temperature approach preferable. Figure 5 shows the normal–mode–coupling behavior of

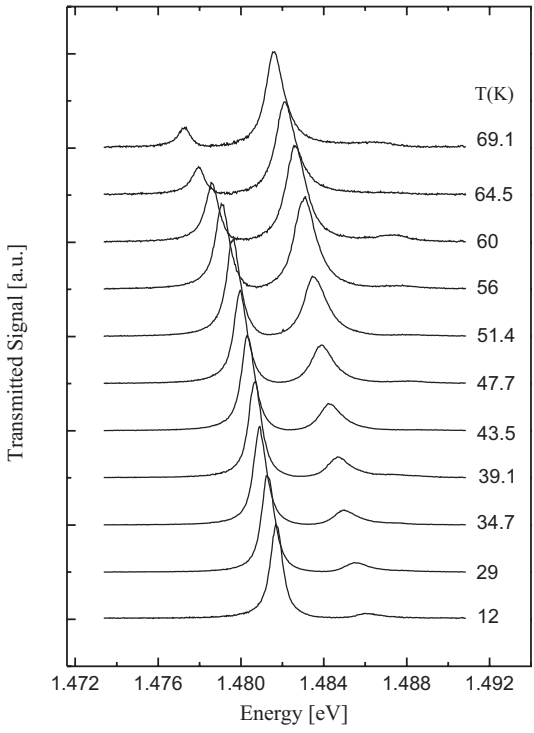

Fig. 5. Transmission spectra of a 2 μm oxide–aperture nanocavity for various temperatures

a 2 μm oxide–aperture cavity measured in transmission. Since the second transverse mode for this small aperture barely shows up in our near–normal–incidence experimental setup as can be seen in Fig. 2, we did not see coupling of the exciton resonance to higher transverse modes; see Fig. 5.

Figure 6 shows the anti–crossing curve and the energy splitting across the resonance for this 2 μm oxide–aperture nanocavity.

The coupling of the quantum well and the first cavity mode results in a minimum splitting (vacuum–field Rabi splitting) of 3.9 meV and a splitting–to–linewidth ratio of 4.9, a value that has not been reached in previous approaches because of broader exciton resonances. In addition, we found that the value 3.9 meV is not much different from the 2D reference value of 4.0 meV, whereas, in pillar shaped nanocavities reported by Gutbrod et al., a relatively larger reduction of $\approx 10\%$ of the Rabi splitting was observed [7] due to the lateral extension of the field in the bottom mirror beyond the etched region. Their physical argument given to the reduction suggests that the oxide–aperture nanocavity may be a more effective way to confine the photon mode laterally.

There is also one notable effect of the dielectric top mirror on our sample. Due to the higher refractive index contrast of the ZnSe and MgF_2 layers of the top mirror, we observe stronger field confinement in the normal direction

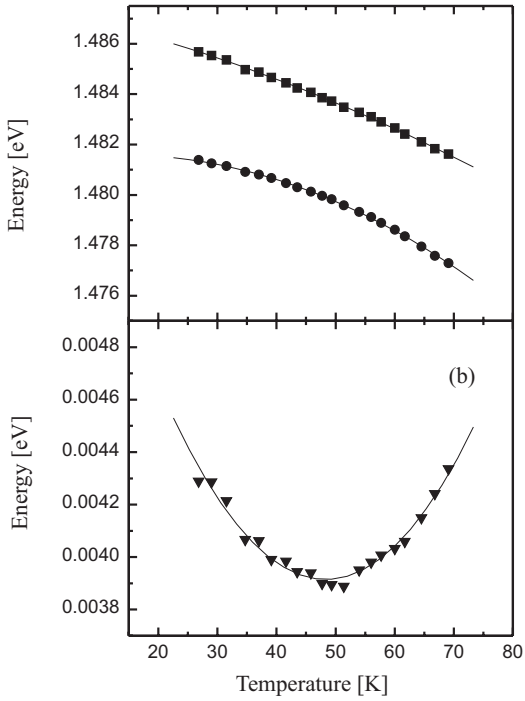

Fig. 6. Spectral positions of the transmission peaks with varying temperature (**a**). Spectral separation of the two peaks with varying temperature. The minimum splitting occurs around 50 K (**b**). Solid lines for guidance

leading to a 16 % larger vacuum-field Rabi splitting for the 2D reference compared to microcavities made with a GaAs/AlAs top DBR mirror.

4 Conclusions

In conclusion, we demonstrated that oxide–aperture nanocavities are well suited to study the nonperturbative regime. The 3D optical–mode confinement gives rise to quantized cavity modes which are energetically well separated. Very well–resolved normal–mode coupling (splitting–to–linewidth ratio of 4.9) between the first quantized cavity mode and the quantum well exciton resonance has been observed for the first time in such nanocavities. Nonlinear single beam experiments have shown that it takes about 400 photons to significantly change the absorption in a 3–μm aperture sample. This value being very close to the estimate made above, we believe that these quantum–well nanocavities are clearly a step toward the quantum statistical limit.

Acknowledgments

We acknowledge support from NSF (EPDT and AMOP), NSA/ARO, JSOP (AFOSR and ARO), and COEDIP. H. M. G. acknowledges support of a Humboldt Research Award.

References

1. C. Weisbuch, M. Nishioka, A. Ishikawa, Y. Arakawa: Phys. Rev. Lett. **69**, 3314 (1992)
2. R.P. Stanley, R. Houdré, U. Oesterle, M. Ilegems, C. Weisbuch: Appl. Phys. Lett. **65**, 2093 (1994)
3. E.K. Lindmark, T.R. Nelson, Jr., G. Khitrova, H.M. Gibbs, A.V. Kavokin, M.A. Kaliteevski Opt. Lett. **21**, 994 (1996)
4. G. Khitrova, H.M. Gibbs, F. Jahnke, M. Kira, S.W. Koch: Rev. Mod. Phys. **71**, 1591 (1999)
5. C. Ell, H.M. Gibbs, G. Khitrova, E.S. Lee, S. Park: D.G. Deppe, D.L. Huffaker, IEEE–LEOS Newsletter **13**, 8 (1999)
6. J.M. Gérard, B. Sermage, B. Gayral, B. Legrand, E. Costard, V. Thierry–Mieg: Phys. Rev. Lett. **81**, 1110 (1998)
7. T. Gutbrod, M. Bayer, A. Forchel, J.P. Reithmaier, T.L. Reinecke, S. Rudin, P.A. Knipp: Phys. Rev. B **57**, 9950 (1998)
8. T. Rivera, J.-P. Debray, J.M. Gérard, B. Legrand, L. Manin–Ferlazzo, J.L. Oudar: Appl. Phys. Lett. **74**, 911 (1999)
9. D.L. Huffaker, D.G. Deppe: Appl. Phys. Lett. **67**, 2594 (1995)
10. D.G. Deppe, T.-H. Oh, D.L. Huffaker: IEEE Photonics Technol. Lett. **9**, 713 (1997)

Cavity QED with Many Atoms

Ullrich Martini and Axel Schenzle

Summary. A new method is presented for describing an arbitrary number of atoms interacting with a resonant cavity mode. The state space of the atoms is symmetrized over permutations of the atoms. The symmetrized states are characterized by collective variables like angular momentum and its projection numbers. It is shown that the collective description is still applicable when spontaneous emission is included. The theory is in good agreement with experimental results.

1 Introduction

Modern quantum optical experiments [1–4] usually investigate systems consisting of very few atoms and photons. Large systems tend to behave more or less classically. Unfortunately, only very small systems can be treated exactly, because the state space required to describe larger systems increases exponentially with the system size. Therefore previous attempts at describing a cavity containing many atoms were restricted to very low photon numbers [5], unitary dynamics [6] or adiabatic elimination of the resonator mode [7]. In this paper we will show how one may use the coupling of two-level atoms [8] to a collective angular momentum [9,10] to solve this problem even when spontaneous emission of photons by individual atoms is included in the description. Our theory allows to treat systems consisting of an intermediate number of atoms where quantum effects and cooperative effects are visible.

There are many possible applications of this new approach. We concentrate on the computation of the normally-ordered intensity correlation function of the light emitted by a cavity that contains a large number of atoms, because in this case we may compare our results directly with experimental observations. We find good agreement between our theory and the experiment.

The model we discuss here is characterized by the master equation $\frac{\mathrm{d}}{\mathrm{d}t}\hat{\rho} = \mathcal{L}\hat{\rho}$ for the density operator $\hat{\rho}$ in Lindblad form [11], where

$$\mathcal{L}\hat{\rho} = \frac{1}{i\hbar}[H,\hat{\rho}] + \mathcal{L}_a\hat{\rho} + \mathcal{L}_f\hat{\rho} \tag{1}$$

with the Hamilton operator

$$H = \hbar\omega a^\dagger a + \frac{\hbar\Omega}{2}\sum_i \sigma_z^{(i)} - \frac{\hbar g}{2}\sum_i (a^\dagger\sigma_-^{(i)} + a\sigma_+^{(i)}) - \frac{\hbar\epsilon}{2}(\mathrm{e}^{iwt}a + \mathrm{e}^{-iwt}a^\dagger), \tag{2}$$

H.J. Carmichael, R.J. Glauber, M.O. Scully (Eds.): LNP 561, pp. 238–249, 2001.

the resonator mode dissipation

$$\mathcal{L}_f\hat{\rho} = -\frac{A}{2}(a^\dagger a\hat{\rho} + \hat{\rho}a^\dagger a - 2a\hat{\rho}a^\dagger) \tag{3}$$

and the atomic dissipation

$$\mathcal{L}_a\hat{\rho} = -\frac{B}{2}\sum_i(\sigma_+^{(i)}\sigma_-^{(i)}\hat{\rho} + \hat{\rho}\sigma_+^{(i)}\sigma_-^{(i)} - 2\sigma_-^{(i)}\hat{\rho}\sigma_+^{(i)}) \tag{4}$$

Here a and $a^\dagger$ are the ladder operators of the resonator mode, ${\sigma_\pm}^{(i)} = \frac{1}{2}(\sigma_x^{(i)} \pm i\sigma_y^{(i)})$ and $\sigma_x^{(i)}, \sigma_y^{(i)}, \sigma_z^{(i)}$ are the 2×2 Pauli spin matrices describing the polarization and inversion of the $i-$th atom.

We assume resonance $\omega = \Omega$. The first two terms of the Hamilton operator vanish in the appropriate interaction picture. This model does not include finite temperatures, because we will compare it to an experiment operating in the optical regime. The method presented can easily be extended to include finite temperatures.

2 Symmetric Atomic Bases

In order to describe an experiment which measures only the state of the resonator mode and not the state of the atoms it is not necessary to know the state of the atoms involved in this experiment.

The dimension of the state space of Z 2-level atoms is 4^Z, since each of these atoms is described by a 2×2-dimensional density operator. This number increases very rapidly with increasing Z and makes it impossible to diagonalize the Liouville operator of a system with a large number of atoms. But there are two effects that reduce the number of dimensions: first, for low photon numbers not all atoms can be excited simultaneously because not enough energy is available to excite all atoms and, second, if one is only interested in the number of atoms found in a particular state, it is possible to symmetrise the atomic state space over all atomic permutations. The dimension of the symmetric subspace is only $\frac{1}{6}(Z+1)(Z+2)(Z+3)$, i.e. it increases polynomially instead of exponentially with the number of atoms.

A two-level system like an atom with two internal states may formally be described as a particle of spin $\frac{1}{2}$. Therefore, a system of Z two-level systems may be described collectively using the angular momentum obtained by coupling the individual spins. In this picture, the projection quantum number m represents the number of excited atoms while the quantum number l gives the maximum and minimum values of m. It can be interpreted as the degree of symmetry of the collective atomic state. In the state with $m = -\frac{Z}{2}$, all atoms are in the ground state, while in a state with $m = \frac{Z}{2}$ all atoms are excited. The general relation between the projection quantum number m and the number n_a of excited atoms is $n_a = m + \frac{Z}{2}$.

R. H. Dicke introduced these collective states in order to describe superradiant emission by a cloud of excited two-level systems [9]. In order to include spontaneous emission, we need a density operator generalization of the Dicke state vectors. This generalization requires that we express the Liouville operator describing spontaneous emission in terms of the Dicke density operators. Before doing so, we will first recapitulate the properties of the Hamiltonian part of the Liouville operator.

Taking the sum over the one-atom operators we obtain collective operators

$$S_- = \sum_i \sigma_-^{(i)}, \quad S_+ = \sum_i \sigma_+^{(i)}, \quad S_k = \frac{1}{2} \sum_i \sigma_k^{(i)}, k = x, y, z \tag{5}$$

which have the same algebraic properties as the well-known angular momentum operators. In this picture, m and $l(l+1)$ are the eigenvalues of S_z respectively $L^2 = S_x^2 + S_y^2 + S_z^2$.

The atomic part $S_\pm$ of the Hamilton operator acts on such an angular momentum eigenstate just like the ladder operator from usual angular momentum theory. In particular, the Hamilton operator commutes with the angular momentum operator.

Unfortunately, the space spanned by the states with $l = \frac{Z}{2}$ is much too small to investigate the effects of atomic spontaneous emission. This can be seen most easily by applying the atomic Lindblad operator $\mathcal{L}_a$ to the operator $\left|Z, \frac{Z}{2}, m\right\rangle \left\langle Z, \frac{Z}{2}, m'\right|$.

The resulting operator is no longer a left or right eigenstate of the angular momentum, but a mixture of density operators with different angular momenta. Therefore a description that contains only the states with highest symmetry is incomplete under the Liouville dynamics. A complete description of the system suitable for calculating the effects of spontaneous emission must contain all values of l. However, the states with $l < \frac{1}{2}$ are not uniquely characterized by Z, l and m. For example, there are two orthogonal states with $Z = 3, l = \frac{1}{2}, m = \frac{1}{2}$: $\frac{1}{\sqrt{2}}(|++-\rangle - |+-+\rangle)$ and $\frac{1}{\sqrt{6}}(|++-\rangle + |+-+\rangle - 2\,|-++\rangle)$. Because of this ambiguity it is necessary to introduce a fourth index, r, in order to label the different states $|Z, l, m, r\rangle$ with the same values of Z, l and m. Since r is only a label we can assign arbitrary numbers to the different states.

We choose Dicke vectors with different values of r to be orthogonal. Using Clebsch-Gordan coefficients one can show that this is possible. From the Dicke vectors we construct symmetric operators by taking the sum over r:

$$\hat{\xi}_{Z,l,m,m'} = \sum_r |Z, l, m, r\rangle \langle Z, l, m', r| \tag{6}$$

$$\check{\xi}_{Z,l,m,m'} = \frac{1}{g(Z,l)} \sum_r |Z, l, m', r\rangle \langle Z, l, m, r| \,. \tag{7}$$

The number $g(Z, l)$ is a normalization factor. Note that m and m' have been exchanged in the definition of the dual base states in order to ensure

the biorthogonality of $\hat{\xi}_{Z,l,m,m'}$ and $\check{\xi}_{Z,l,m,m'}$, i.e. $\mathrm{tr}\left(\hat{\xi}_{Z,l,m,m'}\check{\xi}_{Z,l,m,m'}\right) = 1$. The summation over r is in fact a symmetrization procedure.

The operators $\hat{\xi}$ form a basis of the operator space under consideration, the operators $\check{\xi}$ are the dual basis operators. Since $\mathcal{L}$ is not hermitian, one has to distinguish between base and dual eigenoperators.

The states with $l < \frac{Z}{2}$ are $g(Z,l)$-fold degenerate where [9]

$$g(Z,l) = \binom{Z-1}{\frac{Z}{2}-l} \frac{Z(2l+1)}{(\frac{Z}{2}+l+1)(\frac{Z}{2}+l)}. \tag{8}$$

In a system without atomic spontaneous emission this degeneracy has no consequences, even if unsymmetric states like dark states are considered. But the degeneracy enters explicitly into the calculation of the matrix elements of the atomic Liouville operator, since this operator couples states with different values of l.

The image of a state from the symmetric space under the action of the Liouville operator $\mathcal{L}$ is contained in the symmetric space, because the dissipation does not distinguish between different atoms[1]. Therefore the expansion

$$\mathcal{L}_a\hat{\xi}_{Z,l,m,m'} = \sum_{\bar{Z},\bar{l},\bar{m},\bar{m}'} c_{Z,l,m,m';\bar{Z},\bar{l},\bar{m},\bar{m}'}\hat{\xi}_{\bar{Z},\bar{l},\bar{m},\bar{m}'} \tag{9}$$

is possible.

We need to calculate the matrix elements

$$\begin{aligned}
\lambda_-(Z,l,m,m') &= \mathrm{tr}\left(\check{\xi}_{Z,l,m,m'}\mathcal{L}_{a,\mathrm{nd}}\hat{\xi}_{Z,l+1,m+1,m'+1}\right)\\
\lambda_o(Z,l,m,m') &= \mathrm{tr}\left(\check{\xi}_{Z,l,m,m'}\mathcal{L}_{a,\mathrm{nd}}\hat{\xi}_{Z,l,m+1,m'+1}\right)\\
\lambda_+(Z,l,m,m') &= \mathrm{tr}\left(\check{\xi}_{Z,l,m,m'}\mathcal{L}_{a,\mathrm{nd}}\hat{\xi}_{Z,l-1,m+1,m'+1}\right)
\end{aligned} \tag{10}$$

of the third term

$$\mathcal{L}_{a,\mathrm{nd}}\rho = B\sum_i \sigma_-^{(i)}\rho\sigma_+^{(i)} \tag{11}$$

in (4) which we call occasionally the loss part of the atomic Liouville operator. The remainder of the atomic Liouville operator is diagonal in the Dicke base an will therefore be called the diagonal part. The index refers to the change in the angular momentum due to the action of $\mathcal{L}$. The angular momentum cannot change by more than unity. But since the Liouville operator is a sum of single-atom operators and each single-atom operator can change the angular momentum at most by unity we obtain an analogue to the common selection rules of quantum electrodynamics: Matrix elements of the atomic Liouville operator between Dicke states that differ by more than 1 in their angular momentum quantum number l must vanish.

[1] The formal proof of this statement is given in [12]

Since the Hamilton operator commutes with L^2 this holds also for the complete Liouville operator. This is the angular momentum selection rule: for the matrix elements (10) to be nonzero the condition

$$l - \bar{l} \in \{-1, 0, 1\} \tag{12}$$

must be met.

In the picture of uncoupled atoms the proof of this selection rule goes as follows: We start with a cluster of atoms coupled to a Dicke state with angular momentum l If spontaneous emission or absorption of a photon from the bath or the pump source occurs, the atom affected by that process drops out of the Dicke vector used in the construction of the Dicke states. The remaining atoms are a linear combination of states with angular momentum l' where $|l - l'| = \frac{1}{2}$. Upon recombining the atom with the other atoms we obtain a linear combination of states with angular momentum $\bar{l}$ where $|l' - \bar{l}| = \frac{1}{2}$. Then the triangle inequality gives the desired bound on $\bar{l}$:

$$|l - \bar{l}| = |l - l' + l' - \bar{l}| \leq |l - l'| + |l' - \bar{l}| = 1. \tag{13}$$

The difference $l - \bar{l}$ must have integer values since the angular momenta are half-integers if the number of atoms is odd and integers if the number of atoms is even.

The angular momentum selection rule is the crucial point for the calculation of the matrix elements we are going to present here. This selection rule looks completely analogous to the selection rule known from the interaction of a single atom with an electromagnetic field, but it is of completely different origin.

There are two additional selection rules for the projection quantum numbers $m, m', \bar{m}, \bar{m}'$:

$$m - m' = \bar{m} - \bar{m}'. \tag{14}$$

$$m + m' - (\bar{m} + \bar{m}') = \begin{cases} 1 & \text{loss part} \\ 0 & \text{diagonal part} \end{cases}. \tag{15}$$

2.1 Matrix Elements of the Liouville Operator

The first and second term of the atomic Liouville operator (4) are diagonal in all representations used here. The third term (11) does not commute with the angular momentum. The calculation of its matrix elements will be performed in three steps: First, we find three representative matrix elements, corresponding to $l - \bar{l} = -1, 0$ or 1 from which all other matrix elements can be calculated with the help of ladder operators $S\pm$. Second, we use the angular momentum selection rule (12) to demonstrate that these representative matrix elements may be obtained from a set of three linearly independent equations. Third, we will find these three equations using the recurrence relation (22) and solve them.

The ladder operator S_- commutes with the loss part $\mathcal{L}_{a,\mathrm{nd}}$, since the relation

$$\mathcal{L}_{a,\mathrm{nd}}\left(S_-^{(\nu)}\rho S_+^{(\mu)}\right) = S_-^{(\nu)}\mathcal{L}_{a,\mathrm{nd}}\left(\rho\right)S_+^{(\mu)} \tag{16}$$

holds for any atomic operator ρ. Eqn. (16) connects matrix elements with different values of $m, m', \bar{m}$ and $\bar{m}'$ by expressing the Dicke basis states by other Dicke states multiplied by ladder operators. Then we exchange these ladder operators with the Liouville operator and finally apply them to the Dicke base states of the matrix element.

We have to consider the three cases $\bar{l} = l-1$, $\bar{l} = l$, $\bar{l} = l+1$. In the case $\bar{l} = l-1$, the maximal possible value of $\bar{m}$ or $\bar{m}'$ is $\bar{l}$. But in the case $\bar{l} = l$, the maximal possible value of $\bar{m}$ or $\bar{m}'$ is $\bar{l}-1$ since the maximal possible value of m respectively m' is l and the atomic Liouville operator reduces the number of excited atoms by 1. By the same argument, in the case $\bar{l} = l+1$ the maximally possible value of $\bar{m}$, $\bar{m}'$ is $\bar{l}-2$. In each of these three cases we express arbitrary matrix elements by the one corresponding to the maximal value of $\bar{m}$ and $\bar{m}'$:

$$\begin{aligned}
\lambda_-(Z,l,m,m') &= \frac{\sqrt{(l+m)(l+m-1)(l+m')(l+m'-1)}}{2l(2l-1)}\lambda_-(Z,l,l,l),\\
\lambda_o(Z,l,m,m') &= \frac{\sqrt{(l-m+1)(l+m)(l-m'+1)(l+m')}}{2l}\lambda_o(Z,l,l-1,l-1),\\
\lambda_+(Z,l,m,m') &= \frac{\sqrt{(l-m)(l-m-1)(l-m')(l-m'-1)}}{2}\lambda_+(Z,l,l-2,l-2).
\end{aligned} \tag{17}$$

The square roots are the remainders of the ladder operators.

The three matrix elements on the right side of equation (17) remain to be calculated. To do so we need an additional set of basis states, the spinflip states and the matrix elements between Dicke and spinflip states

$$\hat{R}_{p_+,p_-,n_-,n_+} = \mathcal{S}\prod_{i=1}^{p_+}\pi_+^{(i)}\prod_{i=p_++1}^{p_++p_-}\pi_-^{(i)}\prod_{i=p_++p_-+1}^{p_++p_-+n_+}\sigma_+^{(i)}\prod_{i=p_++p_-+n_++1}^{Z}\sigma_-^{(i)} \tag{18}$$

$$\check{R}_{p_+,p_-,n_-,n_+} = \frac{\hat{R}_{p_+,p_-,n_+,n_-}}{N(p_+,p_-,n_+,n_-)} \tag{19}$$

$$x_{m,n_+}^{(Z,l,m)} = \mathrm{tr}\left(\hat{\xi}_{Z,l,m,m}\check{R}_{Z,m,n_+,n_+}\right) \tag{20}$$

where $\pi_\pm^{(i)}$ is the projector on the upper respectively lower state of the ith atom. We introduce these states because there is a simple recurrence relation between them and the Dicke states and the effect of the atomic dissipation is easily calculated in the spinflip basis:

$$\begin{aligned}
&\mathcal{L}_a\hat{R}_{p_+,p_-,n_-,n_+}\\
&\quad= \frac{B}{2}(2p_+ + n_+ + n_-)\hat{R}_{p_+,p_-,n_-,n_+} - \frac{B}{2}2p_+\hat{R}_{p_{+-1},p_{-+1},n_-,n_+}.
\end{aligned} \tag{21}$$

Since the base states are symmetric with respect to permutations of atoms, the matrix elements of the squared angular momentum operator L^2 with respect to these base states are easily calculated using the expression of L^2 in terms of single-atom Pauli matrices. We project the eigenvalue equation $L^2\hat{\xi}_{l,m,m} = l(l+1)\xi_{l,m,m}$ onto the spinflip states in order to obtain the recurrence relation

$$\begin{aligned} & x^{(Z,l,m,m)}_{m,n_++1}\left(\frac{Z}{2}+m-n_+\right)\left(\frac{Z}{2}-m-n_+\right) \\ & = -\left(\frac{Z}{2}+m^2+Zn_+-2n_+^2-l(l+1)\right)x^{(Z,l,m,m)}_{m,n_+}+n_+^2x^{(Z,l,m,m)}_{m,n_+-1} \end{aligned} \quad (22)$$

for the matrix elements of the Dicke states with respect to the spinflip base.

Because of the angular momentum selection rule (12) and the linearity of the Liouville operator there are coefficients $\lambda_-, \lambda_o, \lambda_+$ such that

$$\begin{aligned} \mathcal{L}_{a,\mathrm{nd}}\hat{\xi}^{(Z,l,m_l,m_l)} = {} & \lambda_-\hat{\xi}^{(Z,l-1,m_l-1,m_l-1)} \\ & +\lambda_o\hat{\xi}^{(Z,l,m_l-1,m_l-1)} \\ & +\lambda_+\hat{\xi}^{(Z,l+1,m_l-1,m_l-1)} \end{aligned} \quad (23)$$

holds. From this equation we obtain three linearly independent equations for the matrix elements λ_-, λ_+ and λ_o if we project the equation on different spin flip base states. We evaluate the projection of (23) on three spinflip base states with $n_+ = 0, 1, 2$ and obtain the three different equations for the matrix elements. At this point the atomic Liouville operator enters via (21). The resulting set of three linear equations is easily solved and we obtain the desired matrix elements

$$\begin{aligned} \lambda_-(Z,l,l,l) &= B\left(\frac{Z}{2}-l\right) \\ \lambda_o(Z,l,l-1,l-1) &= B\frac{Z+2}{2(l+1)} \\ \lambda_+(Z,l,l-2,l-2) &= B\frac{\frac{Z}{2}+l+1}{l(2l+1)}. \end{aligned} \quad (24)$$

Together with the matrix elements of the diagonal part of $\mathcal{L}_a$

$$\mathrm{tr}\left(\check{\xi}^{(Z,\bar{l},\bar{m},\bar{m}')}\left\{\sum_i \sigma_+^{(i)}\sigma_-^{(i)}, \hat{\xi}_{Z,l,m,m'}\right\}\right) = (Z+m+m')\delta_{l,\bar{l}}\delta_{m,\bar{m}}\delta_{m',\bar{m}'} \quad (25)$$

and equation (17) we obtain the expression of $\mathcal{L}_a$ in terms of the Dicke states. Without this expression the Dicke states would be useless in the presence of atomic dissipation.

The numerical calculation of eigenvalues and eigenstates of the Liouville operator in the base of the Dicke states becomes relatively easy now. Using these results we can determine stationary properties like the mean photon

number of the stationary state and dynamical properties like the normally-ordered second-order correlation function

$$g^{(2)}(t) = \frac{\left\langle a^\dagger(0)a^\dagger(t)a(t)a(0)\right\rangle}{\left\langle a^\dagger(0)a(0)\right\rangle} \tag{26}$$

of the stationary state. Using the spectral decomposition of the propagator $\mathrm{e}^{\mathcal{L}t}$ we may express the correlation function in terms of the eigenvalues and eigenstates

$$\begin{aligned} g^{(2)}(t) &= \frac{\mathrm{tr}\left(a^\dagger(0)a(0)\mathrm{e}^{\mathcal{L}t}\left(a(0)\rho_{\mathrm{stat}}a^\dagger(0)\right)\right)}{\mathrm{tr}\left(a^\dagger(0)a(0)\rho_{\mathrm{stat}}\right)^2} \\ &= \sum_i \frac{\mathrm{tr}\left(a^\dagger(0)a(0)\hat{\rho}_i\right)\mathrm{e}^{\lambda_i t}\mathrm{tr}\left(\check{\rho}_i a(0)\rho_{\mathrm{stat}}a^\dagger(0)\right)}{\mathrm{tr}\left(a^\dagger(0)a(0)\rho_{\mathrm{stat}}\right)^2}. \end{aligned} \tag{27}$$

3 Coherently Driven Systems

The results obtained in sec. 2 are quite general and may be applied to any system where one is not interested in the state of the individual two-level systems. As an example we will now compare our results with experimental observations.

In order to obtain a nontrivial stationary state in the presence of dissipative processes, one has to include a pump mechanism, i.e. $\epsilon \neq 0$ in (2). It was shown that light with nonclassical properties was emitted, i.e. with antibunched photon statistics.

Such a coherently driven system has been studied experimentally [1]. The results were, among others, that light with nonclassical properties, namely with antibunched photon counting statistics was emitted. The experimental setup consisted of an atomic beam passing through a high-Q optical cavity. The cavity was excited by a coherent signal beam. The correlation function of the output of the cavity was measured using a coincidence counter.

There is a classical limit on the correlation function: $g^{(2)}(t) \geq \left(\frac{g^{(1)}(t)}{g^{(1)}(0)}\right)^2$. The violation of this inequality, called antibunching, is classically forbidden and hence a pure quantum effect.

The experiment was originally interpreted using a theory which is valid only in the case $|\epsilon| \ll A$ i.e. the weak driving field limit. In this limit $g^{(2)}(0)$ does not depend on the intensity of the driving field [13]. The atom number Z, the coupling constant g and the damping constants A and B were determined by fitting correlation functions from this approximation to the experimental data. The amplitude of the oscillations in the correlation function was four times the observed amplitude while the frequency of the oscillations was predicted correctly by the approximation.

The number of photons in the cavity at constant intensity of the driving field depends on the number of atoms in the resonator. This can be understood by considering the energy balance of the system in the stationary state.

The cavity gains energy through the driving field and loses energy through the mirrors and by spontaneous emission of the atoms, which is unlikely to occur into the resonator mode. Since the atoms interact only with the resonator mode, and not with other atoms, their state is completely determined by the resonator mode. This means that the cavity losses increase with the number of atoms. In order to compensate the losses the intensity of the driving field must be increased.

Another consequence of this argument worth mentioning is that for large numbers of atoms the energy is stored predominantly in the atoms. Therefore, large values of M, the number of photons plus the number excited atoms, are possible even if the mean photon number is low. We have to make sure in our numerical calculations that the maximum value of M is large enough, which can be easily controlled by verifying that the stationary state has vanishing occupation probability at the cutoff. Typical values are $M_{\max} = 4 \ldots 7$ which is three hundred times more than the stationary photon number and well above the number of photons stored in the atoms. For large values of Z the stationary photon number is much smaller than its value at $Z = 1$ and the energy is predominantly stored in the atoms..

The oscillation frequency observed in the correlation functions increases roughly as $\sqrt{Z}$, as expected. In contrast, the value of $g^{(2)}(0)$ depends on the number of atoms only very weakly. This is because in the limit of a very weak driving field the value of $g^{(2)}(0)$ depends only on the saturation photon number [5]. The envelope of the oscillations does not depend on the number of atoms. The reason for this behavior is that the real parts of the matrix elements of the Lindblad operator, which determine the rate of decay of the correlation functions, do not depend on the total number of atoms but instead on the number of excited atoms[2].

The experimental results (the dots in figure 1) of Rempe et al. [1] are not consistent with the weak-field limit $|\epsilon| \ll A$, because the experimentally measured value of $1-g^{(2)}(0)$ is four times smaller than theoretically obtained under the assumption of a weak driving field. Rempe et al. conjectured that the intensity of the driving field exceeded the weak field limit.

Rempe et al have determined the numbers of atoms and the decay rate of $g^{(2)}(t)$ by fitting of correlation functions calculated in the weak field limit to the experimental data. Since our results show that the period of the oscillations still depends on $g\sqrt{Z}$ even if ϵ is of the order of A or larger we will still use their values of Z in comparing their experimental data with our results. Since the experiments were performed at optical frequencies, thermal photons may be neglected.

Figure 2 shows that $g^{(2)}(0)$ does not depend on the strength of the driving field if the dimensionless intensity $y = \frac{\epsilon}{B}$ very small. This is the regime where the weak-field approximation of [5] is appropriate. In our calculations, a value of $y \approx 5$ is used, which still leads to very low mean photon numbers and gives

[2] Remember that $m = -\frac{Z}{2}$ if all atoms are in the ground state.

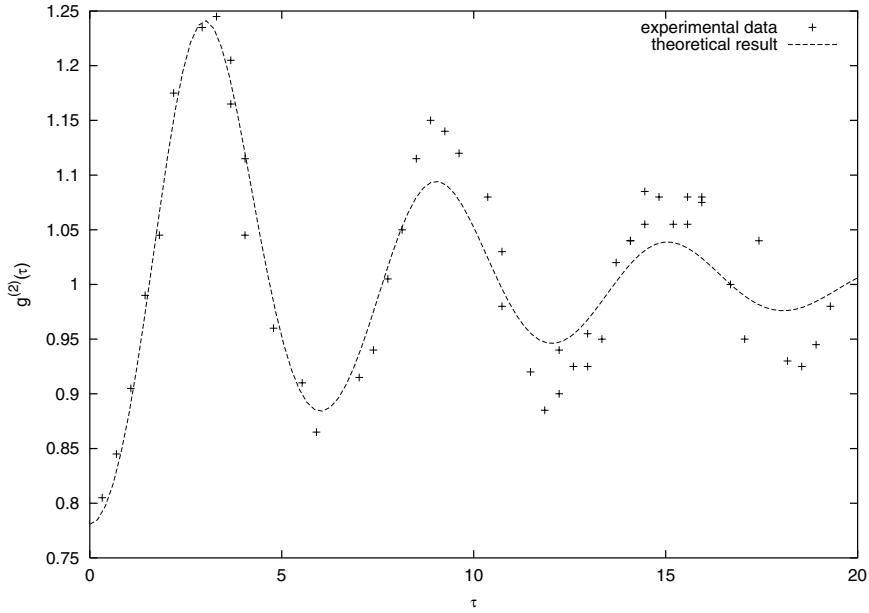

Fig. 1. The experimental values (crosses) of the correlation function in comparison with our theoretical results (solid line). The experimental values were taken from [1]. The atom number is $Z = 110$. The theory describes the experiment quite well with the exception that the damping of the theoretical curve is stronger than that of the experimental curve. Here we use the scaled parameters cooperativity $C = \frac{2g^2}{AB} = 1$ and saturation photon number $n_s = \frac{B^2}{8g^2} = 0.7$. These parameters have been chosen according to the values reported in the experimental publication. The saturation photon number n_s is the mean photon number of the resonator mode where the mean excitation of one atom interacting with the mode is 0.5. The time τ was scaled such the oscillation period is 2π

the experimentally found correlation function. In the regime $4 < y < 6$ the intensity correlation function is still antibunched, but now depends on the intensity of the driving field. For even larger values of y one observes photon bunching $g^{(2)}(0) > 1$.

Our calculations gave the same dependency of the oscillation frequency on the number of atoms as the weak-field approximation. Therefore we will use the number of atoms determined from the experimental data using the weak-field approximation. At $n_s = 0.7$ and $C = 1.0$ we find a good agreement between experimental and theoretical data, as Figure 1 shows. The decay rate of the envelope of the theoretical correlation function is larger than that of the experimental correlation function. The decay rate of the correlation function depends predominantly on the saturation photon number n_s which is fixed by the experimental parameters. This observation is consistent with the weak

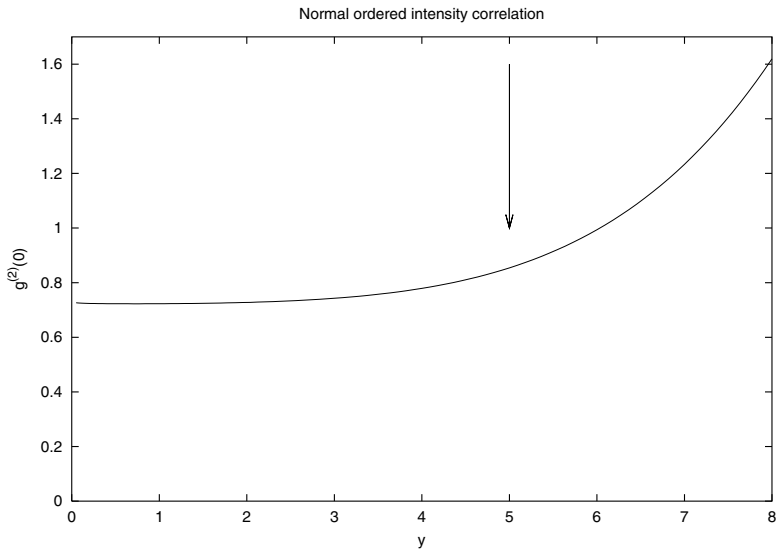

Fig. 2. The normal ordered intensity correlation $g^{(2)}(0)$ at $Z = 110$, $C = 1.0$ and $n_s = 0.7$. For low values of y the intensity correlation does not depend on $y = \frac{\epsilon}{B}$. This is the regime where the weak-field approximation may be used to calculate the intensity correlation function $g^{(2)}$. The arrow marks the value of y used in Fig. 1

driving field approximation where in the limit $Z \gg 1$ the same behavior is predicted.

In summary, we found a new way to reduce the dimension of many-atom cavity QED problems drastically. The method is quite intuitive because it makes use of an analogy to angular momentum. This method has been successfully applied to the description of experimental observations.

4 Outlook

Since we can vary the number of atoms easily in this approach we can test approximations where the atoms are adiabatically eliminated. This procedure leads to one-atom systems where the coupling constant is replaced by a the coupling constant times the square root of the number of atoms. We find that there are regimes where this approximation is valid, but only for rather low photon numbers.

The method developed in this manuscript may be used for any problem where the atomic states are symmetric with respect to permutations of atoms. We have also treated a micromaser model which is pumped by atom clusters instead of single atoms.

The case of finite temperatures can be reduced to the case of zero temperature treated in this manuscript by a simple symmetry transformation.

Other possible applications include ion trap lasers and quantum dot arrays, or in general all systems where permutation symmetry can be used to reduce the dimension of the problem.

References

1. G. Rempe, R.J. Thompson, W.D. Lee, H.J. Kimble: Phys. Rev. Lett. **67**, 1727 (1991)
2. K. An, J.J. Childs, R.R. Dasari, M.S. Feld: Phys. Rev. Lett. **73**, 3375 (1994)
3. G.M. Meyer, H.J. Briegel, H. Walther: Europhys. Lett. **37**, 317 (1997)
4. G. Raithel, C. Wagner, H. Walther, L.M. Narducci, M.O. Scully: 'The micromaser: A proving ground for quantum physics'. In: *Cavity Quantum Electrodynamics*. ed. by P.R. Berman (Academic, New York 1994)
5. H.J. Carmichael, R.J. Brecha, P.R. Rice: Optics Commun. **82**, 73 (1991)
6. M. Kozierowski, S.M. Chumakov, J. Swiatlowski, A.A. Mamedov: Phys. Rev. **46**, 7220 (1992)
7. S. Sakar, J.S. Satchell: Europhys. Lett. **3**, 797 (1987)
8. E.T. Jaynes, F.W. Cummings: Proc. IEEE **51**, 89 (1963)
9. R. Dicke: Phys. Rev. **93**, 99 (1954)
10. M. Tavis, F.W. Cummings: Phys. Rev. **2**, 170 (1968)
11. G. Lindblad: Commun. Math. Phys. **48**, 119 (1976)
12. U. Martini: `http://www.theorie.physik.uni-muenchen.de/~martini/thesis/2000`
13. R.J. Brecha, P.R. Rice, M. Xiao: Phys. Rev. A **59**, 2392 (1999)

The Photonic Band Gap Laser: The Role of Spontaneous Emission in the Theory of Solid-State Lasers and LEDs

Roy Pike, Alison Hughes, and Marzena Szymanska

1 Introduction

1.1 Foreword

It is a pleasure to contribute to this memorial volume for Dan Walls. He was a tireless traveller in the pursuit of his research and we got to know him well, first at RSRE Malvern, where he spent an enjoyable sabbatical in the early days of quantum optics, and later in London and in many other parts of the world. It was an honour to support his case for Fellowship of the Royal Society and this brought him to London even more to speak and participate in our meetings. His untimely death has robbed us of the comfort of his warm humanity and of even further fruits of his unique expertise.

There were a number of possibilities for the content of a commemorative chapter but we have taken the view that Dan would have liked us to describe our latest research rather than to comb over old ground and so we have taken this opportunity to expand a little on a recently published Letter [1] where the four-page limit forces one to leave out some of the more interesting comments one might otherwise make. This is concerned with the theory of a laser operating in a medium with a photonic band gap (PBG), [2]. In the event it will be necessary to comb over quite a bit of old ground dealing with previous theories of the laser!

1.2 Outline

The processes contributing to lasing action include, of course, spontaneous emission. In a PBG medium the spontaneous emission characteristics are altered and a laser operating in such a medium will have a modified performance. This modified performance is expected to reduce greatly the threshold pump rate while increasing the laser output.

It is also expected that other optical devices such as LEDs and amplifiers could also potentially be designed to be more efficient by the use of PBG materials and the theory which we present here can be carried over with little modification to the LED and with a bit more work to the optical amplifier, although this has not yet been done. The impact on optical device technology

H.J. Carmichael, R.J. Glauber, M.O. Scully (Eds.): LNP 561, pp. 250–260, 2001.

of such devices could obviously be significant although, for technical reasons, they have not yet been realised in the optical region in a full three-dimensional medium.

After a discussion of the concept of the photonic band gap we review the various existing theoretical treatments of the laser and highlight their features and differences. The laser of most practical interest to us is the solid-state laser which falls into the so called class-B category when $\gamma_\perp \gg \gamma_\parallel \approx 2\kappa$, where κ is a cavity loss rate and $\gamma_\perp$, $\gamma_\parallel$ are the polarisation and inversion decay rates, respectively. There have been a number of ever more sophisticated laser theories since the mid-sixties but, unfortunately, it seems that none of them can yet satisfactorily describe the properties of class-B lasers with all the spontaneous emission rates built into the model. Thus, surprisingly, none of them can be used to calculate the difference in threshold and output power for lasers, with and without a photonic band gap, which is our aim. We go on, therefore, to describe and extend one methodology, due to Lugiato, that is best suited to solve our problem.

2 Photonic Band-Gap Materials

There is currently considerable interest in materials with a photonic band gap (PBG) i.e. materials in which certain frequencies of light cannot propagate. If an excited atom is placed in such a structure it will be prevented from spontaneously emitting light if its transition frequency lies within the forbidden range. Hence PBG materials can be used to control spontaneous emission. This phenomenon is different from that where the spontaneous emission may be redistributed within a microcavity [3]. The first use of the idea of a photon band structure was probably made by Ohtaka in 1979 [4]. It was, however, Yablonovitch's work of 1987 [5] that really aroused a widespread interest in this area. The idea of being able to control spontaneous emission was introduced as far back as 1946 when Purcell [6] discussed it in the microwave domain. It was much later in 1973 [7] and 1981 [8] that methods of controlling spontaneous emission in the optical region were developed.

Wigner and Weisskopf in 1930 performed the first calculation of the time dependence of the spontaneous emission of an excited atom into an electromagnetic mode continuum [9]. With the advent of cavity QED and PBG materials the theory becomes much more complicated. Kofman [10], [11] has considered an excited atom placed near the edge of the gap in a PBG material to investigate non-Markovian effects which arise. He has also considered a two- level atom interacting with a defect mode in this material. This is effectively a Jaynes-Cummings system with dressed states but these states can decay by coupling to the continuum outside the band gap. John [12] has revisited the Dicke problem. N excited atoms, now close to the edge within the band gap are examined to see how the superradiance is affected, and Vats and

John [13] have discussed spontaneous emission when non-Markovian band-edge influences occur.

Another area of research is the examination of light propagation through optical materials. Smith [14] has looked numerically and experimentally at the propagation through periodic arrays of dielectric scatterers in one and two dimensions to demonstrate the existence of PBGs. He has also considered the introduction of a defect into such a system. Shepherd has numerically calculated light propagation in 2-D photonic crystals using an analytical model [15] and Pendry [16] and others have used transfer-matrix methods.

PBG materials have already been fabricated in three dimensions for the microwave and infrared regions and more recently opal crystals have been used for the visible region [17]. Current research is being undertaken to fabricate PBG optical materials [18]. Two-dimensional structures at nanometer wavelengths have already been realised [19]. By introducing a defect which allows the propagation of only one mode within the forbidden region we could suppress the spontaneous emission to modes other than that particular single laser mode and so these materials could be used to produce new types of lasers. In principle we could make atoms emit almost entirely into one cavity mode which would very much reduce losses from the system and, therefore, achieve a β factor close to unity. The β factor is defined [20] as

$$\beta = \frac{\text{rate of spontaneous emission into lasing mode}}{\text{total rate of spontaneous emission}}. \tag{1}$$

In a recent conference paper presented by Ho and a little earlier in work by Carmichael and Rice [21], the concept of "thresholdless" lasing has been discussed. This is proposed by modifying the β factor to an idealistic value of one. The work has considered photonic wires and wells to make microdisk lasers. The β factor is changed by modifying the density of states in a microcavity (the 'Purcell effect') or by the use of a photonic band-gap material.

The aim of our work is to obtain a theoretical lower bound on the lasing threshold of the PBG laser in order to compare the properties of such an ideal laser with the corresponding conventional laser. To do this we assume that the lasing mode is sufficiently far from the band edges to render spontaneous emission from it to be negligible.

3 Laser Theories

3.1 History

A first insight into laser processes can be given by rate equations which are developed heuristically. The semiclassical laser theory, which involves a classical electromagnetic field, provides a more rigorous derivation but it fails to account for spontaneous emission contributions and therefore field fluctuations. The semiclassical theory and rate equations are equally as good at

describing the laser processes when we consider a single lasing mode. However, the semiclassical theory can be used to describe effects which the rate equations cannot treat, for example, the frequency locking of three lasing modes. When we have more than one lasing mode, the rate equations assume that they have no frequency correlations. For our discussion, however, we are not concerned with these phenomena and are only interested in the case of one lasing mode.

The quantum-Langevin equations improve on the semiclassical theory as the field is now treated quantum mechanically and therefore fluctuation terms are included [22]. Fuller quantum mechanical theories have been given, for example, by Scully and Lamb [23], [24], Lugiato [25], [26], and Pike [27] who employed density matrix methods to examine laser processes, but each has considered a slightly different model.The well-known four-level Scully-Lamb theory of laser photon statistics does not take the spontaneous emission between the lasing levels into account at all and is essentially for class-A lasers. It is the only one, however, to go to all orders in the coupling constant between the cavity modes and the lasing atoms (see below). The quantum-mechanical Langevin equations do have spontaneous emission between the lasing levels built into the model and it is possible to obtain the threshold condition, which, in principle, then could be analysed in the presence of a photonic band gap. However, at and close to the laser threshold no way of solving these equations is known which treats fully the fluctuations. In particular it is also not possible to calculate the photon statistics and the theory is for two-level atoms only. Lugiato's master equation method for the density operator also has spontaneous emission built into the model and all pump and decay rates are represented by explicit interactions between the lasing system and reservoirs with positive and negative absolute temperatures, respectively, but again the theory is for two-level atoms only and only valid below threshold. These equations were solved by Lugiato using the Glauber diagonal P-representation [26]. Other authors have solved this model by transforming into a Fokker-Planck equation [22], [28], [29]. However, all these results have a very complicated form which allow fluctuations to be calculated only numerically and it is still not possible to obtain the photon statistics p_n.

3.2 Beyond Lugiato

We have extended Lugiato's original work by choosing not to employ his "smoothness" assumption for which, unfortunately, we cannot find justification, but instead have been able to solve the model completely, in the photon-number representation, analytically, using computer algebra. We compare this to the Scully-Lamb laser theory and upon inspection we find that Lugiato's theory currently stands to second-order in the coupling constant only (see also the derivation of the Scully-Lamb theory from the Lugiato model described in Pike and Sarkar [29] which at that time also used Lugiato's

smoothness assumption). It is worth commenting on the work Lugiato carried out which compared his two coupled equations in the Glauber representation to the single equation which Mandel [30] developed.

Mandel had one equation which ostensibly included all the terms summed to infinite order in the coupling constant g. The question arises as to why Lugiato's result to second order could possibly be comparable to a result achieved by summing a single equation to infinity. It would appear that coupling two second-order equations produces a result to all orders in the coupling constant g. However, upon inspection of Mandel's work one finds that he has, in fact, employed an ansatz which amounts to factorising the density matrix into a density matrix for the atom and the field, with the atoms always remaining in a steady state. This approximation is only valid when we have weak coupling and so refers to the conditions for threshold and below. Lugiato's equations are also only valid for threshold and below as they are to second order. This somewhat tricky analysis (see [2]) explains why both results are only valid to second order in the coupling constant and expected therefore, to be of comparable form.

Having developed a new two-level-atom, class-A, laser theory in the photon number representation to all orders in the coupling constant, we were then able to extend it to account for three-level atoms. This is desirable since the two-level model has unrealistic behaviour far above threshold and this problem is removed using three-levels. Finally we went on to develop the theory further for a three-level, class-B, PBG laser, the results of which we present here, examining the threshold pump rate and output. We show that even in the case of complete suppression of spontaneous emission into the lasing mode, where the input and output powers are linearly related, there is still a region of incoherent, "sub-threshold", operation before the lasing threshold is reached.

3.3 Master Equation for Three-Level System

The atomic-level structure and the various transitions used in our calculations are shown in Fig. 1.

In the three-level laser model all elements connected with the laser operation are divided into two parts, a small system S and a large heat bath B. S will be described by a Hamiltonian H_S, the bath by H_B, and the interaction between B and S by H_{SB}. The system contains N three-level transitions, a single electromagnetic field mode and the lasing transition-field interaction. Both the three-level transitions and field are treated quantum mechanically and the interaction is taken in the rotating-wave approximation. The bath can be divided into three parts: a field bath which represent losses of the laser mode from the cavity through the partially transmitting output mirror, a bath which represents the interactions of the excited levels with the vacuum modes i.e. spontaneous emission to modes other than the lasing mode, and a bath which represents pumping from the lowest level to the highest one.

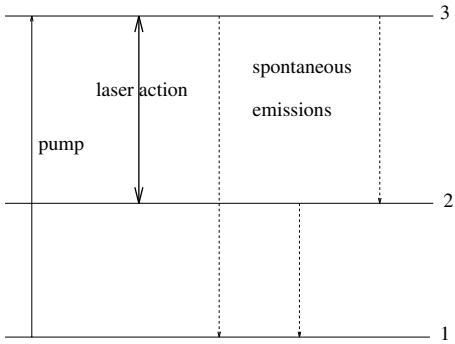

Fig. 1. Atomic-level structure and various transitions in the three-level-atom model

For a semiconductor laser we have an analogy with the three-level model. The gap in a semiconductor material between the conduction and valence bands is where the lasing action occurs. A flow of holes in the valence band corresponds to the depletion of the lower lasing levels [31]. Precise Hamiltonians for the baths are not known but this is not very important since we are only interested in the system behaviour. It is then enough to know the Hamiltonian of the bath-system interaction. We model the baths as sets of harmonic oscillators at temperature T. The spontaneous emission bath is modelled as a set of oscillators at temperature $T = 0K$ and the pumping bath as a set of oscillators at negative temperature $T = -0K$. The field bath is modelled as a set of harmonic oscillators at temperature T. When we are not interested in thermal photons coming back into the laser we may set this temperature to $0K$ (this is like saying that the environment of the laser has zero temperature). The rates of exchange of energy between these baths and the system are expressed by the separate coupling constants of the interactions.

The three types of baths have different influences on the system, but equilibrium between them will be reached and the system will then have a temperature (i.e. inversion) depending on the coupling constants of the two system baths and the lasing transition-lasing mode interaction. The system Hamiltonian is given by:

$$H_S = H_T + H_F + H_{TF}, \tag{2}$$

where

$$\begin{aligned} H_T &= \frac{1}{2}\sum_j \hbar\omega_o S_j^3 \\ H_F &= \hbar\omega_k a_{\mathbf{k}}^\dagger a_{\mathbf{k}} \\ H_{TF} &= i\sum_{j=1}^{N} \hbar g(e^{-i\mathbf{k}.\mathbf{x}_j} a_{\mathbf{k}}^\dagger S_{j23}^- - e^{i\mathbf{k}.\mathbf{x}_j} a_{\mathbf{k}} S_{j23}^+). \end{aligned} \tag{3}$$

S_{j23}^+, S_{j23}^- are creation and annihilation operators, respectively, between lasing levels (levels 2 and 3 in Fig. 1). The bath-system interaction Hamiltonian,

H_{SB}, includes the decay of excited levels to off-resonant modes $\Gamma_{j12\downarrow}$, $\Gamma_{j13\downarrow}$, $\Gamma_{j23\downarrow}$, the pumping of the atoms to the excited state, $\Gamma_{j\uparrow}$, and the decay of the resonant mode. The Hamiltonian is:

$$\begin{aligned} H_{SB} &= \hbar(a_{\mathbf{k}}\Gamma_F^\dagger + a_{\mathbf{k}}^\dagger\Gamma_F) \\ &\quad + \sum_{j=1}^{N} \hbar(S_{j12}^- \Gamma_{j12\downarrow}^\dagger + S_{j13}^- \Gamma_{j13\downarrow}^\dagger + S_{j23}^- \Gamma_{j23\downarrow}^\dagger + S_{j13}^+ \Gamma_{j\uparrow}) \\ &\quad + \sum_{j=1}^{N} \hbar(S_{j13}^- \Gamma_{j\uparrow}^\dagger + S_{j12}^+ \Gamma_{j12\downarrow} + S_{j13}^+ \Gamma_{j13\downarrow} + S_{j23}^+ \Gamma_{j23\downarrow}). \end{aligned} \tag{4}$$

Thus the quantum-optical master equation takes the form:

$$\begin{aligned} \frac{\partial \rho_S}{\partial t} &= -i[H_S, \rho_S] \\ &\quad + \sum_{j=1}^{N} \frac{\gamma_{23\downarrow}}{2}([S_{j23}^-, \rho_S S_{j23}^+] + [S_{j23}^- \rho_S, S_{j23}^+]) \\ &\quad + \sum_{j=1}^{N} \frac{\gamma_{13\downarrow}}{2}([S_{j13}^-, \rho_S S_{j13}^+] + [S_{j13}^- \rho_S, S_{j13}^+]) \\ &\quad + \sum_{j=1}^{N} \frac{\gamma_{12\downarrow}}{2}([S_{j12}^-, \rho_S S_{j12}^+] + [S_{j12}^- \rho_S, S_{j12}^+]) \\ &\quad + \sum_{j=1}^{N} \frac{\gamma_{\uparrow}}{2}([S_{j13}^+, \rho_S S_{j13}^-] + [S_{j13}^+ \rho_S, S_{j13}^-]) \\ &\quad + \kappa(2a_{\mathbf{k}}\rho_S a_{\mathbf{k}}^\dagger - a_{\mathbf{k}}^\dagger a_{\mathbf{k}}\rho_S - \rho_S a_{\mathbf{k}}^\dagger a_{\mathbf{k}}) \\ &= \Lambda\rho_S(t), \end{aligned} \tag{5}$$

Taking the trace over the transition levels, using the dilute-atom approximation and employing the Markov approximation gives us an equation for p_n, the probability of finding n photons in the cavity mode, when we work in the photon-number representation. Multiplying the above expression by $S_{23}^- S_{23}^+$ and $S_{13}^- S_{13}^+$, respectively, we obtain two more coupled equations. When we consider these three equations in the steady state and perform detailed balancing we find:

$$2\kappa p_n(t) = -\frac{A}{1 + nB/A}(p_{n2}(t) - p_{n-1,3}(t)) \tag{6}$$

$$\frac{2g^2 n/\gamma}{1 + nB/A}(p_{n-1,3} - p_{n,2}) - \gamma_{12\downarrow} p_{n,2} + \gamma_{23\downarrow} p_{n,3} = 0 \tag{7}$$

$$\gamma_{13\downarrow} p_{n,3} + \gamma_{12\downarrow} p_{n,2} - \gamma_{\uparrow} p_{n,1} = 0, \tag{8}$$

where

$$\gamma = (\gamma_{23\downarrow} + \gamma_{13\downarrow} + \gamma_{12\downarrow})/2. \tag{9}$$

We also know that

$$p_n = p_{n1} + p_{n2} + p_{n3} \tag{10}$$

where

$$\begin{aligned} p_n(t) &= \langle n|\rho_F^I(t)|n\rangle \\ p_{n,1}(t) &= \langle n|S_{13}^- S_{13}^+(t)\rho_S^I(t)|n\rangle = \langle 1,n|\rho_S^I(t)|n,1\rangle \\ p_{n,2}(t) &= \langle n|S_{23}^- S_{23}^+(t)\rho_S^I(t)|n\rangle = \langle 2,n|\rho_S^I(t)|n,2\rangle \\ p_{n,3}(t) &= \langle n|S_{23}^+ S_{23}^-(t)\rho_S^I(t)|n\rangle = \langle 3,n|\rho_S^I(t)|n,3\rangle. \end{aligned} \tag{11}$$

Solving the above equations we obtain the following recursion relation:

$$\begin{aligned} p_n(t) = {} & A[N\gamma_\uparrow\gamma_{12\downarrow} - 2\kappa(n-1)(\gamma_{12\downarrow} + \gamma_\uparrow)]p_{n-1} \\ & \times\big[2\kappa N(1+nB/A)(\gamma_{13\downarrow}\gamma_{12\downarrow} + \gamma_\uparrow\gamma_{12\downarrow} + \gamma_{12\downarrow}\gamma_{23\downarrow} + \gamma_{23\downarrow}\gamma_\uparrow) \\ & + A(N\gamma_{23\downarrow}\gamma_\uparrow + 2\kappa n\gamma_{13\downarrow} + 2\kappa n\gamma_\uparrow)\big]^{-1}, \end{aligned} \tag{12}$$

where

$$\begin{aligned} A &= 2Ng^2/\gamma \\ B/A &= 4g^2/\gamma^2. \end{aligned} \tag{13}$$

Thus it is possible to express p_n as a product of n elements and to calculate the average and the most probable number of photons in the cavity. The photon statistics determines the coherence of the output. In the region above laser threshold the most probable number of photons is greater than zero and in the region below and at the laser threshold is equal to zero. Thus a physical insight into our results for $\beta = 1$ is given by the realisation that, although always increasing linearly with input power, the cavity output is incoherent until the former condition on the photon statistics is achieved. In order to find the laser threshold we therefore need to calculate the most probable number of photons in the lasing mode.

This becomes equal to the average far above threshold, where the photon statistics are symmetrical and approach the Poisson distribution. It can be shown that the most probable number of photons in the cavity is equal to:

$$\begin{aligned} & n_p \\ & = \frac{\frac{2g^2}{\gamma}N\gamma_\uparrow(\gamma_{12\downarrow} - \gamma_{23\downarrow}) - \frac{2g^2}{\gamma}2\kappa(\gamma_{13\downarrow}+\gamma_\uparrow)}{\frac{2g^2 2\kappa}{\gamma}(\gamma_{\downarrow 12}+2\gamma_\uparrow+\gamma_{\downarrow 13}) + \frac{2\kappa B}{A}(\gamma_{\downarrow 13}\gamma_{\downarrow 12}+\gamma_\uparrow\gamma_{\downarrow 12}+\gamma_{\downarrow 12}\gamma_{\downarrow 23}+\gamma_{\downarrow 23}\gamma_\uparrow)} \\ & \quad - \frac{2\kappa(1+B/A)(\gamma_{13\downarrow}\gamma_{12\downarrow}+\gamma_\uparrow\gamma_{12\downarrow}+\gamma_{12\downarrow}\gamma_{23\downarrow}+\gamma_{23\downarrow}\gamma_\uparrow)}{\frac{2g^2 2\kappa}{\gamma}(\gamma_{12\downarrow}+2\gamma_\uparrow+\gamma_{13\downarrow}) + \frac{2\kappa B}{A}(\gamma_{13\downarrow}\gamma_{12\downarrow}+\gamma_\uparrow\gamma_{12\downarrow}+\gamma_{12\downarrow}\gamma_{23\downarrow}+\gamma_{23\downarrow}\gamma_\uparrow)}. \end{aligned} \tag{14}$$

We can now calculate the threshold pump rate from the condition that the number of photons in the lasing mode must be greater than zero.

$$\gamma_{\uparrow,3} = \frac{2g^2\kappa\gamma_{13\downarrow} + \kappa\gamma_{12\downarrow}\gamma(\gamma_{13\downarrow} + \gamma_{23\downarrow})}{Ng^2(\gamma_{12\downarrow} - \gamma_{23\downarrow}) - 2\kappa g^2 - \gamma\kappa(\gamma_{12\downarrow} + \gamma_{23\downarrow})}, \tag{15}$$

When spontaneous emission between the lasing levels can be suppressed then $\gamma_{23\downarrow} = 0$. Recall that in the development of the theory we employed a Markov approximation. This approximation is still valid even though we use a PBG material as we are positioning our transition levels and defect mode at the centre of the gap, therefore excluding any gap-edge influences. We compare characteristics for lasers with and without a photonic band gap ($\gamma_{23\downarrow} = 0$) for a laser with parameters $N = 10^7/2$, $g = 10^5$, $2\kappa = 10^7$, $\gamma_{13\downarrow} = 10^6$, $\gamma_{23\downarrow} = 10^7/2$ and $\gamma_{12\downarrow} = 10^{10}$, in Fig. 2 and Fig. 3.

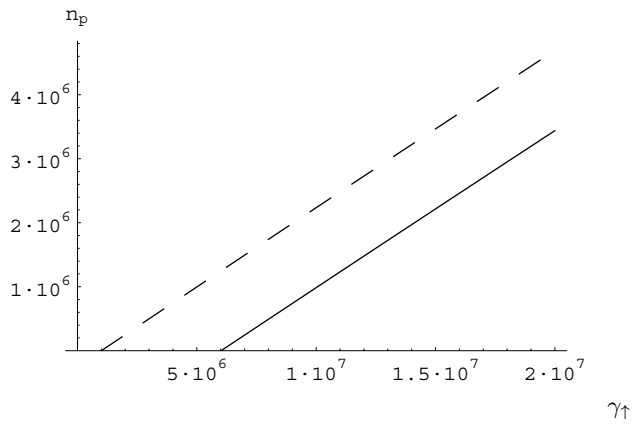

Fig. 2. The most probable number of photons as a function of pumping rate, $\gamma_\uparrow$, for a three-level-lasing model for lasers with PBG

For the case of such a PBG laser the threshold takes place at a pump rate one order of magnitude smaller than that for the case without a PBG. However, the maximum output far above threshold of both types of laser is similar. The PBG laser has a threshold pump rate given by the expression

$$\gamma_{\uparrow,PBG} = \frac{2g^2\kappa\gamma_{13\downarrow} + \kappa\gamma_{12\downarrow}\gamma\gamma_{13\downarrow}}{Ng^2\gamma_{12\downarrow} - 2\kappa g^2 - \gamma\kappa\gamma_{12\downarrow}}. \tag{16}$$

The important point to note for the value of this pump rate is that the threshold is not zero when $\beta = 1$. As for a conventional laser, the output is at first incoherent. This differs from the results of Rice *et al.* [21] where they find a thresholdless laser in this case. We can, in fact, directly compare our work to that of Rice *et al.* Their model is two-level but the lower level rapidly depletes to a lower lying unspecified state. In our model this corresponds to

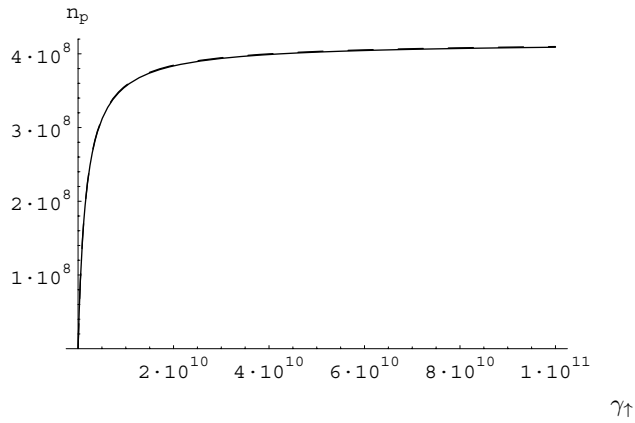

Fig. 3. The most probable number of photons as a function of pumping rate, $\gamma_\uparrow$, for a three-level-lasing model for lasers without PBG. The curves are almost indistinguishable

$\gamma_{13\downarrow}$ being very small and $\gamma_{12\downarrow}$ very large. With these conditions we see, from (8), that $p_{n,2}$ is then very small which implies such a rapidly depleting lower level. The threshold of the PBG laser will then approach zero.

Our new laser theory thus allows the differences between an ideal PBG laser and a conventional laser to be calculated when the numerical values of the relevant parameters are known. A real PBG laser will not have all the spontaneous emission suppressed but our results give an upper bound on the possible improvements in performance. As would be expected, the threshold pump rate is lower. In the region of saturation the stimulated emission dominates the spontaneous emission therefore rendering it negligible. Therefore, when the β factor is one there is little increase in the output power far above threshold and the advantages are marginal at these higher powers. However, when considering LED's we are concerned with lower output powers and in this region we conclude that the output power will indeed be greatly increased due to the use of a PBG material. We are considering an extension of the theory to describe laser amplifiers, where PBG materials are also expected to improve performance significantly.

4 Conclusions

We have presented results for the operation of a three-level solid-state laser both with normal and with completely suppressed spontaneous emission between the lasing levels. The output power difference in these two cases drops as the pump rate is increased above threshold and is not greatly different at higher powers. The threshold pump power, although typically reduced by an order of magnitude, is not zero and our results throw further light on the

concept of "thresholdless" lasing. The theory is also applicable to LED's and amplifiers which function on the same principles as a laser.

References

1. M.H. Szymanska, A.F. Hughes, E.R. Pike: Phys. Rev. Lett. **83**, 69 (1999)
2. A.F. Hughes: A New Theory of Lasers with Applications to Photonic Band-Gap Materials. PhD Thesis, King's College, London (1999)
3. Y. Yamamoto *et al.*: Opt. and Quantum. Electron. **24**, S209 (1992)
4. K. Ohtaka: Phys. Rev. B **19**, 5057 (1979)
5. E. Yablonovitch: Phys. Rev. Lett. **58**, 2059 (1987)
6. E.M. Purcell: Phys. Rev. **69**, 681 (1946)
7. P.W. Milonni, P.W. Knight: Optics Commun. **9**, 119 (1973)
8. D. Kleppner: Phys. Rev. Lett. **47**, 233 (1981)
9. E. Wigner, V. Weisskopf: Z. Phys. **63**, 54 (1930)
10. A.G. Kofman *et. al.*: J. Mod. Optics **41**, 353 (1994)
11. A.G. Kofman *et. al.*: Appl. Phys. B **60**, S99 (1995)
12. S. John, T. Quang: Phys. Rev. Lett. **74**, 3419 (1995)
13. N. Vats, S. John: Phys. Rev. A **58**, 4168 (1998)
14. D.R. Smith *et al.*: J. Opt. Soc. Am. B **10**, 314 (1993)
15. T.J. Shepherd, P.J. Roberts: Phys. Rev. E **51**, 5158 (1995)
16. J.B. Pendry: J. Mod. Optics **41**, 209 (1994)
17. S.G. Romanov *et al.*: App. Phys. Lett. **70**, 2091 (1997)
18. J. Rarity, C. Weisbuch: *Microcavities and Photonic Band Gaps: Physics and Applications*, NATO ASI Series E, Vol 324 (Kluwer, Dordrecht 1996)
19. T.F. Krauss *et al.*: Nature (London) **383**, 699 (1996)
20. T. Baba *et al.*: IEEE J. Quantum. Electron. **QE-27**, 1347 (1991)
21. P.R. Rice, H.J. Carmichael: Phys. Rev. A **50**, 4318 (1994)
22. H. Haken: *Light Vol.2, Laser Light Dynamics* (North-Holland Physics Publishing 1985)
23. M.O. Scully, W.E. Lamb, Jr.: Phys. Rev. **159**, 208 (1967)
24. M.O. Scully, M.S. Zubairy: *Quantum Optics* (Cambridge University Press, Cambridge, England 1997)
25. L.A. Lugiato: Physica (Amsterdam) **81A**, 565 (1975)
26. L.A. Lugiato: Physica (Amsterdam) **82A**, 1 (1976)
27. E.R. Pike: 'Photon Statistics'. In: *The Growth Points of Physics*, Rivista del Nuovo Cimento, Numero Speciale **1**, 277 (1969)
28. C.W. Gardiner: *Quantum Noise* (Springer-Verlag, Berlin 1991)
29. E.R. Pike, S. Sarkar: *The Quantum Theory of Radiation* (Oxford Science Publications, Oxford, England 1995)
30. P. Mandel: Physica (Amsterdam) **77**, 174 (1974)
31. C. Kittel: *Introduction to Solid State Physics* (John Wiley and Sons, New York 1986)
32. R. Loudon *et al.*: Phys. Rev. A **48**, 681 (1993)

Superradiant and Subradiant Behavior of the Overdamped Many-Atom Micromaser

Vasily V. Temnov, Mikhail I. Kolobov and Fritz Haake

Summary. We present the quantum treatment of an overdamped many-atom micromaser. Our model accounts for excited atoms entering the cavity but does not allow them to exit. The limit of overdamped Rabi-oscillations is assumed. We give a temporally coarse-grained description which smoothens over entrance events and compare it with a "microscopic" treatment accounting for each of the entrances and the evolution between them. We find an interesting nonstationary behavior of the micromaser radiation: a sequence of superradiant pulses which converges to a subradiant stationary regime.

In a micromaser [1] or microlaser [2] an atomic beam passing through the cavity usually has such a low atomic density that only a few atoms at a time interact with a single cavity mode. Collective atomic interaction with the cavity mode is interrupted by arrivals of new atoms and their escapes from the cavity. The question arises as to whether collective atomic behavior can persist in such a situation.

It was shown recently [3] by means of Monte-Carlo simulations that two different types of collective behavior are possible in the overdamped many-atom micromaser: superradiance and subradiance [4]. In [3] collective dynamics of superradiance for the density matrix of intracavity atoms [5], interrupted by entrances and escapes, was simulated numerically. Analytical treatment of such a model is extremely difficult because one has to follow the $2^N \times 2^N$ atomic density matrix for large and possibly varying N. In the present paper we discuss another model of the overdamped many-atom micromaser. The difference to [3] is that atoms, once entered into the cavity, are not allowed to escape from it. This assumption greatly simplifies the problem and allows for an analytical treatment.

The scheme of our micromaser is shown in Fig. 1. The atoms first pass through a velocity selector and then a pump field which excites them into the upper level $|e\rangle$. After that they enter the cavity and remain there. The upper atomic level $|e\rangle$ and the lower level $|g\rangle$ constitute the masing transition resonantly coupled to the single cavity mode. The collective atom-field interaction is interrupted by entrances of new excited atoms, to be referred as "kicks". These kicks change both the interaction Hamiltonian and the joint atom⊕field density matrix because the number of atoms inside the cavity grows by one after each kick. The dynamics between the kicks is described

H.J. Carmichael, R.J. Glauber, M.O. Scully (Eds.): LNP 561, pp. 261–270, 2001.

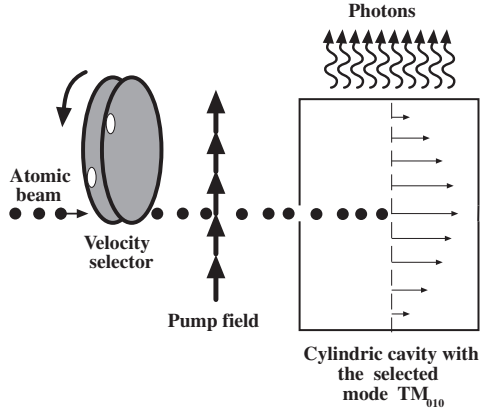

Fig. 1. Physical model of many-atom micromaser

by the following master equation for the atom⊕field density matrix ρ_{AF} in the interaction representation

$$\dot{\rho}_{AF}(t) = -\frac{i}{\hbar}[H, \rho_{AF}] + \Lambda_F \rho_{AF} \,. \tag{1}$$

Here H is the Tavis-Cummings Hamiltonian [6] describing interaction between N two-level atoms and the cavity mode in the dipole- and rotating-wave approximations,

$$H = i\hbar g(aJ_+ - a^\dagger J_-) \,, \tag{2}$$

whereas Λ_F stands for the damping of the cavity mode:

$$\Lambda_F \rho = \kappa\Big([a\rho, a^\dagger] + [a, \rho a^\dagger]\Big) \,. \tag{3}$$

In Eqs. (2) and (3) a and $a^\dagger$ are the annihilation and creation operators of the field mode, $J_\pm = \sum_{i=1}^{N} \sigma_i^\pm$ and $J_z = \sum_{i=1}^{N} \sigma_{zi}$ are the atomic operators of collective polarization and inversion, g is the vacuum Rabi frequency which we assume to be equal for all atoms inside the cavity, and $(2\kappa)^{-1}$ is the photon life time. In our model we neglect all incoherent processes like relaxation of inversion and polarization of atoms. This assumption is fulfilled for long-lived Rydberg atoms [1,7]. In the limit of overdamped Rabi oscillations,

$$\frac{g^2 N}{\kappa^2} \ll 1, \tag{4}$$

the cavity mode can be eliminated adiabatically and the dynamics (1) reduced to the so-called superradiance master equation [5]

$$\begin{aligned} &\dot{\rho}^{(N)}(t) = \Lambda_S \rho^{(N)}(t) \,, \\ &\Lambda_S \rho^{(N)} = \frac{g^2}{\kappa}\big([J_-, \rho^{(N)} J_+] + [J_- \rho^{(N)}, J_+]\big) \,, \end{aligned} \tag{5}$$

for the atomic density matrix $\rho^{(N)} = \mathrm{tr}_F \rho_{AF}$, where N indicates the current number of atoms in the cavity. The Markovian equation (5) holds for sufficiently large times $t \gg \kappa^{-1}$, for which the field follows the motion of atoms adiabatically [5]. In the case of a micromaser the number of atoms in the cavity is changing due to arrivals of new excited atoms. We restrict ourselves to the case of a regular atomic beam and assume that atoms enter the cavity with the entrance rate r. Thus for applicability of Eq. (5) between entrances we must require

$$N_{\mathrm{ex}} = \frac{r}{2\kappa} \ll 1\,, \tag{6}$$

where N_{ex} is the number of atoms entering the cavity during the lifetime of the photon. Note that the number of atoms N inside the cavity appearing in condition (4) grows roughly linear with time $N \sim rt$. Thus we can rewrite Eq. (4) as a restriction for the time interval t,

$$t \ll \frac{\kappa}{2g^2 N_{\mathrm{ex}}}\,, \tag{7}$$

during which our description is valid. By considering small N_{ex} we can increase the range of times t.

The Hilbert space for N two-level atoms has the dimension 2^N [6]. The dynamics (5) conserves the angular momentum quantum number j and it is convenient to use the angular momentum representation for the atomic density matrix [8]:

$$\rho^{(N)} = \sum_{j,m,\alpha;j',m',\alpha'} \rho^{(N)}_{j,m,\alpha;j',m',\alpha'} |j,m,\alpha\rangle\langle j',m',\alpha'|\,, \tag{8}$$

with

$$\begin{aligned} J_\pm|j,m,\alpha\rangle &= \sqrt{j(j+1)-m(m\pm1)}|j,m\pm1,\alpha\rangle\,,\\ J_z|j,m,\alpha\rangle &= m|j,m,\alpha\rangle\,. \end{aligned} \tag{9}$$

The atomic index α defines the symmetry of the state with respect to permutations of atoms.

Our final goal is to calculate the mean intensity $I(t)$ of the emitted light, given by

$$I(t) = 2\kappa\langle a^\dagger(t)a(t)\rangle = I_1\langle J_+(t)J_-(t)\rangle = \sum_{j,m}[j(j+1)-m(m-1)]\rho^{(N)}_{j,m}(t)\,, \tag{10}$$

where $I_1 = 2g^2/\kappa$ is the single-atom rate of spontaneous emission into the cavity mode, and $\rho^{(N)}_{j,m} = \sum_\alpha \rho^{(N)}_{j,m,\alpha;j,m,\alpha}$ is the probability of finding the quantum numbers j and m. The evolution equation for that probability is easily obtained from Eq. (5)

$$\dot\rho^{(N)}_{j,m}(t) = I_1\Big[(j-m)(j+m+1)\rho^{(N)}_{j,m+1} - (j+m)(j-m+1)\rho^{(N)}_{j,m}\Big]\,. \tag{11}$$

Let us look for the change of the probability $\rho_{j,m}^{(N)}$ due to the arrival of a new excited atom. We know that the atomic density operator changes according to

$$\rho^{(N+1)} = |e\rangle\langle e| \otimes \rho^{(N)} \,. \tag{12}$$

This leads to the relation between the probabilities before and after the kick

$$\rho_{j,m}^{(N+1)} = \frac{j+m}{2j}\rho_{j-\frac{1}{2},m-\frac{1}{2}}^{(N)} + \frac{j-m+1}{2j+2}\rho_{j+\frac{1}{2},m-\frac{1}{2}}^{(N)} \,. \tag{13}$$

The derivation of this transformation is based on the coupling of two angular momenta and is performed in [9]. We may note in passing that atomic exits from the cavity could not be accounted for by a closed form evolving only the probabilities $\rho_{j,m}^{(N)}$. The different role of atomic entrances and escapes is clear from a simple physical argument: for an entrance the state of a new atom is uncorrelated with the collective state of atoms of the previously present atoms inside the cavity, while for an escape the state of the leaving atom is strongly correlated with that of remaining ones.

We now consider a time interval $\Delta t \gg 1/r$ and construct a coarse-grained rate of change of $\rho_{j,m}^{(N)}$ due to the $\Delta N = r\Delta t$ atomic entrances and $\Delta\rho_{j,m}^{(N)} \equiv \rho_{j,m}^{(N+\Delta N)} - \rho_{j,m}^{(N)}$. Dropping the superscript N we get

$$\Big(\frac{\Delta\rho_{j,m}}{\Delta t}\Big)_{\rm pump} = r\Big(\frac{j+m}{2j}\rho_{j-\frac{1}{2},m-\frac{1}{2}} + \frac{j-m+1}{2j+2}\rho_{j+\frac{1}{2},m-\frac{1}{2}} - \rho_{j,m}\Big) \,. \tag{14}$$

We add that rate to the superradiant rate given in (11). Employing the rescaled time $t' = rt$ we thus derive a phenomenological "master equation" of the overdamped many-atom micromaser

$$\begin{aligned}\frac{d\rho_{j,m}(t')}{dt'} = &-[1+\chi(j+m)(j-m+1)]\rho_{j,m} + \chi(j-m)(j+m+1)\rho_{j,m+1} + \\ &+\frac{j+m}{2j}\rho_{j-\frac{1}{2},m-\frac{1}{2}} + \frac{j-m+1}{2j+2}\rho_{j+\frac{1}{2},m-\frac{1}{2}} \,.\end{aligned} \tag{15}$$

The single dimensionless parameter

$$\chi = \frac{I_1}{r} = \frac{2g^2}{\kappa r} \,, \tag{16}$$

determines the behavior of our micromaser. Roughly speaking the parameter χ tells us how fast is the dynamics of intracavity atoms on the time scale $1/r$ between two successive kicks. Let us note that the quantum numbers j and m are integer for even number of atoms N inside the cavity ($j = 0, 1, ..., N/2$; $m = -j, -j+1, ..., j$) and half-integer for odd N ($j = 1/2, 3/2, ..., N/2$; $m = -j, -j+1, ..., j$). Since our master equation (15) does not depend on N we can define the elements $\rho_{j,m}$ of the density matrix for both integer and half-integer indices j and m. The atomic expectation

values can be calculated using Eq.(10) with the sum over both integer and half-integer indices j and m.

Since Eq. (15) is too complex for an analytical solution we shall consider a semiclassical approximation. For this we first write the exact equations of motion for the atomic expectation values

$$\begin{aligned}\frac{d}{dt'}\langle J_+J_-\rangle &= 2\chi[\langle J_zJ_+J_-\rangle - \langle J_+J_-\rangle] + 1\,,\\ \frac{d}{dt'}\langle J_z\rangle &= -\chi\langle J_+J_-\rangle + \frac{1}{2}\,,\\ \frac{d}{dt}\Big[\langle J_z^2\rangle - \langle J_z\rangle^2\Big] &= \chi[-2\langle J_zJ_+J_-\rangle + 2\langle J_z\rangle\langle J_+J_-\rangle + \langle J_+J_-\rangle] + \frac{1}{4}\,. \quad (17)\end{aligned}$$

As follows from Eq. (17), the normalized stationary intensity is equal to $\langle J_+J_-\rangle = 1/2\chi$. With the promise of a critical discussion below we here take as a semiclassical approximation the neglect of the dispersion of the inversion operator, $\langle J_z^2\rangle - \langle J_z\rangle^2 = 0$. This implies the factorization $\langle J_zJ_+J_-\rangle = \langle J_z\rangle\langle J_+J_-\rangle + \frac{1}{2}\langle J_+J_-\rangle + 1/8\chi$. We thus get the semiclassical equations of motion for the inversion $\langle J_z\rangle$ and the normalized intensity $\langle J_+J_-\rangle$

$$\begin{aligned}\frac{d}{dt'}\langle J_+J_-\rangle &= \chi[2\langle J_z\rangle\langle J_+J_-\rangle - \langle J_+J_-\rangle] + \frac{5}{4}\,,\\ \frac{d}{dt'}\langle J_z\rangle &= -\chi\langle J_+J_-\rangle + \frac{1}{2}\,. \quad (18)\end{aligned}$$

This nonlinear system has one stable stationary solution $(\langle J_z\rangle, \langle J_+J_-\rangle) = (-\frac{3}{4}, 1/\chi)$. On linearizing we get the eigenvalues

$$\lambda_{1,2} = -\frac{5}{4}\chi \pm i\sqrt{\chi - \frac{25}{16}\chi^2}\,. \quad (19)$$

It follows that quasiperiodic behavior emerges for $\chi < \frac{16}{25}$ (both eigenvalues complex) and aperiodic behavior for $\chi \geq \frac{16}{25}$ (both eigenvalues real and negative). The differential equations (18) can be rewritten as a single equation of second order,

$$\ddot{Z} + (\frac{5}{2} - 2Z)\chi\dot{Z} + \chi Z = 0\,, \quad (20)$$

with $Z = \langle J_z\rangle + \frac{3}{4}$, which describes a damped nonlinear oscillator.

The transformation (13) does not preserve the angular momentum quantum number j. Thus our dynamics is different from the pure superradiant dynamics (5) which does preserve j. To characterize the degree of interatomic cooperation in our micromaser we introduce the effective length of the Bloch vector as

$$B = \sqrt{\langle J^2\rangle} = \sqrt{\langle J_+J_-\rangle + \langle J_z^2\rangle - \langle J_z\rangle} \quad (21)$$

The positively correlated atomic dipole momenta oriented in the same direction (large macroscopic polarization) needed for superradiance can arise

only if the Bloch vector is large. A small Bloch vector corresponds to anti-correlation of atomic dipoles (small macroscopic polarization) and leads to subradiance.

For the sake of comparison we introduce the fictitious *noncollective micromaser* also called an *independent-atom model* [10] in which no correlations between atomic dipole moments arise. Its intensity of radiation is calculated as the incoherent overlap of the 1-atom intensities

$$I_{\rm nc} = I_1 \langle J_+ J_- \rangle_{\rm nc} = I_1 \sum_{i=1}^{N} {\rm e}^{-I_1 t_i} \,, \tag{22}$$

with t_i denoting the time the i-th atom spent in the cavity. We shall call the quantity $\langle J_+ J_- \rangle_{\rm nc} = I_{\rm nc}/I_1$ the normalized intensity of the noncollective micromaser. The stationary (time averaged) intensity of the noncollective micromaser is equal to the atomic pump rate r, because all atoms entering the cavity emit a photon into the cavity mode after sufficiently long time. Thus it is twice as large as the intensity of our overdamped micromaser.

We proceed to compare the results of three different treatments of our model. Two are based on the master equation (15) which is either solved numerically or treated semiclassically in (18). The third "microscopic" treatment amounts to solving the superradiance master equation (5) between the kicks at which we imply the transformation (13). The initial state of the cavity mode is vacuum. We consider the case of the regular pumping, when atoms enter the cavity at equidistant times $t' = 1, 2, ...$ We calculate the normalized intensity of radiation, atomic inversion, and the length of the Bloch vector from the microscopic simulations, the solution of Eq. (15) and its semiclassical approximation (18). We set the initial density matrix in Eq. (15) equal to $\rho_{j,m}(t' = 1) = \delta_{j,\frac{1}{2}} \delta_{m,\frac{1}{2}}$, and for the semiclassical equations (18) we chose $\langle J_z \rangle(1) = \frac{1}{2}$, $\langle J_+ J_- \rangle(1) = 1$ which corresponds to a single excited atom in the cavity. The solution of the master equation and its semiclassical approximation appear to be rather insensitive to the initial values of the atomic density matrix for $\chi \ll 1$ and give the same results for $\rho_{j,m}(t' = 0) = \delta_{j,0}\delta_{m,0}$ and $\langle J_z \rangle(0) = \langle J_+ J_- \rangle(0) = 0$ corresponding to the empty cavity.

In Fig. 2 we represent the evolution of the normalized intensity obtained from the microscopic treatment, the solution of the master equation, and for the noncollective micromaser (22), for different values of parameter χ. The normalized intensity jumps by one after each kick both for noncollective and overdamped many-atom micromaser for any χ. These kicks, which are relatively well pronounced for large χ ($\chi = 0.5$) become invisible on the large intensity scale for small χ ($\chi = 0.005$). The solution of the master equation smoothens the kicks but is still good even for large χ. The normalized intensity of the noncollective micromaser (22) increases quasimonotonically (except for the kicks) until the (stroboscopic) steady state is reached. The intensity of our overdamped many-atom micromaser shows an interesting behavior: (a) it does not oscillate for large χ ($\chi = 0.5$) but does for small χ;

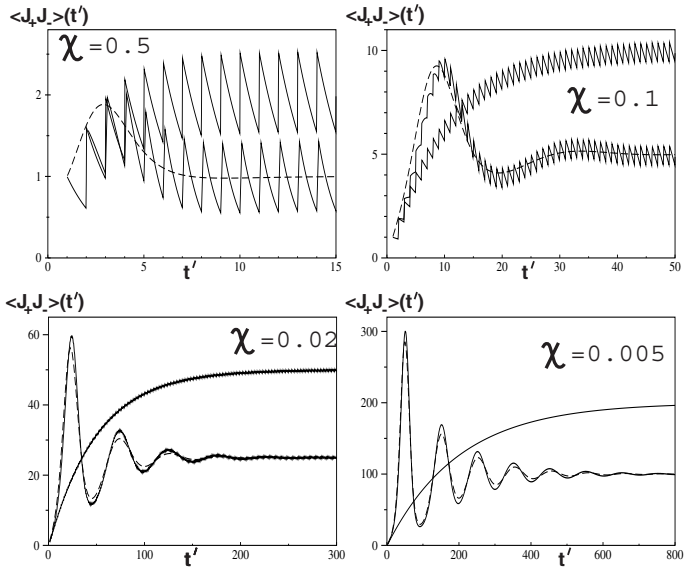

Fig. 2. Normalized intensity of the many-atom micromaser as function of the dimensionless time t' for different χ: noncollective model (bold), solution of the master equation (dashed) and based on the microscopic simulations (normal). The normalized intensity jumps by one when a new excited atom enters the cavity

the smaller χ the larger is the number of oscillations and (b) for any χ the normalized intensity converges against the (stroboscopic) stationary value $\frac{1}{7}2\chi$, which is half as large as the stationary intensity of the noncollective micromaser. In order to understand the physical meaning of the oscillations, we follow the dynamics of intracavity atoms starting with a single atom in the cavity and assuming $\chi \ll 1$.

The first atom enters the cavity at the time $t' = 1$ and starts to interact with the overdamped field mode. At the moment $t' = 2$ when the second excited atom enters, the first atom is excited with probability $\mathrm{e}^{-\chi} \simeq 1-\chi \simeq 1$. Thus the state of the two-atom system is the fully excited state $|1,1\rangle$ with the probability close to unity. Since $\chi \ll 1$ the state of the two-atom system does not change significantly up to the moment $t' = 3$, when the third excited atom enters the cavity. The state of the three-atom system becomes the fully excited state $|\frac{3}{2},\frac{3}{2}\rangle$ with a high probability and so on. It is clear, that the accumulation of atoms in the fully exited state described above cannot last infinitely long. Let us remind that the fully excited collection of N two-level atoms coupled to the bad cavity mode emits the superradiant pulse if the interaction time is longer, than the so-called delay time of the pulse $t'_m = (1/\chi)\ln N/(N+1)$ [8]. In our system the number of atoms inside the

cavity grows linearly with time but the delay time t'_m decreases. After some time the number of atoms inside the cavity exceeds the critical value $N_{\rm cr}$:

$$\frac{1}{\chi}\frac{\ln N_{cr}}{N_{cr}} \sim N_{cr}\,, \tag{23}$$

and atoms emit photons coherently producing the superradiant pulse. After that most atoms are in the ground state and the total inversion is negative. The new excited atoms entering the cavity also start to accumulate in the upper state, as described above. The important difference to the first pulse is that the cavity in no more empty for the new excited atoms: now it contains many unexcited ones. These unexcited atoms interfere with entering atoms in such a way that the amplitude of the second pulse becomes smaller and the duration longer than those of the first pulse, but between the pulses the emission is suppressed. An example of such destructive quantum-mechanical interference is pointed out in [11]: if one adds one excited atom to the collection of N unexcited atoms coupled to the leaky cavity mode, the system will emit a photon with a small probability $1/(N+1)$, because the energy is much more likely to be trapped in the atomic system. This example also provides a qualitative understanding, why the stationary regime of our micromaser is subradiant: as mentioned above, the stationary intensity is half as large as the stationary intensity of the noncollective micromaser. This means that a half of initial atomic excitation is trapped in the atomic system.

More insight into dynamics of our system can be obtained from Fig. 3, where the normalized intensity, inversion, and the length of the Bloch vector are plotted as functions of t' for $\chi = 0.02$. The linear growth of inversion for small times proves that atoms accumulate in the upper state. After the first pulse the inversion becomes negative, the length of the Bloch vector decreases and the radiation rate is suppressed. The maxima of the intensity correspond to maxima of B and zeros of the inversion. In this manner the system reaches the (stroboscopic) stationary state. The normalized intensity and inversion oscillate around their mean values with amplitudes 1 and 0.5 correspondingly, whereas the length of the Bloch vector reaches the stationary value, corresponding to the nearly horizontal orientation of the Bloch vector. The solution of the master equation gives a very good approximation for the results of microscopic treatment (see Fig. 3a). The semiclassical approximation for the normalized intensity and inversion is in a rather good agreement with the exact solution of the master equation; the stationary solution appears to be exact (see Fig. 3b). The semiclassical value of $B = \sqrt{\langle J_+ J_-\rangle + \langle J_z\rangle^2 - \langle J_z\rangle}$ is smaller than the exact one $B = \sqrt{\langle J_+ J_-\rangle + \langle J_z^2\rangle - \langle J_z\rangle}$, because the assumption $\langle J_z^2\rangle - \langle J_z\rangle^2 = 0$ is not valid for large times.

In conclusion we have analyzed the behavior of the overdamped many-atom micromaser. Entering atoms interrupt collective atom-field interaction, but the collectivity survives for any value of parameter χ. For $\chi \ll 1$ an overdamped many-atom micromaser demonstrates an interesting behavior

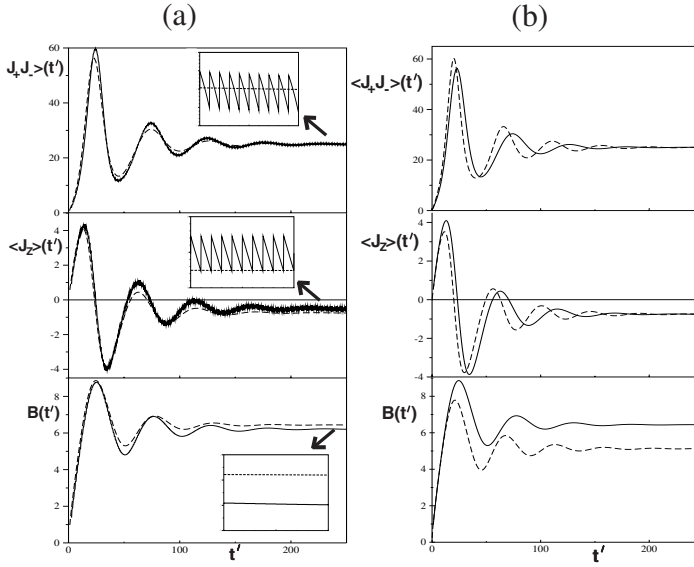

Fig. 3. Evolution of the normalized intensity, inversion and length of the Bloch vector B obtained from (**a**) the microscopic simulations (continuous) and solution of the master equation (dashed) and (**b**) solution of the master equation (continuous) and its semiclassical approximation (dashed) for $\chi = 0.02$

producing the sequence of superradiant pulses which converges to the subradiant stationary regime. For $\chi \sim 1$ and larger there are no superradiant pulses but the stationary regime is subradiant. Such behavior reflects the correlations between the dipole moments of atoms, which arise during the interaction with the common cavity mode.

Acknowledgments

We would like to thank P. Braun and M. Kuś for stimulating discussions. We gratefully acknowledge support by the Sonderforschungsbereich Unordnung und Große Fluktuationen of the Deutsche Forschungsgemeinschaft.

References

1. D. Meschede, H. Walther, G. Müller: Phys. Rev. Lett. **54**, 551 (1985)
2. K. An, J.J. Childs, R.R. Dasari, M.S. Feld: Phys. Rev. Lett. **73**, 3375 (1994)
3. V.V. Temnov: Superradiance and Subradiance in the Overdamped Many-atom Micromaser, unpublished
4. R.H. Dicke: Phys. Rev. **93**, 99 (1954)
5. R. Bonifacio, P. Schwendimann, F. Haake: Phys. Rev. A **4**, 302 (1971)
6. M. Tavis, F.W. Cummings: Phys. Rev. **170**, 379 (1968)

7. G. Raithel, C. Wagner, H. Walther, L.M. Narducci, M.O. Scully: In: *Cavity Quantum Electrodynamics*, ed. by P.R. Berman (Academic Press, San Diego 1994) p. 57
8. R. Bonifacio, P. Schwendimann, F. Haake: Phys. Rev. A **4**, 854 (1971)
9. V.V. Temnov: (Diplomarbeit, Essen University 1999)
10. F. Haake: In: *Quantum Statistics in Optics and Solid-State Physics*, Springer Tracts in Modern Physics, Vol. 66 (Springer, Berlin 1973) p. 98; K.M. Gheri, P. Horak, H. Ritsch, J. Mod. Opt. **44**, 605 (1997)
11. M. Sargent, M.O. Scully, W.E. Lamb: *Laser Physics* (Addison-Wesley, London 1974) p. 408

Bifurcations to Cooperative States in Arrays of Coupled Nonlinear Optical Oscillators

Ken McNeil

1 Introduction

This paper focusses on bifurcations to cooperative states in arrays of linearly coupled identical nonlinear optical oscillators, that is, to states in which each individual oscillator adopts the same state. The general condition on the coupling which allows cooperative states is derived and the examples of coupled gas lasers and coupled parametric oscillators are analysed. These examples show clearly the effects of both the degree of component oscillator phase symmetry and the complexity of the coupling geometry.

Studies of the behaviour of systems of large numbers of coupled nonlinear elements appeared as early as the 1950s [1,2], but it is the last two decades which have seen an explosion of interest in such systems across a number of fields. Relevant theoretical work in the field of optics includes the study of coupled optically bistable systems [3], coupled lasers [4,5] and multimode lasers [6].

A variety of interesting behaviour has been unearthed, including symmetry forming [7–9], wave phenomena [4,10] and phase space clustering [11,12]. Of particular interest for the present work is the attention which has been paid to phase transition behaviour [4,10,13]. We will consider individual elements which exhibit bifurcations from the zero state, and examine the bifurcation behaviour in linearly coupled arrays of such elements, paying particular attention to bifurcations to cooperative states. Such states show the highest possible symmetry, or equivalently, the densest possible phase space clustering. In many practical situations these are the most desired states, since one purpose of an array of oscillators is to enhance the effect of its individual elements.

This paper will present the general condition on the coupling which allows such cooperative behaviour, and then analyse in some detail the features of this behaviour for two particular examples, gas lasers and parametric oscillators. For the laser, we will use the standard simplified model, which describes the near threshold behaviour of the complex output field z:

$$\dot{z} \;=\; pz - \gamma z - |z|^2 z \;. \tag{1}$$

The parametric oscillator has a different pumping phase relationship:

$$\dot{z} \;=\; pz^* - \gamma z - |z|^2 z \;. \tag{2}$$

H.J. Carmichael, R.J. Glauber, M.O. Scully (Eds.): LNP 561, pp. 271–279, 2001.

In both cases, γ is the effective damping and p is the effective pumping strength (throughout this paper the star superscript is used to indicate complex conjugation). The well-known stable steady state of these equations has the magnitude

$$|z|^2 \;=\; \begin{cases} 0 & \text{if } 0 \le p \le \gamma \\ p-\gamma & \text{if } p \ge \gamma\,, \end{cases} \tag{3}$$

with the phase of z arbitrary for the laser and zero or π (relative to the assumed constant phase of the pumping) for the parametric oscillator.

For later reference we note here that the linear stability is governed by a matrix of the following form (taking z and z^* as the phase space variables):

$$A \;=\; \begin{pmatrix} -\mu & -\nu \\ -\nu^* & -\mu \end{pmatrix} \tag{4}$$

where $\mu = 2|z|^2 + \gamma - p$ and $\nu = z^2$ for the laser, and $\mu = 2|z|^2 + \gamma$ and $\nu = z^2 - p$ for the parametric oscillator.

2 Coupled Oscillators and Cooperative States

Consider a system of N linearly coupled identical oscillator elements. If z_j is the complex field amplitude of the jth oscillator, its equation of motion takes the form

$$\dot{z}_j \;=\; f(z_j) \;+\; \sum_{k \ne j} b_{jk} z_k \tag{5}$$

where $f(z)$ is the single oscillator function (the righthand side of (1) or (2), for example) and the b_{jk} are the oscillator coupling strengths. (If there is to be no exchange of energy with the outside world as a result of the coupling between any pair of oscillators, their phases must be related as $b_{jk} = -b_{kj}^*$.)

The stability matrix for the system takes the form

$$\begin{pmatrix} A_1 & B_{12} & B_{13} & .. & .. & .. & B_{1N} \\ B_{21} & A_2 & B_{23} & B_{24} & .. & .. & B_{2N} \\ .. & .. & .. & .. & .. & .. & .. \\ B_{N1} & B_{N2} & .. & .. & .. & B_{NN-1} & A_N \end{pmatrix} \tag{6}$$

where A_j is the 2×2 stability matrix (4) for the jth oscillator, and B_{jk} is the 2×2 matrix $\begin{pmatrix} b_{jk} & 0 \\ 0 & {b_{jk}}^* \end{pmatrix}$.

2.1 Bifurcations from the Zero Steady State

Zero is a steady state for both the laser and the parametric oscillator (although it is not stable for $p \ge \gamma$), and we assume the same is true for the

general oscillator element $f(z)$ in (5). The system state with all oscillators in the zero state is then a solution of (5). The stability of this zero state is governed by the matrix (6) with all the A_j equal to A_0, say, the A for an oscillator in the zero state; whenever the real part of an eigenvalue of this matrix passes through zero there is a bifurcation from the zero state. Roughly speaking, not too far above a bifurcation threshold the nonlinearity in $f(z)$ can be ignored, and (5) becomes the eigenvector equation for any eigenvalue that has gone to zero. In other words, the nonzero solutions $(z_1,\ {z_1}^*,\ z_2,\ {z_2}^*, ...,\ z_N,\ {z_N}^*)$ that emerge at a bifurcation point are stability matrix eigenvectors corresponding to critical eigenvalues.

2.2 Bifurcations to Cooperative States

Obtaining the bifurcation points and the amplitudes of the emergent nonzero solutions is not a trivial exercise: even for simple coupling geometries there can be a large number of bifurcation points, and these can be degenerate, often to a high order [4,10,12,13]. Those bifurcations to cooperative states, however, are relatively easy to deal with.

According to (5), cooperative solutions, where all $z_j = z$, say, must satisfy $\dot{z} = f(z) + (\sum_{k \neq j} b_{jk})\ z$ for all j. This can only hold if the sum over the b_{jk} is independent of j; this is the condition which allows cooperative solutions to occur. Call this sum S. If S is split into its real and imaginary parts $(S = S_R + i\, S_I)$, say, the cooperative state equation takes the form

$$\dot{z} \ = \ f(z) \ + \ \ \Delta z \ + \ i\, \omega\, z\ . \tag{7}$$

$\Delta = S_R$ renormalises terms in $f(z)$ which are linear in z, and represents a global effect of any interaction with the external world through the coupling: the sign of Δ depends on whether the coupling allows loss or gain of energy. For no exchange of energy, $S_R = 0$, which holds if the local condition $b_{jk} = -b^*_{kj}$ holds. (This can be shown by noting that with this local condition, the real part of $\sum_j \sum_{k \neq j} b_{jk}$ is zero. But since each $\sum_{k \neq j} b_{jk}$ is independent of j, the double sum reduces to $N\ \sum_{k \neq j} b_{jk}$, and the result follows.) $\omega = S_I$ looks like an angular frequency, but whether or not the solution actually has an oscillatory component depends on the phase symmetry of $f(z)$, amongst other things.

We can derive a general equation which predicts the point at which a bifurcation from zero to a cooperative state will occur. The eigenvector of the stability matrix ((6) with all A_j equal to A_0) has all $z_j, {z_j}^*$ pairs equal (to z, z^* say), so each 'row' of the eigenvalue equation is

$$(A_0 + S)\ \begin{pmatrix} z \\ z^* \end{pmatrix} \ = \ \lambda\ \begin{pmatrix} z \\ z^* \end{pmatrix}\ . \tag{8}$$

In other words, a bifurcation to a cooperative state occurs when the real part of an eigenvalue of $A_0 + S$ go to zero.

2.3 Stability of a Cooperative State

With all oscillators in the same state, the stability matrix (6) has all A_j equal to the A for the individual oscillator state. This simplifies greatly the problem of determining the stability, but as the examples of the following two sections show, it is still not necessarily a trivial exercise.

3 Example 1: Coupled Lasers

The equation for the coupled laser cooperative state is

$$\dot{z} \;=\; (p - \gamma + \Delta)\; z \;-\; |z|^2\; z \;+\; i\;\omega\, z\;, \tag{9}$$

which has the following long time nonzero solution:

$$z \;\;=\;\; |z|\; e^{i\omega t} \qquad\qquad (p \geq \gamma - \Delta) \tag{10}$$

where the amplitude $|z| = p + \Delta - \gamma$. This inphase solution rotates at angular frequency ω and has an amplitude which is the single laser amplitude renormalised by Δ.

From this point in the analysis we take the coupling to be completely imaginary: $b_{jk} \;\rightarrow\; i\; b_{jk}$, where the redefined b_{jk} is real. This gives $\Delta = 0$. This is the kind of coupling that occurs, for example, through the evanescent fields of devices.

We consider now the stability of the zero state, the emergence of the cooperative state and the stability of this state. Since the stability matrix eigenvalue spectrum depends strongly on the coupling geometry, we must consider this explicitly. We shall look at the cases of global coupling and nearest neighbour ring coupling (sometimes called 'parallel' and 'series' coupling [14]), and take all nonzero couplings to have the same strength b. This clearly satisfies the cooperative state coupling condition and the local condition for no energy exchange with the outside world. ω is $(N-1)b$ for global coupling and $2b$ for ring coupling.

3.1 Global Coupling

For this coupling geometry with all couplings of the same strength, the B_{jk} in the stability matrix (6) are all equal to $B = \begin{pmatrix} ib & 0 \\ 0 & -ib \end{pmatrix}$. In the zero state the A_j are all equal to A_0, and the eigenvalues are the pairs of eigenvalues of the matrices

$$A_0 \;-\; B \qquad\qquad A_0 \;+\; (N-1)B \tag{11}$$

with the first occurring with $(N-1)$ -fold multiplicity [12]. The second is the matrix in (8) which determines the onset of the cooperative state. These two

matrices have the pairs of eigenvalues

$$\begin{aligned} \lambda_{1\pm} &= -\mu \pm \sqrt{|\nu|^2 - b^2}\,, \\ \lambda_{2\pm} &= -\mu \pm \sqrt{|\nu|^2 - (N-1)^2 b^2}\,. \end{aligned} \tag{12}$$

For the zero solution $\mu = \gamma - p$ and $\nu = 0$, so these pairs are

$$\begin{aligned} \lambda_{1\pm} &= p - \gamma \pm i\, b\,, \\ \lambda_{2\pm} &= p - \gamma \pm i\,(N-1) b\,. \end{aligned} \tag{13}$$

The onset of the cooperative state is marked by the real part of $\lambda_{2\pm}$ changing sign: this occurs at the single laser threshold $p = \gamma$. However the real part of the $(N-1)$-fold degenerate $\lambda_{1\pm}$ also changes sign at the same time: all branches appear simultaneously.

Once on the cooperative state branch, the stability is determined by the eigenvalues of the matrix (6) with all A_j equal to the A for the individual oscillator amplitude (10) with z replaced by $|z|$ (after first transforming out a part rotating at angular frequency ω). The eigenvalues thus take the same form as (12), with $\mu = \nu = p - \gamma$:

$$\begin{aligned} \lambda_{1\pm} &= \gamma - p \pm \sqrt{(p-\gamma)^2 - b^2}\,, \\ \lambda_{2\pm} &= \gamma - p \pm \sqrt{(p-\gamma)^2 - (N-1) b^2}\,. \end{aligned} \tag{14}$$

These all have real parts which are negative for any p above threshold, so the cooperative state is stable everywhere.

3.2 Ring Coupling

Here, each oscillator is coupled only to its immediate neighbours, with the Nth coupled to the first to complete the ring. All couplings have the same strength, so the B_{jk} are B for $k = j \pm 1$ (*modulo* N), and zero otherwise. The eigenvalues for the zero state for this stability matrix structure are the eigenvalues of the following N matrices [4,10,13]:

$$A_0 + 2i\, c_k B, \qquad k = 1, 2, \ldots, N \tag{15}$$

where $c_k = \cos(\frac{2\pi k}{N})$. These eigenvalues are the N pairs

$$\lambda_{k\pm} = -\mu \pm \sqrt{|\nu|^2 - 4{c_k}^2\, b^2}, \qquad k = 1, 2, \ldots, N\,. \tag{16}$$

$\mu = \gamma - p$ and $\nu = 0$, so

$$\lambda_{k\pm} = p - \gamma \pm 2i\, c_k\, b, \qquad k = 1, 2, \ldots, N\,. \tag{17}$$

The onset of the cooperative state occurs when the real part of $\lambda_{N\pm}$ changes sign, again at the single laser threshold $p = \gamma$. Also again, the real parts of all the other $\lambda_{k\pm}$ change sign at this point, so all branches appear simultaneously.

Again, the stability matrix for the cooperative state has all A_j equal to the A with z replaced by $|z|$. The eigenvalues thus take the same form as (16), with $\mu = \nu = p - \gamma$:

$$\lambda_{k\pm} \;=\; \gamma - p \;\pm\; \sqrt{(p-\gamma)^2 - \; 4{c_k}^2 b^2}, \qquad\qquad k = 1, 2, \ldots, N\,. \tag{18}$$

These all have real parts which are negative for any p above threshold, so the ring coupling cooperative state is also stable everywhere.

4 Example 2: Coupled Parametric Oscillators

Here, the equation for the cooperative state is

$$\dot{z} \;=\; pz^* + (\Delta - \gamma)\; z \;-\; |z|^2\, z \;-\; i\;\omega\, z \tag{19}$$

In this case, ω is not an angular frequency: the long time nonzero solution has amplitude and phase given by

$$\begin{aligned} |z|^2 \;&=\; \sqrt{p^2 - \omega^2} \;-\; \gamma \;+ \Delta \qquad\qquad (p \geq \sqrt{(\gamma - \Delta)^2 + \omega^2})\,, \\ \tan\theta \;&=\; \pm\, \frac{\omega}{p + \sqrt{p^2 - \omega^2}}\,. \end{aligned} \tag{20}$$

As in the laser case, we have $\Delta = 0$ in what follows.

4.1 Global Coupling

The stability matrix for the zero state again has eigenvalues of the form (12). For the zero solution $\mu = \gamma$ and $\nu = -p$, so these eigenvalue pairs are

$$\begin{aligned} \lambda_{1\pm} \;&=\; -\gamma \;\pm\; \sqrt{p^2 - \; b^2}\,, \\ \lambda_{2\pm} \;&=\; -\gamma \;\pm\; \sqrt{p^2 - \; (N-1)^2 b^2}\,. \end{aligned} \tag{21}$$

The onset of the cooperative state occurs when the real part of λ_{2+} changes sign. This threshold is given by $p^2 \;=\; \gamma^2 + (N-1)^2 b^2$; unlike the laser, the transition to the cooperative state transition is displaced from the single oscillator transition point. In fact, the real part of the $(N-1)$-fold degenerate $\lambda_{1\pm}$ changes sign before this, at $p^2 \;=\; \gamma^2 + b^2$, which means that the other branches appear at a lower value of p than the cooperative state; this emerges from an unstable zero state.

In the cooperative state $\mu = 2\sqrt{p^2 - (N-1)^2 b^2} \;- \gamma$ and $|\nu|^2 = \gamma^2 + (N-1)^2 b^2$, so the eigenvalues on this branch are

$$\begin{aligned} \lambda_{1\pm} \;&=\; -2\sqrt{p^2 - (N-1)^2 b^2} + \gamma \;\pm\; \gamma\,, \\ \lambda_{2\pm} \;&=\; -2\sqrt{p^2 - (N-1)^2 b^2} + \gamma \;\pm\; \sqrt{\gamma^2 + N(N-2) b^2}\,. \end{aligned} \tag{22}$$

Only λ_{2+} is ever positive, so this governs the stability. It is positive when the branch emerges, and remains so until $p^2 \;=\; (N-1)^2 b^2 \;+\; \frac{1}{4}(\gamma +$

$\sqrt{\gamma^2 + N(N-2)b^2})^2$, at which point the cooperative state becomes stable. There is a secondary bifurcation at this point to an unstable state of lower symmetry, but further discussion of this lies outside the scope of the present work.

4.2 Ring Coupling

Here, the eigenvalues for the zero state take the form (16), so with $\mu = \gamma$ and $\nu = -p$,

$$\lambda_{k\pm} \;=\; -\gamma \;\pm\; \sqrt{p^2 - 4{c_k}^2\, b^2} \qquad k = 1, 2, \ldots, N\,. \tag{23}$$

The onset of the cooperative state occurs when the real part of λ_{N+} changes sign, which is when $p^2 = \gamma^2 + 4b^2$. Not only is this transition displaced from the single oscillator transition point, it is the final in a whole sequence of transitions as the λ_{k+} change sign at p values is given by ${p_k}^2 = \gamma^2 + 4{c_k}^2 b^2$. A fuller discussion of the resulting sequence of bifurcations is given in [13], but a typical example of this sequence is shown in Fig. 1. Similar sequences occur in ring arrays of semiconductor lasers [4].

On the cooperative state branch, $\mu = 2\sqrt{p^2 - 4b^2} - \gamma$ and $|\nu|^2 = \gamma^2 + 4b^2$, so the eigenvalues are

$$\lambda_{k\pm} \;=\; \gamma - 2\sqrt{p^2 - 4b^2} + \pm\, \sqrt{\gamma^2 + 4(1 - {c_k}^2)b^2} \qquad k = 1, 2, \ldots, N\,. \tag{24}$$

All λ_{k-} are negative along the whole branch. All λ_{k+} are initially positive, but as p is increased, they change sign in sequence, at points given by

$${p_k}^2 = \tfrac{1}{4}(\sqrt{\gamma^2 + 4(1 - {c_k}^2)b^2} + \gamma)^2 \;+\; 4b^2$$

(with a degenerate bifurcation occuring at each point – the c_k are periodic in k, so that each member of the set of eigenvalues (24) occurs at least twice). It is only when the last eigenvalue in the sequence becomes negative that the branch becomes stable. The corresponding p_k is given by the k values which minimise c_k, and depends on the value of N. Again, similar sequences occur in ring arrays of semiconductor lasers [4]. Further discussion of the secondary bifurcations will not be attempted in the present work, but an example of a typical sequence can be seen in Fig. 1.

5 In Conclusion

When oscillators which individually exhibit bifurcation behaviour are coupled together in large numbers, it is not surprising that the resulting arrays exhibit rich bifurcation behaviour, even when the oscillators are identical and the coupling is linear, as in the present work. This paper has focussed on one particular bifurcation, that to a cooperative state, in which all component oscillators adopt the same state at long times. The condition which allows

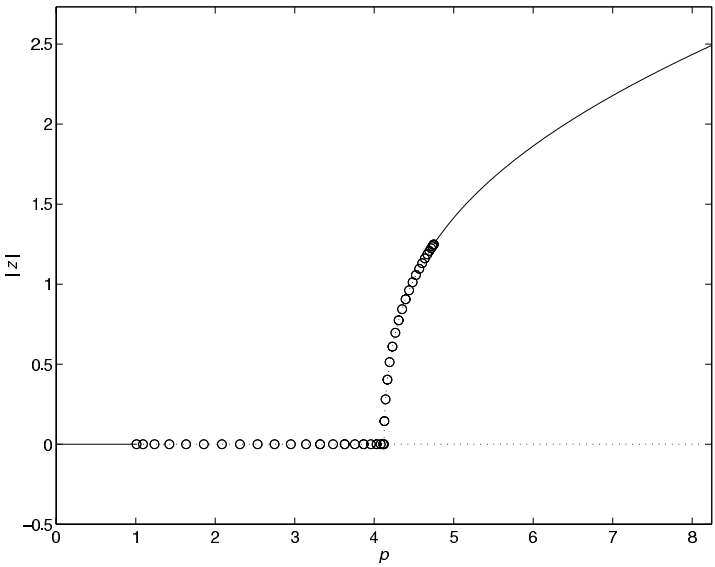

Fig. 1. Oscillator amplitude magnitude as a function of pumping for the zero and cooperative states in 43 parametric oscillators coupled in a ring. $\gamma = 1.0$ and $b = 2.0$. Solid lines indicate stable regions, dotted lines unstable regions. Circles mark the location of bifurcations to non cooperative states. The onset of instability of the zero solution tends to $p = \gamma$ for large N. The graph for the global coupling case has a similar form, except that the sequence of bifurcations from zero (except the one to the cooperative branch) collapses to the leftmost point, and there are no bifurcations on the unstable part of the cooperative state branch. For the laser, there are no bifurcation sequences: all of the bifurcations from zero coincide, and there are no bifurcations from the cooperative state branch

such states requires that in general the coupling be in some sense closed. A linear chain coupling, for example, would not allow a cooperative state unless some rather artificial conditions were imposed on the coupling magnitudes for the end oscillators. (We would expect, however, that for many situations end effects would become less pronounced for large N.)

The particular examples analysed show clearly the effect of the degree of individual oscillator phase symmetry on the long time behaviour: the phase invariance of the laser gives an oscillatory cooperative state, while the parametric oscillator, invariant under reflection only, has no time varying part. The degree of phase invariance is also reflected in the bifurcation structure. In the laser case, all bifurcations from the zero state occur at the same threshold, which is the same as that for the single laser. For the parametric oscillator equation, they occur in a sequence, and only the first is stable when it emerges. The cooperative state emerges as the final in the sequence, and only

stabilises somewhat above threshold. None of the above features are helpful if the cooperative state is the desired operating state.

When there is a sequence of bifurcations, the structure depends on the complexity of the coupling. Uniform global coupling is the least complex possible, and the corresponding sequence has just two members: the bifurcation to the cooperative state and a degenerate bifurcation to all other states. Ring coupling is more complex, and this is reflected in the way the degenerate bifurcation of the global case is 'unfolded' into a whole sequence.

This paper has used examples from nonlinear optics to examine rather regular behaviour in large coupled arrays. Even this simple study, however, hints at the complexity that can lurk behind the seemingly simple coupled equations, a complexity that can be generated as much by the interplay between coupling and oscillators as by the nonlinearity of the oscillators. Understanding of this complexity continues to grow, and the reader is referred to the expanding literature on this subject.

References

1. G.N. Rapaport: Radiotekhnika **6**, 53 (1951)
2. A.M. Turing: Phil. Trans. R. Soc. B **237**, 37 (1952)
3. K. Otsuka, K. Ikeda: Phys. Rev. A **39**, 5209 (1989)
4. R. Li, T. Erneux: Phys. Rev. A **49**, 1301 (1994)
5. J.-Y. Wang, P. Mandel, K. Otsuka: J. Eur. Opt. Soc. B **8**, 399 (1996)
6. D. Pieroux, P. Mandel, K. Otsuka: Optics Commun. **108**, 273 (1994)
7. P. Ashwin, P. Stork: Math. Proc. Camb. Phil. Soc. **116**, 27 (1994)
8. B. Dionne, M. Golubitsky, I. Stewart: Nonlinearity **9**, 559 (1996)
9. B. Dionne, M. Golubitsky, I. Stewart: Nonlinearity **9**, 575 (1996)
10. T. Endo, S. Mori: IEEE Trans. Circuits and Systems **25**, 7 (1978)
11. D. Golomb, D. Hansel, B. Shraiman, H. Sompolinsky: Phys. Rev. A **45**, 3516 (1992)
12. K. Okuda: Physica D **63**, 424 (1993)
13. K. McNeil: Int. J. Bifurcation and Chaos **9**, 107 (1999)
14. R. Li, T. Erneux: Optics Commun. **99**, 196 (1993)

Nonlinear Quantum Fluctuations in the Parametric Amplifier

P.D. Drummond and S. Chaturvedi

Summary. We develop a systematic theory of quantum fluctuations in the parametric amplifier, including the region near threshold. This allows us to treat the limits to quantum squeezing and noise reduction imposed by nonlinearities. In particular, we compute the squeezing spectrum near threshold, and calculate the optimum value. Our analytic results agree well with stochastic numerical simulations.

1 Introduction

The theory of quantum squeezing in the linear parametric oscillator is now well-developed[1]-[9]. Excellent agreement between theory and experiment is obtained[10]-[11], in the region below threshold. However, the usual theory is linearized, and therefore cannot be used in the near-threshold region where the squeezing is largest. The drawback with linearized theories is that they predict that zero quantum noise levels are achievable at threshold. This is clearly unrealistic, since (by the Heisenberg uncertainty principle) it necessarily requires an infinite energy in the conjugate mode. More significantly, this would imply an infinite amount of phase information – which is also impossible, since the coherent pump which drives the parametric oscillator can only supply a finite quantity of phase information.

Accordingly, there have been a number of investigations as to the ultimate limits to the squeezing spectrum of a parametric amplifier/oscillator. This has often involved using many-body Feynman diagram techniques[6] to extend the linear theory [7]-[9]. These have the drawback that they involve infinite sets of diagrams, and are difficult to use systematically at the critical point. This type of problem is common in non-equilibrium quantum physics. It represents a fundamental drawback in the Feynman diagram approach, in which both the coupling to reservoirs and the nonlinear terms are treated as perturbations. Other methods involving number-state expansions – like direct solutions of the master equation, or the stochastic Schroedinger equation - are inapplicable to these large Hilbert spaces. In addition, they are usually insoluble from an analytic approach.

While present experiments are limited by technical noise from approaching the critical point too closely, it is reasonable to expect that progress in integrated optics will lead to more stable, highly miniaturized devices

H.J. Carmichael, R.J. Glauber, M.O. Scully (Eds.): LNP 561, pp. 283–302, 2001.

which could well operate at the quantum limit, even near threshold. We have, for quite some time, been pursuing these questions using the positive P-representation [12], combined with two matched expansion techniques, one valid below the critical point, and one valid at the critical point. These two methods agree in the overlap region below threshold. Results are also verified by the use of direct numerical stochastic equation simulations, which are valid in all regions. In the present paper, we focus on the below-threshold results. We find an $N^{-2/3}$ scaling law for the optimal squeezing predicted by Plimak and Walls [8] is obtained here as well, but with a different spectrum, owing to the use of more systematic expansion techniques that result from using the positive P-representation method. Our analytic results for optimal squeezing, which occurs below the critical threshold, give excellent agreement with accurate numerical simulations for the same parameter values. We also give asymptotic results for the critical region, where the squeezing is less than optimal due to the effects of critical fluctuations.

We dedicate this work to the memory of Dan Walls, who had an enduring interest not only in the questions discussed in this work but also in the technique - the positive P-representation. Indeed, it would be no exaggeration to say that, in some sense, the method had its genesis in work [12] the authors originally did in collaboration with Dan. We fondly remember the exciting time we spent with Dan as graduate students in the Waikato group. The directness and power of the techniques used here, when used to analyze this non-equilibrium many-body quantum statistical problem, is a testament to Dan Wall's love for new yet simple ideas in theoretical physics.

2 Hamiltonian and Stochastic Equations

The Hamiltonian used here is the standard one [1] for a non-degenerate, single-mode parametric amplifier or oscillator:

$$H/\hbar = i\mathcal{E}\left[\hat{a}_2 - \hat{a}_2^\dagger\right] + \frac{i\kappa}{2}\left[\hat{a}_2\hat{a}_1^{\dagger 2} - \hat{a}_2^\dagger\hat{a}_1^2\right] + \sum_k \left[\hat{\Gamma}_k^\dagger\hat{a}_k + \hat{\Gamma}_k\hat{a}_k^\dagger\right] \ . \tag{1}$$

Here $\hat{a}_1, \hat{a}_2$ represent the fundamental and second-harmonic modes respectively, while $\mathcal{E}$ is proportional to the coherent input or driving field at the second-harmonic frequency, assumed to be at exact resonance with the cavity mode. The term κ is a coupling parameter for the $\chi^{(2)}$ nonlinearity of the medium. The operators Γ_1, Γ_2 represent reservoirs of modes external to the interferometer, and are used to describe decay processes. For simplicity, we have chosen the field mode-functions so that $\mathcal{E}$, κ are real. After transforming to the corresponding master equation in the Markovian approximation, we can expand the density matrix in a coherent state representation:

$$\hat{\rho} = \int P\left(\alpha, \alpha^+\right) \frac{|\alpha\rangle\langle(\alpha^+)^*|}{\langle(\alpha^+)^*|\alpha\rangle} d\mu\left(\alpha, \alpha^+\right) \ . \tag{2}$$

The function $P(\alpha, \alpha^+)$ can always be chosen as a positive (generalized) P-representation [12]. Following standard procedures, the assumption of vanishing boundary terms allows the master equation to be re-written as a Fokker-Planck equation in $P(\alpha, \alpha^+)$, and hence as a stochastic equation [13] with real noise. The assumption of vanishing boundary terms is critical to this procedure, and we note here that this is generally valid when the ratio of nonlinearity to damping is small [14], (i.e. $|\kappa/\gamma_k| \ll 1$, where γ_k are the relevant damping rates). The stochastic procedure is best regarded as being generally an asymptotic procedure, valid for small $|\kappa/\gamma_k|$ - in which case the boundary terms are exponentially suppressed. We check this assumption numerically here as well, and point out that the required ratio of nonlinearity to damping is extremely well-satisfied in current experiments, where the ratio is typically 10^{-6} or less. Further analysis of this problem has been given elsewhere [14]. Given this assumption, the following stochastic equations are obtained for any driving field $\mathcal{E}$; that is, either below or above threshold:

$$\begin{aligned}
d\alpha_1 &= \left[-\gamma_1\alpha_1 + \kappa\alpha_1^+\alpha_2\right]dt + \sqrt{\kappa\alpha_2}dW_1(t)\\
d\alpha_1^+ &= \left[-\gamma_1\alpha_1^+ + \kappa\alpha_1\alpha_2^+\right]dt + \sqrt{\kappa\alpha_2^+}dW_2(t)\\
d\alpha_2 &= \left[-\gamma_2\alpha_2 + \mathcal{E} - \frac{1}{2}\kappa\alpha_1^2\right]dt\\
d\alpha_2^+ &= \left[-\gamma_2\alpha_2^+ + \mathcal{E} - \frac{1}{2}\kappa\alpha_1^{+2}\right]dt\ .
\end{aligned} \tag{3}$$

Here the terms γ_k represent the amplitude damping rates. The stochastic correlations are given by:

$$\begin{aligned}
\langle dW_k(t)\rangle &= 0\\
\langle dW_k(t)dW_l(t)\rangle &= \delta_{kl}dt\ .
\end{aligned} \tag{4}$$

This means that $dW_k(t)$ represent two real Gaussian and uncorrelated stochastic processes. Our derivation is formally based on the Itô stochastic calculus. However, in this case, either Itô or Stratonovich stochastic calculus gives identical results [13]. The crucial quadrature variables of the system have the definitions:

$$\begin{aligned}
X_k &= \left(\alpha_k + \alpha_k^+\right) \sim \left(\hat{a}_k + \hat{a}_k^\dagger\right)\\
Y_k &= \frac{1}{i}\left(\alpha_k - \alpha_k^+\right) \sim \frac{1}{i}\left(\hat{a}_k - \hat{a}_k^\dagger\right).
\end{aligned} \tag{5}$$

It is usual to introduce a scaling parameter $g^2 = 1/(2N\gamma_r)$ at this stage – where N is the threshold pump photon number. This determines the ratio of nonlinear to linear rates of change. Defining:

$$g = \frac{\kappa}{\sqrt{2\gamma_1\gamma_2}}\ , \tag{6}$$

we introduce a scaled time $\tau = \gamma_1 t$, and scaled quadrature variables x_k, y_k :

$$x_1 = gX_1$$
$$x_2 = g\sqrt{2\gamma_r}X_2 \ . \tag{7}$$

There is a similar definition of y_k , where we notice the scaling of x_2 and y_2 (involving $\gamma_r = \gamma_2/\gamma_1$) is chosen to give similar fluctuation levels in both types of scaled variables. In terms of these new variables, the relevant equations become:

$$\begin{aligned}
dx_1 &= \left[-x_1 + \frac{1}{2}\left(x_1x_2 + y_1y_2\right)\right]d\tau + \\
&\quad + \frac{g}{\sqrt{2}}\left[\sqrt{x_2 + iy_2}dw_1(\tau) + \sqrt{x_2 - iy_2}dw_2(\tau)\right] \\
dy_1 &= \left[-y_1 + \frac{1}{2}\left(x_1y_2 + x_2y_1\right)\right]d\tau + \\
&\quad + \frac{g}{i\sqrt{2}}\left[\sqrt{x_2 + iy_2}dw_1(\tau) - \sqrt{x_2 - iy_2}dw_2(\tau)\right] \\
dx_2 &= -\gamma_r\left[x_2 + \frac{1}{2}\left(x_1^2 - y_1^2\right) - 2\mu\right]d\tau \\
dy_2 &= -\gamma_r(y_2 + x_1y_1)d\tau \ .
\end{aligned} \tag{8}$$

Here we have introduced a dimensionless driving field as $\mu = \kappa\mathcal{E}/(\gamma_1\gamma_2)$. The stochastic correlations of $dw_k(\tau)$ are exactly those as for $dW_k(t)$, although expressed in terms of τ variables rather than t variables.

2.1 Observable Moments and Spectra

The stochastic method directly reproduces the normally ordered correlations and moments. Of especial interest is $\hat{Y}_1 = (\hat{a}_1 - \hat{a}_1^\dagger)/i$, since $\hat{Y}_1$ is the low-noise, squeezed quadrature. Here we note that the instantaneous correlation functions of the intra-cavity field operators are called the moments. Typically, they are not easily measurable, when compared to output moments or spectra, but they are useful in that they provide a check on the accuracy of the calculation of measurable spectra. We consider the moments of $\hat{Y}_1$ for definiteness, where:

$$\left\langle : \hat{Y}_1\hat{Y}_1 : \right\rangle \equiv Tr\left[\rho_{ss} : \hat{Y}_1\hat{Y}_1 :\right] = \left\langle Y_1^2\right\rangle = \frac{1}{g^2}\left\langle y_1^2\right\rangle \ .$$

The squeezing in terms of the intra-cavity quadrature variances corresponds to an instantaneous measurement of the field moments. If such a measurements were possible, it would include contributions from all frequencies. However, it is the field outside the cavity which is usually measured. The technique for treating external field spectra was introduced by Yurke [2], and by Collett and Gardiner [3]. For measurements averaged over a long time,

it is the low frequency part of the spectrum that is the relevant quantity, and we shall focus on this, as it usually determines the maximum squeezing possible. The output measured spectral variance V_k^θ of a general quadrature

$$\hat{X}_k^\theta = \left(e^{-i\theta}\hat{a}_k + e^{i\theta}\hat{a}_k^\dagger\right)$$

in a cavity with output damping rate γ_{out} can be written

$$V_k^\theta(\omega) = \frac{4\pi\gamma_{out}}{T}\left\langle : \hat{X}_k^\theta(-\omega), \hat{X}_k^\theta(\omega) : \right\rangle + 1 \ . \tag{9}$$

The :: are normal ordering operators, and the frequency argument denotes a Fourier transform:

$$\hat{X}_k^\theta(\omega) = \int \frac{dt}{\sqrt{2\pi}}\hat{X}_k^\theta(t)$$

The output spectrum depends on the spectra of the intra-cavity quadratures. In a cavity where the output coupler provides the dominant loss mechanism, so $\gamma_{out} = \gamma_1$, the result simplifies to:

$$V_k^\theta(\omega) = 2S_k^\theta(\omega) + 1 \ . \tag{10}$$

As usual, the optimal value of the internal squeezing $S_k^\theta(\omega)$ is -0.5 , which corresponds to zero fluctuations in the external squeezed quadrature. Since the P-representation is normally ordered, it automatically provides spectral correlations that correspond to the relevant normally ordered, time-ordered operator correlations of the measured output fields. We therefore define Fourier components of the normalized quadratures as:

$$x_k^\theta(\tau) = \int \frac{d\Omega}{\sqrt{2\pi}} e^{i\Omega\tau}\tilde{x}_k^\theta(\Omega) \ ,$$

This leads to the following result for the general squeezing spectrum, as measured in an external homodyne detection scheme:

$$\left\langle \tilde{x}_k^\theta(\Omega_1)\, \tilde{x}_k^\theta(\Omega_2) \right\rangle = g^2\delta(\Omega_1 + \Omega_2)S_k^\theta(\Omega_1) \tag{11}$$

3 Below-Threshold Perturbation Theory

In order to solve these coupled equations systematically, a formal perturbation expansion in powers of g is now introduced, where:

$$x_k = \sum_{n=0}^{\infty} g^n x_k^{(n)}$$
$$y_k = \sum_{n=0}^{\infty} g^n y_k^{(n)} \ . \tag{12}$$

3.1 Matched Power Equations

The stochastic equations are now solved by the technique of matching powers of g in the corresponding time-evolution equations. This technique can be analyzed diagrammatically, and so can be termed the 'stochastic diagram' method [15]. The zero-th order solution is:

$$\begin{aligned}
dx_1^{(0)} &= \left[-x_1^{(0)} + \frac{1}{2}\left(x_1^{(0)}x_2^{(0)} + y_1^{(0)}y_2^{(0)}\right)\right] d\tau \\
dy_1^{(0)} &= \left[-y_1^{(0)} + \frac{1}{2}\left(x_1^{(0)}x_2^{(0)} - x_2^{(0)}y_1^{(0)}\right)\right] d\tau \\
dx_2^{(0)} &= -\gamma_r\left[x_2^{(0)} + \frac{1}{2}\left(x_1^{(0)2} - y_1^{(0)2}\right) - 2\mu\right] d\tau \\
dy_2^{(0)} &= -\gamma_r\left[y_2^{(0)} + x_1^{(0)}y_1^{(0)}\right] d\tau \ . \qquad (13)
\end{aligned}$$

These equations are the classical nonlinear equations for the cavity, expressed in terms of the quadrature amplitudes of dimensionless scaled fields. The steady-state solution below threshold is well-known, and is given by:

$$x_1^{(0)} = y_1^{(0)} = y_2^{(0)} = 0; \;\; x_2^{(0)} = 2\mu \ . \qquad (14)$$

With no loss of generality, we can set all odd orders of $x_2^{(n)}, y_2^{(n)}$, and all even orders of $x_1^{(n)}, y_1^{(n)}$ to zero. To first order, the equations are given by:

$$\begin{aligned}
dx_1^{(1)} &= -\left(1-\mu\right) x_1^{(1)} d\tau + \sqrt{2\mu} dw_x(\tau) \\
dy_1^{(1)} &= -\left(1+\mu\right) y_1^{(1)} d\tau - i\sqrt{2\mu} dw_y(\tau) \ , \qquad (15)
\end{aligned}$$

where, $dw_{x(y)}(\tau) = \left(dw_1(\tau) \pm dw_2(\tau)\right)/\sqrt{2}$. These equations are the ones that are normally used to predict squeezing. They are non-classical, but correspond to a very simple form of linear, non-classical fluctuation which has a Gaussian quasi-probability distribution. In other words, if no higher-order terms existed, the result would be an ideal squeezed state in the sub-harmonic, together with an ideal coherent state in the pump.

Of more interest to the present paper, is the behaviour to the next order. This is the first order where nonlinear corrections to ideal squeezed-state behaviour will occur. We find the following:

$$\begin{aligned}
dx_2^{(2)} &= -\gamma_r\left[x_2^{(2)} + \frac{1}{2}\left(x_1^{(1)}x_1^{(1)} - y_1^{(1)}y_1^{(1)}\right)\right] d\tau \\
dy_2^{(2)} &= -\gamma_r\left[y_2^{(2)} + x_1^{(1)}y_1^{(1)}\right] d\tau \ . \qquad (16)
\end{aligned}$$

While we do not wish to include any effects beyond the first nonlinear corrections, it is not possible to consistently neglect the third-order in perturbation theory. This is because the first non-trivial correlations arise in terms like $\left\langle \left[x^{(2)}\right]^2 \right\rangle$, which have the same formal order as terms of the type $\left\langle x^{(3)}x^{(1)}\right\rangle$.

Therefore, to obtain a consistent expansion for the correlations that are of interest, we must compute the third-order terms as well. These satisfy the following equations:

$$\begin{aligned} dx_1^{(3)} &= \left[-(1-\mu)\,x_1^{(3)} + \frac{1}{2}\left(x_1^{(1)}x_2^{(2)} + y_1^{(1)}y_2^{(2)}\right)\right]d\tau + \\ &\quad + \frac{1}{2\sqrt{2\mu}}\left[x_2^{(2)}dw_x(\tau) + iy_2^{(2)}dw_y(\tau)\right] \\ dy_1^{(3)} &= \left[-(1+\mu)\,y_1^{(3)} + \frac{1}{2}\left(x_1^{(1)}y_2^{(2)} - x_2^{(2)}y_1^{(1)}\right)\right]d\tau + \\ &\quad + \frac{1}{2\sqrt{2\mu}}\left[y_2^{(2)}dw_x(\tau) - ix_2^{(2)}dw_y(\tau)\right]\ . \end{aligned} \tag{17}$$

3.2 Operator Moments

We now wish to calculate the operator moments. To proceed further, we use Itô calculus to derive stochastic equations for quantities of interest, which in the present calculation are $y_1^{(1)}y_1^{(1)}$ and $y_1^{(1)}y_1^{(3)}$. These equations contain quantities involving variables lower down in the hierarchy, as well as terms generated from the noise correlations. Finally, we compute the steady state averages of the quantities of interest, so that the noise terms vanish. In the present case, this yields,

$$\begin{aligned} \left\langle x_2^{(2)}\right\rangle &= \frac{-\mu}{1-\mu^2} \\ \left\langle y_1^{(1)}y_1^{(1)}\right\rangle &= \frac{-\mu}{1+\mu} \\ \left\langle x_1^{(1)}x_1^{(1)}\right\rangle &= \frac{\mu}{1-\mu} \\ \left\langle y_1^{(1)}y_1^{(3)}\right\rangle &= \frac{\mu}{4\,(1+\mu)\,(1-\mu^2)}\left[\frac{\mu\gamma_r}{\gamma_r+2} + \frac{\gamma_r\left(1-\mu+\mu^2\right)+2\,(1+\mu)}{(1+\mu)\,(\gamma_r+2\,(1+\mu))}\right] \\ \left\langle x_1^{(1)}y_1^{(1)}y_2^{(2)}\right\rangle &= \frac{\gamma_r}{(\gamma_r+2)}\left(\frac{\mu^2}{1-\mu^2}\right)\ . \end{aligned} \tag{18}$$

Hence, the intra-cavity squeezed quadrature fluctuations are obtained as:

$$\begin{aligned} \left\langle \hat{Y}_1^2\right\rangle_{ss} &= 1 + \left\langle :\hat{Y}_1^2: \right\rangle \\ &= \frac{1}{2} + \frac{1-\mu}{2\,(1+\mu)} + \frac{g^2\mu}{2\,(1+\mu)\,(1-\mu^2)} \times \\ &\quad \times \left(\frac{\mu\gamma_r}{\gamma_r+2} + \frac{\gamma_r\left(1-\mu+\mu^2\right)+2\,(1+\mu)}{(1+\mu)\,(\gamma_r+2\,(1+\mu))}\right)\ . \end{aligned} \tag{19}$$

We finally note that another possible method for these calculations is to use the Wigner representation, which also gives stochastic equations –

after certain terms, corresponding to third order moments, are omitted. This turns out to be not only less accurate than the +P method (owing to the approximations), but is considerable more complicated in terms of algebraic complexity.

4 Spectral Correlations

These can be calculated directly from the Fourier transform of the stochastic equations. We also represent the white noise that drives the stochastic equations by its Fourier transform $\xi_{x,y}(\Omega)$, where the spectral moments of the stochastic processes are:

$$\begin{aligned} \langle \xi_a(\Omega) \rangle &= 0 \\ \langle \xi_a(\Omega) \xi_b(\Omega') \rangle &= \delta_{ab} \delta(\Omega + \Omega') \ . \end{aligned} \tag{20}$$

It is also useful to introduce a standard convolution notation, where:

$$[A \star B](\Omega) = \int \frac{d\Omega'}{\sqrt{2\pi}} A(\Omega') B(\Omega - \Omega')$$

The stochastic equations may now be rewritten in the frequency domain as –

- First order:

$$\begin{aligned} \tilde{x}_1^{(1)}(\Omega) &= \frac{\sqrt{2\mu}\xi_x(\Omega)}{[i\Omega + 1 - \mu]} \\ \tilde{y}_1^{(1)}(\Omega) &= \frac{-i\sqrt{2\mu}\xi_y(\Omega)}{[i\Omega + 1 + \mu]} \end{aligned} \tag{21}$$

- Second order:

$$\begin{aligned} \tilde{x}_2^{(2)}(\Omega) &= -\frac{\gamma_r \left[\tilde{x}_1^{(1)} \star \tilde{x}_1^{(1)} - \tilde{y}_1^{(1)} \star \tilde{y}_1^{(1)}\right](\Omega)}{2(i\Omega + \gamma_r)} \\ \tilde{y}_2^{(2)}(\Omega) &= -\frac{\gamma_r \left[\tilde{x}_1^{(1)} \star \tilde{y}_1^{(1)}\right](\Omega)}{(i\Omega + \gamma_r)} \end{aligned} \tag{22}$$

- Third order:

$$\begin{aligned} \tilde{x}_1^{(3)}(\Omega) &= \frac{\left[\tilde{x}_2^{(2)} \star \left(\tilde{x}_1^{(1)} + \xi_x/\sqrt{2\mu}\right) + \tilde{y}_2^{(2)} \star \left(\tilde{y}_1^{(1)} + i\xi_y/\sqrt{2\mu}\right)\right](\Omega)}{2[i\Omega + 1 - \mu]} \\ \tilde{y}_1^{(3)}(\Omega) &= \frac{\left[\tilde{y}_2^{(2)} \star \left(\tilde{x}_1^{(1)} + \xi_x/\sqrt{2\mu}\right) - \tilde{x}_2^{(2)} \star \left(\tilde{y}_1^{(1)} + i\xi_y/\sqrt{2\mu}\right)\right](\Omega)}{2[i\Omega + 1 + \mu]} \end{aligned} \tag{23}$$

4.1 Squeezing Correlation Spectrum

We now calculate the spectrum of the squeezed field y_1, which is given by $\langle \tilde{y}_1(\Omega_1)\,\tilde{y}_1(\Omega_2)\rangle$. Thus, we obtain

$$\langle \tilde{y}_1(\Omega_1)\,\tilde{y}_1(\Omega_2)\rangle = g^2\left\langle \tilde{y}_1^{(1)}(\Omega_1)\,\tilde{y}_1^{(1)}(\Omega_2)\right\rangle + \\ +g^4\left\langle \tilde{y}_1^{(1)}(\Omega_2)\,\tilde{y}_1^{(3)}(\Omega_1) + [\Omega_1 \leftrightarrow \Omega_2]\right\rangle + \cdots \tag{24}$$

The contribution from the first order perturbation theory is the usual linearized squeezing result, given in this case by:

$$\left\langle \tilde{y}_1^{(1)}(\Omega_1)\,\tilde{y}_1^{(1)}(\Omega_2)\right\rangle = -\frac{2\mu\delta(\Omega_1+\Omega_2)}{\left[\Omega_1^2+(1+\mu)^2\right]} \tag{25}$$

Similarly, the complementary (unsqueezed) spectrum is:

$$\left\langle \tilde{x}_1^{(1)}(\Omega_1)\,\tilde{x}_1^{(1)}(\Omega_2)\right\rangle = \frac{2\mu\delta(\Omega_1+\Omega_2)}{\left[\Omega_1^2+(1-\mu)^2\right]} \tag{26}$$

Also, we can obtain the next order contribution to the squeezing, by calculating $\left\langle \tilde{y}_1^{(3)}(\Omega_1)\,\tilde{y}_1^{(1)}(\Omega_2)\right\rangle$. To check the results, we can compare with the moment calculations, since:

$$\left\langle y_1^{(1)}(t)\,y_1^{(3)}(t)\right\rangle_{ss} = \int \frac{d\Omega_1}{\sqrt{2\pi}}\int \frac{d\Omega_2}{\sqrt{2\pi}}\left\langle \tilde{y}_1^{(1)}(\Omega_1)\,\tilde{y}_1^{(3)}(\Omega_2)\right\rangle \tag{27}$$

Using these results, we find that the spectrum of the squeezed quadrature, to this order, is given by

$$\langle \tilde{y}_1(\Omega_1)\,\tilde{y}_1(\Omega_2)\rangle = g^2\delta(\Omega_1+\Omega_2)S(\Omega_1) \tag{28}$$

where the squeezing spectrum is calculated to be:

$$S(\Omega) = \frac{-2\mu}{\Omega^2+(1+\mu)^2} + \frac{2g^2\mu^2\gamma_r}{[\Omega^2+(1+\mu)^2]^2}\times \\ \times\left[\frac{[\Omega^2+1-\mu^2]}{2\mu\gamma_r(1-\mu^2)} + \frac{(1-\mu+\gamma_r)(1+\mu)-\Omega^2}{(1-\mu)[\Omega^2+(1-\mu+\gamma_r)^2]} - \right. \\ \left. -\frac{(1+\mu+\gamma_r)(1+\mu)-\Omega^2}{(1+\mu)[\Omega^2+(1+\mu+\gamma_r)^2]}\right] \tag{29}$$

This equation gives the complete linear and nonlinear squeezing spectrum, including all the nonlinear correction terms that contribute to order g^2 or $1/N$.

4.2 Triple Spectral Correlations

Next, we can calculate the triple spectral correlations, giving as in the moment calculations:

$$\langle \tilde{x}_1(\Omega_1)\,\tilde{y}_1(\Omega_2)\,\tilde{y}_2(\Omega_3)\rangle = g^4\left\langle \tilde{x}_1^{(1)}(\Omega_1)\,\tilde{y}_1^{(1)}(\Omega_2)\,\tilde{y}_2^{(2)}(\Omega_3)\right\rangle \tag{30}$$

Solving for $\tilde{y}_2^{(2)}$, we have

$$\left\langle \tilde{x}_1^{(1)}(\Omega_1)\,\tilde{y}_1^{(1)}(\Omega_2)\,\tilde{y}_2^{(2)}(\Omega_3)\right\rangle = -\frac{\gamma_r\left\langle \tilde{x}_1^{(1)}(\Omega_1)\,\tilde{y}_1^{(1)}(\Omega_2)\,[\tilde{x}_1^{(1)}\star\tilde{y}_1^{(1)}](\Omega_3)\right\rangle}{(i\Omega_3+\gamma_r)} \tag{31}$$

Substituting from the first order spectrum, the final result to this order is obtained to be:

$$\left\langle \tilde{x}_1^{(1)}(\Omega_1)\,\tilde{y}_1^{(1)}(\Omega_2)\,\tilde{y}_2^{(2)}(\Omega_3)\right\rangle = \frac{2\mu^2\sqrt{\gamma_r/\pi}\delta(\Omega_1+\Omega_2+\Omega_3)}{(i\Omega_3+\gamma_r)\left[\Omega_1^2+(1-\mu)^2\right]\left[\Omega_2^2+(1+\mu)^2\right]}$$

To check this result, we can evaluate moments:

$$\left\langle x_1^{(1)}(t)\,y_1^{(1)}(t)\,y_2^{(2)}(t)\right\rangle_{ss} = \int\frac{d\Omega_1}{\sqrt{2\pi}}\int\frac{d\Omega_2}{\sqrt{2\pi}}\int\frac{d\Omega_3}{\sqrt{2\pi}}e^{i(\Omega_1+\Omega_2+\Omega_3)}\times \times\left\langle \tilde{x}_1^{(1)}(\Omega_1)\,\tilde{y}_1^{(1)}(\Omega_2)\,\tilde{y}_2^{(2)}(\Omega_3)\right\rangle \tag{32}$$

On integrating, we obtain the same result as in our moment calculation, given above. We note that these results are greatly different to those that would be generated using the semi-classical truncated [16] Wigner approach to this problem, which neglects third order terms in the evolution equations.

4.3 Optimal Squeezing

It is interesting to evaluate the squeezing or low-noise correlations in the limit of zero frequency, which is generally the frequency of maximum squeezing. We obtain:

$$S(0) = \frac{-2\mu}{(1+\mu)^2} + \frac{\mu g^2}{(1+\mu)^4}\left[1+\frac{4\gamma_r\mu^2(\gamma_r+2)}{(1-\mu)[(1+\gamma_r)^2-\mu^2]}\right] \tag{33}$$

Near threshold, where $\mu\approx 1$, we can set $\mu = 1+\delta$, and expand in powers of δ. This gives the following result, ignoring small terms of order g^2 or $g^2\delta$:

$$S(0) = -\frac{1}{2}+\frac{1}{8}\left[\delta^2-\frac{2g^2}{\delta}\right] \tag{34}$$

Minimizing this result with respect to δ , we find that:

$$V_{opt}(0) = -1 + \frac{3}{4} g^{4/3} \tag{35}$$

This result confirms an approximate calculation of Plimak and Walls [8], although the self-consistent method used by these authors makes it difficult to obtain the relevant driving field. In fact, this minimum level of internal fluctuations occurs at a driving field just below threshold,with:

$$\mu_{opt} = 1 - g^{2/3} \tag{36}$$

This is plotted in Fig. 1:

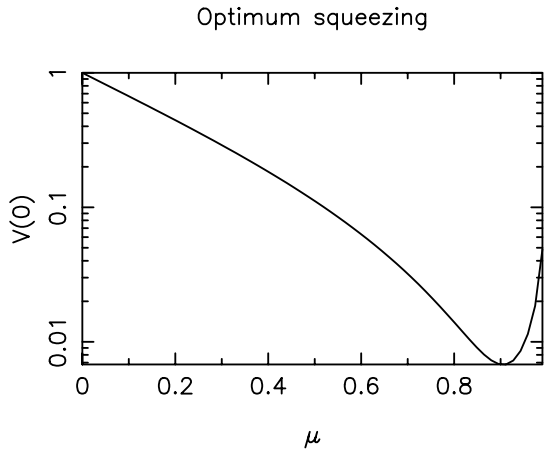

Fig. 1. Optimum squeezing with $g^2 = .001$, $\gamma_r = 0.5$

The physics of this is clearly that the onset of critical fluctuations starts to spoil the noise-reduction even before the critical point is reached at $\mu = 1$. This can be seen from the way that the third order term includes contributions from the critical fluctuations in x_1.

A squeezing measurement is a remarkably sensitive probe for non-equilibrium critical point fluctuations.

5 Asymptotic Critical Theory

In order to avoid the divergences of the previous method at the critical point of this system where $\mu = 1$ or $\delta = 0$, we define new scaled quadrature variables, and use a different expansion [18] valid inside the critical region of $|\delta| < \sqrt{g}$. The new pump mode variable x_2 now corresponds to the real

scaled depletion in the pump mode amplitude, relative to the undepleted value at the critical point. The signal mode variable x_1 now describes the critical fluctuation amplitude scaled to be of order 1 at threshold; while y_1 is simply defined as Y_1. The definitions are

$$\begin{aligned} x_1 &= \sqrt{g}X_1, \\ y_1 &= Y_1, \\ x_2 &= \frac{1}{g}\left[\frac{\kappa X_2}{\gamma_1} - 2\right], \\ y_2 &= \sqrt{2\gamma_r/g}Y_2. \end{aligned} \tag{37}$$

It is convenient to also define a new scaled time and driving field, as:

$$\begin{aligned} \eta &= \frac{1}{g}\left[\frac{\kappa\epsilon}{\gamma_1\gamma_2} - 1\right], \\ \tau &= \gamma_1 g t. \end{aligned} \tag{38}$$

The parameter $\eta = \delta/g$ is a measure of how close the driving field is to its value at the bifurcation threshold. The time has now been scaled both by the decay rate in the signal mode γ_1 and the parameter g. The equations in the new variables are

$$\begin{aligned} dx_1 &= \frac{1}{2}\left[x_1 x_2 + g y_1 y_2\right] d\tau + \sqrt{2} dW_x, \\ g dy_1 &= -\left[2y_1 + \frac{g}{2}(x_2 y_1 - y_2 x_1)\right] d\tau - i\sqrt{2g} dW_y, \\ g dx_2 &= \gamma_r \left[2\eta - x_2 - \left(x_1^2 - g y_1^2\right)/2\right] d\tau, \\ g dy_2 &= -\gamma_r \left[y_2 + x_1 y_1\right] d\tau. \end{aligned} \tag{39}$$

The Gaussian white noise increments dW_i, $(i = X, Y)$, are not independent, and have the following properties

$$\begin{aligned} \langle dW_i \rangle &= 0, \\ \langle dW_x^2 \rangle &= \langle dW_x^2 \rangle = \langle 1 + g x_2/2 \rangle d\tau, \\ \langle dW_y dW_x \rangle &= g^{3/2} \langle y_2 \rangle d\tau. \end{aligned} \tag{40}$$

We can develop an asymptotic theory in the large N limit for the critical region, just as easily as below threshold. The result is a simple theory which correctly predicts the scaling of the critical and squeezing fluctuations, as well as making close predictions of their size for finite N. It is important to note here the presence of the $\sqrt{g}dW_y$ term in these equations. This scaling factor of $\sqrt{g}$, is added to ensure that the fluctuations in this variable occur to an equivalent order to the other mean values. This simplifies the procedure of truncating the deterministic and noise terms to a given order. This procedure is similar to more formal projection operator schemes [13] that can be employed on the equivalent Fokker-Planck equation.

The approximation we use here entails expanding the stochastic trajectories in an asymptotic series in g, and solving the resulting equations on a term by term basis. This entails a similar power series expansion to the one used below threshold, except with new variables. The first set of equations are

$$\begin{aligned} dx_1^{(0)} &= \frac{1}{2}x_1^{(0)}x_2^{(0)}d\tau + \sqrt{2}dW_x^{(0)}, \\ gdy_1^{(0)} &= -2y_1^{(0)}d\tau + \sqrt{2g}dW_y^{(0)}, \\ gdx_2^{(0)} &= \gamma_r\left(2\eta - x_2^{(0)} - [x_1^{(0)}]^2/2\right)d\tau, \\ gdy_2^{(0)} &= -\gamma_r\left(y_2^{(0)} + x_1^{(0)}y_1^{(0)}\right)d\tau. \end{aligned} \tag{41}$$

The Gaussian white noise increments $dW_x^{(0)}$, $dW_y^{(0)}$ have the variance

$$\left\langle [dW_x^{(0)}]^2 \right\rangle = \left\langle [dW_y^{(0)}]^2 \right\rangle = d\tau \ .$$

A significant point about these equations is that the squeezed quadrature, $y_1^{(0)}$ solution can be worked out without reference to any of the other variables, and it gives zero noise in the external quadrature at zero frequency. Of course, couplings between the variables will emerge to higher orders in the expansion, and this generates the actual critical fluctuations in the squeezed quadrature. Also, the $y_2^{(0)}$ variable is simply driven by the other fields, and can be obtained as soon as the other fields are known.

5.1 Critical Fluctuations

We now consider what happens at or near the classical threshold of $\eta = 0$. In a model where the second harmonic generation does not cause the pump mode to deplete, we would have $x_2^{(0)} = 2\eta$, and at threshold the critical fluctuations in x_1 would diffuse outward without any bound. When depletion is included, the critical fluctuations in the quadrature x_1 are finite, but very slowly varying compared to those in the other variables. The pump field can therefore be adiabatically eliminated to first order in the expansion.

Near threshold ($g\eta \ll 1$) the decay term in the un-squeezed quadrature x_1 is roughly $-x_2$, which is of order 1. The pump mode will be depleted, so obviously x_2 must be negative in order for this to be stable. The scaled pump field decay is γ_r/g, and the squeezed quadrature decay is of order $1/g$. If γ_r is much larger than g, it is possible to adiabatically eliminate both the pump amplitude and the squeezed quadrature in the equations for the large critical fluctuations x_1. Since we are taking the limit of small g, we shall assume that this is possible to zero-th order in the asymptotic expansion. In the adiabatic elimination, we must solve for the steady state values of the pump x_2, given

an instantaneous first order critical fluctuation x_1. To leading (zeroth) order this gives -where $x = x_1^{(0)}$:

$$x_2^{(0)} = 2\eta - x^2/2. \tag{42}$$

Substituting in the equation for x_1, we find that

$$dx = \left(\eta x - x^3/4\right) d\tau + \sqrt{2} dW_x. \tag{43}$$

This equation is a standard form of stochastic equation, which is the real cubic process often found at a critical point, even for thermal equilibrium systems. The solution for the distribution of x is given by:

$$P(x) = \exp\left(\eta x^2/2 - x^4/16\right)$$

The steady-state critical variance in x_1 is given to zero-th order by:

$$\left\langle x_1^2 \right\rangle^{(0)} = \left\langle x^2 \right\rangle = \frac{\int x^2 dx \exp\left(\eta x^2/2 - x^4/16\right)}{\int dx \exp\left(\eta x^2/2 - x^4/16\right)} \tag{44}$$

The variance of the critical fluctuations at the critical point, $\eta = 0$, is therefore given to lowest order by the variance of a cubic process, which is a ratio of gamma functions [13],

$$\left\langle x_1^2 \right\rangle^{(0)} = \frac{4\Gamma(3/4)}{\Gamma(1/4)} = 1.3520.. \tag{45}$$

In a normally ordered representation, the normally ordered version of the quadrature variance operator differs by 1 from its symmetric form. However, to this order in the calculation, corrections of this size can be neglected. This is an example of much more general results on representation invariance [17] of the large fluctuations that occur near critical points. In general, these have a behavior to leading order that is rather classical, and does not depend on the operator ordering. Using this, we find the steady state of the un-squeezed quadrature at threshold. Denoting the symmetric expectation value by the subscript S, to leading order we get (at the critical point)

$$\left\langle \hat{X}_1^2 \right\rangle_S^{(0)} = \frac{1}{g} \left\langle x_1^2 \right\rangle^{(0)} = \frac{4\Gamma(3/4)}{g\Gamma(1/4)}$$

This variable has the critical slowing down expected at threshold, that is, the un-squeezed signal quadrature is the one in which the critical fluctuations occur. The value for the size of the critical fluctuations can be used to calculate the depletion of the scaled pump mode amplitude x_2. Using equations (38) and (44), to first order in g it is

$$x_2^{(0)} = 2\eta - \left\langle x^2 \right\rangle /2. \tag{46}$$

The size of the depletion is consistent with an $N^{-1/2}$ conversion efficiency for pump photons to signal photons at the critical point. In summary, by using the fact that a cubic stochastic equation has a potential solution, the quadrature moments can be obtained for any driving field in the critical region [15].

5.2 Critical Squeezing

We can now find the steady state variance of the squeezed quadrature at threshold. Because the fluctuations in the squeezed quadrature are very small, we must work to higher order in the asymptotic expansion to obtain a non trivial result. To achieve this, it is most useful to introduce equations in the higher order moments y_1^2 and $z_1 = x_1 y_1$. The corresponding stochastic equations are derived using Ito rules for variable changes [13], so that:

$$\begin{aligned} gd\left(y_1^2\right) &= -2\left[1 + 2y_1^2 + \frac{1}{2}g(x_2 + x_2 y_1^2 - y_2 z_1)\right] d\tau + 2\sqrt{g} y_1 dW_y, \\ gdz_1 &= \left[-2z_1 + \frac{g}{2} y_2(-x_1^2 + g y_1^2 + 2g)\right] d\tau + \sqrt{g} x_1 dW_y + g y_1 dW_x \end{aligned} \quad (47)$$

The squeezing variance at threshold from equation (47) is obtained by taking expectation values. At the steady-state, $\left\langle d\left(y_1^2\right)\right\rangle = 0$. In addition, the expectation value of any noise term is always zero in an Ito equation, so that

$$\left\langle y_1^2 \right\rangle^{(1)} = -\frac{g}{4}\left\langle (1 + y_1^2)x_2 - y_2 z_1 \right\rangle^{(0)} . \quad (48)$$

The expectation value of the correlation between y_1 and any x_i variable is trivial to zero-th order, as these must factorize. Thus, we can write immediately:

$$\begin{aligned} \left\langle (1 + y_1^2)x_2 \right\rangle^{(0)} &= \left\langle 1 + y_1^2 \right\rangle^{(0)} \left\langle x_2 \right\rangle^{(0)} \\ &= \eta - \left\langle x^2 \right\rangle / 4 . \end{aligned} \quad (49)$$

However, the expectation value of correlations between y_2 and z_1 does not factorize. We first must obtain the equation for this correlation. To lowest order this is

$$gd(y_2 z_1) = -\left[2y_2 + \gamma_r(y_2 + z_1)\right] z_1 d\tau + (\text{noise})$$

The noise correlations do not matter, since we can immediately take expectation values and obtain

$$\left\langle y_2 z_1 \right\rangle^{(0)} = \frac{-\gamma_r}{2 + \gamma_r}\left\langle z_1^2 \right\rangle^{(0)} = \frac{\gamma_r}{4 + 2\gamma_r}\left\langle x^2 \right\rangle$$

To obtain this result we have once again used the factorization properties of the y_1 fluctuations to zero-th order. Combining the above results together, we find the steady state variance of the squeezed quadrature up to first order in g , is

$$\left\langle \hat{Y}_1^2 \right\rangle_S = \frac{1}{2} - \frac{g\eta}{4} + \frac{g(2 + 3\gamma_r)\left\langle x^2 \right\rangle}{16(2 + \gamma_r)} .$$

This is plotted in Fig. 2, with the same parameters as in Fig. 1:

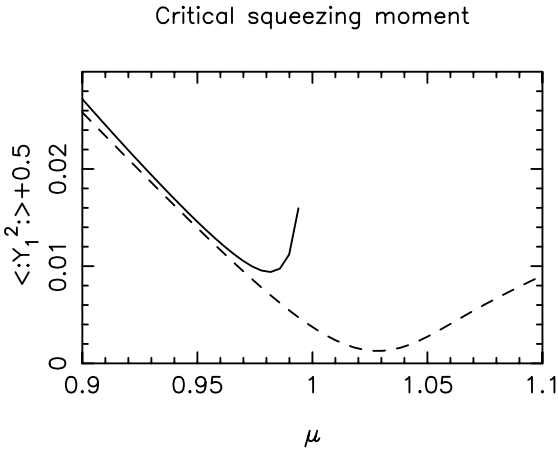

Fig. 2. Squeezing moment with $g^2 = 1000$, $\gamma_r = 0.5$ – dashed lines are the below-threshold expansion

The intra-cavity squeezing moment for a model with a non depleted pump mode is 1/2 [19]. Our theory predicts that a depleted parametric oscillator will get no closer to this intra-cavity lower limit than a term that scales as g , that is as $N^{-1/2}$. The best squeezing in the overall moment is, paradoxically, not just below, but rather just above threshold. It can be seen that in contrast to the un-squeezed quadrature, the dominant term in the decay to the steady state does not depend on the pump mode photon number N. This means the squeezed quadrature does not experience critical slowing down as the un-squeezed quadrature does, and has a line-width similar to the value below threshold. In practical terms, the unsqueezed critical fluctuations would be much easier to observe, as they are the dominant effect at the critical point.

6 Numerical Simulations

The value of the nonlinear correction to the spectrum of the scaled internal squeezed quadrature $S(\Omega)$, can be worked out from a full numerical simulation [20] of the relevant nonlinear stochastic equations. The optimal squeezing in the zero frequency part of the squeezing spectrum is predicted to scale as $N^{-2/3}$. For the simulations, we chose values of $N = g^{-2} = 10^3$, $\gamma_r = 0.5$. The simulations used a total dimensionless time-interval of $\tau_{max} = 1000$. To ensure equilibrium, only the last 500 time units were utilised in the Fourier transforms. Time steps of $\Delta\tau = 0.1$ and $\Delta\tau = 0.2$ were compared to ensure convergence. The algorithmic technique is described elsewhere [21], and uses a semi-implicit central partial difference technique. To obtain the small non-linear corrections near the optimum squeezing, we simulated the difference

between the linear and nonlinear forms of the stochastic equation, in order to minimize sampling errors. It was also useful to initialize the x quadratures with a Gaussian ensemble close to the known steady-state variance, in order to reduce the time taken to achieve equilibrium.

Typically, the relative error in the correlations due to finite step-size was around 10^{-4} with these step-sizes.

6.1 Optimum Squeezing

For these parameters the optimal driving field is predicted to occur at $\mu = 0.9$, or approximately 80% of the critical intensity. We used 10^5 trajectories to improve the relative error due to sampling with a finite trajectory population, giving relative sampling errors of less than 10^{-2}.

The calculated squeezing moment from the SDE simulations was: $\langle Y_1^2 \rangle + 0.5 = .0271 \pm 10^{-5}$. This is in excellent agreement with both types of expansion, as shown in Fig. 2, since the driving field is the transitional region where both expansions are valid. In fact, the agreement is better with the below-threshold expansion, as this is just outside the critical region.

We find that the spectral predictions are also well verified by the simulations. These resulted in a value for the nonlinear correction to the zero-frequency spectrum, of $\Delta S(0) = S(0) - S^{(1)}(0) = 1.874 \times 10^{-3} \pm .01 \times 10^{-3}$. By comparison, the analytic theory, worked to fourth order in g, gives the prediction that $\Delta S(0) = 2.01 \times 10^{-3}$. The residual difference of about 5% can be attributed to the fact that there are higher order corrections that are not included in the analytic theory, and these are more significant in the zero-frequency spectrum than they are in the moment calculation. Fig. 3 shows the detailed results of the simulation.

6.2 Critical Squeezing

At the critical point, where $\mu = 0$, we used 10^4 trajectories, giving relative sampling errors of typically 2×10^{-2}. The calculated squeezing moment from the critical point SDE simulations was: $\langle Y_1^2 \rangle + 0.5 = .0038 \pm 10^{-4}$. This is in poor agreement with the below threshold expansion, which clearly fails closer to threshold than about $\mu = 0.97$, for this value of g . In the region where $|\mu - 1| < g$, much better agreement is naturally obtained with the critical-point expansion, which predicts a value of $\langle Y_1^2 \rangle + 0.5 = .00375$. This agreement verifies our analytic prediction that the total squeezing, integrated over all frequencies, is actually lower at and just above threshold, than it is just below threshold where the zero-frequency squeezing is minimized.

We find that the spectral results for the squeezed quadrature resulted in a value for the nonlinear correction to the zero-frequency spectrum of $\Delta S(0) = 1.01 \times 10^{-2} \pm .2 \times 10^{-3}$ – which gives about three times larger minimum spectral fluctuations in the external transmitted squeezed beam, that at the optimum driving field, just below threshold.

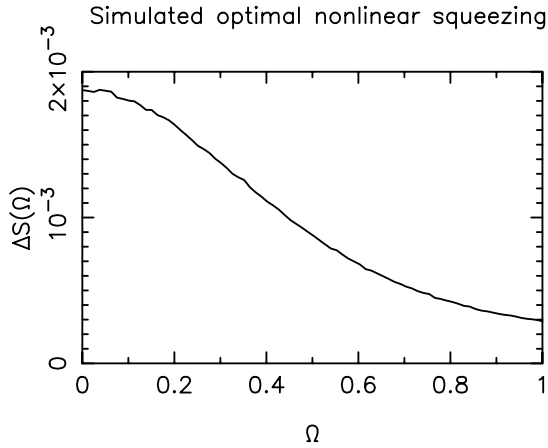

Fig. 3. Numerically simulated nonlinear squeezing with $g^2 = 1000$, $\gamma_r = 0.5$

7 Conclusion

We have calculated the quantum fluctuations in a parametric oscillator below and near the classical threshold, using a nonlinear stochastic theory, and applying both asymptotic approximations and a numerical technique. The important point about this result is the excellent agreement between numerical and analytic calculations, together with the straightforward yet rigorous nature of the perturbation theory. Corresponding results for the Feynman diagram method require a summation over infinite sets of diagrams, in order to fully include the reservoirs. The advantage of the present method is due to the fact that the coherent state basis is a more natural basis set for an open system, since it allows the damping reservoirs to be treated non-perturbatively.

The Hilbert space involved in the simulations had dimension $> 10^6$, and would be difficult to solve using other methods that involve number-state expansions – which would have a Hamiltonian matrix with 10^{12} coefficients, unless simplified, and a density matrix of similar size! The present technique works just as well if $N = g^{-2} = 10^6$ or larger, except for the longer time taken to reach the steady-state, due to critical slowing-down. This represents a more typical experimental photon number, with a Hilbert space dimension of 10^{12}, which appears totally inaccessible with number state techniques.

Optimal squeezing in the output spectra corresponding to these moments were estimated. We found that the best squeezing in the zero frequency part of the squeezing spectrum scales like $N^{-2/3}$ just below threshold. In other words, at the true critical threshold – where the linear squeezing is optimized - the nonlinear corrections are too large to give the lowest overall zero-frequency

squeezing. Instead, one should operate below the critical point to optimize the spectral squeezing.

Using an entirely different method, a calculation by Plimak and Walls [8] also predicted that the zero frequency part of the squeezing spectrum scales like $N^{-2/3}$ somewhat below threshold. Our general scaling results agree with theirs, however, with a different spectrum. We attribute the difference to the simple yet systematic +P stochastic diagram procedure used here to calculate the spectrum, rather than the Feynman diagram method – which involves additional approximations.

We note that at the critical point ($\mu = 1$), the scaling behaviour is quite different to the behaviour just below threshold, and must be calculated by using a distinct asymptotic perturbation theory, valid at the threshold itself. The total squeezing moment is actually minimised at a driving field just above threshold, and this behaviour was confirmed in our simulations. This apparent paradox can be attributed to the fact that the critical fluctuations mostly tend to broaden the squeezing spectrum, which has a strong effect at zero-frequency - but does not diminish the total squeezing moment, which is integrated over all frequencies.

References

1. P.D. Drummond, K.J. McNeil, D.F. Walls: Optica Acta **27**, 321 (1980); P.D. Drummond, K.J. McNeil, D.F. Walls: Optica Acta **28**, 211 (1981)
2. B. Yurke: Phys. Rev. A **32**, 300 (1985)
3. C.W. Gardiner, M.J. Collett: Phys. Rev. A **31**, 3761 (1985); M.J. Collett, D.F. Walls: Phys. Rev. A **32**, 2887 (1985)
4. P. Kinsler, P.D. Drummond: Phys. Rev. A **43**, 6194 (1991)
5. P.D. Drummond, P. Kinsler: Quantum and Semiclass. Opt. **7**, 727 (1995); P.D. Drummond, P. Kinsler: Phys. Rev. A **52**, 783 (1995)
6. J. Schwinger: J. Math. Phys. **2**, 407 (1961); L.V. Keldysh: Sov. Phys. JETP **20**, 1018 (1965)
7. C.J. Mertens, T.A.B. Kennedy, S. Swain: Phys. Rev. Lett. **71**, 2014 (1993); C.J. Mertens, T.A.B. Kennedy, S. Swain: Phys. Rev. A **48**, 2374 (1993); C.J. Mertens, J.M. Hasty, H.H. Roark III, D. Nowakowski, T.A.B. Kennedy, S. Swain: Phys. Rev. A **52**, 742 (1995); C.J. Mertens, T.A.B. Kennedy: Phys. Rev. A **53**, 3497 (1996)
8. L.I. Plimak, D.F. Walls: Phys. Rev. A **50**, 2627 (1994)
9. O. Veits, M. Fleischhauer: Phys. Rev. A **52**, R4344 (1995); Phys. Rev. A **55**, 3059 (1997)
10. L.A. Wu, H.J. Kimble, J. Hall, H. Wu: Phys. Rev. Lett. **57**, 2520 (1986); Z.Y. Ou, S.F. Pereira, H. J. Kimble: Phys. Rev. Lett. **68**, 3663 (1992)
11. A. Heidmann, R.J. Horowicz, S. Reynaud, E. Giacobino, C. Fabre, G. Camy: Phys. Rev. Lett. **59**, 2555 (1987)
12. S. Chaturvedi, P.D. Drummond, D.F. Walls: J. Phys. A **10**, L187-L192 (1977); P.D. Drummond, C.W. Gardiner: J. Phys. A **13**, 2353 (1980)

13. L. Arnold: *Stochastic Differential Equations: Theory and Applications* (John Wiley and Sons, New York 1974); C.W. Gardiner: *Handbook of Stochastic Methods* (Springer, Berlin 1983)
14. A. Gilchrist, C.W. Gardiner, P.D. Drummond: Phys. Rev. A **55**, 3014 (1997)
15. S. Chaturvedi, P.D. Drummond: Eur. Phys. J. B **8**, 251 (1999)
16. P.D. Drummond, P. Kinsler: J. Eur. Opt. Soc. B **7**, 727 (1995); S. Chaturvedi, P.D. Drummond: Phys. Rev. A **55**, 912 (1997)
17. P.D. Drummond: Phys. Rev. A **33**, 4462 (1986)
18. P. Kinsler, P.D. Drummond: Phys. Rev. A **52**, 783 (1995)
19. G. Milburn, D.F. Walls, Optics Commun. **39**, 401, (1981)
20. H.J. Carmichael, J.S. Satchell, S. Sarkar: Phys. Rev. A **34**, 3166 (1986)
21. P.D. Drummond, I.K. Mortimer: J. Comput. Phys. **93**, 144 (1991)

Quantum Phase Transitions in a Linear Ion Trap

G.J. Milburn and Paul Alsing

Summary. We show that the quantum phase transition of the Tavis–Cummings model can be realised in a linear ion trap of the kind proposed for quantum computation. The Tavis–Cummings model describes the interaction between a bosonic degree of freedom and a collective spin. In an ion trap, the collective spin system is a symmetrised state of the internal electronic states of N ions, while the bosonic system is the vibrational degree of freedom of the centre of mass mode for the ions.

1 Introduction

More than two decades ago, when quantum optics was young, the quantum dynamics of collective spin systems interacting with a single bosonic degree of freedom was a major research problem. The model arose as an attempt to describe the interaction between a collection of two level atoms and a single mode of the radiation field. Walls and co-workers [1] were among the first to realise that such models provided ideal examples of the role of quantum fluctuations in the nonlinear interaction between matter and light. Quantum fluctuations were shown to drastically change the predictions of semiclassical theory in such systems. This phenomenon has appeared more recently in the discovery of quantum phase transitions in quantum spin glasses [2] and other many body quantum systems. While the collective spin models did not directly apply to achievable experiments at the time, they did provide insight that subsequently proved important for many other quantum optical experiments including anti-bunching, squeezing [3], and cavity QED [4]. In this paper we show that the models of a collective spin interacting with one or more bosonic modes can now be experimentally realised in modern ion trap systems of the kind proposed for quantum computation [5,6]. An enormous effort has gone into making such systems work at the quantum level, with little interference form classical sources of noise, and a number of such experiments exist today. It would thus appear worthwhile to reconsider the collective spin models, and the associated quantum many-body effects exhibited by such systems, with a view to direct experimental realisation.

In particular we consider the Tavis–Cummings (TC) model [7], which can be realised in a linear ion trap of N ions with the bosonic degree of freedom appearing as the quantised collective centre-of-mass motion. If each ion is coupled to the vibrational motion using an identical external (classical) laser

H.J. Carmichael, R.J. Glauber, M.O. Scully (Eds.): LNP 561, pp. 303–312, 2001.

detuned to the first red-sideband transition, the symmetry is such that the electronic degree of freedom for the ions can be described as a collective spin (N) and the reversible dynamics is well described by the TC model. The TC model is known to exhibit important nonlinear quantum effects including a quantum phase transition [2] in which the (zero temperature) ground state undergoes a morphological change as a parameter is varied and averages of intensive quantities undergo a bifurcation.

2 The Tavis–Cummings Model

The interaction Hamiltonian for N ions interacting with the centre of mass vibrational mode can be controlled by using different kinds of Raman laser pulses. A considerable variety of interactions has already been achieved or proposed [5,6,8]. In this paper we consider the first red-sideband transition. The ion is assumed to be in a three dimensional anisotropic harmonic potential. Two dimensions are very tightly bound and are neglected. In the remaining dimension, an external laser couples the electronic state to the vibrational motion. If the vibrational frequency is large enough and the Lamb-Dicke limit [5] applies the motional sidebands of the absorption of the electronic transition can be resolved and a laser detuned below the electronic resonance by one unit of the trap frequency can excite the electronic transition by absorbing one vibrational phonon, the additional energy required being made up by the laser. We will assume that the laser (or lasers if a Raman process is used) is sufficiently strong that it can be treated classically. Under these assumptions the Hamiltonian, in the interaction picture, is

$$H_I = \hbar\Omega \sum_{i=1}^{N} (a\sigma_+^{(i)} + a^\dagger \sigma_-^{(i)}) \tag{1}$$

where the coupling constant is $\Omega = \eta\Omega_0$ where $\eta^2 = E_r/(\hbar M\omega_0)$ is the Lambe-Dicke parameter with E_r the recoil kinetic energy of the atom, ω_0 is the trap vibrational frequency, and M is the effective mass for the centre-of-mass mode. The Lamb-Dicke limit assumes $\eta << 1$, which is easily achieved in practice. The frequency, Ω_0 is the effective Rabi frequency for the electronic transition involved. The raising and lowering operators for each ion are defined by $\sigma_- = |g\rangle\langle e|$ and $\sigma_+ = |e\rangle\langle g|$. This sideband transition can be used to efficiently cool the ions to the collective centre-of-mass ground state, thus preparing the system in the vibrational ground state [5].

If the external laser field on each ion is identical (in amplitude and phase) the interaction Hamiltonian is

$$H_I = \hbar\Omega(a\hat{J}_+ + a^\dagger \hat{J}_-) \tag{2}$$

where we have introduced the bosonic annihilation operator a for the centre-of-mass vibrational mode and where we have used the definition of the collective spin operators,

$$\hat{J}_\alpha = \sum_{i=1}^{N} \sigma_\alpha^{(i)} \tag{3}$$

where $\alpha = x, y, z$. Identical laser fields could easily be obtained by splitting a single, stabilised laser into multiple beams. The interaction Hamiltonian in Eq (2) specifies the Tavis–Cummings model [7]. This model first appeared in quantum optics where the bosonic mode is the quantised field in a cavity. However this realisation is difficult to achieve experimentally. In contrast the vibrational mode realisation should be readily achieved. The dynamics resulting from this Hamiltonian is quite rich. Collective spin models of this kind were considered many decades ago in quantum optics [9,10]. In much of that work however the collective spin underwent an irreversible decay. In the case of an ion trap model however we can neglect such decays due to the long lifetimes of the excited states. On the other hand heating of the vibrational centre-of-mass mode can induce irreversible dynamics in the system in a manner that has not been previously considered, and that is reminiscent of thermal effects in condensed matter physics.

We are interested in the driven Tavis–Cummings model in which the vibrational mode is subject to a linear forcing term which can easily be achieved by a suitable combination of Raman laser pulses, or by appropriate AC voltages applied to the trap electrodes [5]. In this case the Hamiltonian, in the interaction picture, is given by

$$H_I = \hbar\Omega(a\hat{J}_+ + a^\dagger \hat{J}_-) + \hbar E(a + a^\dagger) \tag{4}$$

This may be written in terms of the hermitian canonical oscillator variables $\hat{X} = (a + a^\dagger)/\sqrt{2}$, $\hat{Y} = -i(a - a^\dagger)/\sqrt{2}$, and the canonical angular momentum variables $\hat{J}_x = (\hat{J}_+ + \hat{J}_-)/2$, $\hat{J}_y = -i(\hat{J}_+ - \hat{J}_-)/2$, $\hat{J}_z = [\hat{J}_+, \hat{J}_-]/2$. It takes the form

$$H = \hat{X}\hat{J}_x - \hat{Y}\hat{J}_y + \chi\hat{X} \tag{5}$$

with $\chi = E/\Omega$ and we have scaled the Hamiltonian by $H \to H/\sqrt{2}\Omega$. This indicates that time is measured in units of $\frac{1}{\sqrt{2}\Omega}$.

Alsing [11] has shown that the ground state of this system, for weak driving, is a product state in which the bosonic mode is squeezed and the electronic states are rotated in the angular momentum space. We provide a direct proof of this statement below. However it is first useful to consider the dynamics of the equivalent semiclassical model as many of the results in the quantum case can be interpreted in terms of the features of the semiclassical model.

2.1 Semiclassical Tavis–Cummings Model

The Tavis–Cummings model represents an interaction between a simple harmonic oscillator and a linear top for which there is a classical model which we now define. We choose the classical model so that the equations of motion are of the same form as the Heisenberg equations of motion for the quantum model. The classical Hamiltonian is defined as

$$\mathcal{H} = X\mathcal{J}_x - Y\mathcal{J}_y + \chi EX \tag{6}$$

where X, Y are respectively the canonical oscillator position and momentum variables with the canonical Poisson bracket $\{X, Y\} = 1$, while $\mathcal{J}_k$ are the three components of angular momentum for a classical top with the canonical Poisson brackets $\{\mathcal{J}_i, \mathcal{J}_k\} = \sum_k \epsilon_{ijk}\mathcal{J}_k$. The equations of motion for a canonical coordinate w is given as usual by Poisson bracket with the Hamiltonian $\dot{w} = \{w, H\}$. The equations of motion are,

$$\dot{X} = -\mathcal{J}_Y \tag{7}$$

$$\dot{Y} = -\mathcal{J}_X - \chi \tag{8}$$

$$\dot{\mathcal{J}}_x = -Y\mathcal{J}_z \tag{9}$$

$$\dot{\mathcal{J}}_y = -X\mathcal{J}_z \tag{10}$$

$$\dot{\mathcal{J}}_z = X\mathcal{J}_y + Y\mathcal{J}_x \tag{11}$$

Note that these equations have a conservation law $\mathcal{J}_x^2 + \mathcal{J}_y^2 + \mathcal{J}_z^2 = \text{constant}$.

We now justify this choice of classical Hamiltonian by noting that the Heisenberg equations of motion for the Hamiltonian Eq(4) have the same form as the semiclassical equations of motion with all variables replaced by the corresponding operators. We thus see that the semiclassical equations result form taking moments of the Heisenberg equations and factorising all product moments. The factorisation assumptions ignores correlations which scale as $1/N$ for the scaled operators $\hat{J}_\sigma/N$. The conservation law $\mathcal{J}_x^2 + \mathcal{J}_y^2 + \mathcal{J}_z = \textit{constant}$ is a reflection of the operator relation

$$\hat{J}^2 = \frac{N}{2}\left(\frac{N}{2} + 1\right) \tag{12}$$

which in the semiclassical limit indicates that $\mathcal{J}_x^2 + \mathcal{J}_y^2 + \mathcal{J}_z = \frac{N^2}{4}$.

The classical equations have one nontrivial fixed point at $X^* = Y^* = \mathcal{J}_y^* = 0$ and $\mathcal{J}_x^* = -\chi$, $\mathcal{J}_z^* = \sqrt{N^2/4 - \chi^2}$. However as the conservation law requires that $|\mathcal{J}_x| \leq N/2$ we see that we must have

$$\frac{2E}{N\Omega} \leq 1 \quad \text{(below threshold)} \tag{13}$$

which corresponds to an energy of $\mathcal{H} = 0$. We will refer to this as the *below threshold* case. As E is increased from zero, the fixed point for the angular momentum system rotates about the $\mathcal{J}_y$ direction eventually reaching the

equatorial plane at $\mathcal{J}_x = -N/2$ at the threshold condition. The oscillator system always has zero amplitude below threshold. If we linearise around this fixed point we discover that it is an unstable hyperbolic point with time constant proportional to $1/\sqrt{\mathcal{J}_z^*}$. Note that this time constant goes to infinity as the fixed point is approached as is typical for a hyperbolic fixed point.

We now consider the *above threshold* case

$$\frac{2E}{N\Omega} \geq 1 \quad \text{(above threshold)} \tag{14}$$

Clearly the value of $|\mathcal{J}_x|$ cannot increase above $N/2$. Indeed there is no fixed point above threshold. However there is a special solution curve that continuously joins to the below threshold case for phase curves with $\mathcal{H} = 0$.

To see this we consider making a canonical transformation by a rotation in both the $X-Y$ plane and in the $\mathcal{J}_x, \mathcal{J}_y$ plane (see figure 1). The canonical transformations are

$$X = \bar{X}\cos\theta + \bar{Y}\sin\theta \tag{15}$$
$$Y = \bar{Y}\cos\theta - \bar{X}\sin\theta \tag{16}$$
$$\mathcal{J}_x = \bar{\mathcal{J}}_x\cos\theta - \bar{\mathcal{J}}_y\sin\theta \tag{17}$$
$$\mathcal{J}_y = \bar{\mathcal{J}}_x\cos\theta + \bar{\mathcal{J}}_y\sin\theta \tag{18}$$

The Hamiltonian then takes the form

$$\mathcal{H} = \bar{X}(\bar{\mathcal{J}}_x + \chi\cos\theta) - \bar{Y}(\bar{\mathcal{J}}_y - \chi\sin\theta) \tag{19}$$

The phase curves with $\mathcal{H} = 0$ now correspond to either

$$\bar{X} = 0 \quad ; \quad \bar{\mathcal{J}}_y = \chi\sin\theta \tag{20}$$

or

$$\bar{Y} = 0 \quad ; \quad \bar{\mathcal{J}}_x = -\chi\cos\theta \tag{21}$$

These phase curves smoothly join the fixed point at threshold if $\mathcal{J}_x = -N/2$ which implies

$$\cos\theta = \frac{N\Omega}{2E} \tag{22}$$

These solutions are illustrated in figure 1. Note that as $E \to \infty$ we have that $\bar{\mathcal{J}}_x$ eventually points in the direction of $-\mathcal{J}_y$ while phase curve in the oscillator phase space points along the Y axis, indicating that for large driving the system is essentially a particle in a linear potential which accelerates at constant rate. These results were first obtained by Alsing and Carmichael [12].

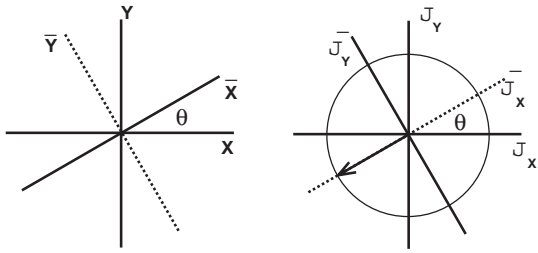

Fig. 1. An illustration of the canonical transformation used in the semiclassical equations above threshold

3 Quantum States

First note that the ground state when there is no driving is $|j,-j\rangle_z \otimes |0\rangle_v$ with a zero eigenvalue. This ground state corresponds to the fixed point of the semiclassical model with zero oscillator amplitude and angular momentum pointing in the $-\mathcal{J}_z$ direction. We postulate that as the driving is increased form zero the ground state of the Hamiltonian Eq(4) is given by

$$|\mathcal{E}_0\rangle = S(r)R(\theta)|j,-j\rangle_z \otimes |0\rangle_v \tag{23}$$

where $|j,-j\rangle_z \otimes |0\rangle_v$ corresponds to all ions in the ground state and the vibrational mode in the ground state. The operator $S(r)$ is a squeezing operator defined by

$$S^\dagger(r)aS(r) = \mu a + \nu a^\dagger \tag{24}$$

with $\mu = \cosh r, \quad \nu = \sinh r.$

The rotation operator $R(\theta)$ is defined by

$$R(\theta) = e^{-\theta(\hat{J}_+ - \hat{J}_-)} \tag{25}$$

and corresponds to a rotation of 2θ around the $\hat{J}_y$ axis. Consider now

$$H_I|\mathcal{E}_0\rangle = SR\left(R^\dagger S^\dagger H S R\right)|j,-j\rangle_z \otimes |0\rangle_v \tag{26}$$

If we now transform the Hamiltonian and require that

$$R^\dagger S^\dagger H S R|j,-j\rangle_z \otimes |0\rangle_v = 0 \tag{27}$$

we find the following conditions,

$$\nu(1+\cos 2\theta) = \mu(1-\cos 2\theta) \tag{28}$$

$$\Omega j \sin 2\theta = E \tag{29}$$

which requires that

$$\cos 2\theta = e^{-2r} \tag{30}$$

and the ground state energy is taken to be $\mathcal{E}_0 = 0$. The ground state is thus a product of a squeezed state for the vibrational mode and a rotated angular momentum state, rotated about the $\hat{J}_y$ axis.

The above results are consistent with the semiclassical approximation. The mean amplitude of a squeezed vacuum state is zero, corresponding to the semiclassical fixed point at $\bar{X} = \bar{Y} = 0$ while the rotation around the $\hat{J}_y$ axis corresponds to the semiclassical fixed point at $\bar{\mathcal{J}}_x = -\chi$.

If we continue to increase E above the threshold value the system adiabatically follows a zero energy state, although this is no longer a ground state. In fact the canonical transformation used in the semiclassical analysis can be applied to the quantum operator valued Hamiltonian. The result is the same as the semiclassical case, Eq (19) with all variables replaced with the corresponding operators. The zero energy state then corresponds to the zero energy eigenstate of $\hat{Y}\cos\theta - \hat{X}\sin\theta$ with $\cos\theta = N\Omega/2E$. This is of course just a rotated, infinitely squeezed state. The electronic state is likewise a angular momentum eigenstate rotated from $|j, -j\rangle$ in the equatorial plane (orthogonal to $\hat{J}_z$). Thus above threshold the zero energy eigenstate deforms continuously from the state at threshold.

Let us summarise these results. For no driving the ground state corresponds to the oscillator in the ground state and all ions in the ground state. As the driving is increased, but kept below threshold, this state deforms to a squeezed oscillator state while the collective spin system begins to rotate about the $\hat{J}_y$ axis. Note that the mean oscillator amplitude $\langle a\rangle$ remains zero as does the mean of the y-component of the collective spin. As the driving increases through the threshold value, this state changes its character so that a non zero value of $\hat{J}_y$ is acquired and the oscillator is infinitely squeezed in a direction at an angle $\cos\theta = N\Omega/2E$ to the below threshold squeezing. This morphological change of the state as the driving passes the semiclassical critical point is a quantum phase transition. The quantum phase transition can be seen in the mean value for $\hat{J}_y$ and $\hat{J}_z$ as shown in figure 2. Below threshold the scaled mean values are given by

$$\frac{\langle \hat{J}_y\rangle}{N/2} = 0 \tag{31}$$

$$\frac{\langle \hat{J}_z\rangle}{N/2} = -\sqrt{1-x^2} \tag{32}$$

and above threshold we have

$$\frac{\langle \hat{J}_y\rangle}{N/2} = -\sqrt{1-\frac{1}{x^2}} \tag{33}$$

$$\frac{\langle \hat{J}_z\rangle}{N/2} = 0 \tag{34}$$

where $x = 2E/N\Omega$.

What are the experimental manifestations of this transition? Needless to say no one is ever going to observe an infinitely squeezed state in an experiment. So what does happen at $2\theta = \pi/2$ when the electronic state is

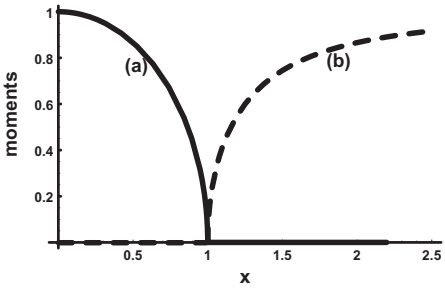

Fig. 2. The scaled moments, (**a**) $2|\langle J_z\rangle|/N$, and (**b**) $2|\langle J_y\rangle|/N$ plotted versus the scaled driving strength $x = 2E/(N\Omega)$

the $\hat{J}_x$ eigenstate $|j-j\rangle_x$ and the vibrational mode appears to be infinitely squeezed ? Is such a state physically possible ? Suppose for example we begin in the ground state of the Hamiltonian with no driving ($E = 0$) which is simply $|j,-j\rangle_z \otimes |0\rangle_v$, and adiabatically increase the driving strength. It would appear that the system would then adiabatically evolve into the squeezed vibrational state described above. If we were ever able to reach the case $2\theta = \pi/2$ we would have reached an infinite energy state for the vibrational mode at a finite driving strength. Clearly this is not possible and to understand why it is useful to reconsider the semiclassical dynamics for this model. The adiabatic approximation requires that we vary the driving strength on a time scale slower than all other time scales in the system. The key time scale for the ground state variation is just the time scale associated with the hyperbolic unstable fixed point, $(N^2/4-\chi^2)^{-1/2}$, which goes to infinity as we approach $\frac{2E}{\Omega N} = 1$. Thus the adiabatic increase of the driving must proceed infinitely slowly, that is it must be switched to the finite value $E = \frac{\Omega N}{2}$ in an infinite amount of time. This pumps an infinite amount of energy into the system and results in infinite squeezing in the centre of mass vibrational mode. Obviously in practice this cannot be achieved so the totally squeezed ground state is not possible. However it will still be possible to achieve some squeezing of the vibrational mode at smaller values of the driving. This would make an interesting observation for current ion trap experiments even with only a few ions. The squeezing of the vibrational mode can be observed using the dynamical method of reference [13]

In current ion trap experiments, laser cooling techniques allow the centre of mass mode to be prepared in the ground state. Unfortunately it does not stay there. Heating due to a variety of sources, including fluctuating linear potentials, lead to an irreversible evolution away from the ground state. If such heating is present during the coupling of the electronic and vibrational motions, irreversible dynamics will be spread to the collective spin degrees of freedom as well.

As an example we consider what happens if we use the Tavis–Cummings interaction (excitation on first red sideband) in the presence of strong heating.

Heating of the centre-of-mass mode due to fluctuating liner potentials may be described in the interaction picture by the master equation,

$$\frac{dW}{dt} = -i\Omega[a\hat{J}_+ + a^\dagger \hat{J}_-, W] + \frac{\gamma}{2}\left(\mathcal{D}[a] + \mathcal{D}[a^\dagger]\right) W \tag{35}$$

where W is the density operator for the spin and vibrational degrees of freedom and the superoperator $\mathcal{D}$ is defined by $\mathcal{D}[A]\rho = 2A\rho A^\dagger - A^\dagger A\rho - \rho A^\dagger A$. The irreversible term corresponds to two point processes in which phonons are removed or added from centre of mass mode at the rates $\gamma\langle a^\dagger a\rangle$ and $\gamma\langle aa^\dagger\rangle$ respectively. This does not change any first order moments, however it does lead to a diffusion in energy as $\frac{d\langle a^\dagger a\rangle}{dt} = \gamma$. The effect of heating can be included in the semiclassical analysis by adding an appropriate stochastic term. In the Ito calculus[14] the effect is to add to the equations for X, Y terms of the form

$$dX = (\ldots) + \sqrt{\gamma} dW_x(t) \tag{36}$$

$$dY = (\ldots) + \sqrt{\gamma} dW_y(t) \tag{37}$$

where $dW_i(t)$ are independent Wiener processes. If the heating rate is small enough these terms can be neglected. However if they are large new steady states can occur in the semiclassical and quantum descriptions which will be described in a future publication.

Acknowledgment

We would like to thank Howard Carmichael for useful discussions.

References

1. D.F. Walls, P.D. Drummond, S.S. Hassan, H.J. Carmichael: Progress of Theoretical Physics, supplement no. 64 (1978)
2. H. Reiger, A.P. Young: In: *Complex Behaviour of Glassy Systems* ed. by M. Rubi; C. Perez-Vicente: Proceedings of the XIV Sitges Conference, Sitges, Barcelona, Spain, 10-14 June, *Lecture Notes in Physics* (Springer Verlag, Berlin 1996), LANL cond-mat/9607005
3. D.F. Walls, G.J. Milburn: *Quantum Optics* (Springer, Heidelberg 1994)
4. Q.A. Turchette, C.J. Hood, W. Lange, H. Mabuchi, H. J. Kimble: Phys. Rev. Lett. **75**, 4710 (1995)
5. D.J. Wineland, C. Monroe, W.M. Itano, D. Leibfried, B.E. King, D.M. Meekhof: Journal of Research of the National Institute of Standards and Technology **103**, 259 (1998)
6. R.J. Hughes, D.F.V. James, J.J. Gomez, M.S. Gulley, M.H. Holzscheiter, P.G. Kwiat, S.K. Lamoreaux, C.G. Peterson, V.D. Sandberg, M.M. Schauer, C.M. Simmons, C.E. Thorburn, D. Tupa, P.Z. Wang, A.G. White: Fortschritte der Physik **46**, 329 (1998)

7. M. Tavis, F.W. Cummings: Phys. Rev. **170**, 379 (1968)
8. M.S. Gulley, A. White, D.F.V. James: 'A Raman approach to quantum logic in Calcium-like ions', unpublished
9. P.D. Drummond: Phys. Rev. A **22**, 1179 (1980), and references therein
10. R.H. Dicke: Phys. Rev. **93**, 99 (1954)
11. P. Alsing: Private communication.
12. P. Alsing, H.J. Carmichael: Quantum Optics **3**, 13 (1991)
13. D.M. Meekhof, C. Monroe, B.E. King, W.M. Itano, D.J. Wineland: Phys. Rev. Lett. **76**, 1796 (1996)
14. C.W. Gardiner: *Handbook of Stochastic Methods* (Springer-Verlag, Berlin 1983)

Quantum Noise Transfer Functions: A Practical Tool in Quantum Optics

H.-A. Bachor and T.C. Ralph

Summary. Abstract: This paper summarises a practical and elegant model for the description of optical systems based on CW lasers and photodetectors. It is based on quantum noise transfer functions and includes all quantum effects, including those of squeezed light. The basic equations are summarised and the model is explained through a series of examples, such as interferometers, resonators and optical parametric oscillators, and electro-optic controls. This model can be extended to include the description of quantum information and quantum control.

1 Introduction

Modern technology uses many different optical systems to create, transfer, control and store information. Examples are optical fibre links, networks and optical memory which contain modulators and sensors, amplifiers, detectors, splitters, optical resonators and lasers. It is useful to have a model which can describe the performance of all these instruments in one consistent way and which applies to classical light, as produced by conventional lasers as well as to the improvements that can be achieved with non-classical or squeezed light [1] [2] [3] [4] [5].

The model deals with classical information , in the form of modulation, but will allow an extension into the new domain of quantum information. The model is to be applied to temporal rather than spatial information, that means it deals with signals in time and not with images. In order to be practical, the model should be modular, so that it can be expanded and adapted easily to a variety of systems.

Such a model is the systematic application of the single mode approximation of light, using quadrature variances. The same model can be looked at, from an engineering point of view, as quantum transfer functions which combine well known electronic noise transfer functions with the quantum features of light. This article summarises this technique which has evolved over the last decade as a practical tool and is used by many researchers. This review highlights the practical aspects of this model with simple recipes and examples. This model is built on detailed theoretical derivations and despite the simplicity it is rigorous and accurate. There are, though rare, cases where the technique is not adequate and these limits are listed.

H.J. Carmichael, R.J. Glauber, M.O. Scully (Eds.): LNP 561, pp. 313–332, 2001.

2 A Linearised Quantum Noise Description

In general a complete description of a beam or state of light, including its quantum properties, can be carried out through quasi probability distributions, such as a Wigner function, Q-function, or P-representation [1]. For the description inside an optical cavity one single function will suffice. In contrast, for a freely propagating beam the situation is more involved [4]. We will find that we need a whole continuum of distribution functions. These functions can be derived as the solutions of complex stochastic differential equations, in many cases master equations [1] [2] [6]. While complete this approach is more general than required in practice. Here we are using an alternative route of linearising the system right from the beginning. This can be done since the modulations and the fluctuations we are concerned with are small compared to the amplitude of the laser beam. This is correct for situations with practical detectable optical powers (larger than micro watts) and where we are using CW or pulsed lasers and electronic spectrum analysers to measure the fluctuations [5]. Note that our approach here is quite different to that applicable in experiments that use single photons and photon counting detection.

The quantum description of the laser beam is in the form of states $|\psi\rangle$ and operators $\hat{A}$. The states are expressed in terms of the standard basis of Glauber coherent states $|\alpha\rangle$. The operators describe both the mean amplitude and the phase of the light, whose mean values are given by one complex number α. The fluctuations and modulations are described by the operator $\delta\hat{A}(t)$, resulting in the total operator

$$\hat{A} = \alpha + \delta\hat{A}(t). \tag{1}$$

The operators for the amplitude quadrature $X1$ and the phase quadrature $X2$ are represented by the operators $X1 = \hat{A} + \hat{A}^\dagger$ and $X2 = -i(\hat{A} - \hat{A}^\dagger)$. The beam can be detected by a photodetector and the operator for the photon flux $\hat{N}$ is given by

$$\begin{aligned}\hat{N} &= \hat{A}^\dagger(t)\hat{A}(t) \\ &= (\alpha + \delta\hat{A}^\dagger(t))(\alpha + \delta\hat{A}(t)) \\ &= \alpha^2 + \alpha\delta\hat{A}^\dagger(t) + \alpha\delta\hat{A}(t) + \delta\hat{A}^\dagger(t)\delta\hat{A}(t) \\ &= \alpha^2 + \alpha\delta X1(t)\end{aligned} \tag{2}$$

where we have taken the arbitrary phase of α real and linearized by neglecting higher than first order terms in the fluctuations. The measurements which are generally performed in experiments are either using a power meter, resulting in the average photon flux $\bar{N}$, or alternatively measurements of the fluctuations in the Photon flux, given by the variance VN, or the fluctuations in the amplitude and phase quadratures , which are represented by the variances $V1$ and $V2$. The results are given by the expectation values:

$$\bar{N} = \langle\alpha|\hat{N}|\alpha\rangle = \langle\alpha|\hat{A}^\dagger\hat{A}|\alpha\rangle = \alpha^2$$

$$
\begin{aligned}
VN &= \langle\alpha|(\hat{A}^\dagger\hat{A})(\hat{A}^\dagger\hat{A})|\alpha\rangle - \langle\alpha|A^\dagger\hat{A}|\alpha\rangle^2 \\
V1 &= \langle\alpha|\hat{X}1\hat{X}1|\alpha\rangle - \langle\alpha|\hat{X}1|\alpha\rangle^2 \\
&= \langle\alpha|(\hat{A}+\hat{A}^\dagger)(\hat{A}+\hat{A}^\dagger)|\alpha\rangle - \langle\alpha|\hat{A}+\hat{A}^\dagger|\alpha\rangle^2 \\
V2 &= \langle\alpha|\hat{X}2\hat{X}2|\alpha\rangle - \langle\alpha|\hat{X}2|\alpha\rangle^2 \\
&= \langle\alpha|(-i(\hat{A}-\hat{A}^\dagger))(-i(\hat{A}-\hat{A}^\dagger))|\alpha\rangle - \langle\alpha| - i(\hat{A}-\hat{A}^\dagger)|\alpha\rangle^2 \qquad (3)
\end{aligned}
$$

For a quantum noise limited (QNL) lasers beam, equivalent to a coherent state, we obtain $VN = \bar{N}$. In contrast, both quadrature variances are normalised, such that for any quantum noise limited beam we have $V1 = V2 = 1$, independent of the optical power. $V1, V2 > 1$ indicates the presence of technical noise or modulations or both. $V1$or $V2 < 1$ can be achieved with squeezed

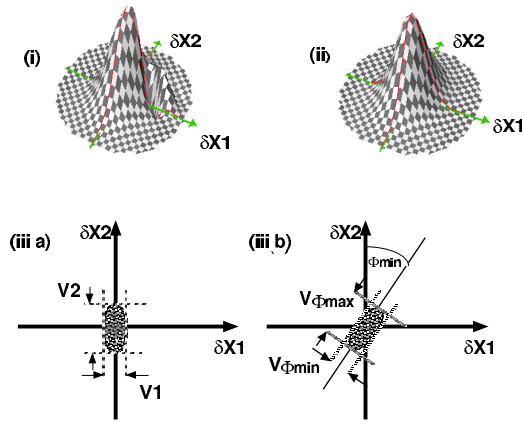

Fig. 1. (**i**) An arbitrary unrealistic 2 dim Q-function, (**ii**) a realistic Q-function, (**iii**) a description of the size of the Q-function by $V1(\Omega)$, $V2(\Omega)$ or alternatively $V_{min}(\Omega)$, $V_{max}(\Omega)$ and $\Theta_{min}(\Omega)$

One complete representation of the quantum system is given by Q-functions, defined as $Q_\psi = |\langle\alpha|\psi\rangle|^2/\pi$. In general Q-functions can have very complex shapes. (see Fig. 1(i)). However, for practical normal detectors and beams with small fluctuations and modulations, $\alpha >> \delta\hat{A}(t)$, we can use linearisation and find that the class of solutions is much more restricted. We only deal here with two dimensional Gaussian Q-functions (see Fig. 1(ii)) with higher order moments that are completely described by their second order moments, i.e. variances, which are a measure of the size of the Q-function.

In the applications information is placed on the laser beams in the form of modulation at various different frequencies Ω_{mod}, usually measured in Hz not Rad/s. Each frequency is one independent information channel. Consequently, we should consider the equivalent of one quantum state to be the properties of the light in a small frequency interval around Ω_{mod}. The

laser beam contains at this frequency both signal and quantum noise in two quadratures. This can be a simple modulation with fixed amplitude, modulation with random amplitude (noise), quantum noise or even noise with correlations between the upper and lower sidebands (squeezing). In general the quadratures can be correlated with each other. All these properties are represented by the Fourier transforms of the operators in equation (1).

$$\begin{aligned} A(\Omega) &= \alpha\delta(\Omega = 0) + \delta A(\Omega), \\ \delta X1(\Omega) &= \delta A(\Omega) + \delta A^{\dagger}(\Omega), \\ \delta X2(\Omega) &= -i(\delta A(\Omega) - \delta A^{\dagger}(\Omega)) \end{aligned} \tag{4}$$

where the absence of hats indicates Fourier transformed operators. The term $\alpha\delta(\Omega = 0)$ represents the carrier at the laser frequency ν_{laser}. This applies to all beams in the experiment. We will have several input and at least one output beam, with $A(\Omega)_{in}$ and $A(\Omega)_{out}$ and their own photon flux, modulation and noise. In analogy to equation (2) we obtain the operator for the photon flux in Fourier space as:

$$N_{out} = \alpha^2\delta(0) + \alpha\delta X1_{out}(\Omega) \tag{5}$$

where the first term describes the average power, concentrated in a DC spike, and the second term describes the fluctuations. In all cases we can define α_{out} as real consequently the variance of the photocurrent at frequency Ω is given by

$$VN_{out}(\Omega) = \alpha_{out}^2\langle\alpha|\delta X1_{out}(\Omega)^2|\alpha\rangle = \alpha_{out}^2\ V1_{out}(\Omega) \tag{6}$$

We now have a compact link between the measured values $VN_{out}(\Omega)$ and the property $V1_{out}(\Omega)$ of the state. Using a homodyne detector it is possible to measure all variances $V(\Theta)_{out}$ at all frequencies (Ω). The properties of the light in a small interval around each frequency can be described by one Q-function $Q(\Omega)$. The interval is assumed small enough such that the frequency response is flat. Since we have small fluctuations and signals, we can apply linearisation.

The variance $V_{\Theta}(\Omega)$ can be determined by first projecting all parts of the Q-function onto one axis at angle Θ. This produces a series of one dimensional distribution functions $DF(\Theta)$ which describe in the form of a histogram the time varying photocurrent in a small frequency range. In a second step the variances of these functions are evaluated which provides information about the width of $DF(\Theta)$. Note that information is lost in this process. Obviously, different functions $DF(\Theta)$ can have the same variance. However, for our restricted class of functions a direct link exists between the Q-functions and the variances and a complete description is given by $V_{min}(\Omega)$, $V_{max}(\Omega)$, $\Theta_{min}(\Omega)$, as shown in Fig. (2). These are the variances in two orthogonal quadratures, the quadrature of maximum and minimum fluctuations, and the orientation Θ_{min} of the minimum axis in regard to two standard directions, $X1$ and $X2$. In many situations we find $\Theta_{min} = 0$ or $\pi/2$. Generally, the values at each

frequency, or channel, are different: the signals appear at certain frequencies only; the noise can also be frequency dependent, as we will find in the case of most lasers; squeezed states have a squeezing spectrum with $V_{min} < 1$ for certain frequencies only and there can also be variations in the orientation $\Theta_{min}(\Omega)$.

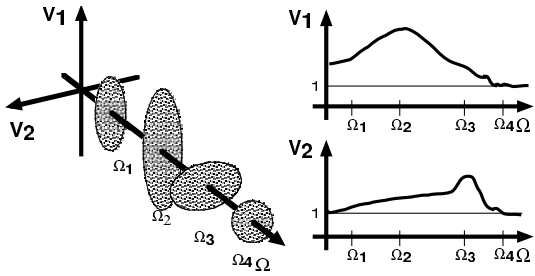

Fig. 2. A laser beam is represented by complete spectra of the variances. Here one typical example is shown. Both V1 and V2 change with frequency. This beam has considerable intensity noise around the frequency Ω_2, it has a phase modulation at Ω_3 and it is quantum noise limited (V2 = V1 = 1) at frequency Ω_4. For simplicity this example beam has in all cases Θ_{min} of either 0 or $\pi/2$

A single CW beam has many of these channels and is represented by the measurement of three spectra $V1(\Omega), V2(\Omega), \Theta_{min}(\Omega)$. It can be regarded as containing many quantum states, which are all distinguishable by their detection frequency. These states are independent from each other, not linked in any classical or quantum sense. Thus this model is also known as the single mode approximation. There are situations, in particular those with very large modulations, where higher harmonics of the modulation frequency can be created, that are linked to each other. These cases would require a more detailed treatment.

Note that we are describing the optical system in the Heisenberg picture, by using the operators, not the states, of the light at the different places of the instrument. Thus we will be concerned with the way these operators are changing through the system. This has the advantage that we obtain compact results and do not have to trace optical states through the system, which can get very complex. This approach is generally used for CW laser beams. In contrast, single photon experiments are more frequently described in the Schroedinger picture, by tracing the propagation of states.

3 Practical Considerations

All calculated variances are automatically normalised. In contrast, in the experiments we measure variances of the photocurrent, and they have to be normalised by the variance measured with a beam of light with the same optical

power and which is quantum noise limited. This requires a beam without any modulation and with no other fluctuations than the standard quantum noise. It also means that $V1(\Omega), V2(\Omega)$ can be interpreted as one plus the signal to noise ratio $(1 + SNR)$ of the two quadratures, provided the dominant noise is quantum noise. Within the spectra $V1(\Omega), V2(\Omega)$ different signals, such as simple harmonic modulations with slowly variable amplitude and fixed modulation phase, and classical noise, such as random changes of the amplitude and modulation phase, are described in the same way. This reflects the actual performance of practical systems, namely that photo detection with a spectrum analyser does not allow a distinction between signals and classical noise other than by their actual frequency distribution, i.e. sharp, narrow spectra for signals and diffuse, broadband spectra for noise.

An alternative experimental approach would be phase synchronous detection, i.e. electronically mixing the photo currents with a copy of the electronic modulation signal used in the modulation process. This is normally not done and consequently not considered here. However, it has been used in quantum tomography [7] where the distribution functions are recorded and Q-functions are reconstructed. This technique allows the distinction between the different states and types of modulation. The spectra, with positive values of Ω, can be traced back to a representation of the light as an electromagnetic wave with one optical carrier frequency ν_{laser}, measured in $[Hz]$, and sidebands at $\nu_{laser} \pm \Omega$. These two sidebands may have common signals, such as for amplitude modulation (AM), phase or frequency modulation (FM). They have uncorrelated noise on both sidebands, such as quantum noise and technical noise. Finally, there could be correlations between the noise sidebands, such as created in squeezed light. In most optical system, such as in beam splitters, attenuators or amplifiers, the two sidebands are affected in the same way [5]. As a consequence the variances $V1$ and $V2$ remain independent. In direct detection, see Fig.(3.(i)) the photo-detector combines the information from both sidebands and produces one contribution to the total photo current $i(\Omega)$. An electronic spectrum analyser is used to select $\mid i(\Omega) \mid^2$ from the total photo current, and this value is proportional to $VN(\Omega)$ and with equation (6) to $V1(\Omega)$.

In order to gain more information a homodyne detector can be used to investigate all quadrature variances $V_{\Theta(\Omega)}$ [8]. This is achieved by mixing the light under investigation, described by $\alpha_{in} + \delta\hat{A}_{in}(t)$ with a local oscillator beam $\alpha_{LO} + \delta\hat{A}_{LO}(t)$, see Fig.3(ii). The two beams are phase locked with a variable phase difference of $\Delta\Phi_{LO}$. The local oscillator beam has a much larger intensity $\alpha_{LO}^2 >> \alpha_{in}^2$. The difference of the photocurrent from the two detectors is formed. This arrangement has the advantage that all the noise of the local oscillator is suppressed, only the fluctuations of the input beam are measured. Scanning $\Delta\Phi_{LO}$ corresponds to projecting the Q-function in different angles onto the quadrature axis. The variance of the photocurrent ,

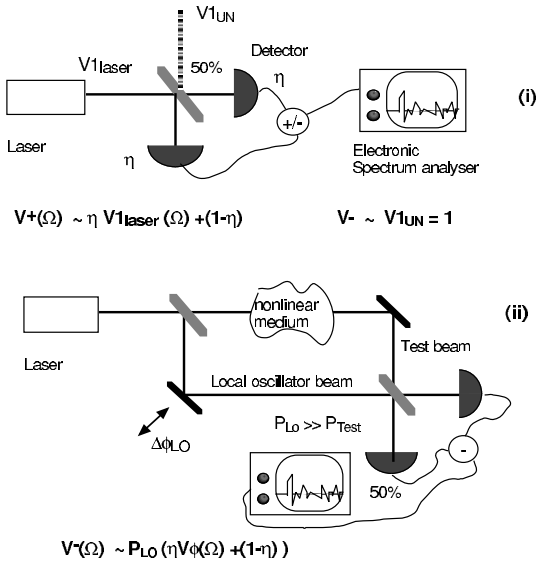

Fig. 3. The optical layout for: (**i**) the direct detector, (**ii**) the homodyne detector

determined by the spectrum analyser is given by

$$V(\Delta\Phi_{LO}) = \sin^2(\Delta\Phi_{LO})V_{in}(\Theta_{min}) + \cos^2(\Delta\Phi_{LO})V_{in}(\Theta_{min} + \pi/2) \quad (7)$$

In many practical cases $\Theta_{min} = 0$ or $\Theta_{min} = \pi/2$ i.e. $V(\Theta_{min}) = V1$ or $V2$. In particular we can measure $V1(\Omega)$ for $\Delta\Phi_{LO} = 0$ or $V2(\Omega)$, for $\Delta\Phi_{LO} = \pi/2$, but note that we can only accurately measure one quadrature at a time.

4 The Transfer of Operators, Signals and Noise: A Simple Recipe

The next step is to describe a complete optical system and to evaluate the propagation of the noise and the signals through the system. Each optical component of the system can be thought of as having several inputs, described by their coherent amplitudes $\alpha_{in1}, \alpha_{in2}, ..etc$, and their fluctuation operators $\delta A_{in1}, \delta A_{in2}, ...etc$. The corresponding spectral variances for each input are $V1_{in1}(\Omega)$, $V2_{in1}(\Omega)$, $V1_{in2}(\Omega)$, $V2_{in2}(\Omega)$, ...etc. Inside the optical component these modes are combined. The algebraic equations for the coherent amplitudes are solved to give the output coherent amplitude. We usually choose the arbitrary overall phase of the input fields such that the output coherent amplitude is real. After linearisation the equations of motion for the fluctuation operators can be solved in frequency space. The frequency space fluctuation operators for one output mode can then be described by equations of the form

$$\delta A_{out}(\Omega) = c_{1a}(\Omega)\ \delta A_{in1}(\Omega) + c_{1c}(\Omega)\ \delta A^{\dagger}_{in1}(\Omega)$$

$$
\begin{aligned}
&+ c_{2a}(\Omega)\ \delta A_{in2}(\Omega) + c_{2c}(\Omega)\ \delta A^{\dagger}_{in2}(\Omega) + ...\\
\delta A^{\dagger}_{out}(\Omega) &= c^{*}_{1c}(-\Omega)\ \delta A_{in1}(\Omega) + c^{*}_{1a}(-\Omega)\ \delta A^{\dagger}_{in1}(\Omega)\\
&+ c^{*}_{2c}(-\Omega)\ \delta A_{in2}(\Omega) + c^{*}_{2a}(-\Omega)\ \delta A^{\dagger}_{in2}(\Omega) + ... \qquad (8)
\end{aligned}
$$

and similarly for all other output modes. The coefficients $c_{kl}(\Omega)$ are complex numbers which describe the frequency response of the component. Note, that the response is not necessarily symmetric about the carrier. The c_{ka} and c_{kc} are linked via commutation requirements. For linear systems the c_{kl} do not depend on the beam intensities and all $c_{kc} = 0$. We can also treat the case of propagation through nonlinear media, such as $\chi^{(2)}$ and $\chi^{(3)}$ media. This includes nonlinear processes such as frequency doubling, parametric amplification, the Kerr effect or nonlinear absorption. The equations (8) remain linear, but in these cases the coefficients $c_{1a}, c_{1c}, c_{2a}, c_{2c}, \ldots$ are dependent on the average optical power of the beams. In the examples given below we will show how the coefficients c_{ij} can be derived from the physical properties of the component, such as reflectivities, conversion efficiencies etc.. Once the operator $\delta A_{out}(\Omega)$ for the output mode in question has been found the variances can be determined using (6) and (7). Let us consider some specific cases:

(1) The simplest case is if firstly all the inputs are independent, i.e. we have $< \delta X1_{ink}(\Omega)\delta X1_{inl}(\Omega) >= \delta_{kl}$. This will be true if all the input beams represent beams from independent sources or different vacuum inputs. Secondly, we require that the coefficients obey $c^{*}_{ij}(-\Omega) = c_{ij}(\Omega)$ i.e. magnitude and phase of the frequency response are symmetric. This will be true if there are no detunings or strong dispersion in the optical system. In this case we obtain the simplest type of transfer function. Indeed, for a linear system ($c_{1c} = c_{2c} = \ldots. = 0$) the transfer functions for both quadratures are identical.

$$
\begin{aligned}
V1_{out}(\Omega) &= |c_{1a}(\Omega) + c_{1c}(\Omega)|^2 V1_{in1}(\Omega)\\
&+ |c_{2a}(\Omega) + c_{2c}(\Omega)|^2 V1_{in2}(\Omega) + \ldots\\
V2_{out}(\Omega) &= |c_{1a}(\Omega) - c_{1c}(\Omega)|^2 V2_{in1}(\Omega)\\
&+ |c_{2a}(\Omega) - c_{2c}(\Omega)|^2 V2_{in2}(\Omega) + \ldots \qquad (9)
\end{aligned}
$$

(2) The coefficients still obey $c^{*}_{ij}(-\Omega) = c_{ij}(\Omega)$ but we allow for inputs that are not independent. Now there can be correlations between the quadrature variances of different inputs. However, we can always regain the form of equ.9 by breaking down each of the inputs into a function of its own inputs until we end up with all the inputs being independent.

(3) The coefficients obey $c^{*}_{ij}(-\Omega) = c^{*}_{ij}(\Omega)$, i.e. the magnitude of the frequency response is symmetric but not the phase. This will occur if the fluctuations suffer a different phase rotation to that of the coherent amplitude. In this case we get cross-coupling between the transfer functions of $V1_{out}$ and

$V2_{out}$ such that now

$$\begin{aligned} V1_{out}(\Omega) &= |c_{1a}(\Omega) + c_{1c}(\Omega)|^2 \cos^2(\theta) V1_{in1}(\Omega) \\ &\quad + |c_{1a}(\Omega) - c_{1c}(\Omega)|^2 \sin^2(\theta) V2_{in1}(\Omega) + ... \\ V2_{out}(\Omega) &= |c_{1a}(\Omega) - c_{1c}(\Omega)|^2 \sin^2(\theta) V2_{in1}(\Omega) \\ &\quad + |c_{1a}(\Omega) + c_{1c}(\Omega)|^2 \cos^2(\theta) V1_{in1}(\Omega) + ... \end{aligned} \tag{10}$$

where θ is defined by $c_{ij}(\Omega) = |c_{ij}(\Omega)|e^{i\theta}$. We have assumed that $V1$ and $V2$ are the quadratures of minimum and maximum fluctuations.

(4) The coefficients obey $c^*_{ij}(-\Omega) \neq c^*_{ij}(\Omega)$. This will occur when the frequency response of the optical components is asymmetric around the carrier frequency, for example due to detunings. It is not possible to represent the output as a transfer function of quadrature variances in this case.

In the detailed examples below we will only consider case (1) applied to both linear and nonlinear components. An example of case (2) would be where either a modulation is common or two or more of the input modes have correlated noise. This is the case when the beams originate from one source, such as two beams formed by a beamsplitter, or where two beams are generated by an above threshold OPO. Examples of case (3) can be as benign as mixing beams on a beamsplitter where the coherent amplitudes of the inputs have different phases, or components with strong dispersion where the refractive index changes within a frequency interval of Ω_{det} and symmetric attenuation, or as complex as single ended cavities with optical detuning. The simplest example of case (4) is a double ended optical cavity with detuning.
Finally, the simplest example of a transfer function describes the influence of loss terms only and has the form: $V1_{out}(\Omega) = |c_{1a}|^2 V1_{in1}(\Omega) + |c_{2a}|^2 + |c_{3a}|^2 + ...$, where all the inputs apart from $V1_{in1}(\Omega)$ are vacuum inputs which have the numerical value of 1.

An appropriate name for equation (9) is quantum noise transfer function. This equation is very similar to the classical transfer functions used by communication engineers. The classical function can be derived using a description of the various inputs as classical waves with modulation at Ω. Noise behaves exactly in the same way as the modulations. Quantum noise is not included. The propagation and interference of these waves is determined and the result is the size of the modulation at the output. In contrast, equation (9) includes all the quantum effects of the light, in particular the effects of quantum noise. We can directly see how the signals vary in comparison to the quantum noise and can evaluate the coefficient for the transfer of the signal to noise ratio from input to output. This approach has been developed since the 1980s by a number of research groups, very prominently by the groups in France who pioneered squeezing [9] and QND[10]. It was extended in the

1990s to include the effects of active systems, such as solid-state lasers [11], and has since been used by many groups. The elegance of this approach is now shown in a number of examples:

5 Examples of Transfer Functions

5.1 Beamsplitter with One Input

The simplest case is that of a beamsplitter which reflects a fraction ϵ of the intensity and transmits the fraction $(1-\epsilon)$. This system has two inputs (see Fig. 4(i)), one is the laser beam (in) , the other is the unused port (UN). The operator for the output is given by: $\delta A_{out}(\Omega) = \sqrt{(1-\epsilon)}\ \delta A_{in}(\Omega) + \sqrt{\epsilon}\ \delta A_{UN}(\Omega)$ The two inputs are not linked, and consequently $\langle \delta A_{in}(\Omega) \delta A_{UN}(\Omega) \rangle = 0$. This results in the transfer function,

$$V1_{out}(\Omega) = (1-\epsilon)\ V1_{in}(\Omega) + \epsilon\ V1_{UN}(\Omega) \tag{11}$$

with the condition $V1_{UN}(\Omega) = 1$. From this well known formula one can find the reduction, T, in the signal to noise ratio is $(1-\epsilon)$. This answer applies to all forms of attenuation. The concept of the beamsplitter can be used to describe absorption, scattering losses and all other forms of linear reduction of the intensity of the beam.

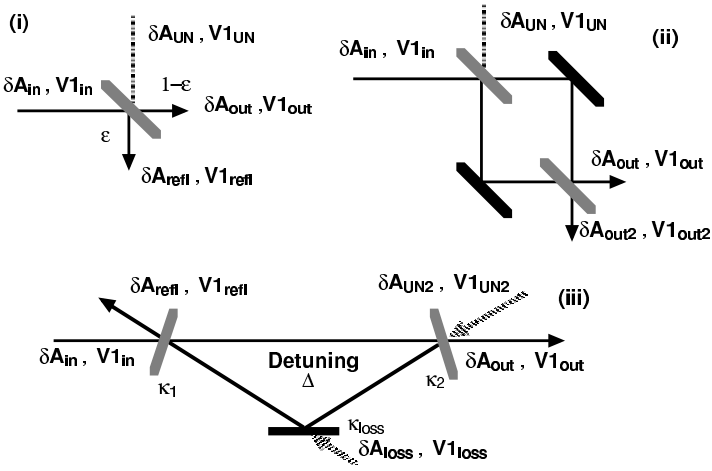

Fig. 4. The optical layout and the various input and output modes for: (**i**) a beam splitter, (**ii**) an interferometer and (**iii**) a cavity

5.2 Interferometer

An interferometer, such as the simple Mach Zehnder interferometer shown in Fig.4(ii) can be analysed by describing the operator $\delta A_{out}(\Omega)$ at the output as a sum of operators for the two beams inside the instrument. Again we keep track of how both the input beam $\delta A_{in}(\Omega)$ and the fluctuations in the unused port of the input beamsplitter $\delta A_{UN}(\Omega)$ propagate through the instrument. At the second beamsplitter, ϵ_2, we have to consider both inputs which are phase linked with a phase shift of $\Delta\Phi$. This results in:

$$\begin{aligned}\delta A_{out}(\Omega) = (\sqrt{(1-\epsilon_1)}\sqrt{\epsilon_2}\ \delta A_{in}(\Omega) + \sqrt{\epsilon_1}\sqrt{(1-\epsilon_2)}\ \delta A_{UN}(\Omega))\ e^{i\Delta\Phi} \\ +\sqrt{(\epsilon_1)}\sqrt{1-\epsilon_2}\ \delta A_{in}(\Omega) - \sqrt{1-\epsilon_1}\sqrt{(\epsilon_2)}\ \delta A_{UN}(\Omega) \qquad (12)\end{aligned}$$

Here we assume that the two sidebands at $+\Omega$ and $-\Omega$ experience the same phase shift $\Delta\Phi$. That means the pathlength difference between the beams is less than c/Ω. For the special case of $\epsilon_1 = \epsilon_2 = 0.5$ we get

$$V1_{out}(\Omega) = \cos^2(\Delta\Phi/2)\ V1_{in}(\Omega) + \sin^2(\Delta\Phi/2)\ V2_{UN}(\Omega) \qquad (13)$$

and again for a single laser input beam, the condition $V2_{UN}(\Omega) = 1$ applies. This is equivalent to a variable attenuator, following equation (11), where $\epsilon = \cos^2(\Delta\Phi/2)$. Equation (13) shows that the noise at the output depends on both the input and the vacuum noise in the quadrature $V2_{UN}(\Omega)$ coupled through the first beamsplitter. Normally this input is unused and we have $V2_{UN}(\Omega) = V1_{UN}(\Omega) = 1$. But the performance of the interferometer can be improved by coupling light, squeezed in the correct quadrature $X2$, into this port. This was demonstrated by Xiao, Wu and Kimble [14].

5.3 Optical Cavities

Next we consider an optical cavity, as shown in Fig.4 (iii). For simplicity we have a triangular cavity with three components and roundtrip length p. An input mirror M1 with an intensity transmission $T_1 = 2\kappa_1 p/c$, an output mirror with transmission $T_2 = 2\kappa_2 p/c$ and one mirror M3 which represents all the losses in the cavity by κ_{loss}. The cavity has one input beam given by $\delta X1_{in}$ at M1 and two vacuum inputs $\delta X1_{UN2}$ and $\delta X1_{loss}$ at M2 and M3 respectively. We write the differential equation for a cavity in terms of δa_{cav} for the internal mode and δA_{ik} for the external fields.

$$\frac{d\delta a_{cav}}{dt} = -(\kappa + i\Delta)\delta a_{cav} + \sqrt{2\kappa_1}\delta A_{in} + \sqrt{2\kappa_2}\delta A_{UN2} + \sqrt{2\kappa_{loss}}\delta A_{loss} \qquad (14)$$

Here the term $i\Delta$ describes the detuning of the cavity from resonance. Note the difference between the intracavity operators a which describe excitations of the cavity mode and the operators A which describe photon fluxes. These operators have different dimensions. The resulting transfer function is obtained by solving equ. (14) together with the boundary conditions for δA at

the mirrors, such as $\delta A_{out} = \sqrt{2\kappa_2}\delta a_{cav} - \delta A_{UN2}$ at mirror M2. This results in the transfer function for a resonant cavity ($\Delta = 0$):

$$V1_{out}(\Omega) = [\kappa^2 + (2\pi\Omega)^2]^{-1}\{4\kappa_2\kappa_1 V1_{in}(\Omega) + [(2\kappa_2 - \kappa)^2 + (2\pi\Omega)^2]V1_{UN2}(\Omega) + 4\kappa_2\kappa_{loss}\ V1_{loss}(\Omega)\} \quad (15)$$

One interpretation of equ. (15) is that it acts like a low pass filter. The cavity has a linewidth $\delta\Omega = 2\pi\kappa$. Inside the cavity linewidth noise is transmitted and not reflected. Outside the cavity linewidth noise is reflected , not transmitted. The cavity can be used to separate low and high frequency noise from each other.

Note that a cavity with detuning away from resonance is an example where terms from both input quadratures mix together. This is one example where all terms in equ. (8) are required and this corresponds to a Q-function with an axis rotated compared to the input. This is particularly noticeable if the input contains single quadrature modulation or squeezing. The reflection of a single ended cavity with detuning has been used as an alternative detector for $V(\Theta)$ [12].

Finally, we mention that all linear optical systems will maintain the properties of a quantum noise limited (QNL) beam $V1 = V2 = 1$. It is not possible to produce a squeezed, ($V(\Theta_{min} < 1)$, output beam by any linear system. This statement allows a practical test: If all the input beams are QNL, including the vacuum states, all output beams will also be QNL. Thus, we can simply replace all values $V1_{inj}$ by 1 and the result should be $V1_{out} = 1$ for all output beams.

5.4 The Subthreshold OPO as Generator for Squeezed Light

One of the most successful sources of squeezed light has been the Optical Parametric Oscillator [13] which generates a squeezed vacuum state. This source of squeezing has produced the best noise suppression on a single beam and has already been used as a lightsource for several applications in interferometry [14], spectroscopy [15] and QND measurements [16].

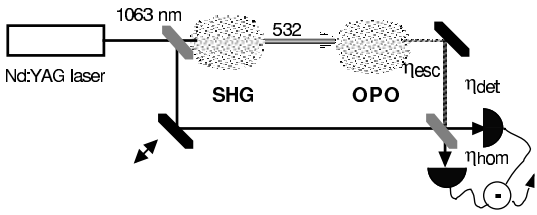

Fig. 5. Schematic diagram of the OPO squeezing experiment

This is an example of the noise transfer through a nonlinear medium, where the coefficients of equ. (8) contain terms which scale nonlinearly with

the average input, or pump intensities. In order to derive the transfer function we can start with the equations of motion of the OPO given by [1]:

$$\begin{aligned}\dot{a} &= Ea^\dagger - \gamma a + \sqrt{2\gamma_b}A_b + \sqrt{2\gamma_l}\ \delta A_l + \sqrt{2\gamma_c}\delta A_c \\ \dot{a}^\dagger &= E^* a - \gamma a^\dagger + \sqrt{2\gamma_b}A_b^\dagger + \sqrt{2\gamma_l}\delta A_l^\dagger + \sqrt{2\gamma_c}\delta A_c^\dagger \end{aligned} \tag{16}$$

These equations have already been linearised with respect to the pump mode. Here the subscripts (b), (c) and (loss) describe the vacuum noise inputs through the mirrors of the cavity and through loss. These two equations can be combined into one equation for the operators $\delta X1_{out}$. By taking the Fourier transform of these equations, we obtain expressions for the fluctuations $\delta X1_{out}(\Omega)$ of the amplitude quadrature and $\delta X2_{out}(\Omega)$ of the phase quadrature of the field inside the cavity.

$$\begin{aligned} i2\pi\Omega\,\delta X1_{out} &= (\Re[E] - \gamma)\ \delta X1 + \Im[E]\ \delta X1 + \sqrt{2\gamma_b}\ \delta X1_b \\ &\quad + \sqrt{2\gamma_l}\ \delta X1_{loss} + \sqrt{2\gamma_c}\ \delta X1_c \\ i2\pi\Omega\,\delta X2_{out} &= \Im[E]\ \delta X1 + (\Re[E] + \gamma)\ \delta X2 + \sqrt{2\gamma_b}\ \delta X2_b \\ &\quad + \sqrt{2\gamma_l}\ \delta X2_{loss} + \sqrt{2\gamma_c}\ \delta X2_c \end{aligned} \tag{17}$$

where $\Re[E]$ and $\Im[E]$ denote the real and imaginary part of the complex number E representing the pump field. The solution for the semi-classical steady state shows oscillations above a threshold pump power P_{thr} and the solution can be scaled by the normalised pump power P/P_{thr}. Using the same boundary conditions as for a linear cavity we obtain the noise spectrum of the squeezed quadrature. In addition we have to include the imperfections of the actual experiment, which can be modelled as losses between the perfect apparatus and the detector. A realistic set of noise transfer functions is

$$\begin{aligned} V2_{out}(\Omega) &= 1 - \eta_{esc}\eta_{det}\eta_{hom}\frac{4\sqrt{P/P_{thr}}}{(\Omega/\gamma)^2 + (1+\sqrt{P/P_{thr}})^2} \\ V1_{out}(\Omega) &= 1 + \eta_{esc}\eta_{det}\eta_{hom}\frac{4\sqrt{P/P_{thr}}}{(\Omega/\gamma)^2 + (1+\sqrt{P/P_{thr}})^2} \end{aligned} \tag{18}$$

The first equation shows the noise suppression in the phase quadrature phase, the second increased noise in the amplitude quadrature. In the case of low losses the beam retains the minimum uncertainty, as was beautifully demonstrated by Wu et al. [13]. Over the years the performance of the components has been improved and the following values for parameters in equation (18) have been achieved by Lam et al.[17]: escape efficiency from the cavity η_{dec} = 0.96, quantum efficiency of the detectors $\eta_{dec} = 0.94$, efficiency of the homodyne detector (mode overlap) $\eta_{hom} = 0.97$, detection frequency, which is limited by laser noise $\Omega/\gamma = 3$ [MHz]/67 [Mhz] = 0.045. The pump power can be continuously varied, $0 < P/P_{thr} < 0.99$. These parameters correspond to a noise reduction by 8.5 [dB] or $V2_{out}(\Omega) = 0.14$. This corresponds to a very narrow minimum in $V(\Theta)$ and the remaining jitter in Θ in the experiment

resulted in measured noise suppression of 7 [db] or $V2_{out}(\Omega) = 0.20$. We can inject a beam into the cavity and lock it to this input such that the medium acts as an optical parametric amplifier (OPA) at a fixed frequency, in this way constant noise suppression (over hours) by 5 [dB], $V2_{out}(\Omega) = 0.32$, has been demonstrated [18]. Comparable and even better results were obtained by the Konstanz group [19].

A similar experiment is the use of the OPO above threshold as a generator of twin photon beams (note that a more complicated set of equations are required above threshold). Individually, each beam is not squeezed, it can actually be noisy. However, the difference between the photon fluxes, or intensities, is below the standard quantum limit. These experiments were pioneered by the Paris group [20] and the best results have been achieved by Mertz et al. [21] and in Shanxi [22] where a noise suppression of 8.5 [dB],V_{diff} = 0.16 was measured. This is the lowest variance observed.

5.5 Quantum Control

The technique of quantum noise transfer function can be applied to optical control situations, for example intensity stabilisation by feedback control using electro-optical modulators [23][24][25]. The feed back is included by following the same derivation as for a classical feedback loop and writing the equation for the beam leaving the apparatus in a closed format that takes into account the roundtrip gain and phase shift $h(\Omega)$ inside the loop. The classical parameters can be replaced by the operators $\delta X_{out}(\Omega)$ and all vacuum input ports have to be included. The resulting transfer functions is

$$V1_{out}(\Omega) = 1 + \frac{(1-\epsilon)\eta(V1_{in} - 1) + |h(\Omega)|^2}{|1 - h(\Omega)|^2} \tag{19}$$

here ϵ is the reflectivity of the beam splitter which diverts the light to the detector in the feedback-loop. The quantum efficiency of the detectors is given by η. For large signals , $V1_{in}(\Omega) >> 1$, this transfer function looks identical to the classical solution, but for signals close to the quantum noise limit it shows dramatic differences. In this case the feedback loop can increase the noise, rather than suppress it. This is an example where classical and quantum noise transfer functions are quite different and care has to be taken in any engineering application that the quantum effects are included.

It is well known that this device cannot produce a squeezed output. The internal light is not squeezed either. It has special properties but cannot be used directly for measurements with improved signal to noise ratio.

An attractive application of quantum control is to use feed forward control as a means of obtaining noiseless AC amplification [26]. With this device it is possible to transfer the information from a non-classical (squeezed beam) onto a classical beam which makes the information robust. The idea is straight forward, see Fig.6. A large fraction of the signal is measured by a detector D1,

the resulting photocurrent is amplified and used to modulate the remaining light with an AM modulator. The transfer function is [26]:

$$\begin{aligned} V1_{out}(\Omega) &= \epsilon_3|\sqrt{\epsilon_1} + \lambda\sqrt{(1-\epsilon_1)\epsilon_2}|^2\ V1_{in}(\Omega) \\ &+ \epsilon_3|\sqrt{1-\epsilon_1} - \lambda\sqrt{\epsilon_1\epsilon_2}|^2\ V1_1 \\ &+ \epsilon_3|\lambda\sqrt{1-\epsilon_2}|^2\ V1_2 \\ &+ (1-\epsilon_3)\ V1_3 \end{aligned} \tag{20}$$

where $V1_1, V1_2, V1_2$ are vacuum noise inputs. $V1_1$ is the vacuum noise entering the beamsplitter M1, $(1-\epsilon_2) = \eta_2$ is the quantum efficiency of the AM detector and $(1-\epsilon_3)$ is the efficiency of the AM modulator. λ is the total gain of the feed forward loop.

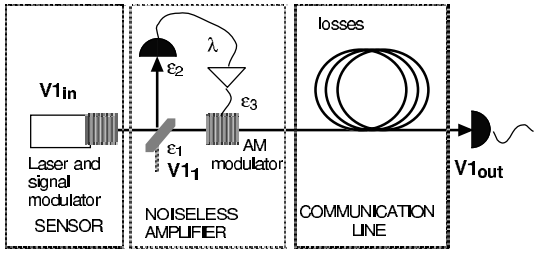

Fig. 6. Schematic diagram for the noiseless amplifier. The components which create the signal (sensor), amplify both signal and noise and transfer it to the detector are shown as individual boxes

The correct choice of λ allows us to cancel the second term in equ. (20). This means that all the noise introduced by the beamsplitter can be cancelled out by the feed forward system. The light at the output is going to be noisy, since both the signal and the noise from the input have been amplified as given by the first term of equation(20). But the signal to noise ratio (SNR) is kept high. In the limit of ϵ_2 and $\epsilon_3 = 0$ the SNR is maintained. We have a noiseless amplifier which transforms a beam with a signal close to standard quantum limit (SQL) into a beam with the same SNR but with both signal and noise well above the SQL. This applies even for input beams with noise less than the SQL, that means modulated squeezed light. The output beam is now all in the classical domain and its SNR is robust in regard to losses. This was experimentally demonstrated by Lam et.al. [26]. One practical application of this device is as a preamplifier after a sensor which uses squeezed light. Inside the sensor losses can be kept low in order to get the improvement to the SNR from the squeezed light. The information can be moved away from the SQL with the feed forward system and can be safely sent along lossy lines.

5.6 Link to Quantum Information

Quantum information can be embedded in a CW laser beam by modulation of a single Fourier frequency Ω_{mod}. The two dimensional operator space $\delta X1, \delta X2$ allows the representation of quantum states, including such quantum features as superposition states and entanglement between the quadratures. This quantum information travels with the beam. Quantum information can be used to enhance the performance of the system. The most publicised example is quantum cryptography. Here the sensitivity of quantum states to loss are used as an advantage to design communication systems where it is possible to guarantee that a message has not been intercepted. While these system normally operate with individual photons [27], an equivalent system exists for CW beams [28]. One particular challenge is to send quantum information from one place to another using classical channels or wires. Such a device would be called a quantum teleporter. Without nonclassical light this is not possible. However, using correlated nonclassical beams it might be possible [29] [30] [31]. The first requirement is to simultaneously measure both quadratures and to thereby determine all the quantities of the state, in this case $V1$ and $V2$. This requires two detectors, one for each quadrature, and consequently the use of at least one beamsplitter which couples in vacuum noise $V_{U!N}(\Omega)$, see Fig.7.

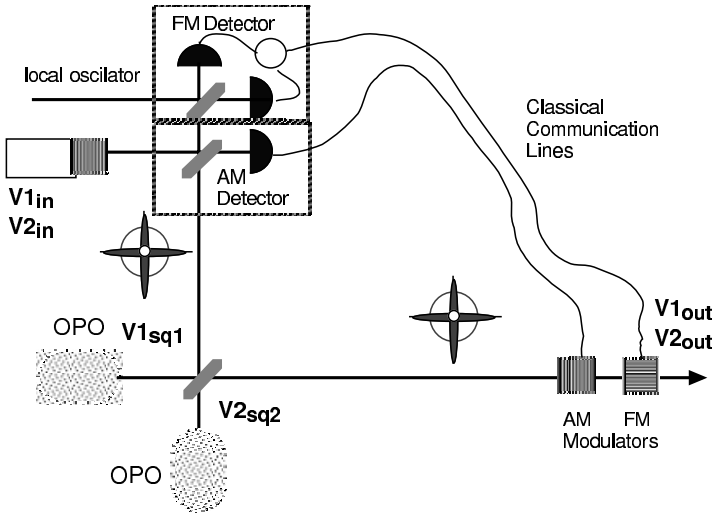

Fig. 7. Optical continuous signal teleporter. The two OPOs provide the pair of nonclassical light beams. One is used for the detection of both the AM and FM signal. The information is carried through classical channels and is reconstructed by modulating the other of the nonclassical beams

The question is, what type of light could we shine into the empty port to suppress the vacuum noise ? If we use squeezed light we can improve the measurement for only one of the quadratures, the one which corresponds to the squeezing axis. The orthogonal quadrature will be much noisier. The solution is to use the superposition of two squeezed states with orthogonal axis, $V1_{sq1} << 1$ and $V2_{sq2} << 1$, which could be called a crossed state, as shown in Fig.7.

The two currents i_{AM}, i_{FM} from both photodetectors are now very noisy. They contain the signal, one $V1_{in}$ and the other $V2_{in}$, but this information is buried in a lot of noise coming from the antisqueezed quadratures within the crossed state. A detection of these currents with a spectrum analyser would show a very small SNR or with strong squeezing, no signal at all. However, it is possible to reconstruct the information of the quantum state by using an identical copy of the crossed state. This can be achieved by generating the crossed state by mixing two squeezed states on a beamsplitter, which generates two entangled beams. The second crossed beam is modulated, both by AM and FM modulators, driven by the two currents i_{AM}, i_{FM}. For this arrangement the transfer function has been derived by Ralph et al. [31]

$$\begin{aligned} V1_{out}(\Omega) &= V1_{in}(\Omega) + V1_{sq1} \\ V2_{out}(\Omega) &= V2_{in}(\Omega) + V2_{sq2} \end{aligned} \tag{21}$$

These elegant transfer functions show that the reconstruction would be perfect if both squeezed states were perfect, that is if $V1_{sq1} = V2_{sq2} = 0$ and no losses occur anywhere. In reality the effect of the uncertainty introduced by the teleporter as given by equation (21) is about as big as the overlap section of the crossed state, which is much smaller than the standard quantum uncertainty area (see Fig.7). One demonstration of this idea has already been done by the Caltech group [32] which showed that the reconstructed state has very similar quantum properties to the input state, as measured by a joint fidelity exceeding 0.5. A challenge for the future is to improve on these experiments and to demonstrate teleportation of nonclassical states.

6 Conclusion

We have shown that the linearised description of the properties of a continuous laser beam is very versatile. By using a spectral description and considering individual frequency intervals, or channels, one by one we have a model which directly relates to the practical applications used in communications and sensing. We can express the properties of light in the format of noise spectra which correspond directly to the measurements with a spectrum analyser or RF mixer. Quantum transfer functions are derived which show how the signals and the noise propagate through optical systems, where additional noise is coupled in. Using these equations we can analyse and optimise

our experiments. The quantum noise transfer functions are a very practical representation of the quantum optical principles.

For very large signals, well above the quantum noise limit, our results correspond exactly to those derived with a fully classical model, as used in many engineering textbooks. However, this approach includes all quantum properties of the light, in particular the effects of losses and imperfections of the equipment. The full quantum transfer functions are essential in situations where nonclassical or squeezed light is used. Engineers will see the need to use these model once the performance of the practical systems approach the quantum noise limit. Our model includes the description of quantum information within the different channels. This fact will prove to be essential once applications of quantum information appear in practice. Presently ideas such as teleportation, cryptography, dense coding are being demonstrated only in rather complex and difficult experiments. But further advances of technology will allow us to explore robust applications of these ideas.

Care has to be taken in some situations where several optical modes are present, that means that we have several carrier frequencies. The noise due to the interaction of all these carriers with their respective sidebands contribute to the measured signal. The most prominent case is diode lasers. They frequently operate in many modes and even if the intensity in these modes is almost undetectable the modes can contribute to the noise spectrum. This is particularly important for lasers which are operated with very quiet currents in order to produce optical noise below the standard quantum limit. It was demonstrated that the noise suppression is distributed over many modes and can only be observed when all mode are equally well detected [33]. The interaction and correlation between the different modes has to be taken into account [34].

Our model is valid for continuous beams with large fluxes of photons that can be converted into detectable photon currents. This model also applies to pulse trains, where each pulse contains many photons, such as the output of strong modelocked lasers or beams containing soliton pulses. Applications with beams that contain very few photons and use single photon detection require a very different model. The detection systems allows the detection of correlations between the events being measured. For example, instead of squeezing, nonclassical properties of the second order correlation coefficient $g^{(2)}(\tau)$ are observed. An overview about this field is given by Mandel and Wolf [35]. For technical applications single photon systems are not used very often, but most of the demonstrations of quantum properties of photons and more recently, the demonstration of optical quantum information were carried out in the single photon regime.

Very recently, alternative detection schemes for laser beams have been proposed which combine CW and single photon detection. The photocurrent is analysed in conjunction, and conditional on the detection of individual photons by a second detector. Such a system cannot be described by the linear approach described here. This approach shows a very strong response to squeezed light as recently predicted by Carmichael [36] and observed by Orozco [37]. This type of detection is required in the search for systems that are so strongly nonlinear that they cannot be described by the linearisation and lead to the measurement of more curious Q- and Wigner functions than described here. Recently, first experimental results were reported by Hansen et al. [38]. We can expect more of these results, which are important from a fundamental point of view but are not directly addressing the question of practical signal sensing and communication.

Acknowledgments

This article reviews the outcome of a long and very productive collaboration which started (for HAB) in 1986 with Marc Levenson and Dan Walls and continued with collaboration with many great colleagues. Here we summarise ideas and innovations made by many of our colleagues in particular, Ping-Koy Lam, Andrew White, Elanor Huntington, Ben Buchler, Charles Harb, Matthew Taubman, David McClelland, Gerd Leuchs, Claude Fabre, Philip Grangier, Juergen Mlynek and many others. This work has been financially well supported by the Australian Research Council.

References

1. D. Walls, G. Milburn: *Quantum Optics* (Springer, Berlin 1994)
2. M. Scully, M.S. Zubairy: *Quantum Optics* (Cambridge University Press, Cambridge 1997)
3. H.J. Kimble: Physics Reports **219**, 227 (1992)
4. C. Fabre: *Quantum Fluctuations in Light Beams*, Les Houches, Session LXIII 1995 (Elsevier, Amsterdam 1997)
5. H.-A. Bachor: *A Guide to Experiments in Quantum Optics* (Wiley, New York 1998)
6. C. Gardiner: *Quantum Noise* (Springer, Berlin 1985)
7. J.W. Wu, P.K. Lam, M. Gray, H.-A. Bachor: Optics Express **3**, 154 (1998)
8. H.P. Yuen, J.H. Shapiro: Opt. Lett. **4**, 334 (1979)
9. C. Fabre: Physics Reports **219**, 215 (1992)
10. P. Grangier: Nature **396**, 537 (1998)
11. T.C. Ralph, C.C. Harb, H.-A. Bachor: Phys. Rev. A **54**, 4370 (1996)
12. M.D. Levenson, R.M. Shelby, S.H. Perlmutter: Opt. Lett. **10**, 514 (1985)
13. L.-A. Wu, M. Xiao, H.J. Kimble: J. Opt. Soc. Am. B **4**, 1465 (1987)
14. M. Xiao, L.-A. Wu, H.J. Kimble: Phys. Rev. Lett. **59**, 278 (1987)
15. E.S. Polzik, J. Carri, H.J. Kimble: Appl. Phys. B **55**, 279 (1992)

16. R. Bruckmeier, H. Hansen, S. Schiller, J. Mlynek: Phys. Rev. Lett. **79**, 43 (1997)
17. P.K. Lam, T.C. Ralph, B.C. Buchler, D.E. McClelland, H.-A. Bachor, J. Gao: J. Opt. B: Qu. Semicl. Optics **1**, 469 (1999)
18. B. Buchler: ANU, private communication (June 2000)
19. K. Schneider, M. Lang, J. Mlynek, S. Schiller: Optics Express **2**, 64 (1998)
20. A. Heidmann, R.J. Horowicz, S. Reynaud, E. Giacobino, C. Fabre: Phys. Rev. Lett. **59**, 2555 (1987)
21. J. Mertz, T. Debuisschert, A. Heidmann, C. Fabre, E. Giacobino: Opt. Lett. **16**, 1234 (1991)
22. K. Peng: J. Phys. D: Appl. Phys. **30**, 1588 (1997)
23. T.J. Kane: IEEE Photon. Technol. Lett. **2**, 244 (1990)
24. C.C. Harb, M.B. Gray, H.-A. Bachor, R. Schilling, P. Rottengatter, I. Freitag, H. Welling: IEEE Jour. Quant. Elect. **30**, 2907 (1994)
25. A.V. Masalov, A.A. Putilin, M.V. Vasilyev: J. Mod. Opt. **41**, 1941 (1994)
26. P.K. Lam, T.C. Ralph, E.H. Huntington, H.-A. Bachor: Phys. Rev. Lett. **79**, 1471 (1997)
27. C.H. Bennett, G. Brassard, A.K. Ekert: Scientific American **10**, 50 (1992)
28. T.C. Ralph: Phys. Rev. A **61**, 010302(R) (2000)
29. L.Vaidman: Phys. Rev. A **49**, 1473 (1994)
30. S.L. Braunstein, H.J. Kimble: Phys. Rev. Lett. **80**, 869 (1998)
31. T.C. Ralph, P.K. Lam: Phys. Rev. Lett. **81**, 5668 (1998)
32. A. Furusawa, J.L. Serensen, S.L. Braunstein, C.A. Fuchs, H.J. Kimble, E.S. Polzik: Science **282**, 706 (1998)
33. F. Marin, A. Bramati, E. Giacobino, T.-C. Zhang, J.-Ph. Poizat, J.F. Roch, P. Grangier: Phys. Rev. Lett. **75**, 4606 (1995)
34. S. Inoue, H. Ohzu, S. Machida, Y. Yamamoto: Phys. Rev. A **46**, 2757 (1992)
35. L. Mandel, E. Wolf: *Optical Coherence and Quantum Optics* (Cambridge University Press, Cambridge 1995)
36. H.J. Carmichael, H.M. Castro-Beltran, G.T. Foster, L.A. Orozco: 'Giant Violations of Classical Inequalities Through Conditional Homodyne Detection of the Quadrature Amplitudes of Light', Phys. Rev. Lett. to be published
37. G.T. Foster, L.A. Orozco, H.M. Castro-Beltran, H.J. Carmichael: 'Quantum State Reduction and Conditional Time Evolution of Wave-Particle Correlations in Cavity QED', unpublished
38. H. Hansen, T. Aichele, A.I. Lvovsky, P. Lohdahl, O. Benson, S. Schiller, J. Mlynek: private communication (March 2000)

Self-Consistency of Thermal Jump Trajectories

Y.-T. Chough and H.J. Carmichael

Summary. It is problematic to interpret the quantum jumps of an atom interacting with thermal light in terms of counts at detectors monitoring the atom's inputs and outputs. As an alternative, we develop an interpretation based on a self-consistency argument. We include one mode of the thermal field in the system Hamiltonian and describe its interaction with the atom by an entangled quantum state while assuming that the other modes induce quantum jumps in the usual fashion. In the weak-coupling limit, the photon number expectation of the selected mode is also seen to execute quantum jumps, although more generally, for stronger coupling, Rabi oscillations are observed; the equilibrium photon number distribution is a Bose-Einstein distribution. Each mode may be viewed in isolation in a similar fashion, and summing over their weak-coupling jump rates returns the net jump rates for the atom assumed at the outset.

1 Introduction

The notion of a quantum jump entered physics with Bohr's model of the atom and was elaborated in a semi-quantitative formulation in Einstein A and B theory [1]. It was, from the beginning, an idea at variance with the usual commitment to a continuous time evolution and with the continuous constitution of light as an electromagnetic wave. The appearance of the Schrödinger equation relieved the situation somewhat, but ultimately, through the use of perturbation theory to make testable predictions about quantum scattering processes, the quantum jump remains with us, though certainly in a more sophisticated and mathematically refined form.

The Monte-Carlo wavefunction and quantum trajectory methods developed in quantum optics [2–4] use quantum jumps as an explicit component of a stochastic time evolution in a manner very reminiscent of Einstein A and B theory. In fact, the only novelty is to combine Einstein's rules for quantum jumps with a coherent evolution between jumps that admits a dynamic involving superpositions of stationary states. In this, these methods achieve something remarkably similar to the proposal of Bohr, Kramers, and Slater (BKS) [5,6] for uniting discontinuous jumps among the stationary states of a material system with a continuous evolution between jumps, during which time material oscillators, possessing coherent amplitudes, are brought into play.

The realistic interpretation sought by BKS may not, however, be entertained. In most circumstances, an interpretation of the jumps employed in quantum trajectory theory is based upon a record of time-resolved photon counts which might be realized in practice by terminating every output channel in a photodetector [4,7].

H.J. Carmichael, R.J. Glauber, M.O. Scully (Eds.): LNP 561, pp. 333–346, 2001.

This scenario is plausible because optical frequencies are sufficiently high that scattered photons can be detected against an essentially vacuum-state background. The measurement-based interpretation is problematic, though, for an atom exchanging photons with a thermal environment. In this situation, incoherent photons are both emitted *and* absorbed; moreover, it is impossible to distinguish a scattered photon from some other photon in the environment. Of course, schemes such as electron shelving exist that are able to monitor thermal quantum jumps [8–10]. They, however, make intrusive measurements by utilizing strong couplings to other inputs and outputs, and are not a suitable foundation for the interpretation of quantum trajectory equations. The relationship, in fact, is exactly the reverse; electron shelving is one of the measurement schemes that quantum trajectories would propose to explain.

In this paper we follow a different direction to give substance, beyond a mere assertion, to the interpretation that an atom exchanging photons with a thermal environment does, in some well-defined sense, execute jumps. We define the sense through a self-consistency argument. Contrary to the notion of quantum jumps, quantum mechanics continuously entangles two interacting systems through the Schrödinger evolution. We show that a single mode, selected from the many modes of a thermal environment, and allowed to evolve in interacting with an atom to produce such an entanglement, is, in fact, seen to undergo jumps in its photon number expectation if it is assumed that all other modes of the environment, treated collectively as a reservoir, induce jumps between the atomic states according to the rules of Einstein theory. The jump evolution for the selected mode emerges from an otherwise continuous evolution in the weak-coupling limit. Thus, assuming jumps induced by the reservoir as a whole leads, self-consistently, to the appearance of jumps in an individual mode of the reservoir when that mode is allowed to entangle with the atom *via* the standard interaction Hamiltonian and Schrödinger evolution. The jumps do bring the individual mode to a Bose-Einstein distribution over photon number, and the jump rates, derived for every mode viewed individually in this way, sum to net rates which agree with Einstein A and B theory.

The underlying theme of this paper is the conflict between a continuous and a discontinuous quantum evolution and the self-consistency of the two in the perturbative weak-coupling limit. In Sect. 2 we therefore briefly review the quantum jump model of Einstein, the BKS proposal to include a continuous evolution, and the quantum trajectory realization of the latter. The argument for the self-consistency of thermal jump trajectories is elaborated in Sect. 3.

2 Einstein *A* and *B* Theory, BKS, and Quantum Trajectories

2.1 Thermal Quantum Jumps

We consider the single two-state atom illustrated in Fig. 1, in thermal equilibrium with Planck radiation at temperature T. In Einstein A and B theory photons are exchanged between the atom and the radiation field as the atom jumps randomly between its two stationary states. The jump rates follow a prescription taking into

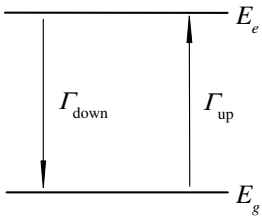

Fig. 1. Thermal quantum jumps in Einstein A and B theory. The jump rates are defined in (1a) and (1b).

account spontaneous emission, stimulated emission, and absorption, with [1]

$$\Gamma_{\text{down}} = A + B\sigma(\omega_0) \,, \tag{1a}$$
$$\Gamma_{\text{up}} = B\sigma(\omega_0) \,, \tag{1b}$$

where

$$\sigma(\omega_0) = \bar{n}(\omega_0)\hbar\omega_0[\rho(\omega_0)/V] \tag{2}$$

is the energy density of the radiation field at the resonance frequency ω_0 of the atom, with average photon number per mode

$$\bar{n}(\omega_0) = [e^{\hbar\omega_0/k_BT} - 1]^{-1} \tag{3}$$

and mode density (in volume V)

$$\rho(\omega_0) = \frac{\omega_0^2 V}{\pi^2 c^3} \,, \tag{4}$$

and the Einstein A and B coefficients must satisfy

$$\frac{B}{A} = \frac{\pi^2 c^3}{\hbar\omega_0^3} \tag{5}$$

in order for the atom to be brought into thermal equilibrium with the radiation.

With the help of the relationship (5), we write (1a) and (1b) in the modern notation

$$\Gamma_{\text{down}} = A[\bar{n}(\omega_0) + 1] \,, \tag{6a}$$
$$\Gamma_{\text{up}} = A\bar{n}(\omega_0) \,. \tag{6b}$$

Einstein theory does not assign a value to the coefficient A. From quantum mechanics, however, using Fermi's Golden rule we obtain

$$A = 2\pi \sum_{\lambda} \int d\Omega \, \rho(\omega_0) |\kappa_{\lambda,\hat{\boldsymbol{n}}}(\omega_0)|^2 \, , \tag{7}$$

where

$$|\kappa_{\lambda,\hat{\boldsymbol{n}}}(\omega_0)| = \sqrt{\frac{\omega_0}{2\pi\epsilon_0 V}} |\hat{e}_{\lambda,\hat{\boldsymbol{n}}} \cdot \boldsymbol{d}_{eg}| \tag{8}$$

is the dipole coupling strength to a mode of the radiation field with polarization λ and direction of propagation specified by the unit vector $\hat{\boldsymbol{n}}$ (polarization vector $\hat{e}_{\lambda,\hat{\boldsymbol{n}}}$); $\boldsymbol{d}_{eg}$ is the atomic dipole matrix element.

Commonly, Einstein theory is discussed at the level of rate equations for the occupation probabilities of the atomic stationary states. The theory does, however, define a stochastic process – one that may be visualized in terms of quantum jumps whose occurrences unfold randomly in time. With each realization of the stochastic process we associate a record of jump types and jump times,

$$\mathrm{REC} \equiv \begin{Bmatrix} \dots & \Gamma_{\mathrm{down}} & \Gamma_{\mathrm{up}} & \Gamma_{\mathrm{down}} & \Gamma_{\mathrm{up}} & \Gamma_{\mathrm{down}} & \dots \\ \dots & t+\tau_1 & t+\tau_2 & t+\tau_3 & t+\tau_4 & t+\tau_5 & \dots \end{Bmatrix} . \tag{9}$$

In Fig. 2 we illustrate the discontinuous evolution of the atom in coordination with its absorption and emission of thermal photons.

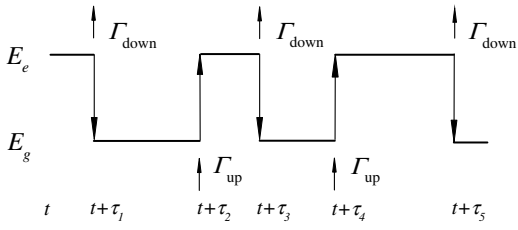

Fig. 2. Sample realization of the Einstein stochastic process. The corresponding record is defined in (9).

2.2 Coherence: The BKS Proposal

Although Bohr had himself put forward the notion of a quantum jump to explain the association of stationary-state energy differences with electromagnetic wave frequencies in his model of the hydrogen atom, he became quite dissatisfied with the idea in the concrete form it acquired under Einstein's proposal. It was the

light quantum, specifically, that troubled him the most. Bohr insisted that since so many optical phenomena rely on the continuity of coherent waves, the wave nature of light simply could not be dismissed. He recognized, on the other hand, that a discontinuous process was definitely needed to account for light emission and detection. What he was unavoidably drawn towards, then, was some sort of merging of the two ideas.

A program to accomplish this was outlined in what has come to known as the BKS proposal [5,6]. The central idea of this proposal is the proposition that during the residence times in a stationary state, represented by the horizontal lines in Fig. 2, an atom is not inactive in its interaction with the electromagnetic field; rather, it acts through a coherent dipole radiator, or "virtual oscillator" in the words of BKS, which is all the time radiating an electromagnetic wave of frequency $\omega_0 = (E_e - E_g)/\hbar$. This wave is either in phase or out of phase with the external radiation at frequency ω_0 depending on whether the residence is in the stationary state with energy E_e or E_g. Thus, there is an energy transfer under the laws of classical electrodynamics either to the electromagnetic field from the dipole, or in the reverse direction, depending on the stationary state [11]. Clearly a double counting of the exchanged energy occurs if one accepts that light quanta are also emitted and absorbed at the times of the jumps. However, the goal was precisely to eliminate these quanta, although still permitting the atom to jump. BKS attempted, thus, to retain, but keep separate, two incompatible mechanisms for energy exchange – a wave (continuous) mechanism for the absorption and emission of radiation and a particle (discontinuous) mechanism for the change of material state energies. Their proposal foundered on its obvious violation of energy conservation at the level of the individual quantum events, a feature that appeared not to be supported in Compton scattering experiments [12,13].

2.3 Coherence: Quantum Trajectories

In retrospect we can see that Bohr had in mind a conception of light that, although supported by numerous wave phenomena in optics, was largely inappropriate for the light sources available at the time. Radiators in thermal equilibrium are not sources of coherent waves. They radiate electromagnetic noise, which, with filtering, can approximate *low intensity* light possessing first-order coherence, but is very far from the classical concept of a coherent wave of large and adjustable amplitude. Modern lasers, however, emit something close to the classical ideal. In their case, the high coherence, if it is to be preserved, disallows the tracking of energy at the level of the individual quanta, so that the energy conservation argument against the BKS proposal does not apply.

Quantum trajectory theory is designed to deal with problems involving the interaction of matter with the high coherence light sources available in modern laboratories. It shows remarkable similarities to the BKS proposal. These are described elsewhere [14,15], and we do not plan to discuss them in any depth here. As an introduction to our main topic, however, itm is useful to contrast Einstein A and B theory with the quantum trajectory description of a coherent field, amplitude $\mathcal{E}$, resonantly exciting the two-state atom of Fig. 1. The connections with BKS emerge automatically through this exercise.

The atom is still located in a thermal environment and quantum jumps still appear as they do in Fig. 2 – but with one notable modification. Due to the induced

coherence, it is necessary that the system state be a superposition of the stationary states $|E_e\rangle$ and $|E_g\rangle$, which we denote by $|\psi_{\rm REC}(t)\rangle$. As suggested by BKS, there is a coherent interaction with the electromagnetic field between the quantum jumps. This we account for by a continuous evolution under the Schrödinger equation [2–4] (for the unnormalized conditional state)

$$\frac{d|\bar{\psi}_{\rm REC}\rangle}{dt} = \frac{1}{i\hbar}\hat{H}_B|\bar{\psi}_{\rm REC}\rangle \,, \tag{10}$$

with non-Hermitian Hamiltonian

$$\begin{aligned}\hat{H}_B = {} & \tfrac{1}{2}\hbar(\omega_0 - i\Gamma_{\rm down})|E_e\rangle\langle E_e| - \tfrac{1}{2}\hbar(\omega_0 + i\Gamma_{\rm up})|E_g\rangle\langle E_g| \\ & + i\hbar\mathcal{E}(e^{i\omega_0 t}|E_g\rangle\langle E_e| - e^{-i\omega_0 t}|E_e\rangle\langle E_g|) \,,\end{aligned} \tag{11}$$

in which the external coherent field is classical, and its interaction with the atom is treated in the dipole and rotating-wave approximations. The quantum jumps are governed by the probabilistic rules of Einstein A and B theory, generalized, in a natural way, to account for the fact that the system at any time is not definitely in a particular stationary state. There are jumps

$$|\bar{\psi}_{\rm REC}\rangle \overset{\Gamma_{\rm down}}{\rightarrow} (|E_g\rangle\langle E_e|)|\bar{\psi}_{\rm REC}\rangle \,, \tag{12a}$$

$$|\bar{\psi}_{\rm REC}\rangle \overset{\Gamma_{\rm up}}{\rightarrow} (|E_e\rangle\langle E_g|)|\bar{\psi}_{\rm REC}\rangle \,, \tag{12b}$$

with jump rates

$$R_{\rm down} = \Gamma_{\rm down}|\langle E_e|\psi_{\rm REC}\rangle|^2 \,, \tag{13a}$$

$$R_{\rm up} = \Gamma_{\rm up}|\langle E_g|\psi_{\rm REC}\rangle|^2 \,. \tag{13b}$$

Figure 3 illustrates how realizations of this stochastic process appear. In (a) the coherent excitation is relatively weak and the overall form of the evolution remains close to that produced by the Bohr-Einstein quantum jumps (Fig. 2). There is, however, in addition to the switching of the energy, a weak induced coherence carried along by the continuous evolution between jumps as a nonvanishing polarization amplitude, quite reminiscent of the BKS virtual oscillator. In Fig. 3(b) the coherent excitation is much stronger. Here, the dominant mechanism for evolution between the stationary states is a coherent Rabi oscillation; we move to a coherent evolution that is nonperturbative and a regime which only became accessible with the invention of the laser. This, specifically, is a form of evolution following from the Schrödinger equation; *nonperturbative* coherence was not anticipated by the BKS proposal. We might note in passing that lasing without inversion and related phenomena acquire their counterintuitive features from such nonperturbative coherence [14].

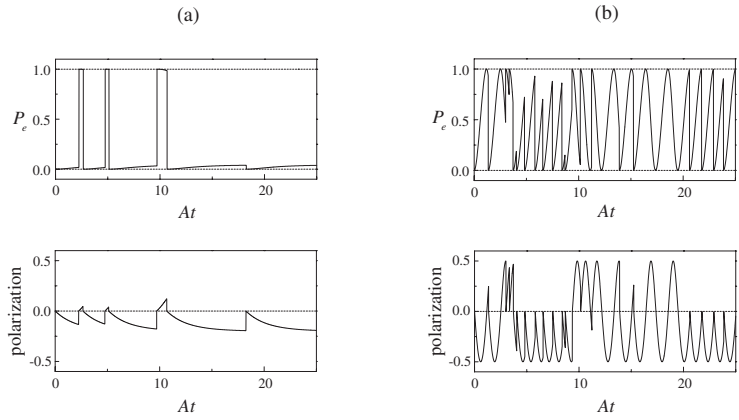

Fig. 3. Sample quantum trajectories with both thermal jumps and induced coherence: $\bar{n}(\omega_0) = 0.25$, $\mathcal{E}/A = 0.1$ and 1.5 [(**a**) and (**b**)].

3 Self-Consistency of Thermal Quantum Jumps

At a sufficiently low temperature, when $\bar{n}(\omega_0) \ll 1$, the jump record that labels the state can reasonably be made by detectors monitoring the scattered light. Almost all jumps will be down-jumps governed by the spontaneous emission rate A which may be identified with emitted photons counted as isolated (in space and time) excitations of the vacuum. For many applications in quantum optics this is the situation in reality. Nonetheless, the thermal jumps, though they might be negligible in practice, cannot be set aside from a fundamental point of view. Considering then those jumps which cannot reasonably be identified with the "click" of a detector, is there any other justification for returning to the language of the old quantum theory, given that, in quantum mechanics, the Schrödinger equation invokes only a continuous evolution? We aim to show that there is, in so far as the jumps are self-consistent – consistent with the Schrödinger evolution – in the weak-coupling limit.

3.1 Trajectories for a Single Field Mode

The Hamiltonian for a two-state atom interacting with the radiation field of a thermal environment (we now take $\mathcal{E} = 0$) is

$$\hat{H} = \tfrac{1}{2}\hbar\omega_0|E_e\rangle\langle E_e| - \tfrac{1}{2}\hbar\omega_0|E_g\rangle\langle E_g| + \sum_{\lambda',\hat{\boldsymbol{n}}',\omega'} \hbar\omega' \hat{r}^{\dagger}_{\lambda',\hat{\boldsymbol{n}}',\omega'} \hat{r}_{\lambda',\hat{\boldsymbol{n}}',\omega'}$$

$$+\sum_{\lambda',\hat{\boldsymbol{n}}',\omega'}\hbar[\kappa_{\lambda',\hat{\boldsymbol{n}}'}(\omega')|E_e\rangle\langle E_g|\hat{r}_{\lambda',\hat{\boldsymbol{n}}',\omega'}+\text{H.c.}]\,, \tag{14}$$

where $\hat{r}^{\dagger}_{\lambda,\hat{\boldsymbol{n}},\omega}$ and $\hat{r}_{\lambda,\hat{\boldsymbol{n}},\omega}$ are creation and annihilation operators for the field mode with polarization λ, propagation direction $\hat{\boldsymbol{n}}$, and frequency ω, and $\kappa_{\lambda,\hat{\boldsymbol{n}}}(\omega)$ is the mode coupling coefficient whose magnitude is defined in (8). The stochastic process (10)–(13b) ($\mathcal{E}=0$) is developed, formally, around the master equation derived from (14) [2–4]. This master equation describes the quantum state of the atom alone, after tracing over every mode of the radiation field. Our idea is to raise one mode of the field to the same status as the atom by including it, along with its interaction with the atom, in the system Hamiltonian. All other modes are to be treated as a reservoir as before and their interaction with the atom described by quantum jumps. The stochastic process is the same as in (10)–(13b), but with the non-Hermitian Hamiltonian $\hat{H}_B$ replaced by

$$\begin{aligned}\hat{H}_B = {} & \tfrac{1}{2}\hbar(\omega_0-i\Gamma_{\text{down}})|E_e\rangle\langle E_e| - \tfrac{1}{2}\hbar(\omega_0+i\Gamma_{\text{up}})|E_g\rangle\langle E_g| \\ & +\hbar\omega\hat{r}^{\dagger}_{\lambda,\hat{\boldsymbol{n}},\omega}\hat{r}_{\lambda,\hat{\boldsymbol{n}},\omega} \\ & +\hbar[\kappa_{\lambda,\hat{\boldsymbol{n}}}(\omega)|E_e\rangle\langle E_g|\hat{r}_{\lambda,\hat{\boldsymbol{n}},\omega}+\text{H.c.}]\,.\end{aligned} \tag{15}$$

Of course removing one mode from the reservoir has no effect on the overall jump rates for the atom. The change is that we can now follow the evolution of an explicit Hilbert space vector for the selected mode, one that entangles this mode with the atom. We ask how does the selected mode evolve in the Hilbert space; in particular, does it also experience quantum jumps?

Figures 4 and 5 show sample trajectories for the selected-mode photon number expectation [16] – for a series of decreasing coupling strengths, (a)–(d), and assuming resonance with the atom, Fig. 4, and a detuning from the atom, Fig. 5. With the coupling strong compared to the Einstein A coefficient coherent Rabi oscillations are seen. There are also discontinuous changes, which in the case of strong coupling are merely a direct manifestation of the assumed quantum jumps for the atom. Note, however, that the atom does not jump monotonously, "up" then "down" then "up" $\cdots$, as in Fig. 2; repeated up-jumps can transfer many energy quanta to the field mode. At an intermediate coupling strength, partial Rabi oscillations are still present. Once the coupling becomes weak, though, the Rabi oscillations apparently disappear altogether, and an entirely new kind of jump evolution sets in. These jumps proceed at a rate far less than the overall jump rate for the atom. Their rate decreases with the square of the coupling constant [(c) to (d)] and also when the detuning is increased (from Fig. 4 to Fig. 5).

Having, then, assumed jumps for the atom in interaction with all but one of the field modes, a jump evolution for the one remaining mode emerges naturally in the weak-coupling limit. We close the self-consistent loop by showing that the one mode samples a Bose-Einstein distribution, and by calculating the rate of the single-mode jumps, to demonstrate that sum over modes returns the rates Γ_{up} and Γ_{down}.

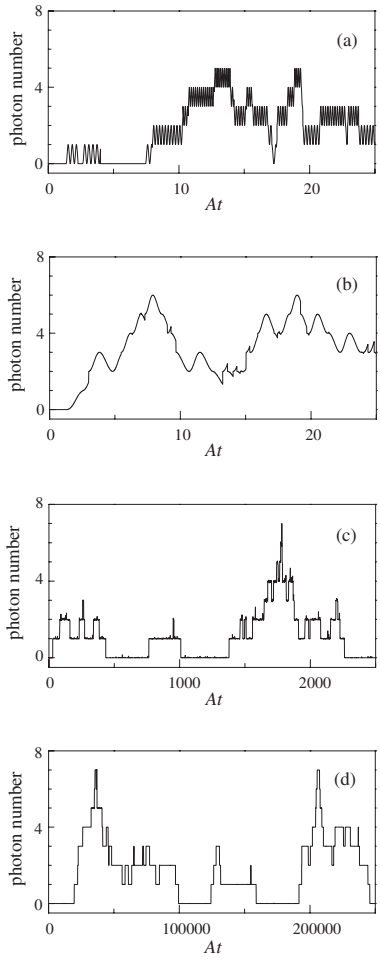

Fig. 4. Sample trajectories for the photon number expectation of a single field mode included as part of the system. The mode is resonant: $\Delta\omega/A = 0$, $\bar{n}(\omega_0) = 1$, and $|\kappa_{\lambda,\hat{\boldsymbol{n}}}(\omega_0)|/A = 10$, 1.0, 0.1, and 0.01 [(**a**), (**b**), (**c**), and (**d**)].

3.2 Self-Consistency

Let us denote the number of energy quanta shared between the atom and the field mode at time t by $n_\omega + 1$. Let t_k be the time of the very last jump of the atom and t_{k+1} be the time of the jump that is to occur next. Then, for $t_k < t < t_{k+1}$, the entangled state of the atom and field mode may be expanded as

$$|\bar{\psi}_{\mathrm{REC}}(t)\rangle = \bar{C}_{e|i}(t)|E_e\rangle|n_\omega\rangle + \bar{C}_{g|i}(t)|E_g\rangle|n_\omega + 1\rangle \ , \tag{16}$$

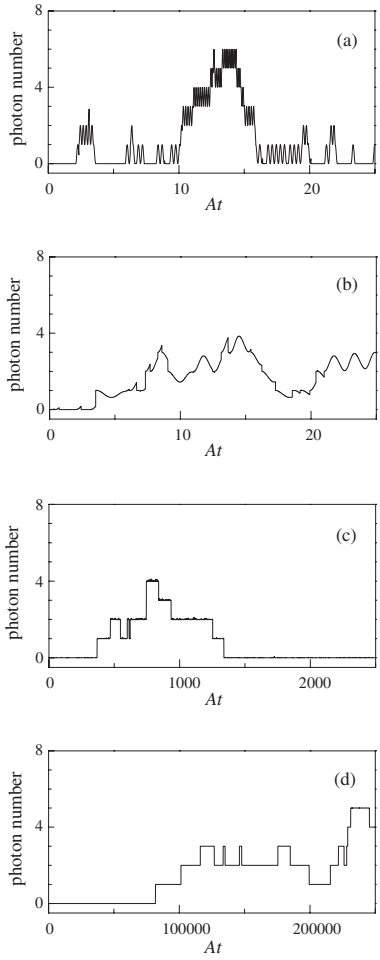

Fig. 5. Sample trajectories for the photon number expectation of a single field mode included as part of the system. The mode is non-resonant: $\Delta\omega/A = 2.0$, $\bar{n}(\omega_0) = 1$, and $|\kappa_{\lambda,\hat{\boldsymbol{n}}}(\omega)|/A = 10,\ 1.0,\ 0.1,$ and 0.01 [(**a**), (**b**), (**c**), and (**d**)].

with $\bar{C}_{e|i}(0) = \delta_{e,i}$ and $\bar{C}_{g|i}(0) = \delta_{g,i}$, where i is e or g for an up- or down-jump at t_k, respectively. Writing

$$\bar{C}_{e|i}(t) = e^{-i(n_\omega + \frac{1}{2})\omega t} e^{i\frac{1}{2}\phi_{\hat{\boldsymbol{n}}}(\omega)} \tilde{C}_{e|i}(t)\ , \tag{17a}$$

$$\bar{C}_{g|i}(t) = e^{-i(n_\omega + \frac{1}{2})\omega t} e^{-i\frac{1}{2}\phi_{\hat{\boldsymbol{n}}}(\omega)} \tilde{C}_{g|i}(t)\ , \tag{17b}$$

with $\phi_{\hat{\boldsymbol{n}}}(\omega) \equiv \arg[\kappa_{\lambda,\hat{\boldsymbol{n}}}(\omega)]$, from (10) and (15), the equations of motion for the conditional state amplitudes are

$$\frac{d\tilde{C}_{e|i}}{dt} = -\tfrac{1}{2}(\Gamma_{\rm down} - i\Delta\omega)\tilde{C}_{e|i} - i|\kappa_{\lambda,\hat{\boldsymbol{n}}}(\omega)|\sqrt{n_\omega + 1}\,\tilde{C}_{g|i}\ , \tag{18a}$$

$$\frac{d\tilde{C}_{g|i}}{dt} = -\tfrac{1}{2}(\Gamma_{\rm up} + i\Delta\omega)\tilde{C}_{g|i} - i|\kappa_{\lambda,\hat{\boldsymbol{n}}}(\omega)|\sqrt{n_\omega + 1}\,\tilde{C}_{e|i}\ . \tag{18b}$$

Consider now the case of an up-jump at t_k, such that the initial state amplitudes are $\bar{C}_{e|i}(0) = 1$ and $\bar{C}_{g|i}(0) = 0$. For weak coupling we will have $\bar{C}_{e|i}(t) \approx 1$ and $\bar{C}_{g|i}(t) \sim |\kappa_{\lambda,\hat{\boldsymbol{n}}}(\omega)|$, with an overwhelming probability that the next jump of the atom will be a down-jump. By a similar argument, it is highly likely that the down-jump is followed by another up-jump; the most probable progression is then "up", "down", "up", ..., just as we illustrated it in Fig. 2 (notice that the number n_ω is unchanged throughout such a progression). Due, however, to the small amplitude – either $\bar{C}_{g|i}(t) \sim |\kappa_{\lambda,\hat{\boldsymbol{n}}}(\omega)|$ or $\bar{C}_{e|i}(t) \sim |\kappa_{\lambda,\hat{\boldsymbol{n}}}(\omega)|$ – excited by the coupling of the atom to the selected mode, there is always a small probability that a jump will occur to break the alternating sequence. An up-jump might be followed by a second up-jump or two down-jumps might occur in a row. These events change n_ω and produce the jumps of the field mode seen in Figs. 4 and 5. In Figs. 4(c) and 5(c), the presence of the small amplitude that underlies the jump mechanism is still seen as a "fuzz" on top of the developing smooth curve. The"fuzz" is even present in Figs. 4(d) and 5(d), though there is it too small there to be visible.

The physical interpretation of the anomalous events in the jump record of the atom is that each represents the scattering of a photon between one of the many field modes of the reservoir and the field mode selected to be viewed. Two up-jumps occur in a row for example, because, in the interval between them, the energy absorbed on the first jump is transferred to the selected mode; the quantum trajectory resolves the transfer at the time of the second up-jump.

Our task now is to calculate rates for the unlikely jumps. We do this using the method of Sect. IVD in [14]. The equations of motion (18a) and (18b) give

$$\frac{d|\tilde{C}_{e|i}|^2}{dt} = -\Gamma_{\rm down}|\tilde{C}_{e|i}|^2 - 2|\kappa_{\lambda,\hat{\boldsymbol{n}}}(\omega)|\sqrt{n_\omega + 1}\,{\rm Im}(\tilde{C}_{e|i}\tilde{C}^*_{g|i})\ , \tag{19a}$$

$$\frac{d|\tilde{C}_{g|i}|^2}{dt} = -\Gamma_{\rm up}|\tilde{C}_{g|i}|^2 + 2|\kappa_{\lambda,\hat{\boldsymbol{n}}}(\omega)|\sqrt{n_\omega + 1}\,{\rm Im}(\tilde{C}_{e|i}\tilde{C}^*_{g|i})\ , \tag{19b}$$

$$\frac{d{\rm Re}(\tilde{C}_{e|i}\tilde{C}^*_{g|i})}{dt} = -\tfrac{1}{2}(\Gamma_{\rm down} + \Gamma_{\rm up}){\rm Re}(\tilde{C}_{e|i}\tilde{C}^*_{g|i}) - \Delta\omega{\rm Im}(\tilde{C}_{e|i}\tilde{C}^*_{g|i})\ , \tag{19c}$$

$$\begin{aligned}\frac{d{\rm Im}(\tilde{C}_{e|i}\tilde{C}^*_{g|i})}{dt} = &-\tfrac{1}{2}(\Gamma_{\rm down} + \Gamma_{\rm up}){\rm Im}(\tilde{C}_{e|i}\tilde{C}^*_{g|i}) + \Delta\omega{\rm Re}(\tilde{C}_{e|i}\tilde{C}^*_{g|i}) \\ &+|\kappa_{\lambda,\hat{\boldsymbol{n}}}(\omega)|\sqrt{n_\omega + 1}\,(|\tilde{C}_{e|i}|^2 - |\tilde{C}_{g|i}|^2)\ .\end{aligned} \tag{19d}$$

We define

$$W_e \equiv \int_{t_k}^{\infty} dt\, |\tilde{C}_{e|i}(t)|^2 \,, \qquad W_g \equiv \int_{t_k}^{\infty} dt\, |\tilde{C}_{g|i}(t)|^2 \,, \tag{20}$$

and

$$U \equiv \mathrm{Re}\left[\int_{t_k}^{\infty} dt\, \tilde{C}_{e|i}(t)\tilde{C}^*_{g|i}\right] \,, \qquad V \equiv \mathrm{Im}\left[\int_{t_k}^{\infty} dt\, \tilde{C}_{e|i}(t)\tilde{C}^*_{g|i}\right] \,, \tag{21}$$

where $\Gamma_{\rm up}W_g$ and $\Gamma_{\rm down}W_e$ are the probabilities, given i is e and g, respectively, that the unlikely jump will occur. From the Laplace transforms of (19a) – (19d), we then have

$$-\delta_{e,i} = -\Gamma_{\rm down}W_e - 2|\kappa_{\lambda,\hat{\boldsymbol{n}}}(\omega)|\sqrt{n_\omega+1}\,V \,, \tag{22a}$$

$$-\delta_{g,i} = -\Gamma_{\rm up}W_g + 2|\kappa_{\lambda,\hat{\boldsymbol{n}}}(\omega)|\sqrt{n_\omega+1}\,V \,, \tag{22b}$$

$$0 = -\tfrac{1}{2}(\Gamma_{\rm down}+\Gamma_{\rm up})V + \Delta\omega U + |\kappa_{\lambda,\hat{\boldsymbol{n}}}(\omega)|\sqrt{n_\omega+1}\,(W_e - W_g) \,, \tag{22c}$$

$$0 = -\tfrac{1}{2}(\Gamma_{\rm down}+\Gamma_{\rm up})U - \Delta\omega V \,, \tag{22d}$$

and hence

$$\Gamma_{\rm up}W_g|_{i=e} = \frac{\frac{1}{2}(\Gamma_{\rm down}+\Gamma_{\rm up})/\pi}{\left[\frac{1}{2}(\Gamma_{\rm down}+\Gamma_{\rm up})\right]^2+(\Delta\omega)^2}\,\frac{2\pi|\kappa_{\lambda,\hat{\boldsymbol{n}}}(\omega)|^2}{\Gamma_{\rm down}}(n_\omega+1) \,, \tag{23a}$$

$$\Gamma_{\rm down}W_e|_{i=g} = \frac{\frac{1}{2}(\Gamma_{\rm down}+\Gamma_{\rm up})/\pi}{\left[\frac{1}{2}(\Gamma_{\rm down}+\Gamma_{\rm up})\right]^2+(\Delta\omega)^2}\,\frac{2\pi|\kappa_{\lambda,\hat{\boldsymbol{n}}}(\omega)|^2}{\Gamma_{\rm up}}(n_\omega+1) \,, \tag{23b}$$

where we have solved (22a)–(22d) to lowest order in the coupling strength.

Equations (23a) and (23b) specify the probability for the unlikely jump to occur following any preparation of the initial state i. To obtain photon-number jump rates, we must multiply by the rate at which the state i is prepared, i.e., by the jump rates for the atom; (23a) is multiplied by $\Gamma_{\rm up}p_e^{\rm eq}$ and (23b) by $\Gamma_{\rm down}p_g^{\rm eq}$, where $p_g^{\rm eq}$ and $p_e^{\rm eq}$ are the state occupation probabilities in thermal equilibrium. We also set $n_\omega = N_\omega$ in (23a) and $n_\omega + 1 = N_\omega$ in (23b), where N_ω is the photon number expectation plotted in Figs. 4 and 5 (recall that $n_\omega + 1$ is the number of quanta *shared* with the atom at t_k). The photon-number jump rates are then

$$\gamma_{N_\omega}^{\rm up} = \frac{\frac{1}{2}(\Gamma_{\rm down}+\Gamma_{\rm up})/\pi}{\left[\frac{1}{2}(\Gamma_{\rm down}+\Gamma_{\rm up})\right]^2+(\Delta\omega)^2}\,2\pi|\kappa_{\lambda,\hat{\boldsymbol{n}}}(\omega)|^2(N_\omega+1)\,p_e^{\rm eq} \,, \tag{24a}$$

$$\gamma_{N_\omega}^{\rm down} = \frac{\frac{1}{2}(\Gamma_{\rm down}+\Gamma_{\rm up})/\pi}{\left[\frac{1}{2}(\Gamma_{\rm down}+\Gamma_{\rm up})\right]^2+(\Delta\omega)^2}\,2\pi|\kappa_{\lambda,\hat{\boldsymbol{n}}}(\omega)|^2 N_\omega\,p_g^{\rm eq} \,. \tag{24b}$$

The self-consistency of the thermal jump picture is now easy to demonstrate. On the one hand, we use (24a) and (24b) to set up rate equations for the selected mode photon number and, using detailed balance, solve these in steady state. Hence, we obtain the equilibrium probability to find N_ω photons in the selected mode:

$$p_{N_\omega}^{\rm eq} = \left(1 - p_e^{\rm eq}/p_g^{\rm eq}\right)\left(\frac{p_e^{\rm eq}}{p_g^{\rm eq}}\right)^{N_\omega} = \left[\bar{n}(\omega_0)+1\right]^{-1}\left[\frac{\bar{n}(\omega_0)}{\bar{n}(\omega_0)+1}\right]^{N_\omega}, \tag{25}$$

where we have used $p_e^{\rm eq}/p_g^{\rm eq} = \Gamma_{\rm up}/\Gamma_{\rm down}$ and the Einstein formulas (6a) and (6b). We obtaine a Bose-Einstein distribution with average photon number $\bar{N}_\omega = \bar{n}(\omega_0)$; note that specific mode coupling strength and frequency affects only the rate of approach to equilibrium. Of course, in reality, each field mode couples to a vast number of two-state systems, and most strongly to those with which it is nearly resonant. For the realistic situation we would therefore find the expected $\bar{N}_\omega = \bar{n}(\omega)$, consistent with the Planck radiation formula.

On the other side we must demonstrate the self-consistency of the jump rates. To this end, we sum (24a) and (24b) over all modes (all λ, $\hat{\boldsymbol{n}}$, ω), with N_ω replaced by its average value, and neglecting the frequency dependence of the density of states and dipole coupling constant (in light of the Lorentzian resonance). The resulting jump rates for the gain and loss of photons by the thermal environment should equal the jump rates assumed initially for the atom. The sums do, indeed, return $\Gamma_{\rm down}\, p_e^{\rm eq}$ and $\Gamma_{\rm up}\, p_g^{\rm eq}$, showing that the net jump rates are in accord with the Einstein rules (6a) and (6b) and Fermi's golden rule, (7) and (8). This completes our demonstration that thermal jump trajectories are self-consistent.

Acknowledgments

This work was supported by the National Science Foundation under Grant No. PHY-9531218 and by a Research Award of the Alexander von Humboldt-Stiftung. HJC thanks Professor W. Schleich for his support and hospitality during his stay at the University of Ulm.

References

1. A. Einstein: Verh. Dtsch. Phys. Ges. **18**, 318 (1916); Phys. Z. **18**, 121 (1917). An English translation of the second paper appears in B.L. van der Waerden: *Sources of Quantum Mechanics* (North Holland, Amsterdam 1967), Chap. 1
2. J. Dalibard, Y. Castin, K. Mølmer: Phys. Rev. Lett. **68**, 580 (1992)
3. R. Dum, P. Zoller, H. Ritsch: Phys. Rev. A **45**, 4879 (1992)
4. H.J. Carmichael: *An Open Systems Approach to Quantum Optics*, Lecture Notes in Physics: New Series m: Monographs, Vol. M18 (Springer, Berlin, Heidelberg 1993)
5. N. Bohr, H.A. Kramers, J.C. Slater: Philos. Mag. **47**, 785 (1924); Z. Phys. **24**, 69 (1924)
6. J.C. Slater: Nature (London) **113**, 307 (1924)

7. H.J. Carmichael: 'Quantum Jumps Revisited: An Overview of Quantum Trajectory Theory'. In: *Quantum Future: From Volta and Como to the Present and Beyond*, Proceedings of the Xth Max Born Symposium, Przesieka, Poland, 24–27 September, 1997. ed. by Ph. Blanchard and A. Jadczyk (Springer, Berlin, Heidelberg 1999) pp. 15–36
8. W. Nagourney, J. Sandberg, H. Dehmelt: Phys. Rev. Lett. **56**, 2797 (1986)
9. Th. Sauter, W. Neuhauser, R. Blatt, P.E. Toschek: Phys. Rev. Lett. **57**, 1696 (1986)
10. J.C. Bergquist, R.G. Hulet, W.M. Itano, D.J. Wineland: Phys. Rev. Lett. **57**, 1699 (1986)
11. It is interesting to note that Einstein motivated his inclusion of stimulated emission jumps (as we would now call them) along with absorption jumps by recalling just this wave-based physics [1]: "If a Planck resonator is located in a radiation field, the energy of the resonator is changed through the work done on the resonator by the electromagnetic field of the radiation; this work can be positive or negative depending on the phases of the resonator and the oscillating field. We correspondingly introduce the following hypothesis. . . ."
12. W. Bothe, H. Geiger: Z. Phys. **32**, 639 (1925)
13. A.H. Compton, A.W. Simon: Phys. Rev. **26**, 290 (1925)
14. H.J. Carmichael: Phys. Rev. A **56**, 5065 (1997)
15. H.J. Carmichael: 'Taming the Paradox of Lasing Without Inversion'. In: *Mysteries, Puzzles, and Paradoxes in Quantum Mechanics*, Proceedings of the workshop, Lake Garda, Italy, August–September, 1998. ed. by R. Bonifacio (American Institute of Physics, New York 1999) pp. 208–219
16. This is to be understood in the sense of a true expectation – i.e., what is likely to be the case – and not in the sense of the quantum mechanical mean value.

Complementarity in Spontaneous Emission: Quantum Jumps, Staggers and Slides

Howard Wiseman

1 Introduction

Dan Walls is rightly famous for his part in many of the outstanding developments in quantum optics in the last 30 years. Two of these are most relevant to this paper. The first is the prediction of nonclassical properties of the fluorescence of a two-level atom, such as antibunching [1] and squeezing [2]. Both of these predictions have now been verified experimentally [3,4]. The second is the investigation of fundamental issues such as complementarity and the uncertainty principle [5,6]. This latter area is one which has generated a lively theoretical discussion [7], and, more importantly, suggested new experiments [8]. It was also an area in which I had the honour of working with Dan [9], and of gaining the benefit of his instinct for picking a fruitful line of investigation.

In this paper I will be considering an undriven atom, rather than the resonantly driven atom of [1,2]. Nevertheless, a general feature of these investigations still applies, namely that there is more to the fluorescence of a two-level atom than meets the eye (literally). For example, it is only when something else intervenes between atom and eye (such as a beam splitter with a local oscillator) that the squeezing of the emitted light is revealed [2]. This is an example of complementarity in quantum measurement [5]: there is always more than one way to observe a system. Different choices of "detector basis" [5] give different (complementary) descriptions for the system.

The premier example of complementarity in quantum physics is the wave-particle duality [10]. This applies to the spontaneous emission of an atom as follows. The emitted photon is particle-like in that it appears to be emitted at a definite time (the time the atom jumps from excited to ground state). The detection of photons at definite times, with errors much less than the lifetime of an atom, is now commonplace in quantum optics laboratories. At the same time, however, it is obvious from interferometric measurements that the photon has a wave nature, and that the photon's wave-packet has a duration of order the atomic lifetime. The resolution is the principle of complementarity: the aspect (wave-like or particle-like) which we observe depends on our choice of observation technique.

In this paper I will examine three different ways of observing the light spontaneously emitted by an initially excited atom, and the stochastic dynamics of the atomic state which results. The first, direct photodetection, requires only a photodetector, and hence yields information only about the intensity of the field (photon number). The second and third require the light from the atom to be interfered with a strong local oscillator prior to detection, and as such are members of a class I have dubbed "dyne" detection. The second, heterodyne detection, yields

H.J. Carmichael, R.J. Glauber, M.O. Scully (Eds.): LNP 561, pp. 347–357, 2001.

information about both the intensity and phase of the field. The third, a particular adaptive dyne detection scheme, yields information only about the phase of the field. The implications of this curious fact for the evolution of the atomic state are investigated here for the first time. I will then show how the three sorts of stochastic dynamics are compatible with the behaviour of the atom when the emitted field is not detected at all. Finally, I conclude with a discussion of the insight which complementarity gives into the stochastic dynamics of the atom.

2 Direct Detection: Quantum Jumps

Consider a two-level atom with lowering operator $\sigma = |g\rangle\langle e|$ and radiative lifetime γ^{-1}. If the initial state of the atom is pure, and all of the light emitted by the atom is focussed onto detectors, then no information is lost in the spontaneous emission process so the atomic state will remain pure. Specifically, it will evolve according to the following equation [11–14]

$$\left|\bar{\psi}(t+\mathrm{d}t)\right\rangle = \left[\left(1-\mathrm{d}t\frac{\gamma}{2}\sigma^\dagger\sigma\right)+\mathrm{d}N(t)\left(\sqrt{\gamma}\sigma-1\right)\right]\left|\bar{\psi}(t)\right\rangle \ . \tag{1}$$

Here the line over ψ indicates that the state is being represented by an unnormalized vector. The infinitesimal $\mathrm{d}N(t)$ is the increment in the number of photons detected in the time interval $[t, t+\mathrm{d}t)$. It is equal to either zero or one, and the probability for it to equal the latter is

$$\mathrm{E}[\mathrm{d}N(t)] = \gamma\left\langle\sigma^\dagger\sigma\right\rangle\mathrm{d}t = \gamma\frac{\left\langle\bar{\psi}(t)\right|\sigma^\dagger\sigma\left|\bar{\psi}(t)\right\rangle}{\left\langle\bar{\psi}(t)\right|\left.\bar{\psi}(t)\right\rangle}\mathrm{d}t \ . \tag{2}$$

Here E denotes expectation value. As expected, the rate of photoemissions is simply equal to the spontaneous emission rate by the excited state fraction.

When a photon is detected, the atom jumps into the ground state. This results from the above equation since $\sqrt{\gamma}\sigma\left|\psi\right\rangle \propto \left|g\right\rangle$ for any state $\left|\psi\right\rangle$, and the other term is of order $\mathrm{d}t$. If, as in this case, there are no processes to re-excite the atom, it will remain in the ground state thereafter. Furthermore, if the atom begins in the excited state, it will remain in the excited state until the photon is detected. These results are evident from the fact that $\left(1-\gamma\mathrm{d}t\sigma^\dagger\sigma/2\right)\left|e\right\rangle \propto \left|e\right\rangle$ and $\left(1-\gamma\mathrm{d}t\sigma^\dagger\sigma/2\right)\left|g\right\rangle \propto \left|g\right\rangle$.

Thus in the case of initially exited atom the evolution is trivial. The scaled excitation energy of the atom

$$E/hf = \varepsilon = \left\langle\sigma^\dagger\sigma\right\rangle \tag{3}$$

simply remains equal to one until the time t at which $\mathrm{d}N(t) = 1$, when it jumps to zero:

$$\varepsilon = 1 - N(t) \ . \tag{4}$$

This jump time is determined randomly from an exponential distribution $w(t)\mathrm{d}t = \mathrm{E}[\mathrm{d}N(t)] = \gamma \mathrm{e}^{-\gamma t}\mathrm{d}t$. Figure 1 shows a typical quantum trajectory [13], in terms of the atomic excitation ε and the dipole phase

$$\phi = \arg \langle \sigma \rangle \ . \tag{5}$$

In this case ϕ is always undefined, since $\langle \sigma \rangle = 0$ when the atom is in the ground state or excited state.

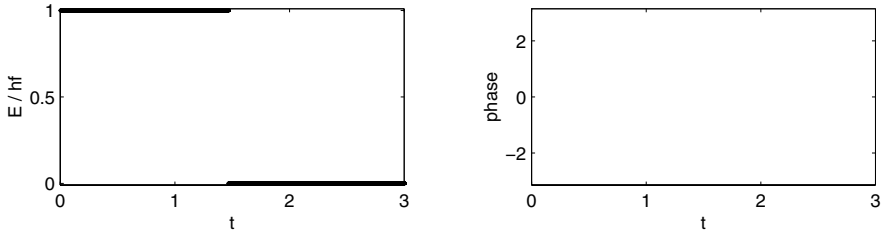

Fig. 1. A typical quantum trajectory for the atomic state under direct detection. The scaled energy $\varepsilon = E/hf$ simply jumps from 1 to 0, and the dipole phase ϕ is always undefined

3 Dyne Detection

Direct detection leads, as exemplified above, to jumps in the dynamics of the observed system. Such dynamics are easily simulated for a wide variety of atomic systems, and the numerical advantages of such stochastic simulations [15] have lead to their wide-spread adoption. Other measurement schemes lead to more complicated dynamics and are less widely used as numerical tools. Nevertheless they are equally applicable to the laboratory; witness the homodyne detection used [4] to verify the squeezing of resonance fluorescence.

Homodyne detection is a special case of a class of measurements which I have called, for want of a better name, "dyne" detection. The defining feature of this sort of measurement is that the light from the system is passed through a beam splitter with a very strong local oscillator (a coherent light source) entering at the other port. The exiting light, a superposition of the field from the system and the local oscillator (LO), is then detected using a photoreceiver (or two if a 50/50 beam splitter is used).

The dynamics of the quantum system conditioned on the photocurrent produced by the receiver was first determined by Carmichael [13] for the case of homodyne detection. This is the case where the local oscillator has the same frequency as the system, so that its phase Φ relative to the system remains fixed. The generalization to an arbitrary local oscillator phase $\Phi(t)$ is trivial [16]. For a spontaneously emitting

atom and with unit efficiency detection, the instantaneous photocurrent $I(t)$, scaled so that the spectrum of shot-noise is unity, is

$$I(t)\mathrm{d}t = \sqrt{\gamma}\left\langle \sigma \mathrm{e}^{-\mathrm{i}\Phi(t)} + \sigma^\dagger \mathrm{e}^{\mathrm{i}\Phi(t)} \right\rangle \mathrm{d}t + \mathrm{d}W(t)\ . \tag{6}$$

Here $\mathrm{d}W(t)$ is a Wiener increment [17] with $\mathrm{E}[\mathrm{d}W(t)] = 0$, $[\mathrm{d}W(t)]^2 = \mathrm{d}t$.

The equation generating the conditioned evolution of the system (that is, its quantum trajectory [13]) is

$$\mathrm{d}\left|\bar{\psi}(t)\right\rangle = \left[-\mathrm{d}t\frac{\gamma}{2}\sigma^\dagger\sigma + I(t)\mathrm{d}t\mathrm{e}^{-\mathrm{i}\Phi(t)}\sqrt{\gamma}\,\sigma\right]\left|\bar{\psi}(t)\right\rangle\ . \tag{7}$$

This equation, which is to be interpreted in the Itô [17] sense, describes the diffusion of the system state in its Hilbert space. This is the effect of the very large LO amplitude: most of the light entering the photoreceiver is from the LO so the photon flux is very large but each photodetection (if it were resolvable) would give only a small amount of information about the system and so cause only a small jump in its state. In the ideal limit of an infinitely strong local oscillator, the jumps in the system state become infinitely frequent and infinitely small, giving rise to diffusion.

The general solution of the dyne detection quantum trajectory for an initially excited atom is easy to find. It is

$$\left|\bar{\psi}(t)\right\rangle = R^*(t)\left|g\right\rangle + \mathrm{e}^{-\gamma t/2}\left|e\right\rangle\ , \tag{8}$$

where

$$R(t) = \int_0^t \mathrm{e}^{\mathrm{i}\Phi(s)}\mathrm{e}^{-\gamma s/2}\sqrt{\gamma}\,I(s)\mathrm{d}s\ . \tag{9}$$

Note that this solution is for a given photocurrent record $I(s)$ up to time t. To find the solution for a given noise process $\mathrm{d}W(t)$ is complicated because the other term in $I(s)$ depends upon

$$\langle\sigma\rangle(t) = \frac{R(t)}{\mathrm{e}^{-\gamma t} + |R(t)|^2}\ , \tag{10}$$

so that the equations become nonlinear.

4 Heterodyne Detection: Quantum Staggers

In the absence of driving there is no preferred phase of the dipole of the two-level atom. Thus there is no reason to choose any particular local oscillator phase Φ for

homodyne detection. A more natural choice of detection is heterodyne detection, in which the local oscillator has a significantly different frequency from the system. This can be encompassed in the equations of the preceding section by choosing

$$\Phi(t) = t\Delta \,, \tag{11}$$

with the detuning $\Delta \gg \gamma$. In this limit we can make the approximation

$$R(t) = \int_0^t \mathrm{e}^{\mathrm{i}s\Delta}\mathrm{e}^{-\gamma s/2}\left[\gamma\left\langle\sigma\mathrm{e}^{-\mathrm{i}s\Delta} + \sigma^\dagger\mathrm{e}^{\mathrm{i}s\Delta}\right\rangle \mathrm{d}s + \sqrt{\gamma}\,\mathrm{d}W(s)\right] \tag{12}$$

$$\simeq \int_0^t \mathrm{e}^{-\gamma s/2}\left[\gamma\,\langle\sigma\rangle\,\mathrm{d}s + \sqrt{\gamma}\,\mathrm{d}W(s)\mathrm{e}^{\mathrm{i}s\Delta}\right] \,, \tag{13}$$

since the terms rotating at rate 2Δ will not contribute to the integral. The noise process does not average to zero because it is white.

Using (10) we can rewrite this integral equation as

$$dR = \frac{R\mathrm{e}^{-\gamma t}}{\mathrm{e}^{-\gamma t} + |R|^2}\mathrm{d}t + \sqrt{\gamma}\,\mathrm{e}^{-\gamma t/2}\mathrm{d}V(t) \,, \tag{14}$$

with the initial condition $R(0) = 0$. Here $\mathrm{d}V(t)$ is the coarse-graining (over a time intermediate between γ^{-1} and Δ^{-1}) of the noise process $\mathrm{e}^{\mathrm{i}s\Delta}\mathrm{d}W(s)$ [14]. It is obviously complex and satisfies

$$\mathrm{E}[\mathrm{d}V(t)] = 0 \,, \quad \mathrm{d}V(t)\mathrm{d}V(t) = 0 \,, \quad \mathrm{d}V^*(t)\mathrm{d}V(t) = \mathrm{d}t \,. \tag{15}$$

Using the Itô calculus it is possible to obtain equations for the atomic excitation

$$\varepsilon = \frac{|R|^2}{\mathrm{e}^{-\gamma t} + |R|^2} \tag{16}$$

and dipole phase

$$\phi = \arg\frac{R\mathrm{e}^{-\gamma t/2}}{\mathrm{e}^{-\gamma t} + |R|^2} = \arg R \,. \tag{17}$$

These are

$$\mathrm{d}\varepsilon = -\gamma\varepsilon\,\mathrm{d}t - \varepsilon^2\sqrt{\gamma(\varepsilon^{-1} - 1)}\,2\mathrm{Re}[\mathrm{e}^{-\mathrm{i}\phi}\mathrm{d}V(t)] \,, \tag{18}$$

$$\mathrm{d}\phi = \sqrt{\gamma/(\varepsilon^{-1} - 1)}\,\mathrm{Im}[\mathrm{e}^{-\mathrm{i}\phi}\mathrm{d}V(t)] \,. \tag{19}$$

Evidently, *on average*, the excitation energy decays exponentially. But in any individual trajectory it will have random fluctuations due to the noise term in (18). The phase dynamics consists entirely of random fluctuations, independent of the energy fluctuations. When the atom is close to the excited state ($\varepsilon \approx 1$), these fluctuations are enormous, and are divergent when $\varepsilon = 1$ (as at $t = 0$). Thus the phase the atomic dipole acquires during the measurement is completely random.

As the measurement progresses, and ε decays (on average), the system tends towards the ground state. Then both phase and amplitude fluctuations become relatively smaller, as the above equations become

$$\mathrm{d}\varepsilon = -\gamma\varepsilon\,\mathrm{d}t - \varepsilon^{3/2}\sqrt{\gamma}\,2\mathrm{Re}[\mathrm{e}^{-\mathrm{i}\phi}\mathrm{d}V] \tag{20}$$

$$\mathrm{d}\phi = \sqrt{\gamma\varepsilon}\,\mathrm{Im}[\mathrm{e}^{-\mathrm{i}\phi}\mathrm{d}V]\,. \tag{21}$$

As $t \to \infty$ the system behaves like a classical oscillator, with an exponentially decaying excitation ε and a constant phase ϕ. This is as expected, since a two-level atom near the ground state is isomorphic to a harmonic oscillator near its ground state. This can be visualized using the Bloch sphere: near the ground state the sphere is identical to a paraboloid.

A typical trajectory illustrating the features discussed above is shown in Fig. 2, again in terms of ε and ϕ. Note that whenever the system approaches the excited state (through fluctuations in the excitation), the phase becomes randomized. As energy is lost the system 'staggers' down the Bloch sphere, with comparable noise in both excitation energy and phase. As it approaches the ground state both sorts of fluctuation vanish.

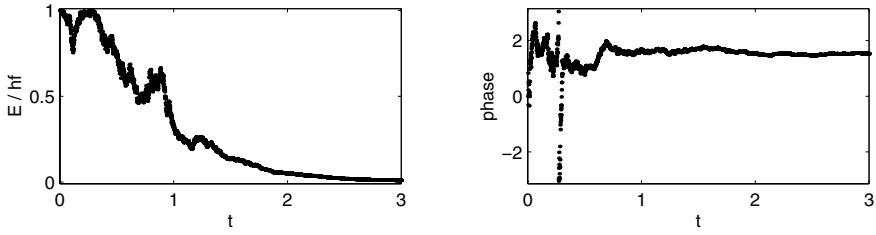

Fig. 2. A typical quantum trajectory for the atomic state under heterodyne detection. The scaled energy $\varepsilon = E/hf$ staggers downwards. The dipole phase ϕ is always defined but evolves stochastically

5 Adaptive Phase Detection: Quantum Slides

It was stated above that homodyne detection is not a natural choice for observing a spontaneously emitting atom because there is no preferred phase of the atomic dipole if it begins in the excited state. Because of this, we were led to consider heterodyne detection, in which both dipole quadratures are measured simultaneously.

However there is another sort of dyne detection with no predefined phase, adaptive phase detection. This was first proposed in [18], and is like doing a homodyne measurement where the phase of the local oscillator is continually adjusted so as to measure the *estimated* phase quadrature of the system. That is, the LO phase is chosen to be

$$\Phi(t) = \hat{\varphi}(t) + \pi/2 \,, \tag{22}$$

where $\hat{\varphi}(t)$ is an *estimate* of the system phase ϕ based on the measurement record up to time t.

For the atom spontaneously decaying from the excited state under dyne detection, the *actual* dipole phase at time t is, from (17) and (9)

$$\phi(t) = \arg R(t) = \arg \int_0^t \mathrm{e}^{\mathrm{i}\Phi(s)} \mathrm{e}^{-\gamma s/2} \sqrt{\gamma}\, I(s) \mathrm{d}s \,. \tag{23}$$

Since this is written purely in terms of the measurement record, it follows that we actually know $\phi(t)$ exactly so we can set $\hat{\varphi}(t) = \phi(t)$. From (22) this means that

$$\mathrm{e}^{\mathrm{i}\Phi(t)} = \mathrm{i}\mathrm{e}^{\mathrm{i}\hat{\varphi}(t)} = \mathrm{i}\frac{R}{|R|} \,. \tag{24}$$

Substituting this into the definition of $I(t)$, and using (10), gives

$$I(t)\mathrm{d}t = \mathrm{d}W(t) \,. \tag{25}$$

That is, the deterministic part of $I(t)$ vanishes. Thus, again using (24), it can be seen that R obeys the nonlinear stochastic differential equation

$$dR = \mathrm{i}\frac{R}{|R|} \mathrm{e}^{-\gamma t/2} \sqrt{\gamma}\, \mathrm{d}W(t) \,. \tag{26}$$

Remarkably, this equation has an exact solution which can be found by solving separately for $|R|^2$ and $\phi = \arg R$. The result for $|R|^2$ is $|R(t)|^2 = 1 - \mathrm{e}^{-\gamma t}$. Converting this into the excitation ε gives

$$\varepsilon(t) = \mathrm{e}^{-\gamma t} \,, \tag{27}$$

while the dipole phase is

$$\phi = \int_0^t \sqrt{\gamma}\, \mathrm{d}W(s) / \sqrt{\mathrm{e}^s - 1} \,. \tag{28}$$

What these equations show is that the energy decays exactly exponentially, with all of the noise being in the phase. At least as far as the atomic excitation is concerned, the system slides smoothly to the ground state, rather than jumping or staggering down.

For comparison with heterodyne detection, we can write the stochastic equation for the phase as

$$\mathrm{d}\phi(t) = \sqrt{\gamma/(\varepsilon^{-1}-1)}\,\mathrm{d}W(t)\ . \tag{29}$$

This shows that the phase noise is exactly twice as large as that in heterodyne detection, since $\{\mathrm{Im}[\mathrm{e}^{-\mathrm{i}\phi}\mathrm{d}V(t)]\}^2 = \mathrm{d}t/2$ compared to $[\mathrm{d}W(t)]^2 = \mathrm{d}t$. It seems that suppressing the stochasticity in ε has doubled the amount of noise in the evolution of the complementary variable ϕ. As with heterodyne detection, the initial phase chosen by the atom is completely random, due to the divergence of (29) at $t = 0$. As $t \to \infty$ the increment in the phase vanishes exponentially, so that the phase becomes stable as the atom approaches the ground state, as in the preceding section. These results are illustrated in the typical trajectory shown in Fig. 3.

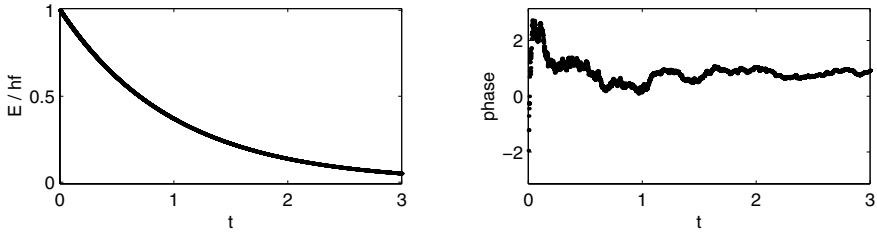

Fig. 3. A typical quantum trajectory for the atomic state under adaptive phase detection. The scaled energy $\varepsilon = E/hf$ slides exponentially downwards. The dipole phase ϕ is always defined and again evolves stochastically

6 No Detection

The three types of quantum trajectory analyzed above apply for three different detection schemes. What happens if there is no detection scheme, with the atom's radiation irretrievably lost? What happens if there is a detection scheme but the experimenter fails to record the results? The answer, as far as the experimenter is concerned, should be the same in both cases. In the absence of any measurement information the system obeys the master equation

$$\dot{\varrho} = \gamma\left(\sigma\varrho\sigma^\dagger - \{\sigma^\dagger\sigma, \varrho\}/2\right)\ . \tag{30}$$

Starting at the excited state, the solution to this equation follows a line down the vertical axis of the Bloch sphere, with

$$\varepsilon = \mathrm{e}^{-\gamma t} \tag{31}$$

and the phase ϕ undefined.

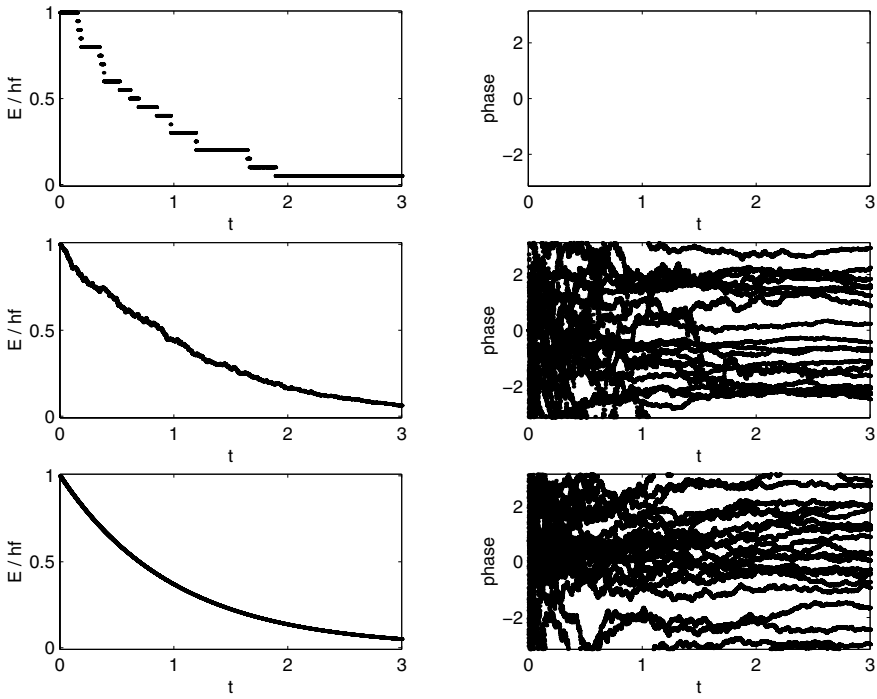

Fig. 4. Average over 20 trajectories of the atomic evolution. The top line shows direct detection, the middle line heterodyne detection and the bottom line adaptive phase detection. For each of the three cases the ensemble average of the scaled energy $\varepsilon = E/hf$ is plotted, and this is seen to decay exponentially on average. (This is true for any single trajectory under adaptive phase detection.) For each of the three cases the dipole phases for all 20 trajectories is plotted, and this is seen to be undefined on average. (This is true for any single trajectory under direct detection)

How is this compatible with the experimenter making a measurement but ignoring the result? The answer is that these are the dynamics which are reproduced *on average* by all three detection schemes. This is shown in Fig. 4 by an average of ε over 20 trajectories, and the phases ϕ for those same trajectories. In the case of direct detection and heterodyne detection the ensemble average has smoothed

the mean energy ε to a curve approximating exponential decay. For the adaptive phase detection, this exponential decay is exact for all members of the ensemble. For direct detection the phase is always undefined, as it is if there is no detection. For the two dyne schemes the phase is always well defined in individual trajectories, but is random across the ensemble of trajectories so there is no defined phase on average.

7 Conclusion

I have shown that three different ways of observing the field spontaneously radiated by an initially excited atom lead to three very different sorts of stochastic evolution for the atomic state. Specifically, under direct, heterodyne, and adaptive phase detection, the atomic energy ε undergoes quantum jumps, staggers and slides respectively. To conclude, I wish to discuss how complementarity can help explain the distinctive features of the evolution of the excitation ε and the complementary quantity, the dipole phase ϕ.

The general principle which emerges from the above analysis is that if and only if the measurement yields no information about a variable (such as ε or ϕ) then that variable will evolve in the same way as it does in the ensemble average. That is, there is no distinction between the different members of the ensemble. Under direct detection, which yields information only about the atomic excitation, the dipole phase is the same in all trajectories as it is on average (i.e. undefined). Under adaptive phase detection, which yields information only about the dipole phase, the atomic excitation is the same in all trajectories as it is on average (i.e. exponentially decaying). Under heterodyne detection, which yields information about both the atomic excitation and the dipole phase, both the phase and the energy evolve stochastically and only reproduce the master equation results under the ensemble average.

This neat correlation, between the nature of the evolution of the complementary variables and the information yielded by the measurement scheme, breaks down when one considers initial states other than the excited state of the atom. This could be explained on the basis of correlations between the variables (ε and ϕ) which do not exist if the system is in the excited state but which do exist in the (quasi)probability distributions for other states [19]. It remains to be seen whether a precise formulation of the above principle is possible taking into account such correlations. In any case, it seems that complementarity is still useful for understanding the surprisingly diverse array of behaviours which that apparently simple quantum system, a spontaneously decaying excited atom, can exhibit.

References

1. H.J. Carmichael, D.F. Walls: J. Phys. B **9**, L43 (1976); *ibid.* 1199 (1976)
2. M.J. Collett, D.F. Walls, P. Zoller: Opt. Commun. **52**, 145 (1984)
3. H.J. Kimble, M. Dagenais, L. Mandel: Phys. Rev. Lett. **39**, 691 (1977)
4. Z.H. Lu, S. Bali, J.E. Thomas: Phys. Rev. Lett. **81**, 3635 (1998)
5. S.M. Tan, D.F. Walls: Phys. Rev. A **47**, 4663 (1993)
6. E.P. Storey, S.M. Tan, M.J. Collett, D.F. Walls: Nature **367**, 626-628 (1994)

7. B.-G. Englert, M.O. Scully, H. Walther: Nature **375**, 367-368 (1995); E.P. Storey, S.M. Tan, M.J. Collett, D.F. Walls: Nature **375**, 368 (1995)
8. S. Dürr, T. Nonn, G. Rempe: Nature **395**, 33 (1998); *ibid.* Phys. Rev. Lett. **81**, 5705 (1998)
9. H.M. Wiseman, F.E. Harrison, M.J. Collett, S.M. Tan, D.F. Walls, R.B. Killip: Phys. Rev. A **56**, 55 (1997)
10. N. Bohr: Nature **121**, 580 (1928)
11. J. Dalibard, Y. Castin, K. Mølmer: Phys. Rev. Lett. **68**, 580 (1992)
12. C.W. Gardiner, A.S. Parkins, P. Zoller: Phys. Rev. A **46**, 4363 (1992)
13. H.J. Carmichael: *An Open Systems Approach to Quantum Optics*, Lecture Notes in Physics, Vol. m18 (Springer, Berlin 1993)
14. H.M. Wiseman, G.J. Milburn: Phys. Rev. A **47**, 1652 (1993)
15. R. Dum, P. Zoller, H. Ritsch: Phys. Rev. A **45**, 4879 (1992)
16. H.M. Wiseman: Quantum Semiclass. Opt. **8**, 205 (1996)
17. C.W. Gardiner: *Handbook of Stochastic Methods* (Springer, Berlin 1985)
18. H.M. Wiseman: Phys. Rev. Lett. **75**, 4587 (1995)
19. H.M. Wiseman: Quantum Semiclass. Optics **7**, 569 (1995)

Ergodicity of Quantum Trajectory Detection Records

J.D. Cresser

Summary. An examination is made of the conditions under which the detection record generated by the quantum trajectory simulation of the output of a detector continuously monitoring an open Markovian system is ergodic, i.e. where the time averages of a single realization of such a record will yield the same result as an ensemble average over many such realizations. It is shown, in the case of discrete counting, that ergodicity holds in the mean and to first order if the long time steady state of the system is independent of the initial state of the system. A two-photon dissipative process is used as an example of a situation in which ergodicity does not hold.

1 Introduction

The past decade or so has seen the development of a theoretical formalism, variously known as the Monte-Carlo, stochastic wave function, or quantum trajectory method [1–5], in terms of which the continuous observation of a quantum system can be consistently described. Generally speaking, the theory is concerned with Markovian open systems in which a system of interest is coupled to a reservoir, this resulting in the irreversible, dissipative evolution of the system. Typically, this dissipation is manifested in decay products – particles – irreversibly propagating away from the system (acting as a source) such as photons radiated from an atom, atoms exiting from a micromaser cavity [6], or even atoms escaping from a Bose-Einstein condensate, as in an atom laser. Measurements – which can take many different forms – then involve the detection of these particles, each detection event resulting, via an amplification process, in the production of a macroscopic, classical signal such as a photodetector current pulse. The theory, in principle, is then able to describe the time dependent classical output of the detector continuously monitoring the reservoir which, due to the entanglement between the reservoir and system, will also represent an indirect measurement of some property of the system. Simulations of possible detector outputs can be generated numerically by these methods. One simple example of a situation that can be described in this way is the simulation of the photocurrent produced by a detector absorbing the photons scattered by an atom driven by a strong laser field [5]. The simulated detection records obtained represent results that could in principle arise in a real experiment, and can be analyzed in the same fashion. In particular, the records will be stochastic in nature: each record, or equivalently the output of one run of an experiment, will be one

H.J. Carmichael, R.J. Glauber, M.O. Scully (Eds.): LNP 561, pp. 358–369, 2001.

realization of a classical stochastic process whose statistical properties are determined by the quantum properties of the system, as well as noise introduced by the detection process itself. Mean values and correlation functions are the sort of information on the statistical properties of the records that could be obtained from the numerically generated data.

In many cases of interest, the processes are stationary, or at least asymptotically stationary, so the most direct approach to obtaining these quantities would be to calculate them by taking suitable time averages of a single, sufficiently long, detection record. Implicit in doing so is the assumption that the stochastic process is ergodic, i.e. that these time averages will yield the same results as would be obtained by taking ensemble averages over very many realizations of the process. It is the aim of this paper to explore the circumstances under which this assumption holds true for detection records generated by the quantum trajectory method. Essentially, it is found that if the steady state of the system is independent of its initial state, then time and ensemble averages are the same, i.e. the detection records are realizations of an ergodic stochastic process. If not, then *depending on what is actually being measured*, time and ensemble averages may differ.

2 The Quantum Trajectory Method

The method is based on the fact that under the Born and Markov approximations, the master equation for the density operator ϱ of an open system will satisfy a master equation of Lindblad form [7]

$$\dot{\varrho} = i\hbar^{-1}[H_S, \varrho] - \tfrac{1}{2}\sum_m (L_m^\dagger L_m \varrho + \varrho L_m^\dagger L_m - 2L_m \varrho L_m^\dagger) = \mathcal{L}\varrho \tag{1}$$

where H_S is the system Hamiltonian and the operators L_m are system operators. The full equation is summarized in terms of a linear superoperator $\mathcal{L}$ acting on the density operator. Introducing a "jump operator" $\mathcal{J}$ defined by

$$\mathcal{J}\varrho = \Omega^\dagger \varrho \Omega \tag{2}$$

where Ω could be any system operator such that $0 \leq \mathrm{Tr}[\mathcal{J}\varrho] \leq 1$, the solution to the master equation can be expressed as

$$\begin{aligned} \varrho &= e^{\mathcal{L}t}\varrho(0) \\ &= \varrho_c(t) + \sum_{n=1}^{\infty} \int_0^t d\tau_n \int_0^{\tau_n} d\tau_{n-1} \ldots \int_0^{\tau_2} d\tau_1 \qquad (3) \\ &\quad \times \varrho_c(\tau_1, \tau_2, \ldots, \tau_n; t) P_n(\tau_1, \tau_2, \ldots, \tau_n; [0, t]). \qquad (4) \end{aligned}$$

where

$$\varrho_c(t) \ = e^{\mathcal{L}_0 t}\varrho(0) \tag{5}$$

$$\varrho_c(\tau_1,\tau_2,\ldots,\tau_n;t) = \frac{e^{\mathcal{L}_0(t-\tau_n)}\mathcal{J}e^{\mathcal{L}_0(\tau_n-\tau_{n-1})}\mathcal{J}\ldots\mathcal{J}e^{\mathcal{L}_0\tau_1}\varrho(0)}{P(\tau_1,\tau_2,\ldots,\tau_n;[0,t])} \tag{6}$$

$$P_n(\tau_1,\tau_2,\ldots,\tau_n;[0,t]) = \mathrm{Tr}\left[e^{\mathcal{L}_0(t-\tau_n)}\mathcal{J}e^{\mathcal{L}_0(\tau_n-\tau_{n-1})}\ldots e^{\mathcal{L}_0\tau_1}\varrho(0)\right] \tag{7}$$

and where

$$\mathcal{L}_0 = \mathcal{L} - \mathcal{J}. \tag{8}$$

The interpretation of this result is well-known. The operator $\mathcal{J}$ is responsible for inducing instantaneous changes ("quantum jumps") in the state of the system:

$$\begin{aligned}\varrho_c(\tau_1,\tau_2,\ldots,\tau_{i-1};\tau_i-\varepsilon) &\to \varrho_c(\tau_1,\tau_2,\ldots,\tau_{i-1},\tau_i;\tau_i+\varepsilon)\\ &= \frac{\mathcal{J}\varrho_c(\tau_1,\tau_2,\ldots,\tau_{i-1};\tau_i-\varepsilon)}{\mathrm{Tr}\left[\mathcal{J}\varrho_c(\tau_1,\tau_2,\ldots,\tau_{i-1};\tau_i-\varepsilon)\right]}\end{aligned} \tag{9}$$

these jumps occurring at the times $\tau_1,\tau_2,\ldots,\tau_n$, during the time interval $[0,t)$, while $\exp\left[\mathcal{L}_0(\tau_i-\tau_{i-1})\right]$ represents evolution of the system "between jumps". The state $\varrho_c(\tau_1,\tau_2,\ldots,\tau_n;t)$ is then the conditioned state of the system at time t, given that jumps have occurred at the times $\tau_1,\tau_2,\ldots\tau_n$. The joint probability $P_n(\tau_1,\tau_2,\ldots,\tau_n;[0,t])$ gives the probability density of jumps occurring at the times $\tau_1,\tau_2,\ldots\tau_n$ within the interval $[0,t)$ and none at any other time. The set of probability densities P_n, for $n=0,1,2,\ldots$ satisfy the normalization condition (obtained by taking the trace of (4)):

$$P_0(t) + \sum_{n=1}^{\infty}\sum_{n=1}^{\infty}\int_0^t d\tau_n\int_0^{\tau_n}d\tau_{n-1}\ldots\int_0^{\tau_2}d\tau_1 P_n(\tau_1,\tau_2,\ldots,\tau_n;[0,t]) = 1 \tag{10}$$

and therefore define a classical point process [8], the point events being, of course, the sequence of quantum jumps. These results can be readily generalized in the case of there being more than one jump operator acting i.e. if $\mathcal{J}\varrho = \Omega_1^\dagger\varrho\Omega_1 + \Omega_2^\dagger\varrho\Omega_2 + \ldots$.

From the above, it is possible to show that the (non-exclusive) joint probability density for N detections occurring at times $\tau_1,\tau_2,\ldots,\tau_N$, during the interval $(0,t)$, with any number of detections occurring elsewhere within this interval is given by [10]:

$$G^{(n)}(\tau_1,\tau_2,\ldots,\tau_N) = \mathrm{Tr}\left[\mathcal{J}e^{\mathcal{L}(\tau_N-\tau_{N-1})}\ldots\mathcal{J}e^{\mathcal{L}(\tau_2-\tau_1)}\mathcal{J}e^{\mathcal{L}\tau_1}\varrho(0)\right]. \tag{11}$$

This can be recognized as the usual time ordered multitime correlation function for the Heisenberg operator $\Omega^\dagger(t)\Omega(t)$. Equation (11) will be important later in the evaluation of various mean values.

Given the set of joint probabilities, it is possible to generate sequences of condition states $\varrho_c(\tau_1, \tau_2, \ldots, \tau_n; t)$, $\tau_n < t < \tau_{n+1}$ as a function of time. Each such sequence defines a quantum trajectory, and the ensemble of all possible quantum trajectories is then equivalent to the original density operator in the sense that all the properties of the system that could be obtained from ϱ can also be obtained by suitable averages over the members of the ensemble.

The decomposition of a density operator into an ensemble of quantum trajectories is not unique: different choices of Ω used in defining $\mathcal{J}$ lead to what is known as different unravellings of the dynamics. The form of the master equation above suggests any or all of the L_i as possible choices for Ω (or Ω_i). For purposes of obtaining numerical solutions to the original master equation, the choice of unravelling would be guided by considerations of computational efficiency, without necessarily any concern for the physical meaning, if any, of the quantum trajectories obtained. However, as pointed out earlier, these quantum trajectories can be provided with a very useful physical interpretation [5] as describing the dynamics of a system coupled to a reservoir subject to continuous observation. From a quantum measurement theory perspective, each detection of a reservoir quantum (for instance a photon scattered by an atom) represents the acquisition of information by the observer, and with each detection the system will be projected (undergo a "quantum jump") into a new state conditioned on the information gained by this detection having occurred. This projection can be described in terms of a jump operator of the form (2), with the specific nature of Ω determined by the details of the measurement that is being performed, i.e. different kinds of measurements are described in terms of different kinds of jump operators. A sequence of such detections is then accompanied by the conditioned evolution of the state of the system as it evolves i.e. a quantum trajectory of just the form discussed above.

The joint probabilities of a sequence of quantum jumps derived in the quantum trajectory theory will then equally well describe the probabilities for a sequence of detection events. Each elementary detection event will be amplified to produce a macroscopic (classical) signal e.g. a current pulse, so the jump statistics embodied in the joint probabilities P_n will characterize also the classical statistical properties of the macroscopic signal produced. Consequently, the statistical properties of the detection signal can be analyzed in terms of the mean values, correlation properties and so on calculated from the P_n.

The discussion above has been confined to the particular case in which the detection events are discrete in time. Detection schemes which produce a continuous output also arise, but will not be treated here.

3 The Detection Current

As discussed above, what would be observed is a detector current $I(t)$ consisting of a random sequence of macroscopic current pulses. Thus if in one realization, the jumps occur at times $\tau_n, n = 1, 2, \ldots$, this will result in the production of identical macroscopic current pulses $j(t-\tau_n)$ (ignoring retardation effects) where $j(t)$ is such that

$$j(t) = 0 \quad t \leq 0 \quad \text{and} \quad \int_0^\infty j(\tau) d\tau = J. \tag{12}$$

The total current at time t, if detections have occurred at times $\tau_1 < \tau_2 < \ldots < \tau_N$ in the time interval $(0, t)$, is

$$i(t) = \sum_{n=1}^{N} j(t - \tau_n). \tag{13}$$

As the times of detection, and the number of detections in the interval $(0, t)$ are random quantities, the current $i(t)$ will itself be a stochastic function of time.

The detection record could be finite – consisting of a single current pulse if, say, it is the spontaneous decay of a single atom that is being monitored, or the detection records may be finite samples of an infinitely long realization of what would be, in general, a non-stationary stochastic process. However, if the system approaches a steady state for which, as $t \to \infty$, $\dot{\varrho} = 0$, e.g. an atom fluorescing in response to continuous irradiation by a steady laser field, the process generated will be stationary, or at least asymptotically stationary after going through an initial transient period. By generating a sufficient number of realizations of the stochastic process, the statistical properties of the detector current can be obtained by the usual procedure of taking ensemble averages. Thus for instance, the mean current will be

$$M[I(t)] = \lim_{N\to\infty} \frac{1}{N} \sum_{n=1}^{N} i_n(t). \tag{14}$$

and the correlation function for the current

$$M[I(t)I(t+\tau)] = \lim_{N\to\infty} \frac{1}{N} \sum_{n=1}^{N} i_n(t) i_n(t+\tau) \tag{15}$$

where $i_n(t)$ is the n^{th} member of the ensemble. By use of the properties of the non-exclusive probability distributions (11), the mean value and correlation function can be shown to be

$$M[I(t)] = \int_0^t j(t-\tau) G^{(1)}(\tau) d\tau \tag{16}$$

and

$$\begin{aligned} M\left[I(t)I(t+\tau)\right] = &\int_0^t d\tau_2 \int_0^{\tau_2} d\tau_1 j(t-\tau_2) j(t+\tau-\tau_1) G^{(2)}(\tau_1, \tau_2) \\ &+ \int_0^{t+\tau} d\tau_2 \int_0^{\tau_2} d\tau_1 j(t-\tau_1) j(t+\tau-\tau_2) G^{(2)}(\tau_1, \tau_2) \\ &+ \int_0^t d\tau_1 j(t-\tau_1) j(t+\tau-\tau_1) G^{(1)}(\tau_1). \end{aligned} \tag{17}$$

These quantities will be become independent of t as $t \to \infty$ (asymptotically stationary) if, as is often the case, the underlying quantum system evolves to a steady state $\dot{\varrho}(t) \to 0$ as $t \to \infty$, after initially ($t = 0$) being prepared in some arbitrary state $\varrho(0)$.

In this last circumstance there is a further option open to calculate the mean values, one that would be more convenient in practice, and that is to run one simulation for a long period of time and to take time averages of this single record, thus yielding

$$\overline{I(t)} = \lim_{T\to\infty} \frac{1}{T} \int_0^T i(t)dt \tag{18}$$

and

$$\overline{I(t)I(t+\tau)} = \lim_{T\to\infty} \frac{1}{T} \int_0^T i(t)i(t+\tau)dt. \tag{19}$$

In general, the expectation is that these two approaches will yield the same result, i.e. that the process is ergodic. It is the aim of the discussion to be presented below to determine the circumstances under which this ergodicity is indeed a property of the detector record. The general conclusion reached is that if the steady state of the system is independent of its initial state, then the detection record is ergodic.

4 Mean Square Tests for Ergodicity

Suppose the detector current $I(t)$ is an asymptotically stationary stochastic process, and let $i(t)$ be one realization of this process. The process will be ergodic to second order if the time and ensemble averaged mean values are equal:

$$\overline{I(t)} = \lim_{t\to\infty} M[I(t)] \tag{20}$$

and if the time and ensemble averaged correlation functions are equal

$$\overline{I(t)I(t+\tau)} = \lim_{t\to\infty} M[I(t)I(t+\tau)]. \tag{21}$$

In order to test whether or not the first condition, (20) is satisfied, it is recognized that the quantity

$$\lim_{T\to\infty} \frac{1}{T} \int_0^T i(t)dt \tag{22}$$

is itself a randomly fluctuating function of the parameter T. Nevertheless, what is required is that in some sense the time average must converge to the ensemble

mean in the limit of $T \to \infty$. There are, however, a number of ways of defining this limiting process. One definition that would be appropriate here, known as almost certain convergence [9], is to require that the time average of each individual realization (except for a set of probability zero) equals the ensemble average in the limit of $T \to \infty$. However use will be made here of a mathematically more tractable condition, which is to demand that the time averaged mean approach the ensemble mean in the sense of a mean square limit or limit in the mean [9], that is to say, the mean square deviation of the time average from the ensemble mean approaches zero as $T \to \infty$:

$$\Delta^{(1)} = \lim_{T\to\infty} M\left[\left(\frac{1}{T}\int_0^T I(t)dt - M[I(\infty)]\right)^2\right] = 0 \tag{23}$$

usually written

$$\underset{T\to\infty}{\text{ms}-\lim}\,\frac{1}{T}\int_0^T i(t)dt = \lim_{t\to\infty} M[I(t)]. \tag{24}$$

Unlike almost certain convergence, this is not a statement about individual detection records, but it still a physically reasonable way of defining what is meant by the limiting process.

An equivalent statement of the condition (23) is

$$\lim_{T\to\infty} M\left[\left(\frac{1}{T}\int_0^T I(t)dt\right)^2\right] - \left(M[I(\infty)]\right)^2 = 0. \tag{25}$$

Similarly, for (21) to be satisfied the requirement will be that

$$\begin{aligned}\Delta^{(2)} &= \lim_{T\to\infty} M\left[\left(\frac{1}{T}\int_0^T I(t)I(t+\tau)dt\right)^2\right] - \lim_{t\to\infty}\left(M[I(t)I(t+\tau)]\right)^2 \\ &= 0.\end{aligned} \tag{26}$$

in which case

$$\underset{T\to\infty}{\text{ms}-\lim}\int_0^T i(t)i(t+\tau)dt = \lim_{t\to\infty} M[I(t)I(t+\tau)].$$

In the following Section, the consequences of the above requirement for the ergodicity of the mean current will be presented.

5 Ergodic Property of Mean Current

The task here is to determine the conditions under which $\Delta^{(1)}$ defined in (23) vanishes. The first step is to calculate the mean value

$$\lim_{T\to\infty} M\left[\left(\frac{1}{T}\int_0^T I(t)dt\right)^2\right] = \lim_{T\to\infty}\frac{2}{T^2}\int_0^T dt_2\int_0^{t_2} dt_1 M\left[I(t_2)I(t_1)\right] \tag{27}$$

appearing in (25), with realizations of $I(t)$ being given by (13).

From (17), the correlation function $M[I(t_2)I(t_1)]$ is given by

$$\begin{aligned} M[I(t_2)I(t_1)] = &\int_0^{t_1} d\tau_1\int_{\tau_1}^{t_2} d\tau_2 j(t_1-\tau_1)j(t_2-\tau_2)G^{(2)}(\tau_1,\tau_2)\\ &+\int_0^{t_1} d\tau_2\int_0^{\tau_2} d\tau_1 j(t_1-\tau_2)j(t_2-\tau_1)G^{(2)}(\tau_1,\tau_2)\\ &+\int_0^{t_1} d\tau j(t_1-\tau)j(t_2-\tau)G^{(1)}(\tau). \end{aligned} \tag{28}$$

Substituting this expression into (27), making a number of simple changes of variable, including $t_i = Tx_i$ and $\tau_i = Ty_i$, yields

$$\begin{aligned} &\frac{1}{T^2}\int_0^T dt_2\int_0^{t_2} dt_1 M\left[I(t_2)I(t_1)\right]\\ &= \int_0^1 dy_1\int_{y_1}^1 dy_2\int_0^{1-y_2} dx_2\int_0^{x_2+y_2-y_1} dx_1 G^{(2)}(Ty_1,Ty_2)\left[Tj(Tx_1)\right]\left[Tj(Tx_2)\right]\\ &\quad+\int_0^1 dy_2\int_0^{y_2} dy_1\int_{y_2-y_1}^{1-y_1} dx_2\int_0^{x_2-y_2} dx_1 G^{(2)}(Ty_1,Ty_2)\left[Tj(Tx_1)\right]\left[Tj(Tx_2)\right]\\ &\quad+\int_0^1 dy\int_0^{1-y} dx_2\int_0^{x_2-y} dx_1 G^{(1)}(Ty)j(Tx_1)\left[Tj(Tx_2)\right]. \end{aligned} \tag{29}$$

In the limit of $T\to\infty$,

$$Tj(Tx)\to J\delta(x) \tag{30}$$

where J is the area under the pulse $j(t)$ and where here

$$\int_0^\infty \delta(x)dx = 1. \tag{31}$$

In this limit, only the first term in (29) survives, so that the right hand side of (27) becomes

$$\lim_{T\to\infty}\frac{2}{T^2}\int_0^T dt_2\int_0^{t_2} dt_1 M\left[I(t_2)I(t_1)\right]$$
$$=\lim_{T\to\infty} J^2\int_0^1 dy_1\int_{y_1}^1 dy_2 G^{(2)}(Ty_1,Ty_2). \tag{32}$$

From the defining expression (11), the limit of $G^{(2)}(Ty_1,Ty_2)$ as $T\to\infty$ becomes

$$\lim_{T\to\infty}\left[\mathrm{Tr}\left[\mathcal{J}e^{\mathcal{L}Ty_1}\mathcal{J}e^{\mathcal{L}Ty_2}\varrho(0)\right]=\lim_{T\to\infty}\left[\mathrm{Tr}\left[\mathcal{J}e^{\mathcal{L}Ty_1}\mathcal{J}\varrho(\infty)\right]\right. \tag{33}$$
$$=\mathrm{Tr}\left[\mathcal{J}\overline{\varrho}(\infty)\right]\mathrm{Tr}\left[\mathcal{J}\varrho(\infty)\right] \tag{34}$$

where

$$\lim_{T\to\infty}e^{\mathcal{L}Ty_2}\varrho(0)=\varrho(\infty) \tag{35}$$
$$\lim_{T\to\infty}e^{\mathcal{L}Ty_1}\mathcal{J}\varrho(\infty)=\overline{\varrho}(\infty)\mathrm{Tr}\left[\mathcal{J}\varrho(\infty)\right]. \tag{36}$$

and where the possibility has been explicitly recognized that the limit of $\exp\left(\mathcal{L}Ty_1\right)$ $\mathcal{J}\varrho(\infty)$ as $T\to\infty$ may differ from $\varrho(\infty)$, i.e. that the steady state density operator may not be unique – it may depend on the initial state.

In a similar way

$$\lim_{t\to\infty}M[I(t)]=J\mathrm{Tr}\left[\mathcal{J}\varrho(\infty)\right] \tag{37}$$

from which it follows that overall

$$\Delta^{(1)}=\lim_{T\to\infty}M\left[\left(\frac{1}{T}\int_0^T I(t)dt\right)^2\right]-\left(M[I(\infty)]\right)^2$$
$$=J^2\mathrm{Tr}\left[\mathcal{J}\varrho(\infty)\right]\left(\mathrm{Tr}\left[\mathcal{J}\overline{\varrho}(\infty)\right]-\mathrm{Tr}\left[\mathcal{J}\varrho(\infty)\right]\right). \tag{38}$$

It then follows that only if $\mathrm{Tr}\left[\mathcal{J}\overline{\varrho}(\infty)\right]=\mathrm{Tr}\left[\mathcal{J}\varrho(\infty)\right]$ will (38) vanish, which in general would occur if $\varrho(\infty)=\overline{\varrho}(\infty)$. In other words, a sufficient condition for the time and ensemble averages to produce the same result, in the sense of limit-in-the-mean, is that the steady state density operator of the system be independent of the initial state.

This last condition is generally the case in most situations encountered in quantum optics, so that ergodicity is almost always guaranteed. However, if the situation should occur in which the steady state does depend on the initial state, the possibility exists that the detection record is non-ergodic. An example of this is given in the following Section.

6 Non-Ergodicity of a Two-Photon Dissipative Process

An example of a situation in which the above non-ergodicity of quantum trajectory detector records can arise is provided by the case of a two photon absorber pumped by a two photon parametric process [11,12]. In this case, the master equation is of the form

$$\dot{\varrho} = -\frac{i}{\hbar}\left[H, \varrho\right] - \kappa\left(a^{\dagger 2}a^2\varrho + \varrho a^{\dagger 2}a^2 - 2a^2\varrho a^{\dagger 2}\right) \tag{39}$$

where

$$H = \tfrac{}{2}i\left(\lambda a^2 - \lambda^* a^{\dagger 2}\right). \tag{40}$$

Because of the two-photon nature of both the coherent and dissipative dynamics, the operator $P = (-1)^N$ where $N = a^\dagger a$ is the photon number operator, is a conserved quantity. Thus states with differing initial mean values of P will evolve into different final steady states. In particular, as shown in [12] any initial state containing an even or odd number of photons ($\langle P\rangle = +1$ or -1 respectively), $\varrho_\pm(0)$ say, will evolve into the even or odd final (pure) states $\varrho_\pm(\infty)$ given by $\varrho_\pm(\infty) = |\beta\rangle_{\pm\pm}\langle\beta|$ where

$$|\beta\rangle_\pm = \frac{|\beta\rangle \pm -|\beta\rangle}{\sqrt{2\left(1 \pm \exp(-2|\beta|^2\right)}} \tag{41}$$

and where $|\beta\rangle$ is a coherent state with $\beta = \sqrt{-\lambda/2\kappa}$. More generally, the steady state solution for an arbitrary initial state is shown to be of the form

$$\varrho(\infty) = P_+|\beta\rangle_{++}\langle\beta| + P_-|\beta\rangle_{--}\langle\beta| + a_{+-}|\beta\rangle_{+-}\langle\beta| + a_{-+}|\beta\rangle_{-+}\langle\beta| \tag{42}$$

for which $\langle P\rangle = P_+ - P_-$.

Thus the final steady state depends on the initial state of the system. Non-ergodic detection records will be produced if the detection process results in the steady state of the system undergoing a jump to a state with a different value for $\langle P\rangle$. For a "two photon detector" for which the jump operator $\mathcal{J}\varrho = \kappa a^2\varrho a^{\dagger 2}$, it is clear that (with $\varrho(\infty)$ given by (42))

$$\mathcal{J}\varrho(\infty) = \varrho(\infty)\mathrm{Tr}[\mathcal{J}\varrho(\infty)] \tag{43}$$

so that, from (36), $\overline{\varrho}(\infty) = \varrho(\infty)$, and $\Delta^{(1)}$ in (38) will vanish.

However, as pointed out in Sect. 2, the possibility exists of using other kinds of detection schemes. If a single photon detection is performed so that $\mathcal{J}\varrho = \kappa_1 a\varrho a^\dagger$ then the post jump state $\mathcal{J}\varrho(\infty)$ will have a different value for $\langle P\rangle$, so that $\overline{\varrho}(\infty) \neq$

$\rho(\infty)$. Consequently, it is possible for $\Delta^{(1)}$ in (38) not to vanish, implying a non-ergodic detection output. To see this explicitly, consider the particular case of an initial state $\varrho_+(0)$ of well-defined parity. The steady state post jump state $\overline{\varrho}$ will then be $\varrho_-(\infty)$ and (38) becomes

$$\begin{aligned}\Delta_+^{(1)} &= J^2 \mathrm{Tr}\left[\mathcal{J}\varrho(\infty)\right]\Big(\mathrm{Tr}\left[\mathcal{J}\overline{\varrho}(\infty)\right] - \mathrm{Tr}\left[\mathcal{J}\varrho(\infty)\right]\Big) \\ &= J^2\kappa_1^2 \mathrm{Tr}[a^\dagger a\varrho_+(\infty)]\Big(\mathrm{Tr}[a^\dagger a\varrho_-(\infty)] - \mathrm{Tr}[a^\dagger a\varrho_+(\infty)]\Big) \end{aligned} \tag{44}$$

The steady state mean photon numbers for even and odd steady states are given in [12]. Substituted here yields for (44)

$$\Delta_+^{(1)} = J^2\kappa_1^2 \frac{|\beta|^4}{\cosh^2|\beta|^2}. \tag{45}$$

If the initial state has odd parity, then a similar calculation yields

$$\Delta_-^{(1)} = -J^2\kappa_1^2 \frac{|\beta|^4}{\sinh^2|\beta|^2}. \tag{46}$$

Interesting features of these results can be seen in the limits of $|\beta|^2 = |\lambda/2\kappa|$ large or small. In the limit of large $|\beta|$, $\Delta_\pm^{(1)} \to 0$. In contrast, in the limit of $|\beta| \to 0$, $\Delta_+^{(1)} \to 0$, whereas $\Delta_-^{(1)} \to -J^2\kappa_1^2$. Thus if there is strong two-photon dissipation (or a weak parametric oscillator) the condition for ergodicity is satisfied for the even parity state, but not for the odd parity state. In the opposite limit of weak dissipation, ergodicity is satisfied for both odd and even states.

7 Conclusion

It appears that in almost all cases of interest, if an open Markovian system reaches a steady state, then this steady state is independent of the initial state. The above result then shows that time and ensemble averages used to calculate the statistical properties of quantum trajectory simulations will yield the same results. In those rare cases in which there is dependence on the initial state, then depending on what information is extracted by the measurement process, it is possible that the detection records are not ergodic. What remains to be investigated is the degree to which ergodicity is not satisfied in such cases, i.e. by how much the time and ensemble averages differ.

The above analysis does not consider ergodicity to all orders. Similar arguments to those presented above can be followed when looking for the conditions under which $\Delta^{(2)}$ defined in (26) vanishes. The same condition i.e. that the final steady state be independent of the initial state, is obtained. But full ergodicity requires equality of time and ensemble averages of correlation functions of arbitrary order,

so a more general analysis is required. It is also of interest to see if the results obtained here are in any way changed if the condition of almost certain convergence is imposed. Finally, the important case in which the detection records are continuous in time also needs to be considered.

References

1. V.P. Belavkin: Phys. Lett. A **140**, 355 (1989)
2. A. Barchielli: Phys. Rev. A **34**, 1642 (1986)
3. J. Dalibard, Y. Castin, K. Mølmer: Phys. Rev. Lett. **68**, 580 (1992)
4. C.W. Gardiner, A.S. Parkins, P. Zoller: Phys. Rev. A **46**, 4363 (1992)
5. H.J. Carmichael: *An Open Systems Approach to Quantum Optics*, Lecture Notes in Physics, Vol. m18 (Springer, Berlin 1993)
6. J.D. Cresser, S.M. Pickles: Quantum Semiclass. Opt. **8**, 73 (1996)
7. G. Lindblad: Comm. Maths. Phys. **48**, 119 (1973)
8. N.G. Van Kampen: *Stochastic Processes in Physics and Chemistry* (North-Holland, Amsterdam 1981)
9. C.W. Gardiner: *Handbook of Statistical Methods for Physics, Chemistry and the Natural Sciences* (Springer, Berlin 1983)
10. H.J. Carmichael, S. Singh, R. Vyas, P.R. Rice: Phys. Rev. A **39**, 1200 (1989)
11. L. Gilles, P.L. Knight: Phys. Rev. A **48**, 1582 (1993)
12. L. Gilles, B.M. Garraway, P.L. Knight: Phys. Rev. A **49**, 2785 (1994)